Edited by
Alexander V. Kolobov

WILEY-VCH

Photo-Induced Metastability in Amorphous Semiconductors

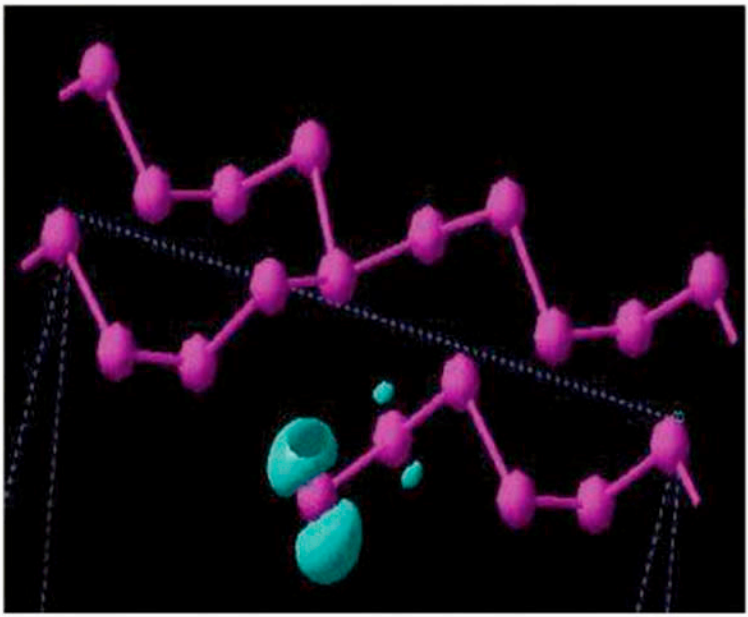

Alexander V. Kolobov

Photo-Induced Metastability in Amorphous Semiconductors

With a Foreword of Kazunobu Tanaka

WILEY-VCH GmbH & Co. KGaA

Alexander V. Kolobov

Photo-Induced Metastability in Amorphous Semiconductors

Alexander V. Kolobov

Photo-Induced Metastability in Amorphous Semiconductors

With a Foreword of Kazunobu Tanaka

WILEY-VCH GmbH & Co. KGaA

Editor
Prof. Dr. Alexander V. Kolobov
Laboratory for Advanced Optical Technology
National Institute of Advanced Industrial Science and Technology (AIST), Tsukuba, Japan
a.kolobov@aist.go.jp

Cover Picture
A valence alternation pair in Se, extracted from a local spin density calculation (from Chapter by Drabold/Zhang/Li).

Library of Congress Card No.: applied for
British Library Cataloging-in-Publication Data:
A catalogue record for this book is available from the British Library

Bibliographic information published by Die Deutsche Bibliothek
Die Deutsche Bibliothek lists this publication in the Deutsche Nationalbibliografie; detailed bibliographic data is available in the Internet at <http://dnb.ddb.de>.

Printed in the Federal Republic of Germany
Printed on acid-free paper

Printing Strauss Offsetdruck GmbH, Mörlenbach

Bookbinding Litges & Dopf Buchbinderei GmbH, Heppenheim

ISBN 3-527-40370-1

This book is dedicated to the fond memory of Professor Boris T. Kolomiets, father of amorphous semiconductors.

Preface

As far as I know, the systematic study on chalcogenide glasses as semiconductors was initiated around the 1950s by a research group headed by B.T. Kolomiets of the Ioffe Physico-Technical Institute. During the half-century that followed, amorphous semiconductors have acquired their own citizenship as an unchallenged, independent area of science. Their applications are being expanded in industry to include many diverse areas, such as solar cells, thin-film transistors, optical data storage, and so on.

The amorphous semiconductors belong to the class of disordered solids which exist in a thermodynamically non-equilibrium state, and their structures are readily affected, in principle, by external disturbances, such as light, heat and pressure, resulting in quasi-stable states. In particular, it has been found recently that photo-induced metastable structural changes are inherent to most amorphous semiconductors, although the observed phenomena are quite diverse.

I, myself, encountered photostructural changes in the beginning of the 1970s and was fully caught by their charms and immersed in the study of these effects for almost a decade. Subsequently, photo-induced metastability attracted a number of scientists, and has grown to become one of the central themes in amorphous semiconductors. In the latest decade, laser technology has achieved remarkable progress, bringing pico- and femto-second technologies into laboratories, and research in this area is entering a new phase both scientifically and technologically. The frontier is expanding to include most of amorphous materials such as chalcogenides, tetrahedrally bonded semiconductors, oxides and so on.

Enough knowledge has accrued in the field to warrant summing up the diverse achievements into a single book. It is a wonderful sight to see that respectable pioneers and up-and-coming young researchers are contributing to this volume. And happiest of all, Dr. Alex Kolobov, who planned and took charge of the overall construction and editing, came from the Kolomiets Group and has been my colleague and intimate friend for 20 years.

Kazunobu Tanaka

March, 2003, Tsukuba

Introduction

The idea of this book has first occurred to the editor during an occasional visit to an electronic shop. Numerous laptop computers, flat-panel TVs and portable DVD players were attracting attention. Having taken one in my hands I suddenly realized that I was literally touching two of the major applications of amorphous semiconductors and, yet more, none of the above mentioned devices would exist if not for amorphous semiconductors. Indeed, flat-panel monitors strongly depend on thin-film transistors (TFTs) which utilize hydrogenated amorphous silicon, and re-writable CDs and DVDs are based on a phase transition in Te-based chalcogenides. No doubt, Si technology and optoelectronic devices based on III-V semiconductors play a far more important role in modern technology but the progress made by amorphous semiconductors is, nevertheless, fascinating.

Strange as it may seem now, just 50 years ago nobody would even have dreamt of *amorphous semiconductors*. The idea of allowed energy bands in classic semiconductors was developed based on long-range order in solids. It was in the 1950s that Professors Nina A. Goryunova and Boris T. Kolomiets at the A.F. Ioffe Physico-Technical Institute in Leningrad started their experiments on ternary semiconductors. Great was their surprise when they found that one of their compositions, exhibiting the typical semiconductor behavior of conductivity, was amorphous. It was this discovery that opened up the novel field of amorphous semiconductors, a field that is now actively being developing and has already given us numerous applications.

Amorphous semiconductors, possessing typical semiconductor properties, also exhibit a number of features unique to the amorphous phase. Intrinsically metastable, they can be easily transformed from one metastable state to another by means of external stimuli, visible light being a characteristic example. This structural transformation can be either beneficial or undesirable. An example of the former are photo-induced changes in amorphous chalcogenides, alternatively called chalcogenide glasses, or chalcogenide vitreous (glassy) semiconductors, which have found applications in high-density optical memories, Xerox machines, photolithography etc. On the other hand, photo-induced degradation of amorphous silicon solar cells is one of the major reasons why these devices are still not on the wide market.

This book compiles, under a single cover, chapters on different optoelectronic phenomena in amorphous semiconductors, primarily phenomena related to photo-induced metastability. Some of the chapters are written by scientists whose contributions in the field started essentially from the day of the discovery of amorphous semiconductors, some chapters are authored by physicists and chemists who joined the field later – all are written by leading experts.

Whilst each chapter itself is a valuable source of information, what is also important is that they all appear under a single cover. The reader is given a chance to get acquainted, first hand,

with the latest achievements in the field seen from different points of view. These points of view, often complimentary but sometimes quite different and even opposing each other, help to create a more complete picture of the phenomena in question. It is hoped that comparison of different opinions will provoke critical thinking which should, eventually, lead to a better understanding of the variety of the described phenomena.

The book starts with a chapter on structure, defects and electronic properties of amorphous semiconductors. This is followed by several experimental chapters on scalar and vectorial phenomena in various classes of amorphous semiconductors: chalcogenide glasses, liquid chalcogenides and hydrogenated amorphous silicon.

While in the previous decade the greatest progress has been achieved in experimental investigations of amorphous semiconductors, recent years have also witnessed significant theoretical progress and this is described in several subsequent chapters.

The physics of photo-induced metastability in amorphous semiconductors has remained a challenge and has attracted numerous investigators but it is their applications which are the driving force for further research. On the application side we should start with the major application of hydrogenated amorphous silicon in flat-panel displays and in solar cells already mentioned above. For amorphous chalcogenides, a major application is in phase-change recording media commercially utilized in re-writable CDs and DVDs. These and other applications are the subject of the remaining part of the book.

I am very much grateful to all the authors for the time and efforts they invested to write their chapters. I would like to express my deep gratitude to Professors Victor M. Lyubin and Kazunobu Tanaka for years of collaboration and their continuous encouragement. I would also like to thank my friends Elena Solovyova for useful hints on Word-to-LaTeX conversion and Paul Fons for keeping me updated on the latest versions of editing and drawing software and for patience answering my numerous questions. Last but not least, I am grateful to my family and my immediate colleagues for the support I got from them. Finally, I would like to express my thanks to Uwe Krieg for the excellent job he did typesetting the manuscript.

The editor and the authors sincerely hope that this book will be a useful source of information for scientists and engineers working in the fields of optoelectronics, semiconductor technology and materials science, as well as for graduate and post-graduate students specializing in these fields.

Alexander V. Kolobov

Tsukuba, 2003

Contents

List of Contributors

- *Thierry Cardinal*

  Institut de Chimie de la Matiére Condensée de Bordeaux (ICMCB),
  University of Bordeaux,
  87 Av. du Dr. A. Schweitzer,
  33608 Pessac, France

- *Elena A. Chechetkina*

  Institute of General and Inorganic Chemistry,
  Leninsky Pr. 31,
  Moscow 119991, Russia
  e-mail: eche@hotbox.ru

- *Sergei A. Dembovsky*

  Institute of General and Inorganic Chemistry,
  Leninsky Pr. 31,
  Moscow 119991, Russia

- *David A. Drabold*

  Department of Physics and Astronomy,
  Ohio University,
  Athens, OH 45701, USA
  e-mail: drabold@helios.phy.ohiou.edu

- *Stephen R. Elliott*

  Department of Chemistry,
  University of Cambridge,
  Lensfield Road,
  Cambridge CB2 1EW, UK
  e-mail: sre1@cam.ac.uk

- *Peter J.S. Ewen*

  Department of Electronics and Electrical Engineering,
  University of Edinburgh,
  Mayfield Road,
  Edinburgh EH9 3JL, UK
  e-mail: Peter.Ewen@ee.ed.ac.uk

- *Miloslav Frumar*

  University of Pardubice,
  Department of General and Inorganic Chemistry and Research Centre,
  53210 Pardubice, Czech Republic
  e-mail: Miloslav.Frumar@upce.cz

- *Božena Frumarová*

  Joint Laboratory of Solid State Chemistry of Academy of Sciences of Czech Republic and University of Pardubice,
  Studentská 95,
  53210 Pardubice, Czech Republic

- *Juan Maria Gonzáles-Leal*

  Department of Chemistry,
  University of Cambridge,
  Lensfield Road,
  Cambridge CB2 1EW, UK
  e-mail: jmg62@cam.ac.uk

- *Janos Hajto*

  School of Engineering,
  Napier University,
  Colinton Road,
  Edinburgh EH10 5DT, UK
  e-mail: J.Hajto@napier.ac.uk

- *Kazuyuki Hirao*

  Faculty of Engineering,
  Kyoto University,
  Sakyu-ku,
  Kyoto 606-8501, Japan
  e-mail:
  hirao@bisco1.kuic.kyoto-u.ac.jp

- *István Jánossy*

  Central Research Institute of Physics
  P.O.Box 49, H-1525 Budapest,
  Hungary

- *Takeshi Kawaguchi*

  Instrument and Analysis Center,
  Nagoya Institute of Technology,
  Showa-ku,
  Nagoya 466-8555, Japan
  e-mail: kawa@elcom.nitech.ac.jp

- *Matvei L. Klebanov*

  Department of Physics,
  Ben-Gurion University of the Negev,
  Beer-Sheva 84105, Israel

- *Michael I. Klinger*

  Department of Physics,
  Bar-Ilan University,
  Ramat-Gan 52900, Israel
  e-mail: klingem@mail.biu.ac.il

- *Alexander V. Kolobov*

  Center for Applied Near-Field Optics Research,
  National Institute of Advanced Industrial Science and Technology,
  Tsukuba Central Research Site 4,
  1-1- 1 Higashi,
  Tsukuba,
  Ibaraki 305-8562, Japan
  e-mail: a.kolobov@aist.go.jp

- *Michio Kondo*

  Thin Film Silicon Solar Cell Laboratory,
  National Institute for Advanced Industrial Science and Technology,
  Tsukuba Central Research Site 2,
  1-1-1 Umezono,
  Tsukuba,
  Ibaraki 305-8568, Japan
  e-mail: michio.kondo@aist.go.jp

- *Pavel Krecmer*

  Department of Chemistry,
  University of Cambridge,
  Lensfield Road,
  Cambridge CB2 1EW, UK

  and

  Polight Technologies,
  Unit 291 Cambridge Science Park,
  Milton Road,
  Cambridge CB4 0WF, UK

- *Jun Li*

  Department of Physics and Astronomy,
  Ohio University,
  Athens, OH 45701, USA

- *Victor M. Lyubin*

  Department of Physics,
  Ben-Gurion University of the Negev,
  Beer-Sheva 84105, Israel
  e-mail: vlyubin@bgumail.bgu.ac.il

- *Kiyotaka Miura*

  Optical Device Development Department,
  Central Glass Corporation,
  5253 Okiube,
  Ube-city, Yamaguchi 755-0001, Japan

- *Eugenia Mytilineou*

  Physics Department,
  University of Patras,
  26500 Patras, Greece
  e-mail: mytilin@physics.upatras.gr

- *Petr Nemec*

  University of Pardubice,
  Department of General and Inorganic Chemistry and Research Centre,
  53210 Pardubice, Czech Republic

- *Shuichi Nonomura*

  Environmental & Renewable Energy Systems,
  Graduate School of Engineering,
  Gifu University,
  Yanagido, 501-1193, Gifu, Japan
  e-mail: nonomura@cc.gifu-u.ac.jp

- *Takeo Ohta*

  Energy Conversion Devices Inc.,
  2956 Waterview Drive,
  Rochester Hills,
  MI 48309, USA
  e-mail: ohta@ovonic.com

- *Stanford R. Ovshinsky*

  Energy Conversion Devices Inc.,
  2956 Waterview Drive,
  Rochester Hills,
  MI 48309, USA

- *Mihai Popescu*

  National Institute of Materials Physics,
  Bucharest-Magurele,
  Romania
  e-mail: mpopescu@alpha1.infim.ro

- *Jiri Prokop*

  Department of Chemistry,
  University of Cambridge,
  Lensfield Road,
  Cambridge CB2 1EW, UK

  and

  Polight Technologies,
  Unit 291 Cambridge Science Park,
  Milton Road,
  Cambridge CB4 0WF, UK

- *Kathleen Richardson*

  Schott Glass Technologies,
  400 York Avenue,
  Duryea, PA 18643, USA
  (on leave from the School of Optics,
  University of Central Florida)
  e-mail: kathleen.richardson@us.schott.com

- *Martin Richardson*

  School of Optics,
  Center for Research and Education in Optics and Lasers (CREOL),
  University of Central Florida,
  Orlando, FL 32816,
  USA

- *Yoshifumi Sakaguchi*

  Department of Materials Science and Engineering,
  Graduate School of Engineering,
  Kyoto University,
  Kyoto 606-8501, Japan

- *Sudipta Seal*

  Advanced Material Processing and Analysis Center,
  Department of Mechanical,
  Materials and Aerospace Engineering,
  University of Central Florida,
  Orlando, FL 32816, USA

- *Koichi Shimakawa*

  Department of Electrical and Electronic Engineering,
  Gifu University,
  Gifu 501-1193, Japan
  e-mail: koichi@cc.gifu-u.ac.jp

- *Alfons Schulte*

  School of Optics,
  Center for Research and Education in Optics and Lasers (CREOL),
  Department of Physics,
  University of Central Florida,
  Orlando, FL 32816, USA

- *Paul Stradins*

  National Renewable Energy Laboratory,
  Golden, CO 80401,
  USA
  e-mail: Pauls_Stradins@nrel.gov

- *Marek Stuchlik*

  Department of Chemistry,
  University of Cambridge,
  Lensfield Road,
  Cambridge CB2 1EW, UK
  e-mail: ms344@cam.ac.uk

- *Kozaburo Tamura*

  Department of Materials Science and Engineering,
  Graduate School of Engineering,
  Kyoto University,
  Kyoto 606-8501,
  Japan
  e-mail: tamura@mtl.kyoto-u.ac.jp

- *Keiji Tanaka*

  Department of Applied Physics,
  Faculty of Engineering,
  Hokkaido University,
  Sapporo 060-8628,
  Japan
  e-mail: keiji@eng.hokudai.ac.jp

- *Junji Tominaga*

  Center for Applied Near-Field Optics Research,
  National Institute of Advanced Industrial Science and Technology,
  Tsukuba Central Research Site 4,
  1-1-1 Higashi,
  Tsukuba,
  Ibaraki 305-8562, Japan
  e-mail: j-tominaga@aist.go.jp

- *Tomáš Wágner*

  University of Pardubice,
  Department of General and Inorganic Chemistry and Research Centre,
  Pardubice 53210, Czech Republic
  e-mail: tomas.wagner@upce.cz

- *Spyros N. Yannopoulos*

  Foundation for Research and Technology Hellas,
  Institute of Chemical Engineering and High Temperature Chemical Processes,
  (FORTH-ICE/HT), P.O. Box 1414,
  26500 Patras, Greece
  e-mail: sny@terpsi.iceht.forth.gr

- *Xiaodong Zhang*

  Department of Physics and Astronomy,
  Ohio University,
  Athens, OH 45701, USA

1 Structure, Defects and Electronic Properties of Amorphous Semiconductors

Mihai Popescu

1.1 Structural States of Solids

Solids represent a particular state of condensed matter characterized by strong interactions between the constituent particles (atoms, molecules) so that every particle is maintained localized in a narrow space of the assembly of condensed particles.

The solids can be found or prepared in two fundamentally different states:

– the ordered (crystalline or quasi-crystalline) state

– the disordered (non-crystalline) state

While the ordered state of a solid, if it is not unique, is, nevertheless, limited to only a few structural forms, the disordered (non-crystalline) state is quite different. A given disordered material is neither unique, nor clearly defined.

1.1.1 Ordered State

Crystalline State

The ideal crystalline state of a solid corresponds to a regular arrangement of atoms (molecules) on the sites (positions, nodes) of a lattice with well defined symmetry, where a structural unit can be defined, the elementary cell, which, by translation along the three coordinate axes, reproduces the whole assembly of atoms (molecules). In the ideal crystal, knowledge of the coordinates of the atoms (molecules) in the elementary cell gives a possibility to know exactly the spatial positions of *all* atoms of the condensed body.

As opposed to the ideal crystal, the real crystal does not exhibit a perfect periodicity in the positions of the atoms (molecules). It is said that the real crystal shows various kinds of imperfections or defects which will be briefly discussed later.

Quasi-Crystalline State

The quasi-crystalline state of a solid body is that corresponding to a perfect arrangement of the atoms on the sites of a lattice possessing five-fold symmetry axes without elementary cell and, therefore, without translational periodicity.

The quasi-crystals were discovered in 1984 by Schechtman et al. [1] on the basis of a detailed analysis of the electronic diffraction pattern observed on a sample of manganese–aluminum alloy. These authors observed the Bragg spots disposed in configurations with five-fold symmetry. The structure could not be described as that of an incommensurate modulated crystal. The very narrow diffraction spots prove that a long distance order in the lattice exists. These observations were later confirmed by X-ray diffraction, and crystallographers have shown that in quasi-crystals the positional correlation of the atoms extends up to several tens of nanometers. The quasi-crystals pose a fundamental challenge to our understanding of nature because they are well ordered on an atomic scale without being periodic.

1.1.2 Disordered (Non-Crystalline) State

Solids which lack the spatial periodicity of the atoms are called non-crystalline solids, or in particular, amorphous, vitreous or glassy solids. Glasses are characterized by similar structure in the solid state and in the liquid state just above the softening temperature. It can be said that a glass is a liquid having the atoms frozen in the spatial positions occupied at the moment of the transition from the liquid to solid state (this means frozen at the softening or transition temperature, T_g).

As opposed to glasses, *amorphous* solids usually refers to materials that are difficult to prepare in the bulk form but can be obtained by vapor deposition as thin films.

1.2 Atomic Scale Ordering in Crystalline and Non-Crystalline Solids

1.2.1 Long-Range Order

In an ideal crystal, if three fundamental vectors are defined, then a position of each and every atom is well defined at any distance from an initial atom taken as origin. It is said that the crystal possesses *long-range order* (LRO).

The LRO can be rigorously defined with the help of the atomic density function, ρ(r), i.e. the density of atoms at a position r calculated from an arbitrary atom of origin. In a crystal the correlation function $< \rho(r) \cdot \rho(r+R) >$ fluctuates around the value ρ_0^2, for increasing R, while in the non-crystalline solid it tends to the limit value of ρ_0^2 for very large R.

1.2.2 Short-Range Order

If the LRO is lost then what remains is not a complete disorder but a special type of ordering that was called short-range order (SRO). In fact, between a solid in the crystalline and a solid in the amorphous state there is strong resemblance, particularly within the first coordination sphere around each atom. For example, the number and the spatial position of the neighbors are maintained because the same chemical forces act in both types of structures. Without doubt, the second coordination sphere is influenced by the position of the first sphere, due to small angular and bond length deviations, that permit the accommodation of the atoms with a larger freedom. The third coordination sphere starts to “forget” the first one because the

spatial constraints are attenuated by large fluctuations of the atomic positions around the ideal positions in the crystal in the second coordination sphere.

One can say that, step by step, the constraints dictated by the directional covalent bonding are lost (along the first 3-4 interatomic distances). This can be regarded as the limit of the short-range order. The energetic price to be paid for the loss of the LRO is an appearance of fluctuations in angles and distances between the bonds, proper to the SRO. Therefore, the SRO in a non-crystalline solid is not perfectly identical with that of the homologous crystal.

The ordered, crystalline state is the state that corresponds to the most favorable positions of the atoms from the energetic point of view, i.e. the atoms occupy the positions corresponding to the ideal values of the bond distances and bond angles dictated by the valence theory. When all the covalent bonds are perfectly satisfied the free energy, F, of the crystal vanishes. Any deviation from the ideal chemical bonds implies some addition of free energy, i.e. the free energy of the non-crystalline solid is higher than that of the crystal.

While the energetic state of an ideal crystal is unique, a non-crystalline material can have quite different states. This is related to a possibility to have various types of disorder, even in the case when all the covalent bonds are fully satisfied.

The ideal non-crystalline network is difficult to define. Practically, there exist various non-crystalline arrangements of atoms that can be obtained by different thermal treatments in different regimes. Some authors consider a continuous random network of atoms as an ideal non-crystalline network. While there are obvious divergences concerning the definition of the ideal amorphous state, physicists are unanimous in defining the disordered, amorphous, vitreous, glassy or generally non-crystalline state as a structure lacking long-range order but retaining the short-range order.

The non-uniqueness or multiplicity of the non-crystalline state is the basis of the most important feature of the amorphous and glassy solids: the modification of the physical properties by external factors such as light, temperature, particle irradiation or electrical and magnetic fields.

1.2.3 Medium-Range Order

A possible multiplicity of the non-crystalline state and the specific features of the diffraction patterns in chalcogenide glasses as well as in other semiconductors and polymeric or carbonaceous materials, lead physicists to introduce the concept of medium-range order (MRO) or intermediate-range order.

The problem of the existence of an extended order in amorphous solids, that extends above the SRO limit was revealed during 1973-1975 by Grigorovici and Popescu [2] who wrote that "many low coordinated elements and compounds exhibit a more complex disorder or even a special kind of ordering at not too large a scale" [3]. A year later, Phillips [4] and later Lucovsky and Galeener [5] introduced concepts of medium-range order and intermediate-range order, respectively, with the same meaning.

The MRO is specific and well evidenced in non-crystalline chalcogenide alloys. This ordering is dictated by the propagation of the order from the first coordination spheres towards the following ones, due to the flexibility of the network with weak connectivity (two and three covalent bonds between the atoms). The MRO extends up to the fourth–eighth sphere

of coordination. The extension of MRO is a decisive factor for the control of the physical properties of the non-crystalline semiconductors.

The definition of the MRO is closely related to its measurement. The particular features in the X-ray, electron and neutron diffraction patterns of the non-crystalline semiconductors can be ascribed to MRO.

After Elliott [6] the following three types of MRO can be distinguished:

(i) *small-scale medium-range order (SSMRO)*

This order is associated with four-atoms correlations and is really applicable to the case of covalently-bonded solids, where a dihedral angle, Φ, can be defined; this is the relative angle of rotation of two connected atoms around the common covalent bond. Any deviation from the random distribution of the dihedral angles in the amorphous network gives rise to non-zero SSMRO. The SSMR extends up to 0.3–0.5 nm in the semiconductor network.

(ii) *intermediate-scale medium-range order (ISMRO)*

This ordering scale consists in non-random structural correlations extending over distances larger than those characteristic of SSMRO, namely 0.5–0.8 nm. The network is characterized by "super-structural" units, that is, well defined structural arrangements whose dimensions are considerably in excess of those typical of the basic structural units (i.e. coordination polyhedra) characterizing SRO.

(iii) *large-scale medium-range order (LSMRO)*

This order implies the dimensionality of the network. The ordering extends to 0.8–1 nm. The chain-like, layer-like structures and big clusters are the main constituents of this type of order.

(iv) *extended-range order (ERO)*

An extended ordering of atoms in amorphous silicon has been demonstrated by Uhlherr and Elliott [7]. This order corresponds to weak, quasi-periodic fluctuations in atomic density. The ERO oscillations extend beyond 3.5 nm and arise from propagated short-range order. It contributes significantly to the formation of the first sharp diffraction peak in the X-ray diffraction pattern, the most obvious signature of the existence of the MRO and larger scale order in the non-crystalline materials.

1.3 Fundamental Problems of Structure of Non-Crystalline Semiconductors

1.3.1 Tetrahedrally Bonded Amorphous Semiconductors

The problem of the structure of elemental semiconductors (Si, Ge) in the amorphous state became a subject of large interest with the advent of device quality hydrogenated (fluorinated) amorphous silicon.

The continuous random network model (CRN) developed by Polk [8] and later built independently and relaxed by Steinhardt et al. [9] and Popescu [2] seemed to be a very attractive model due to the satisfactory explanation of the experimental data (X-ray diffraction pattern, atomic-electronic radial distribution function (AERDF), density, crystallization enthalpy, etc.). On the other hand, some fine details in the AERDF at large distances, poor reproduction of the low-angle part of the X-ray diffraction pattern and, last but not least, the observation of a small first sharp diffraction peak (FSDP) in amorphous silicon by Višor [10] have thrown some doubts on the absolute validity of the CRN models.

An interesting contribution to the modeling of the amorphous semiconductors germanium and silicon was the demonstration that the continuous random network does not support a large scale growth [11]. From the energetic point of view, the splitting of a homogeneous spherically symmetric network into amorphous domains called *amorphites* is a favorable process.

The general structure of the apparently homogeneous amorphous silicon films (a-Si or a-Si:H) may then be regarded as consisting of amorphous domains with very few, if any, inner dangling bonds (active or passivated by hydrogen) separated by thin distorted layers containing the major part of the dangling bonds and hydrogen.

The structure of non-crystalline tetrahedrally bonded semiconductors, as well as the structure of other materials can be regarded from the thermodynamic point of view as a direct consequence of the action of the factors governing the formation kinetics. By limiting the energy and/or time scale during the formation of a disordered solid (either from the melt or by evaporation), the system is effectively forced to search for a minimum energy state on a progressively smaller spatial scale. The thermal vibrations and diffusion processes allow for changes in bonding, and, therefore, in the topology of the atomic network. On a larger scale, the steric hindrance becomes so important that a discontinuity of the atomic network is possible. Donth [12] has estimated a correlation length for the cooperatively arranged regions of $1 - 2$ nm in certain glasses. The special topological structure of the medium-range scale order in a-Si:H seems not only to be necessary but also sufficient to explain various experimental data. The a-Si:H seems to exhibit a wider range of defect states than expected, which gives an additional flexibility to the material. A possible two-dimensional confinement of carriers between the amorphous grains could be an important factor in transport theories and in applications.

Hydrogenated amorphous silicon of improved quality for photovoltaic devices can be prepared by hydrogen dilution of the processing gas. The increase in quality, as measured, for example, by a decrease of the Staebler-Wronski degradation, is accompanied by an increase in the concentration of chain-like objects, recently observed [13] by transmission electron microscopy. These are quasi-one-dimensional configurations, $2 - 3$ nm in width and ~ 30 nm or more in length. They show a high degree of order along their length, implying very low bond-angle distortions. These features can be explained on the basis of self-organization in CRN networks of amorphous silicon by splitting the rather uniform structure in homogeneous and less constrained domains linked through low distortion boundaries. It seems that hydrogen (H) or fluorine (F) are playing in amorphous silicon the role of glass modifiers as Na or Ca atoms in a-SiO_2 when silicate glasses are formed, i.e. conferring to the structurally deficient, but interconnected network a polymeric character.

As opposed to microcrystalline and nanocrystalline silicon, which are composed from crystalline domains surrounded by amorphous boundary layers, device quality amorphous

silicon can be viewed as composed from amorphous nano-domains surrounded by crystalline boundaries [14]. The crystalline arrangement can be a mixture of diamond-like and wurtzite-like configurations due to constraints at boundaries, which allow for a cis (eclipsed) orientation of the bonds. High quality amorphous silicon is in fact a new-type of self-organized structure characterized by meander-like crystalline configurations that define the rather homogeneous amorphous domains. We shall refer to this type of silicon as nano-amorphous silicon because it is a reverse structure of nano-crystalline silicon, a well-known material.

The importance of d-orbital bonding both in amorphous tetrahedrally bonded semiconductors and in chalcogenide glasses is remarkable. In amorphous silicon (germanium) models the contribution of d-orbital bonds has an essential effect in relieving the stresses in the region between the amorphous domains. Thus, the boundaries become thin low-dimensional unstressed and undistorted regions protruding deeper into the material, as observed by transmission electron microscopy. Grigorovici et al. [15] have shown earlier that the distortion of the local tetrahedral symmetry of atomic bonds in a semiconductor like silicon always leads to such a change in the bond character as to eliminate elastic stresses. This can be achieved for metastable silicon phases by adding a small d contribution to the usual sp^3 orbitals. On the basis of a tight binding calculation of the valence band density of states they have demonstrated that the atomic spd orbitals ensuing from this approach yield the correct valence band density of states in the CRN models with 155 and 2052 atoms.

The stability of the nanostructured amorphous material depends on the way of impeding grain boundary motion. The driving force for such motion is simply the reduction of the total area of the grain boundary. This is because the boundaries exhibit a larger free energy, as shown in the CRN models. If the specific energy of the boundary can be made zero or negative, then the driving force for the grain growth vanishes. The domain structure is stable. Weissmüller [16] advanced this idea in a quantitative form. The basic mechanism was suggested to consist in the segregation of a minor constituent solute. If the hydrogen is the minor constituent solute in amorphous silicon, when the CRN grain grows, less segregated hydrogen is needed because the area of the boundary per unit volume decreases and, thus, the excess hydrogen returns in the grain. The return of hydrogen into the amorphite enhances the free energy of the amorphite, so that the total free energy change is positive. If this occurs, then the driving force for the amorphite growth vanishes. We are dealing with a grain structure stabilized by segregation. If the hydrogen dilution rate in silane increases, a motion of the boundary takes place in the inner part of the amorphite at the temperature of $300\ ^\circ$C through hydrogen diffusion. Consequently, the inter-domain region becomes labile and suffers an ordering process, by forming CLO configurations, i.e. two-dimensional crystalline zones. These crystalline-like configurations stabilize the structure with small-size amorphous domains, well ordered as an ideal amorphous phase.

Molecular hydrogen seems to be the most important constituent solute for the migration in the amorphites, because other fragments obtained during silane decomposition are heavier and their diffusion is greatly impeded. As concerns the diffusion process we must observe that high electronegative hydrogen or/and fluorine are able to break up the rather perfect covalent network of silicon. Halogens can be regarded as network modifiers.

1.3.2 Amorphous Non-Tetrahedrally Bonded Semiconductors

The nature and the extent of MRO in covalent amorphous non-tetrahedrally bonded semiconductors remains one of the outstanding problems of non-crystalline solids. The so-called "first sharp diffraction peak" (FSDP) in the X-ray diffraction pattern of such materials has often been taken as a signature of MRO, although its origin still remains controversial. Although every diffraction pattern obviously possesses a first peak, the FSDP for covalent amorphous solids, especially for non-tetrahedrally bonded ones, is unique in that it exhibits an anomalous behavior in its temperature, pressure and composition dependence compared with other peaks and as such would seem to have a qualitatively different origin. The FSDP has often been assumed to arise from a particular distance in real space in the range corresponding to MRO ($0.5 - 1$ nm) but this is extremely unlikely in view of the anomalously narrow width of the peak [17]. It is more likely that the FSDP can be regarded as a pseudo-Bragg peak associated with some type of quasi-periodicity in the real space structure of the amorphous material, with a period given by $R = 2\pi/Q_1 \approx 0.3 - 0.6$ nm (where Q_1 is the position of the FSDP), extending over a correlation range given by $D = 2\pi/\Delta Q_1$ (where ΔQ_1 is the half-width of the FSDP), with correlation lengths of $D \approx 2$ nm.

One of the possible interpretations of FSDP is the presence of distinct layer-like features in the glass. In glasses derived from layered crystals, e.g. As, As_2S_3, As_2Se_3, the sharp and high diffraction peak at or near the reciprocal layer spacing has been interpreted as evidence for the formation of disordered layers. The FSDP is influenced by preparation and thermal treatment. X-ray measurements carried out by Tanaka [18] and Busse [19] have shown that the intensity of FSDP in well-annealed samples of As_2S_3 increases reversibly with temperature in contrast to the behavior of other peaks situated at higher diffraction angles. This anomalous behavior has been interpreted in terms of increased ordering of the layers in the glass, made possible by the reduction in viscosity. Calculation of a quasi-crystalline model does, in fact, show the formation of a peak at the right position but of small height, impossible to correct by realistic modifications of the structural parameters.

It is most unlikely that the quasi-crystalline picture involving inter-layer correlations is generally valid. Some glasses (e.g. SiO_2) clearly exhibit FSDP, yet there is no evidence for the structure in either crystalline or amorphous state being layer-like or locally two-dimensional. Furthermore, the FSDP of e.g. $GeSe_2$ persists into the liquid state [20], seeming to rule out the microcrystalline explanation for its origin. Finally, X-ray scattering is independent of the film thickness [21] and this fact could be an indication that preferential layer-like correlations probably do not exist.

A new picture for MRO emerged from the modeling studies of amorphous arsenic. As early as in 1979 Greaves et al. [22] pointed out that the continuous random network model of amorphous arsenic is somewhat cavern-like. The structural relaxation and concomitant ordering of the caverns can (via a Babinet argument) produce a sharper FSDP. At the same time the comparison between the diffraction pattern of initial amorphous and annealed arsenic allows one to conclude that the local order (evidenced at high diffraction angles) is not affected by longer-range organization of the basic structural units.

We have compared [23] various models of amorphous arsenic for the FSDP profile and for the void structure. The void radius distribution has been determined as the distribution of the radii of the largest spheres, which can be introduced into the free spaces of the network. The results are shown in Fig. 1.1.

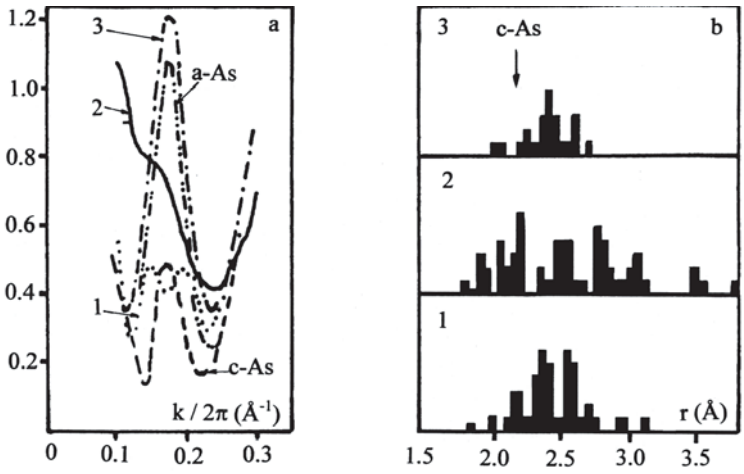

Figure 1.1: FSDP in amorphous arsenic (a-As), in crystalline arsenic (c-As) and in three models for amorphous arsenic: (1) Beeman model, (2) Greaves model, and (3) Popescu model (a) and the void distribution in the models (b).

While the CRN model of Greaves et al. [22] gives only a very faint FSDP and exhibits a very large void distribution, the model with disordered layer packing developed by Popescu [24] gives a very strong FSDP but exhibits a narrow void distribution. The Popescu model is built by stacking three disordered layers (3×146 atoms) with the distance between layers corresponding to that from the crystalline layered arsenic. It is interesting to remark that the Beeman model (private communication of the coordinates) is mainly a CRN model but, in a deeper analysis, we have found regions of very high and very low densities. This bimodal distribution of densities (and voidsizes) gives rise to a split FSDP. The above observations could be regarded as a proof that void size distribution contributes essentially to the control of FSDP. The crystalline arsenic is, nevertheless, intriguing by its small FSDP, because there is only one definite void radius and the distribution of voids is regular. In order to explain this feature we start from the observation that the radius of the crystal void is significantly smaller than the mean void radius in the models. When the layer spacing in the Popescu model [24] is increased, a strong increase of FSDP is observed (Fig. 1.1b). Therefore, the FSDP intensity in arsenic crystals can be theoretically amplified by increasing the layer spacing. Our last simulations on crystalline models proved this observation.

We have found by modeling of amorphous arsenic in the frame of the Popescu model that is not necessary to have well defined structural entities in order to produce a large FSDP and that the position of the FSDP changes significantly and linearly with the change in the layer spacing (Fig. 1.2).

It is interesting to observe that MRO in non-tetrahedrally bonded amorphous and glassy solids can be very complex. The FSDP, that comprises the major information on MRO, varies in intensity, position and width as a function of various parameters: temperature, pressure, type of material and thermal treatment, etc. Even a split FSDP has been observed in a continu-

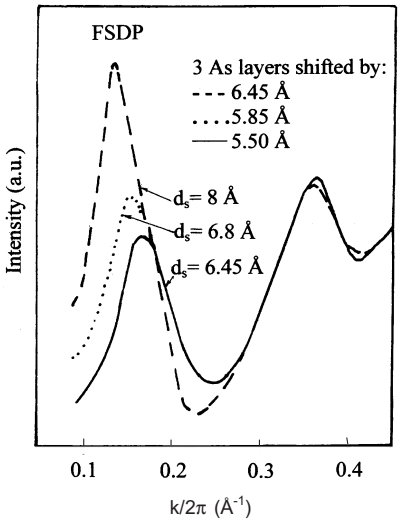

Figure 1.2: The relation between the quasi-distance extracted from FSDP position (d_{FSDP}) and the layer spacing in the model developed by Popescu [23] for amorphous arsenic, with three disordered layers.

ous random model of amorphous arsenic. The understanding of the MRO in non-tetrahedrally bonded amorphous or glassy semiconductors based on the layer-like model, the cluster model and the void ordering model.

Taking into account the fact that quasi-spherical symmetry of the as-quenched semiconducting glass can be broken with a significant gain in the distortion (free) energy (as is the case for tetrahedral CRN models) the appearance and variation of the FSDP as a quasi-Bragg peak can be easily understood. The structure becomes goffered after the glass formation. The periodicity of goffering and its perfection are the main parameters that govern the position and intensity of the FSDP. The goffering is mainly dictated by the distribution of the voids in the structure that arrange in a more or less ordered fashion during the melt quenching or heat treatment. The void arrangement is made easier when a chalcogenide glass is heated just above the melting point and the constraints due to layer configurations vanish. As a consequence, the goffering effect is maximum, the void ordering is excellent and the FSDP approaches the Bragg peak for a multilayer ordered structure. In fact we are dealing with the atomic arrangement, which gives rise to voids as a function of packing of the structural units. The spatial and energetic constraints impose the rearrangement of the system of voids and even the change in size and shape of a void from one position to another. Therefore the voids easily change, more so than the network does, and this flexibility allows the atoms to be accommodated in the limited space of the non-crystalline body.

This point of view can explain more simply the assembly of experimental data on the structure of amorphous covalent semiconductors. For example, the increase of FSDP in high temperature melts (e.g. in binary chalcogenides) is due to the strong goffering of the network, induced by the system of voids. Rearrangement of the atomic network that contains

small remnants of layers or other configurations gives rise to a larger scale modification of the void system. As a consequence of this modification and of the network expansion the quasi-distance increases and, as expected, the FSDP intensity increases. Illumination in As_2S_3 results in a decrease of the height of FSDP, broadening of this peak and its shift towards lower quasi-distances calculated from the angular position of the FSDP in the X-ray diffraction pattern [18]. This effect can be readily explained in the framework of the goffering model. The photostructural transformations of the network are more likely to occur in regions with larger voids. The collapse of larger voids is easier to trigger and, therefore the larger voids split into smaller ones. As a consequence, smaller correlation lengths appear that are accompanied by a decrease of the FSDP intensity. Because local structural modifications are propagating with more difficulty, the goffering is altered and regions with different structure of voids are randomly distributed in the network. This is a non-equilibrium situation. The material looks more disordered and FSDP width increases. Thermal annealing can restore the state before the illumination, and this fact was indeed observed experimentally.

In general, the quasi-periodic structural fluctuations in amorphous semiconductors can be understood in terms of bonding frustration inherent in maintaining the network connectivity at large distances from a given atom of origin. The density fluctuations are related to the fluctuation of short-range order in tetrahedrally bonded semiconductors and of medium-range order in chalcogenide glasses.

1.4 Defects in Non-Crystalline Solids

In crystalline solids structural defects are defined in terms of deviation from the ideal long-range order of a given lattice. Basically three types of defects can be defined:

- intrinsic pointdefects (vacancies, interstitials);
- extended defects (dislocations, stacking faults, lattice distortions, grain boundaries);
- chemical impurities (substitutional atoms or interstitial atoms or molecules).

In the case of non-crystalline solids an important problem to be discussed is whether there are defects which can be described as counterparts of the well-defined defects in crystals. Although most defects seem to have lost their meaning, the structurally sensitive changes in the properties of non-crystalline solids show, at least qualitatively, the same trend as corresponding properties of crystals [25]. In crystals the change of properties is governed by the behavior of lattice defects. For example, annealing leads to the annihilation of dislocations and point defects whilst plastic deformation increases the density of both these lattice defects. The above observations allow one to conclude that structural defects, which are akin to defects in crystals, should exist in non-crystalline materials. The deviation of the structure of a non-crystalline solid from its low energy equilibrium state could be, therefore, described in terms of increase or decrease of the density of defects. Thus, the structural relaxation is a process of annihilation of some defects and is an exothermic process, whereas the mechanical deformation leads to an increase of the defect concentration and is an endothermic process [26, 27].

Several attempts have been made to define the structural defects in non-crystalline solids on a general basis [28]. First, an ideal reference structure is defined and the defects are introduced using geometrical concepts analogous to those used for crystal defects. The strains

are measured with respect to the reference structure and they are always very high. However, this definition of defects, using the local strain seems to be valid only for covalently bonded solids [29].

The defects in covalently bonded networks of atoms can be roughly classified into two groups, namely, microdefects and macrodefects. The microdefects are:

- local or point defects (dangling bonds, quasi-vacancies, quasi-interstitials);
- diffuse or collective defects (extended defects);
- chemical defects (wrong bonds, impurities);
- electronic-structural defects (valence alternation pairs, quasi-molecular defects).

The macrodefects can be classified as columns, voids, network of pores, pinholes, and cracks.

Several types of defects are correlated. Local or point defects are usually extended on a larger scale in the network. Change of coordination of the atoms and, therefore, a local structural change accompany electronic defects. Chemical defects generally distort the network around the impurity location.

1.4.1 Local Defects

Quasi-Vacancies and Quasi-Interstitials

In covalently bonded solids, the vacancy-like defect or quasi-vacancy can occur and can be defined as a local arrangement of atoms which implies a local lower density than the average density of the material. Although the quasi-vacancies could not be observed experimentally, simulation of the amorphous networks using computer modeling allows for characterization the structure of the quasi-vacancies, their distribution and dynamic properties. In the ideal amorphous network the density distribution is uniform. In the real amorphous network the bonding fluctuations give rise to density fluctuations and these fluctuations can be interpreted as quasi-vacancies and interstitial-like defects (quasi-interstitials) distributed randomly in the network. It may be interesting to note that what is a point defect in a crystalline lattice is transformed into a narrow defected region in a non-crystalline network.

Dangling Bonds and Floating Bonds

An important defect proved to exist and to play an important role in non-crystalline semiconductors is a dangling bond. A single dangling bond defect, i.e. an unsatisfied bond can be incorporated within the network of an amorphous semiconductor without much perturbation of the surroundings; in contrast the dangling bonds help to reduce the strains accumulated during the network formation. The dominant paramagnetic center in non-crystalline films based on amorphous silicon (a-Si) and hydrogenated amorphous silicon (a-Si:H) has been identified as a dangling bond [30]. Close correlation between the photoluminescence efficiency and the spin density in a-Si:H indicates a nearly random distribution of the paramagnetic defect centers [31].

Pantelides [32] has brought arguments in favor of the existence of both three-fold and five-fold coordinated atoms as defect centers. One argument is that in amorphous silicon a vacancy, which introduces a three-fold coordinated system and a tetrahedral self-interstitial (which introduces four five-fold coordinated silicon atoms), has roughly the same formation energy. A number of examples of that nature show that five-fold coordination of silicon can be preferred over the three-fold one. Another argument is the development of techniques for routine synthesis of chemical compounds involving five-fold coordinated silicon atoms (called penta-coordinated silicon) [33].

Pantelides defined the counterpart of dangling bonds in silicon as a *floating* bond. Ideal dangling bonds and floating bonds are rarely produced. In general, an intermediate state is produced and this configuration was called a frustrated bond. Pantelides proposed that the defect center is likely to be mobile because of the ease to switch bonds. The enhanced hydrogen diffusion caused by doping [34] and by illumination [35] is explained in unified and simple manner in terms of excess defect centers which are mobile and "kick out" the hydrogen atoms from Si–H bonds [36].

1.4.2 The Diffuse or Collective Defects (Extended Defects)

The extended defects in amorphous semiconductors are controversial. Disjunction, dislocations or disclination lines with variable Burgers vectors are discussed in the literature. The disclinations are defined in elastic bodies as line defects similar to dislocations but differing in that rotations rather than translations constitute the operations involved. Gilman [37] used this concept in order to explain the flow properties of glassy materials.

In the example shown in Fig. 1.3, crystalline and vitreous silica (SiO_2) are compared. In the crystalline case, there is a constant Burgers vector along the dislocation line and the structure left behind as the dislocation moves is the perfectly restored crystal. In the non-crystalline material, the local translations that are needed to restore the bonding vary along the line length, so that the Burgers vector fluctuates in magnitude and direction.

Rivier [38] has shown that odd-member rings in CRN [39] constitute line defects and that the disclination line can be described as threading its way through the glass by connecting the centers of the odd-member rings. The disclination lines tend to approach the dislocation characteristics. The disclinations can be regarded as defective dislocations.

Recently, the existence of boundaries between rather ideal non-crystalline regions has been suggested. The ideal amorphous domain, the amorphite, is naturally introduced, because it was demonstrated by simulation experiments that the total distortion energy diminishes when the homogeneous random network splits into domains with nanometric size (Fig. 1.4) [40]. The interconnected amorphites exhibit distorted bonds at the boundary but not necessarily not satisfied or dangling bonds. The boundaries between amorphites seem to be responsible for the specific properties of a-Si:H, especially for the reduced gap states characteristic of this material.

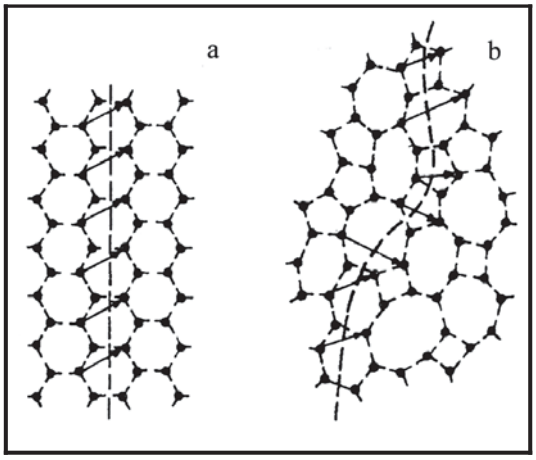

Figure 1.3: Dislocation line in crystalline SiO_2 (a) and disclination line in vitreous silica (b). The arrows indicate the Burgers vectors.

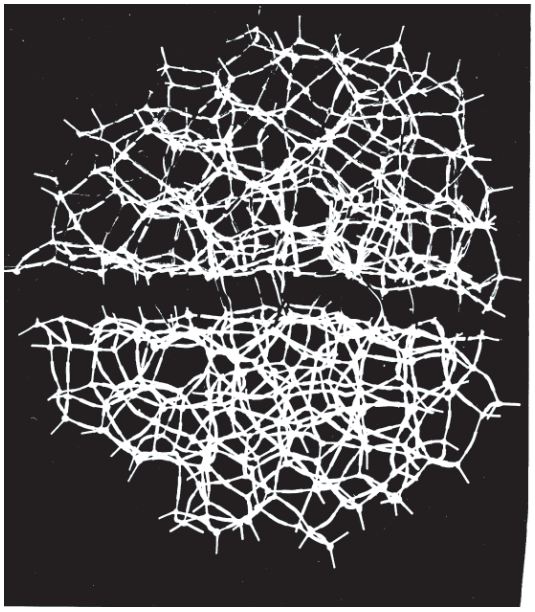

Figure 1.4: The structural model of non-crystalline silicon with two amorphous domains (amorphites).

1.4.3 Chemical Defects

Wrong Bonds

A wrong bond is the most representative chemical defect in amorphous semiconductors. In the case of non-crystalline networks of binary or polynary alloys the deviation of the structure

from the chemically ordered network is mainly dictated by the wrong position of some atoms on the network sites. Thus, in binary covalently bonded alloy (e.g. GaAs) the configuration of minimum free energy corresponds to a network of bonds where every arsenic atom is bonded to gallium atoms and every gallium atom is bonded to arsenic atoms. The Ga–As bond is the most favorable bond from the energetic point of view. Nevertheless, defects can be produced as bonds between atoms of the same type. These are the *wrong* bonds.

In the classical structural models of amorphous semiconductors (Ge, Si) the six-fold rings of atoms, which represent the basic configuration in crystals, alternate with five- and seven-fold rings. These models, when applied to binary alloys will necessarily include wrong bonds. Although these wrong bonds cannot be avoided, their amount will be minimized, as demonstrated by the simulation of the structure of e.g. $CdGeAs_2$ glass [41] compared with the experimental structural data.

Chemical Impurities

Chemical additives can be incorporated into the basic network of the amorphous semiconductors. As a rule, the amorphous semiconductors are difficult to dope because of the large number of states in the forbidden gap and because of the possible easy accommodation of the impurity atoms, determined by the network flexibility.

The elemental amorphous semiconductor most sensitive to doping is amorphous selenium [42]. Only a few hundred ppm of oxygen, potassium or chlorine [43] introduced in the melt increase the dark conductivity by several orders of magnitude. A change to n-type conduction was reported when traces of chlorine were added.

The chemical impurities are of leading importance in controlling the transport properties in amorphous semiconductors.

1.4.4 Electronic-Structural Defects

Valence Alternation Pairs

In 1969 Cohen et al. [44] assumed that in amorphous solids the valence and conduction bands have tails of localized states and, therefore, a mobility edge exists that separates the localized states from the extended ones. The band tails extend into the forbidden gap and, due to their superposition, the Fermi level is pinned. In the case of chalcogenide materials, Davis and Mott [45] considered that this mechanism for pinning of the Fermi level is improbable and suggested that pinning is due to deep levels caused by defects.

It is remarkable that although the Fermi energy is pinned, the chalcogenide glasses do not possess unpaired electrons. This contradiction has been resolved by Anderson [46] who suggested that all spins are paired because of a very strong electron–lattice interaction. In such a case, the repulsion within the pair (characterized by the so-called Hubbard energy, U) is compensated by the energy gained as a consequence of the distortion of the chemical bond. Such defects are called negative-U centers.

Mott et al. [47] used the following notations for the centers defined as a dangling bond in three charging states: D^0 (neutral center), D^+ (positively charged center) and D^- (negatively

charged center). It was suggested that the reaction: $2D^0 \rightarrow D^+ + D^-$ is exothermic, i.e. all the spins become paired, which explains the absence of an ESR signal.

Kastner et al. [49] came up with a more detailed description of the defects. It was shown that the energetically least-costly bonding deviations in non-crystalline chalcogenides can be achieved when the defects are created in pairs: a positively charged over-coordinated atom and a negatively charged under-coordinated atom. These defects were called *valence alternation pairs* (VAP) because the valence or coordination is alternated for the defect atoms. The notations C_1^-, C_3^+ and C_3^0, where the subscript represents the number of neighbors of the defect atom, and the superscript represents the charge state of that atom, were introduced. The a D^+D^-, or $C_3^+C_1^-$ pair is considered as a fundamental defect in amorphous chalcogenide semiconductors.

In an amorphous selenium matrix two selenium atoms, each of which is triply bonded, serve to cross-link two molecular chains of doubly bonded atoms. A VAP can be produced by a spontaneous breaking of the cross-linkage, combined with a simultaneous transfer of an electron from one of the triply bonded selenium atoms to an atom near that where the cross-link was broken. Since such an electronic transfer reduces the total energy of the solid, nearly all the trigonally bonded selenium atoms become members of such valence alternation pairs.

Since the total number of bonds in the solid does not change by creating these defects (two at a time), the energy needed for the creation of a pair is relatively small. It is approximately the energy required to place the negative charge onto the under-coordinated atom (reduced by relaxation effects of the surrounding matrix). In typical chalcogenide glasses this results in a VAP defect density of about 10^{17} cm^{-1}, in agreement with the defect density measured by photo-induced ESR, mid-gap absorption, and photo-luminescence [50].

Kastner et al. [50] has suggested that Coulomb and exchange forces act between the VAP partners, so that the VAPs can become associated and form *intimately bonded valence alternation pairs* (IVAP). The difference between VAP and IVAP defects is illustrated in Fig. 1.5.

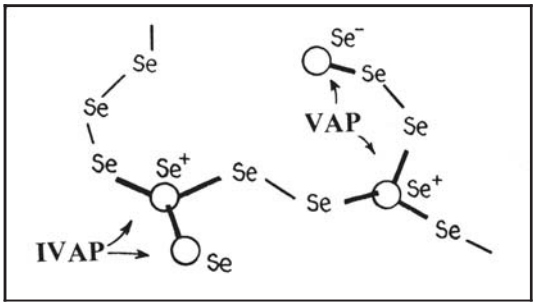

Figure 1.5: Schematic representation of the IVAP and VAP defects.

Quasi-Molecular Defects

A more general defect in chalcogenide semiconductors was proposed by Popov [51], namely, the *quasi-molecular defect* (QMD), which is a single orbital-deficient bond against the covalent background. The idea was later elaborated by Dembovsky and Chechetkina [52]. In

contrast to a covalent bond, which is established by electron pairing between two atoms, an orbital-deficient bond is a multi-centered one, so a QMD is a multi-atomic (or molecular) defect. From the properties of orbital deficient bonds, it follows that the three atoms in QMD under consideration are bound more weakly than in the covalent case and are arranged along a straight line with definite length.

QMDs plays the dominant role in the glass-forming substances because they take part in all the processes, including the VAP formation.

1.4.5 Macrodefects

Strongly anisotropic density fluctuations have been considered as a major class of defects in thin films prepared by various techniques. Both crystalline and amorphous thin films produced by vapor deposition commonly exhibit a columnar structure. This structure consists of a network of low-density material that surrounds an array of parallel rod-shaped or columnar regions of higher density.

The columnar structures commonly form in deposits in which the mobility of the deposited atoms is low and, although they have been observed in both crystalline and amorphous materials, they occur predominantly in amorphous films whose formation requires a limited atom mobility.

In non-crystalline chalcogenide films, it was observed that the photo-induced changes in volume and band gap can be greatly enhanced by the oblique deposition [53–55].

Other macrodefects are beyond the scope of this chapter.

1.5 Electronic States in Amorphous Semiconductors

All solids, crystalline or amorphous, contain atoms which are coordinated differently from their normal structural bonding. These are called defects and were discussed in Section 1.4. The defects are intimately related to specific energy states of the electrons that play an important role in defining the optical and electrical properties of the material. The electronic states of solids are grouped in bands, in narrow sub-bands, or in isolated levels in between the electronic energy bands. The main parameter that characterizes the electronic properties of the semiconductors is the density of electronic states.

1.5.1 Electronic States in Tetrahedrally Bonded Semiconductors

In crystalline semiconductors the valence and conduction band are separated by a forbidden gap of electronic states. The situation in amorphous semiconductors is different. According to the band model developed by Cohen, Fritzsche and Ovshinsky (CFO model) [44], in amorphous semiconductors, due to the absence of the long-range order, the valence and conduction bands are prolonged by tails, which tend to zero with different slopes. The energetic domain corresponding to the permitted bands defines the region of the extended states, while the band tail states are localized. In the extended states the mobility of the carriers are 4-5 orders of magnitude higher than in the localized states. The extended and localized states are separated by the mobility edge.

The tetrahedrally coordinated amorphous semiconductors (amorphous germanium, silicon, etc.) are well described by a model which separates the distribution of states into extended states, tail states and deep localized states (Fig. 1.6). The tail states arise from deformed but intact bonds whereas the deep states are due to incorrect coordination of some atoms.

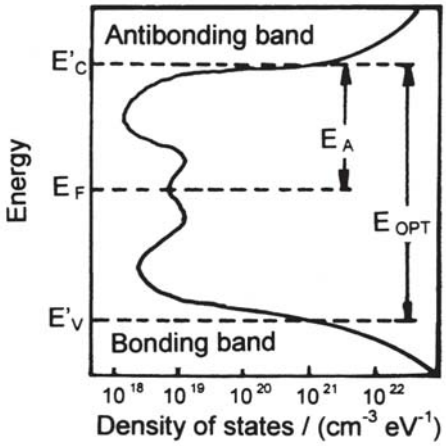

Figure 1.6: Distribution of density of states, $g(E)$, in amorphous semiconductors.

The dangling bond is energetically very unfavorable (the bond strength is $\sim$2–6 eV). Nevertheless, they characterize the tetrahedral amorphous semiconductors because: (i) the lowest energy deviant electronic configuration of a tetravalent atom contains a dangling bond and (ii) the rigid three-dimensional structure required by tetrahedral bonding leads, particularly in amorphous solids deposited from the vapor phase, to structures in which it is difficult to avoid a certain number of three-fold coordinated sites since the latter tends to relieve the stresses inherent in a rigid tetrahedral network. In practice, evaporated films tend to contain relatively large voids, and they must contain some dangling bonds in addition to many strained bonds. The strained bonds are similar to surface states, but dangling bonds are qualitatively different in several respects. Each dangling bond involves an unpaired spin, and thus should contribute to both an ESR signal and a Curie term in the magnetic susceptibility. Moreover, the dangling bonds produce a very different density of electronic states. The occupied states are non-bonding and so are higher in the gap than those resulting from strained bonds (Fig. 1.7).

Upon hydrogenation, all three types of states (extended states, tail states, and deep localized states) are affected but the most prominent effect occurs for the tail states and for the deep localized states. Hydrogen tends to remove states from the top of the valence band [57], which leads to an increase of the optical band gap, E_g, with increasing hydrogen content. In most cases the density of states, $g(E)$, around the Fermi level, E_F, is reduced by a factor of 10^2 to 10^3 from the values observed in its unhydrogenated counterpart (10^{20} cm^{-1} eV^{-1}); this is attributed to the passivation of the dangling bonds. Low defect state density (2×10^{15} cm^{-1} eV^{-1}) was achieved only in hydrogenated (glow discharge or sputtered [58]) and fluorinated amorphous silicon-type materials [59]. In the following we discuss

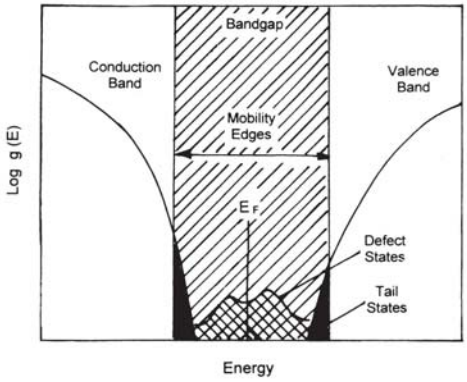

Figure 1.7: Sketch of the electronic density of states of as-deposited evaporated amorphous silicon. The Fermi energy is pinned by the large dangling-bond density ($\sim 10^{-19}$ cm^{-3}).

in detail the problems of the electronic states in amorphous tetrahedrally bonded semiconductors.

The dangling bond defect is neutral when is occupied by one electron (non-bonding). The charge of the defect is +e when the dangling bond is not occupied by electrons, and it is –e when is occupied by two electrons. Following the notation of Adler (T_z^q is a tetrahedral atom with the coordination z and local charge q) we can say that the normal configuration of a tetrahedral atom is T_4^0. The dangling bond defect is T_3^0. If an electron is removed from a T_3^0 center, the latter is transformed into a T_3^+ center (Fig. 1.8c). This electronic modification can induce strong chemical forces, which lead to local distortions of the neighboring shell of the defect. Adler has shown that the optimum situation for a center T_3^0 is realized for the hybridization sp^2 with angles between bonds of 120°. Bringing an extra electron transforms the T_3^0 center into T_3^-, that induces, after Adler, a decrease of the angle between bonds down to 95°.

Different opinions exist as to the sign of the correlation energy in amorphous silicon [56]. Thus, Dersh et al. [60] found from ESR measurements that correlation energy of Si dangling bonds was positive ($U_{eff} > 0$) while Adler deduced a negative correlation energy $U_{eff} < 0$ [61]. Silver argues [62] that in a given material centers with negative and positive correlation energy can coexist.

1.5.2 Electronic States in Non-Tetrahedrally Bonded Semiconductors

Comparison of the optical properties of crystalline and amorphous As_2S_3 and As_2Se_3 demonstrated that the effect of disorder on the electronic structure is relatively small. Apart from the loss of the details related to the symmetry points in the Brillouin zone, and some broadening of around several tenths of electronvolts, the spectra of the amorphous chalcogenide solids are very near to those of the crystalline analogues. The major differences between crystal and amorphous solid are a higher density of traps, and a larger scattering of the trapping levels in the amorphous solid.

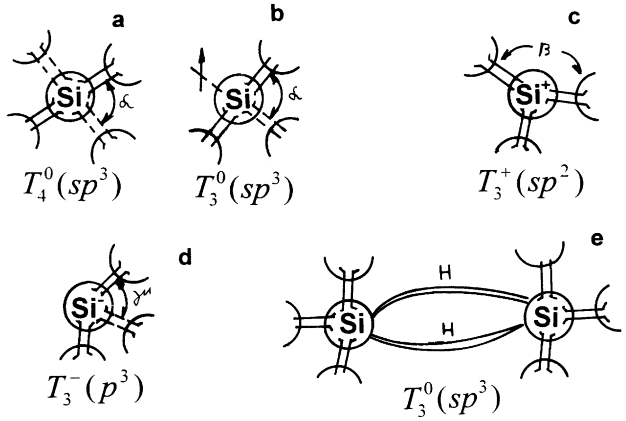

Figure 1.8: Sketch of the tetrahedral bonding in amorphous silicon (germanium) for the cases of a correct bonding (a), a dangling bond defect (b), a missing electron (c), an extra electron (d) on that atom, and the hydrogen bonding between two silicon atoms (e).

The electrical band gap is 1.1 eV, which is considerably smaller than the optical gap (1.9 eV). In general, the properties of the materials belonging to the family of As_2Se_3 (e.g. As_2S_3, As_2Te_3, Sb_2S_3, and Sb_2Se_3) are analogous, with the exception of quantitative variations of the band gap. The optical gap is the double of the electrical gap which indicates that the Fermi level is situated near the middle of the mobility gap.

In the first model of the band structure in amorphous semiconductors (CFO model) it was assumed that the valence and conduction bands contain tails of localized states and, consequently, a mobility edge exists that separates the extended from localized states. The tails extend deeply in the forbidden gap, superpose, and thus pin the Fermi level. At the same time, already in early studies it was demonstrated that the chalcogenide glasses behave like intrinsic semiconductors with the band gap of 1 eV or more and they are transparent for red and infrared rays and the density of unpaired spins was $\sim 10^{10}$–10^{14} cm^{-3}. This controversy was solved by introduction of the concept of negative-U centers described above.

In a chalcogen, e.g. selenium, the four 4p electrons occupy two bonding orbitals representing covalent bonding and one orbital named a lone-pair orbital, that does not participate in the bonding. The p electrons gives rise to strong covalent bonds. Lone-pair electrons determine the dihedral angles and, being the uppermost electrons, play an important role in defining the energy bands.

The energy levels in the chalcogen solid have been calculated in the framework of the molecular orbital theory [63]. They give an image on the distribution of the six electrons on the hybridized orbitals and their participation in the bonding with the neighbors. A general picture for the density of extended states in amorphous chalcogenides has been obtained using photoemission [64].

To determine the density of localized states in the gap, various techniques have been used. In early papers, from transient decay measurements (over almost nine decades of time) it

was concluded that the density of tail states decreases exponentially and does not have any defined structure. The characteristic energy kT_0 was determined to correspond to $T_0 = 500$ K in As_2Se_3 [65]. However, it was argued back in 1983 that a combination of non-exponential arrays of localized traps can also generate current decays of the power law form [66]. It is now generally believed that on top of featureless distribution of state in the tails, structured density of states exists attributed to VAPs [67] whose concentration is around 1% at temperatures near T_g. For arsenic triselenide time-of-flight and transient photoconductivity measurements suggest a feature located 0.6 eV above the valence band edge which dominates the transport.

There was some controversy in the literature related to the sign of correlation energy in amorphous selenium. Thus, in an early paper by Kastner et al. [48] the correlation energy was assumed to be negative. Later, Vanderbilt and Joannopoulos [68] argued that in elemental selenium the correlation energy was likely to be positive. It was only recently that Kolobov et al. have convincingly demonstrated, using light-induced ESR, that the correlation energy was, indeed, negative [69].

Popescu et al. [70] stated, after Mott, that in amorphous selenium the states C_3^+ give rise to discrete traps situated at around 0.33 eV below the bottom of the conduction band (concentration 10^{18} cm^{-3}) and they control the electron mobility. The C_1^- states are situated 0.17 eV above the top of the valence band and control the hole conduction. Both types of traps are distorted by trapping the charge carriers, and, as a consequence, their energies do not correspond to that found from the light absorption experiments and charge carriers generation. A somewhat different value of 0.25 eV for the states above the valence band was reported by Pfister [71].

Combined analysis of xerographic potentials and transient transport data was applied to determine the energy positions of the localized states in amorphous selenium [72]. Four different energy levels were identified, namely located 0.26 eV above the valence band and 0.35 eV below the conduction band attributed to VAPs as well as two deep states located around the Fermi level and separated by 0.13 eV It should be noted, however, that the energy difference between the deep states claimed in [72] is less than the experimental uncertainties for each level reported in the original papers cited therein.

The issue of defects in selenium has been recently revisited [73]. The authors used post-transient photocurrent analysis and found two levels located 0.55–0.66 eV below the conduction band and $0.4 - 0.5$ eV above the valence band attributed to D^+ and D^- intrinsic negative-U defects. While these values differ somewhat from those reported earlier [72], which may be due to differences in samples, the technique used, or the data analysis procedure, the conclusion that well defined states exist in the gap of chalcogenides can be considered a well-established fact.

References

[1] D. Schechtman, I. Blech, D. Gratias and J. W. Cahn, Phys. Rev. Lett. **53**, 1951 (1984).

[2] M. Popescu, Ph. D. Thesis, Bucharest, 1975.

[3] M.Popescu, in Proc. Intern. Conf. "Amorphous Semiconductors '78", Pardubice, Czechoslovakia, Vol. 1, 1978, p. 189.

[4] J. C. Phillips, J. Non-Cryst. Solids **34**, 153 (1979).

[5] G. Lucovsky and F. L. Galeener, J. Non-Cryst. Solids **37**, 53 (1980).
[6] S. R. Elliott, Adv. Physics **38**, 1, 1989.
[7] A. Uhlherr and S. R. Elliott, J. Non-Cryst. Solids **192&193**, 98 (1995).
[8] D. E. Polk, J. Non-Cryst. Solids **5**, 365 (1971).
[9] P. Steinhardt, R. Alben, M. S. Duffy and M. S. Polk, Phys. Rev. B **18**, 6021 (1973).
[10] P. Višor, J. Non-Cryst. Solids **101**, 156 (1988).
[11] M. Popescu, J. Non-Cryst. Solids **192&193**, 140 (1995).
[12] E. Donth, J. Non-Cryst. Solids **52**, 325 (1982).
[13] D. V. Tsu, S. Chao, S. R. Ovshinsky, S. J. Jones, J. Yang, S. Guha and R. Tsu, Phys. Rev. B **63**, 125338 (2001).
[14] R. Grigorovici and M. Popescu, in Physics and Applications of Disordered Materials, Ed. M. Popescu, INOE, Bucharest, 2002, p. 19.
[15] R. Grigorovici, P. Gartner and I. Corcotoi, J. Non-Cryst. Solids **114**, 256 (1989).
[16] J. Weissmüller, Nanostruct. Mater. **4**, 261 (1993).
[17] S. R. Elliott, J. Phys. Cond. Matt. **4**, 7661 (1992).
[18] Ke. Tanaka, Appl. Phys. Lett. **26**, 243 (1975).
[19] L. E. Busse, Phys. Rev. B **29**, 3639 (1984).
[20] S. Susman, D. L. Price, K. J. Volin, R. J. Dejus and D. G. Montague, J. Non-Cryst. Solids **106**, 26–29 (1988).
[21] P.H. Fuoss and A. Fischer-Colbrie, Phys. Rev B **38**, 1875 (1988).
[22] G. N. Greaves, S. R. Elliott and E. A. Davis, Adv. Phys. **28**, 49 (1979).
[23] M. Popescu, Proc. Intern. Conf. "Amorphous Semiconductors '80", Chisinau, Moldova, Vol. 1, 1980, p. 21.
[24] M. Popescu, in Proc. Intern. Conf. "Amorphous Semiconductors '78", Pardubice, Czechoslovakia, Vol. 1, 1978, p. 203.
[25] T. Egami, K. Maeda and V. Vitek, Phil. Mag. A **41**, 883 (1980).
[26] R. S. Williams and T. Egami, IEEE Trans. Magn. **12**, 927 (1976).
[27] H. Chen and E. Coleman, Appl. Phys. Lett. **28**, 245 (1976).
[28] R. C. Morris, J. Appl. Phys. **40**, 3250 (1979).
[29] M. F. Ashby and J. Logan, Scripta Met. **7**, 513 (1973).
[30] W. B. Jackson and S. B. Zhang, in Transport, Correlation and Structural Defects (Advances in Disordered Semiconductors, Vol. 3), Ed. H. Fritzsche, World Scientific Publ. Co., Singapore 1990, pp. 63–128.
[31] R. A. Street, J. C. Knights and D. K. Biegelsen, Phys. Rev. B **18**, 1880 (1978).
[32] S. T. Pantelides, Phys. Rev. Lett. **57**, 2979 (1986).
[33] R. M. Laine, K. Y. Blohowiak, R. R. Robinson, M L. Hoppe, P. Nardi, J. Kampf and J. Uhm, Nature **353**, 642 (1991).
[34] R. A. Street, C. C. Tsai, J. Kakalios and W. B. Jackson, Phil. Mag. B **56**, 305 (1987).
[35] P. V. Santos, N. M. Johnson and R. A. Street, Phys. Rev. Lett. **67**, 2686 (1991).
[36] S. C. Pantelides, Solid State Comm. **84**, 221 (1992).
[37] J. J. Gilman, J. Appl. Phys. **44**, 675 (1973).

[38] N. Rivier, Phil. Mag. **40**, 859 (1979).
[39] G. A. N. Connel and R. J. Temkin, Phys. Rev. B **9**, 5323 (1974).
[40] M. Popescu, J. Non-Cryst. Solids **192&193**, 140 (1995).
[41] M. Popescu, R. Manaila and R. Grigorovici, J. Non-Cryst. Solids **23**, 229 (1977).
[42] E. Mytilineou, J. Optoelectron. Adv. Mater. **4**, 705 (2002).
[43] V. A. Twaddell, W. C. Lacourse and J. D. Mackenzie, J. Non-Cryst. Solids **8–10**, 831 (1972).
[44] M. H. Cohen, H. Fritzsche and S. R. Ovshinsky, Phys. Rev. Lett. **22**, 1065 (1969).
[45] E. A. Davis and N. F. Mott, Phil. Mag. **22**, 903 (1970).
[46] P. W. Anderson, Phys. Rev. Lett. **34**, 953 (1975).
[47] N. F. Mott, E. A. Davis and R. A. Street, Phil. Mag. **32**, 961 (1975).
[48] M. Kastner, D. Adler and H. Fritzsche, Phys. Rev. Lett. **34**, 1346 (1975).
[49] M. Kastner and H. Fritzsche, Phil. Mag. B **37**, 199, 1978.
[50] S. G. Bishop, U. Strom and P. C. Taylor, Phys. Rev. **36**, 543 (1976); Phys. Rev. B **15**, 2278 (1977).
[51] N. A. Popov, Fiz. Tehn. Poluprovod. (Russ.) **15**, 369, 1981; **16**, 384 (1982).
[52] S. A. Dembovsky and E. A. Chechetkina, J. Non-Cryst. Solids **64**, 95 (1984).
[53] Y. Kuzukawa, A. Ganjoo, K. Shimakawa and Y. Ikeda, J. Non-Cryst. Solids **227–230**, 715 (1998).
[54] S. Rajagopalan, K. S. Harshavardhan, L. K. Malhotra and K. L. Chopra, J. Non-Cryst. Solids **50**, 29 (1982).
[55] K. Starbova, J. Dikova and N. Starbov, J. Non-Cryst. Solids **210**, 261 (1997).
[56] J. Hubbard, Proc. Roy. Soc. (London) A, **276**, 238 (1963).
[57] B. von Roedern, R. Ley, M. Cardona and F. W. Smith, Phil. Mag. B **40**, 433 (1979).
[58] R. L. Weisfield, J. Appl. Phys. **54**, 6401 (1983).
[59] A. Madan, S. R. Ovshinsky and E. Benn, Phil. Mag. **40**, 259 (1979).
[60] H. Dersh, J. Stuke and J. Bechler, phys. stat. sol. (b) **105**, 265 (1981).
[61] D. C. Adler, Semiconductors and Semimetals, Vol. 21, Part A, Academic Press, New York 1984.
[62] M. Silver and L. Cohen, Phys. Rev. B **15**, 3276 (1977).
[63] L. Chen, Phys. Rev. B **7**, 3672 (1973).
[64] S. Hosokawa, Y. Hari, K. Nishihara, K. Tamura and M. Taniguchi, J. Non-Cryst. Solids **166**, 1199 (1993).
[65] D. Monroe and A.A. Kastner, Phys. Rev. B **33**, 8881 (1986).
[66] J.M. Marshall, Rep. Progr. Phys. **46**, 1235 (1983).
[67] R.P. Barclay, J. Phys.: Condens. Matter **6**, L431 (1994).
[68] D. Vanderbilt and J. D. Joannopoulos, Phys. Rev. Lett. **49**, 823 (1982).
[69] A. Kolobov, M. Kondo, R. Durny, A. Matsuda and K. Tanaka, Phys. Rev. B **56**, R485 (1998).
[70] M. Popescu, A. Andriesh, V. Chumash, M. Iovu and S. Shutov, Tsiuleanu, Fizica Sticlelor Calcogenice (in Roumanian), Shtiintsifica, Bucharest-Stiintsa, Chishinau, 1996, p. 154.
[71] G. Pfister, Contemp. Phys. **20**, 449 (1979).
[72] M. Abkowitz, Philos. Mag. Lett. **58**, 53 (1988).
[73] H.Z. Song, G.J. Adriaenssens, E.V. Emelianova and V.I. Arkhipov, Phys. Rev. B **59**, 10607 (1999).

2 Photo-Induced Phenomena in Amorphous and Glassy Chalcogenides

Miloslav Frumar, Božena Frumarová, Tomáš Wágner, and Petr Němec

A review of optically induced changes of structure and properties of amorphous and glassy chalcogenides (AGC) and amorphous chalcogenide films is given. Isotropic effects, chemical aspects, and new results are emphasized.

2.1 Introduction

Photo-induced effects (PE) include changes of electronic and atomic structure, composition, phase, and physicochemical properties of chemical compounds induced by exposure of the material to light (radiation) of appropriate energy and intensity. In a broader sense, they also include photoconductivity, photovoltaics, photoluminescence, and non-linear optical phenomena that are connected with purely electronic effects. The latter group of processes will be discussed in this chapter only marginally. Intense illumination can also partly or fully damage (or evaporate) the material. Such processes will be also beyond the scope of our review.

PE are not rare in solids and have been found (and exploited) also in crystalline compounds, e.g. in Ag–X (X = Cl, Br, I), in the so-called photochromic materials, as well as in many molecular organic compounds, etc. [1–5]. PE have been also observed in many amorphous and glassy chalcogenides (AGC) (see, e.g. [1, 3, 6–107] etc.).

The mechanism of PE can be very different. The first step of interaction of radiation (UV, VIS, NIR light, neutrons, γ- or X-rays) with the substance is nearly always energy absorption, excitation of electrons and/or holes, displacement of atoms, creation or amplification of phonons. Such processes can induce changes of structure, electrical conductivity, electric charges and temperature; they can even lead to melting or evaporation of the material. Electronic or atomic defects can be also formed. Exposure can lead to chemical bond redistribution or reorientation, to photo-induced crystallization or amorphization, to formation of products of synthetic or photolytic chemical reactions, to change of chemical reactivity, surface profile, optical transmittivity and reflectivity, index of refraction, hardness, thickness, fluidity, etc. [1, 3, 6–107].

One photon is usually absorbed by each molecule or structural unit and is responsible for primary photochemical or photo-induced processes (Stark–Einstein rule [4, 5]). This rule is broken when high-intensity lasers are the source of radiation and more than one photon is absorbed. Such an effect is probably behind a large increase of efficiency of PE when very intense pulses are used for excitation [63]. Optically excited states relax, after a time, to the original or to a new state, either directly or via intermediate steps. The relaxation can be purely

electronic, or it can involve changes in positions of individual atoms or atomic groups. The time of relaxation varies from picoseconds to years, depending on the system, its structure, temperature, and wavelength of the excitation light [57].

In crystalline compounds, the optically induced changes of atomic structure are confined to the surface of the crystals or its vicinity or to the neighborhood of defects because the dense packing of the atoms only rarely allows larger changes in their positions and the photo-induced changes (PC) are small or relax back after the exposure is finished.

The situation in AGC is different. The disorder of such materials is high, their density is generally lower than in crystalline counterparts (when they exist) and, therefore, a larger free volume is available [7, 27, 28, 35, 42, 51, 108]. The larger free volume and broad composition regions of AGC are favorable for the formation of compositional and coordination defects. In amorphous films or in powdered glasses, the disorder is even larger than in bulk glasses and movement of atoms is easy [27, 29, 51, 55]. The PC of atomic structure can be larger and the PE are stronger.

2.2 Photo-Induced Effects in Amorphous and Glassy Chalcogenides

The AGC are favored materials. The PE in them are strong and numerous and they are transparent in the IR region, which is favorable for their applications. PE in AGC have been extensively studied as an interesting subject of fundamental research of disordered solids and due to present and potential applications in optics and optoelectronics (see, e.g. [1, 3, 6–107]). A systematic study of PE in AGC was started in the 1960s, stimulated by the work of Ovshinsky, Berkes and others [8–14, 16–18, 79] and motivated by an effort to apply PE in optics and optical data storage.

The fact that the PC of structure and of many properties are larger in AGC than in other compounds is probably caused by several reasons:

- The chalcogens in AGC are usually two-fold coordinated and the valence angles between two covalent bonds of chalcogens (S, Se), are between 90–109° [102]. Such structure is flexible and the angle between two bonds can be easily deformed. Vibrations of structural units interconnected via such chalcogen atoms are practically independent (strongly localized) and can be interpreted as vibrations of nearly free oscillators [102].

- The chalcogens and also pnictogens (As, Sb and partly Bi) and group IV elements (Si, Ge) can form chemical bonds between like atoms (e.g. As–As, Sb–Sb, Si–Si, Ge–Ge, generally M–M, where M is metalloid or a metal [109]). The energies of such bonds are not far from the energies of heteroatomic bonds M–C, where C is for a chalcogen (Table 2.1, [6, 111]). This fact enables the changes of coordination of individual atoms [46, 51]. The energies necessary for the optically induced or optically enhanced reactions

$$2|\text{M–C}| \overset{h\nu_i, I_i, T_i}{\longleftrightarrow} |\text{M–M}| + |\text{C–C}| \tag{2.1}$$

  are lower than in oxides. Here $h\nu_i$ and I_i are energy and intensity of the exposure light, T is temperature and $i = 1, 2$ for the direct and backward reactions, respectively. The

Table 2.1: Bond energies E (kJ/mol) for various atom pairs [6, 111]

Bond	E	Bond	E	Bond	E
S–S	280	P–Se	240	Sb–Te	195
Se–Se	225	As–As	200	Si–Si	225
Se–Te	195	As–S	260	Si–Te	220
S–Se	255	As–Se	230	Ge–Ge	185
Se–Te	220	As–Te	205	Ge–S	265
P–P	225	Sb–Sb	175	Ge–Se	230
P–S	270	Sb–S	230	Ge–Te	200

exposure to light or annealing shift the the reaction equilibrium to the right- or left-hand side depending on the system, its temperature, energy and intensity of light. For $h\nu_1 > h\nu_2$ and $I_1 > I_2$, the forward reaction is enhanced while annealing ($T_2 > T_1$), or exposure to $I_1 < I_2$ light shifts the reaction in the backward direction.

- Over- and under-coordinated atomic defects are common in AGC and they can be induced by exposure. Such defects are usually charged, they can increase the densities of the localized states in the band-tails and cause the shift of the absorption edge. Although the density of charged defects is much lower ($10^{15} - 10^{17}$/cm^3) than the expected density of defects which are behind the photostructural changes [52], they can act as intermediate defects in PC of structure and properties (see, e.g. [1, 6, 53, 58, 60] and papers cited therein).

- The chalcogens and pnictogens possess non-bonding orbitals (lone pairs), which form the upper part of valence band states [1, 6, 92]. These orbitals can be transferred to the bonding ones and vice versa, and can be used for the formation of new bonds with changed geometry of local structural units.

- The "free volume" of AGC is relatively high, which makes the structure flexible [7, 51, 108]. The largest PC of optical properties were found for systems with the largest "free volume" [27–29, 43]. It should be noted that the composition corresponding to maximal free volume is close to the one corresponding to the mean coordination number of the Tanaka threshold (~ 2.7) [42].

- The AGC are non-equilibrium substances. The glasses (films) that are close to, or even outside, the glass-forming region can be prepared. Such materials are highly metastable and the exposure can initiate their transformation (e.g. crystallization) to a state closer to equilibrium.

The PE in AGC can be irreversible and reversible. Processes within each group are described below.

2.2.1 Irreversible Photo-Induced Changes

Irreversible PC of structure and properties of AGC are found after the exposure of as-evaporated films, in crystallization processes, they accompany PC of reactivity, photo-induced oxidation or hydrolysis, photo-induced dissolution and diffusion of metals in AGC, interdiffusion of chalcogenide compounds and photo-decomposition of materials (see, e.g. [1, 6–8, 18, 21, 56, 60, 64, 81]).

Changes of Structure

For preparation of thin chalcogenide films, high-temperature, high-energy radiation, particles, or laser pulses have to be used. During the evaporation, the effective temperature of vapors is relatively high and chalcogenides can dissociate into fragments with lower molecular mass. Fractional evaporation of materials containing more- and less-volatile species or fragments can also take place. After condensation of the vapors on a cold substrate, non-homogeneous films are obtained. The "synthetic" chemical reactions among fragments, which would result in original material, are generally slow at lower temperatures [7, 46, 51]. Nano-regions of different composition distributed in the volume or gradient of composition can be obtained. As a result, such films are non-homogeneous, and their composition and structure are strongly influenced by the preparation conditions.

Glasses in the As–S system can serve as an example of the dissociation of evaporated substances to low molecular mass fragments. They dissociate according to the following simplified reaction [41, 42, 51, 56]:

$$2(\mathrm{As_2S_3})_n \longleftrightarrow n\mathrm{As_4S_4} + n\mathrm{S_2} \tag{2.2}$$

where $n \gg 1$. Other reactions also proceed in the vapors because other particles, such as $\mathrm{As_4}$, $\mathrm{S_8}$, $\mathrm{As_4S_3}$, and $\mathrm{As_2S_6}$ are also present in the vapors [56]. Some of them can be identified in the deposited films (Figs. 2.1 and 2.2). The presence of $\mathrm{As_4S_4}$ and S_n molecules in thin films can be seen in Raman spectra in the region between $120 - 260$ cm^{-1} and the bands with maxima near 145, 168, 190, 214, 223 and 361 cm^{-1} can be assigned to $\mathrm{As_4S_4}$ vibrations; the band near 495 cm^{-1} is due to S–S vibrations [7, 42, 46–48] (Figs. 2.1 and 2.2).

The exposure of as-evaporated films can induce synthetic chemical reactions among the fragments, which result in their chemical homogenization (Eq. (2.2), backward direction) and polymerization. This process is accompanied by a decrease of amplitudes of the bands with maxima near 136, 146, 169, 191, 215, 223, 235, 361, and 495 cm^{-1} in the Raman spectrum [7] of As–S films (Figs. 2.1 and 2.2). The Raman bands corresponding to As–As (235 cm^{-1}) and S–S bonds (495 cm^{-1}) and $\mathrm{As_4S_4}$ vibrations (see above) lower their amplitudes. This process is irreversible.

The homogenization of fresh evaporated films can be also achieved by their annealing close to the glass-transition temperature, T_g, when atoms or structural groups are relatively mobile and chemical reactions among them can progress quickly. The structure of annealed films is not fully identical with the structure of fresh evaporated films after their exposure, due to some photolytic reactions, which proceed simultaneously with synthetic ones during the exposure (Figs. 2.1 and 2.2). Similar photostructural and the photochemical effects as in the

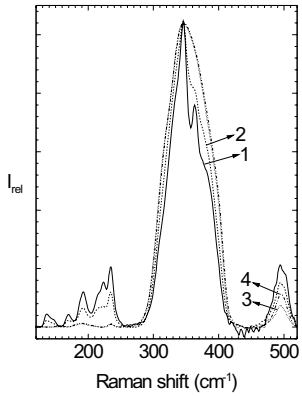

Figure 2.1: Reduced Raman spectra of $As_{38}S_{62}$ thin films and bulk glass. (1) as-evaporated film (2) exposed film (3) annealed film (4) bulk glass. Curves 3 and 4 are overlapping in the spectral region up to $420\ cm^{-1}$. Some narrow bands of the spectrum ($130 - 250\ cm^{-1}$, $361\ cm^{-1}$) can be assigned to As_4S_4 molecules, the band $235\ cm^{-1}$ can be assigned to As–As bonds vibrations, the band $495\ cm^{-1}$ to S–S bonds vibrations.

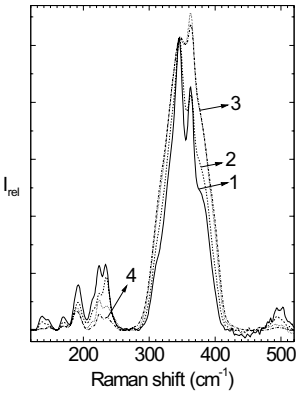

Figure 2.2: Reduced Raman spectra of $As_{42}S_{58}$ thin films and bulk glass. (1) as-evaporated film (2) exposed film (3) annealed film (4) bulk glass. The amplitudes of curves 1–4 were normalized to the same value for the band 345 cm^{-1} (AsS_3 pyramid vibrations). For assignment see Fig. 2.1.

As–S system were found in As–Se, As–Ga–S, Ge–Sb–S and Sb–S systems [7, 22, 26–28, 38, 43, 45, 47].

The Ge–Sb–S system with a relatively broad glass-forming region can serve as an example with different PE. In thin films of this system, prepared by flash evaporation of $Ge_5Sb_{45}S_{50}$, $Ge_5Sb_{40}S_{55}$, $Ge_{10}Sb_{40}S_{50}$ and $Ge_{10}Sb_{50}S_{40}$ glasses, crystallization, photobleaching or pho-

todarkening were observed [22]. It is supposed that dissociation of vapors into fragments analogously to Eq. (2.2) takes place. During the condensation of the vapors, local inhomogeneities are formed. Samples with a low content of Ge and with mSb/nS$\geq$ 2/3 (excess Sb over stoichiometry of Sb_2S_3) were darkened after exposure [23, 24, 46]. Such films are oversaturated by Sb and are chemically metastable. During the exposure, they can lose the excess metal (Eq. (2.3)) resulting in absorption edge shift towards longer wavelengths (darkening):

$$\begin{array}{l} \mathrm{Sb}_m\mathrm{S}_n \quad \xrightarrow{h\upsilon} \quad \mathrm{Sb}_{m-x}\mathrm{S}_n + x\mathrm{Sb} \\ (m/n) \rangle\, 2/3, (m-x)/n \cong 2/3. \end{array} \tag{2.3}$$

The Ge–Sb–S films with lower Sb content, or films with $x_{Ge}/y_S < 1/2$ were photobleached which can be explained as follows. During the evaporation of Ge–Sb–S glasses, the vapors of GeS_2 are formed as fragments; they can be further thermally dissociated according to the scheme [112]

$$2\mathrm{GeS}_2 \rightarrow \mathrm{Ge}_2\mathrm{S}_3 + 1/2\mathrm{S}_2 \rightarrow 2\mathrm{GeS} + \mathrm{S}_2; \qquad T \geq 1098\ \mathrm{K} \tag{2.4}$$

The GeS_x, $x < 2$, and S_2 or S_8 molecules are thus formed and, after condensation, local inhomogeneities appear again. The backward reaction of (Eq. (2.4)) or the reaction (Eq. (2.5)) is facilitated by exposure, the GeS_2 is formed and the transmission of the layers is increased ($E_g^{opt}(\mathrm{GeS}_2) > E_g^{opt}(\mathrm{Ge}_2\mathrm{S}_3$ or GeS)); the chalcogenides are photobleached. In films, due to exposure, the following reaction could also proceed:

$$\mathrm{GeS}_x + \mathrm{S}_y \rightarrow \mathrm{GeS}_{x+y}, \qquad x < 2 \leq (x+y) \tag{2.5}$$

This reaction leads to stoichiometric or sulfur-rich films, and, consequently, to photobleaching as well. Amorphous GeS_x, $x < 2$, contains excess of Ge as compared with GeS_2; its optical gap is lower than that of GeS_2.

Changes of Optical Transmission, Photodarkening, and Photobleaching

The exposure of fresh evaporated films shifts their absorption edge either towards longer wavelengths (red shift, photodarkening) or towards shorter wavelengths (blue shift, photobleaching) (see, e.g. [1]). The explanation of these shifts based on photosynthetic or photolytic reactions was given above. In many papers, the photodarkening is assigned to the formation of defects and localized electronic states in the tails of conduction and valence bands, which lower the energy gap [1]. Such a description may be identical, because the photolytic or photosynthetic reactions change the density or create new defects with energy inside the energy gap of amorphous solid (see above).

Changes of Index of Refraction

Exposure of fresh evaporated or annealed films also changes their index of refraction [6, 48, 49, 59, 85]. The changes of index of refraction, Δn, of fresh evaporated films of As–Se, Ge–S, Ge–Sb–S are larger than those of annealed films and can be as large as $\Delta n = 0.78$ (e.g. for $As_{0.6}Se_{0.4}$) [59, 89]. The spectral dependence of the index of refraction of amorphous

chalcogenide films can be described by the Wemple–DiDomenico relationship using a single-oscillator approach (Fig. 2.3) [113, 114]:

$$n^2(\hbar\omega) - 1 = \frac{E_0 E_d}{E_0^2 - (\hbar\omega)^2} \quad , \tag{2.6}$$

where $\hbar\omega$ is the photon energy and E_0 is the single oscillator energy, E_d is the dispersion energy. As an example, values of E_g^{opt}, E_0, E_d, n, of the thickness, d, and of relative permittivity, ε_r, for the system As–S are given in Table 2.2 [48].

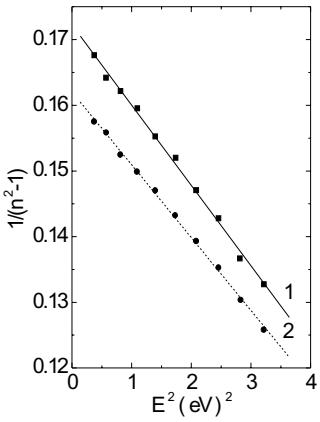

Figure 2.3: Spectral dependence of $(n^2 - 1)^{-1}$ for thin films of Sb_2S_3, where n is index of refraction. (1) as-evaporated film (2) exposed film.

The index of refraction of fresh evaporated $As_{38}S_{62}$ and $As_{40}S_{60}$, as well as of $As_{42}S_{58}$ films is increased by illumination and, even more, by subsequent annealing ([48], Table 2.2). Part of these changes can be caused by film densification, polymerization, and homogenization. It can be connected also with an increase of the dispersion energy, E_d, [113, 114]. $E_d = \beta N_c Z_a N_e$, eV, where N_c is the coordination number of the cation nearest neighbor to the anion, Z_a is the formal chemical valence of the anion, N_e is the effective number of valence electrons per anion, and β is a constant ($\sim$0.37 for amorphous materials) [113, 114]. Values of E_d, increase with illumination and increase further after annealing (Table 2.2). The decreased content of S–S and As–As bonds (Eq. (2.1), backward direction) and increased content of AsS_3 structural units in illuminated or annealed films increase the mean coordination number of the cation to the anion N_c; As–As bonds are replaced by As–S bonds. It is still an open question whether the value of Z_a is changed during the exposure, too.

The changes of index of refraction cause changes of third-order non-linear effect χ^3. Its behavior is discussed elsewhere [93].

Changes of Reactivity

The exposure of chalcogenide films also changes their solubility in chemical solvents (see, e.g. [29–36, 40, 78]). The difference in dissolution rates of exposed and unexposed parts can

Table 2.2: The values of the optical band gap E_g^{opt}, of the single-oscillator energy E_0, of the dispersion energy E_d, of the index of refraction n (extrapolated to $E = 0$), of the thickness d and of the relative dielectric constant ε_r

$As_{38}S_{62}$ films	E_g^{opt} (eV)	E_0 (eV)	E_d (eV)	n $(E = 0)$	d (nm)	ε_r $(E = 0)$
unexposed	2.41	4.8	21.22	2.24	1 007	5.02
exposed	2.39	4.73	22.35	2.4	980	5.74
annealed	2.39	4.56	22.59	2.44	953	5.96
exposed after annealing	2.38	4.53	22.27	2.43	956	5.91
$As_{40}S_{60}$ films	E_g^{opt} (eV)	E_0 (eV)	E_d (eV)	n $(E = 0)$	d (nm)	ε_r $(E = 0)$
unexposed	2.39	4.76	21.22	2.34	988	5.46
exposed	2.37	4.78	22.31	2.38	982	5.67
annealed	2.35	4.54	22.68	2.45	970	5.99
exposed after annealing	2.33	4.51	22.37	2.44	975	5.96

be increased using specific reactants [31–36] (Figs. 2.4 and 2.5). The dissolution rates can also be influenced by the presence of oxidizing (I_2, $KClO_3$) or reducing agents (methol, etc.) in the solution [31]. The process can be illustrated on dissolution of As–S films. As we have mentioned above, the fresh evaporated films of the As–S system contain a large amount of As_4S_4 [31, 39, 41, 42, 51]. Dissolution of As_4S_4 in alkaline solutions is relatively slow, partly because of elemental arsenic formed on the surface of the film and partly because As_4S_4 is relatively resistant to alkaline solutions:

$$3As_4S_4 + 24OH^- = 4AsS_3^{3-} + 4AsO_3^{3-} + 4As + 12H_2O \tag{2.7}$$

The dissolution of As_2S_3, that is the prevailing compound in the exposed parts of films, is much faster:

$$As_2S_3 + 6OH^- = AsO_3^{3-} + AsS_3^{3-} + 3H_2O \tag{2.8}$$

Reducing agents, added to the alkaline etchant, can increase the content of As on the surface of the film and slow the dissolution. The blocking effect of As deposited on the surface of film, was confirmed in [34]. Oxidizing agents speed up the dissolution of the unexposed films oxidizing As_4S_4 (Fig. 2.5 [31]). Similar effects were observed when the films were dissolved in dimethylamine [30].

The dissolution rates of films with overstoichiometry of As (e.g. $As_{42}S_{58}$) are lower in alkaline solutions than those of stoichiometric films. This supports the above idea because these films contain larger amounts of As and As_4S_4 [7, 40, 41] (Figs. 2.1 and 2.2), which are poorly soluble in alkaline solutions.

The solubilities of as-evaporated and exposed films can be drastically influenced by chemisorption of some organic compounds, e.g. of aryl- or tetraalkylammonium salts [34, 36, 39],

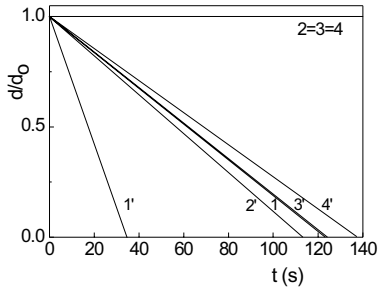

Figure 2.4: Kinetics of dissolution of as-evaporated and exposed thin As_2S_3 films ($d_0 = 0.3\mu$m) in an aqueous solution of 100 g/l 150 g/l Na_2CO_3 + 150 g/l $Na_3PO_4.12H_2O$ with methol, pH = 12.0. Concentration of methol (g/l): $(1, 1')0; (2, 2')0.1; (3, 3') - 0.2; (4, 4')0.3$. Samples $1' - 4'$ were exposed before etching for 1 h.

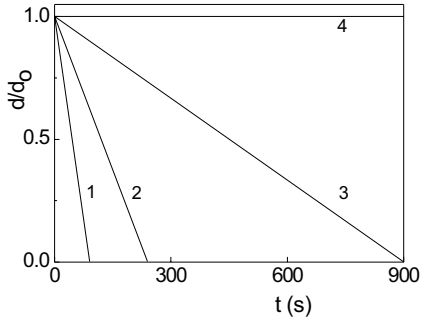

Figure 2.5: Dissolution rates of As_2S_3 thin films in CS_2 solution of I_2 (0.5 g/100 ml). (1) As evaporated film; (2–4) the film was exposed before etching for 1 min (2), 5 min (2.1) or 20 min (4).

in which at least one alkyl group is long enough (e.g. cetyl-, $C_{16}H_{33}$-). These compounds can be selectively chemisorbed on the unexposed parts of films; As-rich parts or fragments of the film are apparently preferred. After such a sorption, the dissolution of the unexposed films can be completely blocked (Fig. 2.6) [39]. The effect is not fully understood; a possible model is suggested in [34]. The nitrogen of $[N^+R_4]$, or $-[N^+R_3]$, $=[N^+R_2]$ and similar groups is positively charged and can be bonded to As–As structural units, which act as Lewis bases. The long alkyl- (aryl-) chain of alkylammonium salts is hydrophobic; when the compound is chemisorbed it protects the surface against the attack of the alkaline solution [34, 36, 39].

Both positive and negative etching can be obtained [36]. The etching of As_xS_{100-x} thin films in alkaline solvents is positive (exposed part was dissolved more quickly), while the films with excess As, $x \geq 40$, which were treated before etching by CS_2, were etched negatively. The CS_2 can dissolve free sulfur or sulfur-rich fragments of the film that are present in fresh evaporated films (Eqs. (2.2) and (2.4)). Because of removal of S-rich fragments, the surface becomes rough and the surface area is considerably increased. Subsequent dissolution of the film in alkaline solvents is then quicker [36].

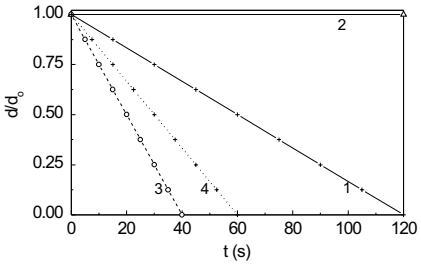

Figure 2.6: The change of relative thickness (d/d_0) of $As_{42}S_{58}$ films ($d_0 = 500$ nm) during dissolution in alkaline solution (150 g/l Na_2CO_3 + 150 g/l $Na_3PO_4.12H_2O$, pH = 12,5). (1) Fresh evaporated film; (2) fresh evaporated film, which was immersed for 5 min in cetyltetraammonium bromide solution (1 g/l) before etching; (3) illuminated film; (4) illuminated film, which was immersed for 5 min in cetyltetraammonium bromide solution (1 g/l) before etching. The lines are drawn as guides for the eye.

Oxidation and Hydrolysis

The sensitivity of many chalcogenides to oxidation and hydrolysis when they are exposed to light has been well known for a long time [25]. The photo-induced reaction of films or glass surfaces with oxygen and/or moisture can cause their bleaching [25, 94] because the formed Ge–O–Ge bonds in the glass matrix, or some Ge–O^-, or Ge–OH bonds on the surface are formed. As the E_g^{opt} of oxides and hydroxides is larger than that of sulfides and selenides, E_g^{opt} is shifted towards shorter wavelengths. ≡Ge–O–Ge≡, Ge–O^- or Ge–OH bonds are relatively strong, and, consequently, their formation is mostly irreversible.

Crystallization

The absorption of light with photon energy near to E_g^{opt} can result in weakening of chemical bonds [16] (lower bonding order due to electrons in anti-bonding orbitals [109]), in possible bonds breaking, which can facilitate structural changes and start nucleation and crystal growth. From the thermodynamic point of view, the light supplies the energy for overcoming energy barriers of nucleation and kinetic barriers for crystal growth. Optically induced crystallization was observed in many amorphous systems (Se, S, Se–Te, Sb–S, Ge–Sb–S–Te, Ge–Se, Ge–Sb–S, Ge–Sb–Te, Ge–In–Te, $GeSb_2Te_5$, $Ag_{10}In_4Sb_{58}Te_{28}$ [1, 3, 6, 8, 16, 21, 22, 57, 84, 85, 95–97] etc.), mostly in materials which form unstable glasses.

The time necessary for optically induced irreversible crystallization of thin films can be very short ($\sim 10^{-9}$ s). The effect has been applied in optical memories [3, 21, 57].

2.2.2 Reversible Photo-Induced Changes

The structure and physico-chemical properties of AGC can also be changed reversibly (crystallization–amorphization, vectorial effects, non-linear and other electronic effects, changes of optical transmittivity and reflectivity, absorption edge shift [1, 6, 23, 24, 32, 42, 60], index of refraction [48–50, 58], hardness and fluidity [15, 59], volume [71, 83], reactivity [28, 29,

34, 39, 42, 71], etc.). Reversible PE include also defect formation and annihilation, changes of chemical bonds statistics, optomechanical effects, [1, 3, 6, 23, 24, 26, 42, 43, 60, 61, 72]. Usually, the reversible processes are observed in bulk glasses and well-annealed films. The original state before exposure can be restored after relaxation, or after their treatment (annealing at the glass-transition temperature, T_g, exposure to light with lower photon energy or intensity [23, 24, 48, 51, 91]). When non-polarized light is used for exposure, the final state of the exposed material is also optically isotropic.

The chemically simplest system, in which the small stable reversible PC of structure and properties were observed, is amorphous selenium [72, 75]. The photo-induced transformation can proceed via changes of Se_8 rings to Se_n chains, by their reorientation, by change of the polymerization level, or by defect formation. An unambiguous explanation of PE in Se is still lacking. The reversible changes were also found most of binary, ternary and more complex chalcogenide systems.

Changes of Structure, Photodarkening, and Photobleaching

The exposure of AGC generally causes darkening. Reports on reversible photobleaching are rare [68]. Reversible photodarkening can also be seen in powdered glasses, where the effect is more pronounced than in massive samples [46, 51].

Many models of reversible PE have been proposed. Some of them are phenomenological (configuration coordinate approach), some are purely electronic, others involve bond switching and atom movement. These models have already been discussed and reviewed more than once (see e.g., [1, 6, 7, 26, 33, 41, 42, 53, 54, 58, 60, 69, 81, 86, 107]).

In the phenomenological configuration coordinate model, the adiabatic potential has two minima (double-wells) in the ground state with different energies of the wells. Optical excitation transfers the system to an excited state and, after relaxation, the system overcomes the potential barrier and ends up to the second potential well with a higher energy.

It has been suggested [7, 23, 24, 43, 48, 51] that (at least in some binary and ternary chalcogenides), the exposure changes the bond distribution (photolytic reaction) according to Eq. (2.1). The shift of the reaction (Eq. (2.1)) towards the left-hand side can be described by increasing homogenization (the system is approaching the chemically ordered model of AGC), the shift of equilibrium towards the right-hand side can be ascribed to the increased disorder and the system is shifted towards a random covalent network model. The photolytic reaction (Eq. (2.1), formation of As–As and S–S bonds) in the As–S system can proceed either directly or via the formation of self-trapped excitons [29, 69, 81]. The bonds between the like atoms remain embedded in glassy matrix without any phase separation. In the As–S system, the excess As–As bonds are apparently behind the shift of the absorption edge (photodarkening), because a similar shift of the absorption edge can be obtained in bulk glasses of the As–S system by increasing the As content without any exposure (Fig. 2.7) [51]. A similar process proceeds in thin As–S–Ga films [7]. It should be noted that in many papers (e.g. in [61]), a result of Myers and Felty [98] is cited, which states that the overstoichiometry of both S and As increases the optical gap of the As_2S_3 glasses. Our results, however, demonstrated a different behavior, namely, the gap decreased when excess As was added and new As–As bonds were formed (Figs. 2.1, 2.2 and 2.7), which is similar to photodarkening. In broader concentration ranges (e.g. in As–Se with high content of As, As_4Se_4 or As_nSe_m particles can be formed and the shift of E_g becomes more complex.

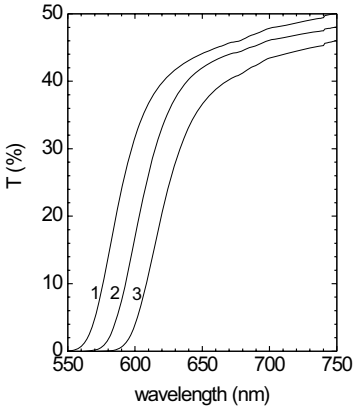

Figure 2.7: Optical transmittance of bulk glasses of the As–S system. (1) $As_{38}S_{62}$; (2) $As_{40}S_{60}$; (3) $As_{42}S_{58}$. Thickness of the samples $d = 2.45$ mm.

The processes described by Eq. (2.1) require changes of atomic positions and proceed more easily in materials with a larger free volume [27, 28].

Another type of photochemical reaction, namely PC of coordination of individual atom, can probably also be found in AGC, e.g.

$$2\mathrm{MX}_n \Leftrightarrow \mathrm{MX}_{n+y} + \mathrm{MX}_{n-y}, y \leq (\sim 0.03-0.1) \tag{2.9}$$

Here again, the left-hand side represents the state closer to the thermodynamic equilibrium, and MX_{n+y} and MX_{n-y} represent over- and under-coordinated atoms of metal or metalloid, respectively. The changes of the coordination numbers due to exposure have been found in many chalcogenides [1], e.g. in GeS_2 and $GeSe_2$ [99].

The model based on reactions described by Eqs. (2.1) and (2.9) is supported in the As–S system by following facts:

- It explains the reversible shift of the absorption edge by a change of the density of As–As bonds; glasses with a larger As content also possess a smaller band gap (Fig. 2.7).
- The amplitude of the Raman band with maximum near 235 cm^{-1} is reversibly increased by exposure of the annealed samples and decreased by their annealing. This band can be assigned to the vibrations of As–As bonds embedded in a glassy matrix but not as a part of As_4S_4 molecules [7, 23, 24, 41]. The intensity of this band in bulk As–S glasses increases with increasing As content (Figs. 2.1 and 2.2 [7, 51]).

While the two issues mentioned above strongly support the model of photo-induced bonds redistribution or photochemical reactions presented earlier, we also wish to mention two more factors which support any model involving changes of atomic structure:

- The reversible PE is strong in thin films, weaker in powdered bulk glasses [7, 41, 42, 51] and relatively weak in bulk samples. This behavior is apparently connected with disorder

of AGC. The increasing disorder and increasing free volume allow the movement of atoms. This makes any structural change easier and supports all models based on changes of atomic structure.

- The process of structural changes and of photodarkening is a dynamic one [23, 24, 67] (Fig. 2.8) as can be expected from Eq. (2.1). An increase in intensity of exposing light moves the equilibrium of Eq. (2.1) to the right-hand side (photodarkening) and vice versa. The values of the photo-induced shift of absorption edge, ΔE, decrease with temperature and vanish near the T_g [87]. Near the T_g, the atoms are relatively mobile and the system can approach the equilibrium state.

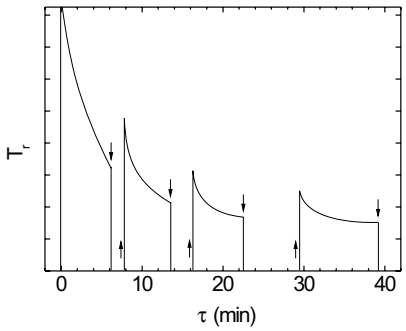

Figure 2.8: The change in the transmissivity of annealed As_2S_3 thin films during illumination at a constant intensity by 514.5 nm laser light. The vertical arrows correspond to the closing ($\downarrow$) and opening ($\uparrow$) of a shutter. The measurements were made at room temperature.

It can be objected that the exposure-induced shift of the absorption edge (photodarkening) has also been observed in a-S or a-Se, where no bonds among heteroatoms can be formed [60]. Some authors believe that the photostructural changes in a-Se can be explained by transformation of Se_8 rings into chain polymers Se_n and vice versa[1]. The chemical bonds in octagonal (Se_8) and chain structural units (Se_n) differ only slightly, octa-chalcogen molecules being cis-form, while chains are formed in trans-form. Very small differences in the bonding energies of these two forms result in only very small differences in IR and Raman spectra and their interpretation is therefore difficult. In liquid sulfur, the changes of optical transmission due to exposure are explained by destruction of S_8 rings. Charged polymeric diamagnetic chains are then created and are supposedly responsible for the photodarkening [64, 100].[2]

The exposure of annealed chalcogenides also reversibly changes the index of refraction The values are usually smaller than in the irreversible process and part of the changes may be due to the exposure-induced volume changes.

Until now, we have only discussed the changes in the short-range order range. The optically induced changes are not confined to the short-range order changes, but change also

[1] An alternative explanation encompasses photo-induced bond switching via photoexcitation of lone-pair electrons and formation of dynamic interchain bonds. This process has been extensively studied experimentally by in-situ EXAFS and ESR (Chapter 3) and by ab-initio simulations (Chapter 15). (Editor's comment)

[2] For photo-induced phenomena in liquid chalcogenides see also Chapter 12. (Editor's comment)

medium-range order as follows, for example, from the shift and lowering of the first sharp diffraction peak of As_2S_3 after exposure of the annealed samples [80]. This peak is typical for glasses and is associated with the medium-range order. Its decrease corresponds to a decrease of the medium-range order.

Changes of Thickness and Volume

Exposure of amorphous chalcogenides can cause photo-contraction or photo-expansion [1, 3, 6, 23, 24, 83]. The photo-contraction is mainly observed in obliquely deposited films (during the deposition, the angle between the vapor flux direction and substrate is $<90^\circ$, the largest effects were found for an angle $\sim 40^\circ$). Obliquely deposited films possess a column-like structure with a large space around the columns [101, 102]. After the exposure, the columns can collapse and atoms interact among themselves; a homogeneous film of higher density and lower thickness is then obtained. If the film with a columnar structure is annealed before exposure, or the vapors are deposited on a heated substrate, the photo-contraction is lowered or completely vanishes.

Photo-induced expansion has been found in many amorphous chalcogenides [1, 6, 24, 71, 83], when the exposure is made by light of wavelengths corresponding to the Urbach tail of the absorption edge of the amorphous chalcogenide. The effect can probably be explained also by bonds redistribution. In crystalline As_4S_n ($n = 3, 4$), and probably in the whole amorphous As–S system, As–As bonds are longer than As–S bonds (for example, in As_4S_4: As–As = 0.259 nm and As–S = 0.221 nm [115]). It is supposed [24] that the band-gap illumination facilitates rupture of a small fraction ($\sim 4-8\%$) of As–S bonds creating longer As–As bonds (Eq. (2.1)). The direction of chemical bonds is random in a-chalcogenides. Only the part of changes of the bond lengths that is perpendicular to the substrate plane, or the projection of length changes in this direction, can contribute to the layer thickness change ΔX. The contribution of individual bonds according to Eq. (2.1), $\Delta x = \Delta b \sin\varphi$ [24], where the change in the bond length per bond can be given by $\Delta b = {}^1\!/_2\,(b_{\text{As–As}} + b_{\text{S–S}}) - b_{\text{As–S}}$ and the φ is the angle between a given bond direction and the substrate plane. The mean value of the layer thickness changes as

$$\overline{\Delta X} = (\Delta b/\pi) \int_0^\pi \sin\varphi \, \mathrm{d}\varphi = 2\Delta b/\pi \tag{2.10}$$

As similar expression can be obtained for the average layer thickness $\overline{X}_0$ of original As–S bonds. For the bond lengths quoted above, and for $b_{S-S} = 0.22$ nm, one obtains [24] $\overline{\Delta X}/X_0 = 0.068$, for photolysis of all bonds. When compared with the experimentally found thickness increase (0.04 [13]), the fraction of As–S bonds changed by exposure = 6% of total can be evaluated. This value is in accordance with other results [6].

Tanaka [83] also observed the so-called giant photo-expansion. The glassy As_2S_3 illuminated by laser light increased its thickness $\sim$4%, which is 10 times more than in conventional photoexpansion [13, 24]. The photoexpansion is specific to AGC and has been proposed for applications.

Changes of Viscosity, Changes of Hardness

Optically induced changes of viscosity have been observed in several chalcogenides [6, 15, 50, 60, 66]. In a-Se, it was described as photomelting; the surface profile of bulk Se was changed due to exposure. The effect was demonstrated to be purely optical [66]. In As_2S_3 [15] it is supposed that light can excite and break van der Waals bonds and excite the tail states of the valence band electrons into the antibonding orbitals (conduction band) and lower the order of chemical bonds [109]. These bonds can then be broken. The glass becomes less interconnected and can flow. Sub-band-gap illumination also strongly decreases the viscosity of As_2S_3 glass, which is apparently caused by excitation of weaker or van der Waals bonds connecting some blocks in the glass structure [15]. After exposure, the bonds can be formed again restoring the original state and the viscosity then increases.

In As_2S_3 bulk glasses, PC of hardness were also observed. The samples were hardened by annealing and softened by exposure [6]. Analogously, the exposure decreases the viscosity [82]. Parallel to observed changes of hardness, reversible changes of E_g^{opt} (photodarkening) and of the index of refraction were observed. The effect in thin films is substrate dependent [6], which is probably due to different coefficients of dilatation of individual substrates.

Crystallization and Amorphization

The exposure of some AGC can induce their crystallization, especially for unstable glasses and films with composition close to the borders of the glass-forming region as was mentioned above.

In some cases, the reverse process was observed, namely the exposure-induced amorphization of crystalline samples below their melting point. The effect was first observed in films of $As_{50}Se_{50}$ [61, 62]. The process is athermal, reversible and its nature is not fully understood.

Photo-induced amorphization was also found in powder of crystalline As_2S_3 [37]. The amorphization proceeded also when the samples were exposed at low temperatures (36 K, Fig. 2.9 [37]); the process is athermal. As the preparation of As_2S_3 crystals from their melt is an extremely difficult task and even several months of annealing of As_2S_3 glass at temperatures close to its T_g does not crystallize the glass, it can be supposed [37] that the difference between the Gibbs free energy of crystals and glasses (ΔG) is very small. Even more, the As_2S_3 crystals are very soft with a layered structure and their powdering creates a large amount of defects. The density of defects in powdered crystalline As_2S_3 can be so high that its value of G becomes even closer to the value of G of the glassy state. The kinetic effect can also play a role; the rate of transformation of crystals to non-equilibrium amorphous state could be higher than that from the amorphous to crystalline state.

2.3 Applications

The AGC are transparent in the near- and mid-infrared regions of the spectrum ($\sim 0.5-10$ μm for sulfides, $0.8-12$ μm for selenides, up to 20 μm for tellurides) and have been applied as optical materials in this region (lenses, coatings, prisms, plates, filters). The refractive index of chalcogenides is larger (typically $2.2-2.9$) than that of silica and silicates; chalcogenides can match with high refractive index materials, such as Si, GaAs, ZnSe, InSb and others. Many

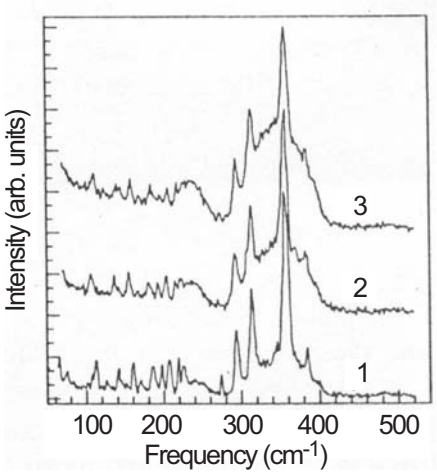

Figure 2.9: Raman spectra for As_2S_3 (orpiment) at $T = 36$ K, excited by a Kr laser ($\lambda = 568.2$ nm): (1) $I = 10$ mW ($\sim$1 W/cm^2); (2) $I = 30$ mW ($\sim$3 W/cm^2); (3) $I = 80$ mW ($I \sim 8$ W/cm^2). Relatively intense bands near 340 cm^{-1} and 231 cm^{-1}, corresponding to AsS_3 pyramid vibrations and As–As vibrations, respectively, can be seen for curve 3. The narrow bands from crystalline As_2S_3 are of low intensity.

AGC can be obtained using simple technologies; in many cases they do not need high purity starting materials, and they also manifest relatively large resistance to hard radiation.

The PC of properties of amorphous chalcogenides have been applied in xerography, as photovoltaic and photoconductive elements, in laser printers, light-sensitive camera tubes (Saticon, etc.), high-speed optical switches, in X-ray radiography (see, e.g. [1, 3, 6, 57, 60, 89, 116]). The important PE, found in rare-earth doped chalcogenides concerns their photoluminescence in the visible, near-IR and mid-IR regions, where they can be applied as light amplifiers, lasers, sensors etc.

A very important application of PE in chalcogenide amorphous films is connected with their crystallization (optical data storage, e.g. [1, 3, 6, 21, 88] and papers cited therein). The process was initially suggested by Ovshinsky [8,9,21,57,60] and has been successfully applied to optical disc production. At the moment of writing, the maximum density in commercially available phase-change discs is 4.7 GB/disc but considerably higher density discs are expected to reach the market in the near future. A detailed description of the use of chalcogenides in optical storage is given elsewhere in this book.

Another major application of PE concerns photoresists. Photoresists of large size (areas) can be prepared from amorphous chalcogenides and very high resolution of 5000–10000 lines/mm and sensitivity $\sim$0.1 J/cm^2 can be obtained [43,44,75]. The sensitivity of PE can be increased by several orders of magnitude when short pulses are used (see, e.g. [63] and papers cited therein) instead of continuous-light exposure. The resolution capability can be further increased to the sub-wavelength region by the near-field optical technique [70]. Nano-writing is then possible and can be applied for holographic recording [76]. In this case, the absorption

of light in band tails in the optical gap plays a role. Such tails in films and glasses are formed mainly by fluctuations in bond angles and lengths. The effect under these conditions has some different features: the changes of local structure, optical transmittivity, and index of refraction are not permanent and the thickness of the films is not changed.

Using chalcogenide photoresists, optical elements, optical circuits and diffractive gratings can be produced by holographic or electron beam lithography techniques. They have found wide application in various optical and optoelectronic devices and elements (see, e.g. [1, 3, 6, 60, 76, 77] and papers cited therein). The diffraction efficiency of gratings can be very high.

For some pattern production, e.g. for IR gratings, deep etching is necessary. Sharp edges with a height up to $5 - 10$ μm were obtained (see, e.g. [73]). The etching solutions for As chalcogenides are based on alkylamines or on other alkaline solutions; pure, or solutions containing surface-active additives have been applied [73]. Solutions containing H_2O_2 are used for Ge-chalcogenide based photoresists [71]. The contrast obtained after etching can be very high. It can be also very gentle or low, and gray tones or gray scale can be achieved by variation of exposure and etching conditions [63].

The exposure can also change the volume and surface profile. Gratings and micro-lenses or micro-lens arrays can be fabricated from photoresists of As–Se and As–S systems [15, 44, 81–83, 90] by exposure through a mask with microhole(s). Lenses or cylindrical microlenses with focal lengths several tens of μm and diameters of several microns can be produced. Such microlenses can be applied in CCD cameras, imaging machines, optical communication and in IR technology.

2.4 Summary

Amorphous chalcogenides and glasses exhibit a large number of optically induced phenomena resulting in changes of structure and physico-chemical properties. Some of them, together with the corresponding models, were described in this chapter. Some effects are still not fully understood in spite of the fact that they have already been applied or are potentially applicable in optoelectronics, optical memories, optical elements and circuits production.

Acknowledgments

The study was supported by project LN00A028 of the Ministry of Education of the Czech Republic and by project AV 0Z 4050913 of the Czech Academy of Sciences, Prague, which is gratefully acknowledged.

References

[1] H. Fritzsche, in P. Boolchand (Ed.), Insulating and Semiconducting Glasses, World Scientific Publ., Singapore, 2000, pp. 653–690.

[2] F.A. Kröger, The Chemistry of Imperfect Crystals, Vol. 3, North-Holland Publ. Co., Amsterdam, 1974, pp. 216–230.

[3] M. Mitkova, in P. Boolchand (Editor), Insulating and Semiconducting Glasses, World Scientific Publ., Singapore, 2000, pp. 813–843.
[4] A.W. Adamson and P.D. Flaischauer: Concepts of Inorganic Photochemistry, J. Wiley, New York, 1975.
[5] R. Roberts, R.P. Oullette, M.M. Muradaz, R.F. Cozzens, P.N. Cheremisinoff: Applications of Photochemistry, Technomic Publ. AG, Basel, 1984.
[6] M.A. Popescu: Non-Crystalline Chalcogenides, Kluwer Academic Publ., Dordrecht, 2000, pp. 209–292.
[7] M. Frumar, Z. Cernosek, J. Jedelsky, B. Frumarova, and T. Wagner, J. Optoelectron. Adv. Mat. **3**, 177 (2001).
[8] S.R. Ovshinsky, J. Appl. Photographic Eng. **3**, 35 (1977).
[9] S.R. Ovshinsky, Phys. Rev. Lett. **21**, 1450 (1968).
[10] J.Z. Liu, and P.C. Taylor, Phys. Rev. Lett. **59**, 1938 (1987); Phys. Rev. B **41**, 3163 (1990).
[11] V. Lyubin, T. Tada, M. Klebanov, N.N. Smirnova, A.V. Kolobov, and K. Tanaka, Materials Lett. **30**, 79 (1997).
[12] H. Hamanaka, K. Tanaka, A. Matsuda, and S. Iizima, Solid State Commun. **19**, 499 (1976).
[13] H. Hamanaka, K. Tanaka, and S. Iizima, Solid State Commun. **23**, 63 (1977).
[14] J.S. Berkes, S.W. Ing, and W.J. Hillegas, J. Appl. Phys. **42**, 4908 (1971).
[15] H. Hisakuni, and Ke. Tanaka, Science **270**, 975 (1995).
[16] J. Feinleib, J.P.D. Neufville, S.C. Moss, and S.R. Ovshinsky, Appl. Phys. Lett. **18**, 254 (1971).
[17] S.A. Keneman, Appl. Phys. Lett. **19**, 205 (1971).
[18] M. Janai, and P.S. Rudman, in Proc. 5th Internat. Conf. on Liq. and Amorphous Semicond., Eds. J. Stuke and W. Brenig, Taylor and Francis, London, 1974, p. 425.
[19] M. Janai, Phys. Rev. Lett. **47**, 726 (1982).
[20] J. Dresdner, and G.B. Stringfellow, J. Phys. Chem. Solids **29**, 303 (1968).
[21] T. Ohta, J. Optoelectron. Adv. Mat. **3**, 609 (2001).
[22] M. Frumar, H. Tichá, M. Vlček, J. Klikorka, and L. Tichý, Czech. J. Phys. **B31**, 441 (1981).
[23] M. Frumar, A.P. Firth, and A.E. Owen, J. Non-Cryst. Solids **59-60**, 921 (1983).
[24] M. Frumar, A.P. Firth, and A.E. Owen, Phil. Mag. **B50**, 483 (1984).
[25] L. Tichý, A. Tříska, H. Tichá, and M. Frumar, Phil. Mag. **B54**, 219 (1986).
[26] M. Frumar, Czech. J. Phys. A **37**, 574 (1987) (in Czech).
[27] M. Vlček, M. Frumar, and A. Vidourek, J. Non-Cryst. Solids **90**, 513 (1987).
[28] M. Vlček, and M. Frumar, J. Non-Cryst. Solids **97-98**, 1223 (1987).
[29] M. Frumar, M. Vlček, and J. Klikorka, Reactivity of Solids, **5**, 341 (1988).
[30] M. Frumar, M. Vlček, and T. Wágner, in V.V. Khiminets (Ed.), Physical Phenomena in Non-crystalline Semiconductors. Proc. Internat. Conf. on Non-Crystalline Semiconductors 89, Vol. II, Uzghorod, 1989, Acad. Nauk USSR, Gos. Univ. Uzghorod, 1989, p.161.

[31] M. Vlček, M. Frumar, M. Kubový, and V. Nevšímalová, J. Non-Cryst. Solids **137-138** 1035 (1991).

[32] K. Petkov, M. Vlček, and M. Frumar, J. Mat. Sci. **27**, 3281 (1992).

[33] M. Frumar, and L. Tichý, in J. Šesták, Z. Strnad, A. Tříska (Editors), Advanced Technologies and Materials, Academia, Prague, 1993, pp. 391–406, in Czech.

[34] M. Frumar, M. Cvrkal, M. Vlček, and T. Wágner, J. Non-Cryst. Solids, **164-166**, 1243 (1993).

[35] M. Frumar, M. Vlček, and T. Wágner, Chem. Listy, **87**, 78 (1993) (in Czech).

[36] M. Vlček, J. Prokop, and M. Frumar, Int. J. Electronics **77**, 969 (1994).

[37] M. Frumar, A.P. Firth, and A.E. Owen,. J. Non-Cryst. Solids, **192-193**, 447 (1995).

[38] M. Vlček, C. Raptis, T. Wágner, A. Vidourek and M. Frumar, J. Non-Cryst. Solids, **192-193**, 669 (1995).

[39] M. Frumar, M. Vlček, and T. Wágner, J. Non-Cryst. Solids, **221**, 27 (1997).

[40] M. Frumar, M. Vlček, Z. Černošek, and T. Wágner, J. Non-Cryst. Solids, **213-214**, 215 (1997).

[41] M. Frumar, Z. Polák, Z. Černošek, M. Vlček, and B. Frumarová, in Physics and Applications of Non-crystalline Semiconductors in Optoelectronics, Proc. NATO Workshop, Kishinau, 1996 (M. Bertolotti, A. Andriesh, Eds.), Kluwer Acad. Publ., Dordrecht, 1997, pp. 123–139.

[42] M. Frumar, Z. Polák, Z. Černošek, B. Frumarová and T. Wágner, Chem. Papers, **57**, 310 (1997).

[43] C. Raptis, I.P. Kotsalas, D. Papadimitriou, M. Vlček, and M. Frumar, in M. Bertolotti, A. Andriesh (Eds.), Physics and Application of Non-Crystalline Semiconductors in Optoelectronics, Kluwer Acad. Publ., Dordrecht, 1997, pp. 291–305.

[44] M. Vlček, K. Nejezchleb, T. Wágner, M. Frumar, Mil. Vlček, A. Vidourek, and P.J.S. Ewen, Thin Solid Films **317**, 228 (1998).

[45] P. Kotsalas, C. Raptis, D. Papadimitriou, M. Vlček, and M. Frumar, J. Non-Cryst. Solids, **226**, 910 (1998).

[46] M. Frumar, Z. Polák, and Z. Černošek, J. Non-Cryst. Solids, **256-257**, 105 (1999).

[47] M. Frumar, J. Jedelský, Z. Polák, and Z. Černošek, Thin Solid Films, **343-344**, 488 (1999).

[48] Z. Polák, M. Frumar, and B. Frumarová, Thin Solid Films, **343-344**, 484 (1999).

[49] R. Prieto-Alcon, E. Marquez, J.M. Gonzáles-Leal, R. Jiménez-Garay, A.V. Kolobov, and M. Frumar, Appl. Phys. **A68**, 653 (1999).

[50] A.V. Kolobov, H. Oynagi, K. Tanaka and Ke. Tanaka, Phys. Rev. B **50**, 726 (1997).

[51] M. Frumar, Z. Polák, J. Jedelský, Z. Černošek, and B. Frumarová, in M.F. Thorpe and L. Tichý (Eds.), Properties and Applications of Amorphous Materials, Kluwer Acad. Publ., Dordrecht, 2001, pp. 321–328.

[52] Ke. Tanaka, J. Optoelectron. Adv. Mat. **3**, 189 (2001).

[53] K. Shimakawa, A. Kolobov, and S.R. Elliott, Adv. Phys. **44**, 475 (1995).

[54] H. Fritzsche, Phys. Rev. B **52**, 15854 (1995).

[55] I.P. Kotsalas, D. Papadimitriou, C. Raptis, M. Vlcek, and M. Frumar, J. Non-Cryst. Solids **226**, 85 (1998).

[56] S.A. Solin, and G.V. Papatheodorou, Phys. Rev. B **15**, 2087 (1977).

[57] S.R. Ovshinsky, in P. Boolchand (Ed.), Insulating and Semiconducting Glasses, World Scientific, Singapore, 2000, pp. 729–779.

[58] S.R. Elliott, J. Non-Cryst. Solids **81**, 71 (1986).

[59] V.M. Lyubin, in A.C. Kartuzhanskyi (Ed.), Neserebrjanye Fotograficheskie Processy, Khimiya, Leningrad, 1988, p. 145 (in Russian).

[60] A.V. Kolobov, and Ka. Tanaka, in H.S. Nalwa (Ed.) Handbook of Advanced Electronic and Photonic Materials and Devices, Vol. 5, Academic Press, San Diego, 2001, pp. 47–85.

[61] S.R. Elliott, and A.V. Kolobov, J. Non-Cryst. Solids **128**, 216 (1991).

[62] A.V. Kolobov, V.A. Berstein, and S.R. Elliott, J. Non-Cryst. Solids **150**, 116 (1992).

[63] V.M. Lyubin, S. Rosenwaks, V.P. Eisemberg and M. Bonevich, J. Vac. Sci. Tech. **B15**, 823 (1997).

[64] Z. Ogorelec, and A. Tonejc: Mat. Letters **42**, 81 (2000).

[65] L. Tichý, H. Tichá, P. Nagels, and R. Callaerts, J. Non-Cryst. Solids **240**, 177 (1998).

[66] V.V. Poborchii, A.V. Kolobov, and K. Tanaka, Appl. Phys. Letters **74**, 215 (1999).

[67] A. Ganjoo and K. Shimakawa, J. Optoelectron. Adv. Mat. **3**, 221 (2001).

[68] S.H. Messaddeq, M. Siu Li, D. Lezal, S.H. Ribeiro, and Y. Messaddeq, J. Non-Cryst. Solids **284**, 282 (2001).

[69] S.R. Elliott, Physics of Amorphous Materials, 2nd Edition, Longman, Essex, 1990.

[70] Y. Isbi, S. Sternklar, E. Granot, V. Lyubin, M. Klebanov, and A. Lewis, Optics Commun. **171**, 219 (1999).

[71] R. Loeffer, T. Schwarz, H. Sautter, and D. Lezal, J. Non-Cryst. Solids **232-234**, 526 (1998).

[72] A.V. Kolobov, B.T. Kolomiets, O.V. Konstantinov, and V.M. Lyubin, J. Non-Cryst. Solids **45**, 335 (1981).

[73] S. Noach, M. Manevich, M. Klebanov, V. Lyubin, and N.P. Eisenberg, Proc. SPIE, **3778**, 158, (1999)q.

[74] H. Hisakuni, and Ke. Tanaka, Optics Lett., **20**, 958 (1995).

[75] A.V. Kolobov, and Ke. Tanaka, Fiz. Tekh. Poluprovodnikov (Phys. Tech. Semiconductors), **32**, 899 (1998).

[76] A. Ozols, N. Nordman, O. Nordman, and P. Riihola, Phys. Rev., Condens. Matter, **B55**, 14216 (1997).

[77] J. Teteris, M.J. Reinfelde, Neorg. Materialy **22**, 584 (1986) (in Russian).

[78] K. Petkov, M. Sachatchieva, and J. Dikova, J. Non-Cryst. Solids **101**, 37 (1988).

[79] J.P. Neufville, S.C. Moss, and S.R. Ovshinsky, J. Non-Cryst. Solids **13**, 191 (1973/74).

[80] K. Tanaka, Appl. Phys. Lett. **26**, 243 (1975).

[81] Ke. Tanaka, Rev. Solid State Sci. **4**, 641 (1990).

[82] H. Hisakuni, and K. Tanaka, Appl. Phys. Lett. **65**, 2925 (1994).

[83] Ke. Tanaka, in A. Andriesh, and M. Bertolotti (Eds.) Physics and Applications of Non-Crystalline Semiconductors in Optoelectronics, Kluwer Acad. Publ., Dordrecht, 1997, pp. 31–44.
[84] V.M. Lyubin, M. Klebanov, M. Mitkova, and T. Petkova, J. Non-Cryst. Solids **227**, 739 (1998).
[85] A.V. Kolobov, and J. Tominaga, J. Optoelectron. Adv. Mat. **4**, 679 (2002).
[86] K. Shimakawa, and S.R. Elliott, Phys. Rev. **B38**, 12479 (1988).
[87] K. Tanaka, J. Non-Cryst. Solids **59-60**, 926 (1983).
[88] T. Ohta, Private communication (2002).
[89] J. Teteris, J. Optoelectron. Adv. Mat. **4**, 687 (2002).
[90] J. Turunen, in H.P. Herzig (Ed.), Micro-Optics, Elements Systems and Applications, Taylor and Francis, London, 1998.
[91] M. Kastner, D. Adler, and H. Fritzsche, Phys. Rev. Lett. **37**, 1504 (1976).
[92] M. Kastner, and H. Fritzsche, Phil. Mag. **B37**, 199 (1978).
[93] M. Frumar, J. Jedelský, B. Frumarová, and T. Wágner, J. Non-Cryst. Solids (2003), in press.
[94] L. Tichy, H. Ticha, M. Vlcek, J. Klikorka, and K. Jurek, J. Mat. Sci. Lett. **5**, 1125 (1986).
[95] I.A. Paribok-Alexandrovitch, Fiz. Tverd. Tela **11**, 2019 (1969).
[96] T. Fukaya, J. Tominaga, T. Nakano, and N. Atoda, Appl. Phys. Lett. **75**, 3114 (1999).
[97] J. Tominaga, H. Fuji, A. Sato, T. Nakano, and N. Atoda, Jpn. J. Appl. Phys., Part 1, **39**, 957 (2000).
[98] M.B. Myers and E.J. Felty, Mater. Res. Bull. **2**, 715 (1967).
[99] L.F. Gladden, S.R. Elliott, and G.N. Greaves, J. Non-Cryst. Solids, **106**, 189 (1988).
[100] M.F. Kotkata, J. Mater. Sci., **27**, 4858 (1992).
[101] S. Rajagopalan, K.S. Harshavardhan, L.K. Malhorta and K.L. Chopra, J. Non-Cryst. Solids **50**, 29 (1982).
[102] Y. Kuzukawa, A. Ganjoo, and K. Shimakawa, Phil. Mag. **B79**, 249 (1999).
[103] J. Tominaga, H. Fuji, A. Sato, T. Nakano, T. Fukaya, and N. Atoda, Jpn. J. Appl. Phys., **37**, L1323 (1998).
[104] T. Nagase, S. Ashida, and K. Ichihara, Jpn. J. Appl. Phys., Part 1, **38**, 1665 (1999).
[105] K. Hirota, and G. Ohbayashi, Jpn. J. Appl. Phys., **37**, 1847 (1998).
[106] K. Sakai, T. Uemoto, H. Yokoyama, A. Fukuyama, K. Yoshino, T. Ikari, and K. Maeda, J. Non-Cryst. Solids, **266-269**, 933 (2000).
[107] K. Shimakawa, and A. Ganjoo, J. Optoelectron. Adv. Mat. **3**, 167 (2001).
[108] R. Zallen, The Physics of Amorphous Solids, John Wiley, New York, 1983.
[109] F.A. Cotton, G. Wilkinson, C.A. Murillo, and M. Bochman, Advanced Inorganic Chemistry, 6th Edition, John Wiley, New York, 1999.
[110] P.V. Sen, and M.F. Thorpe, Phys. Rev. B **15**, 4030 (1977).
[111] D. Linke, Proc. Internat. Conf. Amorph. Semiconductors '78, Pardubice Czechoslovakia, 1978, Vol. I, Inst. Phys. Czechosl. Acad. Sci., Prague, 1978, p.78.
[112] H. Spandau, and F. Klanberg, Z. Anorg. Allgem. Chem. **295**, 292 (1958).

[113] S.H. Wemple, and M. DiDomenico, Phys. Rev. B **3**, 1338 (1971).

[114] S.H. Wemple, J. Chem. Phys. **67**, 2151 (1977).

[115] E.J. Porter, and G.M. Sheldrick, J. Chem. Soc., Dalton Trans., 1347 (1972).

[116] S.O.Kasap, and J.A. Rowlands, in P. Boolchand (Ed.), Insulating and Semiconducting Glasses, World Scientific, Singapore, 2000, pp. 781–811.

3 Short-, Medium- and Long-Range-Order Structural Transformations in Amorphous Semiconductors

Eugenia Mytilineou and Alexander Kolobov

This chapter reviews a wide variety of metastable phenomena induced by illumination in amorphous chalcogenides and compares them with those in a-Si:H in an attempt to point out similarities and differences between two very important classes of amorphous semiconductors. The light-induced effects scale from the creation of metastable point defects that is common to both classes of materials, to long-range order structural rearrangements that are a characteristic property of amorphous chalcogenides and are facilitated by the presence of lone-pair electrons of the chalcogen atoms and also by the flexibility of the lattice.

3.1 Introduction

One of the characteristic properties of an amorphous lattice is the existence of a wide range of effects when exposed to light. Depending on the stability of the photoinduced changes they can be permanent, metastable (when they completely reverse upon heating) or transient (when they reverse simply with the cessation of the illumination). Point or coordination defects are induced rather easily when a photon producing an electron–hole pair is absorbed. As the illumination time increases, a considerable amount of energy, derived from the non-radiative recombination of the exited carriers, is accumulated over the lattice causing bond rearrangements around the photo-induced defects and further movements of atoms that produce medium- (MRO) and/or long-range-order (LRO) structural changes. As the light affects a large fraction of atoms and locations, the induced movement of atoms and bond rearrangement produce a light-soaked structure that is characterized by higher energy and lower MRO than that in the annealed state. The temperature at which the sample is annealed or is exposed to illumination is very important and the final stabilized configuration is a state in *dynamic equilibrium* that depends also on the intensity and/or the wavelength of the excitation light. Similar light-induced effects are not observed in the crystalline counterparts, suggesting that the light-induced structural rearrangement is an *intrinsic property of the amorphous state* [1].

In the annealed state in the dark a low concentration of defects ($\sim 10^{15}$–10^{16} cm^{-3}) exists in the mid-gap of amorphous semiconductors. These defects are called intrinsic, native, or deposition defects in order to distinguish them from the metastable light-induced defects. The equilibrium concentration of the dangling bonds strongly depends on the preparation conditions (particularly in hydrogenated amorphous silicon, a-Si:H) and the annealing temperature. Extended experimental studies of the various light-induced phenomena showed that they are created through two different processes: a *fast process* that is connected with the creation of

individual point defects and a *slow process* that is related to the lattice rearrangements (M- or LRO effect) [2]. It is believed that the dominant metastable coordination defects (fast process) in a-Si:H, are singly occupied dangling bonds, D^0, while in the chalcogenide alloys they are pairs of charged dangling bonds, D^- and D^+.

A slower stabilization process accompanies the formation of the point defects, such as hydrogen diffusion in a-Si:H or lattice rearrangements in the chalcogenide semiconductors. The latter class of materials exhibits additionally a variety of medium- and long-range-order isotropic or anisotropic metastable photo-induced effects that are not necessarily directly related to the creation of charged defects. These effects seem to be due to a combination of the unique properties of the lone-pair electrons of the chalcogen elements and high flexibility of the lattice. For a detailed review see [3].

In the following we give a brief review of light-induced metastable effects that produce short-, medium- and long-range-order metastable structural changes in a-Si:H and in amorphous chalcogenide semiconductors.

3.2 Short-Range-Order (SRO) Effects

In this section we refer to the light-induced effects that are related to the creation of point defects in amorphous chalcogenides and a-Si:H and are completely restored upon thermal annealing or proper illumination. The metastable defects induced by prolonged illumination at low temperature cause an increase in the mid-gap absorption and in the electron spin density; they may also cause a decrease in the photoconductivity and fatigue of photoluminescence intensity (PL). In accordance with the discussion in the previous section, only the creation of the dangling bonds and of under- (over-)coordinated sites will be considered as an SRO effect. It should be kept in mind that some MRO structural effects may also accompany the defect creation as time proceeds.

The modifying effect of light was first studied in amorphous chalcogenide glasses. In the early 1970s it was observed that at low temperatures (<150 K) and under prolonged band-gap illumination a wide mid-gap absorption band was induced [4]. The states responsible for this absorption disappear upon low temperature annealing (above 150 K) or as a result of subsequent sub-band illumination. Exposure to light also produces a red shift of the absorption edge (photodarkening, PD). However, in order to anneal the photodarkening much higher temperatures, namely close to the glass transition temperature, are needed [5].

Intense illumination was found to decrease the efficiency of a-Si:H solar cells (the Staebler–Wronsky (SW) effect [6]) which was related to the observed decrease of the photoconductivity and the increase, by about one order of magnitude, of the mid-gap absorption and of the electron spin resonance (ESR) signal. The original parameters were restored after annealing at temperatures close to the deposition temperature. The magnitude of the SW effect is an important device parameter of the film and depends strongly on the preparation conditions, the geometry of the deposition chamber and the gas mixture used.

In contrast to glasses, direct measurements of the mid-gap optical absorption in thin films are prohibited by the very low absorption of the samples in this energy range, so techniques such as the constant photocurrent method (CPM) [7, 8], photoacoustic spectroscopy (PAS) [9] and photothermal deflection spectroscopy (PDS) [10] have been developed for measuring the mid-gap absorption of thin films.

In order to apply these techniques, e.g. CPM, to thin chalcogenide films, one has to make sure that the assumptions made for a-Si:H are also valid for other films. One of the main assumptions of CPM is that the photogeneration quantum efficiency remains constant in the energy range of the measurements. Although this requirement is not satisfied for a-Se [11], it can be fulfilled under certain experimental conditions for binary chalcogenide alloys such as stoichiometric As_2Se_3 [11–13] and As_2Te_3 [12] or mixed alloys with As and Si or Ge [14].

Figure 3.1a shows the PDS results for two glow-discharge deposited a-Si films before and after prolonged illumination. Both films were deposited in the same chamber; the sample H1 is a device quality a-Si:H, while the sample F1 is an optimized a-Si:H:F film [15]. The results demonstrate that the saturated density of the light-induced defects is lower in the fluorinated sample than in the hydrogenated film, even though the initial density of defects is higher. In a pure a-Si:H film prepared under similar conditions to the fluorinated sample, the initial and the final defect density were also higher than those of the sample F1 [15]. One can also see that prolonged illumination of a-Si:H induces only the mid-gap-state density increase but no shift of the absorption edge occurs.

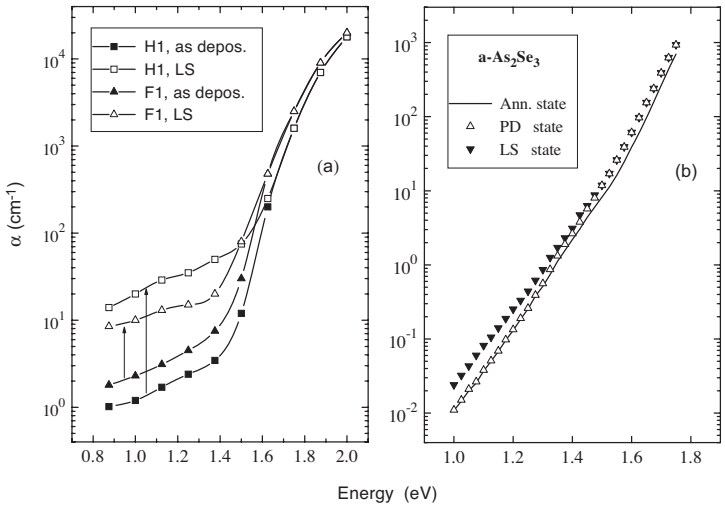

Figure 3.1: The effect of illumination on the gap states in amorphous semiconductors. (a) PDS spectra of device quality a-Si:H (H1) film and an optimized a-Si:H:F (F1) film before and after light soaking; (b) CPM spectra of a-As_2Se_3 sputtered film in three characteristic states during a light soaking cycle.

Figure 3.1b shows the CPM of annealed (at 150 °C) a-As_2Se_3 films measured at different times during prolonged illumination by 50 mW/cm^2 white light from a 100 W halogen lamp at room temperature [16]. It was found that, during the first 20 min of the illumination, the absorption edge is shifted to lower energies (photodarkening, PD) and only when this shift is saturated does the mid-gap absorption start to increase. Upon thermal annealing, the different phenomena are restored in the reverse order. First, the original defect density was completely restored at 120 °C and later, at 150 °C, the band edge was shifted back to its original value [16, 17]. These results indicate that the bond breaking process is absent at the

beginning of the illumination when the PD occurs. The bond breaking sets in only 20 min after the light is turned on and when enough *strain has been accumulated* in the lattice. In a-Si:H [17] a similar time delay in the creation of the metastable defect density is also observed, as will be discussed later.

We note that in most cases information about photo-induced defects in chalcogenides is mainly obtained from ESR and PL fatigue experiments performed at low temperatures as ESR active centers are not induced at $T > 250$ K. Under these circumstances, in most previous experiments the defects have been induced and detected *at low temperatures* from the very initial stages of illumination. The experiment described above was performed entirely at room temperature. It is reasonable then to assume that light soaking can only induce defects that are stable at higher temperatures, possibly charged VAPs, that do not manifest themselves either in ESR and PL fatigue or in mid-gap absorption. For this reason, short time (20 min) photo-excitation does not produce any detectable amount of defects responsible for the mid-gap absorption (or they may anneal instantaneously). It is possible that the strain, accumulated in the structure during the initial period of illumination, modifies the atomic adiabatic potentials, making possible the creation of defects that are stable at a higher temperature.

A study of the degradation of photocurrent and its relation with the metastable light-induced defects has been performed in both a-Si:H and a-As_2Se_3 films [17, 18]. For a-Si:H, it was found that the dependence of the photocurrent on the mid-gap defects density during an annealing cycle *does not* follow the same curve as during the light-soaking cycle. A characteristic hysteresis loop is then observed (Fig. 3.2a), in agreement with previous reports [19, 20]. In contrast to a-Si:H, the photocurrent of a-As_2Se_3 films seems to be a single-value function of the mid-gap defects density. The creation and the recovery of the light-induced defects as a function of the photocurrent are identical (Fig. 3.2b).

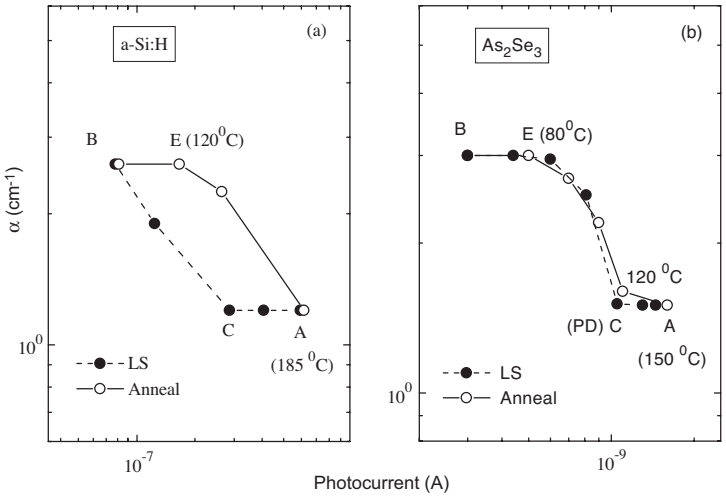

Figure 3.2: Mid-gap absorption as a function of the photocurrent during light soaking–annealing cycles: (a) in a-Si:H and (b) in a-As_2Se_3 films.

It is evident from Fig. 3.2 that in *both materials*, during the first minutes of the LS there is no creation of deep defects even though i_{ph} decreases (branch AC, Fig. 3.2). *The bond breaking process is absent at the initial stage of illumination*. The bond breaking sets in only after 20 min of light soaking, at room temperature, in both materials (branch CB, Fig. 3.2), indicating that at first, strained bonds and/or structural disorder are induced in the lattice and only later are the defects created when some highly strained bonds break, enhancing the sub-gap absorption. It has also been found that at the beginning of the illumination, the ratio of the capture coefficient to the free carrier mobility (c/μ) increases [18], by $\sim$86% in a-Si:H and by $\sim$30% in a-As_2Se_3, indicating that the *induced strain*, responsible for the increase of c, may cause the degradation of the i_{ph}. In a-Si:H, where extensive studies of the light soaking effects have been performed, many researchers agree that the metastable defects show capture cross-sections larger that the native defects [19, 21, 22]. In the case of a-As_2Se_3, we may suggest that the induced strain during the first 20 min of illumination is probably consumed by the structural modifications needed for the PD effect and thus the changes of i_{ph} and c/μ are smaller than those observed in a-Si:H. The localized absorption of the photon energy during the light-soaking increases the dihedral angles, bond length distortions and also in the chalcogenides increases the lone-pair interactions [23] while in the case of a-Si:H [2], it facilitates hydrogen diffusion. These atom rearrangements, even though do not create deep band-gap states, seem to be responsible for the increase of c and the degradation of i_{ph} at the beginning of light soaking (branch AC, Fig. 3.2).

Under illumination that is able to create free electron–hole pairs, a broad photoluminescence (PL) band appears in amorphous semiconductors close to the center of the energy gap. The shift from the absorption edge, the so-called Stokes shift, is determined by the strength of electron–phonon interaction. The intensity of the peak represents the number of radiative recombination centers present in the energy gap. For more details see a review [24]. At low temperatures and under prolonged bandgap illumination, the PL peak shows a strong decrease (fatigue), which indicates that illumination increases the density of the non-radiative recombination centers. The fatigue recovers upon heating or with exposure to IR radiation. The existence of the fatigue implies [24, 25] that after the excitation the recombination center (a charged defect) can acquire a new metastable configuration that is not suitable for luminescence, for example a D^0 center. According to this mechanism, the fatigue corresponds to a change in the occupancy of the recombination center that becomes ESR active, explaining the complimentary behavior of PL and ESR signals. At high temperatures these metastable effects are no longer present, but as a certain concentration of holes remains, transient effects may be expected. It was found that the intensity and wavelength of the illumination, as well as the temperature at which the illumination is performed, strongly influence the characteristics of the photoinduced defects. For a review, see [1]. It was also found that the duration of the illumination strongly affects the annealing properties of the centers.

Most chalcogenide alloys show a single PL peak and a single excitation peak. As exceptions we should mention a-As_2S_3 [26], where under certain illumination conditions changes in the position of the PL peak were observed, and some Ge sulfides [27] alloys with a narrow range of compositions close to the stoichiometric GeS_2 where, a double PL peak observed. It is worth mentioning that bulk a-As [12, 24, 25] shows a single PL, but a double excitation peak. In contrast, a-P – another group V elemental semiconductor [28] – exhibits a narrow single excitation peak and a single PL peak, similar to most chalcogenide alloys.

In a-Si:H two wide PL bands have been found independent of the preparation technique used [24,29]: the main band is at 1.3 eV and the second band at 0.9 eV. Their relative intensity depends on temperature, namely, the 0.9 eV peak dominates at room temperature while the 1.3 eV peak is stronger at low temperatures (2 K). The existence of two bands indicates that in a-Si:H two different recombination centers are induced. For both the 1.3 eV band of a-Si:H and the PL band of the chalcogenides were found to decay with two different characteristic times. In the chalcogenides the slow process (10^{-4} s) is the dominant one in steady-state experiments. Comparing the shape of dark- and light-induced ESR spectra with the decay of PL, and the induced optical absorption spectra of the chalcogenide glasses, it was suggested [30] that the fast process is due to excitation of pre-existing defects [31] while the slow decay is due to the creation of new centers [30].

ESR is a very sensitive probe for detecting singly occupied defects. Even though the chalcogenides show no ESR signal in the dark, after low temperature illumination with bandgap light, an ESR signal is induced (LESR) [30]. In a-Se, *in situ* LESR studies have found that two kinds of ESR centers were created *in pairs*. The two centers were identified as a singly coordinated dangling bond, C_1^0, and a triply coordinated defect, C_3^0. The C_3^0 center is less stable and is *converted* into a dangling bond at a temperature of $\sim$90 K. See refs. [32, 33] for more details.

In arsenic chalcogenides (As_2S_3 and As_2Se_3), low-intensity (<10 mW/cm^2) illumination creates two district LESR centers: a hole center localized on a p-orbital of a singly coordinated chalcogen atom and an electron center localized predominantly on an s–p hybridized orbital of a doubly-coordinated arsenic atom [34]. In contrast, high-intensity light (>100 mW/cm^2) induces in As_xS_{1-x} glasses [35] two types of centers, with different annealing behaviors. Each type of centers consists of two different defects. Type I centers anneal out at low temperatures (<180 K) while the type II centers anneal out at higher temperatures (<300 K). In general, centers that are induced with short-time or low-intensity illumination are annealed at lower temperatures than those induced by prolonged or high-intensity illumination, a fact that demonstrates the accumulative effect of the illumination. Type I centers constitute about 15% of the total ESR signal and are identified as a hole on a non-bonding 3p orbital of a sulfur atom (S_I) and an electron center localized predominantly on a s–p hybridized orbital of an arsenic atom (As_I). The identical generation and annealing behavior suggests that these centers are generated simultaneously as a result of the rupture of an As–S bond. The close kinetic relation observed between the type I centers and the mid-gap absorption suggests that both effects originate from the same electronic states. Type II centers represent 85% of the ESR signal and are identified as a hole on a non-bonding 3p orbital of a sulfur atom (S_{II}) and an electron center on a non-bonding 4p orbital of a doubly-coordinated arsenic atom (As_{II}). The origin of these centers is suggested to be the breaking of As–As and S–S bonds. A different assignment of type II centers, namely to bonds broken in the immediate vicinity of homopolar bonds, was suggested in [36].

In a-As, light induces one type of ESR centers that is suggested to be an unpaired spin localized predominantly on an As p-orbital, with 95% s–p hybridization [25]. The similarity of the dark- and light-induced ESR signals suggests that, possibly, illumination simply increases the concentration of some localized paramagnetic centers that are present in the dark and does not produce new kinds of defects.

LESR is also observed in a-Si:H (see, e.g. [1]). The dark ESR signal with a g value of 2.0055 is attributed to dangling bonds [37, 38]. Using the electron-spin-echo envelope-modulation method of pulsed ESR it was found that dangling bonds are formed in the hydrogen-depleted regions, being separated from the closest hydrogen atom by a distance of 4.2 Å [39].

Light-induced ESR at low temperature in undoped a-Si:H possesses two components with g values of 2.004 and 2.01 [40]. For the explanation of the light-induced ESR in a-Si:H two major models were suggested. One model is that of electrons and holes trapped at week Si–Si bonds [41]. In the other model, electrons and holes are trapped at positively and negatively charged dangling bonds with negative-U, resulting in $g = 2.004$ and 2.01, respectively [42, 43]. Based on hyperfine structures of LESR signals it was concluded [44] that the origin of light-induced ESR with $g = 2.004$ is electrons trapped at weak Si–Si bonds whose energy is located at the conduction-band tail. By analogy, it was suggested that the $g = 2.01$ center is due to holes trapped at the weak Si–Si bonds (in the valence-band tail) [44].

3.3 Medium-Range-Order (MRO) Effects

The best-studied metastable structural effect in vitreous chalcogenides is photodarkening. Under band gap illumination, the absorption edge shifts to lower energies, and the magnitude of the shift increases at low temperatures. The shift depends on the composition of the material – As–S alloys generally show a greater effect than the As–Se alloys – and scales with the glass transition temperature [1]. Thermal annealing near the glass transition temperature restores the initial edge position. In as-deposited evaporated films irreversible effects are additionally observed. These effects are due to irreversible structural transformations such as polymerization [45], partial crystallization or Se segregation on the surface [46].

Already at early stages of research it was realized that the PD effect is a reversible structural modification wherein medium-range-order lattice rearrangement takes place during illumination. The PD were found to be accompanied by reversible changes in the IR spectra [47] and in the first-sharp diffraction peak (FSDP) [48]. Reversible photostructural changes were also found to modify the "Boson peak" [49, 50], i.e. the features at the low-frequency region ($\omega < 100$ cm^{-1}) in the Raman spectra. Both FSDP and the Boson peak are strongly related to the randomness of the amorphous lattice and are associated with certain medium-range-order structural units in the glass. The above facts strongly suggest, therefore, that the photo-induced structural modifications of the amorphous chalcogenide semiconductors occur on a medium-range-order scale.

In situ extended absorption fine structure (EXAFS) measurements performed on both elemental a-Se and As_2Se_3 glass [51] found that the average coordination number of Se increases reversibly by about 5% in the photo-excited state and extra disorder is created. After cessation of the illumination, the local change of coordination disappears *while the light-enhanced structural disorder remains.* This extra disorder represents the metastable change while the dynamic increase in the coordination number is related to dynamic changes [52].

The observed light-induced *increase* in the coordination number indicates the formation of higher than two-fold coordinated Se sites. This may look unusual since normally one would expect the occurrence of photo-induced bond *breaking*, and hence a decrease in the average coordination. This unusual behavior observed in a-Se is explained as follows. Under

light irradiation, electrons from the top of the valence band, which is formed by lone-pair (LP) electrons of Se, are excited into the conduction band leaving unpaired electrons in the initially filled LP-orbital. If an excited atom finds itself close to the neighboring chain, its unpaired electron in the former LP-orbital interacts with LP-electrons of a neighboring chain creating an interchain bond [51, 53] and a pair of triply coordinated defects. Comparison of the total energies for the two configurations (states b and c in Fig. 3.3) shows that such a process is energetically favorable. Further evidence for the photo-induced change in the bonding geometry comes from Raman scattering when two new peaks were observed in the sample in the photoexcited state [53].

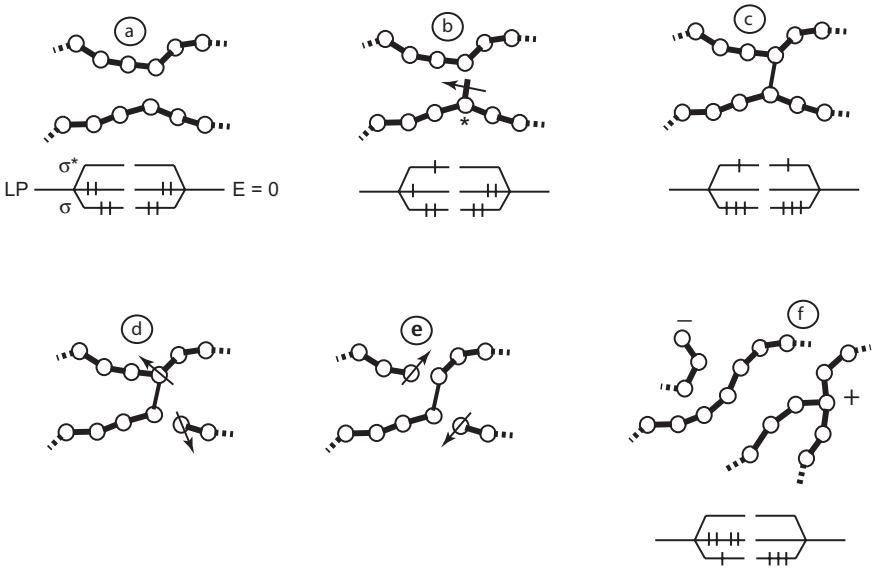

Figure 3.3: Structural evolution of amorphous selenium unveiled by *in situ* EXAFS and ESR studies. Usual configuration (a), photo-excited state (b), formation of interchain bonds (c) and subsequent bond breaking/switching (d–f). Diagrams present electronic cinfugurations of the corresponding states. The lone-pair electron level is taken as $E = 0$.

The above results are also supported by resent studies of X-ray photoelectron spectroscopy of light-induced changes in As–Se glasses [46]. Reversible changes are found in the valence band only upon illumination, indicating transfer of lone pair states of Se to a new kind of bonding state deeper in the band. The population of these states is reduced with the cessation of light.

After the photo-excitation is turned off, non-equilibrium electrons recombine. However, when the two excited C_2^* sites form an interchain bond moving an LP-electron to the bonding state, the corresponding empty LP-state is pushed up to the antibonding state. Recombination in the excited state is therefore impossible since in this configuration there is no empty state in the valence band. Bond breaking is a necessary condition for the recombination, which means that the newly formed bonds are essentially *dynamical* and disappear after cessation of the irradiation. The dynamical bonds manifest the transient, or dynamical, component of PD.

The bond breaking and their subsequent rearrangement result in the generation of VAP pairs, which are responsible for the metastable PD [33]. It should be kept in mind that creation of the dynamical bonds necessarily involves movement of the neighboring atoms, changing the dihedral angles within the Se chains, which is a medium-range-order change. It is believed that this change of the dihedral angle and the resulting increase in the LP–LP interaction are the origin of the observed photodarkening.

In the case of binary chalcogenides, the so-called wrong bonds are created during the photostructural change, as was evidenced by Raman scattering and EXAFS [50, 54]. The creation of wrong bonds at "weak" sites may cause the layer deformation as suggested in [55]. This geometric change results in changes in dihedral angles and can be responsible for the observed photodarkening.

Illumination with polarized light induces reversible optical anisotropies which is, perhaps, the most intriguing photo-induced effect observed in amorphous chalcogenides [56, 57].

3.4 Long-Range-Order (LRO) Effects

Long-range-order (LRO) effects are structural rearrangements that involve correlations between atoms located at distances exceeding MRO. The better-known effects that require long-range modifications are volume expansion (construction), photo melting, photo-crystallization, photo-fluidity, and photo-vitrification, or photo-amorphization. Also the photodiffusion of metals, particularly of Ag in amorphous chalcogenides and the light-enhanced hydrogen diffusion in a-Si:H, could be considered as LRO photo-induced effects. The latter two effects are irreversible.

The photoinduced expansion (contraction) and fluidity provide probably the best manifestation of correlated light-induced atomic movements. Metastable volume photoexpansion has been observed in chalcogenide alloys [58] and more recently a-Si:H [59]. The effect is more pronounced in obliquely evaporated chalcogenide films that are characterized by a columnar structure [60]. Various experiments demonstrated [61] that the effects of the photoexpansion and photodarkening are not directly related.

The effect of photo-induced fluidity of chalcogenide glasses has been observed [62]. When a 50 μm thick flake of evaporated a-As_2S_3 was illuminated locally by a focused laser light the fluidity increased. The athermal nature of the effect is demonstrated by the unusual temperature dependence of the photo-induced viscosity that decreases as the illumination temperature decreases. The pure photoelectronic nature of the effect has been attributed to the cumulative effect of the energy released during the non-radiative recombination events that cause motions of a lot of atoms and are accompanied by bond switching [63].

Athermal optical melting of selenium was reported in [64]. It was found that linearly polarized light weakens the interchain interaction in the direction parallel to its polarization plane, resulting in a preferred orientation of the chains perpendicular to the polarization of the light inducing the anisotropy [65, 66].

Exposure to intense light may result in crystallization of amorphous chalcogenides. The effect is most strongly pronounced in a-Se. While thermal effects of the light cannot be completely neglected, we believe that the underlying mechanism is essentially optoelectronic and consists in the following. Photoexcitation results in the creation of ESR-active defect pairs.

The constituents of such pairs are electrically neutral and can diffuse away from the place of origin. The diffusion occurs by bond switching and does not require much energy. As time elapses, neutral defects are converted into charged defects with Coulomb interaction between them attracting the two defects towards each other.

When the concentration of photo-induced defects (roughly proportional to the light intensity) is small, the photo-created defects recombine geminately and their recombination results in recovery of the initial structure. If, on the other hand, the light intensity is high, the inverse concentration of the photo-induced defects becomes smaller than the distance between the diffused defects originating from the same site. In such a case, after acquiring the charged state, the defects find themselves under the action of Coulomb potential centered at a place different from that of their origin. In such a case the structure resulting after the recombination is different from the initial structure. Since the process develops in the direction which lowers the total energy, the material gradually crystallizes. This process is facilitated at high excitation levels when the local changes can take place collectively. Here, too, exposure to linearly polarized light leads to anisotropic crystallization, as was observed in [65] using polarized Raman scattering (Fig. 3.4).

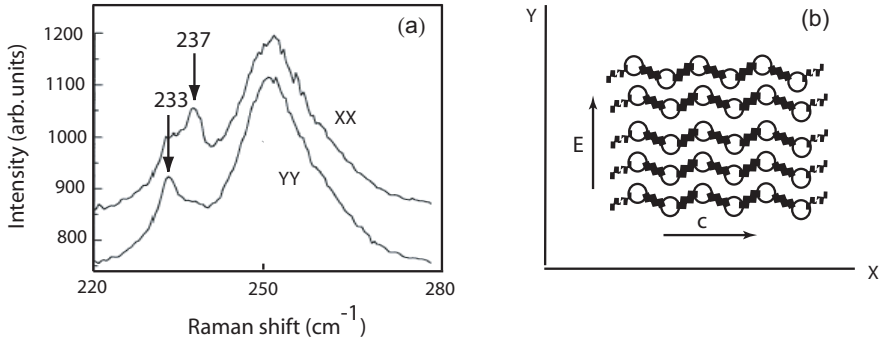

Figure 3.4: Polarized Raman spectra of initial stages of photocrystallization of an amorphous Se film under linearly polarized light (a) and the orientation of Se chains deduced from the obtained spectra (b).

Interestingly, not only can light crystallize the amorphous films but it can also amorphize crystallized films. This effect was first observed for $As_{50}Se_{50}$ films [67]. It was argued that the origin of the process is rupture of intramolecular bonds within the As_4Se_4 molecules, which are the building blocks of the formed crystal and the formation of a three-dimensional continuous glass network. It was believed that the process is energetically favorable since it reduces the strain accumulated in the film during the crystallization. It may be worth noticing that this process was only observed in films supported by a substrate; the scraped film did not crystallize even after 50 times longer annealing at the same temperature. Photoamorphization has also been observed for As_2S_3 [68].

Finally, a reversible photo-induced phase transition should be mentioned. When a chalcogenide film (usually Te-based) is exposed to a laser pulse it crystallizes; the same film re-exposed to a shorter more intense pulse is reamorphized [69]. Whilst it is often believed that the effect of light is simply to heat the sample, an optoelectronic process, similar to the one

described above, may be operative and further studies are needed to investigate the role of electronic excitation.

The photo-induced reversible phase transition has found a major application in CD-RW, DVD-RW and DVD-RAM technology. The materials used in these devices are multicomponent chalcogenides in the Ge–Sb–Te and Ag–In–Sb–Te systems [70].

3.5 Conclusion

Absorption of light creates a wide variety of metastable effects in a-Si:H and the chalcogenide alloys. The energy released during the recombination events is absorbed by the whole lattice, inducing spatial strain fluctuations, bond rearrangements and atom movements. The presence of lone pair electrons and flexibility of the lattice seem to be the decisive factors for the observed effects.

References

[1] A.V. Kolobov and K. Tanaka, in Handbook of Advanced Electronic and Photonic Materials and Devices Vol. 5, H.S. Nalwa (Ed.), Academic Press, San Diego, 2001, p. 47.
[2] H. Fritzsche, Solid State Commun. **99**, 153 (1996).
[3] K. Shimakawa, A.V. Kolobov, and S.R. Elliott, Adv. Phys. **44**, 475 (1995).
[4] S.G. Bishop, U. Strom, and P.C. Taylor, Phys. Rev. Lett. **36**, 543 (1975).
[5] J.S. Berkes, S.W. Ing, and W.J. Hillegas, J. Appl. Phys. **42**, 4908 (1971).
[6] D.L. Steabler, and C.R. Wronski, Appl. Phys. Lett. **28**, 671 (1977).
[7] G. Moddel, D.A. Anderson and W. Paul, Phys. Rev. B **22**, 1918 (1980).
[8] M. Venecek, J. Koska, J. Stuchlik, and A. Triska, Solid State Commun. **39**, 1199 (1981).
[9] K. Tanaka and Y. Yamasaki, Solar Energy Mater. **8**, 277 (1982).
[10] N.M. Amer, and W.B. Jackson, Hydrogenated Amorphous Silicon, in Semiconductors and Semimetals, Vol. 21B, J. Pankove (Ed.), 1984, p. 83.
[11] N.F. Mott, and E.A. Davis, Electronic Processes in Non-Crystalline Materials, Clarendon Press, Oxford, 1979.
[12] J.M. Marshall, C. Main, and A.E. Owen, J. Non-Cryst. Solids **8–10**, 760 (1972).
[13] R.P. Barklay, M. Sarr, and J.L. Brebner, J. Non-Cryst. Solids **97–98**, 687 (1987).
[14] E.A. Fagen, and H. Fritzcshe, J. Non-Cryst. Solids **2**, 180 (1970).
[15] X. Deng, E. Mytilineou, R.T. Young, and S.R. Ovshinsky, Mat. Res. Soc. Symp. Proc. **258**, 491 (1992).
[16] P. Kounavis, and E. Mytilineou, Phil. Mag. Lett. **72**, 117 (1995).
[17] E. Mytilineou, in Future Directions in Thin Film Science and Technology, J.M. Marshall, N. Kirov, A. Vavrek, and J.M. Maud (Eds.), World Scientific, Singapore, 1996, p. 242.
[18] P. Kounavis, and E. Mytilineou, J. Phys: Condens. Matter **11**, 9105 (1999).
[19] D. Han, and H. Fritzsche, J. Non-Cryst. Solids **59–60**, 397 (1983).
[20] G. Schumm, E. Lotter, and G.H. Bauer, Appl. Phys. Lett. **60**, 3262 (1992).

[21] Ka. Tanaka, and H. Okushi, J. Non-Cryst. Solids **66**, 205 (1984).
[22] M. Hack, and M. Shur, J. Appl. Phys. **58,** 1656 (1985).
[23] A.V. Kolobov, K. Tanaka, Semiconductors **32**, 801 (1998).
[24] R.A. Street, Adv. Phys. **25**, 397 (1976).
[25] S.G. Bishop, U. Strom, and P.C. Taylor, Solid State Commun. **18**, 573 (1976).
[26] T. Tada, and T. Ninomiya, J. Non-Cryst. Solids **137–138**, 998 (1991).
[27] K. Arai, U. Itoh, H. Komine, and H. Namikawa, Proc. of the 6th Int. Conf. on Amorphous and Liquid Semiconductors, B.T. Kolomiets (Ed.), 1976, p. 222.
[28] P.B. Kirby, and E.A. Davis, J. Non-Cryst. Solids **35–36**, 945 (1980).
[29] R.A. Street, Adv. Phys. **30**, 593 (1981).
[30] D.K. Biegelsen, and R.A. Street, Phys. Rev. Lett. **44**, 803 (1980).
[31] S.G. Bishop, U. Strom, and P.C. Taylor, Phys. Rev. B **15**, 2278 (1977).
[32] A.V. Kolobov, M. Kondo, H. Oyanagi, R. Durny, A. Matsuda, and K. Tanaka, Phys. Rev. B **56**, R485 (1997).
[33] A.V. Kolobov, M. Kondo, H. Oyanagi, A. Matsuda, and K. Tanaka, Phys. Rev. B **58**, 12004 (1998).
[34] S.G. Bishop, U. Strom, and P.C. Taylor, Proc. of the 7th Int. Conf. on Amorphous and Liquid Semiconductors, W.E. Spear (Ed.), Univ. of Edinburgh, 1977, p. 595.
[35] J. Hautala, W.D. Ohlsen, and P.C. Taylor, Phys. Rev. B **38**, 11048 (1988).
[36] S.R. Elliott, and K. Shimakawa, Phys. Rev. B **42**, 9766 (1990).
[37] D.K. Biegelsen and M. Stutzmann, Phys. Rev. B **33**, 3006 (1986).
[38] T. Umeda, S. Yamasaki, J. Isoya, and K. Tanaka, Phys. Rev. B **59**, 4849 (1999).
[39] J. Isoya, S. Yamasaki, H. Okushi, A. Matsuda, and K. Tanaka, Phys. Rev. B **47**, 7013 (1993).
[40] J.C. Knight, D.K. Biegelsen, and I. Solomon, Solid State Commun. **22**, 133 (1977).
[41] M. Stutzmann, W.B. Jackson, and C.C. Tai, Phys. Rev. B **32**, 23 (1985).
[42] D. Adler, Sol. Cells **9**, 133 (1983).
[43] S. Yamasaki, H. Okushi, A. Matsuda, K. Tanaka, and J. Isoya, Phys. Rev. Lett. **65**, 756 (1990).
[44] T. Umeda, S. Yamasaki, J. Isoya, and K. Tanaka, Phys. Rev. B **62**, 15702 (2000).
[45] J.P. deNeufville, S.C. Moss and S.R. Ovshinsky, J. Non-Cryst. Solids **13**, 191 (1973/74).
[46] H. Jain, S. Krishnaswami, A.C. Miller, P. Krecmer, S.R. Elliott, and M. Vlcek, J. Non-Cryst. Solids **274**, 115 (2000).
[47] Y. Utsugi and Y. Mizushima, J. Appl. Phys. **49**, 3470 (1978).
[48] K. Tanaka, Appl. Phys. Lett. **26**, 243 (1975).
[49] M. Frumar, A. Firth, and A.E. Owen, Philos. Mag. **50**, 463 (1984).
[50] K. Matsuishi, R. Arima, K. Kagota, and S. Onari, J. Non-Cryst. Solids **266–269**, 938 (2000).
[51] A.V. Kolobov, H. Oyanagi, K. Tanaka, and Ke. Tanaka, Phys. Rev. B **55**, 726 (1997).
[52] A. Ganjoo, K. Shimakawa, K. Kitano, and E.A. Davis, J. Non-Cryst. Solids **299**, 917 (2002).

[53] A.V. Kolobov, H. Oyanagi, and K. Tanaka, Mater. Res. Soc. Bull. **24**, 32 (1999).
[54] C.Y. Yang, M. Paesler, and D.E. Sayers, Phys. Rev. B **36**, 9160 (1987).
[55] A.V. Kolobov and G. Adriaenssens, Philos. Mag. B **69**, 21 (1994).
[56] V.M. Lyubin, J. Optoelectronics Adv. Mater. **3**, 265 (2001).
[57] K. Tanaka, in Handbook of Advanced Electronic and Photonic Materials and Devices, H.S. Nalwa (Ed.), Vol. 5, Academic Press, San Diego, 2001, p. 120.
[58] H. Hamanaka, K. Tanaka, and S. Iizima, Solid State Commun. **23**, 63 (1977).
[59] T. Gotoh, S. Nonomura, M. Nishio, and S. Nitta, Appl. Phys. Lett. **72**, 2978 (1998).
[60] A. Ganjoo, Y. Ikeda, and K. Shimakawa, J. Non-cryst. Solids **266**, 919 (2000).
[61] Ke. Tanaka, Phys. Rev. B **57**, 5163 (1998).
[62] H. Hisakuni and Ke. Tanaka, Science **270**, 275 (1995).
[63] H. Fritzsche, Solid State Commun. **99**, 153 (1996).
[64] V.V. Poborchii, A.V. Kolobov, and K. Tanaka, Appl. Phys. Lett. **74**, 215 (1998).
[65] V.V. Poborchii, A.V. Kolobov, and K. Tanaka, Appl. Phys. Lett. **72**, 1167 (1998).
[66] A.V. Kolobov, H. Oyanagi, and K. Tanaka, Phys. Rev. Lett. **87**, 145502 (2001).
[67] S.R. Elliott and A.V. Kolobov, J. Non-Cryst. Sol. **128**, 216 (1991).
[68] M. Frumar, A.P. Firth, and A.E. Owen, J. Non-Cryst. Solids **192/193**, 447 (1995).
[69] R.T. Young, D. Strand, J. Gonzalez-Hernandez and S.R. Ovshinsky, J. Appl. Phys. **60**, 4319 (1986).
[70] T. Ohta, J. Optoelectronics Adv. Mater. **3**, 609 (2001).

4 Dynamics of Photo-Induced Metastability in Amorphous Chalcogenides

Koichi Shimakawa

Recent understanding of the dynamics of photo-induced metastable changes, e.g. defect creation and structural changes, in amorphous chalcogenides is reviewed. The quantum efficiency (QE) of the defect creation by the bandgap and sub-gap illuminations is discussed. New results on the occurrence of transient and metastable components in photostructural changes are described. It is suggested that the defect creation occurs within the layers of a chalcogenide while the structural change is attributable to inter-layer interactions. i.e. the defect creation and the structural change may have different origins.

4.1 Introduction

Two types of reversible photo-induced effects are well known in amorphous chalcogenides, namely the defect creation and structural changes [1, 2] Although these changes have been discussed in numerous papers, their microscopic origin is still not clear [1–5].

Photo-induced defect creation was first found in hydrogenated amorphous silcon (a-Si:H) and later also in amorphous chalcogenides (see, e.g. [1]). Such defects act as recombination centers and cause device degradation. Flexible or deformable structural networks in amorphous materials may facilitate the degradation and self-trapped exciton (STE) states are often considered to be the origin of such defects [1].

The structural changes, on the other hand, produce a change in the bandgap and refractive index (n) and can be used for optical memory applications. In obliquely deposited films *giant* reversible photo-induced volume changes [$\Delta V/V \approx +0.04$ (expansion) in $As_2Se(S)_3$ and $\Delta V/V \approx -0.08$ (contraction) in $GeSe(S)_2$] have been observed [6, 7] accompanied by *giant* changes of the bandgap. Recent detailed study of photo-induced volume expansion (PVE) of a-As_2S_3 indicates that there seems to be no direct relation between PVE and the decrease of the bandgap (photodarkening) [8].

Photostructural change (PSC) and the related photodarkening are phenomena unique to glassy or amorphous chalcogenides and are not observed in amorphous group IV and V semiconductors (a-Si, a-As, etc.), or in crystalline chalcogenides [9]. It is noted also that the photodarkening disappears in some metal-doped chalcogenide glasses (e.g. by doping with Cu, Mn, etc.) [10, 11]. It is believed that an increased interaction of chalcogen lone-pair (LP) electrons is responsible for photodarkening. The existing models can be classified into the following major categories: (1) change in the atomic (chalcogen) positions [4], (2) bond breaking and/or alternations between the atoms [12, 13] and (3) macroscopic repulsion and slip motion

of structural layers (RS model) [14]. Recent *in situ* measurements of photodarkening or PVE etc., may contribute to better understanding of these changes [13, 15–17].

In this chapter, recent results obtained on defect creation (in particular, quantum efficiency), reversible photodarkening and PVE in As-based chalcogenides are reviewed. We concentrate on the time evolution of these changes (*in situ* measurements, etc.), which is useful in order to understand the dynamics of these processes.

4.2 Light-Induced Metastable Defect (LIMD) Creation

As mentioned above, the self-trapped exciton (STE), which requires a strong carrier–lattice interaction, may be the origin of the defect generation [1, 18, 19]. Subsequent non-radiative recombination (multiphonon process) after photo-excitation may act to stabilize the defects.

We discuss here LIMD creation. We define the quantum efficiency (QE) of LIMD creation as $\eta = N(n_p)/n_p$, where N is the number of the created defects and n_p (= Gt, G is the generation rate and t is time) is the total number of the absorbed photons. It is of interest to know how QE depends on n_p and on the photon energy. We also discuss the effect of structural flexibility on QE. To address these issues we have studied the temporal evolution of the photocurrent in normal and obliquely deposited a-As_2Se_3 films [20].

Figure 4.1 shows the experimentally obtained photocurrent I_p as a function of the exposure time t at 300 K and 250 K. For the bandgap illumination, the photocurrent I_p first decreases with time and approaches a minimum and then increases for both the obliquely and normally deposited films. For the sub-bandgap illumination, no pronounced decrease in I_p is observed.

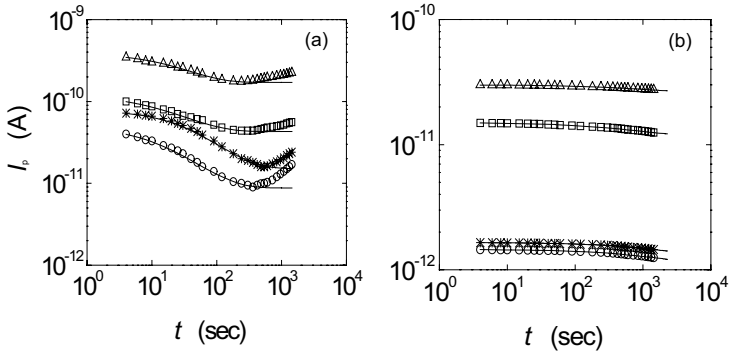

Figure 4.1: Variation of photocurrent with exposure time measured at 300 K and 250 K for a-As_2Se_3 films for the bandgap illumination (a), and sub-bandgap illumination (b). Open circles and squares represent the photocurrents for obliquely deposited films measured at 250 and 300 K, respectively. Open triangles and stars represent the photocurrents for normally deposited films measured at 300 and 250 K, respectively. The solid curves are the calculated results using Eq. (4.4).

The initial decrease of the photocurrent may result from the photo-induced creation of the recombination centers (defects) [18, 19]. The photo-induced random defect pairs are believed to result from bond-switching reactions involving optically induced intimate defect pairs. For

the sub-bandgap illumination (Fig. 4.1(b)) the number of random pairs is smaller, resulting in a smaller decrease of I_p.

The subsequent increase in photocurrent I_p for the band gap illumination is probably caused by an increase of optical absorption due to photodarkening [20]. The magnitude of the photocurrent increase is larger at 250 K in agreement with the fact that photodarkening increases at lower temperatures.

We now turn to the defect creation $N(t)$ during the illumination. We assume that the change in the photocurrent is dominated by LIMD creation itself. The photocurrent can be expressed as

$$I_p(t) = \frac{C}{N_0 + N_t} = \frac{C}{N_0(1 + N_t/N_0)} = \frac{I_p(0)}{1 + N_t/N_0}, \tag{4.1}$$

where C is a constant and $I_p(0)$ $(= C/N_0)$ is the initial photocurrent. $N(t)/N_0$ can be estimated from the ratio $I_p(0)/I_p(t)$, with N_0 being the initial number of defects in the film. Figure 4.2 shows the kinetics of the defect creation $(N(t)/N_0)$, for the bandgap and sub-gap illuminations. N_t increases with time during the illumination in obliquely and normally deposited films being larger for obliquely deposited films which may be due to a larger structural flexibility in the latter.

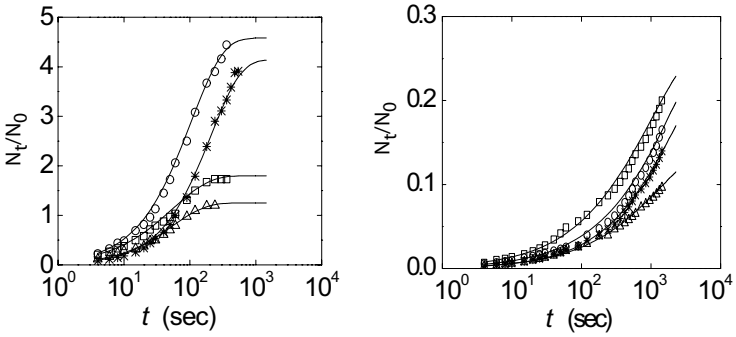

Figure 4.2: Variation of N_t/N_0 with exposure time estimated from changes in photocurrent using Eq. (4.1) for the bandgap illumination (a), and sub-bandgap illumination (b). The notations are the same as in Fig. 4.1. The solid lines show the fitting obtained using Eq. (4.3).

Various descriptions of LIMD creation have been proposed [1, 21, 22] and we use the following rate equation for LIMD creation:

$$\frac{dN_t}{dt} = k_p(N_T - N_t) - k_r N_t, \tag{4.2}$$

where N_T is the total number of sites available for LIMD creation, and k_p and k_r are the generation and recovery rates, respectively [1, 20]. Assuming time dispersive reactions for generation and recovery reactions ($k_p = At^{\alpha-1}$ and $k_r = Bt^{\alpha-1}$, respectively; A and B are constants), the solution of Eq. (4.2) is given as

$$N_t = N_s \left[1 - \exp\left\{-\left(\frac{t}{\tau}\right)^{\alpha}\right\}\right], \tag{4.3}$$

where $N_s = N_T A/(A+B)$ is the saturated density of N_t and $\tau = [\alpha/(A+B)]^{1/\alpha}$ is the effective creation time; the dispersion parameter α $(0 < \alpha < 1)$ is assumed to be the same for the forward and backward reactions.

Using Eqs. (4.1) and (4.3), the expression for the photocurrent can be written as

$$I_p = \frac{I_s}{1 - \gamma \exp\{-(t/\tau)^\alpha\}}, \tag{4.4}$$

where I_s is a constant current reached after prolonged illumination and $\gamma = N_s/(N_0 + N_s)$. The solid lines in Figs. 4.1 and 4.2 are the calculated results obtained using α, τ, and N_s/N_0 (or γ) as the fitting parameters (listed in Table 4.1).

Table 4.1: Results of the fitting of the photocurrent curves. In the sample description O stands for obliquely deposited and N for normally deposited films.

Sample (temperature)	Illumination	α	$\tau(s)$	N_s/N_0	γ
O (300 K)	Bandgap	0.80	55	1.80	0.64
O (250 K)		0.90	105	4.58	0.82
N (300 K)		0.90	55	1.25	0.56
N (250 K)		0.96	210	4.10	0.81
O (300 K)	Sub-gap	0.65	1000	0.28	0.22
O (250 K)		0.65	2300	0.32	0.24
N (300 K)		0.66	1300	0.15	0.13
N (250 K)		0.71	2100	0.26	0.21

The following conclusions can be drawn. For both the bandgap and sub-gap illuminations the values of N_s/N_0 and γ for the obliquely deposited samples are larger than those for the normally deposited ones. The effective creation time τ for the sub-gap illumination is larger than that for the bandgap illumination and increases with decreasing temperature. The dispersion parameter α is smaller for the sub-gap illumination.

We now define the quantum efficiency (QE) η of LIMD creation:

$$\eta = N_t/n_p, \tag{4.5}$$

where N_t is the number of defects created by illumination and n_p is the total number of absorbed photons. The QE, η, as a function of the total number of absorbed photons n_p for the bandgap and sub-gap light is shown in Fig. 4.3.

QE decreases with increasing number of the absorbed photons for both the bandgap and sub-bandgap illumination. At the studied temperatures, all the results show a similar behavior. The solid lines in Fig. 4.3 represent the calculated results of QE using Eqs. (4.3) and (4.5), which are in good agreement with the experimental results. QE is larger in obliquely deposited films. Intuitively one would expect QE to increase for higher photon energies. In the experiment, however, such a dependence was not observed – a somewhat surprising result.

The thermalization energy of the photocarriers (from the extended state to the tail state) may not be important for LIMD creation [21]. As already stated, the self-trapped exciton can be an origin of LIMD creation [1]. The self-trapped excitons can be as easily created by the

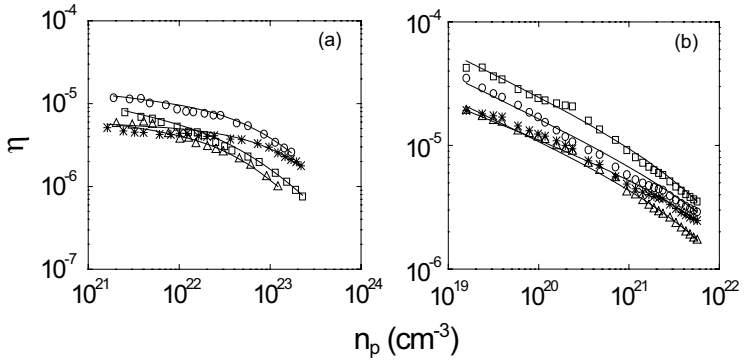

Figure 4.3: Variation of quantum efficiencies η with the number of absorbed photon n_p for bandgap illumination (a) and sub-bandgap illumination (b). The notations are the same as in Fig. 4.1. The solid lines show the fitting obtained using Eq. (4.5).

sub-gap illumination as by the bandgap illumination, and hence QE for sub-gap illumination may be comparable to that for the bandgap illumination.

The QE is larger for a-As_2Se_3 than for a-Si:H (not shown). This can be attributed to the higher degree of flexibility of the atomic structure in amorphous chalcogenides. It should be noted that for a-Si:H the bandgap and sub-gap illuminations also produce almost the same QE, which indicates that similar mechanisms of the defect creation could be operative in these two different materials. In fact, self-trapped holes have been suggested to initiate LIMD creation in a-Si:H [23, 24].

Finally, we discuss the case of pulsed excitation. It is known that illumination of a-Si:H [25] and amorphous chalcogenides [26] with short intense light pulses creates LIMDs more efficiently than continuous-wave irradiation with the *same average intensity* and photon energy, which may be due to highly non-equilibrium conditions under pulsed excitation. For this reason, the kinetic equation applied above to the equilibrium conditions is not appropriate for pulsed excitation.

4.3 Photostructural Changes

We start with the metastable changes in photodarkening and PVE. It has long been believed that photodarkening and PVE were two different sides of the same phenomenon and hence a one-to-one correlation should exist between photodarkening and PVE. However, it has been demonstrated [8] that the time constants of the photodarkening and the PVE in As_2S_3 are different: the PVE saturated earlier than the photodarkening. These experimental observations suggested that the two phenomena are not directly related to each other.

In order to understand the dynamics of photodarkening and PVE during the illumination, *in situ* measurements were performed [15, 16]. Figure 4.4 shows the time-dependent thickness change, $\Delta d/d$, for an illuminated a-As_2S_3 film [16]. As soon as the light (a mercury lamp, 150 mW/cm^2) is switched on, the thickness increases rather rapidly, reaches a maximum after

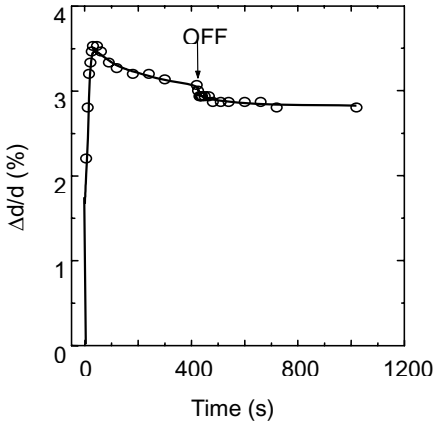

Figure 4.4: Relative changes in thickness $\Delta d/d$ with time on switching the illumination on and off for an obliquely deposited film of a-As_2S_3. The solid line is a guide to the eye.

approximately 30 s, and then gradually decreases. This behavior *during* the illumination is similar to the degradation of photocurrent in amorphous chalcogenides [1, 18, 19]. When the illumination is turned off, the thickness decreases slowly due to relaxation of the structure, and eventually reaches the metastable state value. This relaxation behavior of PVE (after the illumination is switched off) is also very similar to the decay of photocurrent [15]. In Ge-based chalcogenides, where volume *contraction* is observed during and after illumination [6, 7], no transient volume changes could be observed.

In situ measurements of the optical absorption coefficient have been performed for As_2S_3 [16]. The variation of changes in the absorption coefficient ($\Delta\alpha$) with the number of absorbed photons (n_p) at different temperatures is shown in Fig. 4.5. Note that $\Delta\alpha$ is defined as $\Delta\alpha = (-1/d)\ln(\Delta T)$, where d is the film thickness and ΔT the change in optical transmission which is defined here as $\Delta T = T/T_0$ (T_0 is the transmission when the illumination is put on and T is the transmission at any time t). The details of the experiment are described elsewhere [16].

Initially, $\Delta\alpha$ increases slowly with n_p, followed by a faster increase and then almost levels off. The magnitude of the changes decreases with increasing temperature with $\Delta\alpha$ being the largest at 50 K (in spite of a slow initial variation). At low temperatures, the changes are initially very slow but increase rapidly as n_p increases. The slow initialization at low temperatures is attributed to a smaller number of the absorbed photons, as the initial absorption coefficient is small at lower temperatures ($\alpha_0 = 150$ cm^{-1} at 50 K). As the illumination time increases, the resulting photodarkening causes a positive feedback increase in the absorption change.

Next we show the results of transient photodarkening in normally deposited a-As_2Se_3 films (Fig. 4.6 (a)) during the repeated cycles of Ar laser illumination at 50 and 300 K [16]. $\Delta\alpha$ first exhibits a rapid increase at both temperatures and then almost saturates. When the Ar laser illumination is switched off, a fast drop in $\Delta\alpha$ is observed. This drop corresponds to the

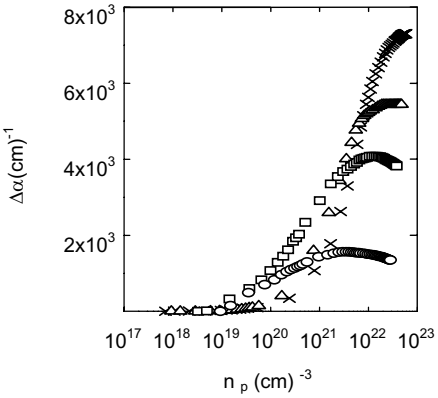

Figure 4.5: *In situ* variation of changes in absorption coefficient $\Delta\alpha$ as a function of absorbed photons n_p at various temperatures. Crosses, triangles, squares and circles correspond to the changes at 50, 100, 200, and 300 K, respectively. Illumination is performed by an Ar^+ laser (20 mW/cm^2).

transient component of photodarkening and whatever remains corresponds to the metastable photodarkening. The transient component of the changes is found to be about 60% and 30% of the total changes induced at 300 and 50 K, respectively. After the metastable component saturates, only the transient photodarkening can be observed. Figure 4.6(b) shows the initial kinetics of $\Delta\alpha$. $\Delta\alpha$ increases and decreases very rapidly when the illumination is switched on and off, but in neither case does it return to the original value, i.e. the metastable photodarkening is accumulated with each successive illumination.

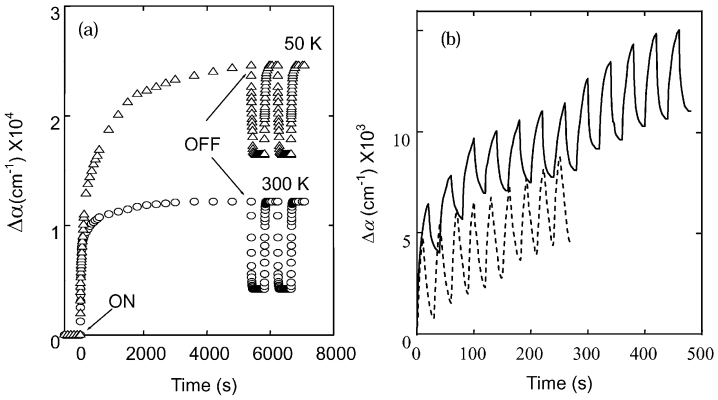

Figure 4.6: (a) Time evolution of changes in absorption coefficient, $\Delta\alpha$, for a-As_2Se_3 films at 50 (triangles) and 300 K (circles). ON and OFF stages of the Ar laser are indicated by the arrows. (b) Changes in absorption coefficient, $\Delta\alpha$, with time for short-duration illumination for a-As_2Se_3 films at 50 K (solid line) and 300 K (dashed line). Ar laser ON and OFF states are 20 s each at 50 K, and 10 s and 20 s respectively at 300 K.

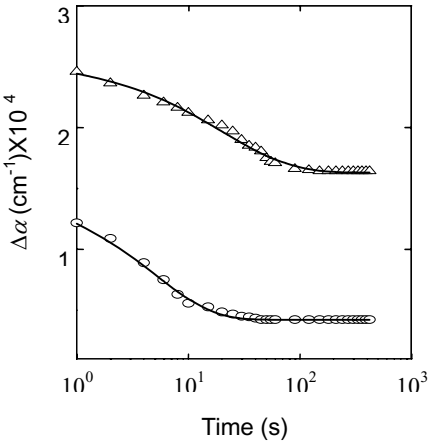

Figure 4.7: The decay of the transient photodarkening after switching off the Ar laser for a-As_2Se_3 films at 50 K (triangles) and 300 K (circles). The solid lines are the fits using Eq. (4.6).

Figure 4.7 shows the time dependence of the decay of the transient part at 50 and 300 K. The solid lines are stretched exponential fits to the data. The logarithmic scale is adjusted so that the starting time in the plot is the time when the Ar-laser illumination is switched off. The decay is faster at 300 K as compared with 50 K and it can be described by a stretched exponential function:

$$\Delta\alpha = C \exp\left[-\left(\frac{t}{\tau}\right)^{\beta}\right] + \Delta\alpha_s, \tag{4.6}$$

where t is the time after the illumination is switched off, τ is the effective decay time, β is a dispersion parameter ($0 \leq \beta \leq 1$) and $\Delta\alpha_s$ is the saturated value of $\Delta\alpha$ (i.e. the metastable part of the changes). C is a temperature-dependent quantity (equal to the total amount of transient photodarkening) and its value is obtained by fitting to the experimental data. The solid line in Fig. 4.7 shows the results. The fitting yields the values of β and τ to be 0.7 and 20 s at 50 K and 0.85 and 5 s at 300 K, respectively. The effective decay time τ decreases and the dispersion parameter β increases with increasing temperature.

4.4 Discussion

The microscopic models proposed for elemental Se [4, 9, 13, 27] cannot account for the occurrence of PVE because they only consider very local structural transformations. We believe that overall network changes, which are initiated by bond twisting or bond alternation, should be taken into consideration in PVE. The basic models consider only *particular atoms* that are excited by photoirradiation. On the other hand, the top of the valence band is formed by the LP *bands*, and hence we suggest that "mesoscopic or macroscopic" interaction plays a decisive role because LP electrons have equal probabilities of being excited. Therefore, electrons

or holes in the extended states (or band-tail states) can be regarded as being responsible for photodarkening or PVE, rather than individual atoms [14].

Now, we briefly review the model of repulsion and slip motion of structural layers (RS model) proposed by the present author and shown schematically in Fig. 4.8. As a typical example, we consider a-$As_2Se(S)_3$ which is known to possess a layered structure. During the illumination, the photocreated electrons reside mostly in the CB tails, while the photocreated holes diffuse away to the unilluminated region through VB and VB tails (since the mobility of electrons is much lower than that of holes in amorphous chalcogenides). As a result, the layers become negatively charged, giving rise to a repulsive Coulomb interaction between layers and causing an increase in the interlayer distance (PVE).

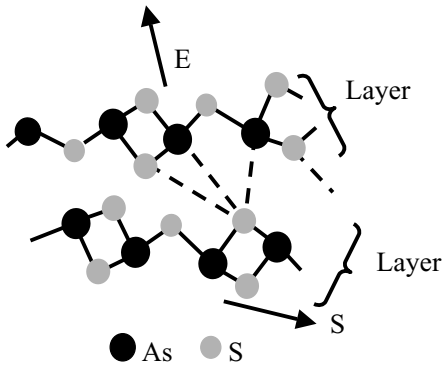

Figure 4.8: The repulsion and slip motion of layered cluster model. The arrows E and S indicate the expansion (due to repulsion) and the slip motions, respectively. The difference in local environments (and hence LP interactions) between chalcogen atoms is indicated by the dashed lines.

This expansion process is indicated by the arrow E (the "E" process) in Fig. 4.8. The experimentally observed widening of the valence angle subtended at S atoms within a layer [28] and hence the increase in the distance between two arsenic atoms bridged by a chalcogen atom upon illumination can be explained by the repulsive force involved in the "E" process (see arrow). The repulsive force between layers acts as a compressive force for each individual layer. It is expected, however, that no change in the LP–LP interaction occurs in this process and hence the photodarkening is not induced at this stage.

A slip motion along the layers should also take place with the occurrence of the "E" process between neighboring clusters. A slip motion is shown by the arrow S (the "S" process). As the energy required for the slip motion along layers is expected to be greater than that for expansion normal to the layers, the rate of the "S" motion may be lower than that of "E" which is supported by the fact that cleaving is very easy for layered materials, for example graphite.

Both processes occur due to the same repulsion force between the layers, but only the "S" process is expected to be directly related to photodarkening [14]. If the neighboring layer slips away from the equilibrium position, an increase in the energy of the highest occupied states (VB) is expected due to an increase in the total LP–LP interactions. This leads to a widening of the VB (while the CB remains almost unchanged [29]), which results in photodarkening.

The RS model may be further supported by the following experimental results. As already stated, the photodarkening effect disappears in metal-doped chalcogenides [10, 11]. This can be explained as follows. The metal atoms may act as bridging atoms between the layers and hence reduce the flexibility of the layered network. Such bridging reduces the ability of both PVE and the slip motion. Furthermore, the introduction of such a strong constraint also induces dangling bonds which act as recombination centers and which considerably reduce the number of photo-excited free carriers [30].

As already suggested, a very important factor in order for the structural changes to occur is the *charge separation* during illumination [14]. Application of an electric field may assist charge separation if the field is properly applied and may enhance photodarkening. This point remains unclear: whilst enhancement of photodarkening has been reported [31], Lyubin and Kolobov could not observe such an effect [32].

From the similar spectral dependences of the photodarkening and photoconductivity in As_2S_3, and the similar behaviors of PVE and photoconductivity during and after the illumination [15], we argue that free-carrier generation rather than geminate (excitonic) pairs is responsible for the structural changes, This conclusion is consistent with the RS model.

We now discuss the transient changes of photodarkening observed in a-As_2Se_3 *during* the illumination. The total changes consist of transient and metastable components. The transient component decays when the illumination is switched off and only the metastable photodarkening is observed after cessation of the light. The mechanism can be understood as follows. Upon absorbing a photon a "cluster" in the ground state is transferred to the excited state *via* the transient state. The relaxation of the transient state may proceed along two different pathways, either back to the ground state (the transient component) or into the metastable or a new equilibrium state (the metastable component).

4.5 Conclusions

The current understanding of the dynamics of photo-induced defect creation, volume changes (in particular, photo-induced volume expansion), and photodarkening in amorphous chalcogenides, has been reviewed. The quantum efficiency of light-induced creation of metastable defects in a-As_2Se_3 for the bandgap and sub-gap illumination has been determined from the photocurrent measurements.

It has been also demonstrated that the defect creation is more efficient in the obliquely deposited films which can be caused by greater flexibility of the latter due to a larger number of voids.

Time evolutions of PVE and photodarkening (*in situ* measurements) were performed. During the illumination, the total changes comprise both transient and metastable effects. The transient component decays when the illumination is switched off to give the usually observed metastable photodarkening or expansion. After the metastable change has been saturated, only transient changes can be observed. The origin of PVE and photodarkening was discussed in terms of the model of repulsion and slip motion of clustered layers.

References

[1] K. Shimakawa, A.V. Kolobov, and S.R. Elliott, Adv. Phys. **44**, 475 (1995).

[2] A. Ganjoo, N. Yoshida and K. Shimakawa, Recent Research Developments in Applied Physics, ed. M. Kawasaki, N. Ashgriz and R. Anthony, Research Signpost, Trivandrum, 1999, p. 129.

[3] K. Tanaka, J. Non-Cryst. Solids **35**&**36**, 1023 (1980).

[4] Ke.Tanaka, Rev. Solid St. Sci. **4**, 641 (1990).

[5] G. Pfeiffer, M.A. Paesler, and S.C. Agarwal, J. Non-Cryst. Solids **130**, 111 (1991).

[6] Y. Kuzukawa, A. Ganjoo and K. Shimakawa, J. Non-Cryst. Solids **227–230**, 715 (1998).

[7] Y. Kuzukawa, A. Ganjoo, K. Shimakawa, and Y. Ikeda, Philos. Mag. B **79**, 249 (1999).

[8] Ke. Tanaka, Phys. Rev., B **57**, 5163 (1998).

[9] A. V. Kolobov and K. Tanaka, Handbook of Advanced Electronic and Photonic Materials and Devices, Vol. 5, ed. H.S. Nalwa, Academic Press, San Diego, 2001, p. 47.

[10] J.Z. Liu and P.C. Taylor, Phys. Rev. Lett. **59**, 1938 (1987); Phys. Rev. B **41**, 3163 (1990).

[11] M. Iovu, S. Shutov, S. Rebeja, E. Colomeyco, and M. Popescu, J. Optoelectron. Adv. Mater., **2**, 53 (2000).

[12] S.R. Elliott, J. Non-Cryst. Solids **81**, 71 (1986).

[13] A.V. Kolobov, H. Oyanagi, K. Tanaka, and Ke. Tanaka, Phys. Rev. B **55**, 726 (1997).

[14] K. Shimakawa, N. Yoshida, A. Ganjoo, A. Kuzukawa, and J. Singh, Philos. Mag. Lett. **77**, 153 (1998).

[15] A. Ganjoo, Y. Ikeda, and K. Shimakawa, Appl. Phys. Lett. **74**, 2119 (1999); J. Non-Cryst. Solids **266–269**, 919 (2000).

[16] A. Ganjoo, K. Shimakawa, H. Kamiya, E.A. Davis, and J. Singh, Phys. Rev. B **62**, R14601 (2000).

[17] A. Ganjoo and K. Shimakawa, J. Optoelectron. Adv. Mater. **4**, 595 (2002).

[18] K. Shimakawa, S. Inami, and S.R. Elliott, Phys. Rev. B **42**, 11857 (1990).

[19] K. Shimakawa, S. Inami, T. Kato, and S. R. Elliott, Phys. Rev. B **46**, 10062 (1992).

[20] M. Nessa, K. Shimakawa, A. Ganjoo, J. Optoelectron. Adv. Mater. **4**, 93 (2002).

[21] M. Stutzmann, W.B. Jackson, and C.C. Tsai, Phys. Rev. B **32**, 23 (1985).

[22] M. Senda, N. Yoshida, and K. Shimakawa, Philos. Mag. Lett. **79**, 375 (1999).

[23] K. Morigaki, Jpn. J. Appl. Phys. **28**, L2128 (1989).

[24] K. Imagawa, K. Shimakawa, and A. Kondo, J. Non-Cryst. Solids **266–269**, 428 (2000).

[25] M. Stutzmann, J. Nunnenkenkamp, M.S. Brandt, and A. Asano, Phys. Rev. Lett. **67**, 2347 (1991).

[26] G. Rosenbaum, B.G. Sfez, Z. Kotler, V. Lyubin and M. Klebanov, Appl. Phys. Lett. **75**, 3249 (1999).

[27] Ke. Tanaka, Philos. Mag. Lett. **79**, 25 (1999).

[28] C.Y. Yang, M.A. Paesler, and D.E. Sayers, Phys. Rev. B **36**, 9160 (1987).

[29] T. Watanabe, H. Kawazoe, and M. Yamane, Phys. Rev. B **38**, 5677 (1988).

[30] J. Hautala, S. Yamasaki, and P.C. Taylor, J. Non-Cryst. Solids **114**, 85 (1989).

[31] W.R. Salaneck and J.S. Berkes, Solid State Commun. **13**, 1721 (1973).

[32] V.M. Lyubin and A.V. Kolobov, private communicaton.

5 Sub-Gap Photo-Induced Phenomena in Chalcogenide Glasses

Keiji Tanaka

Prominent optical and shape changes appear in covalent chalcogenide glasses such as As_2S_3 when exposed to photons with energy in the Urbach-edge region. The phenomena are reviewed, and the mechanisms are discussed.

5.1 Introduction

Semiconductors can generally be photoexcited by bandgap illumination, while in amorphous semiconductors sub-bandgap illumination can also give some effects. Specifically, in a kind of amorphous semiconductors, the chalcogenide glasses, the sub-gap photoexcitation can trigger atomic motions, which appear as dramatic macroscopic changes. Why can less energetic photons produce such motions? Are these phenomena relevant to some applications?

In this chapter, we review the present status of the sub-gap photo-induced phenomena in chalcogenide glasses. After a brief introduction to chalcogenide glasses and photo-induced phenomena, several sub-gap photo-induced phenomena are described. Mechanisms of these phenomena are then discussed. Related observations in other materials, such as a-Si:H, oxide glasses, and organic materials, are also referred to whenever possible.

5.2 Chalcogenide Glass

A chalcogenide glass is the glass containing a large amount of chalcogen atoms, i.e. S, Se, and Te, and a variety of compounds have been synthesized so far [1–3]. Glasses can be characterized as covalent, metallic, and ionic. In covalent chalcogenide glasses such as Se and As_2S_3, the so-called 8-N rule applies to the coordination number of constituent atoms, e.g. the coordination number of chalcogens is 2. The bandgap is 2–3 eV, and electrical conduction in many materials is governed by holes. Accordingly, these glasses can be regarded as amorphous semiconductors. On the other hand, in a glass containing large amounts of Te, the bandgap is $\sim$1 eV, and metallic character increases. For instance, the electrical conductivity in AsTe is reported to be $\sim 10^4$ S/cm [1]. Telluride films also exhibit the so-called optical Ovonic effect, i.e. amorphous–crystalline phase changes induced by Joule heat, which is now commercially utilized in digital versatile discs (DVDs). Finally, in glasses such as Ag–As(Ge)–S, the coordination number of S is demonstrated to be 3–4, and ionic conduction of Ag^+ governs the electrical conductivity. Such glasses can therefore be regarded as ionic glasses or ion-

conducting amorphous semiconductors. In this chapter, we will mostly deal with the covalent chalcogenide glasses.

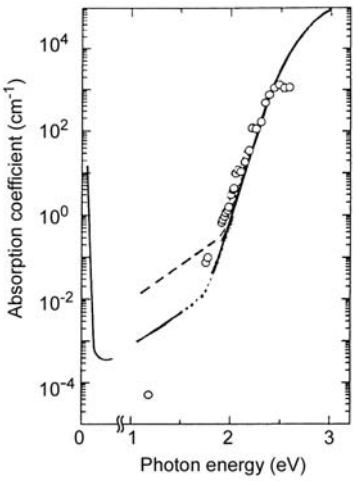

Figure 5.1: Optical absorption edges in As_2S_3 glasses at room temperature [4]. The two lines in the visible region (solid and dashed) show absorption spectra for different samples; circles correspond to the data obtained using the constant-photocurrent method in which the 1.2 eV point is obtained using laser light with sufficient accuracy.

As shown in Fig. 5.1 [4], the optical absorption edge in amorphous semiconductors is not as steep as that in crystalline semiconductors. The spectrum $\alpha(\hbar\omega)$ can be divided into three parts [2]. For $\alpha \geq 10^4$ cm^{-1}, the spectrum shows a square-root dependence $\alpha\hbar\omega \propto (\hbar\omega - E_g^T)^{1/2}$. For $10^4 \geq \alpha \geq 10^0$ cm^{-1}, the so-called Urbach edge with the form of $\alpha \propto \exp(\hbar\omega/E_U)$ appears. For $\alpha \leq 10^0$ cm^{-1}, a weak-absorption tail $\alpha \propto \exp(\hbar\omega/E_W)$ exists. Here, it is usual to define the optical bandgap energy by E_g^T, the optical Tauc gap. In As_2S_3 glass at room temperature, for instance, $E_g^T = 2.36 \pm 0.02$ eV, $E_U \simeq 50$ meV, and $E_W \simeq 250$ meV [2,4,5]. It should be noted that, despite extensive studies, the origins of these characteristics have not been elucidated. On the other hand, the mobility gap, which can be evaluated from photoconduction spectra, appears to be located at $\sim$2.5 eV [4, 6].

5.3 Photo-Induced Phenomena

Many optically-induced phenomena have been discovered for chalcogenide glasses. Such phenomena as photodoping [7, 8] occur through photochemical reactions, where the role of interfaces is important. Others (e.g. photostructural change) are bulk processes (see Fig. 5.2) [9–16], which can be divided into two groups, viz., dynamical changes which appear only under illumination, and memory effects which can be detected after illumination. The memory effect is regarded as reversible or irreversible if it can or cannot be erased by annealing at around the glass transition temperature. In addition, a bulk effect may be scalar

or vectorial. In the latter case, the effect depends on the polarization or propagation direction of the light which illuminates the sample [17]. Among scalar reversible phenomena, photo-darkening (photo-induced red shift of optical absorption edges) and related refractive-index increase are the ones most extensively studied. Note that these photo-induced phenomena appear mainly in glasses containing S and Se. The telluride glasses exhibit the Ovonic effect.

	S	Se	Te
Photon			
polymerization	○	△	
darkening	○	○	△
fluidity	○		
expansion	○	○	
Photo-thermal			
anisotropy	○	○	
crystallization	△	○	
Thermal			
phase change			○

Figure 5.2: Some optically-induced phenomena in sulfide, selenide, and telluride glasses. Irreversible changes are written in italics. Circles and triangles represent the magnitudes (circles correspond to larger changes).

It may be fair to say that, despite extensive studies, microscopic mechanisms of photo-induced phenomena have not been elucidated. The main reason is that the atomic structure of chalcogenide glasses itself, specifically the medium-range-order and defective structures, has not been identified. In addition, in order to understand the reversible changes, we need microscopic pictures of the glass transition in chalcogenide glasses, which are ambiguous. However, some consensus seems to have been obtained for the photo-electronic configuration models. Possible applications to micro-optics are continuously investigated.

To make the present chapter concise, we shall focus upon bulk, reversible (dynamical), and scalar phenomena induced by the sub-gap illumination. The photo-induced anisotropy, even though it can be induced by the sub-gap illumination, is beyond the scope of the present work. Interested readers may refer to a recent review [17] and related studies [18–21]. Also, we shall not deal with dynamical effects induced by sub-gap and bandgap illumination [22–24].

Selection of materials is crucial for investigation of sub-gap photo-induced phenomena. Among many covalent chalcogenide glasses [1–3], As_2S_3 bulk glass appears to be the most appropriate for several reasons. One reason is that the glass is stoichiometric and stable. High-purity samples are now available [5, 25]. The other reason is that a variety of fundamental properties of this glass such as optical absorption spectra are well known [1–3].The optical gap of 2.4 eV and the glass-transition temperature of $\sim$480 K are appropriate for experiments. Other glasses may also be employed. For instance, Se has a special advantage of the elemental glass, and the simple amorphous structure is suitable for investigations of fundamental mecha-

nisms. However, the glass transition temperature is $\sim$320 K, i.e. just above room temperature, and because of this thermal property, photo-induced phenomena in amorphous phases should be investigated at cryogenic temperatures. Ge-chalcogenide glasses such as $GeS(Se)_2$ can also be employed, while production of these glasses which provide reproducible characteristics is more difficult. The reason may be due to the high average coordination number of 2.67 and the existence of two types of crystals, namely, with layered and cross-linked structures.

5.4 Sub-Gap Photo-Induced Phenomena

5.4.1 Background

In some pioneering reports on photostructural changes in chalcogenide glasses, it is written that the phenomena appear upon bandgap illumination [9]. This assertion is very reasonable, since in principle only the bandgap light can give rise to electronic excitation, which may trigger successive structural changes. However, in quantitative analyses, the phenomena should be evaluated taking absorption spectra into account.

Figure 5.3 summarizes some absorption-corrected spectral variations of the photodarkening and related refractive-index increase in As_2S_3. Fig. 5.3(a) shows the quantum efficiency [26], which is normalized to an absorbed photon, and Fig. 5.3(b) shows saturated magnitudes ΔE and Δn [27, 28], which are obtained after prolonged illumination. Here, ΔE is a photo-induced red shift of the absorption edge, which can be a measure of the photodarkening. Note that all these data have been taken using excitation light with intensity of $\sim$5 mW/cm^2. These results clearly demonstrate that sub-gap illumination ($\hbar\omega < 2.4$ eV) is less effective than bandgap illumination, which confirms that *the photo-induced phenomena are induced by the bandgap illumination* [11–16]. It is mentioned here that a similar spectral dependence has been reported for the Staebler–Wronski effect and related phenomena in a-Si:H [29, 30].

The dependence upon the intensity I of light inducing the photodarkening has also been investigated for bandgap illumination. Some researchers have demonstrated that $\Delta E \propto \ln I$ [31, 32], which can be interpreted using a configurational model [33]. It has also been demonstrated that, for pulsed bandgap light with a peak intensity of $\sim$500 kW/cm^2, the time-averaged intensity is responsible for ΔE [33].

In contrast to these observations, it was discovered in the 1990s that, in some cases, sub-gap illumination can produce prominent changes. For instance, As_2S_3 with the Tauc gap of 2.4 eV exhibits marked changes when exposed to a He–Ne laser emitting photons of 2.0 eV [34–37]. The sub-gap phenomena can be divided into two groups. One is attributable to the photo-induced refractive-index increase, which produces Bragg gratings (Section 5.4.2) and self-focusing structures (Section 5.4.3). In other phenomena, *intense* sub-gap light seems to be essential, which can give rise to changes in sample shapes, i.e., photo-induced fluidity (Section 5.4.4) and giant photoexpansion (Section 5.4.5).

Photo-induced phenomena induced by pulse (fs–ns) lasers emitting sub-gap light have also been studied [38–44]. For instance, Efimov et al. reported an increase in the refractive index in As_2S_3 which is exposed to 100 fs light pulses with photons of 1.5 eV [43]. The peak intensity is estimated to be greater than 1 TW/cm^2, and underlying mechanisms seem to be different from those induced by continuous-wave (cw) sub-gap illumination. Nonlinear

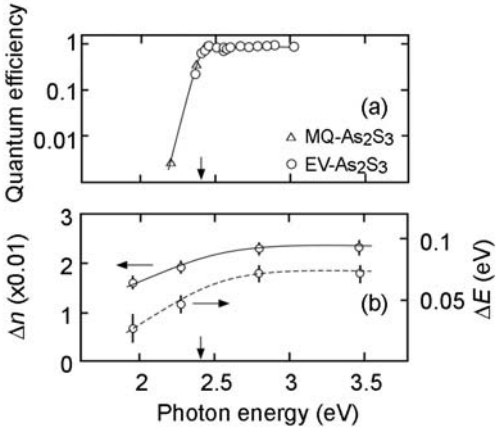

Figure 5.3: Dependence of the photodarkening (and related refractive-index increase) in As_2S_3 at room temperature on the excitation photon energy: (a) shows the quantum efficiency [26], where the triangles and the circles are obtained for bulk samples and annealed films; (b) shows the saturated values of the photodarkening ΔE and the refractive-index increase Δn, which are evaluated at $\hbar\omega \simeq 2.6$ and 2.0 eV [27].

absorption processes and/or temperature rises may be responsible for pulsed exposures. These phenomena are not covered in the following.

5.4.2 Photo-Induced Bragg Grating

If a polished As_2S_3 sample with a thickness of 0.1–5 mm is exposed to weak ($\sim$10 W/cm^2) He–Ne laser light of 633 nm ($\hbar\omega = 2.0$ eV), a spectral dip emerges at the laser wavelength [34]. An example is shown in Fig. 5.4. If, after producing a dip at 633 nm, the sample is exposed to light with a different wave length, say, 578 nm, the 633 nm dip disappears and a new dip at 578 nm grows [45]. The dip also disappears if the sample is annealed at $\sim$450 K, i.e. just below the glass-transition temperature.

Photo-induced Bragg gratings in oxide glass fibers have been fabricated by Hill's group [46, 47], and we can assume that a similar process takes place in our case. We believe that the dip is caused by a photo-induced sinusoidal pattern of the refractive index, which can be produced by mutual interference of incident and reflected light in the glass. Such a model gives a refractive-index change of $\sim$0.002 for the present case [48]. This value is smaller than that ($\sim$0.02 [27, 28]) induced by bandgap illumination, which is consistent with the result shown in Fig. 5.3b.

This model is also consistent with several other observations. First, neither the 2.3 eV nor the 1.7 eV photons can produce Bragg gratings in a 1 mm thick As_2S_3 sample [34]. Probably, this is because the penetration length ($\sim$0.1 mm) of the 2.3 eV light is smaller than the sample

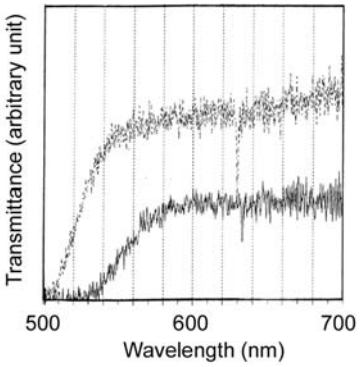

Figure 5.4: Optical transmission spectra of a 0.15 mm thick As_2S_3 sample, which has been exposed to 633 nm light at room temperature. The spectra are measured at 300 K (solid line) and 100 K (dashed line), in which the dip wavelengths are different by 3.4 nm. The 300 K spectrum is scaled to make differences in the dips clearly visible.

thickness, and accordingly, interference patterns cannot be formed. On the other hand, the 1.7 eV photons may be short of energy for inducing the refractive-index change. Secondly, when the light intensity is higher, the dip does not appear. Under intense illumination a volume expansion described in Section 5.4.4 appears, and the deformed surface probably distorts the wavefront of the reflected light. Then, mutual light-interference cannot occur. Thirdly, in a compositional study for As_xS_{100-x} (x = 25, 30, 35, 40, and 43) glasses using a He–Ne laser, it has been found that the dip is prominent in a sample with $x = 40$ and scarcely observed in the glass with $x = 25$. We can assume that the 2.0 eV photons may not be energetic for the sample with $x = 25$, since its Tauc gap is estimated to be $\sim$2.5 eV [2]. In addition, the photo-induced refractive-index increase by the bandgap light is known to become smaller in S-rich samples [49].

Photo-induced Bragg gratings are promising for applications. The grating can be produced in As_2S_3 optical fibers, which operate as wavelength-notch filters [48]. As shown in Fig. 5.4, the dip wavelength can be utilized for sensing temperatures, since the chalcogenide glass has relatively large thermal expansion coefficients of $\sim 2 \times 10^{-5}$/K [50]. Recently, it has also been demonstrated that light illumination from fiber side-surfaces can induce refractive-index modulations in chalcogenide-glass fibers [51, 52]. As mentioned above, Bragg gratings in oxide glasses have been produced, and a comparison may be important to recognize some characteristic differences between chalcogenides and oxides. A marked one is the greater refractive-index changes in chalcogenides, which is favorable to produce shorter ($\sim$5 mm) Bragg-reflector fibers than those ($\sim$1 m) in oxide fibers [46,47]. However, since the refractive index ($\sim$2.5) of chalcogenides is much higher than that ($\sim$1.5) of oxides, the coupling between the chalcogenide fiber and oxide optical components may be problematic.

5.4.3 Photo-Induced Persistent Self-Focusing Structure

Lyubin and Tikhomirov discovered that when thick (1–50 mm) As_2S_3 samples are exposed to He–Ne laser beams of 633 nm and $\sim$5 W/cm^2, the transmitted beam gradually spreads with the exposure time [35]. Based on this observation, they speculated that the spreading is caused by photo-induced light scattering [53], i.e. the laser beam produces some small particles, which scatter the transmitted light.

However, Hisakuni and Tanaka argued that the light spreading is caused by the formation of persistent self-focusing structures [17, 54, 55]. The situation is illustrated in the inset to Fig. 5.5. These authors noticed, as shown in Fig. 5.5, that the intensity of directly transmitted light first increases, which cannot be explained by the light-scattering model. In contrast, the observed fact can be understood quantitatively by the self-focusing model, in which the light-intensity increase is a manifestation of GRIN (graded refractive index) lens formation through the photo-induced refractive-index increase. With prolonged exposure, the index increases further, so that the illuminated region behaves as a defocusing structure, which gives rise to the light spreading. Note that such self-focusing structures can only be produced by the sub-gap light, since a long penetration length ($\sim$1 cm) is a prerequisite.[1]

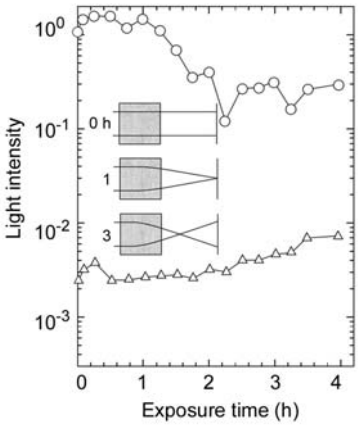

Figure 5.5: Intensity changes of directly-transmitted (circles) and diffuse light (triangles) at a diffuse angle of 2° in a 3 mm thick As_2S_3 glass, which is exposed to He–Ne laser light of $\sim$5 W/cm^2 [54]. The inset illustrates the self-focusing structures (cross-sectional views) at various exposure times.

The persistent self-focusing structure has been applied to optical devices. For instance, Saitoh et al. have fabricated photo-induced GRIN microlenses on end surfaces of optical fibers [56]. Self-written waveguides have also been fabricated [57, 58].

5.4.4 Photo-Induced Fluidity

A stressed As_2S_3 glass shows viscous relaxation when exposed to 2.0 eV light [36]. The inset to Fig. 5.6 shows a sample which has been employed to evaluate the photo-induced fluidity.

[1] See Chapter 6 (p. 99) for alternative arguments. (Editor's comment)

Here, an As_2S_3 flake is subjected to an elongating stress, and the sample is illuminated from the side with a focused He–Ne laser beam with photon energy of 2.0 eV and intensity of 10^2 W/cm^2. Changes in the sample length are monitored using an optical lever technique (not shown). Then, as exemplified in the figure, marked elongations are detected only under illumination. The viscosity (the inverse of fluidity) calculated from this elongation behavior is $\sim 10^{12}$ poise, which is smaller by one order of magnitude than that obtained at the glass transition temperature. On the other hand, Fig. 5.7 shows that an illuminated region of As_2S_3 is smoother than peripheral unilluminated regions, which may also be a manifestation of the photo-induced fluidity.

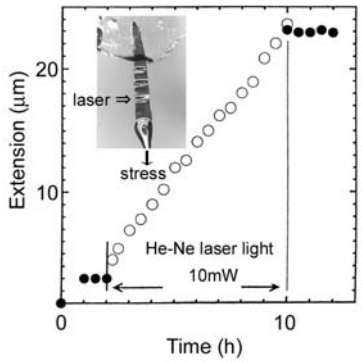

Figure 5.6: Elongation behavior of an As_2S_3 flake (with approximate dimensions of 2 mm, 0.2 mm, and 50 μm) under illumination of focused He–Ne laser light with intensity of $\sim 10^2$ W/cm^2 and a load of 4.5 grams. The inset shows an experimental setup, in which the flake has been illuminated three times.

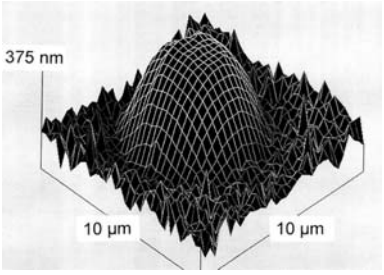

Figure 5.7: An AFM image of an As_2S_3 flake (4 μm thick) which has been exposed to He–Ne laser light with an intensity of $\sim 10^4$ W/cm^2 for 10 min [45].

A thermal mechanism might be envisaged straightforwardly for this phenomenon, i.e. one can think that a temperature rise higher than the glass transition temperature causes the fluidity. However, the photo-induced fluidity becomes more prominent if a sample is illuminated at lower temperatures [36, 45]. This result cannot be accounted for by thermal models. Alternatively, the fluidity enhancement triggered by photoelectronic processes is quite plausible.

Features in other materials are of interest. However, since the photo-induced fluidity appears only under illumination, quantitative evaluations are more-or-less restricted. Accordingly, the investigation has been done only for As_2S_3 layers and fibers, in which some differences have been marked [45]. In other covalent chalcogenide glasses, the photo-induced fluidity seems to occur universally, since the giant photoexpansion appears in the glasses (see Section 5.4.5). Note that similar photo-induced relaxation phenomena have been reported for some chalcogenide glasses such as Se [59–61], while in those studies bandgap light was, or seems to have been, employed. As a result, photoelectronic and thermal effects cannot be clearly distinguished. Lastly, it is also noted the photo-induced fluidity has not been detected in Pyrex glass and polyethylene films which were exposed to ultraviolet light [45].

5.4.5 Giant Photoexpansion

If a surface of As_2S_3 is exposed to a focused intense ($\geq 10^2$ W/cm^2) He–Ne laser beam for several minutes, a prominent volume expansion appears [37]. Figure 5.7 shows a typical result, in which the fractional expansion $\Delta L/L$ amounts to $\sim$5%, where ΔL ($\simeq$ 250 nm) is the expansion height and L ($\simeq$ 4 μm) is the sample thickness. Previously, Hamanaka et al. discovered that bandgap light could produce volume expansions of $\Delta L \simeq 90$ nm, which corresponds to a fraction of 0.4% [62–64]. Accordingly, the expansion of $\sim$5% by sub-gap light could be referred to as *giant*.

Since it is relatively easy to evaluate the photoexpansion by using profile monitors, several characteristics in As_2S_3 have been investigated in detail. First, regarding the spectral dependence, light having photon energy in the Urbach-edge region is effective to produce the giant expansion [37]. The bandgap illumination ($\sim$2.4 eV) gives the conventional volume expansion of 0.4 % [62,63], and sub-gap light ($<$1.7 eV) in the weak-absorption tail cannot produce appreciable effects [37, 65]. We can, therefore, assume that *Urbach-edge light* is responsible for this phenomenon. Second, the expansion occurs only when a sample is illuminated by intense light, i.e. higher than 10^2 W/cm^2 [37]. Above this threshold intensity, ΔL increases as $\Delta L \propto \ln I$ (see Fig. 5.8 in which α is $\sim$1 cm^{-1} for 2.0 eV light). Weaker light may produce Bragg gratings (Section 5.4.2) and/or the self-focusing structures (5.4.3). Third, the expansion becomes more prominent if a sample is illuminated at lower temperatures [66]. For instance, the expansion produced at 10 K is four times larger than that produced at 300 K, the magnitude being measured at room temperature in both cases. If the measurements could be performed at 10 K, greater magnitudes would have been obtained, since the expansion produced at 10 K in an optical cryostat could be seen with the naked eye. Finally, annealing at 490 K erases the expansion [37].

Giant photoexpansion of 1–5% seem to be inherent to covalent chalcogenide glasses [45]. Actually, the expansion patterns with diameters of 5–10 μm have been produced at room temperature in As_2Se_3 ($E_g \simeq 1.8$ eV) exposed to focused light from a laser diode (1.6 eV and 5 mW), in GeS_2 ($E_g \simeq 3.2$ eV) by an Ar ion laser (2.7 eV and 5 mW), and in $GeSe_2$ ($E_g \simeq 2.2$ eV) by a He–Ne laser (2.0 eV and 5 mW). However, it has not been examined if expansion occurs in pure amorphous Se.

The giant photoexpansion is assumed to occur as a combined effect of expansive forces and the photo-induced fluidity (Section 5.4.4) [37]. That is, provided that the experimentally detected surface expansion is a manifestation of volume expansion with an intrinsic fractional

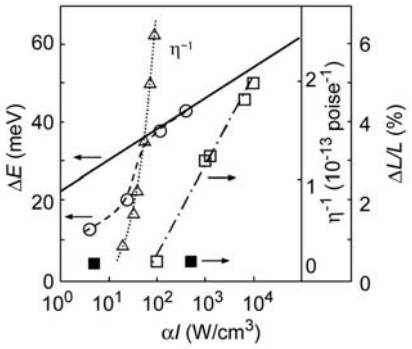

Figure 5.8: Light intensity dependence of photodarkening, ΔE (circles), expansion $\Delta L/L$ (squares) and fluidity η^{-1} (triangles) upon 2.4 eV bandgap (solid line and symbols) and 2.0 eV sub-gap (open symbols) illumination.

ratio of $\Delta L_0/L$ of an illuminated cylinder with a length of L and a diameter of $2r$, the apparent expansion $\Delta L/L$ is given as $\Delta L/L = (\Delta L_0/L)(1 + L/r)$. This can dramatically increase when $L \gg r$, which has been quantitatively confirmed. This quantitative agreement also suggests that the intrinsic expansion $\Delta L_0/L$ induced by intense sub-gap illumination is the same as that by the bandgap illumination ($\sim$0.4% at room temperature [62, 63]).

The giant photoexpansion has been applied to fabrication of optical components such as microlenses [56, 67, 68].

5.4.6 Spectral Light-Intensity Dependence

Figure 5.8 summarizes the dependence of photo-induced optical and shape changes in As_2S_3 upon the absorbed light intensity αI for the bandgap ($\sim$2.4 eV) and sub-gap ($\sim$2.0 eV) illumination [36, 37, 63, 65, 69]. Above 10^5 W/cm^3, As_2S_3 is likely to thermally vaporize. Note that, for 2.4 and 2.0 eV light, the absorption coefficients are 10^3 cm^{-1} and 10^0 cm^{-1}, so that the incident light intensities are different by three orders of magnitude.

For the photodarkening ΔE, the bandgap and sub-gap illumination exhibit contrasting light-intensity dependences [65]. The bandgap illumination provides the known intensity dependence of $\Delta E \propto \ln I$ [31–33]. For the sub-gap light, when the intensity is small ($\sim$10 W/cm^3), ΔE is smaller than that induced by bandgap illumination, which is consistent with the spectral dependence shown in Fig. 5.3b. However, at αI = 10^2 W/cm^3, ΔE markedly increases and approaches to the curve corresponding to the bandgap illumination. Accordingly, when $\alpha I \geq 10^2$ W/cm^3, the dependence of ΔE upon the photon energy of excitation becomes flat at $\hbar\omega \simeq$ 2.0–2.4 eV. (A flat spectrum also appears at low temperatures [65]). Note that ΔE can be a measure of the refractive-index increase (see Fig. 5.3b), while it can be evaluated more easily than the index change.

The shape changes show two interesting characteristics. One is that the photo-induced fluidity becomes prominent at $\alpha I \simeq 10^2$ W/cm^3 [36], where sub-gap illumination exhibits a similar ΔE to that of bandgap illumination. The other is that the giant photoexpansion

becomes prominent above this intensity level [37]. This correlation between fluidity and expansion is very reasonable, since photoexpansion necessarily requires fluidity.

5.5 Mechanism

A photo-induced change can occur through two processes; photoelectronic excitation and successive structural changes. Accordingly, in order to understand the photo-induced change, we must know the structural change and the photo-electro-structural process. In this context, mechanisms of the sub-gap photo-induced phenomena, which can be grouped into the two, have not been elucidated. The known features can be summarized as follows.

Photo-induced Bragg gratings and photo-induced persistent self-focusing structures are produced by sub-gap illumination of moderate intensities ($\alpha I \leq 10$ W/cm^3). These changes are undoubtedly induced by the photo-induced refractive-index increase, which can be connected through the Kramers–Kronig relation with the photodarkening. It is known that, at such intensity level, the bandgap illumination can induce optical changes more efficiently (Fig. 5.3b). However, since its penetration length is short ($\leq$10 μm), the changes are restricted to the neighborhood of illuminated surfaces. On the other hand, in the case of the sub-gap light, despite smaller refractive-index increases, the longer penetration length ($\sim$1 cm) can give rise to bulk changes. As a result, the effect becomes seemingly prominent. Then the question is why the sub-gap photons in the Urbach-edge region can provide similar, but smaller, optical changes to those induced by bandgap light.

The photo-induced fluidity and the giant photoexpansion, which appear under intense sub-gap illumination, may be more complicated. Here, the first problem is related to the photoelectronic excitation. This means the role of the intense sub-gap illumination, or more precisely, the meaning of the threshold of 10^2 W/cm^3 should be interpreted (see Fig. 5.8). It is noted here that the bandgap illumination with intensity of 0.5–500 mW/cm^2 produces the photoexpansion [63, 69] and probably the photo-induced fluidity as well, since fluidity is a necessary condition for transferring an atomic expansion in a sample interior to its surface. Accordingly, the qualitative features are assumed to be the same with those characteristic of the intense sub-gap illumination. However, we can expect that the longer penetration length of sub-gap light can provide *bulk* effects. Then, why can the intense sub-gap light cause similar changes to those by bandgap light? The next problem may be atomic structural changes which are responsible for the fluidity and the expansion.

5.5.1 Temperature Rise

A temperature rise inevitably occurs in a sample when it absorbs light energy. The magnitude of ΔT upon continuous-wave illumination is estimated roughly to be $\sim I_a/(2\pi r\kappa)$ [70], where I_a is the absorbed light energy, κ is the thermal conductivity of the sample, and r is the radius of the light spot. In an experiment on giant photoexpansion, where the temperature rise may be maximal, an As_2S_3 flake with a thickness of 0.1 mm is exposed to the light with $I = 10$ mW, $r = 5$ μm (10^4 W/cm^2), and the wavelength 633 nm, where $\alpha \simeq 1$ cm^{-1}. Then, using $\kappa \simeq 3$ mW/cm.K [71], we obtain $\Delta T \simeq 10$ K.

This value can be neglected in the present context. Optical changes induced by the temperature rise are small, e.g., $\mathrm{d}E_g/\mathrm{d}T = 10^{-3}$ eV/K [72, 73] and $\mathrm{d}n/\mathrm{d}T = 10^{-4}$ K^{-1}, where $n = 2.6$ [74]. The fluidity changes due to heating can be neglected, since the glass transition temperature is $\sim$450 K, at which the viscosity is known to be $\sim 10^{13}$ poise. Thermal expansion may also be neglected, since the expansion coefficient is of the order of 10^{-5}/K [50].

5.5.2 Two-Photon Absorption

It may be instructive to examine the role of two(multi)-photon absorption in the sub-gap phenomena. Actually, several kinds of photo-induced phenomena, which are assumed to be triggered by non-linear excitation, have been reported for wide-gap materials such as oxide glasses and organic polymers (see, for instance, [75] and [76]). Similar processes may be responsible for the sub-gap photo-induced phenomena in chalcogenide glasses.

However, the following three features strongly suggest that the non-linear absorption can be neglected in the present phenomena. The first is the spectral dependence. It is noted in Section 5.4.5 that an exposure to the Urbach-edge light is needed for the giant photoexpansion to occur (see also Fig. 5.11). If the two-photon absorption were responsible for the observed phenomenon, the light absorption at $\hbar\omega \geq E_g/2$ ($\simeq$1.2 eV) would have induced some effects, which is not the case in the present observation. Second, an insight is obtained from a quantitative consideration. The two-photon absorption coefficient in As_2S_3 at $\hbar\omega$ = 2.0 eV is evaluated at $\sim$10 cm/GW [77]. Since the one-photon absorption coefficient at 2.0 eV is ~ 1 cm^{-1}, two-photon absorption processes can become dominant when the light intensity is greater than 10^8 W/cm^2. This intensity is higher than the present maximum level by four orders of magnitude. Third, the intensity dependence proportional to I^2 has not been observed. Actually, the fluidity increase shown in Fig. 5.8 depends roughly linearly on the light intensity [45], and the giant photoexpansion appears to be proportional to $\ln I$ [37]. Based on these arguments, we can reject the two-photon effects as being responsible for the observed processes.

5.5.3 Gap States and Microscopic Structure

When considering the mechanisms of sub-gap photo-induced phenomena, we should know the density of states which is responsible for the sub-gap optical absorption. However, related studies seem to be limited. For instance, although extensive publications upon the well-known charged-defect model originally proposed by Mott et al. are available [2,3], optical absorption spectra have not been considered in detail [78]. Different ideas for the gap states have also been suggested [79], but the role of the Urbach-edge light cannot be specified in these models.

The present author has recently proposed [80, 81], on the basis of several experimental results, that the realistic density of states can be considered to be like the one illustrated in Fig. 5.9a. Assuming this electronic density, spatial potential fluctuations and atomic structures in As_2S_3 are exemplified in Fig. 5.9b and c. The model assumes that the Urbach edge, which is connected with the exponential density of states above the valence band, arises from fluctuations of the van der Waals type interlayer bonds and/or disordered interaction among the intralayer lone-pair electrons. On the other hand, the weak absorption tail is ascribed to

antibonding states of As–As wrong bonds, which can produce unoccupied deep states below the conduction band.

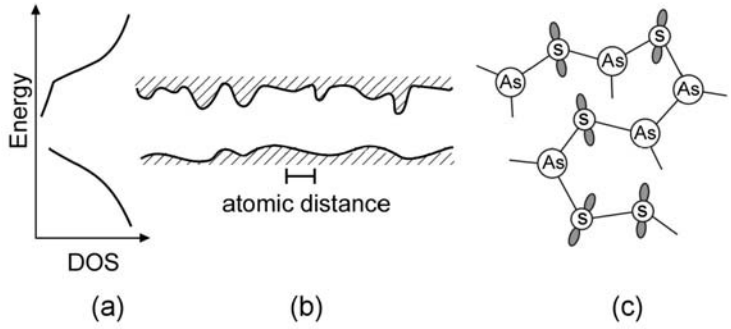

Figure 5.9: Density of states (a), the spatial potential fluctuation (b), and the corresponding atomic structure (c) proposed for As_2S_3 glass [80, 81].

In this model, the Urbach-edge light is assumed to produce the following electronic excitations. One possibility is generation of localized holes in the valence-band edge and delocalized electrons in the conduction band, and the other is generation of delocalized holes in the valence band and localized electrons in the conduction-band tail. Simultaneous excitation of localized electrons and holes may be less probable, since the localized states are spatially separated as illustrated in Fig. 5.9b. The delocalized carriers are immediately ($\sim 10^{-12}$ s) trapped into the localized states. Then, what kinds of structural changes follow these excitations?

5.5.4 Refractive-Index Change

A configurational model as shown in Fig. 5.10 can be applied to interpret the refractive-index increase which produces Bragg gratings and self-focusing structures. In the model, which has been proposed for understanding the photon-energy dependence of the photodarkening and related refractive-index increase [27, 28], a number of defective sites are envisaged, each being assumed to have a configurational energy with single-well excited state, Z, and double-well ground-state potentials, X and Y [82, 83]. It is also assumed that the optical change is proportional to the site density having the quasi-stable configuration Y. In the defective site having such a single-and-double well configuration, the main process induced by bandgap illumination is a configurational transfer of $X \rightarrow Z \rightarrow Y$. On the other hand, Urbach-edge light can induce relatively efficiently the backward process, $Y \rightarrow Z \rightarrow X$, since the excitation from Y to Z can be induced by photons with smaller energy. Accordingly, the sub-gap illumination produces smaller optical changes than those induced by the bandgap illumination, which is consistent with the results shown in Fig. 5.3b. Later, the configurational model has been connected to an atomic model, which assumes bond twisting motions of the chalcogen atoms [84, 85].

Taking the density of states described in Section 5.5.3 into account, we can improve the above model as follows. Irrespective of whether the bandgap or Urbach-edge light is used, a photon excites an electron (X to Z' in Fig. 5.10). Then, after some electronic relaxation, the

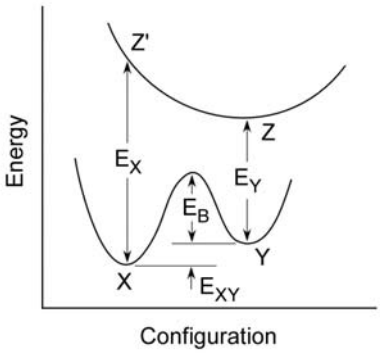

Figure 5.10: A configurational model for the photodarkening and related refractive-index changes [85].

electron and hole are trapped in the conduction-band tail state (antibonding state of As–As in Fig. 5.9) and in the valence-band edge state. The distance between these trapped carriers may be either short or long. If the distance is long so that immediate geminate recombination ($\sim 10^{-8}$ s) does not occur, a polaron-like structural change can take place (Z' to Z); e.g., an As–As bond may be severed and/or the interlayer van der Waals distance may be shortened (or lengthened) temporally, which can appear as a C_3 configuration. This temporal C_3 may correspond to the three-fold coordinated atoms detected in recent EXAFS experiments on Se by Kolobov et al. [86]. Then, after the structural change, the carriers recombine, and the disordered structure is frozen in (Z to Y). Through repeating such photo-electro-structural processes at the configurational sites, the amorphous structure becomes more disordered. Specifically, the interlayer distance of van der Waals type becomes more random, which gives rise to broadening of the valence band. As a result, photodarkening occurs, and the refractive index at visible wavelengths increases. This model is consistent with the reported intensity decrease in the first-sharp diffraction peak [11] (see Fig. 5.12).

Several researchers proposed the so-called thermal spike models [3, 9, 87] for the photodarkening, although this idea seems to be less probable. In this model, it is assumed that localized vibrations (thermal spikes) excited through recombination of electron–hole pairs induce some structural changes. However, if this model were correct, the excitation in the weak-absorption-tail region would have also given some structural changes. However, no photo-induced changes have been detected after illumination of the sample with such low-energy photons. Therefore, geminate recombination is assumed not to play an important role in the photostructural process.

5.5.5 Fluidity and Volume Expansion

Electronic Excitation

Spectral experiments using pulsed light may be valuable for understanding the role of intense sub-gap illumination [88–90]. As shown in Fig. 5.11, when the light intensity is not high,

excitation spectra of the photoconduction and the volume expansion have thresholds at around the Tauc gap, $\sim$2.4 eV, which is reasonable. However, when the pulsed light is strengthened to a peak intensity of $\sim 10^7$ W/cm^2 (5 ns width and 10 Hz repetition), the spectra red-shift to a threshold of $\sim$2.0 eV. Note that, for cw illumination, the sub-gap (2.0 eV) illumination can give the giant expansion when the intensity is higher than 10^2 W/cm^2 (see Section 5.4.5).

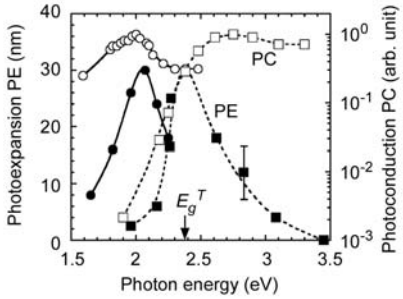

Figure 5.11: Spectral dependence of the photoexpansion PE (solid symbols) and the photoconduction PC (open symbols) in As_2S_3 exposed to cw light of 10^{-2} W/cm^2 (square) and pulsed light of 10^8 W/cm^2 (circles) [90]. The Tauc gap E_g^T is indicated.

Although the light intensities of the pulse and cw experiments appear to be very different, we can see that both exposures produce a similar number of trapped carriers. For cw light of 10^2 W/cm^2, since the absorption coefficient is 10^0 cm^{-1} at 2.0 eV, the absorbed energy is 10^2 W/cm^3, i.e. 10^{20} photons/s cm^3, which can produce 10^{20}/s cm^3 trapped carriers. The trap depth may typically be $\sim$0.5 eV (2.5–2.0 eV), for which the thermal excitation time ($\tau = \Omega^{-1} \exp(E/kT)$) is evaluated as 10^{-4} s. Accordingly, the number of steadily trapped carriers under cw illumination is estimated as 10^{16} cm^{-3}. On the other hand, pulsed excitation of 10^7 W/cm^2 and 5 ns yields an energy of 50 mJ/cm^3, which leads to a carrier density of 10^{17} cm^{-3}, which is nearly the same as that of the cw excitation.

It is important to grasp the implication of this carrier density, 10^{16}–10^{17} cm^{-3}. This density seems to be comparable to that of the tail states below $\sim$2.0 eV, which can be estimated from the optical absorption spectrum assuming that the optical transition probability is not strongly dependent on the photon energy. This similarity in values allows us to assume that *the required carrier density should be sufficient to fill the available tail states* [90]. When the tail states are filled with carriers, successively-photoexcited carriers can no longer be trapped, or detrapped immediately. These excess carriers produce photocurrent, which explains the red-shifted photocurrent spectra in Fig. 5.11 [88]. In this way, intense sub-gap illumination can work as if it were bandgap illumination. We can assume that the giant photoexpansion and the photo-induced fluidity occur under such circumstances [89].

Consideration of the temperature dependence gives further support to the above idea. As mentioned in Section 5.4.5, prominent giant photoexpansion appears with intense 2.0 eV illumination at low temperatures such as 10 K, where the Tauc gap is $\sim$2.5 eV. At low temperature, the thermal excitation of trapped carriers is practically impossible since $\tau \simeq 10^{12}$ s. Therefore, the trap filling is accomplished in an ideal way. Then, what kinds of structural changes follow?

Structural Changes

Structural changes responsible for the volume expansion may be identified through detailed X-ray diffraction experiments. We note here that the features induced by bandgap and sub-gap illumination appear to be similar; i.e., the same intrinsic volume expansions ($\sim 0.4\%$ in As_2S_3 at room temperature) and similar changes in the X-ray diffraction patterns [65]. However, since the bandgap illumination can induce the expansion with larger areas and a depth of ~ 10 μm, it is more suitable for X-ray studies.

Figure 5.12 shows a typical result [69]. We see in the upper pattern that the first sharp diffraction peak is located at wavenumber of $Q \simeq 1.2$ Å^{-1}, which is consistent with previous studies [2]. The lower pattern shows the intensity difference between the annealed and illuminated states, with positive difference values indicating a decreases in the X-ray intensity with illumination. This pattern manifests that the peak intensity decreases with illumination, which is also consistent with previous results [11]. In addition, a closer look reveals that the peak broadens asymmetrically. That is, the intensity enhancement at ~ 0.8 Å^{-1} appears to be broader than that at ~ 1.5 Å^{-1}.

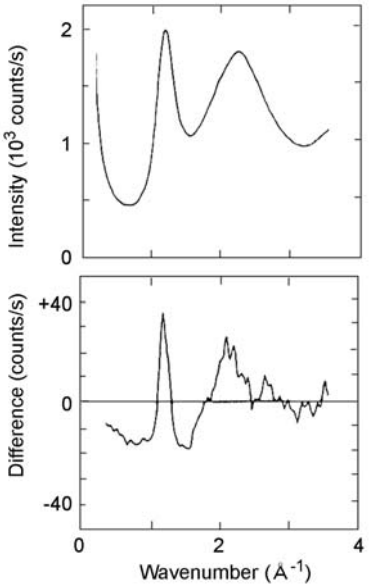

Figure 5.12: An X-ray diffraction pattern of As_2S_3 (top) and the intensity decrease (bottom) induced by bandgap illumination [69]. A positive difference means the intensity reduction upon illumination.

On the basis of the so-called distorted-layer model originally proposed by Vaipolin and Porai-Koshits [91], this asymmetric change can be interpreted as a manifestation of interlayer cracking [69]. That is, in distorted layer structures with a typical interlayer distance of ~ 0.5 nm, in a few places the interlayer distance becomes as wide as ~ 1 nm. A preliminary calculation suggests that such a change can give rise to a macroscopic volume expansion of $\sim 0.5\%$ [69]. Therefore, it is plausible that the volume expansion is caused by cracking the layered structure.

Structural changes responsible for fluidity are more difficult to examine, since the change occurs only *under* illumination. No changes in the X-ray diffraction have been detected by the author (unpublished). On the other hand, some Raman-scattering studies on the photo-induced fluidity have been reported recently [21,92]. However, relations between microscopic and macroscopic changes remain to be studied.

Models

Regarding the photo-electro-structural process giving rise to the volume expansion and fluidity, at least two ideas have been proposed. Shimakawa et al. try to explain these structural changes using a Coulomb-repulsion model [93–95]. Tanaka [90] and some other researchers [92] envisage atomic motions, which enhance structural randomness, and successive relaxation. These models are summarized below.

Shimakawa et al. assume macroscopic carrier diffusion and Coulomb repulsion among the layer fragments [93–95]. They emphasize that, in conventional chalcogenide glasses such as As_2S_3, illuminated regions tend to be negatively charged due to the difference of diffusion constants of holes and electrons. Such charge separations are actually detected as Dember voltages [96]. Then, As–S layer fragments in illuminated regions may be negatively charged, and the Coulomb repulsion among the fragments can cause mutual expansions. In this model, they try to explain the expansive force and the fluidity in a unified way. This model is similar to that proposed for the deformation induced by an electron beam [66, 97].

The present author assumes the bond twisting motion and interlayer relaxation. It is supposed that, as illustrated in Fig. 5.13 [90], illumination induces bond twisting motions and so forth (a), which produce strain in the interlayer regions (b). This strain relaxes with segmental expansion (c). In this case, for the internal expansions to manifest themselves as macroscopic surface expansions, atomic fluidity is needed, which may occur through interchanges of covalent bonds producing dynamical dangling bonds [15, 16, 60]. In these processes, it is plausible that strained regions behave as localized states, which can be selectively photoexcited by the sub-gap photons [45]. Alternatively, the fluidity may occur in ionized structures due to trapped electrons and holes [45], just as an ionic crystal can deform more easily than a covalent crystal. In essence, the photo-induced fluidity can be regarded as a kind of electronic melting, which was originally proposed by Van Vechten et al. [99] and which has been demonstrated recently [100].

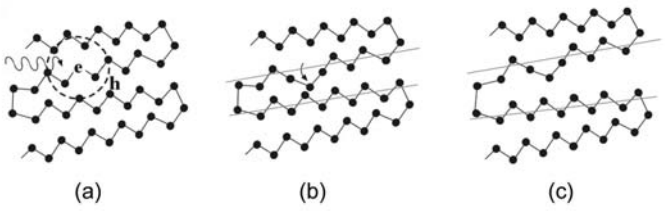

Figure 5.13: An atomic model for the photoexpansion, which is illustrated for Se for simplicity [90].

It may be fair to conclude this section with a statement that all existing models are speculative. The above two models are consistent with the fact that, if expansions are suppressed with pressure, the photodarkening becomes greater [98]. However, it seems to be problematic how the Coulomb-repulsion model explains the photo*depression* in $GeAs_4Se_5$ [62]. In the atomic model, the depression can be assumed to be a manifestation of compressive structural relaxation, which has been widely observed in oxide glasses [69]. Finally, it should be emphasized that no quantitative models are available at present. For instance, why does As_2S_3 at room temperature exhibit an intrinsic expansion ($\Delta L_0/L$) of $\sim$0.4% ?

5.6 Summary

Photo-induced phenomena induced by continuous-wave sub-gap illumination seem to be inherent to covalent chalcogenide glasses. The reason is the existence of gap states into which the carriers can be photoexcited. Further excitation from the localized to extended states may be possible through thermal activation. In the photo-induced Bragg grating and self-focusing formations, the refractive-index increase occurs through these gap states. In the photo-induced fluidity and giant expansion, the majority of these gap states are excited, giving rise to dramatic structural changes. This kind of sub-gap excitation cannot occur, in principle, in a perfect crystal in which no gap states exist [101].

In addition, it is suggested that the sulfide and selenide glasses exhibit photostructural changes for two reasons. One reason is the existence of lone-pair electrons, which give a variety of bonding configurations. The other is a flexible structure consisting of two kinds of atomic bonds (covalent and van der Waals). In telluride glasses, this dual bonding character tends to merge into a single metallic bonding, so that photostructural changes become smaller. On the other hand, in most oxide glasses, although the oxygen atom possesses lone-pair electrons, rigid three-dimensional continuous-random-network structures prohibit prominent photostructural changes.

Acknowledgments

Most pioneering experiments on sub-gap photo-induced phenomena in my laboratory were carried out by one of my ex-students, H. Hisakuni, and it is my pleasure to thank him for his skillful and passionate work. I also thank Dr T. Gotoh for preparing the publication-quality figures.

References

[1] Z.U. Borisova, Glassy Semiconductors, Plenum Press, New York, 1981.

[2] S.R. Elliott, Chalcogenide Glasses, in Materials Science and Technology, Vol. 9, J. Zarzycki (Ed.), VCH, Weinheim, 1991, p. 375.

[3] M.A. Popescu, Non-Crystalline Chalcogenides, Kluwer, Dordrecht, 2000.

[4] K. Tanaka and S. Nakayama, Jpn. J. Appl. Phys. Pt. 1 **38**, 3986 (1999).

[5] K. Tanaka, T. Gotoh, N. Yoshida, and S. Nonomura, J. Appl. Phys. **91**, 125 (2002).

[6] K. Tanaka and S. Nakayama, J. Optoelectron. Adv. Mater. **2**, 5 (2000).

[7] A.V. Kolobov and S.R. Elliott, Adv. Phys. **40**, 625 (1991).

[8] K. Kawaguchi, K. Tanaka, and S.R. Elliott, Photo-Induced and Electron-Beam Phenomena in Ag-Rich Amorphous Chalcogenide Semiconductors, in Handbook of Advanced Electronic and Photonic Materials and Devices, Vol. 5, H.S. Nalwa (Ed.), Academic Press, San Diego, 2001, p. 92.

[9] J.P. deNeufville, Photostructural Transformations in Amorphous Solids, in Optical Properties of Solids – New Developments, B.O. Seraphin (Ed.), North-Holland, Amsterdam, 1975, p. 437.

[10] B.T. Kolomiets and V.M. Lyubin, Mat. Res. Bull. **13**, 1343 (1978).

[11] K. Tanaka, Photo-Induced Phenomena in Amorphous Semiconductors, in Fundamental Physics of Amorphous Semiconductors, F. Yonezawa (Ed.), Springer-Verlag, Berlin, 1981, p. 104.

[12] K. Tanaka, Rev. Solid State Sci., **4**, 511 (1990).

[13] G. Pfeiffer, M.A. Paesler, and S.C. Agarwal, J. Non-Cryst. Solids **130**, 111 (1991).

[14] K. Shimakawa, A. Kolobov, and S.R. Elliott, Adv. Phys. **44**, 475 (1995).

[15] H. Fritzsche, Light-Induced Structural Changes in Glasses, in Insulating and Semiconducting Glasses, P. Boolchand (Ed.), World Scientific, Singapore, 2000, p. 653.

[16] A. Kolobov and K. Tanaka, Photo-Induced Phenomena in Amorphous Chalcogenides: From Phenomenology to Nanoscale, in Handbook of Advanced Electronic and Photonic Materials and Devices, Vol. 5, H.S. Nalwa (Ed.), Academic Press, San Diego, 2001, p. 47.

[17] K. Tanaka, Photo-Induced Anisotropy in Chalcogenide Glass, in Handbook of Advanced Electronic and Photonic Materials and Devices, Vol. 5, H.S. Nalwa (Ed.), Academic Press, San Diego, 2001, p. 120.

[18] A. Saliminia, T.V. Galstian, and A. Villeneuve, Phys. Rev. Lett. **85**, 4112 (2000).

[19] H-Y. Lee, S-J. Jang, E-S. Kim and K-B. Chung, Jpn. J. Appl. Phys. Pt. 1. **40**, 3965 (2001).

[20] T. Gotoh and K. Tanaka, J. Appl. Phys. **89**, 4697 (2001).

[21] K. Matsushita, K. Kagota, and S. Onari, J. Non-Cryst. Solids **299–302**, 929 (2002).

[22] A. Matsuda, H. Mizuno, T. Takayama, M. Saito, and M. Kikuchi, Appl. Phys. Lett. **24**, 3 (1974).

[23] A.M. Andriesh, N.A. Enachi, I.P. Cleac, T.N. Copaci, and V.A. Binchevici, J. Non-Cryst. Solids **189**, 147 (1995).

[24] A. Roy, A.V. Kolobov, and K. Tanaka, J. Appl. Phys. **83**, 4951 (1998).

[25] M.F. Chubanov, I.V. Scripachev, G.E. Snopatin, V.S. Shiryaev, and V.G. Plotnichenko, J. Optoelectron. Adv. Mater. **3**, 341 (2001).

[26] K. Tanaka, Proc. 7th Intern. Conf. Amorphous and Liquid Semicond., W.E. Spear (Ed.), 1977, p. 787.

[27] K. Tanaka, Solid State Commun. **34**, 201 (1980).

[28] K. Tanaka, J. Non-Cryst. Solids **35 & 36**, 1073 (1980).

[29] M. Fathallah, Philos. Mag. B **61**, 403 (1990).

[30] B. Ogihara, H. Takemura, T. Yoshimura, and K. Morigaki, J. Non-Cryst. Solids **299-302**, 637 (2002).
[31] K. Kimura, H. Nakata, K. Murayama, and T. Ninomiya, Solid State Commun. **40**, 551 (1981).
[32] H. Hamanaka, J. Non-Cryst. Solids **57**, 401 (1983).
[33] K. Tanaka, Thin Solid Films **157**, 35 (1988).
[34] K. Shiramine, H. Hisakuni, and K. Tanaka, Appl. Phys. Lett. **64**, 1771 (1994).
[35] V.M. Lyubin and V.K. Tikhomirov, JETP Lett. **52**, 78 (1990).
[36] H. Hisakuni and K. Tanaka, Science **270**, 974 (1995).
[37] H. Hisakuni and K. Tanaka, Appl. Phys. Lett. **65**, 2925 (1994).
[38] V. Chumash, I. Cojocaru, E. Fazio, F. Michelotti, and M. Bertolotti, Nonlinear Propagation of Strong Laser Pulses in Chalcogenide Glass Films, in Progress in Optics XXXVI, E. Wolf (Ed.), Elsevier, Amsterdam, 1996, p. 1.
[39] A.V. Belykh, O.M. Efimov, L.B. Glebov, Yu.A. Matveev, A.M. Mekryukov, M.D. Mikhailov, and K. Richardson, J. Non-Cryst. Solids **213 & 214**, 330 (1997).
[40] K. Hirao and K. Miura, J. Non-Cryst. Solids **239**, 91 (1998).
[41] A. Meneghini and A. Villeneuve, J. Opt. Soc. Am. B **15**, 2946 (1998).
[42] G. Rosenblum, B.G. Sfez, Z. Kotler, V. Lyubin, and M. Klebanov, Appl. Phys. Lett. **75**, 3249 (1999).
[43] O.M. Efimov, L.B. Glebov, K.A. Richardson, E. Van Stryland, T. Cardinal, S.H. Park, M. Couzi, and J.L. Brunêel, Opt. Mater. **17**, 379 (2001).
[44] A.P. Aleksandrov, A.A. Babin, A.M. Kiselev, D.I. Kulagin, V.V. Lozhkarev, and A.N. Stepanov, Quantum Electron. **31**, 398 (2001).
[45] K. Tanaka, C. R. Chimie 5, 805 (2002).
[46] K.O. Hill, Y. Fujii, D.C. Johnson, and B.S. Kawasaki, Appl Phys. Lett. **32**, 647 (1978).
[47] B.S. Kawasaki, K.O. Hill, D.C. Johnson, and Y. Fujii, Opt. Lett. **3**, 66 (1978).
[48] K. Tanaka, N. Toyosawa, and H. Hisakuni, Opt. Lett. **20**, 1976 (1995).
[49] K. Tanaka and Y. Ohtsuka, Thin Solid Films **57**, 59 (1979).
[50] G.J. Morgan, G.K. White, and J.G. Collins, Philos. Mag. B **43**, 1039 (1981).
[51] M. Asobe, T. Ohara, I. Yokohama, and T. Kaino, Electron. Lett. **32**, 1611 (1996).
[52] A. Saliminia, T. Galstian, A. Villeneuve, K. LeFoulgoc, and K. Richardson, J. Opt. Soc. Am. B **17**, 1348 (2000).
[53] V.M. Lyubin and M.L. Klebanov, Semiconductors **32**, 817 (1998).
[54] H. Hisakuni and K. Tanaka, Solid State Commun. **90**, 483 (1994).
[55] K. Tanaka and H. Hisakuni, Asian J. Phys. **19**, 723 (2000).
[56] A. Saitoh, T. Gotoh, and K. Tanaka, J. Non-Cryst. Solids **299–302**, 983 (2002).
[57] K-B. Song, J. Lee, J-H. Kim, and K. Cho, Phys. Rev. Lett. **85**, 3842 (2000).
[58] A.M. Ljungstrom and T.M. Monro, J. Lightwave Technol. **20**, 78 (2002).
[59] O.U. Vonwiller, Nature **104**, 347 (1919).
[60] H. Koseki and A. Odajima, Jpn. J. Appl. Phys. **21**, 424 (1982).
[61] D.K. Tagantsev and S.V. Nemilov, Sov. J. Glass Phys. Chem. **15**, 220 (1990).

[62] H. Hamanaka, K. Tanaka, A. Matsuda, and S. Iizima, Solid State Commun. **19**, 499 (1976).

[63] H. Hamanaka, K. Tanaka and S. Iizima, Solid State Commun. **23**, 63 (1977).

[64] H. Hamanaka, K. Tanaka and S. Iizima, Solid State Commun. **33**, 355 (1980).

[65] K. Tanaka and H. Hisakuni, J. Non-Cryst. Solids **198–200**, 714 (1996).

[66] K. Tanaka, Electronic Micro-Fabrication of Chalcogenide Glass, in Physics and Applications of Non-Crystalline Semiconductors in Optoelectronics, A. Andriesh and M. Bertolotti (Eds.), Kluwer, Dordrecht, 1997, p. 31.

[67] H. Hisakuni and K. Tanaka, Opt. Lett. **20**, 958 (1995).

[68] S. Ramachandran, J.C. Pepper, D.J. Brady, J. and S.G Bishop, J. Lightwave Technol. **15**, 1371 (1997).

[69] K. Tanaka, Phys. Rev. B **57**, 5163 (1998).

[70] A. Arun and A.G. Vedeshwar, Physica B **229**, 409 (1997).

[71] D.G Cahill and R.O. Pohl, Phys. Rev. B **35**, 4067 (1987).

[72] J.R. Zakis and H. Fritzsche, Phys. Stat. Sol. B **64**, 123 (1974).

[73] R.A. Street, T.M. Searle, I.G. Austin, and R.S. Sussmann, J. Phys. C: Solid State Phys. **7**, 1582 (1974).

[74] W.S. Rodney, I.H. Malitson, and T.A. King, J. Opt. Soc. Am. **48**, 633 (1958).

[75] E.N. Glezer and E. Mazur, Appl. Phys. Lett. **71**, 882 (1997).

[76] R. Sivaraman, S.J. Clarson, B.K. Lee, A.J. Stecki, and B.A. Reinhardt, Appl. Phys. Lett. **77**, 328 (2000).

[77] K. Tanaka, Appl. Phys. Lett. **80**, 177 (2002).

[78] J.A. Freitas, Jr., U. Strom, and S.G. Bishop, Phys. Rev. B **35**, 7780 (1987).

[79] Y. Watanabe, H. Kawazoe, and M. Yamane, Phys. Rev. B **38**, 5677 (1988).

[80] K. Tanaka, J. Optoelectron. Adv. Mater. **3**, 189 (2001).

[81] K. Tanaka, J. Optoelectron. Adv. Mater. **4**, 505 (2001).

[82] K. Tanaka and A. Odajima, J. Non-Cryst. Solids **46**, 259 (1981).

[83] K. Tanaka, J. Appl. Phys. **65**, 2042 (1989).

[84] K. Tanaka, J. Non-Cryst. Solids **59 & 60**, 925 (1983).

[85] K. Tanaka, Jpn. J. Appl. Phys. **25**, 779 (1986).

[86] A. Kolobov, H. Oyanagi, K. Tanaka, and K. Tanaka, Phys. Rev. B **55**, 726 (1997).

[87] V.K. Malinowsky and V.G. Zhdanov, J. Non-Cryst. Solids **51**, 31 (1982).

[88] K. Tanaka, Appl. Phys. Lett. **73**, 3435 (1998).

[89] K. Tanaka, Philos. Mag. Lett. **79**, 25 (1999).

[90] K. Tanaka, J. Non-Cryst. Solids **266–269**, 889 (2000).

[91] A.A. Vaipolin and E.A. Porai-Koshits, Sov. Phys. Solid State **5**, 497 (1963).

[92] A. Th. Kastrissios, G.N. Papatheodorou, and S.N. Yannopoulos, Phys. Rev. B **64**, 21203 (2001).

[93] K. Shimakawa, N. Yoshida, A. Ganjoo, Y. Kuzukawa, and J. Singh, Philos. Mag. Lett., **77**, 153 (1998).

[94] K. Shimakawa and A. Ganjoo, J. Optoelectron. Adv. Mater. **3**, 167 (2001).

[95] A. Ganjoo and K. Shimakawa, J. Optoelectron. Adv. Mater. **4**, 595 (2001).
[96] K. Tanaka, M. Itoh, N. Yoshida, and M. Ohto, J. Appl. Phys. **78**, 3895 (1995).
[97] K. Tanaka, Appl. Phys. Lett. **70**, 261 (1997).
[98] K. Tanaka, Phys. Rev. B **30**, 4549 (1984).
[99] J.A. Van Vechten, R. Tsu, and F.W. Saris, Phys. Lett. **74A**, 422 (1979).
[100] A. Rousse, C. Rischel, S. Fourmaux, I. Uschmann, S. Sebban, G. Grillon, Ph. Balcou, E. Forester, J.P. Geindre, P. Audebert, J.C. Gauthier, and D. Hullin, Nature, **410**, 65 (2001).
[101] D. Vanmaekelbergh and L. van Pieterson, Phys. Rev. Lett. **80**, 821 (1998).

6 Photo-Induced Anisotropy in Chalcogenide Glassy Semiconductors

Victor M. Lyubin and Matvei L. Klebanov

6.1 Introduction

Photo-induced anisotropy (PA) in chalcogenide glassy semiconductors (ChGS) has been discovered in experiments of Zhdanov, Kolomiets, Lyubin and Malinovskii [1,2] who studied the polarization state of light transmitted through glassy films of different composition irradiated by a linearly polarized laser beam. The possible role of PA of light scattering was also mentioned in these papers. Later, investigation of photo-induced optical anisotropy was carried out by different groups on thin films [3–8], bulk glasses [9–13] and As_2S_3 fibers [10].

It has also been shown that photo-induced circular dichroism of transmittance, referred to as photo-induced optical gyrotropy, appears in both bulk ChGS and thin films exposed to circularly polarized light [9, 14]. Photo-induced elliptical birefringence and photo-induced elliptical dichroism were also reported [15, 16] as well as photo-induced light scattering [9] and photo-induced scattering anisotropy and gyrotropy [17, 18].

In early publications, PA in chalcogenide films was explained by the interaction of polarized light with some optically anisotropic structural elements whose optical axes are oriented randomly [1,2]. According to this assumption, linearly polarized light interacts more strongly with structural elements oriented with their optical axis parallel to the electrical vector of the light, destroying them, This process results in the appearance of optical anisotropy. Later, more detailed models of PA in thin chalcogenide films were proposed but in most cases these models developed the initial proposed idea [1, 2]. Thus Fritzsche [19] discussed the photo-induced redistribution of anisotropic microvolumes in ChGS when the microvolumes with the axis parallel to the electric vector of the excitation light are transformed into ones with the axis orthogonal to this vector. In other models, different kinds of possible microanisotropic structural elements of ChGS were considered. Several review papers on PA have been published recently [20, 21] of which the review by Tanaka [20] is especially recommended since both the history of PA research and the modern state of experiment and theory are considered in detail. The study of photo-induced optical anisotropy is in constant progress and new papers in this field have been published recently [22–24].

In this chapter we limit ourselves to a summary of recent results of the PA studies performed by the authors, predominantly at the laboratory of amorphous semiconductors of the Ben-Gurion University of the Negev (Beer-Sheva, Israel), either independently or in collaboration with other groups. First, we consider processes of photo-induced optical anisotropy and describe successively the results obtained on excitation of ChGS samples by the above-

bandgap, sub-bandgap and super-bandgap light. The last term is used for the case when the excitation energy substantially exceeds the optical gap of ChVS. This part of the review is followed by a description of other manifestations of PA. Finally, we propose a general understanding of the essence of anisotropic phenomena in ChGS.

6.2 Samples and Experimental Procedures

Two major kinds of samples were investigated, namely thin films and bulk glasses. The thin film glassy samples of As_2Se_3, $As_{50}Se_{50}$, As_2S_3, $Ge_{28.5}Pb_{15}S_{56.5}$, Se, $Se_{80}Te_{20}$, $Ge_xAs_{40-x}S_{60}$, and $Ge_xAs_{40-x}Se_{60}$ were prepared by conventional thermal evaporation of the starting glassy materials from quartz crucibles onto suitably cleaned Corning glass substrates in a vacuum ($p \sim 10^{-6}$ Torr). $Se_{70}Ag_{15}I_{15}$ films were prepared by evaporation from a closed evaporator with a small opening [25]. Thicknesses of all films studied were in the range of 0.3–4.0 μm. The bulk samples were prepared by polishing melt-quenched chalcogenide glass ingots and had a typical thickness of several millimeters.

Most experiments were performed at room temperature using experimental setups shown schematically in Fig. 6.1. The setup shown in Fig. 6.1(a) was used for investigation of linear dichroism and linear birefringence in thin film samples upon excitation by the above-bandgap light. Beams of two lasers hit the same area of the studied film. The photon energy of one of the lasers (the anisotropy-inducing laser) is selected to be above the bandgap of the ChGS. The linear polarization of this beam could be changed to the orthogonal one using a $\lambda/2$ plate. A much less intense beam from the other laser (the probing beam) passed through an electrooptical modulator which modulated the light polarization discontinuously between two orthogonal states at a frequency of 1 kHz. This laser beam then passed through the sample and was detected by a Si photodiode permitting to measure photo-induced transmission anisotropy, $T_y - T_x = 2(I_y - I_x)/(I_y + I_x)$, where I_y and I_x are the intensities of the beams with two orthogonal electric vectors. We used synchronous detection to measure the difference signal $I_y - I_x$. If the photon energy of the probing laser is selected such that it is larger than the bandgap, one can measure photo-induced dichroism. In order to study the photo-induced birefringence, the wavelength of the probing laser must be selected in a range of transparency of the studied film. In most cases, we used He–Ne ($\lambda = 633$ nm) and Ar^+ ($\lambda = 515$ nm) lasers. This two-beam set-up allowed us to study very initial periods of PA kinetics and relaxation.

To study the transmission PA in bulk chalcogenide samples excited by the sub-bandgap light we also used the setup of Fig. 6.1(a). Additionally, for simultaneous measurements of laser radiation transmitted through the bulk sample and that scattered by the sample to various angles up to 230 mrad, we have used the setup shown in Fig. 6.1(b). A collecting lens, placed behind the sample, focused the scattered light onto a photodiode window and a small mirror, fixed in the central part of the lens, reflected the transmitted beam to another photodiode. The He–Ne laser radiation ($\lambda = 633$ nm) which is the sub-bandgap radiation for the studied bulk glass samples (As_2S_3 glass) played, in turn, the role of either inducing or probing light. This set-up allowed us to study the transmission and scattering anisotropy and gyrotropy in bulk samples.

The experimental setup for reflectance difference measurements is shown in Fig. 6.1(c). The anisotropy in this case was induced using either the light of a 1000 W xenon lamp (which generated radiation in a wide energy range including the sub-bandgap, above-bandgap light

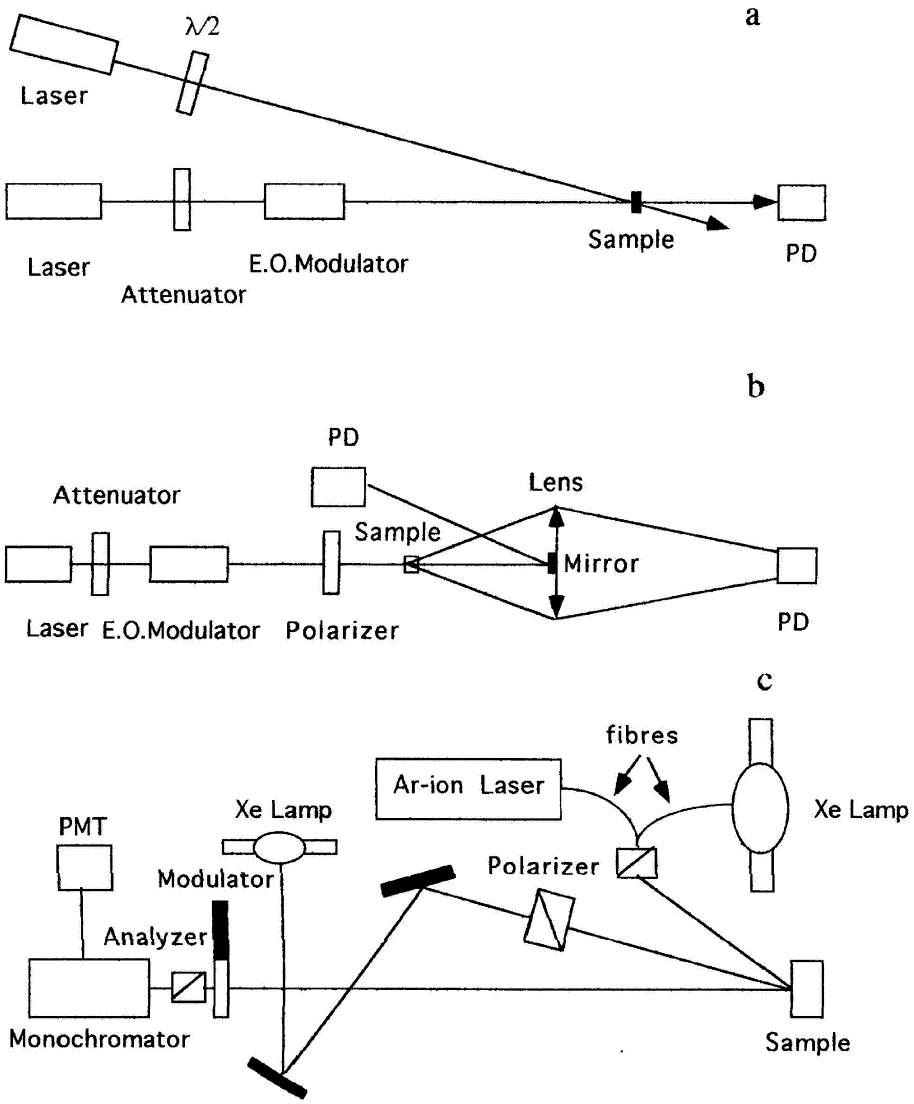

Figure 6.1: Experimental installations for investigation of photo-induced anisotropy. (a) Absorption, (b) scattering, and (c) reflection measurements.

and super-bandgap light) or an Ar^+-ion laser ($\lambda = 488$ nm) generating the above-bandgap light for the studied As_2S_3 samples. The inducing light passed through a Glan-prism polarizer and the light intensity on the surface of the sample was around 100 mW/cm^2. The intensity of the probing linearly polarized light generated by the xenon lamp was about 5 mW/cm^2. Use of a monochromator allowed us to investigate the spectra of PA in the light reflection mode. For a detailed description of the reflection difference spectroscopy, see Ref. [26].

6.3 Photo-Induced Optical Anisotropy

6.3.1 Above-Bandgap Light Excitation

Most of early experiments on the PA were performed on thin ChGS films using the above-bandgap light. Both photo-induced linear dichroism and photo-induced linear birefringence were revealed. PA could be decreased to zero by subsequent irradiation by non-polarized or circularly polarized light. Multiple reorientation of PA was observed at successive irradiation cycles of the studied film by linearly polarized light with two orthogonal polarizations [7]. All these features are illustrated in Fig. 6.2.

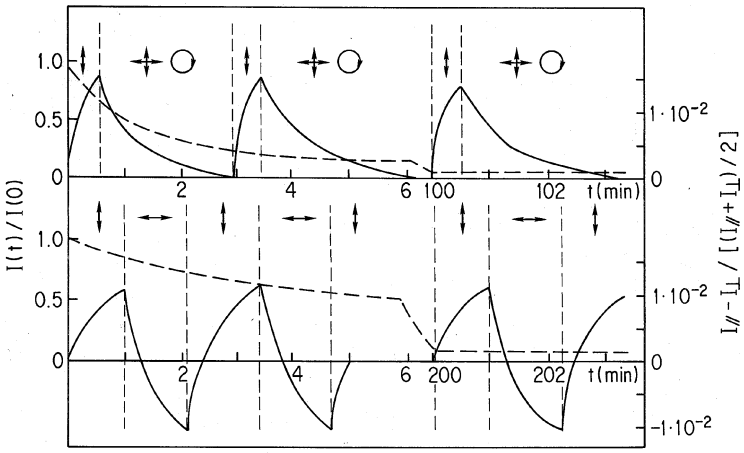

Figure 6.2: Kinetics of changes in relative transmission $I(t)/I(0)$ and in photo-induced dichroism $(I_{\parallel} - I_{\perp})/2(I_{\parallel} + I_{\perp})$ in an $As_{50}Se_{50}$ film at successive irradiation by linearly polarized light and the non-polarized or circularly polarized light of a He–Ne laser ($\lambda = 633$ nm, 350 mW/cm^2) (a) and at successive irradiation by linearly polarized light with a beam power density of 50 mW/cm^2 with the orthogonal directions of electrical vector (b). The polarization of the light is marked by arrows.

Different models have been put forward to account for PA generation by the above-bandgap light excitation. The best one, in our opinion, is the model by Tikhomirov and Elliott [27]. Their model is based on photo-induced orientation of valence alteration pairs (VAPs), i.e. the charged defects with negative correlation energy, characteristic of chalcogenide glasses [28]. The authors predominantly refer to native VAPs, existing in the non-irradiated glass with a concentration $\sim 5 \times 10^{17}$ cm^{-3} and in order to explain an appearance of strong anisotropy related to such a small concentration of defects they suggested a very strong interaction of VAPs with their environment.

Our experiments have shown that along with the native VAPs, photo-induced VAPs play a very important role in generation of PA in the case of the above-bandgap light excitation [29]. In these experiments, we used a 0.6–2.0 μm thick $As_{50}Se_{50}$ film. The photo-induced dichroism generation and reorientation are illustrated in Fig. 6.3 for a case of a 1.2 μm thick $As_{50}Se_{50}$ film. The initial dichroism growth in the non-treated film is rather slow (10–20 min) while the dichroism reorientation occurs much faster ($<$1 min). Quick reorientation is ob-

served not only after the dichroism has reached its saturation but also in the initial stages of the dichroism generation as is shown in Fig. 6.3(b). In the case of long enough irradiation of a ChGS film with unpolarized light, subsequent irradiation with linearly polarized light results in rapid appearance of the dichroism (Fig. 6.3(c)). It is important that the dichroism saturates at approximately the same values for various excitation light intensities. Similar behavior of the kinetics of dichroism generation and reorientation was also observed in other films.

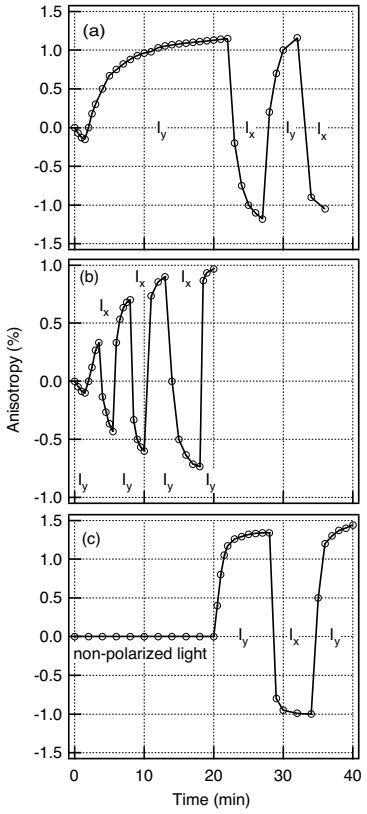

Figure 6.3: Kinetics of dichroism generation and reorientation in an $As_{50}Se_{50}$ film under the action of linearly polarized laser light with two orthogonal directions of electrical vector (**y** and **x**), when the reorientation starts after the dichroism saturation (a), when the reorientation takes place during the initial stages of the dichroism growth (b), and when the polarized light irradiation starts after prolonged illumination with non-polarized light (c).

Figure 6.4 shows room temperature kinetics of repeated photo-induced dichroism generation at room temperature after annealing an $As_{50}Se_{50}$ film at various temperatures for 10 min. The kinetics of room temperature dichroism reorientation in the non-annealed film are also shown. It can be seen that a gradual increase in the annealing temperature results in a form of the curve characterizing the growth of the dichroism closer to that of the virgin film. Complete coincidence of these two curves was observed after annealing at a temperature of 170–180 °C,

i.e. close to the softening temperature of the $As_{50}Se_{50}$ film where thermal bleaching of photodarkened films is observed.

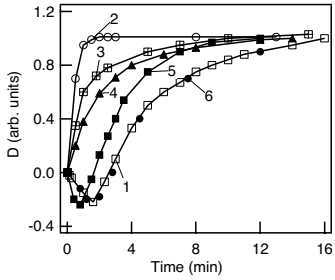

Figure 6.4: Kinetics of room temperature dichroism generation in a virgin 1.2 μm thick $As_{50}Se_{50}$ film (1), and repeated dichroism generation after annealing at 75 °C (3), 95 °C (4), 140 °C (5) and 180 °C (6) for 10 min. Kinetics of one of the cycles of room temperature dichroism reorientation in the film are also shown (2). The intensity of linearly polarized He–Ne laser light is 2.75 W/cm^2.

These data and other results described in [29] permitted us to conclude that irradiation with both polarized and non-polarized above-bandgap light creates some centers in the non-irradiated film that can be oriented quickly by linearly polarized light. The constant dichroism saturation value at different light intensities strongly suggests that the number of centers that can be created and/or oriented is limited to a certain value. The results of the annealing experiments allow us to assume that the same centers, or a part thereof, are capable of being oriented and are responsible for both photodarkening and PA. Such centers can be regarded as VAPs (photo-induced VAPs) in the reaction [28]:

$$2C_2^0 + h\nu \rightarrow C_1^- + C_3^+ \quad \text{and} \quad C_2^0 + P_3^0 + h\nu \rightarrow C_1^- + P_4^+ \tag{6.1}$$

where C and P refer to chalcogens and pnictides, respectively.

Combining the ideas proposed in [19] and [27], we assume that the polarized light initiates the following reactions:

$$C_1^- + C_3^+ + h\nu \rightarrow C_1^+ + C_3^- \quad \text{and} \quad C_1^- + P_4^+ + h\nu \rightarrow C_1^+ + P_4^- \tag{6.2}$$

and that these reactions occur more efficiently for VAPs with the dipole moment oriented parallel to the electrical vector of the excitation light. Afterwards, energetically advantageous reactions:

$$C_1^+ + C_3^- \rightarrow C_1^- + C_3^+ \quad \text{and} \quad C_1^+ + P_4^- \rightarrow C_1^- + P_4^+ \tag{6.3}$$

take place with the $(C_1^- + C_3^+)$ and $(C_1^- + P_4^+)$ defects oriented randomly this time.

The whole process is accompanied by a decrease in the number of VAPs which have dipole moments co-directed with the electrical vector of the inducing light and by the corresponding growth of the anisotropy.

In previous experiments, ChGS films exhibiting photodarkening (both reversible and *irreversible*) were studied. At the same time, in some Ge-containing ChGS films, light irradiation

of as-deposited films induces photobleaching (instead of photodarkening) while the irradiation of the annealed films results in photodarkening.

We have investigated PA in photobleached $Ge_{25}As_{15}S_{60}$, $Ge_{32}As_8S_{60}$, $Ge_{36}As_4S_{60}$, $Ge_{32}As_8Se_{60}$ and $Ge_{36}As_4Se_{60}$ films, in which large scalar photobleaching effect was earlier investigated in detail [30, 31]. The results were qualitatively identical for all studied films. An example is shown in Fig. 6.5

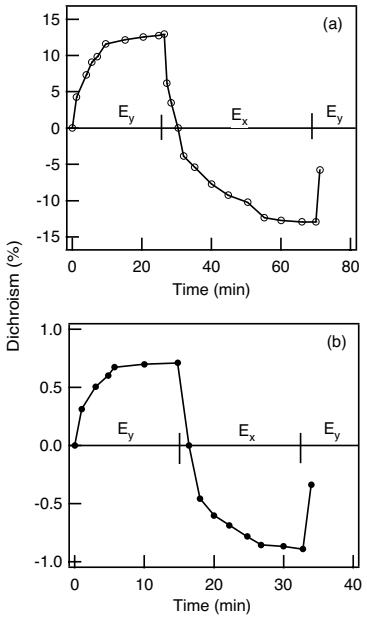

Figure 6.5: . Kinetics of dichroism generation and reorientation in as-prepared (a) and annealed at 210 °C (b) $Ge_{32}As_8S_{60}$ glassy film. Inducing light, a 2.5 W/cm^2 linearly polarized Ar^+-laser ($\lambda = 488$ nm); probing light, a 0.5 mW/cm^2 linearly polarized 515 nm Ar^+-laser.

Maximum values of PA (10–15%) were recorded in as-prepared $Ge_{25}As_{15}S_{60}$ and $Ge_{32}As_8S_{60}$ films. These values are substantially larger than those in most of the previously studied elementary or binary chalcogenide glassy films. Annealing of such films does not result in a change of the sign of dichroism. However, the value of dichroism is much smaller in the annealed films (Fig. 6.5b). In this respect, the studied films differ from the binary films where the annealing causes a very small decrease in the dichroism value. Generation and reorientation of birefringence were also observed and studied in these photobleached films. More details about the study of the photobleached Ge–As–S and Ge–As–Se films could be found in [32, 33]. We conclude that the characteristics of PA do not depend on whether the as-prepared chalcogenide glassy films exhibit photodarkening or photobleaching.

6.3.2 Sub-Bandgap Light Excitation

In early experiments on the interaction of linearly and circularly polarized sub-bandgap light with bulk samples, several photo-induced phenomena – viz. anisotropy, gyrotropy and light scattering – were observed and investigated [9]. It was also shown that the polarization of the light changed significantly when it passed through the bulk sample: both rotation of the polarization plane (optical activity) and ellipticity were observed [9].

Photo-induced light scattering in bulk ChGS, excited by the sub-bandgap light manifested itself as a change of the shape of the transmitted laser beam, as the appearance of a speckled structure and as a photo-induced modification of the trace of the laser beam inside the irradiated ChGS bulk sample [9]. Observation of the trace of the laser beam inside the bulk sample of the glass unequivocally indicates the scattering of the passing light at 90° and the observed change of this trace, induced by the sub-bandgap light, is a clear proof of the photo-induced light scattering change at 90°. Semi-quantitative data confirming the light scattering at smaller angles were also obtained in the early stages of this work [9].

In a later series of experiments we investigated the photo-induced light scattering at room temperature in bulk As_2S_3 and, primarily, the anisotropy and gyrotropy of light scattering [34, 35]. The He–Ne laser light ($h\nu = 1.96$ eV, $W = 10$ mW), i.e. the sub-bandgap light for the As_2S_3 glass ($E_g = 2.3$ eV), has been used. See [34] for more details.

We studied the kinetics of the change of the scattered light intensity induced by intense linearly or circularly polarized light with two orthogonal polarizations (E_y-radiation, E_x-radiation, E_r-radiation and E_l-radiation). It was found [34] that the E_y-radiation, for example, induces an increase of scattering of the corresponding (I_s^y) light. Simultaneously, the intensity of I_s^x-light usually decreases. These results are illustrated in Fig. 6.6a. Similar results were recorded in the case of circularly polarized light [35].

Figure 6.6(b,c) show typical kinetics of photo-induced changes of the scattered and transmitted light anisotropy and gyrotropy, respectively. It can be seen from the figures that scattering anisotropy (gyrotropy) and transmittance anisotropy (gyrotropy) always change in antiphase (Fig. 6.6b). In another experiment, the sample was first pre-irradiated by non-polarized light and only then exposed to linearly or circularly polarized light. The non-polarized light induced additional isotropic light scattering, while the subsequent exposure to linearly or circularly polarized light resulted in an appearance of scattering anisotropy or gyrotropy – again in antiphase with transmission changes – which could be reoriented. This result is demonstrated in Fig. 6.6c for the case of the photo-induced gyrotropy.

The observed opposite changes of photo-induced anisotropy (gyrotropy) of transmittance and scattering allow us to draw an important conclusion that the creation of anisotropically or gyrotropically scattering centers is the basis of the whole lot of photo-induced vectorial phenomena in bulk chalcogenide glasses excited by the sub-bandgap light. This idea makes understandable the fact that anisotropy can be induced by the sub-bandgap light. The energy of the corresponding light quanta is insufficient either for electron–hole pair excitation, or for breaking the interatomic covalent bond, but these quanta can be absorbed by defect states and their energy is sufficient to produce certain changes in the subsystem of weaker bonds, for example, intermolecular van der Waals bonds. These changes can result in an appearance of scattering centers in the glass. These centers scatter light isotropically, anisotropically or gyrotropically depending on the polarization state of the light that was the origin of their creation.

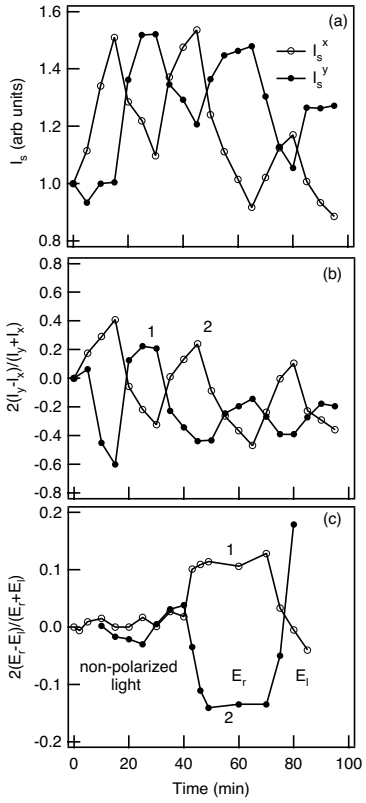

Figure 6.6: Kinetics of scattered light intensity induced by polarized light (a); antiphase correlation between transmittance anisotropy (1) and scattering anisotropy (2) in an As_2S_3 bulk sample induced by successive $\mathbf{E}_y$ and $\mathbf{E}_x$ laser excitation (b); and kinetics of scattering gyrotropy (1) and transmittance gyrotropy (2) changes in an As_2S_3 bulk glass sample induced by successive $\mathbf{E}_r$- and $\mathbf{E}_l$-laser excitation (c).

The above conclusion has been disputed in [12, 13, 36], where an alternative explanation of the observed phenomena based on an assumption of photo-induced creation of persistent self-focusing structures has been suggested. We adhere to our original explanation. First, we argue that the observation of the laser-beam trace in the bulk glass and its photo-induced change are evidences of the initial and photo-induced light scattering. Second, we believe that differences between our results and those reported in [12, 13, 36] are largely due to different experimental conditions, viz. in the cited papers light focusing was used. In such a case, the light beam impinging upon the sample is no longer parallel and this fact can seriously complicate the interpretation of the results obtained. We maintain that the photo-induced generation of the scattering centers in the bulk glass is a decisive factor for all the observed anisotropic phenomena induced by the sub-bandgap excitation.[1]

[1] See Chapter 5 (p. 75) for alternative arguments. (Editor's comment)

6.3.3 Super-Bandgap Light Excitation

For the super-bandgap excitation, we used reflectance difference spectroscopy which allowed us to investigate the photo-induced anisotropy in a broad spectral range [37–39]. The measured value of the reflected light dichroism is defined as $\Delta r/r = 2(r_y - r_x)/(r_y + r_x)$, where r_y and r_x are the reflectance values for the polarizations of the probing beam in the direction parallel or perpendicular to the polarization of the inducing beam. The samples studied were polished bulk glasses and thin films of As_2S_3, $As_{50}Se_{50}$ and $Ge_{20}As_{20}S_{60}$.

Figure 6.7 shows the PA of light reflection and its reorientation for bulk $Ge_{20}As_{20}S_{60}$ (Fig. 6.7(a)) and As_2S_3 (Fig. 6.7(b,c)) samples induced by unfiltered linearly polarized light of a Xe lamp (polychromatic light) and/or an Ar^+-laser (monochromatic light). One can see that the PA appeared in the whole 1.5–5.0 eV range. It should be noted that for the sample excited by the Xe lamp light, the trend in the reflectance change was the same (positive or negative depending on the polarization) throughout the whole studied spectral range while for the Ar^+-laser excitation, the sign variation of the effect has been observed. Whilst an increase in $\Delta r/r$ (positive value) is observed for larger photon energies (above 4.0 eV) similar to the previous case of polychromatic light excitation, for smaller photon energies an opposite change (negative value) is detected. This behavior was characteristic for all samples studied.

The possibility to observe PA at energies much larger than the exciting photon energy indicates that by irradiation with linearly polarized light not only the defects or the scattering centers in the glass can be oriented and/or reoriented by light but that the main covalent bonds also become oriented and reoriented. We believe that the Ar^+-laser radiation ($\lambda = 488$ nm), that is the above-bandgap radiation for the As_2S_3 samples, exciting and orienting the VAPs or the lone pair (LP) orbitals [37], simultaneously induces anisotropy in the 4.5 to 5.5 eV spectral range corresponding to the excitation of the bonding electrons.

The most interesting result to be explained is the essential difference of the reflection spectra for the cases of the Xe lamp and the Ar^+-laser light excitation (Fig. 6.7(a,b) and (c)). One way to explain this difference is demonstrated in Fig. 6.8 for the simplest case of elemental amorphous selenium. In the initial state, atom 3 is three-fold coordinated and atom 10 is one-fold coordinated. Following the photoexcitation by the Ar^+-laser light (above-bandgap light) with the polarization shown in the figure, LP electrons oriented parallel to this orientation will predominantly be excited. As a result, atom 10 may form a covalent bond with a neighboring atom 8, making the latter three-fold coordinated. To keep the defect concentration and charge balance, the initially three-fold coordinated atom 3 decays into a singly coordinated defect and a two-fold coordinated "regular" atom. We see here a redistribution of LP and bonding orbitals. Before the photoexcitation, the bond between atoms 2 and 3 was covalent (parallel to the x-axis), while atoms 8 and 10 had LP orbitals parallel to the z-axis. After the photoexcitation, atoms 8 and 10 became bonded by a covalent bond in the z direction, while the bond between atoms 2 and 3 is broken, and two LP orbitals parallel to the x-axis are created. As a result, the total number of bonding electrons along the z-axis decreases, while the number of non-bonding electrons along the x-axis increases, which explains the opposite change in the anisotropy probed at lower and higher energies. In other words, conversion between bonding and non-bonding electrons takes place.

In the case of the broad spectrum light of the Xe lamp, the above considered process also exists but, additionally, direct excitation of bonding electrons by the high-energy light quanta

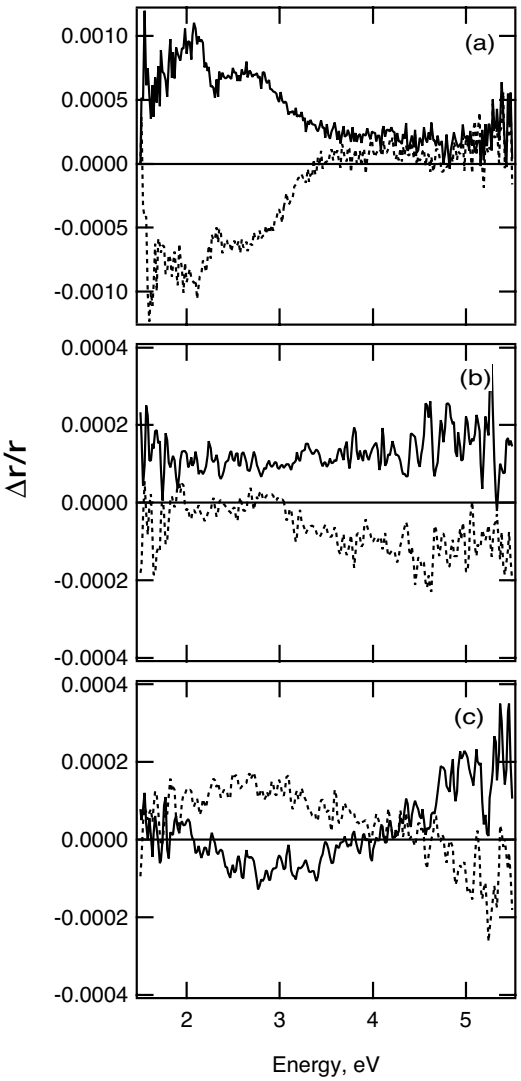

Figure 6.7: PA (solid lines) and its reorientation (dotted lines) spectra for $Ge_{20}As_{20}S_{60}$(a) and As_2S_3 (b,c) bulk glasses excited by a Xe lamp (a,b) and Ar^+-laser (c) light.

becomes possible, resulting in a decrease in the number of bonding electrons in the direction of the light polarization. This latter process can compensate/overcompensate a decrease in the number of covalent bonds caused by the excitation with the above-bandgap light, leading to the same change in the sign of anisotropy for both lower and higher energies.

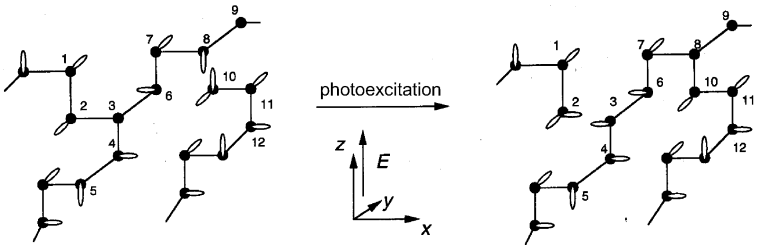

Figure 6.8: Schematic representation of photostructural changes induced by the above-bandgap light.

6.4 Photo-Induced Anisotropy of Other Properties of ChGS

Photo-induced optical anisotropy is accompanied by an appearance of anisotropy of other properties. In this section we consider polarization-dependent photocrystallization, photodoping, and photoconductivity.

6.4.1 Polarization-Dependent Photocrystallization

We found that the polarization state of the excitation light influences the photocrystalization process first described in [40] and the properties of the crystallized samples (anisotropic photocrystallization) [41, 42]. Irradiation of glassy $Se_{70}Ag_{15}I_{15}$, Se and $Se_{80}Te_{20}$films with linearly polarized He–Ne and Ar^{+}-laser light was shown to result in the formation of polycrystalline films with strong optical anisotropy (dichroism), the sign of which is determined by the polarization of the excitation light. This conclusion was originally made on the basis of observation of some peculiarities of photo-induced dichroism in these films, namely, a change of reorientation kinetics and of the dichroism sign (Fig. 6.9). At the beginning of the experiment, when the film was amorphous, the vertical polarization vector stimulated an increase of positive dichroism while the horizontal polarization vector diminished the positive dichroism and led to negative dichroism. In the following stages, the reverse processes were observed. The induced dichroism was stable, it did not relax in the dark and could not be erased even by annealing at the glass transition temperature.

The results obtained (unusual kinetics, the opposite sign and the large value of the photo-induced dichroism, absence of relaxation and thermal erasure) permitted us to conclude that we are dealing with photo-induced *crystallization* [42]. This conclusion was confirmed by direct structural investigations including optical microscopy, electron microscopy and an X-ray diffraction study. The X-ray analysis of the irradiated Se–Ag–I films showed the presence of Se, Ag_2Se and AgI microcrystals. Polarization dependence of the photocrystallization of Se films was also reported at almost the same time, simultaneously and independently, by two groups [43, 44].

In [45], a different polarization-dependent phenomenon in amorphous Se films was observed for photocrystallization induced by simultaneous action of two lasers, one with the above-bandgap energy photons and the other one with the below-bandgap energy photons. A

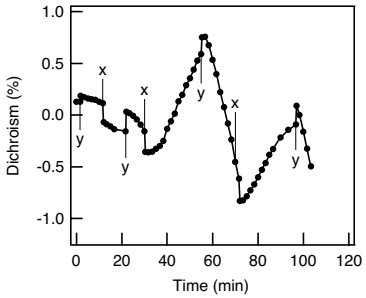

Figure 6.9: Kinetics of dichroism generation and reorientation in a thermally treated $Se_{80}Te_{20}$ film induced by a linearly polarized He–Ne laser beam with horizontal (x) and vertical (y) polarizations.

drastic decrease of the crystallization rate was detected when the polarizations of both beams were parallel to each other. If, on the other hand, the polarizations were orthogonal, a significant increase of the photocrystallization rate was observed.

6.4.2 Polarization-Dependent Photodoping of ChGS Films by Silver

ChGS films can be photodoped with silver and other metals which is accompanied by drastic changes in their properties (see review article [46]). It was shown also that the silver photodoping of As_2S_3 glassy films by linearly polarized light is accompanied by the generation of strong dichroism with the sign opposite to that generated in Ag-free ChGS films [47]. This phenomenon was termed "polarized photodoping".

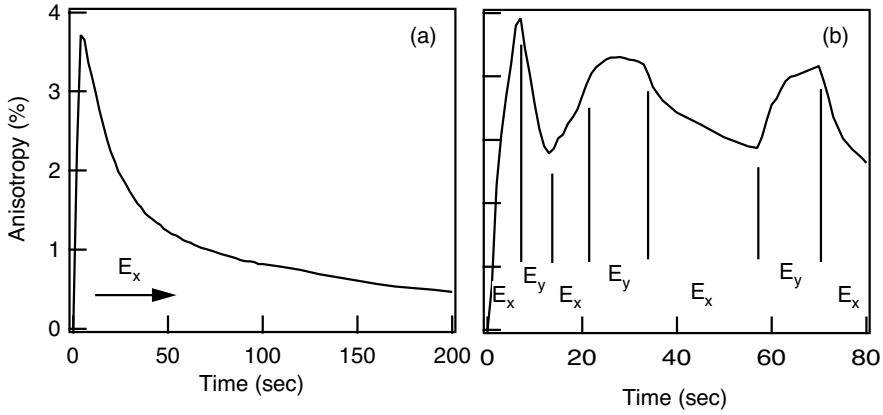

Figure 6.10: Kinetics of dichroism generation (a) and reorientation (b) in a Ag-photodoped $As_{50}Se_{50}$ film under the action of linearly polarized laser light with two orthogonal polarizations (E_x and E_y).

Recently, we investigated the polarized photodoping of ChGS films of other compositions, namely, As_2Se_3, AsSe and $GeS_{2.2}$, and found a very similar behavior in all samples. Some peculiarities observed in the kinetics of the dichroism reorientation are demonstrated

in Fig. 6.10 for the case of the $As_{50}Se_{50}$ film. When the Ag/$As_{50}Se_{50}$ structure is exposed to the He–Ne laser beam of a certain, say horizontal, polarization, positive dichroism appears and increases quickly. Then, after passing through a maximum value, the dichroism starts to decrease (Fig. 6.10(a)). Very unusual were the kinetics of the dichroism reorientation. In the first cycles of the dichroism reorientation, the horizontal polarization caused an increase of the positive dichroism, while the vertical polarization decreased the dichroism value. In the later cycles, a reverse picture was observed (Fig. 6.10(b)). This situation resembles the previous case of the photo-induced polarized crystallization. Further studies confirmed that prolonged laser-induced photodoping does indeed lead to partial polarization-dependent photocrystallization of three-component As(Ge)–Se(S)–Ag materials obtained in the process of photodoping.

6.4.3 Photo-Induced Anisotropy of Photoconductivity

Recently, we demonstrated that photo-induced optical anisotropy in amorphous $As_{50}Se_{50}$ chalcogenide films is accompanied by anisotropy of photoconductivity and that this effect is optically reversible [48, 49]. In these experiments we used 0.3–2.0 μm thick amorphous $As_{50}Se_{50}$, Sb_2S_3 and $Ge_{28.5}Pb_{15}S_{56.5}$ films. The anisotropy of the photoconductivity was measured on films with gold electrodes. Further details can be found in [48, 49].

When the $As_{50}Se_{50}$ sample was illuminated by a non-polarized He–Ne laser beam (the laser spot was set between the electrodes), the appearance and saturation of photocurrent is observed. Subsequent irradiation by linearly polarized light with the electric vector E either parallel, E_x, or orthogonal, E_y, to the electrodes resulted in an appearance of anisotropy of photocurrent (Fig. 6.11(a)). The values of anisotropy achieved $\sim 0.5\%$. A change in the polarization state of the inducing light resulted in the respective change of the sign of the resultant current. Kinetics of the change of resultant current were similar to the kinetics of reorientation of the optical dichroism generated in the studied film. Qualitatively similar results were obtained with amorphous Sb_2S_3 and $Ge_{28.5}Pb_{15}S_{56.5}$ films (Fig. 6.11(b)). It can be seen that while a variation of the inducing light polarization to the orthogonal results in a change of the sign of anisotropy, the secondary illumination with circularly polarized light leads to a gradual decrease and disappearance of the anisotropy. Values of the photocurrent anisotropy in the Sb_2S_3 and $Ge_{28.5}Pb_{15}S_{56.5}$ films were 2–3 times larger than those in the $As_{50}Se_{50}$ films.

Based on these results we concluded [48,49] that the observed anisotropy of photoconductivity is due to different transport properties (mobility) of charge carriers when they move in the direction parallel or perpendicular to the electrical vector of inducing light, i.e. anisotropy of carriers mobilities μ ($\mu_x \neq \mu_y$) can be photo-induced.

The data obtained indicate that the microanisotropic species, such as charged valence-alternation pairs, affect not only the light absorption process but also the process of transport of non-equilibrium charge carriers. While normally these microanisotropic species are randomly oriented which results in the isotropic photoconductivity, illumination with linearly polarized light induces the alignment of these species and the resulting anisotropic photoconductivity.

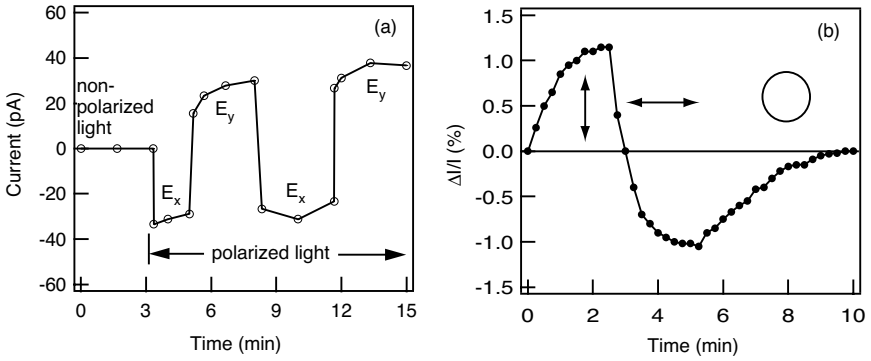

Figure 6.11: Kinetics of photocurrent following the change of the polarization E of the inducing beam of a He–Ne laser using a three-electrode configuration [48] (a), and kinetics of relative anisotropy generated in a 1.5 μm thick Sb_2S_3 film (b). Arrows and a circle indicate the polarization of the inducing He–Ne laser beam ($\lambda = 633$ nm, 1W/cm^2).

6.4.4 Anisotropic Opto-Mechanical Effect and Ionic Transport

Finally we would like to mention two important recent findings by other groups. The first effect, viz. an anisotropic opto-mechanical effect, consists in the appearance of optically controllable, reversible nanocontraction and nanodilatation induced in a chalcogenide glassy film ($As_{50}Se_{50}$ film) by linearly polarized light [50]. A very good correlation of this effect with photo-induced dichroism was observed. The mechanism of this effect, as well as mechanisms of other photo-induced vectorial effect, are in need of further investigation.

Another interesting phenomenon was observed recently in ion-conducting chalcogenide glasses [51, 52]. It was found that excitation of Ag–As–S films by linearly polarized light caused large reversible positive birefringence and anisotropic surface deformation. The anisotropic shape of the deformation correlated with the polarization direction and the shape changed from a crater-like to anticrater-like shape following a change in the illumination direction (from the free surface of the film or through the substrate [52]. The authors related the formation of such patterns to photo-induced migration of Ag^+ ions in the film.

6.5 Conclusion

Concluding this review, we can say that the investigation of the interaction of polarized light with chalcogenide glasses is still in its initial stage. One is tempted to compare the development of research of scalar and vectorial photo-induced phenomena in ChGS. The photo-induced *optical* effects (photodarkening and photorefraction) were observed and studied first. Later, it was shown that these effects are accompanied by changes in photoconductivity, microhardness, glass softening temperature, velocity of surface acoustic waves, density, rate of dissolution in some solvents, photodoping by metals, etc.

Similarly, the investigation of PA started from observation and study of photo-induced *optical* anisotropy. Then it was demonstrated that irradiation of ChGS with polarized light also results in the appearance of numerous polarization-dependent phenomena, such as polarization-dependent photocrystallization and metal photodoping, anisotropy of photoconductivity, opto-mechanical effect, and anisotropic surface deformation. We believe that other polarization-dependent phenomena will be observed in the future.

We would like to stress that anisotropy of different properties is a characteristic property of ChGS, especially of As-containing ChGS. This anisotropy can be induced not only by visible light but also by X-rays and high-energy electron irradiation [53, 54], by uniaxial compression [55] and even by some impurities introduced into the glass during the synthesis [56].

As to the photo-induced optical anisotropy and gyrotropy, we are of the opinion that the mechanisms are different for excitation in different spectral ranges. At the sub-bandgap excitation, light creates scattering centers in the glass. Such centers scatter the light isotropically, anisotropically or gyrotropically depending on the polarization state of the inducing light. This process is also displayed in isotropy, anisotropy or gyrotropy of the light transmitted trough the sample. In the case of the above-bandgap excitation, the polarized light orients the native VAPs existing in the film, additionally creating and orienting the photo-induced VAPs. Finally, in the case of the super-bandgap light, excitation is able to orient and reorient the interatomic covalent bonds of the glass.

Our present knowledge allows us to give only speculative explanations of various PA phenomena but we hope that more detailed understanding will be achieved in the near future. We also hope that some of these phenomena will find novel applications in modern technology, primarily in microelectronics, electrooptics and photonics.

Acknowledgments

It is a pleasure to acknowledge the participation and important input of our collaborators – V.K. Tikhomirov, A.V. Kolobov, T. Yasuda, K. Tanaka, L. Boehm, M. Mitkova, T. Petkova, E. Vateva, D. Arsova, E. Skordeva and E. Savova – in various parts of this research, which was partly supported by the Israel Science Foundation administered by the Israel Academy of Science and Humanities.

References

[1] V.G. Zhdanov and V.K. Malinovskii, Sov. Tech. Phys. Lett. **3**, 943 (1977).

[2] V.G. Zhdanov, B.T. Kolomiets, V.M. Lyubin and V.K. Malinovskii, Phys. Stat. Sol. A **52**, 621 (1979).

[3] J. Hajto, I. Janossy and C. Forgaes, J. Phys. C **15**, 6293 (1982).

[4] R. Grigorovici, A. Vancu and L. Ghita, J. Non-Cryst. Sol. **59-60**, 903 (1983).

[5] K. Kimura, K. Murayama and T. Ninomiya, J. Non-Cryst. Sol. **77-78**, 1203 (1985).

[6] J.M. Lee and M.A. Paesler, J. Non-Cryst. Sol. **97–98**, 1235 (1987).

[7] V.M. Lyubin and V.K. Tikhomirov, J. Non-Cryst. Sol. **114**, 133 (1989).

[8] V.K. Tikhomirov, G.J. Adriaenssens and S.R. Elliott, Phys. Rev. B **55**, R660 (1997).

[9] V.M. Lyubin and V.K. Tikhomirov, J. Non-Cryst. Sol. **135**, 37 (1991).

[10] V.M. Lyubin and V.K. Tikhomirov, Sov. Tech. Phys. Lett. **15**, 804 (1989).

[11] V.K. Tikhomirov and S.R. Elliott, Phys. Rev. B **49**, 1746 (1994).

[12] H. Hisakuni and K. Tanaka, Sol. St. Commun. **90**, 483 (1994).

[13] K. Tanaka, M. Notani and H. Hisakuni, Sol. St. Commun. **95**, 461 (1995).

[14] V.M. Lyubin, V.K. Tikhomirov and M.M. Chervinskii, Semicond. Sci. Technol. **6**, 807 (1991).

[15] V.M. Lyubin and V.K. Tikhomirov, J. NonCryst. Sol. **137–138**, 993 (1991).

[16] V.K. Tikhomirov, Sov. Phys.: Semiconductors **26**, 1415 (1992).

[17] V. Lyubin, M. Klebanov, S. Rosenwaks and V. Volterra, J. Non-Cryst. Sol. **164–166**, 1165 (1993).

[18] M. Klebanov and V. Lyubin, Physica B **245**, 206 (1998).

[19] H. Fritzsche, Phys. Rev. B **52**, 15854 (1995).

[20] K. Tanaka, in Handbook of Advanced Electronic and Photonic Materials and Devices, H.S. Nalva (Ed.), Chalcogenide Glasses and Sol–Gel Materials, Vol. 5, Academic Press, New York, 2001, pp. 119–139.

[21] H.Y. Lee, J.Y. Chun, C.H. Yeo and H.B. Chung, J. Vac. Sci. Technol. A **18**, 485 (2000).

[22] A. Saliminia, V. Galstian and A. Villeneuve, Phys. Rev. Lett. **85**, 4112 (2000).

[23] T. Gotoh and K. Tanaka, J. Appl. Phys. **89**, 4703 (2001).

[24] V.M. Lyubin and M.L. Klebanov, Semiconductors **32**, 817 (1998).

[25] T. Petkova and M. Mitkova, Thin Solid Films **205**, 25 (1991).

[26] D.E. Aspnes, J.P. Harbison, A.A. Studna and L.F. Florez, J. Vac. Sci. Technol. A **6**, 1327 (1988).

[27] V.K. Tikhomirov and S.R. Elliott, Phys. Rev. B **51**, 5538 (1995).

[28] M. Kastner and H. Fritzsche, Philos. Mag. **37**, 199 (1978).

[29] V. Lyubin and M. Klebanov, Phys. Rev. B **53**, R 11924 (1996).

[30] E. Vateva, E. Skordeva and D. Arsova, Philos. Mag. B **67**, 225 (1993).

[31] E. Vateva, D. Arsova, E. Skordeva and E. Savova, in Electronic, Optoelectronic and Magnetic Thin Films, J. Marshall, N. Kirov and A. Vavrek (Eds.), Research Studies Press, 1995, p. 604.

[32] M. Klebanov, V. Lyubin, D. Arsova, E. Vateva, and V. Pamukchieva, Physica B 3**01**, 399 (2001).

[33] E. Vateva, E. Skordeva, D. Arsova, V. Pamukchieva, M. Klebanov and V. Lyubin, in Materials for Information Technology in the New Millenium, J. Marshall, A.G. Petrov, A. Vavrek, D. Nesheva, D. Dimova-Malinovska and J.M. Maud (Eds.), Research Studies Press, 2001, p. 300.

[34] V. Lyubin, M. Klebanov, S. Rosenwaks and V. Volterra, J. Non-Cryst. Sol. **164–166**, 1165 (1993).

[35] M. Klebanov and V. Lyubin, Physica B **245**, 206 (1998).

[36] K. Tanaka and H. Hisakuni, Asian J. Phys. **19**, 723 (2000).

[37] A.V. Kolobov, V. Lyubin, T. Yasuda and K. Tanaka, Phys. Rev. B **55**, 23 (1997).

[38] A.V. Kolobov, V. Lyubin, T. Yasuda, M. Klebanov and K. Tanaka, Phys. Rev. B **55**, 8788 (1997).

[39] V. Lyubin, A.V. Kolobov, T. Yasuda, M. Klebanov, L. Boehm and K. Tanaka, J. Non-Cryst. Sol. **227–230**, 677 (1998).

[40] J. Dresner and G.B. Stringfellow, J. Phys. Chem. Sol. **29**, 303 (1968).

[41] V. Lyubin, M. Klebanov, M. Mitkova and T. Petkova, Appl. Phys. Lett. **71**, 2118 (1997).

[42] V. Lyubin, M. Klebanov and M. Mitkova, Appl. Surf. Sci. **154–155**, 135 (2000).

[43] K. Ishida and K. Tanaka, Phys. Rev. B **56**, 206 (1997).

[44] V.K. Tikhomirov, P. Hertogen, C. Glorieux and G.I. Adriaenssens, Phys. Stat. Sol. A **162**, R1 (1997).

[45] A. Roy, A.V. Kolobov and K. Tanaka, J. Appl. Phys. **83**, 4951 (1998).

[46] A.V. Kolobov and S.R. Elliott, Adv. Phys. **40**, 625 (1991).

[47] A.V. Kolobov, V.M. Lyubin and V.K. Tikhomirov, Phil. Mag. Lett. **65**, 67 (1992).

[48] V. Lyubin, M. Klebanov and V.K. Tikhomirov, Phys. Rev. Lett. **87**, 216806 (2001).

[49] V. Lyubin, M. Klebanov and V.K. Tikhomirov, J. Non-Cryst. Sol. **299–302**, 945 (2002).

[50] P. Krecmer, A.M. Moulin, R.J. Stephenson, T. Rayment, M.E. Welland, and S.R. Elliott, Science **277**, 1799 (1997).

[51] K. Tanaka, T. Gotoh and H. Hayakawa, Appl. Phys. Lett. **75**, 2256 (1999).

[52] T. Gotoh and K. Tanaka, J. Appl. Phys. **89**, 4703 (2001).

[53] E.V. Berlin, B.T. Kolomiets, V.M. Lyubin, S.I. Nesterov, V.V. Rudnev and V.P. Shilo, Sov. Phys.-Tech. Phys. Lett. **7**, 1526 (1981).

[54] O.I. Shpotyuk, V.O. Balitska, Phys. Stat. Sol. A **165**, 295 (1998).

[55] K. Tanaka, J. Non-Cryst. Sol. **119**, 243; 254 (1990).

[56] T.F. Mazets, E.A. Smorgonskaya and V.K. Tikhomirov, J. Non-Cryst. Sol. **166**, 1215 (1993).

7 The Optomechanical Effect in Amorphous Chalcogenide Films

Marek Stuchlik, Pavel Krecmer, and Stephen R. Elliott

7.1 Introduction

Chalcogenide glasses are remarkable for the wide variety of metastable photo-induced phenomena that they exhibit. Exposure of these semiconducting materials to near-bandgap light can induce metastable changes in their opto-electronic properties (e.g. refractive index, optical absorption coefficient, etc.), structure (e.g. volume) and mechanical properties (e.g. elastic modulus). These changes can be reversible (either optically or thermally) or irreversible. Furthermore, optically induced changes can be scalar (i.e. isotropic) in nature or vectorial (i.e. anisotropic, induced by polarized light). For a review of these phenomena, see refs. [1–3]. Although there is now an extensive body of experimental results on such optically-induced metastabilities, a proper theoretical understanding of the microscopic mechanism(s) involved is still lacking. However, there has been some recent progress from *ab initio* quantum-chemical calculations on small clusters of atoms simulating As_2S_3 [4] and *ab initio* molecular-dynamics simulations of small supercell models of As_2S_3 [5]. Non-radiative electron–hole recombination, following optically-induced electronic excitation, can produce a range of bond-breaking or conformational changes.

One particularly intriguing phenomenon is the influence of light on the mechanical behavior of chalcogenide glasses, although it has been little studied. Hisakuni and Tanaka [6] discovered an athermal "photofluidity" effect, whereby the viscosity of a fiber of glassy As_2S_3 decreased so much during light illumination that the fiber deformed under gravity. A related effect, namely optical field-induced mass transport, has also been observed [7] in glassy films of As_2S_3, in which anisotropic surface-relief modulations occur on exposure to linearly polarized bandgap light. This behavior has been linked to the photofluidity effect [7].

However, perhaps the most interesting photomechanical effect that has been observed in chalcogenide glasses is the so-called optomechanical effect [8, 9], wherein linearly polarized light incident on an amorphous chalcogenide film deposited on an inert substrate, forming a clamped cantilever, causes a reversible upward or downward displacement of the cantilever, depending on whether the electric vector of the light is respectively parallel or perpendicular to the cantilever axis. In other words, light polarized parallel to the cantilever axis causes a volume contraction of the chalcogenide and light polarized perpendicularly causes a volume expansion. This vectorial effect is dynamic, i.e. the contraction/expansion persists only during the illumination, and it is also superimposed upon a (larger) scalar volume-expansion effect which is probably a combination of a conventional thermal ("bi-metallic strip") expansion and normal scalar photoexpansion (see e.g. [10]).

The optomechanical effect is an example of direct optical actuation, where the light energy is directly converted into mechanical work, rather than indirectly via heating or the generation of an electrical current, etc. Direct optical processes can be faster and take place at lower light intensities than indirect ones, and they permit greater simplicity, versatility and parallelism of the actuator. This effect can form the basis of MOMS (micro-opto-mechanical system) devices, controlled by varying the light intensity, wavelength or polarization direction. There are a number of advantages that the use of chalcogenide materials exhibiting the optomechanical effect has over other kinds of actuation:

(i) the optomechanical effect is highly reversible and non-hysteretic (in contrast to piezoelectric actuators);

(ii) the effect is strongly wavelength-selective (the maximum, and fastest, response is for light having a photon energy comparable to the bandgap energy of the chalcogenide);

(iii) light, rather than electricity (as in piezoelectric devices), is used as the stimulus, allowing remote actuation and operation in hazardous (e.g. flammable) environments;

(iv) optical actuators are suitable for miniaturization, and large arrays of independent cantilevers can be envisaged for applications requiring massively parallel processing;

(v) the optomechanical actuators are potentially cheap and easy to manufacture.

7.2 Experimental

The first experiments on the optomechanical effect [8] were performed on vee-shaped silicon nitride AFM cantilevers (200 μm in length, 20 μm in width and 0.6 μm in thickness) coated with a thin ($\sim$250 nm) film of amorphous $As_{50}Se_{50}$. (This material was chosen because it exhibits one of the largest *optical* anisotropy responses when illuminated by linearly polarized light.) Optically-induced deflections of the cantilevers when the chalcogenide layer was illuminated were detected by an optical-lever arrangement, whereby a laser beam was directed at, and reflected from, the underside of the cantilever, the position of the reflected beam being detected by a linear position-sensitive photodiode.

Recent, more systematic studies of the optomechanical effect have been performed on calibrated rectangular etched, single-crystal silicon cantilevers, of width 35 μm, thickness 2.8 μm and lengths ranging from 80 to 380 μm (three cantilevers being attached to a single 4 mm $\times$1.6 mm chip). The cantilever chips were mounted in a cryostat fixed to a positioning stage. An improved deflection-detection system was used (Fig. 7.1), in which a near-IR laser ($\lambda = 655$ nm), whose output was modulated at 38 kHz, was focused onto the end of the underside of a cantilever, the reflected beam being directed onto a split quadrupole photo-diode for positional measurements. Lock-in detection of the resulting photo-current has produced a great improvement in the signal-to-noise ratio of the cantilever-displacement measurements.

A variety of lasers have been used as illumination sources for exposing the chalcogenide films: a 10 mW He–Ne laser ($\lambda = 633$ nm), a 5 W Nd:YAG laser ($\lambda = 532$ nm) and a $\sim$1 W dye ring laser ($\lambda = 560$–615 nm). In all cases, the laser beams were focused onto the chalcogenide side of the cantilever such that the central, approximately uniform part of the

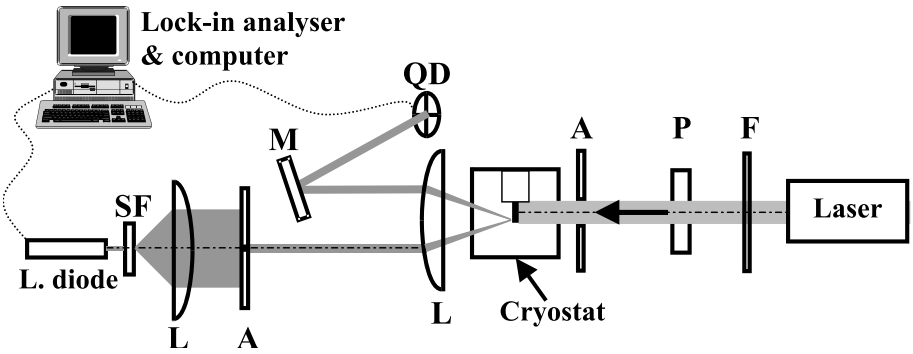

Figure 7.1: A schematic illustration of the experimental set-up used to measure the optomechanical effect: F is a neutral-density filter, P is a $\lambda/2$ waveplate or two Glan–Thompson prisms, A is an iris attenuator, L is a lens, SF is a spatial filter, M is a mirror and QD is a quadrupole diode.

gaussian intensity profile extended over the entire length of the cantilever, thereby assuring (approximately) uniform illumination of the chalcogenide film.

Amorphous chalcogenide thin films (of thickness $\sim$1 μm) have been deposited by standard thermal-evaporation techniques onto the cantilever substrates attached to a rotating planetary substrate holder to ensure homogeneous deposition. A variety of arsenic chalcogenide materials have been studied, including the composition $As_{50}Se_{50}$ ($E_g = 1.96$ eV, $\lambda_g = 628$ nm) studied previously [8, 9], but also the $As_{40}(S_xSe_{1-x})_{60}$ system $(0 < x < 1)$, for which the bandgap, E_g, varies between 1.79 and 2.43 eV $(688 > \lambda > 507$ nm), spanning the available laser tuning range.

As well as varying the wavelength, the illuminating laser light was altered systematically by changing the (linear) polarization state by means of a $\lambda/2$ waveplate for 633 nm illumination or otherwise by two Glan–Thompson polarizers, and the light intensity was controlled by neutral-density filters.

7.3 Results

7.3.1 Polarization Dependence

Representative optomechanical time-dependent displacement results (for a-$As_{50}Se_{50}$) are shown in Fig. 7.2. Two features of the effect are evident from this plot, namely reversibility and controllability. It can be seen that, following illumination with linearly-polarized light with the electric-field vector at an angle θ $(0 < \theta < 90^\circ)$ to the normal to the cantilever axis (see inset to Fig. 7.2), subsequent illumination with θ = 0° polarized light (the perpendicular, $\perp$, state) always produces the *same* (downward) displacement of the cantilever. This reversibility of the effect was demonstrated previously [8, 9] by cycling the light electric-vector polarization direction between $\theta = 0^\circ(\perp)$ and $\theta = 90^\circ$ (parallel to the cantilever axis, $\|$) states, whereupon it was observed that the cantilever displacement oscillated between two fixed values, i.e. there was no apparent fatigue in displacement amplitude on repeated cycling.

The second feature of note evident from Fig. 7.2 is the controllability of the optomechanical response: the displacement of a cantilever can be set simply by varying the angle between the light electric-vector polarization and the cantilever axis for illumination with light of a given wavelength and intensity. This simple method of controlling the actuator response is unique to the optomechanical effect.

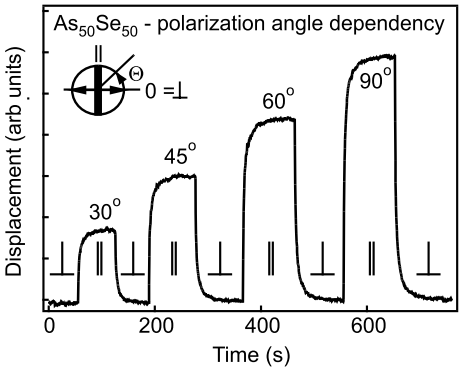

Figure 7.2: Dependence of the deflection of a cantilever, coated with a-$As_{50}Se_{50}$, as a function of the angle θ between the electric vector of the illuminating linearly polarized light and the normal to the cantilever axis (see inset).

7.3.2 Light-Intensity Dependence

Pronounced, and surprising, changes are observed in the optomechanical response on changing the intensity of the illuminating light (at constant wavelength and polarization angle). The time-dependent optomechanical response for a-$As_{50}Se_{50}$ films illuminated with light (λ = 633 nm) having intensities in the range 7–1140 mW cm^{-2} is shown in Fig. 7.3. Again, two features are evident from this figure. The first is that the kinetics of the cantilever displacement on changing, say, the light-polarization state from parallel ($\parallel$) to perpendicular ($\perp$) speed up markedly with increasing light intensity: the saturation level is reached more quickly with increasing light intensity. The growth curve of cantilever displacement versus time obeys stretched-exponential kinetics:

$$(A_0 - A_t) = A_0 \exp[-(t/\tau)^{\beta}], \tag{7.1}$$

where A_0 is the maximum (saturated) amplitude and A_t is the value at time t, τ is the characteristic time constant and β ($0 \leq \beta \leq 1$) is the stretching coefficient. A plot of $\ln(\ln[A_0/(A_0 - A_t)])$ versus $\ln t$ should therefore give a straight line if the growth kinetics obey the Kohlrausch–Williams–Watts (KWW) function, Eq. (7.1). Such a plot is shown in Fig. 7.4 for the representative case of a cantilever coated with a-$As_{50}Se_{50}$. It can be seen that, indeed, the cantilever displacement exhibits stretched exponential kinetics, but with apparently *two* different time and stretching constants, τ_1 and β_1, the short-time values, and τ_2 and β_2, the long-time values ($\tau_2 \simeq \tau_1, \beta_2 < \beta_1$). A plot of τ_2 versus the incident light intensity, I, for the $As_{50}Se_{50}$ system is shown in Fig. 7.5: it can be seen that τ_2 decreases by about

two orders of magnitude for an approximately 100-fold increase in I, and becomes constant at high light intensities, greater than about 400 mW cm^{-2} in this case.

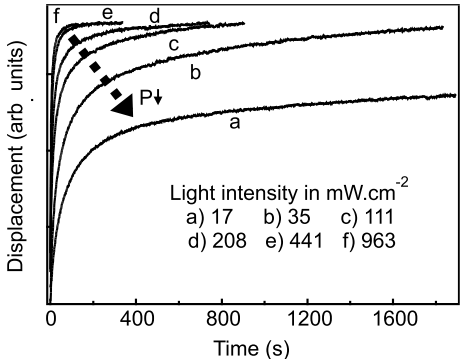

Figure 7.3: Kinetics of the deflection of a cantilever coated with a-$As_{50}Se_{50}$ as a function of light intensity.

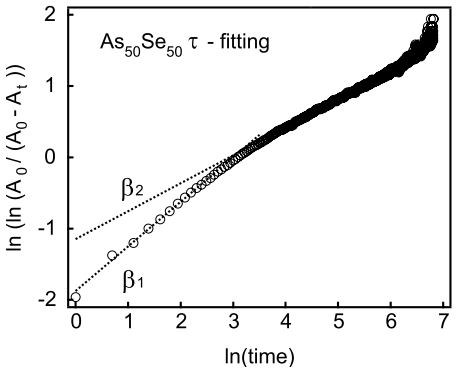

Figure 7.4: Double-logarithmic plot of the time dependence of the deflection of a cantilever coated with a-$As_{50}Se_{50}$, revealing two regimes of stretched-exponential (KWW) behavior.

The other significant, and surprising, point to glean from examination of Fig. 7.3 is that the saturated cantilever-displacement amplitude, A_0, is *independent* of the illuminating light intensity, even though the kinetics vary strongly with I.

7.3.3 Wavelength Dependence

It is of great interest to investigate the cantilever response (e.g. kinetics, maximum displacement) as a function of the wavelength of the illuminating light, in particular in relation to the bandgap wavelength (λ_g) of the chalcogenide material.

The wavelength response of the optomechanical effect has been studied both by varying the polarized illumination-light wavelength for a given material and by varying the composi-

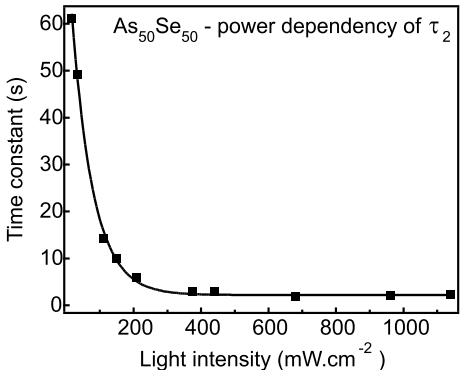

Figure 7.5: Plot of the long-time KWW time constant, τ_2, for a-$As_{50}Se_{50}$ as a function of light intensity.

tion of a chalcogenide system ($As_{40}[S_xSe_{1-x}]_{60}$) so that the bandgaps, E_g, of the materials span the available tuning range of the polarized laser source.

Representative results of the effect of illumination wavelength (at a fixed light intensity and polarization state) on the kinetics of cantilever displacement are shown in Fig. 7.6 for the case of the chalcogenide $As_{40}S_{40}Se_{20}$. It can be seen that the behavior is superficially similar to that shown in Fig. 7.3 for the light-intensity dependence. With decreasing wavelength (increasing photon energy), the kinetics of the cantilever displacement get faster, as for increasing light intensity. The wavelength dependence of the KWW (long-time) time constant τ_2, for a-$As_{40}S_{40}Se_{20}$, extracted from Fig. 7.6, is shown in Fig. 7.7. It can be seen that τ_2 decreases by a factor of 100 or so (50 to 0.5 s) for the wavelength tuning range available, and that the time constant becomes wavelength-independent for wavelengths shorter than λ_g (or super-bandgap photon energies greater than E_g). However, a marked difference with the light-intensity results of Fig. 7.3 is that the *saturated* cantilever displacement amplitude, A_0, is rather strongly wavelength dependent. This is not particularly evident at first sight from the kinetic data shown in Fig. 7.6, but is shown explicitly in Fig. 7.8. Here, A_0 values for different compositions in the system $As_{40}[S_xSe_{1-x}]_{60}$ are shown for different wavelengths in the tuning range of the illumination laser, with the wavelength ranges shifted in each case so that the bandgap wavelengths, λ_g, of each material coincide. In this manner, it is hoped that Fig. 7.8 represents the wavelength-dependent optomechanical behavior that would be exhibited by any chalcogenide glass in the As–S–Se system, were a sufficiently wide range of illumination wavelengths available to probe deep into both the sub-bandgap and super-bandgap regions. It can be seen from Fig. 7.8, in this respect, that the saturated displacement response appears to exhibit a maximum for wavelengths comparable to the bandgap wavelength, λ_g, of the material. Indeed, a couple of the compositions studied (x = 35, 40) clearly show extremal behavior of the wavelength dependence of the saturated cantilever displacement, since for them the value of λ_g lies within the available laser tuning range.

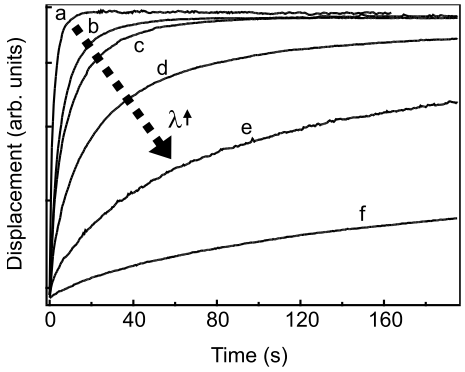

Figure 7.6: Kinetics of the deflection of a cantilever coated with a-$As_{40}S_{40}Se_{20}$ as a function of illumination wavelength. The saturated displacement values for each wavelength are shown in parentheses in arbitrary units: (a) 532 nm (77.2), (b) 564 nm (75.6), (c) 584 nm (75.3), (d) 595 nm (68.4), (e) 604 nm (63.3), (f) 633 nm (38.1).

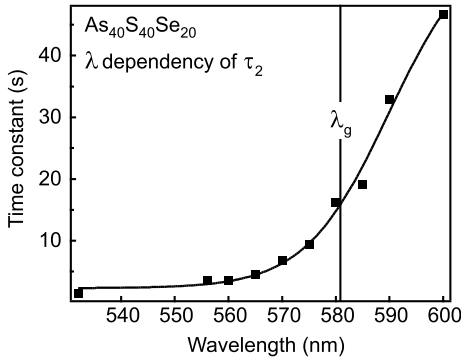

Figure 7.7: Plot of the long-time KWW time constant, τ_2, for a-$As_{40}S_{40}Se_{20}$ as a function of wavelength (the wavelength corresponding to the bandgap of the material is marked).

7.4 Discussion

From the above results it follows that, at least for the $As_{40}[S_xSe_{1-x}]_{60}$ system studied in detail, there is the happy coincidence for the performance of the optomechanically-driven cantilever that illumination with bandgap light causes *both* the largest (saturated) displacement amplitude and the fastest response. In addition, increasing the illumination light intensity up to a limiting value (e.g. 400 mW cm^{-2} for the case of a-$As_{50}Se_{50}$) also speeds up the response. However, rather counter-intuitively, increasing the light intensity does *not* produce a corresponding change in saturated displacement amplitude. The cantilever-displacement response kinetics have mostly been analyzed in terms of the *long-time* KWW time constant, τ_2, since this is experimentally the most precise. The short-time time constant, τ_1, is rather difficult to measure precisely in many cases.

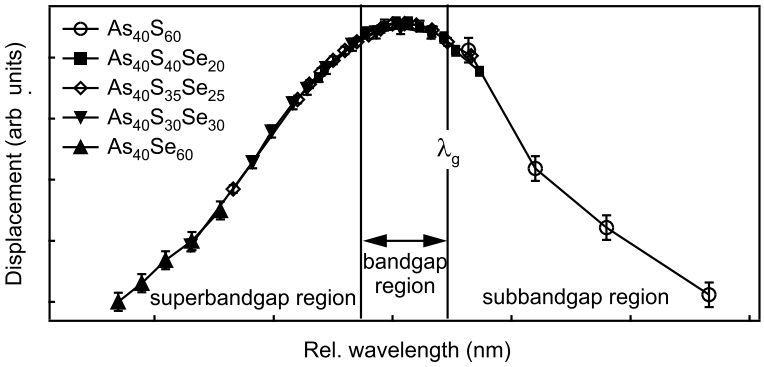

Figure 7.8: Saturated cantilever displacement as a function of relative wavelength (shifted relative to the bandgap wavelength) for the a-$As_{40}(S_xSe_{1-x})_{60}$ system.

Currently, a thorough theoretical understanding of the experimental optomechanical results is still lacking. We do not have a sound understanding of the microscopic mechanism involved in the transformation of light energy into mechanical motion of the chalcogenide-cantilever system. Nor can we account in detail yet for many of the features of the optomechanical effect that are observed experimentally.

In our paper first reporting the optomechanical effect [8], we postulated a mechanism that could plausibly account for this effect, namely a light-induced bond-twisting motion involving the two-fold-coordinated chalcogenide atoms. Optical excitation of electron states forming the top of the valence band (mainly chalcogen non-bonding p–π states) to (localized) states at the conduction-band edge causes a change in the repulsive interaction between the excited lone-pair orbital on the photoexcited chalcogen and the lone-pair orbitals on surrounding atoms. Since the recombination time for photoexcited carriers in localized states is much longer than for extended states, there is time for appreciable local structural rearrangement to take place before recombination occurs. Moreover, non-radiative recombination is more likely for carriers trapped in localized states, and the (vibrational) energy liberated by such recombination events will also promote local structural changes, even bond-breaking. The intrinsic anisotropy of the p-like electron orbitals associated with the chalcogen atoms means that only certain chalcogen atoms, having favorable orientations with respect to the electric-field vector of linearly-polarized light, will absorb photons and thus participate in photostructural changes. This restriction leads automatically to an anisotropic response [8]. However, it is still not clear to what extent light-induced charged-defect creation plays a role [4].

The above scenario can be used to account, for example, for the wavelength dependence of the optomechanical effect (Fig. 7.8). If (near-) bandgap light is the most efficient at inducing the effect, as assumed above, the response is expected to decrease with increasing wavelength (decreasing photon energy) in the absorption-tail sub-gap region because increasingly less light is absorbed there with decreasing photon energy. For shorter wavelengths (greater photon energies) in the super-bandgap region, preferential surface recombination of the light absorbed close to the top surface of the chalcogenide may be responsible for the decrease in the response, although this suggestion needs to be verified. As a result, the peaked response curve as a function of wavelength shown in Fig. 7.8 can be expected.

Concerning the light-intensity-dependent behavior evident in Fig. 7.3, it is plausible that increasing the light intensity speeds up the kinetics of the optomechanical effect, since the rate of light-induced atomic reconfigurations will concomitantly increase. What is harder to understand is why the magnitude of the saturated cantilever displacement should be *independent* of the light intensity (Fig. 7.3) when, naively, it might be thought that the greater the light intensity, the greater the number of light-induced atomic reconfigurations and hence the larger should be the magnitude of the (saturated) cantilever displacement. The only explanation for this behavior that comes readily to mind is that there exists a competing process with that responsible for the opto-mechanical effect. One candidate for such a competing process might be the photo-induced fluidity observed originally in glassy As_2S_3 by Hisakuni and Tanaka [6]. If the viscosity or shear modulus, and hence Young's modulus, E, which is linearly related, of the chalcogenide glass layer is reduced by optical illumination, a given strain e induced in the material by light (the optomechanical effect) will give rise to a correspondingly smaller stress, σ, i.e. displacement of the cantilever, since $\sigma = Ee$. The near-constancy of displacement amplitude with light intensity is therefore understandable if the functional dependence of induced strain on light intensity for constant modulus (e.g. $e \propto I^{\alpha}$) is comparable to the inverse of the dependence of the modulus on light intensity (e.g. $E \propto I^{-\alpha}$). This hypothesis remains to be tested.

7.5 Conclusions

One of the most intriguing of all photo-induced phenomena exhibited by chalcogenide glasses is the optomechanical effect, wherein illumination with linearly-polarized light of an amorphous chalcogenide film deposited on a cantilever support causes the chalcogenide to contract or expand (leading to a deflection of the cantilever), depending on whether the electric vector of the light is parallel or perpendicular to the cantilever axis, respectively. It is found that the speed of the cantilever-displacement response is greatly increased by increasing the illuminating light intensity or alternatively by decreasing the wavelength of the light until it is comparable to that corresponding to the bandgap of the semiconductor. The saturated (long-time) displacement of the bilayer cantilever is also a function of the wavelength, being a maximum for near-bandgap illumination. However, surprisingly, the saturated displacement is independent of the light intensity, for a given wavelength. This behavior is ascribed to a simultaneous softening of the chalcogenide glass (reduction in elastic modulus) during illumination (photoplasticity effect). The optomechanical effect lends itself to a variety of potential applications for optical actuators where the deflection of a cantilever can be controlled precisely by simply varying the angle between the electric-field vector of the linearly polarized light and the cantilever axis.

References

[1] K. Shimakawa, A. Kolobov and S. R. Elliott, Adv. Phys. **44**, 475 (1995).

[2] K. Tanaka, Semiconductors **32**, 861 (1998).

[3] A.V. Kolobov and K. Tanaka, in Handbook of Advanced Electronic and Photonic Materials and Devices, H.S. Nalwa (Ed.), Academic Press, San Diego 2001, vol. 5, p. 47.
[4] T. Uchino, D.C. Clary and S.R. Elliott, Phys. Rev. Lett. **85**, 3305 (2000); Phys. Rev. B **65**, 174204 (2002).
[5] J. Li and D. Drabold, Phys. Rev. Lett. **85**, 2785 (2000).
[6] H. Hisakuni and K. Tanaka, Science **270**, 975 (1995).
[7] A. Saliminia, T.V. Galstian and A. Villeneuve, Phys. Rev. Lett. **85**, 4112 (2000).
[8] P. Krecmer, A.M. Moulin, R.J. Stephenson, T. Rayment, M.E. Welland, and S.R. Elliott, Science **277**, 1799 (1997).
[9] M. Stuchlik, P. Krecmer and S.R. Elliott, J. Optoel. Adv. Mat. **3**, 361 (2001).
[10] K. Shimakawa and A. Ganjoo, J. Optoel. Adv. Mat. **3,** 167 (2001).

8 Photo-Plastic Effects in Chalcogenide Glasses: Raman Scattering Studies

Spyros N. Yannopoulos

8.1 Preamble

Over the last two decades we have witnessed growing interest in the external-stimuli control of the structure for a particular class of amorphous semiconductors, the so-called chalcogenide glasses. Light is a convenient stimulus that is extensively employed to induce, as well as to detect, subtle structural modifications in amorphous media which are the precursors of a variety of exceptional physical and chemical effects [1–3]. Apart from the interest from the fundamental point of view in this kind of studies, that is, the need to decipher the microscopic origin of light-induced (or photo-induced) metamorphoses, the technological aspects of these glasses are also abundant and important. Indeed, recent seminal achievements in this field have demonstrated that practical applications do not seem remote any more [4, 5]. The fact that physicochemical properties can be controlled, in a desired way, by excitation with visible light justifies the motivation over the past years for intense and fertile research efforts on metastable photo-induced phenomena.

Numerous light-induced effects have been realized in chalcogenide glasses manifesting themselves in the long body of (mainly) experimental work [1–3] and lately molecular dynamics simulations [6] and quantum chemical calculations [7] that have appeared thus far, aiming either to reveal new aspects of photo-induced effects or to elucidate their microscopic origin.

Reversible photo-induced effects in amorphous chalcogenide semiconductors are observed when they are illuminated with light having energy ($E^{ill} = h\nu$) comparable to or even lower than the energy bandgap E_g of the material. Various physicochemical properties, such as structural, mechanical, rheological, optical, electrical, etc., experience changes after illumination. The changes are caused through a process that involves the photo-creation and the subsequent non-radiative recombination of electron–hole pairs. Chalcogenide glasses display a dazzling variety of photo-induced phenomena. Among the most thoroughly studied and sufficiently understood such effects we can mention photodarkening [2], photo-induced anisotropy [2], giant photoexpansion [8], athermal photo melting at low temperatures [9], photo-induced mass transport [10], reversible nano-contraction and dilation in thin amorphous films induced by polarized light [4], etc. Athermal plastic changes in the structure of a crystalline semiconductor have been known for more than 30 years [11], while photo-plastic effects in chalcogenide glasses have also been reported [12]. One of the many facets of photo-plastic effects is the athermal photo-induced fluidity (PiF) [13]. This effect pertains to the permanent

deformation (shape change) of a glassy semiconductor under the combined action of light illumination and mechanical stress. Changes in rheological and mechanical properties upon bandgap light illumination, such as decrease of the glass transition temperature T_g [14] as well as softening of the elastic constants [15] have also been observed. Very recently, the athermal ultrafast melting of an amorphous semiconductor InSb [16] and single-crystal Ge films [17] has been studied by ultrafast time-resolved X-ray diffraction techniques, showing that non-thermal or electronic melting of materials might be a universal property. Despite their potential technological importance and the challenge from the scientific viewpoint, photo-plastic effects have not yet been put under focus.

In this chapter we present a brief survey on the PiF effect, putting emphasis on the changes of vibrational modes taking place during the effect. Section 8.2 contains a brief survey on the PiF effect. The temperature dependence of the changes of intramolecular and intermolecular vibrational modes in the athermal PiF regime of As_xS_{100-x} ($x = 40, 25$) glasses are described in Sections 8.3, 8.4 and 8.5. Section 8.6 presents some relevant microscopic models for photo-plastic changes in chalcogenide glasses and finally Section 8.7 concludes this chapter, advancing some suggestions for future work.

8.2 The Photo-Induced Fluidity Effect: A Synopsis

In a relatively recent report, Hisakuni and Tanaka demonstrated that a glassy semiconductor, i.e. As_2S_3, could "flow" under intense sub-bandgap light illumination, without heat provision. The effect takes place at temperatures much below the glass transition temperature [13]. A local increase of the network fluidity emerges as a result of light illumination and can be revealed through application of external stress. Specifically, the consequence of laser light (632.8 nm or 1.92 eV) irradiation was to facilitate viscous flow, reducing the viscosity by more than two orders of magnitude. The effect is macroscopically manifested through an increasing elongation of a glassy As_2S_3 fiber ($d \approx 100$ μm) under light illumination and uniaxial stress. As a result a "necking" effect is evidenced at the illuminated point. Since PiF was observed only after the simultaneous action of illumination and stretching the effect, as regards the fiber, it could also be conceived as a kind of *photo-induced ductility*.

The photo-electronic or athermal origin of this effect can be evidenced through the unexpected temperature dependence it exhibits [13]. Specifically, while ordinary flow of glass-forming liquids follows either a strong or mild temperature dependence, being always facilitated when the temperature of the material increases [18], it was observed that photo-induced fluidity was hindered at elevated temperatures. This was manifested through the considerable suppression of the material's ability to flow or to plastically deform at the illuminated point as the temperature increased. This finding reassured the athermal origin of PiF since a thermal effect should follow the opposite trend.

A possible explanation of PiF has been offered by Fritzsche [19], who attempted its rationalization by employing the self-trapped exciton idea. In that sense, the photo-excited electron–hole pairs are considered to recombine non-radiatively through an intermediate transient exciton state. The final recombination may yield a bonding arrangement different from the initial configuration. Then the observed macroscopic changes in the fluidity arise from the cumulative effect of the local configuration changes. First-principles molecular dynamics

simulations have also been utilized to calculate light-induced structural changes and diffusive motion in As_2Se_3 [6]. Diffusive motions occurring at short time scales were interpreted as the initial stage of the athermal PiF.

The structural mechanism underlying PiF can be elucidated by tracking changes in vibrational modes during the time that the effect takes place. For this, Raman spectroscopy is an ideally suitable probe that can provide information concerning both short and intermediate length scales. It is therefore feasible, by using Raman spectroscopy, to study both intramolecular and intermolecular vibrational modes and to monitor specific effects of photostructural changes on them. A brief survey of the results obtained from detailed Raman scattering investigations on the PiF effect, recently undertaken by the author and co-workers, follows in the next sections.

8.3 Changes of Vibrational Modes in the Athermal PiF Regime at Ambient Temperature

8.3.1 High-Frequency Modes: Intramolecular Vibrations

Experimental details concerning fiber preparation and light scattering apparatus can be found elsewhere [20, 21]. Representative Stokes-side, polarized (VV: vertical electric field of the incident radiation – vertical analysis of the electric field of the scattered radiation) and depolarized (HV: horizontal electric field of the incident radiation – vertical analysis of the electric field of the scattered radiation) Raman spectra for a fiber ($d \approx 150$ μm) under stress are shown in Fig. 8.1. The fiber axis was fixed at a perpendicular (V) configuration relative to the scattering plane. It should be stressed here that PiF can be induced with a range of laser power densities on the sample. In our studies we have used a power density in the range 20–30 W cm^{-2}; this was close to the lowest threshold value above which the effect was measurable and it was chosen in order to avoid undesired sample heating. The spectra shown in Fig. 8.1 correspond to different magnitudes of the applied stress given in parentheses in 10^7 dyn/cm^2 units. The most obvious feature made out from this figure is the monotonic increase of the depolarization ratio $\rho = I^{HV}/I^{VV}$ when increasing the magnitude of the external stress, S. The spectral region 260–430 cm^{-1}, shown in Fig. 8.1, includes according to the "molecular model" analysis [22] at least three vibrational peaks, in particular, the ν_1 and ν_3 vibrational modes of the C_{3v} symmetry AsS_3 pyramidal unit at 342 and 310 cm^{-1}, respectively, and the ν_3' vibrational mode of the C_{2v} symmetry water-like unit As–S–As at 392 cm^{-1}.

The stress dependence of the depolarization ratio, found by integrating the VV and HV scattered intensities in the spectral region 260–430 cm^{-1}, is illustrated in Fig. 8.2 for fibers of various diameters. One can easily discern from this figure that the depolarization ratio exhibits a systematic, monotonic increase for all fibers used. This finding shows that the measured effect is well reproduced and repeatable. It therefore becomes obvious that the depolarization ratio is a rather reliable indicator apt to quantify the structural changes that occur in the glass structure during the illumination/stretching procedure. This is also supported by the fact that no detectable changes are perceived from the measured spectra, i.e. ρ remains constant regardless of the exposure time, if no stress is applied. Thus, the changes observed in the depolarization ratio are due to the *combined* effect of illumination and the application

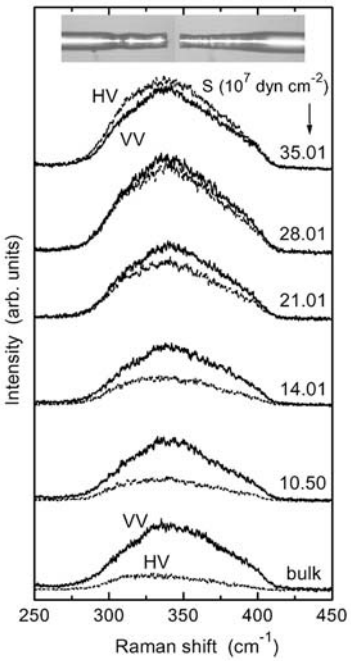

Figure 8.1: Representative polarized (VV) and depolarized (HV) Stokes-side Raman spectra of As_2S_3 at various magnitudes of the applied elongation stress. The inset in the upper part of the figure illustrates a typical example of an optically processed fiber, which has experienced the simultaneous effect of light illumination and elongation stress.

of the external stress. This implies that illumination alone does not engender fluidity, it rather brings the structure to a state amenable to flow or to plastically deform; the plastic change is achieved with the aid of an external mechanical stimulus. This justifies the term photo-induced ductility for this effect that we coined in the previous section.

A few remarks should be added here to prevent possible misinterpretations of the observed structural changes in fibers. One could argue that the fiber drawing procedure from the melt might induce some ordering in the glass structure as has been reported for As_2Se_3 [23]. However, one has to emphasize the important differences of the fiber drawing procedure between the present study and that in Ref. [23]. In the latter, fibers were pulled from the melt at a speed greater than 100 m/min with a final fiber diameter $d \approx 1$ μm, while in our experiment much lower drawing rates (at least one order of magnitude) are used leading to a fiber diameter $d \approx 100$–300 μm. More importantly, the drawing-induced "crystallites" were shown to survive only at 77 K, and seemed to anneal to the amorphous phase at 300 K [23]. Finally, the depolarization ratios (quite sensitive to such ordering effects) of the unstressed fiber and the bulk glass are found to be equal [21]. Therefore, the procedure we follow for fiber drawing does not induce traces of crystallization in the glass structure. From the above it becomes evident that the depolarization ratio can be used rather satisfactorily to infer structural mod-

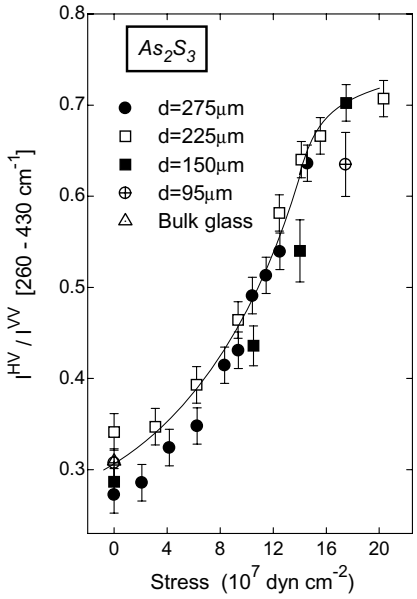

Figure 8.2: Stress dependence of the depolarization ratio area in the spectral region 260–430 cm^{-1} for As_2S_3 fibers with various diameters. The sigmoid solid line is a guide to the eye.

ifications of the glass structure. Strictly speaking, the structural (ordering) changes that the stress-dependence curves of ρ unveil are related to the atomic configurations to which the system ends up after the illumination/stretching procedure.

8.3.2 Medium Range Structure: the Boson Peak Region

One of the most spectacular differences between the amorphous and crystalline states has its origin in the lack of long-range periodicity and is epitomized in the universal presence of excess low-energy excitations in the amorphous state [24]. The term low-energy excitations has been coined to account for properties such as anomalies of the specific heat at very low temperatures, anomalous attenuation of sound waves, and the presence of extra low-energy scattering mechanisms in Raman and inelastic neutron scattering. Indeed, inelastic (Raman and neutron) scattering data have revealed that the low-frequency part of the spectrum (below ca. 10 meV, 80 cm^{-1}, or 3 THz) consists of two contributions: (a) the first order vibrational spectrum, around 1 THz, called the *Boson peak*, and (b) the *quasi-elastic* contribution appearing as a zero-centered mode, ascribed to fast (ps) relaxations. The interpretation of these two overlapping spectral features in the low-frequency part of the spectrum, as well as their interrelation and spectral properties, is today one of the most debated issues of glassy physics eluding a commonly accepted explanation. Experimental remarks contradicting putative universalities have recently been addressed by our group [25–27].

The Boson peak is usually assigned to the concerted vibrational motion of a number of molecules and hence information about a spatial region beyond the short-range order can in principle be gained [28]. Therefore, it becomes quite tempting to check for possible changes in the spectral features of the Boson peak in optically processed fibers. A representative series of low-frequency depolarized Raman spectra for various magnitudes of the applied stress are shown in Fig. 8.3. To unravel possible subtle spectral changes a quantitative treatment (fitting) is necessary. One of the simplest approaches employs the log-normal distribution to account for the Boson peak and a Lorentzian line to represent the relaxational contribution (for details see [21]). The results obtained are illustrated in Fig. 8.3 where it can be seen that the total fitted curve (continuous line) conforms almost perfectly to the experimental data (open circles) in the whole frequency range of the fitting. It is also obvious that the position of the maximum to the Boson peak does not depend on the magnitude of the applied stress. The insensitivity of the Boson peak maximum on the external stress implies that the structural changes that occur during the effect do not involve changes in the size distribution of the layer-like clusters. We draw this conclusion based on the physics underlying the log-normal model which invokes the existence of clusters of atoms/molecules in the glassy phase whose sizes are described by a log-normal statistical distribution.

On the other hand, the frequency dependence of the depolarization ratio in the region of the Boson peak exhibits a much more interesting behavior (see Fig. 6 in [21]). In particular, apart from an overall increase of the depolarization ratio when increasing the magnitude of the external stress it is also clear that the frequency dependence of the bulk glass and the unstressed (or slightly stressed) fiber smoothes over at higher stress values leading finally to a frequency-independent depolarization ratio. This finding implies a modification in the scattering mechanism since polarization properties of the scattered light are described by the photon–phonon coupling coefficient which represents the strength of the polarizability modulation of the vibrational modes. The constant depolarization ratio of the optically-processed fiber indicates that both isotropic and anisotropic vibrational motions modulate the polarizability of the medium in a similar way.

Closing this section, we should mention that stress-dependence studies of the Boson peak have revealed that this significant structural feature is not the privilege of only isotropic amorphous media; it can also be found in systems with enhanced order [29]. This was essentially accomplished by analyzing the Boson peak spectral features when the glassy structure under study was driven from the isotropic state to the state where the isotropic orientational symmetry is violated.

8.4 Temperature Dependence of the Photo-Induced Fluidity Effect

Perhaps the most fascinating feature of PiF is the anomalous behavior it exhibits against temperature variations, namely the fact that the effect becomes less appreciable at higher temperatures. Indeed, it was observed an Arrhenius-like increase of PiF by almost one order of magnitude over the temperature interval 10–50 °C [13]. This stimulated the study of vibrational modes at high temperatures. To achieve this, we have undertaken [30, 31] a Raman

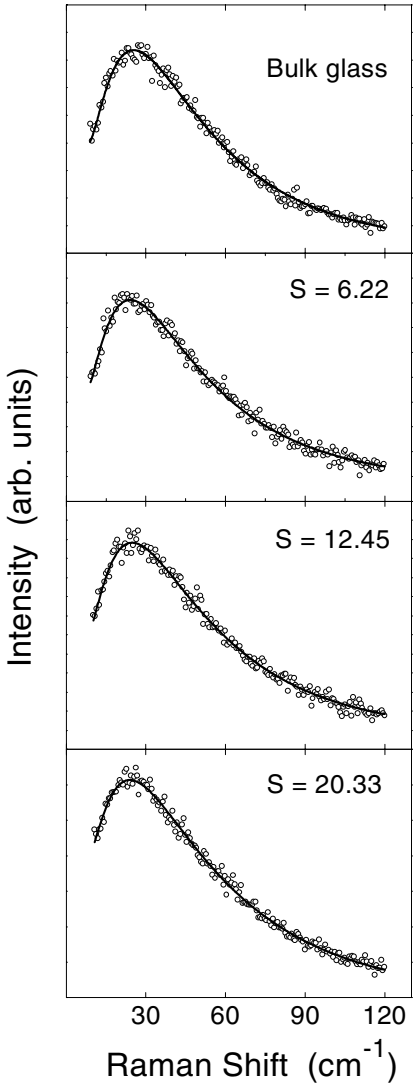

Figure 8.3: Representative depolarized low-frequency Raman spectra (Boson peak) of As_2S_3 at various magnitudes of the applied elongation stress (dyn/cm^2). The bulk glass data are also shown for comparison. Open circles, experimental data; solid lines, best fit curve according to the log-normal model as described in the text.

spectroscopic study in the temperature interval 20–120 °C, thus extending the information over a region much broader than that used in Ref. [13], but still much below T_g so as to avoid

introducing heating. Analyzing the Stokes-side polarized and depolarized Raman spectra it was found that the main changes taking place at each temperature pertain to a monotonic increase of the depolarization ratio. However, what interestingly emerges from the temperature-dependence study is that the rate of increase of the depolarization ratio is not constant, even non-monotonic, as a function of the temperature, as Fig. 8.4 reveals for four different temperatures. We observe that at 40 °C the sigmoid increase of the depolarization ratio curve reaches a plateau that hardly exceeds half of the corresponding plateau value of the room temperature curve. Subsequent temperature rise, up to 60 °C, renders the effect even less appreciable. Evidently, structural reorganization during PiF seems to be hindered at higher temperature.

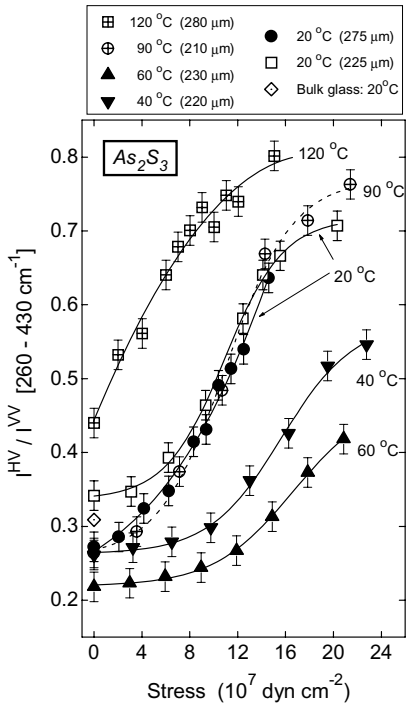

Figure 8.4: Stress dependence of the depolarization ratio area in the spectral region 260–430 cm^{-1} for As_2S_3 fibers at various temperatures. Sigmoid dashed and solid lines are guides to the eye. The data illustrate the anomalous characteristics of the photo-plastic effect (PiF) through the reversal of the temperature dependence above 60 °C.

Up to this point, the obtained behavior of the depolarization ratio is reminiscent of the temperature dependence of the photo-induced viscosity [13], which provides further support to the idea that the changes of the depolarization ratio can indeed be utilized as a rather sensitive indicator of PiF. This picture changes drastically when the measurements are extended over a wider temperature range than that of Ref. [13]. Indeed, as is illustrated in Fig. 8.4, the depolarization ratio (and presumably the fluidity) increases again at 90 °C, where the ρ versus S curve essentially coincides with that of the room temperature study. A further increase

of temperature to 120 °C leads to more noticeable changes of the depolarization ratio even at low values of the applied stress. Bearing in mind that the glass transition temperature of the material ($T_g \approx 210$ °C) is still well above the highest temperature employed in our experiment, it seems highly unlikely that a substantial softening of the glass structure at 120 °C takes place. Indeed at 120 °C the "dark" viscosity of As_2S_3 is two orders of magnitude higher than the viscosity at T_g. To preclude any possibility of thermal structure softening at the highest temperature reached in the present work we undertook the following experiment. A fiber was stressed (8×10^7 dyn/cm^2) with the laser held "off" at 120 °C for 3 h. Then, the fiber was cooled down to room temperature and the magnitude of the depolarization ratio was found to be identical with that measured before the thermal treatment. This indicates that at least up to 120 °C no thermal softening occurs and thus the features illustrated in Fig. 8.4 are indeed photo-induced.

Finally, it would be useful to note here that the narrowing of the bandgap caused by the temperature rise up to 120 °C cannot affect the observed behavior of the depolarization ratio. Indeed, the bandgap energy change is of the order of 3% (see [31] for details) which is too small a difference to account for the immense, even non-monotonic, changes of the depolarization ratio.

Let us now discuss the origin of the experimental data shown in Fig. 8.4 in terms of possible structural mechanisms. Having established a link between PiF and the monotonic increase of the depolarization ratio, at a particular temperature, we conclude from Fig. 8.4 that the rise of temperature – at least up to 60 °C – causes a hindrance in the flow process, as was also demonstrated in [13]. A simplistic model to account for this finding was the adoption of an intramolecular structural mechanism, namely, the geminate recombination process [19]. Since the increase of temperature facilitates the diffusion of the excited carriers, a decrease of the geminate recombination rate is expected hindering bond-reforming processes. However, because of the linear dependence of the diffusion constant of charge carriers on temperature, it seems no very likely that within 40 °C – where PiF was studied [13] – such a dramatic decrease of photo-induced viscosity could solely be accounted for by a decrease of the geminate recombination rate. Further, we must bear in mind that the inducing light energy is sub-bandgap and thus less effective in producing electron–hole pairs than bandgap light. Critical analysis of our experimental data has revealed the destruction of As_4S_4 molecules, which are sporadically present in the glass structure [32]. This finding is suggestive of another intramolecular structural mechanism which might be responsible for the observed decrease of PiF at high temperatures and is discussed in Section 8.6 in more detail.

More intriguing is the apparent reversal in the temperature dependence of PiF shown in Fig. 8.4. Evidently, to rationalize the reversal of PiF one has to reckon on structural mechanisms other than, and competing with, those mentioned previously. The buckling model [33] has been mentioned as one possible candidate for intermolecular structural changes [13, 21, 31]. This model is based on the widely adopted idea that particular chalcogenides, including As_2S_3 glass, retain to some degree the layered structure of the crystalline phase, thus containing two types of bonds, i.e. strong covalent ones within the layer and weak van der Waals bonds between the layers. The covalent bonds are responsible for the glass structure integrity of the chalcogenide layers and other properties such as the glass transition temperature and are affected by temperature only close to and above T_g. On the other hand, the sub-lattice of the weak bonds is the one that contains the entities that are easily responsive to

incident light and is ultimately responsible for the photo-induced phenomena. Owing to the smaller energy barriers that are involved in this case, weak-bond restructuring may occur even at temperatures much lower than T_g.

Temperature dependence diffraction studies of As_xS_{100-x} glasses have revealed an unexpected increase in the first-sharp-diffraction peak intensity with increasing temperature while the second-diffraction peak intensity normally decreased [34]. These findings have been interpreted as evidence of an increasing layer ordering with temperature. This is expected to occur since, as the temperature rises, the thermal energy provided may allow the atoms to relax their strained bonding arrangement rendering the layer smoother. Given the above context, a possible explanation could be offered for the anomalous behavior of PiF observed through the Raman depolarization ratio. Indeed, the non-monotonic dependence on temperature of the ρ versus S curves shown in Fig. 8.4 may arise from the competition of two opposing effects. The first one is the decreasing geminate recombination rate and the gradual elimination of As_4S_4 molecules discussed above. The second effect, namely ordering effects through enhanced layering, has the opposite temperature trend compared with the previous mechanism, tending to facilitate the plastic deformation imposed by the external stress. The reversal of the fluidity versus temperature curve occurring around 60 °C signifies the predominance of the second mechanism above this temperature. The enhancement of layer ordering is presumably the origin of the increased $S = 0$ value of ρ at 120 °C (Fig. 8.4).

8.5 PiF in Non-Stoichiometric As_xS_{100-x} Glasses

So far, the studies on the athermal PiF effect have been focused only on the stoichiometric composition As_2S_3 or $As_{40}S_{60}$. To examine whether the effect is quite general, studies on other glasses would be desirable. The As_xS_{100-x} glass-forming family is an advantageous candidate because by varying x one can almost smoothly pass from the layer-like structure ($x = 40$) to the more flexible arrangement containing the chain-like or ring-like fragments characteristic of sulfur-rich mixtures. The $As_{25}S_{75}$ glass composition is a convenient one since it corresponds to a much softer or more flexible structure characterized also by a high enough glass transition temperature ($T_g \approx 140$ °C), implying that the glass is quite stable at room temperature. Selected spectra of the $As_{25}S_{75}$ glass composition are shown in Fig. 8.5 for various magnitudes of the elongation stress. The established analysis of the depolarization ratio has also been applied to these data (for the spectral range 260–430 cm^{-1}) and the results obtained are reported in Fig. 8.6 where for comparison the stoichiometric glass data at 20 °C and 60 °C are also shown. The room temperature results for the $As_{25}S_{75}$ composition are shown in Fig. 8.6 as crossed squares. It is clearly seen in this case that the changes of the depolarization ratio and hence of PiF are much weaker than those of $As_{40}S_{60}$ at room temperature.

The $As_{25}S_{75}$ glass has a wider bandgap than the stoichiometric glass, $E_g \approx 2.55$ eV, and therefore the 514.5 nm (or 2.41 eV) laser line can also be used as a sub-bandgap illuminating source. The depolarization ratios as a function of the applied stress for the $As_{25}S_{75}$ concentration measured with the 514.5 nm laser line are shown in Fig. 8.6 as open and solid diamonds for two different runs (fiber diameter) of the experiment. These results demonstrate the obvious ineffectiveness of the 514.5 nm laser line, which lies below but very close to the bandgap

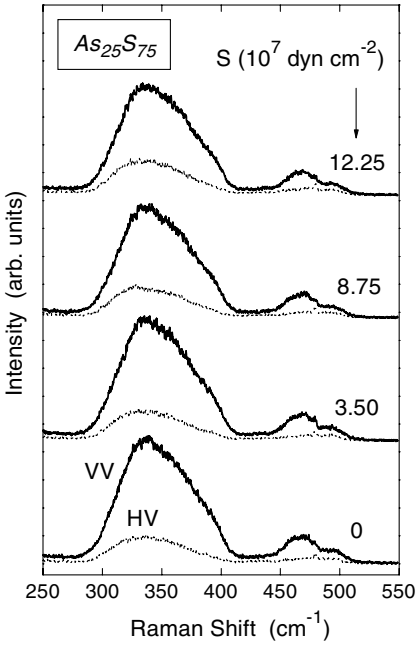

Figure 8.5: Representative polarized (VV) and depolarized (HV) Stokes-side Raman spectra of $As_{25}S_{75}$ at various magnitudes of the applied elongation stress.

of the glass, to produce the particular structural changes which are responsible for the plastic deformation of the fiber. The considerably smaller penetration depth of bandgap laser light is presumably associated with this behavior.

The above-mentioned results imply that that PiF of $As_{25}S_{75}$ glass might be less prominent than that of the stoichiometric composition ($As_{40}S_{60}$). In the following we attempt to address the role of two possible factors that might contribute to these findings, viz. (i) the relation between incident light energy and bandgap energy, and (ii) the role of the glass-transition temperature.

8.5.1 The Role of Illumination-to-Bandgap Energy Ratio in PiF

Since the $As_{25}S_{75}$ glass has a wider bandgap than the stoichiometric one it would be instructive to examine the role of the illumination energy E^{ill} to bandgap energy ratio $r = E^{ill}/E_g$. Indeed, one could argue that the observed difference in the ρ versus S curves at room temperature for the two studied glasses could be due to the effectiveness of the light inducing the structural changes or equivalently to the ratio of the illuminating light energy to the bandgap energy. The modification of the glass structure by increasing the sulfur content causes an increase in the bandgap of the material changing also the ratio r. For example, in the case of $As_{40}S_{60}$ and $As_{25}S_{75}$ we have $r = 0.80\ (1.0)$ and $0.75\ (0.94)$, respectively for the $647.1\ (514.5)$ nm laser

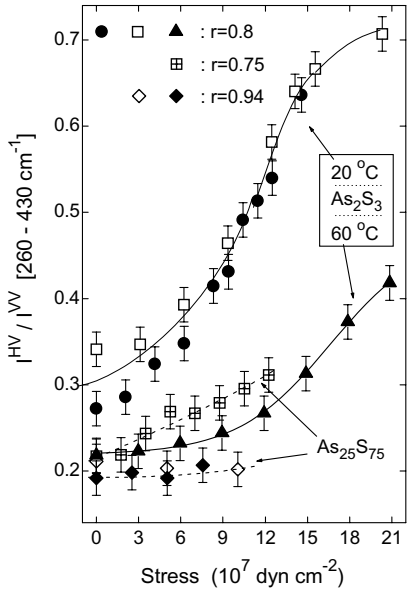

Figure 8.6: Stress dependence of the depolarization ratio area in the spectral region 260–430 cm^{-1} for As_2S_3 ($As_{40}S_{60}$) and $As_{25}S_{75}$ fibers at ambient temperature for different illumination sources as determined by the parameter $r = E^{ill}/E_g$. Data for $As_{40}S_{60}$ corresponding to 60 °C are also present for comparison. Open squares and filled circles: ambient temperature data for $As_{40}S_{60}$ (647.1 nm or $r = 0.8$); filled triangles: 60 °C data for $As_{40}S_{60}$ (647.1 nm or $r = 0.8$); crossed squares: ambient temperature data for $As_{25}S_{75}$ (647.1 nm or $r = 0.74$); open and filled diamonds: ambient temperature data for $As_{25}S_{75}$ (514.5 nm or $r = 0.94$).

energy. For $r = 1.0$ (that is, illumination of $As_{40}S_{60}$ with the 514.5 nm laser line) strong absorption/heating conditions make it impossible to discriminate between thermal and athermal effects. A wavelength-dependence study was carried out only for the $As_{25}S_{75}$ glass. The fact that the structural changes of this glass for $r = 0.75$ (647.1 nm) are less significant than those of the $As_{40}S_{60}$ glass for $r = 0.80$ is not likely to be due to the minor difference in r.

Let us now see what is the impact of different wavelengths on the same structure, that is $r = 0.75$ and 0.94 in the case of $As_{25}S_{75}$. It is obvious from the data in Fig. 8.6 that when near-bandgap light illumination is used ($r = 0.94$) structural changes leading to PiF do not occur. This is expected for the reason that although the efficiency of light in producing electron–hole pairs is higher with near-bandgap light, the effect occurs only on the surface of the fiber due to strong absorption, resulting in unimportant penetration (only the skin layer is affected) and as a consequence the elongation of the fiber is negligible.

8.5.2 The Role of the Glass Transition Temperature

The glass-transition temperature is an important factor that has to be taken into account for interpreting the difference between the room temperature data (Fig. 8.6) for $As_{40}S_{60}$ and $As_{25}S_{75}$ glasses obtained at wavelength 647.1 nm. The significant role of T_g has been demonstrated in studies of various As_xS_{100-x} glasses [34] where the temperature dependence of the first-sharp-diffraction peak intensity was found to follow a master curve in a T_g-scaled plot. In this context, a direct comparison between the room temperature data for $As_{40}S_{60}$ and $As_{25}S_{75}$ may be not so informative and a comparison should instead be done at T_g-scaled or reduced temperatures, $\tau = T^{exp}/T_g$. The 20 °C data of $As_{25}S_{75}$ ($T_g \approx 140$ °C) correspond to $\tau = 0.71$. In the case of the $As_{40}S_{60}$ glass ($T_g \approx 210$ °C) the τ ratio assumes the same value ($\tau = 0.71$) for $T^{exp} \approx 70$ °C, implying that the room temperature depolarization ratio data for $As_{25}S_{75}$ glass should be compared with the 70 °C data for $As_{40}S_{60}$. The closest available data set for $As_{40}S_{60}$ is that for 60 °C which is re-plotted in Fig. 8.6 for convenience. Interestingly, a considerable proximity is revealed for these two data sets, namely for the 60 °C curve of $As_{40}S_{60}$ and the room temperature data for $As_{25}S_{75}$. This finding allows us to adopt the idea that structural changes accompanying photo-induced fluidity might be governed by glass transition dynamics. If the above hypothesis is correct, then PiF for $As_{25}S_{75}$ cannot be considered as being less prominent than that of the stoichiometric composition. Consequently, study of this glass ($As_{25}S_{75}$) at $T^{exp} \approx -20$ °C would result in depolarization ratio changes similar to the room temperature curve of $As_{40}S_{60}$ if glass transition dynamics does indeed govern the photo-induced fluidity.

8.6 Microscopic Models Related to PiF

Before discussing some relevant structural models underlying PiF and its anomalous temperature dependence it would be instructive to comment on the different behavior of PiF for $As_{25}S_{75}$ and $As_{40}S_{60}$ in relation to structural differences of these glasses. It is well-known that in sulfur-rich glasses the quasi two-dimensional layers of the stoichiometric composition are partially disrupted and chain-like fragments and/or S_8 rings are the main structural elements. Thus, in the framework of the buckling model the less prominent structural changes in the case of the more flexible structure ($x = 25$) seem quite reasonable. The disruption of the layer-like fragments with increasing sulfur softens the structure considerably, reducing also its ability to respond to an external mechanical stimulus. Two such possible ways that can be envisaged are shown in Fig. 8.7. First, the chain-like sulfur configurations could be entangled, thus hindering the flow process (Fig. 8.7(a)). Second, the quasi one-dimensional character of the chain-like fragments offers a possibility of new relaxation pathways, during illumination, for example in directions perpendicular to that of the applied stress (Fig. 7(b)). Such processes are not expected to contribute to orientation enhancement. Both the above mechanisms cannot be realized in the case of two-dimensional layers (Fig. 8.7(c)). Evidently, PiF is also expected to be not so prominent for glasses with highly constrained three-dimensional (3D) network structures. The compactness of 3D structures and the lack of weak van der Waals bonds might be possibly associated with the reluctance of the material to undergo plastic deformation under the action of light illumination and mechanical stress, thus impeding the flow process. As

we have already stressed [31] the particular structural characteristics and the appropriate softness of locally layered (2D) materials are the decisive factors maximizing the possibility of structural changes that lead to the plastic deformation (flow) of the material. In other words, glasses whose structures are dominated by dimensionalities lower or higher than two are not expected to be appreciably amenable to photo-plastic effects.

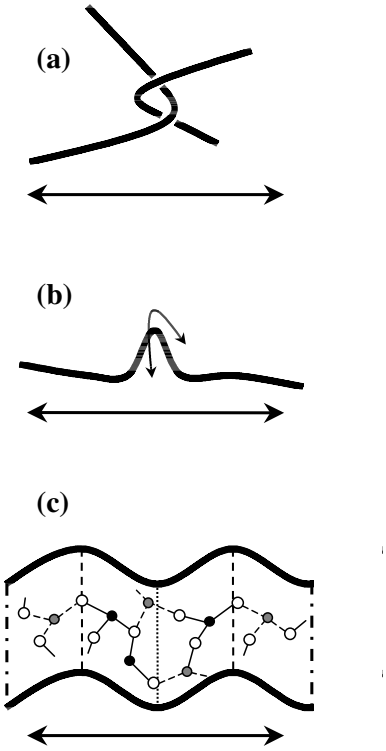

Figure 8.7: Schematic representation of possible local structural arrangements in non-stoichiometric S-rich structurally flexible glasses, (a) and (b) and in the $As_{40}S_{60}$ glass (c). The double-side arrow portrays the direction of a hypothetical external elongation stress. Conformation (a) shows a possible entanglement while (b) delineates a quasi one-dimensional molecular fragment demonstrating the likelihood of this arrangement to relax in another direction, i.e. perpendicular, than that of the imposed mechanical stimulus. Drawing (c) shows a typical atomic configuration of the $As_{40}S_{60}$ glass. In drawings (a) and (b) the structure consists of S-rich chains containing occasionally AsS_3 pyramidal units not shown here for simplicity.

8.6.1 Intramolecular Structural Models for PiF

As it became clear from the foregoing sections, in our previous studies [20, 21, 30, 31] emphasis was given mainly to the polarization properties of scattered light through which ordering

effects or the formation of anisotropic structures could be monitored. However, the appearance and the intensity dependence of vibrational lines on external parameters can also provide valuable information about the presence of certain "chemical species" in the glass structure. A detailed analysis of Raman spectra of As_2S_3 glass fibers (virgin and optically processed), bulk glass at room temperature, and supercooled liquid just above the glass transition temperature [35] revealed that the Raman spectrum of the bulk glass rapidly quenched from 600 °C contains weak but clearly visible peaks characteristic of As–As homopolar bonds in realgar-like As_4S_4 molecules; this is a well-known effect of fast quenched As_2S_3 glass [32].

These peaks are also present in the virgin fiber spectrum with the same relative intensity since the fiber is pulled out from the high-temperature melt. The As_4S_4 peaks gradually disappear when the fiber is subjected to the combined illumination/stretching effect. This finding shows that during the photo-plastic effect As_4S_4 molecules dissociate or open-up giving rise to less symmetric structural units. Such a procedure can be envisaged by the schematic model shown in Fig. 8.8. This particular structural metamorphosis is also compatible with two key features of PiF. On the one hand, it can account for the length increase of the fiber and, on the other hand, it engenders anisotropy (depolarization ratio increase) because of the transformation of a highly symmetric molecule to an asymmetric planar-like configuration. These findings are important since they show that homopolar As–As bonds are most likely dissociating rather than forming in the PiF regime. More details of the aforementioned structural mechanism can be found elsewhere [35].

8.6.2 Implications of Intermolecular Structural Modifications

On the intermolecular level, the structural models envisaged pertain mainly to the motions and conformations of the chalcogenide layers. As noticed above, the release of interlayer buckling can give rise to both an increasing length of the illuminated part of the fiber and a higher structural anisotropy. In addition, the mechanism of interlayer ordering at higher temperatures [34] is also compatible with the reversal of the temperature dependence of the depolarization ratio. However, as the temperature is raised the low potential barriers associated with buckling may be overcome by both light-induced bond breaking and thermal motions. In any case, neither temperature nor light illumination is capable of producing the observed changes; instead, the simultaneous presence of the elongation stress is the key factor. The layer unfolding idea is supported by experimental results showing the stress dependence of the depolarization ratio of individual peaks in the 260–430 cm^{-1} spectral range [31]. It was found that the vibrational mode corresponding to the $S_2As–S–AsS_2$ "water-like" molecule is the most affected while PiF takes place.

The role of both intramolecular and intermolecular bonds was appreciated by Elliott [36] who formulated a unified model for photostructural changes. A basic assertion of that model is that light weakens and finally breaks not only the strong covalent intramolecular bonds but also the weak van der Waals intermolecular "bonds". This idea conforms to the buckling model [33] where the removal of buckling between adjacent layers releases accumulated strains, thus rendering the layers less ruffled. One may also recall here the recently proposed "slip and repulsion" model that aims to account for photostructural changes, such as the photo-induced volume expansion, in chalcogenide glasses [37]. In the context of this model, the volume expansion is the result of the electrostatic repulsion forces between adjacent layers

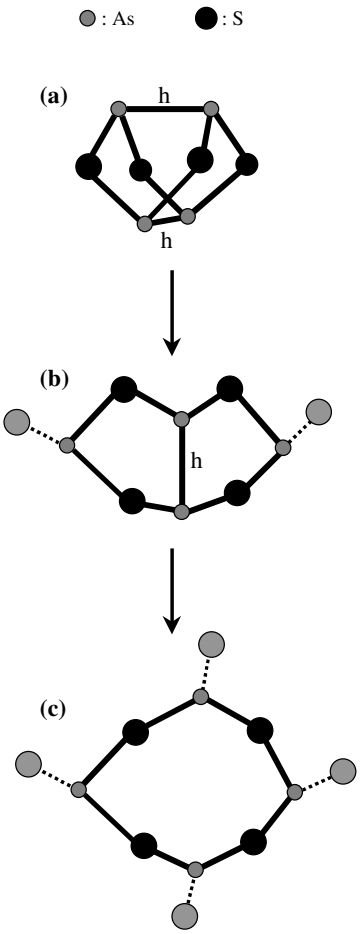

Figure 8.8: A possible route of a locally planar morphogenesis. The highly symmetrical As_4S_4 molecule unfolds giving rise to planar-like configurations. The homopolar As–As bonds are denoted by h. For details see text. The generated planarity of the final configurations can be the source of the observed structural anisotropy and of the increasing fiber length.

after excitation. These forces build up owing to the lower mobility of electrons compared to holes. After volume expansion the mutual slipping between adjacent layers is facilitated. The external elongation stress, in a PiF experiment, can therefore exploit this interlayer instability thus causing the lengthening of the fiber.

8.7 Summary and Outlook

In this brief review, we have tried to outline the characteristics and possible origins of photo-induced fluidity. This effect is one of the different aspects of photo-plastic effects in amorphous solids. In previous paradigms of photo-plastic effects chalcogenide films were attached onto substrates, where the presence of the latter was able to reveal the deformation brought about to the film due to light-illumination [38]. For PiF [13] an external stress is needed either to bend the flake or to elongate the fiber since in this case both the flake and the fiber are in free-standing (substrateless) geometry. In any case, photo-plastic effects seem to have a common origin, that is the athermal increase of $viscoelasticity$ under light illumination. It is a very important fact that light illumination can engender drastic viscoelastic changes of the chalcogenide glass which are comparable to those caused by conventionally heating the glass to a temperature near T_g. Indeed, micro-indentation experiments [12, 39] have shown that the photo-induced viscosity of As_2S_3 at ambient temperature is of the order of 10^{13} P which amounts to the viscosity at T_g (210 °C) of a bulk (dark) glass. In agreement with these data, the photo-induced viscosity obtained through stress–strain relations was estimated as $\sim 5 \times 10^{12}$ P from PiF experiments [13].

As previously noted, despite the fact that photo-plastic effects have been known since many years they still have not attracted a considerable degree of attention and hence many issues of these effects are so far at a speculative level. Raman studies that have been summarized in the preceding sections have unveiled particular aspects of PiF concerning both intramolecular and intermolecular vibrational modes. The data obtained in our work [20, 21, 29–31, 35] have been critically evaluated and specific intramolecular and intermolecular structural models have been supported or discarded. Particularly, the Raman results are compatible with self-trapped exciton models [19], layer unfolding processes [33], and the annihilation of As_4S_4 molecules [35], initially present in the fast quenched glass structure, through the breakage of homopolar As–As bonds.

The inherent viscoelastic nature of photo-plastic effects and the fact that these effects are macroscopic manifestations of atomic bonding changes necessitate the use of other experimental techniques that could furnish complimentary information. *Brillouin scattering* studies, which can provide information on changes of the elastic constants during photo-plastic effects, would be very beneficial. Indeed, Brillouin scattering provides a means to relate microscopic parameters (elastic constants) and macroscopic properties (viscoelasticity, bulk and shear moduli) as well as sound propagation and attenuation. The interlayer shear vibrational modes – and hence the transversal elastic constants – are expected to experience appreciable changes. Their study can be used as a benchmark for distinguishing the relative role of intramolecular and intermolecular models. Raman spectroscopic experiments on new glass compositions and at low temperatures can cast light on the universality of photo-plastic effects and aid the discrimination between short- and medium- range structural models. Further, more detailed studies of the photo-induced viscosity by conventional techniques are also expected to shed light into the microscopic nature of photo-plastic effects.

It is obvious that photo-plastic effects could meet several important applications related to micro-fabrication. The key issue is that a laser beam can be directed with surgical precision to induce the desired plastic deformation on a micro-volume. In contrast, conventional heat methods lack this advantage suffering also from heat conduction. It is, however, not yet defi-

nite whether chalcogenide glasses have the exclusive privilege to exhibit photo-plastic effects or if such effects also characterize other glasses, for example oxides as Fritzsche [19] has suggested. Future experiments will provide or not vindication to this important expectation. The transformation of photo-plastic effects into commercially viable applications will be decided from the improvement of our knowledge on the basic mechanisms underlying the effect. However, even if applications of photo-plastic effects still seem remote, these effects deserve further study since they are of fundamental interest in their own right.

Acknowledgments

Prof. G. N. Papatheodorou and Dr. Th. Kastrissios have contributed considerably to the work presented in this chapter; I would like to thank them for fruitful collaboration. Prof. H. Fritzsche and Prof. G. Fytas are also thanked for bringing the photo-induced fluidity effect to our attention.

References

[1] A.V. Kolobov and K. Tanaka, in Handbook of Advanced Electronic and Photonic Materials and Devices, Vol. 5 (Chalcogenide Glasses and Sol–Gel Materials), H.S. Nalwa (Ed.), Academic Press, San Diego, 2001, pp. 47–90.

[2] H. Fritzsche, in Insulating and Semiconducting Glasses, P. Boolchand (Ed.), World Scientific, Singapore, 2000, pp. 653–690.

[3] K. Shimakawa, A.V. Kolobov, and S.R. Elliott, Adv. Phys. **44**, 475 (1995).

[4] P. Krecmer, A.M. Moulin, R.J. Stephenson, T. Rayment, M.E. Welland, and S.R. Elliott, Science **277**, 1799 (1997).

[5] A. Saitoh, T. Gotoh, and Ke. Tanaka, J. Non-Cryst. Solids **299–302**, 983 (2002), and references therein.

[6] J. Li and D.A. Drabold, Phys. Rev. Lett. **85**, 2785 (2000), and references therein.

[7] T. Uchino, D.C. Clary, and S.R. Elliott, Phys. Rev. B **65**, 174204 (2002).

[8] H. Hisakuni and K. Tanaka, Appl. Phys. Lett. **65**, 2925 (1994).

[9] V.V. Poborchii, A.V. Kolobov, and K. Tanaka, Appl. Phys. Lett. **74**, 215 (1999).

[10] A. Saliminia, T.V. Galstian, and A. Villeneuve, Phys. Rev. Lett. **85**, 4112 (2000).

[11] Y.A. Osipyan and I.B. Savchenko, JETP Lett. **7**, 130 (1968).

[12] M.L. Trunov and A.G. Anchugin, Sov. Tech. Phys. Lett. **18**, (1992) 78, and references therein.

[13] H. Hisakuni and Ke. Tanaka, Science **270**, 974 (1995).

[14] J.P. Larmagnac, J. Grenet, and P. Michon, Phil. Mag. B **45**, 627 (1982).

[15] Ke. Tanaka, N. Kawakami, and A. Odajima, Jap. J. Appl. Phys. **20**, L784 (1981).

[16] A. Rousse, C. Rischel, S. Fourmaux, I. Uschmann, S. Sebban, G. Grillon, Ph. Balcou, E. Forster, J.P. Geindre, P. Audebert, J.C. Gauthier, and D. Hulin, Nature **410**, 65 (2001).

[17] C.W. Siders, A. Cavalleri, K. Sokolowski-Tinten, Cs. Toth, T. Guo, M. Kammler, M. Horn von Hoegen, K.R. Wilson, D. von der Linde, and C.P.J. Barty, Science **286**, 1340 (1999).

[18] L.-M. Martinez and C.A. Angell, Nature **410**, 663 (2001).

[19] H. Fritzsche, Solid State Commun. **99**, 153 (1996).

[20] D Th. Kastrissios, S.N. Yannopoulos, and G.N. Papatheodorou, Physica B **296**, 216 (2001).

[21] D. Th. Kastrissios, G.N. Papatheodorou, and S.N. Yannopoulos, Phys. Rev. B **64**, 214203 (2001).

[22] G. Lucovsky and R.M. Martin, J. Non-Cryst. Solids **8–10**, 185 (1972).

[23] P. Hari, P.C. Taylor, W.A. King, and W.C. LaCourse, J. Non-Cryst. Solids **227–230**, 789 (1998), and references therein.

[24] J. Jackle, in Amorphous Solids: Low-Temperature Properties, W.A. Phillips (Ed.), Springer, Berlin, 1981, p. 135.

[25] S.N. Yannopoulos and G.N. Papatheodorou, Phys. Rev. B **62**, 3728 (2000).

[26] S.N. Yannopoulos, J. Chem. Phys. **113**, 5868 (2000).

[27] D. Th. Kastrissios and S.N. Yannopoulos, Phys. Rev. E **65**, 021510 (2002).

[28] S.R. Elliott, Europhys. Lett. **19**, 201 (1992).

[29] S.N. Yannopoulos, Phys. Lett. A **296**, 295 (2002).

[30] D. Th. Kastrissios and S.N. Yannopoulos, J. Non-Cryst. Solids **299–302**, 935 (2002).

[31] D. Th. Kastrissios, G.N. Papatheodorou, and S.N. Yannopoulos, Phys. Rev. B **65**, 165211 (2002).

[32] As_4S_4 molecular species exist even in the stoichiometric composition if the glass has been produced by fast quenching of the high temperature melt; see for example Z.U. Borisova, Glassy Semiconductors, Plenum Press, New York, 1981.

[33] J. Ihm, J. Phys. C **18**, 4741 (1985).

[34] L.E. Busse, Phys. Rev. B **29**, 3639 (1984).

[35] S.N. Yannopoulos, submitted for publication.

[36] S.R. Elliott, J. Non-Cryst. Solids **81**, 71 (1986).

[37] K. Shimakawa, N. Yoshida, A. Ganjoo, Y. Kuzukawa, and J. Singh, Philos. Mag. Lett. **77**, 153 (1998).

[38] H. Koseki and A. Odajima, Jpn. J. Appl. Phys. **21**, 424 (1982).

[39] M.L. Trunov, J. Non-Cryst. Solids, **192–193**, 431 (1995).

9 Photo-Induced Non-Linearity and Transmittance Oscillation in $GeSe_2$ and As_2S_3

Janos Hajto and Istvan Jánossy

9.1 Introduction

In recent years considerable interest has developed in connection with non-linear optical properties of condensed matter. Of special interest are the non-linear optical phenomena that occur at relatively low levels of light intensity, as these effects may find special applications in integrated optics. Perhaps the most interesting effect is the intrinsic optical bistability in *crystalline semiconductors,* which was observed by several groups [1–3].

It has also been reported that strongly non-linear optical phenomena can also occur in *amorphous semiconductors.* Oscillation of the transmitted light and optical bistability have been observed under the influence of a c.w. He–Ne laser beam both in amorphous $GeSe_2$ films [4–6] and in bulk samples of As_2S_3 [7]. These optical non-linear phenomena have several features significantly different from those observed in crystalline semiconductors. First, they occur at a c.w. incident laser intensity range from 3 to 45 W/cm^2 (self-supporting films) and from 1.4 to 2.7 kW/cm^2 (films adhered to glass or quartz substrate). It is important to note that these intensities are much lower than is needed to produce intrinsic optical bistability in *crystalline semiconductors* ($\sim$MW/cm). Second, in *amorphous semiconductors*, optical bistability and hysteresis were found without placing the samples in an optical resonator. Third, low-intensity (1–30 W/cm^2) linearly polarized laser beam can produce optical optical anisotropy and re-orientation of optical anisotropy in *amorphous* semiconductors [8, 9]. This phenomenon is not observed in *crystalline semiconductors*. Finally, a variety of light-induced structural changes (the term "photostructural changes" is also used) have been observed in amorphous semiconductor (amorphous chalcogenide) films but not in crystalline films [10–12]. The best known of these effects are photodarkening [13] and photobleaching [14, 15] which have been extensively studied.

It is also important to emphasize that these non-linear optical effects are unique to the amorphous structure. If the amorphous films or bulk samples are crystallized (e.g. by heat treatment or by an intense laser beam) the observed non-linearity disappear. Therefore, in this paper, we confine our attention to the interaction between the light (laser) and that of the amorphous material.

The aim of this chapter is to treat laser-amorphous material interactions quantitatively and show how these effects can produce optical non-linearity such as optical anisotropy, optical bistability and transmittance oscillations.

The chapter is organized as follows: the experimental method is described in Section 9.2, the laser-induced anisotropy is described in Section 9.3, the laser-induced optical bistability and oscillatory phenomena are described in Section 9.4, and the final section contains some conclusions.

9.2 Experimental Technique

Amorphous a-$GeSe_2$ and As_2S_3 films are usually prepared by vacuum evaporation at a pressure of 2×10^{-6} Torr onto glass substrates using polycrystalline $GeSe_2$ and amorphous As_2S_3 ingots as an evaporation source. For the optical experiments, the films are usually removed from the glass or quartz substrates in order to reduce the effects of multiple light reflections and of mechanical stress occurring at the amorphous film–glass interface.

The samples are placed in a sample holder, as shown in Fig. 9.1. With this arrangement, it is possible to carry out optical measurements and regulate the temperature of the film. Note that the temperature of the film T_F can be different from the temperature of the illuminated spot T_S. This difference is due to absorption of the laser light within the film. A linearly polarized He–Ne laser beam provides illumination. The Gaussian spot size can be varied between 20 μm and 200 μm.

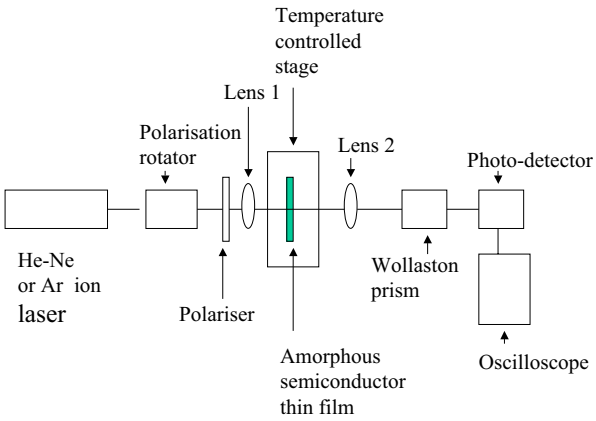

Figure 9.1: Experimental arrangement for the measurements of light-induced optical anisotropy, optical bistability and oscillation

The intensity of the incident, reflected and transmitted light can be measured using Si photodetectors. Also, carrying out measurements with the Wollaston prism and the $\lambda/4$ plate at a different directions of polarization of the incident measuring light beam, the various characteristics of the optical anisotropy of the films can be measured. This way, rotatory power, birefringence, dichroism and the direction of the principal axes of the index ellipsoid can be determined. The optical anisotropy can be measured with the same laser as used for inducing the effect but attenuated by a filter.

It is important to emphasize that intensity of the incident laser light determines which particular type of optical non-linear effects can be observed. Laser-induced optical anisotropy

such as birefringence and dichroism is observed in the low-intensity range ($\sim$1–30 W/cm^2). Laser-induced optical bistability and transmission and reflection oscillations are observed in the intensity range from 30 to 2700 W/cm^2.

9.3 Laser-Induced Optical Anisotropy

9.3.1 Experimental Results on Laser-Induced Birefringence and Dichroism

In the as-deposited films no sign of optical anisotropy was observed. However, as a result of laser irradiation, both birefringence and dichroism were found. The direction of the principal axis of the index ellipsoid coincided with the direction of the incident beam polarization; consequently no optical activity was induced. Typical curves showing the development of the laser-induced dichroism and the simultaneous decrease of the absorption coefficient (photo-bleaching [14, 15]) as a function of time at a given incident laser intensity are presented in Fig. 9.2. The dichroism is defined as $\Delta\alpha = \alpha_x - \alpha_y$ where α_x is the absorption coefficient in the x-direction (direction of the incident laser beam polarization) and α_y is the absorption coefficient in the y direction (perpendicular to x). All of these measurements were obtained at a laser wavelength of $\lambda = 0.6328$ μm. The dichroism is positive if the absorption coefficient is higher in the direction of the incident laser beam polarization. As shown in Fig. 9.2, the dichroism is positive for the first period of illumination. This observation is in accordance with observation of Zhdanov et al. [16] who also found a positive laser-induced dichroism in As–Se films. However, after prolonged illumination, the dichroism changes its sign and becomes negative. This type of time dependence strongly suggest that at least two distinct processes affecting the absorption should be involved during illumination.

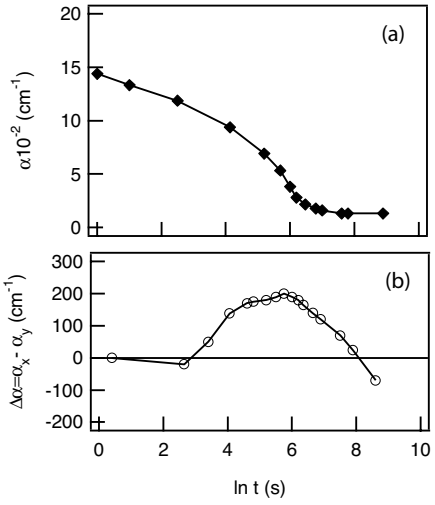

Figure 9.2: Time dependence of the absorption coefficient (a) and laser-induced dichroism (b) and in a-$GeSe_2$ film at incident laser intensity of 30 W/cm^2. Thickness of the film = 6 μm.

As shown in Fig. 9.2, during photobleaching α_x (measured at λ = 0.6328 μm) decreases by one order of magnitude. Note that the final equilibrium value of the absorption coefficient is comparable to the laser-induced optical anisotropy, indicating a very high dichroism.

Figure 9.3 shows the time dependence of the laser-induced birefringence and the absorption with the same experimental conditions as in Fig. 9.2. The birefringence Δn is defined as $n_x - n_y$ (the difference in the refractive indices measured in the direction of laser polarization x and perpendicular to it). The birefringence varies linearly with the logarithm of the time of illumination through several orders of magnitude. No change of sign could be observed, in contrast to the case of dichroism. The logarithmic dependence of the birefringence makes it difficult to determine the saturation value. The highest value of the laser-induced birefringence in the self-supporting $GeSe_2$ films observed is $\Delta n = 6 \times 10^{-3}$ [8].

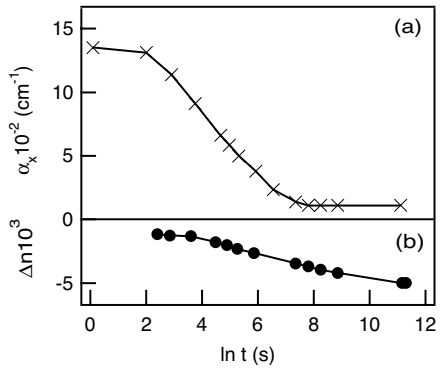

Figure 9.3: Time dependence of the absorption coefficient (a) and laser-induced birefringence (b) with the same experimental condition as in Fig. 9.2.

It is important to note that the laser-induced anisotropic structure in the amorphous network is stable at room temperature (memory state). No sign of relaxation to the isotropic state can be observed after keeping the samples in the dark for days.

A remarkable feature of the laser-induced anisotropy is that its principal axis can be reoriented to any direction by changing the direction of the incident beam polarization. Figure 9.4 shows an example of reorientation. The sample is first irradiated for a long time to reach a saturation value of $\Delta n = -6 \times 10^{-3}$ and then the incident beam polarization is rotated 90°. As a result of the irradiation, the anisotropy first decreases to zero and then starts to increase toward a reoriented (+) saturation value with a magnitude similar that was observed before.

The kinetics of the reorientation can also be measured by reorienting the structure first in a given direction of polarization (say the y direction) and then rotating the incident beam by 90° (to the x direction). It is possible to measure how direction of the principle axes of the index ellipsoid and the absolute values of the anisotropy of the principal refractive indices vary during the reorientation.

The two orthogonal principal axes ξ and η (see Fig. 9.5) are described as

$$E_\xi^{out} = E_\xi^{in} \exp[i(2\pi/\lambda)n_1 d] \tag{9.1}$$

$$E_\eta^{out} = E_\eta^{in} \exp[i(2\pi/\lambda)n_2 d] \tag{9.2}$$

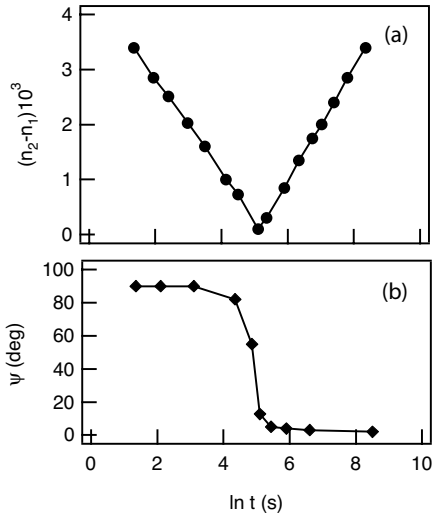

Figure 9.4: Variation of the difference in the principal refractive indices (a) and the 'fast axis' (b) and during the reorientation.

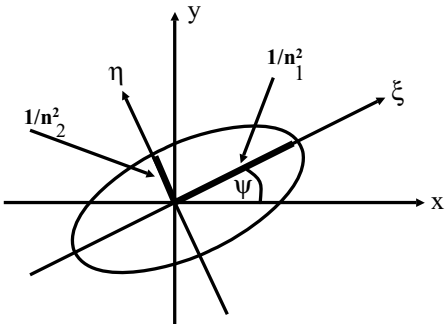

Figure 9.5: The index ellipsoid.

where E^{in} and E^{out} are the electric field vectors of the incoming and outgoing light beams, d is the thickness of the sample, and n_1 and n_2 are the principal refractive indices. ξ is the direction to which the smaller principal index belongs (the 'fast axis') [17]. The birefringence of the sample can be completely described by giving the angle ψ between ξ and x, and the value of $n_2 - n_1$. Note that by definition n_2- $n_1$is always positive. The results can be seen in Fig. 9.4. As can be seen, at first ψ remains almost constant during the illumination, while $n_2 - n_1$ decreases. At a given time $n_2 - n_1$ becomes zero i.e. the sample becomes *isotropic.* On continuing the irradiation, the sample becomes anisotropic again (n_2 - $n_1 > 0$) but now ψ is changed by 90°.

This type of reorientation, which passes through an isotropic state, is unique to the amorphous structure. For example, in the laser-induced reorientation of liquid crystals, $n_2 - n_1$

remains almost constant while ψ changes continuously [18]. The difference arises from the fact that in the case of liquid crystals the reorientation consists of the collective rotation of molecules while in the case of $GeSe_2$ the reorientation takes place through independent atomic events. However, in our case, the x and y axes remain the principal axes during the reorientation process. Therefore, it is sufficient to use the quantity $\Delta n = n_x - n_y$ for describing the kinetics [8]. Δn can be positive or negative, depending on the orientation of the 'fast axis'. The time dependence of the reorientation in a well defined time interval shows a logarithmic behavior; see Fig. 9.6 which can be described by the following equation:

$$\Delta n = n_x - n_y = -A \ln t/t_0 \tag{9.3}$$

The logarithmic type of reorientation kinetics was observed in all cases and the slope was independent of the incident laser intensity. This means that the constant A is determined only by the structure of the amorphous network in $GeSe_2$. However, the time at which the sample becomes isotropic (t_0) depends primarily on the incident laser intensity. This dependence can be described as:

$$t_0 \sim P^{-s} \tag{9.4}$$

where P is the incident laser power density (W/cm^2) and s is between 2 and 3.

9.3.2 Theoretical Results on Laser-Induced Optical Anisotropy

The experimental results show that optical anisotropy can be induced by polarized laser irradiation. The structure of $GeSe_2$ remains amorphous during illumination, no sign of microcrystallites was observed by simultaneous electron diffraction measurements [19]. This fact indicates that the phenomenon of laser-induced optical anisotropy is principally connected to the peculiar structure of the amorphous $GeSe_2$.

The anisotropic structure can be reoriented by changing the polarization direction of the illuminating laser beam or erased by circularly polarized light. The study of reorientation processes is an excellent method for studying the intensity dependence of the kinetics of photostructural phenomena. Reorientation may be repeated several times and there is no need to anneal the samples between successive runs.

The whole process would not necessarily be a one-photon reaction. Grigorovici and Vancu [20] have shown the possibility of a two-photon reaction for the light-induced polymerization (photodarkening) in amorphous As–Se films. Equation (9.4) also suggest that reactions involving at least two photons are involved in the displacement of an atom.

Orientational Dependence of Optical Excitation at Atomic Scale

It is important to note that in the $GeSe_2$, the optical excitation and the associated atomic rearrangement is related to the excitation of chalcogenide atom (Se). This is because the four outermost electrons in the Ge atoms form σ bonds which are more stable than some of the p electrons in the chalcogenide atoms. On the other hand, the chalcogenide atoms have six outer electrons, two of which are in the s state and do not contribute significantly to chemical bonding. Two p electrons form σ bonds with the first neighbors in the amorphous

network (Ge,). The remaining two electrons occupy the third p orbital forming a 'lone pair' [21]. The lone pair electrons are situated at the top of the valence band while the conduction band corresponds to antibonding states. Therefore, the optical edge transition is caused by transitions of lone pair electrons to antibonding states. Figure 9.6 shows the lone pair electron orbital involved in the light excitation process. The probability P_1 of exciting one of the lone pair electron to the C–A_1 antibonding state is proportional to $\cos^2\theta_1$; similarly the probability P_2 of exciting one of the lone pair electron to the C–A_2 antibonding state is proportional to $\cos^2\theta_2$ where θ_1 and θ_2 are the angles between the light polarization direction and the corresponding radius vectors. The total probability of exciting a chalcogenide atom is the sum P_1 and P_2:

$$P = P_1 + P_2 \sim \cos^2\theta_1 + \cos^2\theta_2 = \sin^2\theta \tag{9.5}$$

where θ is the angle between **p** (polarization direction of the light) and **n** (the normal of the plane given by the three atoms A_1–C–A_2). In the case of $GeSe_2$, C refers to the chalcogen atom (Se) and A_1 and A_2 refer to Ge atoms. Therefore, the plane of A_1–C–A_2 gives the bonding plane. The above considerations show that if the light polarization direction is parallel to **n**, the chalcogenide atom is less susceptible to optical excitation compared with the case when **p** is parallel to the bonding plane.

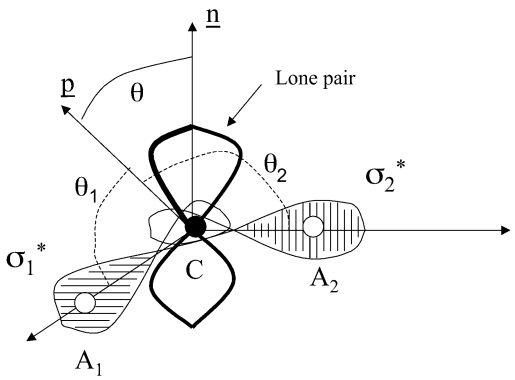

Figure 9.6: Lone pair electron orbitals.

Photostructural Change and Optical Anisotropy at Medium Range Order

The elementary excitation process described above is the first step in initiating photostructural changes in the amorphous network. Kolobov et al. [22] and Guha [23] presented comprehensive descriptions of atomic models of photostructural changes. According to these models the photo-induced process consists of two steps. In the first stage, an electron–hole pair is created by light and certain bonds are weakened. This leads to the displacement of the atoms. As a second step, recombination of the electron–hole pair takes place in a different atomic configuration as compared with its excitation. Consequently, at certain atomic sites, the final equilibrium state might be different from the initial one. The simplest atomic model of photostructural changes was suggested by Tanaka [24]. According to this model, all of the chemical

bonds are unchanged but a chalcogen atom is displaced from its original position to a new one as shown in Fig. 9.7. A more detailed model was described by Elliott [25] who considered the relatively strong interaction between the chalcogen atom and its nearest non-bonding neighbor ("back bonding").

Our observations i.e. the fact that polarized light induces optical anisotropy shows that, in chalcogenides, the role of light is not merely to generate free carriers. Free carriers (once generated by the atomic excitation step described above) move independently of the excitation light which precludes anisotropy. Janossy et al. [26] showed that by the extension of the models of photostructural changes, the phenomena of laser-induced optical anisotropy and laser-induced photostructural changes can be treated by a unified theory.

The comparison of the elementary excitation step (Fig. 9.6) and the subsequent photostructural change (Fig. 9.7) shows that the normal vectors of the bonding planes in the ground state A_1–C'–A_2 ($\mathbf{n}$) and the metastable state A_1–C''–A_2 ($\mathbf{n}'$) are not parallel to each other. When the polarization of the illuminating laser beam is parallel to the normal of the bonding plane of the ground state ($\boldsymbol{p} \parallel \boldsymbol{n}$), the population in the metastable center will be low. However, when $\boldsymbol{p} \parallel \boldsymbol{n'}$, the population in the metastable state will be much higher than at the previous one. This leads to the fact that the population in the metastable state is the function of the relative direction of the metastable state to the polarization of the laser beam. In order to observe optical anisotropy, it is necessary that the bistable centers should have an anisotropic structure. This can be achieved by illuminating the sample in a given polarization direction which "selects and promotes" the creation of metastable state configurations resulting in optical anisotropy on a macroscopic scale. Therefore, if the direction of the incident laser beam polarization changes, the optical anisotropy can be reoriented. This is in good accordance with the experiments [8].

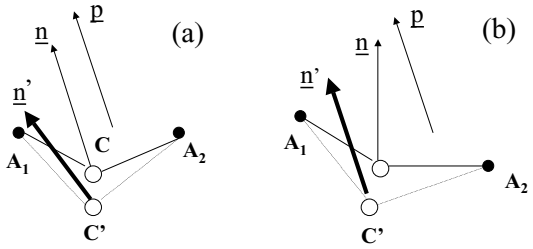

Figure 9.7: Model of photostructural change.

The description of the laser-induced optical anisotropy in terms of bistable centers suggests that it is not necessary to "break" chemical bonds in the amorphous structure. An alternative model proposed by Hajto and Janossy [27] is based on the extension of this model to include chemical bond breaking and subsequent bond rearrangement.

It was shown by Phillips et al. [28] that the molecular structure of chalcogenide glasses is anisotropic on a scale of medium range (30–1000 atoms). There is evidence from x-ray and Raman data [29] that amorphous $GeSe_2$ is built up of medium range anisotropic units, the so-called "outrigger rafts", polymerized along one direction. Without any applied external field, the directions of the polymerized rafts are distributed randomly on the macroscopic scale;

thus the material is optically isotropic. However, irradiation by plane polarized light induces optical anisotropy on a macroscopic scale.

Our suggested model for laser-induced anisotropy is based on the theoretical assumption that light can create electron–hole pairs by bond excitation and during the electron–hole recombination an atomic displacement may occur in the amorphous structure [30]. As a consequence, new atomic configurations might be established. In order to explain the optical anisotropy, it is assumed that the "outrigger rafts" in $GeSe_2$ can continuously rearrange under the influence of the plane polarized laser light. It is further assumed that the cross-section for producing an electron–hole pair depends strongly on the angle between the incident beam polarization and the excited bond. Thus the stability of a given raft depends on its orientation with respect to the direction of incident beam orientation. As a result of the laser irradiation, we obtain an amorphous structure in which there are more polymerized rafts oriented into the more stable direction (directed by the direction of the laser field). This could be the origin of the laser-induced optical anisotropy.

Quantitative Model for the Light-Induced Optical Anisotropy

A quantitative theory for light-induced optical anisotropy was developed by Hajto et al. [8]. In this model it is assumed that in the amorphous network there are N sites per unit volume where atoms can be displaced as a result of laser irradiation. It is also assumed that in the environment of these sites there are two equilibrium atomic configurations. These configurations can be described by a double well potential whose two minima correspond to two equilibrium positions of atoms. Such a double well potential model was originally presented for the linear temperature dependence of the specific heat in an amorphous structure by Anderson [31] and applied by Tanaka [24] and Kolobov et al. [22] to the photostructural changes in chalcogenide glasses. For simplicity, only symmetric potential wells are considered.

The two equilibrium configurations correspond to two different contributions to the anisotropy of the refractive indices. The observed anisotropy according to this model is due to the fact that the atoms are unequally distributed in the two minima. The birefringence Δn is proportional to $N_1 - N_2$ where N_1 and N_2 denote the number of atoms per unit volume in the first and the second minimum respectively ($N_1 - N_2 = \Delta N$). The laser beam can transfer atoms from one minimum to the other one by creating metastable states as described in the previous section. The probability per unit time of the excitation can be written in the form $\gamma_1 f(P)$ and $\gamma_2 f(P)$ for the first and second minimum respectively. P is the laser power density and γ_1 and γ_2 chosen such that $\gamma_1 + \gamma_2 = 1$. The difference $\gamma_2 - \gamma_1$ reflects the fact that the polarized light excites the two different configurations with different probabilities. The probability of per unit time of a transition between the two minima is related to the to the energy barrier height V via $[1/\tau_0]\,\mathrm{e}^{-V/kT}$. [32].

If the barrier height V and other parameters involved were the same for all sites, the time development of $\Delta N = N_1 - N_2$ would be governed by the simple relaxation equation

$$\tau d/dt + \Delta N(t) = \Delta N_{eq} \tag{9.6}$$

with $\Delta N_{eq} = (\gamma_2 - \gamma_1)N$ and $t = [\tau_0/f(P)]\,\mathrm{e}^{V/kT}$ the solution of which is

$$\Delta N(t) = \Delta N(0) + \big[\Delta N_{eq} - \Delta N(0)\big](1 - \mathrm{e}^{t/\tau}) \tag{9.7}$$

However, as the effect takes place in an amorphous system it is reasonable to assume that V has a probability distribution [31]. Hence Equation (9.7) should be replaced by

$$\Delta N(t) = \int \left\{ \Delta c_0(V) + \left[\Delta c_{eq}(V) - \Delta c_0(V) \right] (1 - \mathrm{e}^{-t/\tau}) \right\} dV \tag{9.8}$$

with $\Delta c_{eq} = c(V)(\gamma_2 - \gamma_1)$.

Here $c(V)d(V)$ gives the number of sites per unit volume with barrier height between V and $V + dV$; the value of $\Delta c_0(V)dV$ is the difference between the number of atoms I the first and second minima at these states at time $t = 0$.

As the sites are not too different from each other, it can be assumed that $c(V)$ has a rather sharp maximum at some V_0 and its value is only significant between the energies V_1 and V_2. The simplest form that describes this behavior is

$$c(V) = \begin{cases} N/V_2 - V_1 & \text{if } V_2 < V < V_1 \\ 0 & \text{otherwise} \end{cases} \tag{9.9}$$

In an as-deposited amorphous film $c_0 = 0$. In this case, differentiating Equation (9.8) with respect to t and performing the integral over V using the form of $c(V)$ given above, the following form can be deduced:

$$d\Delta N/dt = \Delta N_{eq}[kT/(V_2 - V_1)](\mathrm{e}^{-t/\tau_2} - \mathrm{e}^{-t/\tau_1})/t \tag{9.10}$$

with $\tau_1 = \tau(V_1)$ and $\tau_2 = \tau(V_2)$.

The observed logarithmic time dependence of the birefringence can be explained by assuming that $V_2 - V_1 \gg kT$. In this case a long time interval exists where the inequalities

$$\tau_1 \leq t \leq \tau_2 \tag{9.11}$$

are satisfied. In this time interval $\mathrm{e}^{t/\tau_1} = 0$, $\mathrm{e}^{t/\tau_2} = 1$, and the solution of Eq. (9.10) is

$$\Delta N(t) = \Delta N_{eq}[kT/(V_2 - V_1)] \ln t + C \tag{9.12}$$

The birefringence for this time interval can be described by the following relationship:

$$\Delta n(t) = A \ln t/t_0 \tag{9.13}$$

with

$$A = -g\Delta N_{eq} kT/(V_2 - V_1) \quad \text{and} \quad \ln t_0 = gC/A \tag{9.14}$$

where g is the factor connecting ΔN and Δn.

The reorientation process can be treated similarly. In this case the initial condition can be written as $\Delta c_0 = \Delta c_{eq}$ (provided that saturation has been reached by the irradiation with the y-polarized light beam). By consideration similar to the above the following relationship can be obtained:

$$\Delta N(t) = 2\Delta N_{eq}[kT/(V_2 - V_1)] \ln t + C \text{ for } \tau_1 \leq t \leq \tau_2 \tag{9.15}$$

$n(t)$ has the same form as given by Eq. (9.13) but A is now given by

$$A = -2g\Delta N_{eq}[kT/(V_2 - V_1)] \tag{9.16}$$

This model also allows one to treat the influence of an unpolarized or circularly polarized light beam on an area where previously anisotropy has been induced. For an unpolarized light beam $\gamma_1 = \gamma_2$. As can be seen from Eq. (9.6), in this particular case ΔN decreases in time and its equilibrium value is 0. In other words, the unpolarized light beam erases the optical anisotropy.

9.3.3 Comparison of the Model with the Experiments

The model described in the previous section gives the following results:

- The saturation value of the induced birefringence should be independent of the intensity of the polarized light beam. It is difficult to measure the precise saturation value in the measurements. Nevertheless, it is generally found that the increase of the birefringence (measured on a logarithmic scale) slowed down at $\Delta n \sim 5 \times 10^{-3}$. This slowing down was observed at slightly different values of Δn but no definite correlation was found between these values and the polarized light intensity. The uncertainty of the Δn values at the slowing down can be explained by the assumption that the number of metastable sites per unit volume, N, varies within the sample.

- The model provides explanation for the observed logarithmic time dependence (see Eqs. (9.12) and (9.13)). The condition for this type of time dependence can be written as $\tau_1 \leq t \leq \tau_2$. The values of τ_1 and τ_2 can also be estimated from the experiments by notifying the deviations from the logarithmic time dependence. This allows the estimate the value of $V_2 - V_1$, i.e. the spread of the barrier height in the excited state. For this estimation see below.

- According to Eqs. (9.14) and (9.16), the slope A of $\Delta n(t)$ plotted on a logarithmic time scale should be independent of the light intensity. This is in good accordance with the experiments.

- Comparison of Eqs. (9.14) and (9.16) shows that the slope A should be twice as large for the re-orientation process as for the orientation process in the as deposited films. This prediction is also in good accordance with the experiments.

- The constant C, or equivalently t_0 in Eq. (9.13) depends on the form of the function $f(P)$. Assuming that $f(P) \sim P^s$ (s photon reaction) the model predicts $t \sim P^{-s}$. This relationship was verified by the experiments, the actual value of s was found to be 2.6.

- It is evident that anisotropy cannot be induced using unpolarized light. The model predicts, in addition, that circularly polarized light should erase the previously induced anisotropy. This is also in good accordance with experiments.

9.3.4 Application of the Optical Anisotropy Effect

The observed optical anisotropy effect can be used to fabricate a novel type of memory device using the laser-illuminated spot as a digital or analogue optical memory element. Assuming an illuminated spot with a diameter of 0.8 μm and a periodicity of 1μm, a digital memory density of $\sim$25 000 MB can be achieved in an active area of 66 cm^2 which is much larger than can be achieved on CD disc memory of the same area (750 MB). Also, using the laser reorientation effect, an extra analogue memory function can be utilized at each illuminated spot. Using 2° as the minimum distinguishable step, 180 analogue steps can be utilized at each spot. The optical memory can also be rather fast. Extrapolation of Eq. (9.3) predicts that the time for reorientation can be less than 1 ns at an applied laser intensity of 1 MW/cm^2. This corresponds to a laser power of 250 mW focused into an illuminated spot of diameter of 1 μm, i.e. not a challenging task from technical point of view.

9.4 Optical Bistability and Light-Induced Transmittance Oscillations in Amorphous Semiconductor Films

The first observations of transmittance oscillation were made on vacuum evaporated amorphous $GeSe_2$ films deposited on glass substrates It was found that under the influence of a continuous focused He–Ne laser beam, the transmittance and the reflectance show periodic oscillations in time above a threshold of $\sim$1.6 kW/cm^2 [4, 5]. The optical behavior of self-supporting amorphous $GeSe_2$ films was also studied [6]. In this case the oscillation of transmittance and reflectance occurs at much lower laser intensity levels ($\sim$40 W/cm^2). Bistability and hysteresis were also found without placing the sample in an optical resonator. Different mechanisms have been suggested to explain this peculiar optical behavior. Fazekas proposed that the observed optical anomalies are due to a collective phenomenon of charged and neutral effects present in vacuum evaporated amorphous $GeSe_2$ films [33]. Phillips et al. suggested that the oscillatory behavior may be associated with laser-induced reversible microcrystallization which was observed in amorphous $GeSe_2$ using Raman spectroscopy [28]. We also proposed that a thermal "runaway" model can explain the main features of optical bistability and hysteresis and the fact that the critical laser intensity for inducing these effects depends on the laser power diameter [6]. This model also gives a natural explanation of the differences in the behavior of self-supporting samples and those on substrates. In the latter case the heat is conducted away much more efficiently from the illuminated spot and consequently in this case a much higher laser intensity is necessary to produce the same thermal effect. The thermal "runaway" model explains the optical bistability in terms of a mixture of "absorptive" and "disperse" types of bistability [34]. On the other hand, it does not explain the oscillatory behavior. The oscillations of transmittance and reflectance at a constant incident laser intensity can be explained by taking into account the combined effect laser heating and photostructural changes [35]. Photostructural changes are usually much slower than the thermal effects. Thus the thermal "runaway" model [6] is relevant for experiments in which the intensity is scanned fast enough to prevent significant photostructural changes.

9.4.1 Experimental Results

Optical Bistability

In this section some experimental results are presented to demonstrate the strongly non-linear nature of the optical effects at moderately high laser light intensities (3–40 W/cm^2). The experimental arrangement is the same as shown in Fig. 9.1 (Section 9.2). In this experiment only the transmittance of the c.w. He–Ne laser is measured as a function of the incident laser intensity (i.e. no optical anisotropy is measured). Figure 9.8 shows the recorded values of transmitted light intensity as a function of the incident laser light intensity at a laser spot diameter of 207 μm (equal to an area of 3.34×10^{-4} cm^2) in an amorphous $GeSe_2$ film having a thickness of 6 μm. The film temperature T_F is 298 K.

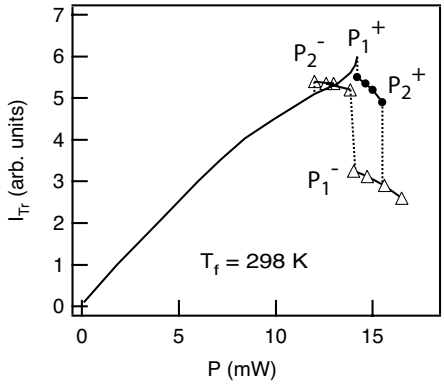

Figure 9.8: Transmitted light intensity as a function of incident laser intensity in a-$GeSe_2$ film.

The first discontinuity is observed at 14.2 mW (P_1^+) incident laser power (equivalent to incident laser intensity of 14.2 mW/3.34×10^{-4} cm^2 = 41.8 W/cm^2, characterized by a sharp increase and subsequent discontinuous decrease in the transmitted light. On increasing further the incident laser power, a switch to the dark state is observed i.e. a significant decrease in the transmitted signal at 15.5 mW (P_2^+).

Starting from the dark state and decreasing the laser power, the transmitted light shows a hysteresis, e.g. the transition to the bright state (higher transmittance values) occurs at 14.1 mW (P_1^-) which is lower than P_1^+. As a consequence, the transmittance has two different stable values at a fixed laser power, i.e. *optical bistability* is observed. On further decreasing the laser power, a second discontinuity is observed at 12 mW (P_2^-) where the hysteresis disappears.

The shape of the optical bistability curve varies somewhat with experimental conditions such as the temperature of the films, spot diameter and the rate of increase of the intensity. Increasing the film temperature T_F by using a sample heater around the sample, the critical laser power for producing the optical bistability decreases [6]. Similarly, the amplitudes of the optical discontinuities decrease with increasing T_F. A decrease of the area of the hysteresis with increasing T_F is also observed. The optical discontinuities and the optical bistability disappear when the film temperature is increased above 500 K.

The critical laser power P_1^- (at which the first switching from the dark to the bright state occurs) was also measured as a function of the incident laser beam diameter. This discontinuity was chosen because it seemed to be the most reproducible one, i.e. it does not depend strongly on the rate of the decrease of the intensity. The critical laser intensity (P_1^- divided by the area of the laser spot) as a function of the laser spot diameter is shown in Fig. 9.11.

Assuming a pure electronic excitation effect for producing optical bistability [34], one would expect the switch to the dark state to occurs at a constant electric field produced by the laser, i.e. at a constant laser intensity independent of the laser beam diameter. Figure 9.11 shows that this is not the case for the amorphous $GeSe_2$ films. The laser intensity increases with decreasing laser beam diameter. This experimental observation indicates the importance of thermal effects. The increase in the laser irradiated spot temperature T_S at a given laser intensity is less when the laser beam diameter is decreased because of the greater heat conduction. Consequently, the laser intensity must be higher to produce a given spot temperature.

Photostructural Changes

As mentioned in the previous section, the shape of the transmittance curves depends on the rate of increase of the intensity. It is established that this dependence can be associated with another effect, namely that the transmittance changes even under the influence of a *constant* laser power. The details of this effect are shown in Fig. 9.9. In this experiment the transmitted light intensity is recorded as a function of time at a fixed laser power (11 mW, laser spot diameter 207 μm) which was smaller than the critical laser power (14.2 mW) at which optical switching occurs into the dark state (see Fig. 9.8). In the first period of illumination a continuous decrease in the transmittance is observed. This decrease cannot be attributed simply to the increase in spot temperature because it possesses a 'memory' behavior. Switching off the light (points 2 and 4 in Fig. 9.9) and keeping the sample in dark for a while do not restore the initial transmittance value. On switching the light on again (points 3 and 5 in Fig. 9.9), the transmittance continues from the same value as before. This is a memory state associated with photostructural changes.

When the transmittance decreases to a critical value (point 6 in Fig. 9.9), a discontinuous switching to the dark state occurs,. Switching off the light at the dark state (point 7 in Fig. 9.9) causes the 'memory' to be erased; the initial transmittance is restored (point 8 in Fig. 9.9) and the whole cycle recommences. This fact indicates that in the dark state a different type of photostructural change takes place which erases the structure of the amorphous network developed in the bright period (above the dashed line in Figure 9.9).

Laser-Induced Oscillation of Transmittance and Reflectance

It is found experimentally that, for an appropriate laser intensity, the dark state is unstable and switches back spontaneously to the bright state. In this case, periodic oscillations of the optical properties occur as seen in Fig. 9.10. The oscillation of the transmitted and reflected light intensity in a 6 μm thick self-supporting $GeSe_2$ film is observed at a constant laser power ($P = 14.5$ mW) and at a fixed laser beam diameter of 207 μm. It is important to note that, for a particular sample thickness, oscillation occurs only in a narrow incident laser intensity range which corresponds to the observed hysteresis (see Fig. 9.8) [6].

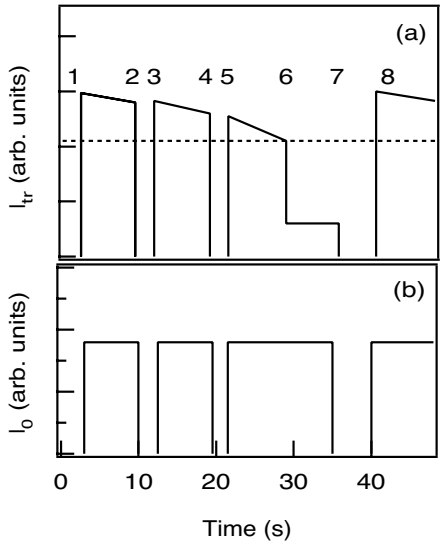

Figure 9.9: Time dependence of the transmitted light intensity at a fixed laser power (a) in relationship with the excitation light intensity (b).

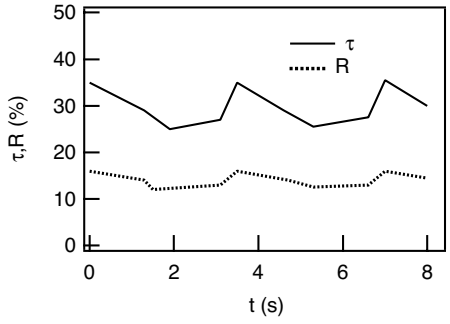

Figure 9.10: Oscillation of the transmitted and reflected light intensity at a fixed laser power.

9.4.2 Theoretical Considerations

The theories for optical bistability and the oscillation effect are based on the combination of thermal and photostructural effects.

Thermal Effects

The treatment of thermal effects is based upon the strong temperature dependence of the absorption coefficient α (at a fixed wavelength) which is observed in most amorphous semicon-

ductors above room temperature [30]. This dependence is described by the Urbach rule:

$$\alpha(T) = \alpha_0 \exp[-(E_g - h\nu)/kT] \tag{9.17}$$

The refractive index n (at a fixed wavelength) is also dependent on the temperature, but the dependence is less pronounced:

$$n(T) = n_0 - \beta T \tag{9.18}$$

where β is the linear temperature coefficient.

The main problem (discussed in [6]) is to describe the temperature rise in the illuminated spot due to the dissipation of the laser beam. This can be calculated by assuming that the heat loss is due to the difference in temperature between the illuminated spot and that of the film (the spot temperature T_s and the film temperature T_F). Thus the spot temperature can be given by the equation

$$\tau_0 \partial T/\partial t = \eta J D(T_s) - (T_s - T_F) \tag{9.19}$$

where η and τ_0 are constants determined by the thermal constants of the material and geometry, J is the incident laser intensity, D is the dissipation coefficient (= dissipation/incident laser intensity) which depends on α and thus on T. The dissipation coefficient D is related to the transmission and reflection coefficients (Q and R respectively) as

$$D = 1 - Q - R \tag{9.20}$$

For self-supporting samples,

$$Q = 1/[n_1^2 \Gamma + (n_2^2/\Gamma) - 2n_1 n_2 \cos 2\delta] \tag{9.21}$$

$$R = n_1 n_2 [\Gamma + (1/\Gamma) - 2\cos 2\delta] Q \tag{9.22}$$

where $n_1 = (n-1)^2/4n$, $n_2 = (n-1)/4n$ and

$$\Gamma = \exp(\alpha L), \quad \delta = (2\pi/\lambda_0) nL$$

where L is the sample thickness and n is the refractive index.

The stationary value of spot temperature can be determined from the equation

$$\eta J D(T_s) = T_s - T_F \tag{9.23}$$

together with the stability condition

$$\partial \{D(T_s) - [(T_s - T_F)/\eta T]\}/\partial T < 0 \tag{9.24}$$

To solve Eq. (9.23) explicitly, the temperature dependences of α and n have to be known. These are described by Eq. (9.17) and (9.18).

To demonstrate how optical discontinuities and bistability can occur, let us first neglect the temperature dependence of the refractive index. A schematic curve describing $D(T)$ is shown in Fig. 9.11. At low temperatures where $\exp[\alpha L] - 1 \ll 1$, $D(T)$ is proportional to

αT. At high temperatures where $\exp[\alpha L] \gg 1$, $D(T)$ reaches a saturation value of $1 - [(n-1)/(n+1)]^2$ (i.e. all light incident on the sample is absorbed). Equation (9.23) can be solved graphically by determining the intercepts of $D(T)$ and the straight line $(T - T_F)/\eta T$. As can be seen from Fig. 9.11, if the incident light intensity I is less than a critical value, $I_-(I < I_-)$ or is larger than a critical value of $I_+(I > I_+)$, there is only one solution for T. However, in the range $I_- < I < I_+$, there are three solutions.

To decide whether a given solution is stable or not, one has to consider what happens if the if the temperature deviates slightly from its equilibrium value. If the sign of $\partial T/\partial t$ is such that the temperature approaches the equilibrium value, the solution is stable, in the opposite case it is unstable. Equation (9.24) gives the stability condition. The inequality described by Eq. (9.24) is satisfied for the solution denoted by T_1 and T_3 (see Fig. 9.11). The first solution (T_1) corresponds to a cold and transparent state of the film. This happens when the laser intensity is increased from 0. The state becomes unstable when $I = I_-$, where a *discontinuous transition* takes place to a warm and strongly absorbing state. On the other hand, when the intensity is decreased from a larger value than I_+, the film remains in this "warm" state down to a critical intensity $I < I_-$. At this intensity the film transforms back to the "cold" transparent state. This behavior described above is typical of optical bistability [34] and is in good accordance with the experimental results shown in Fig. 9.8. Note, however, that in the present mechanism the reflection at the boundaries does no play an important role, and that the switching is from the transparent to the dark state when the light intensity is increased. These features are opposite to what is found in conventional optical bistability.

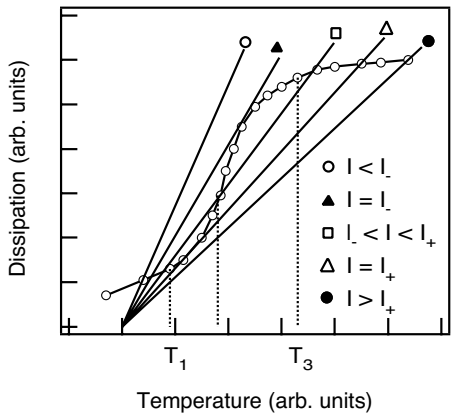

Figure 9.11: Determination of the laser-illuminated spot temperature at different laser intensities: n is considered to be constant.

In the considerations above, the variations of the refractive index with temperature were neglected. This variation, although weak, may itself also lead to bistability. Keeping α a non-zero constant, D oscillates with increasing T because of the temperature dependence of the term of $\cos 2\delta$ in Eqs. (9.21) and (9.22).

Photostructural Changes

A detailed description of photostructural changes in amorphous chalcogenide semiconductors has been given by Tanaka [24]. These structural changes are due to light-induced displacements of chalcogenide atoms as described in the corresponding subsection of the previous section. A fraction of these atoms can sit in two different equilibrium positions. On a configurational coordinate diagram these positions correspond to two minima of the double well potential [31]. One of the minima represents the ground state and the other is associated with the metastable excited state. Transitions from one configuration to the other occur through photo-induced and – near glass transition temperatures – pure thermal processes. According to Kolobov et al. [22], the photo-induced transitions consist of two steps: a thermally activated small displacement of the atom and an electronic excitation by the incoming atoms which is followed by a relaxation to the new equilibrium position.

According to Kolobov et al. [22], the population kinetics are governed by the equation

$$dN/dt = -[1/\tau + J(\sigma_1 + \sigma_2)]N + J\sigma_1 \tag{9.25}$$

where N is the number of units in the metastable state divided by the total number of sites, σ_1 and σ_2 are the cross-sections of the transitions from the ground state to the metastable state and for the inverse transitions, respectively. The temperature dependence of the cross sections can be expressed as

$$\sigma_i = K_i \exp(-E_i/kT) \qquad i = 1, 2 \tag{9.26}$$

where $K_i \sim 1/T$. The activation energies E_i are of the order of tenths of electronvolts.

In Equation (9.25), τ is the relaxation time to the ground state via pure thermal transition. This relaxation is usually very slow, except at near the glass transition temperature T_g and therefore can be neglected.

The stationary solution of Eq. (9.25) is

$$S = \sigma_1/[1/J\tau + (\sigma_1 + \sigma_2)] = 1/[1/q + 1 + f\exp(-\Delta E/kT)] \tag{9.27}$$

with $f = K_2/K_1$, $\Delta E = E_2 - E_1$, and $q = J\tau K_1 \exp(-E_1/kT)$.

Equation (9.25) can be re-written as

$$dN/dt = (\boldsymbol{N} - N)/\tau_0 \text{ with } 1/\tau_0 = J(\sigma_1 + \sigma_2) + 1/\tau \tag{9.28}$$

The main problem to be considered is the connection between the value of N and the optical parameters of the substance. For the sake of simplicity, we assume that the photo-induced processes influence only the value of α_0, otherwise the Urbach rule (Eq. (9.17)) remains valid. It is also assumed that α_0 is proportional to N. With this assumption we derive from Eq. (9.28) an expression describing the kinetics of photostructural changes:

$$d\alpha/dt = (\boldsymbol{\alpha}_0 - \alpha_0)/\tau_s \tag{9.29}$$

where τ_s is the structural relaxation time and $\boldsymbol{\alpha}_0$ is the stationary value of α_0:

$$\boldsymbol{\alpha}_0(T, J) = A/[1/q + 1f\exp(-\Delta E/kT)] \tag{9.30}$$

In this theoretical description, the instantaneous structure of the amorphous network is characterized from the optical point of view by the value of α_0; α_0 represents the fraction of atoms in the metastable state. Under the influence of laser light, the amorphous network approaches an equilibrium structure in which the number of transitions from the ground state to the metastable state equals the number of inverse transitions. This is characterized by the equilibrium value of α_0, $\boldsymbol{\alpha}_0(T, J)$.

It is important to emphasize that the simplifications made in deriving the exact form of $\boldsymbol{\alpha}_0(T, J)$ is not essential in describing the oscillatory phenomenon. The important point is that there exists an equilibrium value of α_0 ($\boldsymbol{\alpha}_0$) which is determined by the temperature and in some cases by the laser light intensity also. However, $\boldsymbol{\alpha}_0$ does not depend on the previous history of the illuminated spot, but the value of α_0 itself does depend on the previous history. At a given moment, it can be larger than smaller than the equilibrium value at a given temperature and light intensity. In the first case ($\alpha_0 > \boldsymbol{\alpha}_0$), α_0 decreases resulting in photobleaching, while in the second case ($\alpha_0 < \boldsymbol{\alpha}_0$), α_0 increases giving rise to photodarkening. Thus whether photodarkening or photobleaching occurs under the influence of the laser beam depends on the *history of the illuminated spot.* This fact was proven experimentally by Averyanov et al. [36].

In order to determine the stationary state and its stability, the laser illuminated spot temperature T_s and its absorption coefficient (at a fixed wavelength) α_0 has to be considered as independent variables which satisfy the following equations:

$$\tau_0(\partial T/\partial t) = \eta J D(\alpha_0, T_s) - (T_s - T_F) \tag{9.31}$$

$$\partial\alpha_0/\partial t = (\boldsymbol{\alpha}_0 - \alpha_0)/\tau_s \tag{9.32}$$

The stationary solutions (i.e. at $\partial T/\partial t = \partial\alpha_0/\partial t = 0$) of Eqs. (9.31) and (9.32) are

$$\eta J D(\alpha_0, T_s) = T_s - T_F \tag{9.33}$$

$$\alpha_0 = \alpha_0(T_s, J) \tag{9.34}$$

For the analysis it is very important to note that under the present experimental conditions the thermal relaxation time τ_0 is much shorter then the structural relaxation time τ_s (this was inferred from the experimental observations) [35]. We found τ_s to be a few seconds at the incident laser intensity $J \sim 50$ W/cm^2. However, measurements with a chopped laser showed another relaxation process with a time constant of a few milliseconds. An estimation of the parameters involved in Eq. (9.31) showed that this latter process can be identified with the establishment of a pseudo-thermal equilibrium, associated with the actual value of α_0.

As a consequence of the large difference between τ_0 and τ_s, it can be assumed that after switching on the laser, a pseudo-thermal equilibrium is first quickly established which corresponds to the actual value of α_0. As α_0 is changed by the laser beam, the spot temperature follows "adiabatically" the pseudo-equilibrium value corresponding to the actual structure. The main point, however, is that this pseudo-equilibrium is not necessarily stable against thermal fluctuations (with fixed α_0).

The stability condition can be written in the form [35]

$$\partial\alpha_0/\partial T^{(s)} > 0 \tag{9.35}$$

The stationary solutions can be found by plotting $\boldsymbol{\alpha}_0(T)$ on the same diagram as the $\alpha_0(T)$ curves. At a given intensity the intercept of $\boldsymbol{\alpha}_0(T)$ and $\alpha_0(T)$ determines the stationary solution. If $\boldsymbol{\alpha}_0(T)$ crosses the unstable region there is an intensity interval where the intercept corresponds to an unstable solution: in this case oscillation occurs.

According to these considerations three laser intensity range can be distinguished:

(1) The intensity is smaller than the lower threshold for oscillation. In this case only photodarkening takes place and a stationary state is established in the illuminated side.

(2) When no stable stationary solutions exists, the time-dependent Eqs. (9.31) and (9.32) have to be used to calculate the time variation of α_0 and T. Because the pseudo-thermal equilibrium is established much faster than structural equilibrium, we can regard the α_0, T point (characterizing the state of the spot) as moving along the $\alpha_0(T^{(s)})$ curve corresponding to fixed intensity. It always moves in the direction in which the absolute value of $\boldsymbol{\alpha}_0 - \alpha_0$ decreases. In the bright state of the curve α_0 is smaller than $\boldsymbol{\alpha}_0$ therefore photodarkening occurs and the point moves towards the unstable region (the temperature of the spot increases). When it reaches the boundary of the unstable region a discontinuous switch takes place into the dark state of the curve. The switch is fast therefore there is no time for photostructural change to take place, i.e. α_0 remains the same. Along the dark state of the curve, α_0 is larger than $\boldsymbol{\alpha}_0$ so photobleaching occurs and the α_0, T point moves back towards the unstable region (the temperature of the spot decreases). At the boundary, the next switch takes place to the bright state again fast enough to avoid any change in α_0. Thus α_0 again becomes smaller than $\boldsymbol{\alpha}_0$ and the whole cycle starts again resulting in oscillation of the optical properties with time.

There is a good correspondence between the theory and the experimental results [35, 37].

9.5 Conclusion

Our model of the optical anisotropy shows clearly that the reorientation of the optical anisotropy cannot consist of collective rotation of atomic or molecular units as is the case in liquid crystal, for example. The rather unusual logarithmic time dependence of the orientation and reorientation processes can be explained by the plausible assumption that the heights of the barriers hindering the atomic displacements have an energy distribution whose spread is much larger than kT.

The observed optical anisotropy and reorientation effect can be used to fabricate fast, high-capacity digital or analogue optical memory devices.

According to our models of optical bistability and oscillation, both phenomena can be expected to occur in any amorphous semiconductor film provided that:

- α_0 is a strongly (exponentially) increasing function of T (Urbach rule)
- the sample thickness, wavelength of the light and film temperature are properly selected
- $\boldsymbol{\alpha}_0(T)$ is a decreasing function of T

The observed optical bistability can be used to fabricated optical switching elements performing “optical transistor” function.

References

[1] A. Szoke, V. Daneu, J. Goldhar, and N.A. Kurnit, Appl. Phys. Lett **15**, 376 (1969).

[2] H.M. Gibbs, S.L. McCall, and T.N.C. Venkatesan, Phys. Rev. Lett. **36** 1135 (1976).

[3] D.A.B. Miller, C.T. Seaton, M.E. Prise, and S.D. Smith, Phys. Rev. Lett. **47**, 197 (1981).

[4] J. Hajto, G. Zentai, and I. Kosa Somogyi, Solid St. Commun. **23**, 401 (1977).

[5] J. Hajto and P. Apai, Journal of Non-Cryst Solids **35 & 36**, 1085 (1980).

[6] J. Hajto and I. Janossy, Phil. Mag. B **Vol 47**, No.4, 347 (1983).

[7] J. Hajto and P.J.S. Ewen, Phys. Stat. Sol. (a), **54**, 385 (1979).

[8] J. Hajto, I. Janossy, and G. Forgacs, J. Phys. C: Solid State Phys. **15,** 6293 (1982).

[9] I. Janossy, A. Jakli, and J. Hajto, Solid State Commun. **Vol. 51**, 761 (1984).

[10] J.P. de Neufville and B.O. Seraphin (Eds.), Optical Properties of Solids, North Holland, Amsterdam, 1975, p. 347.

[11] K.S. Rajogopalan, K.S. Harshavardhan, L.K. Malhorta, and K.L. Chopra, J. Non-Cryst. Solids **50**, 29 (1982).

[12] A.V. Kolobov, B.T. Kolomiets, V.M. Lyubin, N. Sebastian, M.A. Tagirdzhanov, and J. Hajto, Sov. Phys. Solid State **24**, 603 (1982).

[13] B.T. Kolomiets, and V.M. Lyubin, Mater. Res. Bull. **13**, 1343 (1978).

[14] J. Hajto, J. Phys. Colloq., Suppl., **41**, 63 (1980).

[15] J. Hajto and M. Fustoss-Wegner, J. Phys. Colloq., Suppl., **42**, (1981).

[16] V.G. Zhdanov, B.T. Kolomiets, V.M. Lyubin, and V.K. Malinovskii, phys. stat. sol. **52**, 621 (1979).

[17] N. Harshorne, and A. Stuart, Crystals and the Polarising Microscope, Edward Arnold, London, 1970.

[18] L. Csillag, I. Janossy, V.F. Kitaeva, N. Kroo, N.N. Sobolev, and A.S. Zolotko, Mol. Cryst. Liq. Cryst. **78**, 173 (1981).

[19] J. Hajto, G. Radnoczi, L. Pogany, and E. Hajto, Rep. Central Res. Inst. Phys. Budapest **81**, 96 (1981).

[20] R. Grigorovici and A. Vancu, J. Phys. **42-C4**, 391 (1981).

[21] R.A. Street, Solid State Commun. **24**, 363 (1986).

[22] A.V. Kolobov, B.T. Kolomiets, O.V. Konstantinov, and V.M. Lyubin, J. Non-Cryst. Solids **45**, 335 (1981).

[23] S. Guha, Physical Properties of Amorphous Materials, Plenum Press, New York, 1985, p. 423.

[24] K. Tanaka, J. Non-Cryst. Solids **35 & 36**, 1023 (1980).

[25] S.R. Elliott, J. Non-Cryst. Solids **81**, 71 (1986).

[26] I. Janossy, J. Hajto, and W.K. Choi, J. Non-Cryst. Solids **90**, 529 (1987).

[27] J. Hajto and I. Janossy, J. Non-Cryst. Solids **97 & 98**, 1207 (1987).

[28] J.C. Phillips, C. Beevers and S. Gould, Phys. Rev. B **21**, 5724 (1980).

[29] J.C. Phillips, J. Non-Cryst. Solids **43**, 37 (1981).

[30] N.F. Mott and E.A. Davis, Electronic Processes in Non-Crystalline Materials, Clarendon Press, Oxford 1971.

[31] P.W. Anderson, B.I. Halperin, and C.M. Varma, Phil. Mag. **25**, 1 (1971).
[32] K.S. Gilroy and W.A. Phillips, Phil. Mag. B **43**, 391 (1981).
[33] P. Fazekas, Phil. Mag. B. **44**, 435 (1981).
[34] E. Abraham and S.D. Smith, Rep. Prog. Phys. **45**, 815 (1982).
[35] J. Hajto and I. Janossy, A. Firth, Phil. Mag. B **48**, 311 (1983).
[36] V.L. Averianov, A.V. Kolobov, B.T. Kolomiets, and V.M. Lyubin, Phys. Stat. Solidi **57**, 81 (1981).
[37] J. Hajto, I. Janossy, and W.K. Choi, J. Non-Cryst. Solids **77&78**, 1273 (1985).

10 Optically-Induced Diffusion and Dissolution of Metals in Amorphous Chalcogenides

Tomáš Wágner and Miloslav Frumar

10.1 Introduction

A wide range of photo-induced phenomena exhibited by chalcogenide thin films enables them to be utilized in a variety of optical applications [1–4]. Among these phenomena optically-induced diffusion and dissolution (OIDD), also known in the literature as photodoping or photodissolution, of some metals (Ag, Cu, Zn, Cd) in a wide range of compositions in glassy chalcogenide films has been observed [4–10]. In the bilayer or multilayer metal/chalcogenide structure, light illumination induces fast migration of metal atoms into chalcogenides, as shown schematically in Fig. 10.1. The amorphous Ag/$As_{33}S_{67}$ and Ag/$Ge_{30}S_{70}$ films have recently been shown to be useful materials for fabrication of phase gratings and other diffractive optical elements [11, 12] with relief nano-structures. There are also other related phenomena in Ag-rich chalcogenide glasses e.g. in ternary systems Ag–As–Se, Ag–As–S, Ag–Ge–S, which exhibit so-called photo-induced surface deposition of metallic Ag, i.e. photoinduced segregation of fine particles on the glass surface [13, 14]. A similar effect is known for some minerals, e.g. Ag_3AsS_3 or Ag_3SbS_3, during their exposure to light. Furthermore, it was found that silver-containing chalcogenide films exhibit reversibility in optical writing and thermal erasing of the Ag patterns [15].

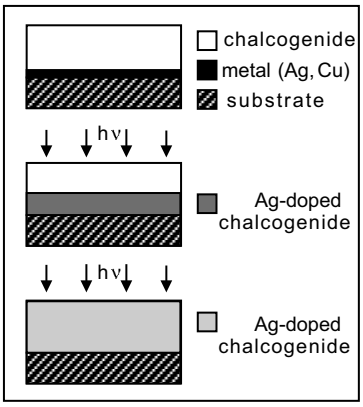

Figure 10.1: A schematic cross-section through a sample of Ag/chalcogenide during the OIDD process.

Another potential option in optical recording of information is to make use of glasses or their films with stoichiometric composition such as $AgAsS_2$ [16]. Such glasses are potentially applicable to phase-change optical recording based on a phase transition between amorphous and crystalline states [17, 18]. Generally, such a transition can be induced by light exposure of different energy to perform irreversible or reversible recording. The glasses of Ag–Ge–S, Ag–Ge–Se, Ag–As–S and Ag–As–Se systems belong to the so-called super ionic conductors [19] and this quality has been demonstrated to be beneficial, e.g. in reversible opto-electrical switching [20].

In order to consider the further development of such applications, it is essential to understand the physical principles of the OIDD and other optically-induced effects. It is also important to know a definite and reproducible way for the preparation of silver-containing chalcogenide glass films and their physico-chemical properties, especially optical, thermal and structural properties, since they are closely related to the mechanism of the above-described phenomenona. Recent methods of amorphous film preparation, description of the physico-chemical origin of the process of silver optically-induced dissolution and diffusion into thin films of amorphous films such as $As_{33}S_{67}$, $Sb_{33}S_{67}$, $Ge_{30}S_{70}$, $Ge_{10}Sb_{30}S_{60}$, $As_{30}Se_{70}$ and $Ge_{20}Se_{80}$, and their physico-chemical properties will be the focus of this review.

10.2 Preparation of Bulk Glasses and Thin Films

Amorphous chalcogenide films are usually prepared using a vacuum evaporation technique [8]. The bulk chalcogenide glasses used as an evaporation source are prepared from the constituent pure elements that are weighed and placed into pre-cleaned and outgassed (by heating under vacuum to 900 °C) quartz ampoules. The ampoules are then evacuated to a pressure of 1×10^{-3} Pa for 30 min and sealed. The synthesis is performed in a rocking furnace with ampoules exposed to a temperature of 700 or 1050 °C for 24 h. The fragments of the bulk material are evaporated from a quartz crucible to avoid any contamination of the prepared films during the evaporation process [8]. The films are usually prepared on glass substrates in a 1×10^{-4} Pa vacuum, at a rate of 1–5 nm/s. Other deposition techniques such as chemical vapor deposition [21], laser ablation [22] or magnetron sputtering [23] are also used to prepare chalcogenide films.

Thin films of chalcogenide glasses can also be prepared from organic amine (e.g. n-propylamine, n-butylamine) solutions of bulk glasses. Organic solutions of chalcogenide glasses are deposited e.g. by spinning, spraying, dipping or casting on substrates and the amorphous films are formed upon evaporation of the volatile solvent [24, 25]. All deposition techniques allow one to obtain films with a uniform thickness in the range 0.1–2 μm. The silver layers are typically evaporated on top of the amorphous chalcogenide films either in full thickness (typically between 80 and 150 nm of silver) [26] for kinetic measurements or in portions ($\sim$10 nm of silver) for the step-by-step optically-induced dissolution technique [27] which allows one to prepare Ag-chalcogenide films with desired composition and silver concentration. Recently, we have succeeded in depositing thin Ag–As–S amorphous films directly from a mixture of organic solutions by the spin-coating method [28].

10.3 Kinetics

10.3.1 Kinetic Measurement Methods and Kinetics of OIDD Process

The OIDD reaction kinetics have been studied using various techniques, e.g. measurement of the optical transmittance [29] or X-ray diffraction of the Ag (111) peak [30]. The most convenient and reliable is the reflectivity technique which was first developed by Firth [7], and later modified by Ewen et al. [31], Wagner et al. [26, 32] and Marquez et al. [33, 34]. The modified computer-controlled reflectivity technique [32] was used to measure the kinetics of OIDD of silver (d = 80 nm) in $As_{30}S_{70}$, $Sb_{33}S_{67}$ and $Ge_{30}S_{70}$ (d = 800 nm) films by monitoring the change of thickness of the undoped chalcogenide. The measurement of the rate of OIDD is based on periodic variations of the reflectivity of a weakly absorbing film with its thickness, due to interference between the light reflected from the top and bottom surfaces of the film. A typical plot of reflectivity as a function of exposure time during one of these experiments is shown in Fig. 10.2. The time between successive maxima or minima on the curve corresponds to a decrease in the thickness of the undoped layer by $\lambda/2n$, or to an increase of the thickness of the doped layer by $z\lambda/2n$, where λ is the wavelength of the detected light (λ = 550 nm), n is the refractive index of the undoped $As_{30}S_{70}$, $Sb_{33}S_{67}$ and $Ge_{30}S_{70}$ layer at this wavelength (n = 2.3, 2.65 and 1.9, respectively) and z is a constant relating the thickness of the doped layer to the thickness of the undoped material consumed ($z = 1.07$).

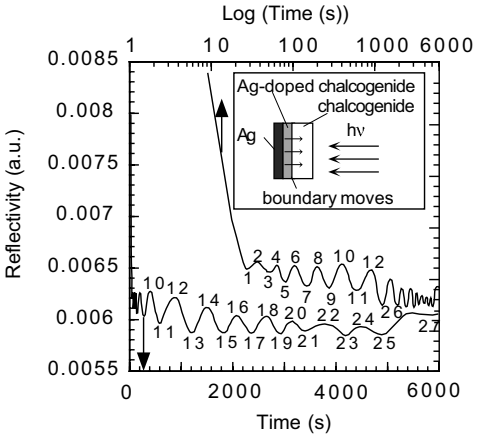

Figure 10.2: A typical reflectivity curve as a function of illumination time, for the Ag/$As_{30}S_{70}$ bilayer system during the OIDD process.

The silver layer thickness during the course of the reaction was determined following the technique proposed by Goldschmidt and Rudman [35] and later improved by Fernandez-Pena et al. [29], which is based on the measurement of the variation of the electrical resistance of the silver film during the OIDD process. Simultaneous measurements of optical transmittance (or reflectivity) and electrical resistance [29, 36] allow one to measure the OIDD kinetics with good accuracy.

10.3.2 Kinetic Curves of the OIDD Process

The kinetics of OIDD in e.g. an Ag/$As_{33}S_{67}$ bilayer was monitored by using simultaneously two independent techniques (reflectivity and resistance measurements) at room temperature using an Ar-ion laser beam (λ = 514 nm) for the sample exposure [36]. The monitoring of the electrical resistance of the silver layer is certainly a very important tool to establish accurately the time when the entire elemental silver source is completely consumed during OIDD. The monitoring of electrical resistance change during the OIDD process helped to calculate the initial silver-consumption rate v_{Ag} ($v_{Ag} = 1.26$ nm/s), which is exactly the same as the rate of Ag-doped/undoped boundary movement obtained from the reflectivity technique [36].

The reflectivity oscillation curve (i.e. the position of the maxima and minima) shown in Fig. 10.2 is used to derive the experimental points for the kinetic curves (Fig. 10.3). As can be seen from the reflectivity curve, the amplitude of oscillations decreases gradually with time and at a certain point they die out, and then the value of the reflectivity increases monotonically to a new level. The intensity change in the reflectivity curve during the OIDD process can be attributed to the changing refractive index value of the reflecting layer, from that of the initial, elemental Ag layer to that of an $As_{33}S_{67}$ layer doped with different levels of Ag. The final increase of the reflectivity at the end of the OIDD effect is certainly due to the leading edge of the boundary (doped/undoped) region, reaching the top surface of the film, so that the Ag concentration at this surface then gradually increases up to a constant value. The electrical resistance and optical reflectivity kinetic curves demonstrate that the OIDD process continues, very efficiently, even after the elemental Ag layer is used up, i.e. the Ag exhaustion has no effect on the OIDD kinetic curve [36].

In order to find the best physical model to describe and interpret such experimental kinetic data corresponding to the metal-dissolution kinetic measurements, four different fitting functions have been tested [36]. It is clear that the measured kinetic curve (i.e. doped layer thickness vs. exposure time), shown in Fig. 10.3 has a more complex character than usually reported. It cannot be fitted by a simple linear term [37] or a square root function [7, 9, 38–40] as suggested earlier.

A more complex character of the kinetic curves during OIDD process of silver is observed in many chalcogenide systems (As–S, Sb–S, Ge–S [12, 26, 32]) depending on the silver-doped chalcogenide film thickness. The kinetics can be fitted using a composite function consisting of a single exponential and steady-state terms [12, 26, 32] or a single exponential and square root terms described in Ref. [36]. The latter function is appropriate when the thickness of the chalcogenide exceeds 1500 nm [36]. The former two-stage exponential/linear function, $f(t) = -a\exp(-bt) + ct + d$, where b and c are the rate coefficients, and a and d are two constants seems, to be appropriate for films with a thickness $d < 1500$ nm. The parameters b and c are reaction rate coefficients ($a = k_{\text{exp}}$, $b = k_{\text{lin}}$ in units of s^{-1}). The parameters a and d correspond to the photodoped layer thickness at the end of stage 1 and at the beginning of stage 2, respectively. The kinetic curve shows that there are two stages of OIDD. The first stage is characterized by the rate coefficient k_{exp} and the second stage by k_{lin}, where $k_{exp} > k_{\text{lin}}$. The OIDD rate, as expressed by two rate coefficients (k_{exp} and k_{lin}), depends strongly on temperature [12, 26, 32], the chalcogenide film thickness [12], exposure light energy [41, 42] and the intensity of the light [43–46]. The values of the activation energies during the two stages (E_{exp} and E_{lin}) calculated from typical Arrhenius plots ($\ln k$ vs. T^{-1} or $\ln k$ vs. I^{-1}) are shown in Table 10.1.

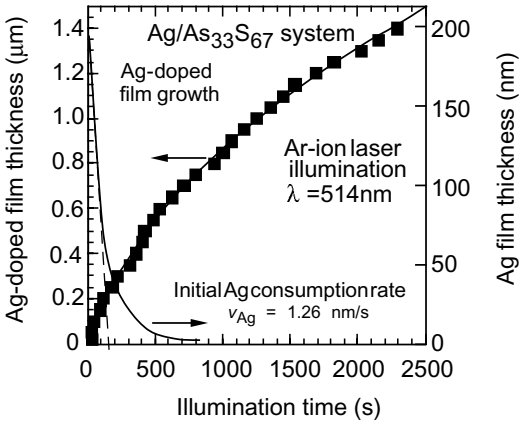

Figure 10.3: A typical kinetic curve for OIDD of Ag into an $As_{33}S_{67}$ glass film. The solid line is a fit to the experimental points [36].

Table 10.1: Comparison of the results of kinetic parameters of OIDD obtained in $Ag/As_{30}S_{70}$ and $Ag/Ge_{30}S_{70}$ systems [46].

Conditions	Sample	k_{exp} (s^{-1}) $T = 120$ °C	k_{lin} (s^{-1}) $T = 120$ °C	$E_{a,exp}$ (kJ mol^{-1}/eV)	$E_{a,lin}$ (kJ mol^{-1}/eV)
$k = f(T)$	$As_{30}S_{70}$	3.4×10^{-2}	6.1×10^{-3}	22.5/0.21	33.3/0.31
$I = 90$ mW/cm	$Ge_{30}S_{70}$	1.2×10^{-2}	4.6×10^{-4}	20.5/0.19	40.2/0.37
$k = f(I)$	$As_{30}S_{70}$	1.7×10^{-2} ($I = 70\%$)	3.0×10^{-3} ($I = 70\%$)	$0.102/9 \times 10^{-4}$	$0.108/1 \times 10^{-3}$
$T = 120$ °C	$Ge_{30}S_{70}$	1.1×10^{-2} ($I = 70\%$)	1.0×10^{-3} ($I = 70\%$)	$0.094/8 \times 10^{-4}$	$0.096/9 \times 10^{-4}$

10.3.3 Mechanism of the OIDD Process

The OIDD process is generally considered to be a solid-state chemical reaction [52]. The detailed physical or physico-chemical interpretation of the process can be found in models [26, 47–56]. The understanding of the OIDD process is still far from being complete and e.g. the kinetics of the process need to be studied.

The measured kinetic curves and different activation energies in different stages of OIDD show the complex character of the process [32, 36]. The composite mathematical functions need to be applied to find the best fit to experimental kinetic data and then the physico-chemical mechanism of the OIDD process can be suggested. The kinetic curves characterize two different velocity constants (exponential and linear stages or exponential and square root stages for different thicknesses of the reaction products), which support the idea of two or three consequent physico-chemical processes, depending on the OIDD product thickness (Fig. 10.4), described also in other systems by Schmalzried [57].

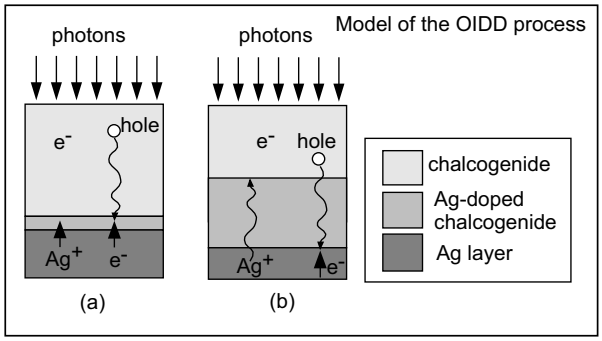

Figure 10.4: A schematic diagram of the proposed model for the OIDD process in the Ag/chalcogenide system.

It is suggested that during the first stage when a very thin film of a reaction product is formed, the OIDD process rate can be determined by space charge at the Ag/Ag-doped/undoped chalcogenide boundary, which is built in after the originally two-layer system Ag/chalcogenide is exposed to light. The light with the energy higher than the optical gap of the chalcogenide $E_{g,opt}$ is absorbed in close vicinity of the chalcogenide surface or of the metal-doped/undoped boundary and electron–hole pairs are excited. The electrons are likely to be trapped within a short distance and form negatively charged centers located at the chalcogen sites while the holes can migrate for much longer distances, e.g. 10 μm [58]. The accumulation of the holes at the Ag/chalcogenide boundary leads to the formation of pairs of Ag^+ ions and electrons. The holes and Ag^+ ions are introduced into the chalcogenide leaving behind a part of silver species bonded to the chalcogen sites and a part of free unbonded Ag^+ ions, which are able to move forward and neutralize the electrons. The electron tunneling from metallic Ag into the chalcogenide can speed up the overall process. The described processes refers to the silver-containing thin chalcogenide film formed during the *exponential stage* of OIDD.

The silver-doped film thickness increases and influences the boundary space charge. At the same time, the electron tunneling diminishes. The rate of the Ag-doped film formation goes through a *linear stage*, when the supply of ions and charged particles (electrons, holes) is sufficient. When the silver-doped film is formed, holes have to migrate through the silver doped part towards the 'Ag/Ag-doped film' boundary and the Ag^+ ions need to migrate in the opposite direction. The slowest part and the driving force of the OIDD is the chemical reaction at the 'Ag-doped/undoped chalcogenide' boundary (e.g. 2Ag + S = Ag_2S). The difference in silver chemical potential $\Delta\mu_{Ag}$ and silver isothermal activity a_{Ag} in the doped part and on the boundary between the doped and undoped parts of the film is the measure of the reaction rate in the studied solid-state system. The silver activity a_{Ag} depends on the silver solubility in amorphous chalcogenide and the phase in which it is present [57]. The source of silver or silver ions is changing during the course of OIDD. At the beginning, the source is elemental Ag, it then changes to a solid solution of silver in chalcogenide but the kinetics are not influenced by this fact [36]. The linear rate (linear reaction law) applies for product film thicknesses of 1–1.5 μm [12, 36].

When the thickness of the Ag-doped chalcogenide becomes larger than 1–1.5 μm, the reaction rate slows down. Gradually, a change to a *parabolic rate* of OIDD is observed. This means that the OIDD is no longer determined by the reaction rate (e.g. 2Ag + S = Ag_2S) but by the diffusion of the silver ions and other charged particles through increasing thickness of the reaction-product film (Ag-doped chalcogenide). The overall process rate becomes diffusion limited. The diffusion coefficient calculated from such kinetic curves [12,36] is $D_{Ag^+,optical} = 1.16 \times 10^{-11}$ cm^2/s (the light intensity used in the experiment was 200 mW/cm^2). The value of thermal diffusion coefficient $D_{Ag^+,thermal} = 4 \times 10^{-14}$ cm^2/s for Ag^+ ion self-diffusion in darkness has been obtained [59]. A similar result, namely that $D_{Ag^+,optical} > D_{Ag^+,thermal}$ by three orders of magnitude, has been also obtained in [60].

The values and origin of the activation energies at the two stages (E_{exp} and E_{lin}) were discussed by Dale et al. [61] and also by the present authors [12]. The activation energy of OIDD ($E_a \sim 0.1$–0.3 eV, temperature range 20–120 °C) decreases by one order of magnitude compared to thermally-activated silver diffusion and dissolution ($E_a \sim 1.3$ eV, in the temperature range 20–120 °C) in the dark [12, 61, 62]. The activation energies of two Ag/chalcogenide systems for stage 1 and stage 2 ($E_{a,\,exp}$, $E_{a,\,lin}$) described earlier are shown in Table 10.1. Their values are close to those characteristic of the activation energy of the diffusion process of Ag^+ ions in ion-conducting chalcogenide glasses, namely, in sulfides $E_a = 0.23$ eV and in selenides $E_a = 0.14$ eV [59] at $T = 175$ °C. In order to explain the differences in activation energies between optically and thermally activated diffusion, the activation energies of ionic conductivity and self-diffusion of Ag^+ ions [63] and the Anderson–Stuart model of strong electrolytes [64] have to be considered. The Anderson–Stuart model correlates the activation energy with the energy needed for metal ion transition between bridging and non-bridging chalcogen atoms [62]. The light energy absorbed generates valence alternation pairs (VAP) which could contribute to a decrease of the activation energy [55] of OIDD.

It is also known from the chemical kinetic theory that processes with activation energies $E_a > 10$ kJ/mol $\sim$0.1 eV can be connected with chemical processes. Ongoing chemical processes during OIDD and the resulting changes of structure of the optically-doped films have been proved, e.g. by EXAFS [65, 66], IR spectroscopy [26, 67], Raman spectroscopy [68, 69] and photo differential scanning calorimetry (DSC) [60].

10.3.4 Location of Actinic Light Absorption During OIDD

A number of models have been proposed to describe OIDD taking into account different kinetics. The models described the kinetics according to where the actinic light is absorbed. We believe that the light most effective for OIDD is absorbed in close vicinity of the metal-doped/undoped boundary [8,9]. The role of the light is to excite the holes (the majority carriers in most chalcogenide glasses) and to enable their diffusion through the boundary. However, on the basis of the observation that the light which is hardly absorbed in the doped or undoped chalcogenide film can also cause, to some extent, silver diffusion and dissolution effects [35, 70, 71] it was concluded that photon absorption in the metal layer could also contribute to OIDD. Within the frame of those observations, Goldschmidt and Rudman [35] and Lis and Lavine [70] concluded that the absorption of light in the silver layer generates hot electrons, which overcome the energetic barrier between metal and chalcogenide films leaving behind Ag^+ ions. The generated electrons are trapped in the chalcogenide. This process produces

electrostatic attraction and starts enhanced transfer of Ag^+ ions into the host chalcogenide film. Recent experiments on a Ag/Sb_2S_3 bilayer films by Lee et al. [71] shed some light on such a mechanism using two different wavelengths of the light, one being absorbed by the silver layer and the other which is not absorbed in the 10 nm film of Ag deposited on top of the chalcogenide film. It was demonstrated [71] that for the OIDD process more effective is the light which was absorbed by the Ag film. In our opinion, however, the question remains open because immediately after the silver-doped chalcogenide is formed the absorption in it cannot be avoided. In fact, the OIDD process can be activated with light in a wide energy range from X-ray [72, 73] through ultraviolet [70] and visible [12] to near-infrared [74], which also determines the light penetration depth and the number of electron–hole pairs excited.

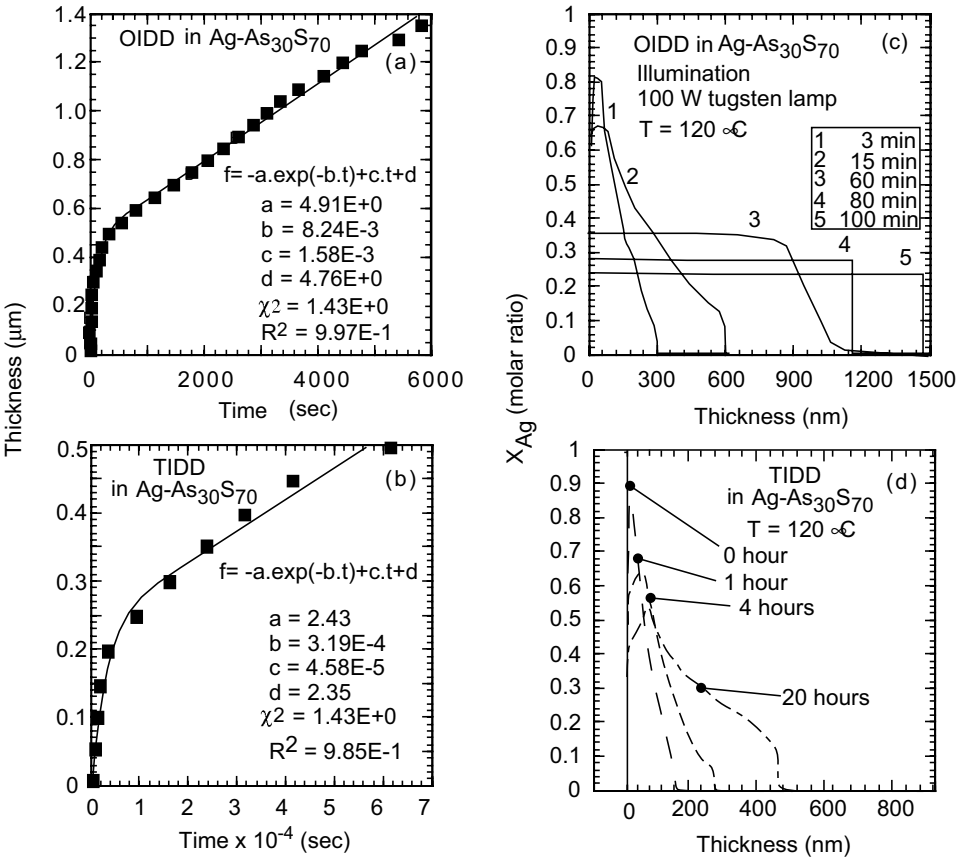

Figure 10.5: Kinetic curves of OIDD Ag in $As_{30}S_{70}$ film (a) and of TIDD Ag in $As_{30}S_{70}$ film. The Ag concentration depth profiles (c) obtained for the sample Ag/a-$As_{30}S_{70}$ during OIDD from the corresponding RBS spectra and Ag concentration depth profiles (d) obtained from the sample Ag/a-$As_{30}S_{70}$during TIDD from the corresponding RBS spectra [60].

The silver diffusion and dissolution process of metals in chalcogenides can be induced by exposure to light of different energies, or at elevated temperature without light, or to a combination of both light and elevated temperature. The OIDD process rates, e.g. in the $Ag/As_{30}S_{70}$ [69] bilayer system (Fig. 10.5a and b), show typical kinetic curves from which the reaction rates can be calculated according to the model discussed above. The OIDD process rate is 2–3 orders of magnitude higher than the rate of thermally induced diffusion and dissolution (TIDD) [69].

10.3.5 Diffusion Profiles

The silver diffusion profiles during OIDD can measured by different techniques such as tracing of the ^{107}Ag and ^{109}Ag isotopes during the process [75, 76] or by Rutherford backscattering spectroscopy (RBS) [76] using α particles or carbon ions (e.g. C^+) as projectiles. RBS is the only method enabling practically non-destructive qualitative and quantitative analysis of the films during OIDD. The depth resolution of the method is from 10 nm to a few micrometers and the accuracy (in the range 2–5%) depends on the knowledge of stopping powers, which enables one to evaluate the depth dependence due to the energy losses of the projectiles.

Typical RBS spectra (Fig. 10.6a, b and c) can be converted into depth-concentration profiles of present elements (e.g. Fig. 10.5c, d and Fig. 10.6d, e, f) using the GISA program [77]. The depth profiles of silver in chalcogenide films exhibit step-like profiles, which cannot be fitted by standard error or Gaussian functions usually used to describe diffusion. The step-like silver profile is a unique feature found in several systems such as Ag/As–S [12, 32, 63, 78, 79], Ag/Ge–S [46] and Ag/Ge–Se [76, 80, 81] during OIDD. Its origin is still a subject of discussion. Some authors suggest that it is due to the presence of two immiscible glass-forming regions in Ag-chalcogenide glass systems [26, 49]. Alternatively, the step-like profile may be due to the space charge [52] formed at the Ag-doped chalcogenide/undoped chalcogenide boundary because the holes, being majority carriers, can migrate a longer distance after the excitation while electrons are trapped and localized in the undoped part of film [58] as is schematically shown in Fig. 10.4.

The step-like silver profiles are found in samples during both OIDD and TIDD. The RBS spectra corresponding to these experimental conditions show similar Ag-diffusion profile development as shown in Fig. 10.5c and d. The final product of OIDD or TIDD of silver in chalcogenide films has, according to RBS measurements, a constant value of silver depth profile [12].

10.4 Reaction Products and Their Properties

The silver diffusion and dissolution process leads to homogeneous products in a wide span of compositions based on the dissolution limits of silver in different compositions of chalcogenides [4, 12, 35, 46, 82–86, 88]. Silver dissolution limits in different chalcogenide films given in Table 10.2 were obtained using step-by-step OIDD, which allows one to prepare films with a wide range of silver concentrations. The silver concentration in chalcogenide films strongly influences their physico-chemical and mechanical properties.

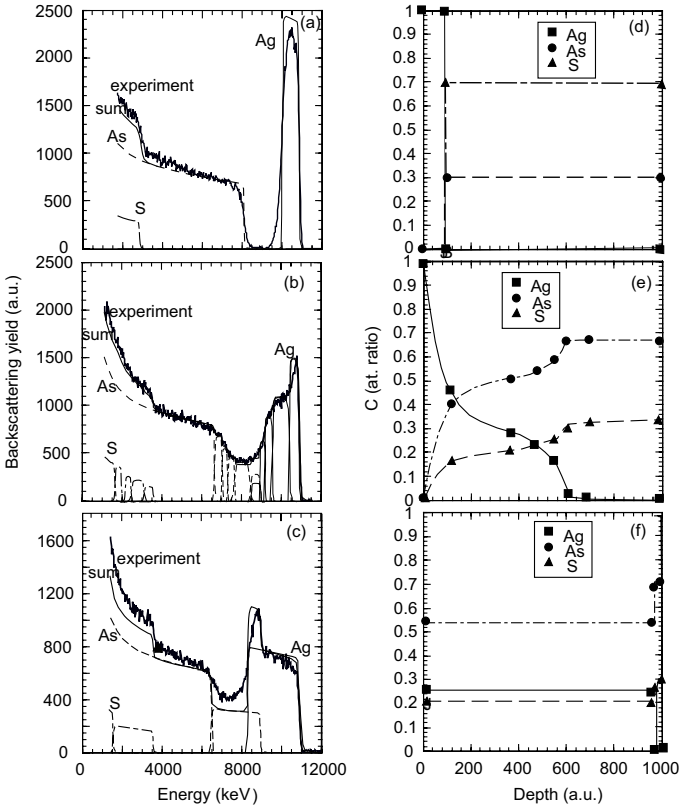

Figure 10.6: Typical RBS spectra are shown in (a)–(c), obtained in an Ag/a-$As_{30}S_{70}$ sample after different illumination times (0, 2000 and 6000 s, respectively). The Ag, As and S concentration depth profiles, shown in (d)–(f), were obtained from corresponding RBS spectra (a)–(c) [83].

Table 10.2: Limits of the silver concentration obtained by OIDD in different chalcogenide systems.

Composition	$As_{33}S_{67}$	$As_{30}S_{70}$	$As_{30}Se_{70}$	$Ge_{30}S_{70}$	$Sb_{33}S_{67}$	$Ge_{10}Sb_{30}S_{60}$
$c_{Ag,OIDD}$ limit (at.%)	30	31	20	25	10	7

10.4.1 Optical Properties

The OIDD process allows the preparation of chalcogenide films with the silver content in a wide concentration range. A silver concentration increase leads to a red shift of the optical absorption edge of the doped films [4, 12, 46, 82–86]. Typical optical transmission curves of the film before and after OIDD are shown in Fig. 10.7 together with the calculated values of the spectral dependence of the refractive indices n shown in the inset. The refractive indices increase with increasing silver content for different film compositions measured at a fixed

wavelength (λ = 800 nm) as shown in Fig. 10.8. As a consequence of optically-induced dissolution and diffusion of silver in chalcogenide films of As–S, As–Se, Sb–S, Ge–Se, Ge–S and Ge–Sb–S systems, the values of the optical bandgap, $E_{g,opt}$, significantly decrease with increasing Ag content in the films (Fig. 10.9).

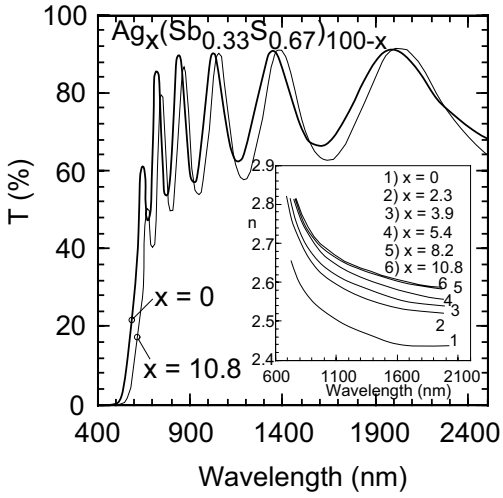

Figure 10.7: Transmission spectra and calculated spectral dependence of the refractive indices (insert) of the undoped and optically doped Ag–Sb–S films prepared by the OIDD process [85].

Optical transmission, T, refractive index, n, and optical gap, $E_{g,opt}$, show strong evidence that silver has been incorporated into and reacted with the host matrix of the chalcogenide films. The decrease of $E_{g,opt}$ with increasing Ag content can be explained by the fact that the binding energies of Ag–S and Ag–Se bonds, As–As and Ge–Ge bonds are higher than those of As–S, As–Se, Se–Se and S–S bonds [89] as shown in Table 10.3. Therefore, it leads to significantly smaller energy splitting between the states forming the valence and conduction bands and the optical bandgap decreases.

Table 10.3: Bonding energies of homopolar and heteropolar bonds present in chalcogenide systems [89].

Bond	As–S	As–Se	Ge–S	S–S	As–As	Ge–Ge	Se–Se	Ag–S	Ag–Se
Energy (kJ/mol)	260	230	265	280	200	185	225	217	202

Non-linear optical properties of Ag–As–S films were studied by Kosa et al. [90]. A high value of the non-linear index of refraction and related parameters, i.e. the third order of non-linear polarizability were established. Ag–As–S amorphous chalcogenides were proved to be optically self-defocusing materials for high light intensities.

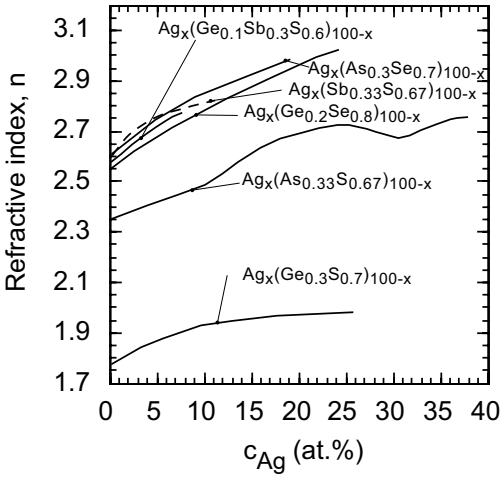

Figure 10.8: Silver content dependence of the refractive index at wavelength $\lambda = 800$ nm in different chalcogenide films prepared by the OIDD process.

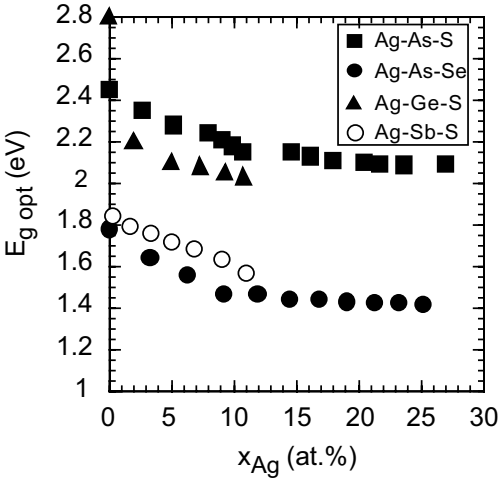

Figure 10.9: Optical bandgap, $E_{g,opt}$ vs. silver content in the prepared chalcogenide films. The experimental points represent average values with typical errors bars comparable to the size of the plotted experimental points.

10.4.2 Mechanical and Thermal Properties

The Vickers hardness, H_v, of the films prepared by OIDD of Ag in $As_{33}S_{67}$ [82] was measured by means of depth-sensing microindentation using a Fischerscope H100 V microindentometer with the Vickers indentor tip. The hardness of the samples was measured in a load range of 10–30 mN. The maximum indentation depth was ca. 0.9 μm, which is about 40% of the film

thickness. The hardness of the glass substrate ($\sim$430 kg/mm^2) is much higher compared with the chalcogenide films which provides good conditions for the measurements. The hardness is load independent in the load range (10–30 mN), as is seen in Fig. 10.10. The elastic modulus, E, which is a measure of the elastic deformation of the materials evaluated from the load-relieving curve [91], was also determined (Fig. 10.10). The values of mechanical parameters such as Vickers hardness, H_v, and elastic modulus, E, increase with increasing silver content in $Ag_x(As_{0.33}S_{0.67})_{100-x}$ films (Fig. 10.10) up to the maximum, where $x = 25$ at.% Ag. This solid solution has a composition close to the stoichiometric one, i.e. $AgAsS_2$ [82].

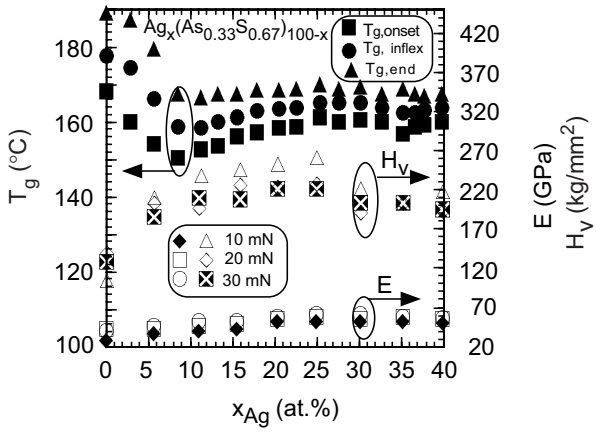

Figure 10.10: Glass transition temperature, T_g, Vickers hardness, H_v, and elastic modulus, E, vs. silver content in prepared Ag–As–S films [82].

The dependence of the glass transition temperature T_g (taken at three important points on the sigmoidal curve C_p versus T curve [92], namely, $T_{g,onset}$, $T_{g,inflex}$ and $T_{g,end}$), on the composition of the Ag/$As_{33}S_{67}$ [82] films is shown in Fig. 10.10. The glass transition temperature in all three datasets first decreases with increasing Ag concentration down to a local minimum at 10 at.% Ag, then T_g increases up to a local maximum at 25 at.% Ag. After that, T_g decreases again for Ag contents, exceeding 25 at.% Ag. Similar results were obtained in other systems (Fig. 10.11).

Because T_g, H_v, and E are structurally sensitive parameters [92], the measured thermal and mechanical properties also support the idea of an optically-induced solid-state reaction of silver with $As_{33}S_{67}$ films [82]. The silver atoms play a glass-forming role in the composition of $AgAsS_2$ and because they are three-fold coordinated, the structure of the glass is strengthened. The minimum at 10 at.% Ag on T_g vs. x_{Ag} curves is not fully understood. It could be phenomenologically described as due to a change in the role of silver from that of a glass modifier to a glass former. Alternatively, it can be related to the glass-formation region gap in the Ag–As–S system between 10 and 15 at.% of Ag described in melt-quenched bulk glasses. The role of silver as a glass modifier or maybe as a depolymerizer is evident from the Raman spectra [82] (Fig. 10.12) for an Ag concentration of about 10 at.%.

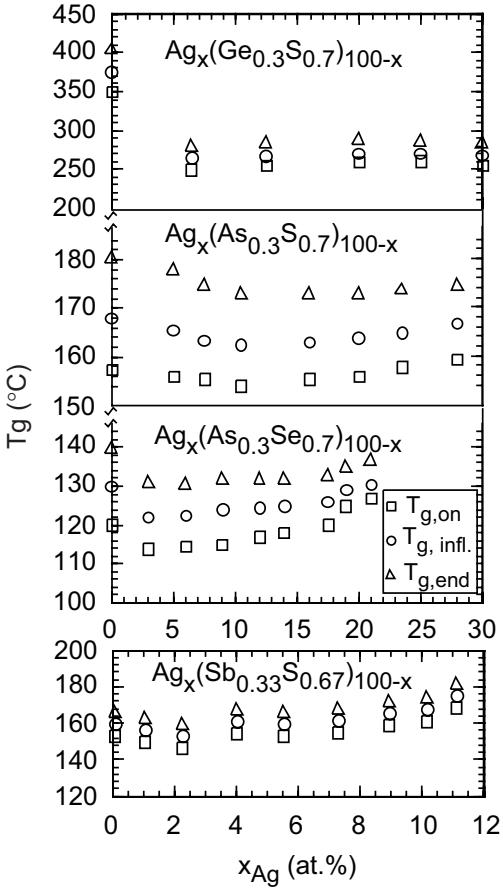

Figure 10.11: Glass transition temperature, T_g, vs. silver content in the different chalcogenide films prepared by the OIDD process, Ag–As–S. The experimental points in represent average values with typical errors bars smaller then the size of the plotted experimental points.

10.4.3 Structure

Optically induced diffusion and dissolution of metals results in changes of structure of the optically-doped chalcogenide films. Such changes of structure were identified by several methods, e.g. EXAFS [65, 66]. Four-fold coordination of Cu atoms was found in As_2Se_3 glass [93] and also in the As_2S_3 glass [94] with low Ag concentrations. For higher concentration of Ag in chalcogenide glasses, silver atoms were found to be three-fold coordinated in Ag–As–S [94], Ag–As–Se [95] and Ag–Ge–Se [96].

Far-IR spectroscopy of optically doped materials [26, 67] also proves the existence of Ag–S or Ag–Se bonds. Raman spectroscopy results described in [68] and applied to our recent Raman measurements for films of Ag–As–S, Ag–As–Se, Ag–Ge–S and Ag–Sb–S systems [82–85] verified and expanded the knowledge about the changes of structure due to

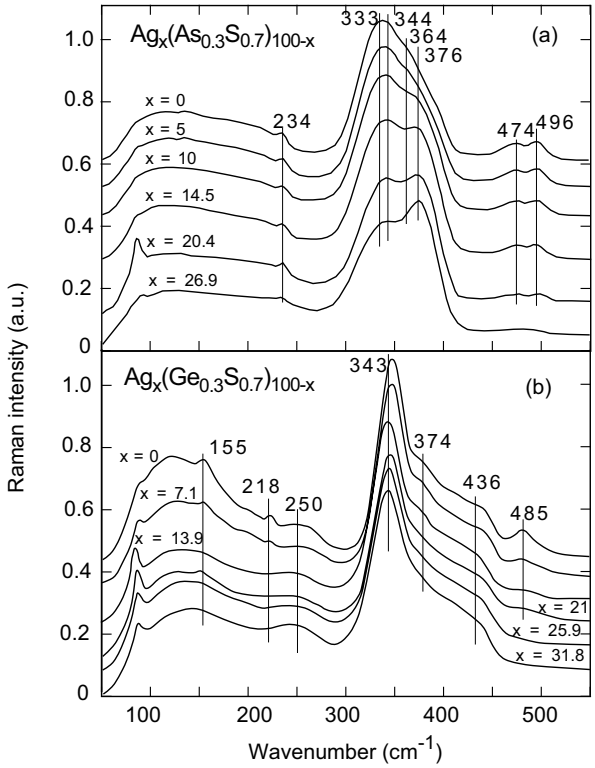

Figure 10.12: Raman spectra of Ag–As–S films (a) and Ag–Ge–S (b) prepared by the OIDD process.

OIDD (Figs. 10.12 and 10.13). The spectra of Ag–As–S films [82, 83] were interpreted using references [97–99]. The illuminated $As_{30}S_{70}$ film (Fig. 10.12a, $x = 0$) contains strong bands at 333, 344 ($AsS_{2/3}$ units) and 364 cm^{-1}(As_4S_4 units), and also weak bands at 474 and 496 cm^{-1}(S_8 rings or S ring fragments), respectively. The consequent step-by-step silver photodoping leads to the appearance of a new strong band at 376 cm^{-1}(AsS_3 pyramids connected by an S–Ag–S linkage), and to a decrease of intensities of the main bands and weak bands described for $As_{30}S_{70}$ film, S_8 rings or S ring fragments included (Fig. 10.12a, curves from $x = 0$ to $x = 27$ at.%).

The Raman spectra measured in Ag–Ge–S [46] films are shown in Fig. 10.12b. The spectra were interpreted using references [100–103]. The $Ge_{30}S_{70}$ film (Fig. 10.12b) contains strong bands at 343 cm^{-1} (units $GeS_{4/2}$, corner sharing type [102]), 374 cm^{-1}and 436 cm^{-1} ($GeS_{4/2}$ units, edge sharing type [102]), and also a weak band at 250 cm^{-1}($GeS_{4/2}$ units, ethane-like type "ETH" [102]), and at 485, 218 and 155 cm^{-1} (S_8 rings or S ring fragments), respectively. The consequent step-by-step silver photodoping leads to an increase of intensity of the Raman band at 250 cm^{-1} (GeS_4, ETS units), and to a decrease of intensities of the main bands 374 and 436 cm^{-1} ($GeS_{4/2}$, edge-sharing units), and the disappearance of the weak bands 485, 218 and 155 cm^{-1} assigned to S–S bonds (Fig. 10.12b, curves from $x = 0$

to $x = 31$ at.%).

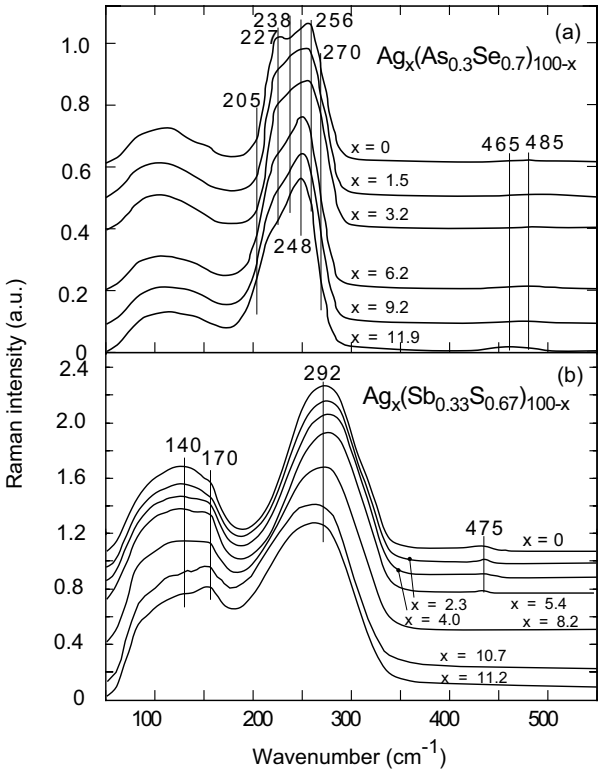

Figure 10.13: Raman spectra of Ag–As–Se films (a) and Ag–Sb–S (b) prepared by OIDD.

The results of Raman spectroscopy studied in Ag–As–Se [84] films are shown in Fig. 10.13a. The spectra were interpreted using references [104–106]. The $As_{30}Se_{70}$ film (Fig. 10.13a) contains strong bands at 227, 238, 256 and 270 cm^{-1} ($AsSe_3$ pyramids), multiple weak bands in the spectral region 50–180 cm^{-1} and a weak band at 485 cm^{-1}. A silver step-by-step concentration increase leads to the appearance of new strong bands at 248 and 205 cm^{-1}, which can be assigned to As-rich structural units (e.g. As_4Se_4), and to an increase of the main band intensity 238 cm^{-1} (development of the Se-chain vibration). The decrease of the 270 cm^{-1}band intensity and a further shift of the main vibration band from 256 to 248 cm^{-1} can be assigned to a decrease of Se "ring-like" unit and –Se–Se– unit vibrations.

The Raman spectra measured in Ag–Sb–S films [85] are shown in Fig. 10.13b. The spectra were interpreted using reference [107]. The illuminated $Sb_{33}S_{67}$ film (Fig. 10.13b, $x = 0$) contains a strong band at 292 cm^{-1}(units SbS_3), band at 170 cm^{-1} due to Sb–Sb vibrations in S_2Sb–SbS_2 units and also bands at 140 and 475 cm^{-1}(S ring fragments). The consequent step-by-step silver photodoping leads to a decrease of intensities of S–S unit bands and an increase of the intensity of the 170 cm^{-1} band and shift of the main band at 290 cm^{-1} to lower frequencies as shown in Fig. 10.13b (curves from $x = 0$ to 11.2).

Based on the observed results we conclude that silver can either form a bond with the S- or Se-chain end or it can break S–S or Se–Se bonds in chains or rings. Their disappearance during OIDD is clearly seen in the Raman spectra (Figs. 10.12 and 10.13).

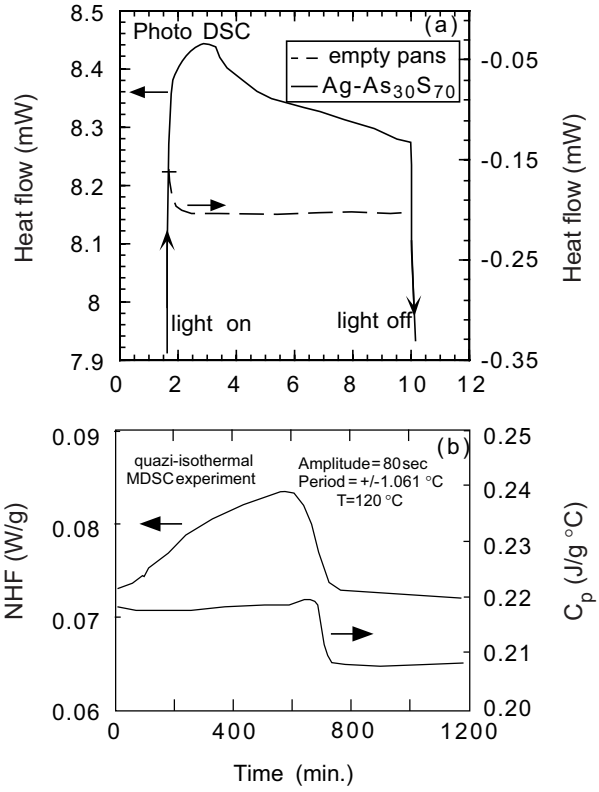

Figure 10.14: A typical photo DSC heat flow curve during obtained OIDD process in a sample of Ag/a-$As_{30}S_{70}$ (a) and typical quasi-isothermal modulated DSC non-reversing heat flow and heat capacity curves during TIDD in a sample of Ag/a-$As_{30}S_{70}$ (b) [60].

Raman spectroscopy together with the results obtained by other methods demonstrate that OIDD is a photo-induced solid-state reaction. The enthalpic changes connected with OIDD and TIDD were measured for the Ag/$As_{30}S_{70}$ system (Fig. 10.14) [60]. The enthalpy change could represent the Ag^+ ion formation or the formation of new Ag–S bonds (2 Ag + S = Ag_2S; $\Delta G^0_{298} = -19.9$ kJ/mol [8]), which is a part of the overall chemical reaction reaction, i.e. Ag + AsS_2 = $AgAsS_2$. Such a solid-state chemical reaction leads to the same reaction products as a high temperature synthesis of chalcogenide glasses by the melt-quenching technique [82].

10.5 Applications

The optically-induced diffusion and dissolution of metals in chalcogenide films has many potential applications in areas requiring the fabrication of high resolution or high aspect ratio surface relief or embedded structures such as gratings, microlenses, photonic bandgap devices and also for high-resolution optical recording. In view of the good transparency of these materials in the IR region, the technique is also suited to producing components for operation at IR wavelengths inclusive of optical switches. Various applications of this process are reviewed elsewhere in this book.

Acknowledgments

The authors acknowledge grants 203/02/0087 and 203/00/0085 from the Grant Agency of the Czech Republic, Research Center project LN00A028 of the Ministry of Education, Youth and Sports of the Czech Republic and the University of Saskatchewan, Canada (Prof. S. O. Kasap), for providing financial support for this project.

References

[1] Ke. Tanaka, Rev. Solid State Sci. **4**, 641 (1990).

[2] M. Cable and J.M. Parker (Eds.), High-Performance Glasses, Blackie, Glasgow, 1992.

[3] M. Frumar, Z. Polak, Z. Cernosek, B. Frumarova, and T. Wagner, Chem. Papers **51**, 310 (1997).

[4] A.V. Kolobov and Ka. Tanaka, Handbook on Advanced Electronic and Photonic Materials, Academic Press, New York, 2000.

[5] M.T. Kostyshin, E.V. Mikhajlovskaya, and P.F. Romanenko, Soviet Phys. Solid State **8**, 451 (1966).

[6] V.M. Lyubin and A.V. Kolobov, J. Non-Cryst. Solids **90**, 489 (1987).

[7] A.P. Firth, P.J.S. Ewen, and A.E. Owen, J. Non-Cryst. Solids **77–78**, 1153 (1985).

[8] T. Wagner, M. Frumar, and V. Suskova, J. Non-Cryst. Solids **128**, 197 (1991).

[9] A.V. Kolobov and S.R. Elliott, Adv. Phys. **40**, 625 (1991).

[10] Ke. Tanaka, J. Non-Cryst. Solids **170**, 27 (1994).

[11] J. Eneva, A. Gushterov, B. Tomerova, and B. Mednikarov, J. Mat. Sci.: Mat. Electron. **10**, 529 (1999).

[12] T. Wagner, G. Dale, P.J.S. Ewen, A.E. Owen, and V. Perina, J. Appl. Phys. **87**, 7758 (2000).

[13] T. Kawaguchi and S. Maruno, J. Appl. Phys. **77**, 628 (1995).

[14] T. Kawaguchi, S. Maruno, and S.R. Elliott, J. Appl. Phys. **79**, 9096 (1996).

[15] T. Kawaguchi and S. Maruno, Jpn. J. Appl. Phys. **33**, 6470 (1994).

[16] T. Wagner, M. Frumar, S.O. Kasap, Mir. Vlcek and Mil. Vlcek, J. Optoelectr. Adv. Mat. **3**, 227 (2001).

[17] S.R. Ovshinsky, Applications of Non-Crystalline Materials, in Insulating and Semiconducting Glasses, Series on Directions in Condensed Matter Physics, Vol. 17, P. Boolchand (Ed.), World Scientific, Singapore, 2000.
[18] T. Ohta, J. Optoelectr. Adv. Mat. **3**, 609 (2001).
[19] E. Robinel, B. Carette and M. Ribes, J. Non-Cryst. Solids **57**, 49 (1983).
[20] M. Mitkova and M.N. Kozicki, J. Non-Cryst. Solids **299**, 1023 (2002).
[21] P. Nagels, L. Tichy, R. Mertens, and R. Callaerts, Mat. Lett. **46**, 234 (2000).
[22] D.I. Florescu and R.L. Cappelletti, J. Non-Cryst. Solids **246**, 150 (1999).
[23] M. Bruns, H. Klewe-Nebenius, G. Pfennig, E. Bychkov, and H.J. Ache, Surf. Coat. Technol. **97**, 707 (1997).
[24] G.C. Chern and I. Lauks, J. Appl. Phys. **54**, 2701 (1983).
[25] E. Hajto, P.J.S. Ewen, P.G. Hill and A.E. Owen, phys. stat. sol. (a) **114**, 587 (1989).
[26] T. Wagner, M. Vlcek, V. Smrcka, P.J.S. Ewen, and A.E. Owen, J. Non-Cryst. Solids **164–166**, 1255 (1993).
[27] T.I. Kosa, T. Wagner, P.J.S. Ewen, and A.E. Owen, Phil. Mag. B **71**, 311 (1995).
[28] T. Wagner, T. Kohoutek, Mir. Vlcek, Mil. Vlcek, M. Munzar, and M. Frumar, Physicochemical properties and structure of the $Ag_x(As_{0.33}S_{0.67})_{100-x}$ films prepared by spin-coating technique, in Proceedings XIIIth Int. Symp. On Non-Oxide Glasses and New Optical Glasses, Vol. 1, M. Frumar, P. Nemec, T. Wagner, B. Frumarova, E. Cernoskova (Eds.), University of Pardubice, Pardubice, 2002, p. 157–160.
[29] J. Fernandez-Pena, J.B. Ramirez-Malo, J.J. Ruiz-Perez, C. Corrales, E. Marquez, P. Villares and R. Jimenez-Garay, J. Non-Cryst. Solids **196**, 173 (1996).
[30] T. Wagner, M. Frumar and L. Benes, J. Non-Cryst. Solids **90**, 517 (1987).
[31] P.J.S. Ewen, A. Zakery, A.P. Firth, and A.E. Owen, Phil. Mag. B **57**, 1 (1988).
[32] T. Wagner, M. Vlcek, K. Nejezchleb, M. Frumar, V. Zima, V. Perina, and P.J.S. Ewen, J. Non-Cryst. Solids **198 & 200**, 744 (1996).
[33] E. Marquez, R. Jimenez-Garay, A. Zakery, P.J.S. Ewen, and A.E.Owen, Phil. Mag. B **63**, 1169 (1991).
[34] E. Marquez, J. Fernandez-Pena, J.M. Gonzalez-Leal, and R. Jimenez-Garay, Mat. Lett., **25**, 143 (1995).
[35] D. Goldschmidt and P.S. Rudman, J. Non-Cryst. Solids **22**, 229 (1976).
[36] T. Wagner, E. Marquez, J. Fernandez-Pena, J.M. Gonzales, P.J.S. Ewen, and S.O. Kasap, Phil. Mag. B **79**, 223 (1999).
[37] T. Yaji, and S. Kurita, J. Appl. Phys. **54**, 647 (1983).
[38] M.T. Kostyshin and Y.V. Ushenin, Fiz. Tekh. Poluprovodn. **16**, 119 (1982)
[39] E. Inoue, H. Kokado and I. Shimitsu, Oyo Butsuri **43**, 101 (1974).
[40] T. Shirakawa, I. Shimizu, H. Kokado, and E. Inoue, J. Photogr. Sci. Eng. **19**, 139 (1975).
[41] H. Kokado, I. Shimizu, and I. Inoue, J. Non-Cryst. Solids **20**, 131 (1976).
[42] R. Ressel, G. Kluge, and P. Suptitz, J. Non-Cryst. Solids **97–98**, 1247 (1987).
[43] T. Yaji and S. Kurita, J. Appl. Phys. **54**, 647 (1983).
[44] J.M. Oldale, J.H.S. Rennie, and S.R. Elliott, Thin Solid Films **164**, 467 (1988).
[45] M. Krbal, MSc Thesis, University of Pardubice, 2002.

[46] T. Wagner, J. Optoelectr. Adv. Mat. 4, 717 (2002).
[47] J. Malinovski and A. Buroff, Contemp. Phys. **19**, 99 (1978).
[48] G. Kluge, Phys. Stat. Sol.(a) **101**, 105 (1987).
[49] T. Wagner and M. Frumar, J. Non-Cryst. Solids **116**, 269 (1990).
[50] S.R. Elliott, J. Non-Cryst. Solids **137–138**, 1031 (1991).
[51] K. Tanaka and H. Sanjoh, Defect and Diffusion Forum, **95–98**, 1213 (1993).
[52] I.Y. Indutnyi, V.A. Danko, A.A. Kudryatsev, F.V. Michailovskaya and V.I. Minko, J. Non-Cryst. Solids **185**, 176 (1995).
[53] M. Aniya, J. Non-Cryst. Solids **198–200**, 762 (1996).
[54] A.V. Kolobov, H. Oyanagi, Ka. Tanaka and Ke. Tanaka, Phys. Rev. B **55**, 726 (1997).
[55] H. Fritzsche, The Chemical Bonding of Silver Photodissolved in Chalcogenide Glasses, in Homage Book – Andrei Andriesh, M. Popescu (Ed.), INOE & INFM Publishing House, Bucharest, 1999.
[56] V.V. Poborchii, A.V. Kolobov, and K. Tanaka, Appl. Phys. Lett. **74**, (1999)
[57] H. Schmalzried, Solid State Reactions, Academic Press, New York, 1974.
[58] Ke. Tanaka, J. Non-Cryst. Solids **137–138**, 1021 (1991).
[59] G.A. Holmquist and J.A. Pask, J. Am. Ceram. Soc. **62**, 183 (1979).
[60] T. Wagner, A. Mackova, V. Perina, E. Rauhala, A. Seppaala, S.O. Kasap, M. Frumar, Mir. Vlcek, and Mil. Vlcek, J. Non-Cryst. Solids **299–302**, 1028 (2002).
[61] G. Dale, A.E. Owen, and P.J.S. Ewen, Metal-photodissolution in Amorphous Semiconductors of the As–S System, in Proceedings of the NATO Advanced Research Workshop on Physics and Applications of Non-Crystalline Semiconductors in Optoelectronics, 3. High Technology, Vol. 36, A. Andriesh, M. Bertolotti (Eds.), Kluwer Academic Publishers, Dordrecht.
[62] T. Wagner, Assoc. Prof. Thesis, University of Pardubice, 2000.
[63] Y. Kawamoto and M. Nishida, Phys. Chem. Glasses **18**, 19 (1977).
[64] S.R. Elliott, Physics of Amorphous Materials, Longman, New York, 1990.
[65] J.M. Oldale, J.H.S. Rennie, and S.R. Elliott, Thin Solid Films **164**, 467 (1988).
[66] A.T. Steel, G.N. Greaves, A.P. Firth, and A.E. Owen, J. Non-Cryst. Solids **107**, 155 (1989).
[67] L. Jun, J.J. Videau, B. Tanguy, J. Portier, J.M. Reau, and P. Hagenmuller, Mater. Res. Bull. **23**, 1315 (1988).
[68] A.P. Firth, PhD. Thesis, University of Edinburgh, 1985.
[69] T. Wagner, M. Vlcek, S.O. Kasap, Mil. Vlcek, and M. Frumar, J. Non-Cryst. Solids **284**, 168 (2001).
[70] S.A. Lis and J.M. Lavine, Appl. Phys. Lett. **42**, 673 (1983).
[71] H.-Y Lee, J.-K. Kim, and H.-B. Chung, J. Non-Cryst. Solids **279**, 209 (2001).
[72] M.S. Chang, J. Vac. Sci. Technol. **16**, 1973 (1979).
[73] T. Suzuki, phys. stat. sol. (a) **72**, K165 (1982).
[74] H. Mizuno, Ke. Tanaka, and M. Kikuchi, Solid State Commun. **12**, 999 (1973).
[75] B.I. Boltaks, I.D. Dzafarov, and V.C. Kudojarova, Rus. Phys. Techn. Semiconductors **13**, 41 (1979).

[76] R. El Ghrandi, J. Calas, G. Galibert and M. Averous, Thin Solid Films **218**, 259 (1992).

[77] J. Saarilahti and E. Rauhala, Nucl. Instrum. Methods B **64**, 734 (1992).

[78] Y. Yamamoto, T. Itoh, Y. Hirose, and H. Hirose, J. Appl. Phys. **47**, 3603 (1976).

[79] D. Goldschmidt, T. Bernstein, and P.S. Rudman, phys. stat. sol. (a) **41**, 283 (1977).

[80] J. Rennie, S.R. Elliott, and C. Jeynes, Appl. Phys. Lett. **48**, 1430 (1986).

[81] J. Calas, R. El Ghardi, G. Galibert, and A. Traverse, Nuclear Instrum. Methods Phys. Res. B **63**, 462 (1992).

[82] T. Wagner, S.O. Kasap, Mir. Vlcek, M. Frumar, P. Nesladek, and Mil. Vlcek, Appl. Surf. Sci. **175–176**, 117 (2001).

[83] T. Wagner, V. Perina, A. Mackova, E. Rauhala, A. Seppala, Mir. Vlcek, S. O. Kasap, Mil. Vlcek, and M. Frumar, Solid State Ionics **141–142**, 387 (2001).

[84] T. Wagner, M. Frumar, Mir. Vlcek, S.O. Kasap, and Mil. Vlcek, Int. J. Inorg. Mat. **3**, 497 (2001).

[85] T. Wagner, J. Gutwirth, M. Krbal, Mir. Vlcek, Mil. Vlcek, and M. Frumar, Ag–Sb–S Amorphous Chalcogenide Thin Films Prepared by Photo-Induced Dissolution of Silver – Prospective Materials for Rewritable Optical Memories, in Proceedings XIIIth Int. Symp. on Non-Oxide Glasses and New Optical Glasses, Vol. 1, M. Frumar, P. Nemec, T. Wagner, B. Frumarova, and E. Cernoskova (Eds.), University of Pardubice, Pardubice, 2002, p. 394–397.

[86] E. Marquez, T. Wagner, J.M. Gonzalez-Leal, R. Jimenez-Garay, P.J.S. Ewen, J. Non-Cryst. Solids **274**, 62 (2000).

[87] M. Yamaguchi, I. Shimizu, and E. Inoue, J. Non-Cryst. Solids **47**, 341 (1982).

[88] A.V. Kolobov, S.R. Elliott, and A.T. Steel, Phys. Rev. B **41**, 9913 (1990).

[89] A. Feltz, Amorphous Inorganic Materials and Glasses, VCH, Weinheim, 1993.

[90] T.I. Kosa, R. Rangel-Rojo, E. Hajto, P.J.S. Ewen, A.E. Owen, A.K. Kar, and B.S. Wherrett, J. Non-Cryst. Solids **164–166**, 1219 (1993).

[91] H.-H.Behncke, VDI Berichte **33**, 1194 (1995).

[92] T. Wagner and S.O. Kasap, Phil. Mag. B **74**, 667 (1996).

[93] S.H. Hunter, A. Bienenstock, and T.M. Hayes, in Amorphous and Liquid Semiconductors, W.E. Spear (Ed.), Centre for Industrial Consultancy and Liaison, University of Edinburgh, 1976.

[94] I.T. Penfold and P.S. Salmon, Phys. Rev. Lett. **64**, 2164 (1990).

[95] C.J. Benmore and P.S. Salmon, J. Non-Cryst. Solids **156–158**, 720 (1993).

[96] R.J. Dejus, S. Susman, K.J. Volin, D.G. Montague, and D.L. Price, J. Non-Cryst. Solids **143**, 162 (1992).

[97] G. Lukovski, F.L. Geils, and R.C. Keezer, The Structure of Non-Crystalline Materials, Taylor and Francis, London, 1977.

[98] A.P. Firth, A.E. Owen, and P.J.S. Ewen, The Structure of Non-Crystalline Materials, Taylor and Francis, London, 1983.

[99] T. Wagner, S.O. Kasap, M. Vlcek, A. Sklenar, and A. Stronski, J. Mat. Sci. **33**, 5581 (1998).

[100] G. Lucovski, F.L. Galeener, R.C. Keezer, R.H. Geils, and H.A. Six, Phys. Rev. B **10**, 5134 (1974).

[101] A. Sklenar, M. Vlcek, and P. Bezdicka, in Proceedings of the 5th ESG Conference "Glass Science and Technology For 21st Century", A. Helebrant, M. Maryska, and S. Kasa (Eds.), Czech Glass Society, Prague, 1999, CI–99.

[102] K. Jackson, A. Briley, S. Grossman, D.V. Porezag and M.R. Pederson, Phys. Rev. B **60**, R14985 (1999).

[103] H. Takebe, H. Maeda and K. Morinaga, J. Non-Cryst. Solids **291**, 14 (2001).

[104] G. Lukovski and R.M. Martin, J. Non-Cryst. Solids, **8–10**, 185 (1972).

[105] T. Mori, S. Onari, and T. Arai, Jpn. J. Appl. Phys. **19**, 1027 (1980).

[106] P. Nagels, E. Sleeckx, R. Callaerts, and L. Tichy, Solid State Commun. **94**, 49 (1995).

[107] I. Watanabe, S. Noguchi, and T. Shimizu, J. Non-Cryst. Solids **58**, 35 (1983).

11 Photo-Induced Deposition of Silver Particles on Amorphous Semiconductors

Takeshi Kawaguchi

11.1 Introduction

Glasses which contain chalcogen elements (S, Se, Te) as a constituent are called "chalcogenide glasses or chalcogenide amorphous semiconductors". A wide variety of photo-induced phenomena have been discovered in these glasses and amorphous films and numerous studies on the phenomena are now in progress [1, 2].

Ion-conducting glasses, containing a metallic element, can exhibit ionic conduction of the metal at room temperature. In the case of silver, for example, the Ag atoms usually exist in the glass as ions with the valence of +1. When an electric field is applied to the glass, the Ag^+ ions migrate toward the negative electrode and an ionic current flows through the glass. Chalcogenide glasses containing more than 5 at.% Ag are an example of ion-conducting glasses [3]. Ag-rich glasses with Ag content above 30 at.% exhibit a marked ionic conduction of Ag (superionic conductors) [4]. These glasses exhibit several unique photo-induced phenomena, a major role in which belongs to Ag^+ ions [5, 6].

Photodoping (or photodissolution) of metallic Ag into chalcogenide glasses is the best known photo-induced phenomenon accompanied by the long-range movement of Ag^+ ions [7]. Photodoping is observed in samples in which the chalcogenide glass is in contact with an Ag layer. The Ag atoms dissolve into the glass and move into its interior as Ag^+ ions during illumination (light with a photon energy equal to the bandgap of the glass is usually effective). A similar process may also be induced by heat treatment (thermal doping) but the rate is much lower than that of photodoping. The depth profiles of the doped Ag atoms are also different in the cases of photodoping and thermal doping. The light absorbed in the glass affects the diffusion process of Ag^+ ions and enhances the diffusion rate. The Ag photodoping process is a photochemical reaction, producing e.g., an Ag–As–S glass ($\sim$25 at.% Ag) from Ag and As–S glass. According to Elliott [8] and Tanaka [9], the Ag–As–S glass is a mixed ion–electron (hole) conductor and the electronic properties are essential in order to understand the photodoping mechanism.

Ag-rich chalcogenide glasses containing more than 30 at.% Ag have long been studied for applications as solid-state electrolytes for batteries, since they exhibit a marked ionic conduction [4]. In 1975, Maruno and Kawaguchi [10] reported that Ag-rich Ag–As–S glasses exhibit a phenomenon opposite to photodoping. When the bandgap light illuminates the surface, a large number of fine particles are deposited in the illuminated region. The particles are pure metallic silver and are formed from Ag^+ ions in the glass. This phenomenon is referred to as

"photo-induced surface deposition" (PSD) of silver. The PSD phenomenon is a purely optical phenomenon and any thermal effects are secondary [11].

In 1993, Tanaka et al. [12] reported that Ag–As–S glass with 25 at.% Ag exhibits a photo-induced phenomenon which they referred to as "photo-induced chemical modification" (PCM). The Ag concentration increases under illumination by the bandgap light ($25 \rightarrow \sim 30$ at.%). Since the increase is caused by Ag^+ migration from the dark region to the illuminated region in a sample, the PCM phenomenon seems to be similar to the PSD phenomenon. However, no deposition of Ag particles occurs and the PCM process is reversible without annealing [13].

Figure 11.1 illustrates a comparison of the Ag photodoping, PCM and PSD phenomena. These phenomena are due to the long-range movement of Ag^+ ions under illumination but the direction of the ionic migration is opposite between photodoping and the other two effects, as shown by the arrows in the figure.

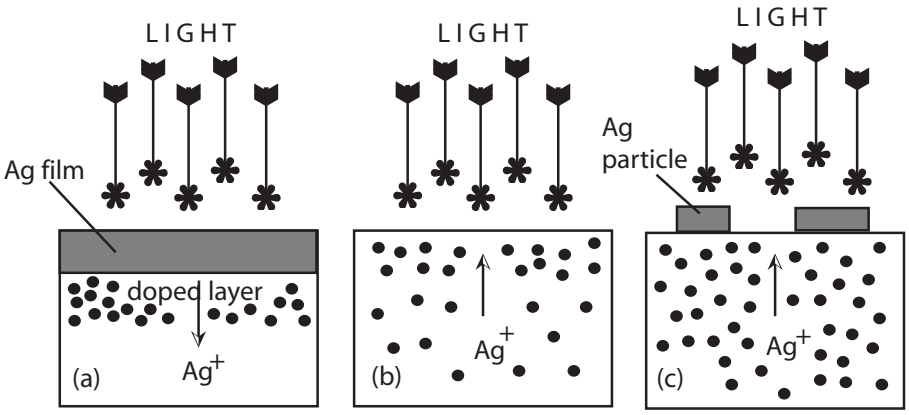

Figure 11.1: Comparison of (a) photodoping, (b) photochemical modification (PCM) and (c) photo-induced surface deposition (PSD) phenomena. The arrow shows the direction of the Ag^+ migration. The small dots schematically represent the Ag concentration.

The PSD phenomenon resembles a photochemical reaction of silver halide crystals in conventional photographic films but the basic process is different from the silver halide photographic process. Strangely, the electrical properties of the Ag-rich glasses (mixed ion–hole conductors) may also be responsible for the PSD process, although the Ag migration in the PSD effect is seemingly opposite to that in photodoping [14].

The segregation of Ag in the PSD process is due to the long-range movement of Ag^+ ions caused by illumination with the bandgap light. The ionic flow towards the illuminated surface is caused by the counterflow of photoexcited holes, since the mobility of electrons is negligibly small. This idea proves a unified concept for the photodoping, PSD and PCM phenomena [5, 6]. On the other hand, these phenomena can also be related to the thermodynamic metastability of glasses [5, 15]. The PSD phenomenon may be considered to be a photochemical reaction leading towards a thermodynamically more stable state caused by the segregation of excess Ag^+ ions [5].

The PSD phenomenon is potentially applicable in novel high-density rewritable optical recording devices. Direct positive patterning with high contrast can be obtained by photodeposited Ag particles [5]. The Ag pattern can be completely fixed by coating with a semitransparent metallic film such as Au [16]. The Ag deposits are less than 0.2 μm in diameter, i.e. the resolving power of the Ag pattern is superior to that of conventional photographic films [17]. Furthermore, the Ag pattern can be erased by annealing at temperatures below the glass transition temperature [18]. The processes of optical recording and thermal erasure can be successfully repeated for at least 20 cycles although the recovery after the thermal erasure gradually degrades with the number of repetitions [18].

Holographic and/or bit-by-bit Ag patterns can be recorded by photodeposited Ag nanoparticles on Ag-rich films. Recording is performed using a blue laser beam and for read-out of the signal a red or infrared laser beam is usually used [17]. If a simple optical system is required, very weak blue light can also be used as the probing light in the read-out process. If the Ag pattern is fixed by a semitransparent Au film, intense blue light can be used in both the recording and and read-out processes.

11.2 Photodeposited Ag Particles

The As-based bulk glasses were prepared by conventional melt-quenching from 1000 °C into water or ice-water. The surface of the glass was mechanically polished with alumina powder (0.3 μm diameter) and subsequently with AB MIROMET polishing compound (Buehler) [11].

The S(Se)-based films (100–700 nm thick) were prepared by co-evaporation of Ag metal and $Ge_{30}S(Se)_{70}$ glass fragments onto cleaned Pyrex glass or quartz glass substrates. The substrate temperature was usually maintained at 20 ± 2 °C by cooling with water. The Ag content of the films was evaluated from the thicknesses of the $Ge_{30}S(Se)_{70}$ and Ag films individually measured using two monitors, as reported [19]. In addition, the composition of the films was checked using an electron-probe microanalyzer (EPMA) with an energy-dispersive X-ray instrument (EDX) [19]. The Ag content determined by the monitor system was almost equal to that obtained by the EPMA analysis. The Ge content of the films was slightly greater than that of the raw $Ge_{30}S(Se)_{70}$ glasses, but this difference was within the experimental error of the EPMA analysis.

The PSD phenomenon was investigated using light from an ultrahigh-pressure Hg lamp (500 W) or Xe lamp (500 W) passing through an IR-cut filter. Illumination was usually made in air at room temperature. For the film samples, the chalcogenide surface was illuminated directly (i.e. not through the substrate).

Figure 11.2 shows SEM photographs of photodeposited Ag particles on (a) Ag-rich Ag–As–S bulk glass (hereafter, As-based glass) and (b) Ag-rich Ag–Ge–S amorphous film (hereafter, S-based film). In (a), the overall shape of Ag deposits is disc-like but on a finer scale each disc consists of an assembly of many dendrites growing radially. The profile was measured using a mechanical stylus instrument [11]. The profile suggests that the deposits stand out from the surface of the glass, as if they are adsorbed on the surface. The profile is approximately flat except around the center. The height of the flat part is 0.5–0.6 μm and is independent of the radial size of the deposits. In (b), the Ag deposits are pebble-like and are much smaller than those found on the As-based glass. It should be noted that all the deposits

consist of pure Ag polycrystallites with no preferred orientation [10]. The photograph (c) is an optical micrograph of the Ag pattern formed on an S-based film by Ag nanoparticles. It is a demonstration of an optical recording device using the PSD phenomenon (direct positive patterning). The contrast is very high because of the brilliant white color of the Ag deposits and the dark brown color of the Ag-rich chalcogenide film itself.

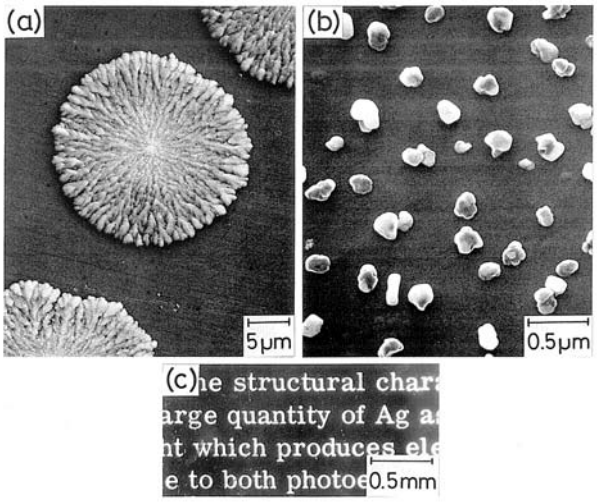

Figure 11.2: SEM photographs of photodeposited pure Ag particles on (a) bulk glass and (b) amorphous film. Light from an ultrahigh-pressure Hg lamp with an IR-cut filter illuminated the samples: (a) at an intensity of 200 mW/cm^2 for 15 min on $Ag_{45}As_{15}S_{40}$ bulk glass; (b) 80 mW/cm^2 for 2 min on $Ag_{65}(Ge_{0.3}S_{0.7})_{35}$ film. The optical microphotograph (c) shows an Ag pattern formed by Ag nanoparticles on $Ag_{60}(Ge_{0.3}S_{0.7})_{40}$ film by illumination (Xe lamp, 110 mW/cm^2, 3 min). In this study, the SEM photographs were usually taken with an acceleration voltage of 20 kV after carbon-coating the samples ($\sim$200 Å thick).

Figure 11.3 shows SEM photographs of (a) an as-prepared and (b) an illuminated S-based film and (c) an illuminated Ag-rich Ag–Ge–Se film (hereafter, Se-based film). The Ag deposits occur densely on the S-based film and sparsely on the Se-based film. The reason is due to the difference in Ag content of the films. The size and density (number per unit area) of the Ag deposits depend significantly on the composition of the sample (especially the Ag content), photon energy, intensity of light, illumination time, sample temperature and surface condition, atmosphere, etc. [5].

11.3 Compositional Dependence of Photodeposition

The compositional dependence of the PSD effect was examined for three kinds of systems: (i) $Ag_xAs_{60-x}S_{40}$ system ($35 \leq x \leq 45$) for As-based glasses, (ii) $Ag_x(Ge_{0.3}S_{0.7})_{100-x}$ system ($0 \leq x \leq 80$) for S-based films and (iii) $Ag_x(Ge_{0.3}Se_{0.7})_{100-x}$ system ($0 \leq x \leq 50$) for Se-based films [5].

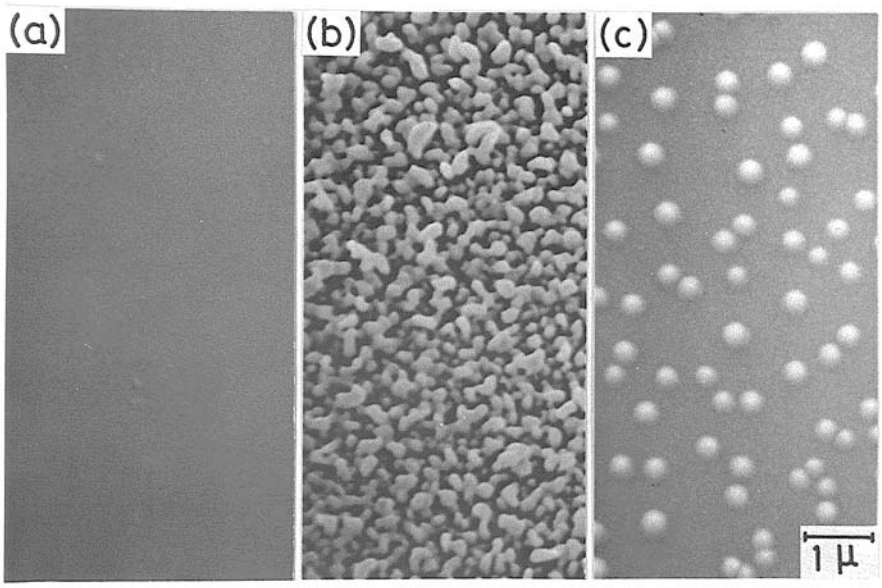

Figure 11.3: PSD phenomenon of $Ag_x(Ge_{0.3}S(Se)_{0.7})_{100-x}$ films [20]: (a) as-prepared S-based film ($x = 60$); (b) after illumination of (a); (c) illuminated Se-based film ($x = 35$). Illumination (Xe lamp, 110 mW/cm^2) was performed for (b) 5 and (c) 30 min.

Figure 11.4 shows the $Ag_xAs_{60-x}S_{40}$ system studied, together with the glass-forming region of the Ag–As–S system. The hatched area shows the region ($38 \leq x \leq 45$) in which the PSD phenomenon is effectively observed. Below 38 at.% Ag, the sample was a partially crystalline ($x = 25$) or phase-separated glass ($30 \leq x \leq 35$) [11]. Above 45 at.% Ag, the samples are partially crystalline, containing β-Ag_2S (acanthite) ($x = 50$). On the other hand, crystals of β-Ag_2S, Ag_3AsS_3 (xanthoconite, proustite), and Ag_7AsS_6 (billingsleyite) exhibit no PSD effect, even if the Ag content is larger than that of the glasses showing the PSD effect [11].

Similar results were obtained for the $Ag_x(Ge_{0.3}S(Se)_{0.7})_{100-x}$ systems [20]. In S-based glasses the PSD is effectively observed for $55 \leq x \leq 67$ while for Se-based glasses it is observed for $30 \leq x \leq 40$. The films with lower Ag content are amorphous but do not exhibit PSD effect. The films with higher Ag content are partially crystalline and also do not exhibit the PSD effect [20]. We thus conclude that the PSD phenomenon is only observed for amorphous films in a special region which is close to the maximum Ag content of the system.

Figure 11.5 shows the PSD phenomenon in As-based glasses ($35 \leq x \leq 45$). The SEM photographs suggest that the size of the Ag deposits increases with the Ag content, while their density (number per unit area) decreases. The Ag deposits in (c) and (d) possess a disc-like shape. The occurrence of the disc-shaped particles is confined to finely polished surfaces. If the surface is rough and/or polishing scratches are prevalent, the growth of Ag particles is affected significantly by the surface roughness and the scratches.

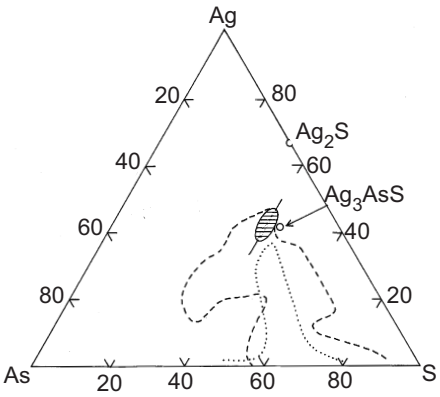

Figure 11.4: A phase diagram of the Ag–As–S system and the glass-forming region: dashed curve, the glass-forming region determined experimentally [34]; dotted curve, the glass-forming region predicted from condensed phase relation above 575 °C [35, 36]. The PSD effect in bulk glasses was examined in the $Ag_xAs_{60-x}S_{40}$ system. The hatched region represents the glasses which exhibit strong PSD effect [20].

The photosensitivity of the PSD effect is evaluated by the total amount of segregated Ag metal [11]. For the As-based glass, the total amount is obtained from the surface area occupied by the Ag deposits, since the height of the Ag deposits is almost constant (0.5–0.6 μm) irrespective of the radius. The total amount is also obtained from the area of the Ag(111) peak in the X-ray diffraction pattern using a suitable scaling [21]. The PSD effect of As-based glass appears at around 38 at.% Ag and the photosensitivity increases with increase in the Ag content of the sample up to the maximum Ag content (45 at.%) of the glass-forming region [21].

In the case of film samples, measurement of optical properties or X-ray diffraction are suitable for evaluation of the PSD photosensitivity rather than the method used for As-based glass, because the Ag deposits on the film samples are much smaller. In view of a possible application in an optical recording device, we have mainly used changes in the optical properties at 800 nm for evaluation of the PSD effect, since the X-ray diffraction method has considerable errors for low-sensitivity films [18].

Two methods are considered for the evaluation based on optical properties. One is the detection of a change in the reflectivity before and after the illumination, and the other makes use of a change in the transmission. The reflectivity method is not suitable in the present case, since the shape and orientation of photodeposited Ag particles are random and cannot be controlled. In contrast, the transmission method is useful, since the transmission change in the longer wavelength region depends only on the surface area occupied by the Ag deposits [16]. Thus, the PSD photosensitivity of film samples can be evaluated using the parameter $-\Delta T/T(0) = -[T(t) - T(0)]/T(0)$, where $T(t)$ is the transmission after illumination for time t.

The PSD effect of the S-based film appears at around 55 at.% Ag and the photosensitivity increases with Ag content up to the maximum Ag content (67 at.%) in the amorphous region.

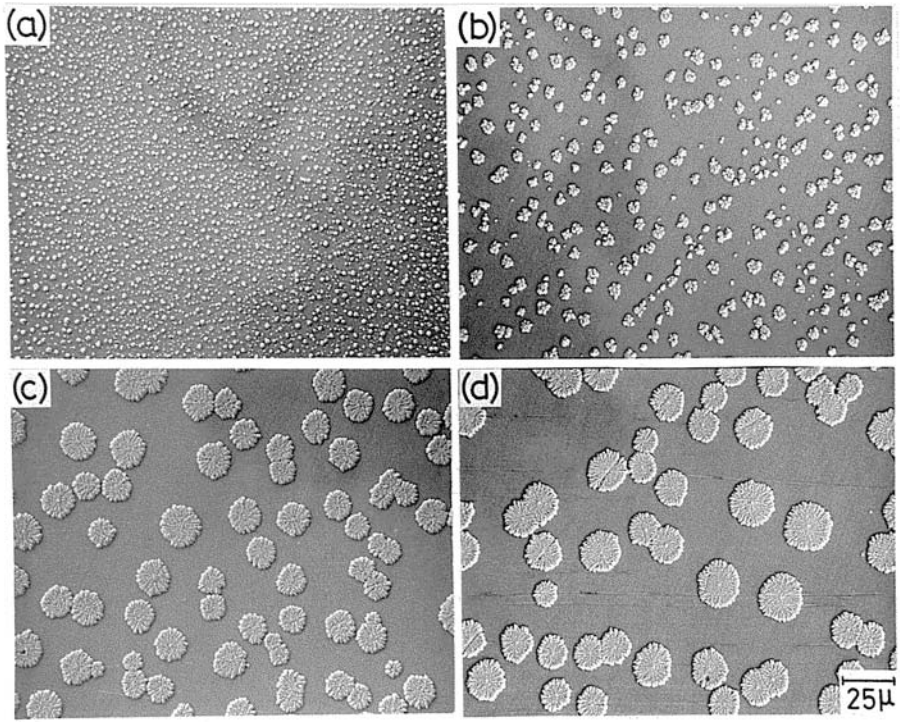

Figure 11.5: Compositional dependence of the PSD phenomenon for $Ag_xAs_{60-x}S_{40}$ bulk glasses [11]: $x =$ (a) 37.5; (b) 40; (c) 42.5; (d) 45. Illumination (Hg lamp, 110 mW/cm^2) was performed for 15 min at 21 °C.

The photosensitivity of Se-based films is very different from that of S-based films but the compositional trend against the As concentration is similar. For the film samples, the size and morphology of the Ag deposits do not depend significantly on the Ag concentration.

In summary, the PSD phenomenon is characteristic of Ag-rich glasses or amorphous films and the photosensitivity increases with increase in the Ag content. None of the related crystalline materials exhibit the PSD effect, even if the Ag content is sufficiently high. This point is essentially different from the photochemical reaction in conventional photographic films.

11.4 Effect of Light Intensity, Photon Energy and Temperature

The As-based bulk glasses are suitable for the study of the basic properties and the mechanism of the PSD phenomenon because of the large Ag deposits that are found. The sample with 45 at.% Ag was mainly used for this study, since the PSD effect is the most sensitive and the photodeposited Ag particles are the largest in this glass.

Figure 11.6 shows the change in morphology of the Ag deposits as a function of the intensity of the illumination light. In (a) and (b), the disc-like deposits are seen and their size decreases with increasing light intensity. In (c), which is representative of relatively large deposits, the peripheral region is higher than the central region, so that the particles have the appearance of a flower. Numerous small deposits are also observed between the flower-like deposits. The nucleation of small deposits seems to occur after the growth of the flower-like deposits.

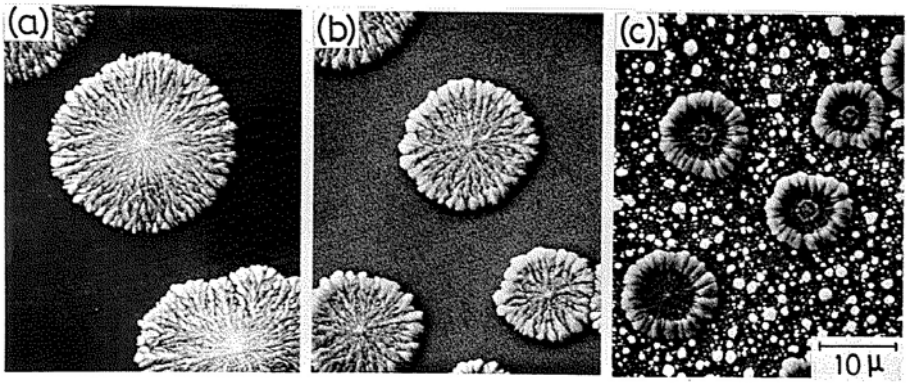

Figure 11.6: Effect of light intensity for $Ag_{45}As_{15}S_{40}$ bulk glass [11]. Illumination with light (Hg lamp) of (a) 80, (b) 200 and (c) 530 mW/cm^2 was performed for 15 min at 21 °C.

For various illumination times, a marked difference in density is not seen over all the intensity ranges. The nucleus formation of Ag deposits may be completed at an early stage of the illumination. The amount of Ag segregated by the PSD effect increases in proportion to the logarithm of the light intensity in the range 40–300 mW/cm^2, as does the optical density curve of photographic films [22].

A photon energy higher than the optical band gap is needed to induce PSD and the photosensitivity of the PSD effect increases with increase in the photon energy [23]. These results suggest that photoexcitation of electron–hole pairs is vital for the PSD to take place.

The effect of temperature on the PSD phenomenon was examined in a temperature range of 0 to 50 °C [11]. The temperature dependence of the size of the Ag deposits shows a maximum at around 30 °C, but the density decreases with increasing temperature. Thus, the photosensitivity, proportional to (density) × (area), shows a maximum at around 20 °C. The PSD effect could not be observed at low temperatures (e.g. 77 K) and at temperatures above 80 °C [11].

11.5 Erasing, Rewriting and Fixing of Ag Patterns

The As-based bulk glasses are not suitable for optical recording devices, because the Ag deposits are large and the photosensitivity is low. We have thus carried out basic research for applications using S-based films with 60–67 at.% Ag [18]. The photosensitivity of the PSD

effect in these films is much larger than that of the As-based glasses. The photodeposited Ag particles are less than 0.2 μm in diameter, i.e. smaller than the Ag particles found in conventional photographic films. Thus, it can be expected that the films are superior to photographic films in the resolving power of the Ag pattern; 200–300 nm thick S-based films with an Ag content of 60–65 at.% are optimal for applications in optical recording devices [24].

Figure 11.7 shows the alternate photodeposition and thermal erasure below the glass transition temperature (T_g) of Ag deposits. Figure 11.7(a) is an SEM photograph of an as-prepared S-based film. The particles in Fig. 11.7(b) are the Ag deposits resulting from the first illumination. In Fig. 11.7(c), the disappearance of the deposits can be recognized, but very small white particles and dark spots of relatively large size are observed. The white particles possibly are the residue of Ag deposits and the dark spots may be due to an inhomogeneous Ag distribution caused by the thermal erasing.

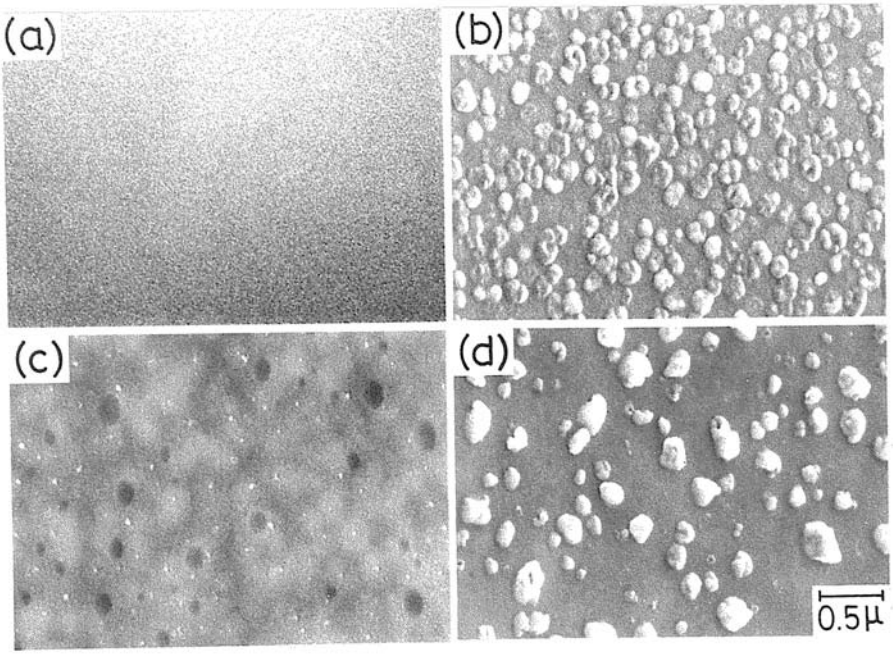

Figure 11.7: SEM photographs of as-prepared and variously treated $Ag_{61.5}(Ge_{0.3}S_{0.7})_{38.5}$ films [18]: (a) as-prepared film (1400 Å thick); (b) after the first illumination (Hg lamp, 160 mW/cm^2, 10 min, 20 °C); (c) after annealing of (b) (150 °C, 10 min, in Ar gas); (d) after illumination of (c) (Hg lamp, 160 mW/cm^2, 10 min, 20 °C)

The particles in Fig. 11.7(d) are the Ag deposits caused by the second illumination. They are larger in size and fewer in number than those in (b). The PSD effect in the second illumination seems to appear preferentially at the Ag-rich region and/or around the residual fine Ag particles on the erased sample. The increase in the particle size and the decrease in the number of particles with repetitions are not desirable for applications, since these quantities

are related to the resolving power of the Ag pattern. Further changes in the size and number are rarely observed for repetitions after the first cycle.

The PSD effect does not occur in the region overlaid by metallic films. This is illustrated in Fig. 11.8, which shows fixation of the Ag pattern by an overlaying semitransparent Au film. This suggests that the Ag pattern printed by PSD can be fixed by coating the sample surface with a semitransparent metallic film. Au film is the most suitable with respect to chemical stability. In fact, the fixation by the Au film was very effective and almost permanent under sunlight. No fixing effect was observed for electrically non-conducting films such as MgF_2 [16]. Thus, the mechanism of the suppression of PSD effect can be considered as follows [11]. The dendritic shape of Ag deposits shown in Fig. 11.2(a) suggests the existence of diffusion-limited growth associated with lateral diffusion of Ag^+ ions at the glass surface. The diffusion can be induced by the Coulomb force of the negatively charged Ag deposits, as discussed in Section 11.6.1. The metallic overlayer can lead to a constant surface potential, eliminating the surface fields, and thereby stopping the lateral surface diffusion of the Ag^+ ions.

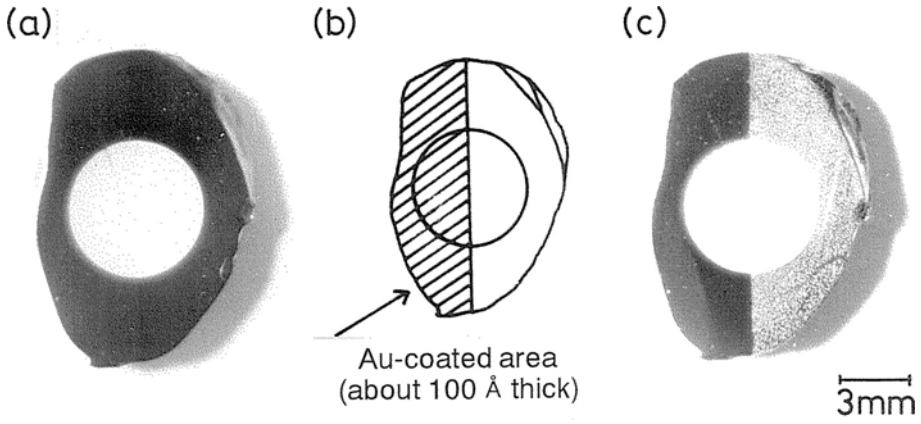

Figure 11.8: Fixation of Ag pattern by coating with a semitransparent Au film [16]. (a) A test sample; a white circular pattern was recorded at the center of $Ag_{45}As_{15}S_{40}$ bulk glass by the PSD effect. Then, the left side of the sample was coated with Au film, as illustrated in (b). (c) A test sample after exposure to Hg lamp light of 30 mW/cm^2 for 2 h. The color of the uncoated region (right side) changed from black to white due to the PSD effect, while no change was observed for the coated region (left side).

11.6 Mechanism of Photodeposition

The formation of Ag particles by illumination in the PSD phenomenon resembles the photochemical reaction in conventional photographic films. In the case of photographic films, the formation of Ag particles on AgBr(Cl) crystals is induced by photoexcited electrons trapped at the crystal surface [25]. The theory is based on the fact that the crystals are n-type for electronic conduction (the mobility of electrons is larger than that of holes). However, the glasses exhibiting the PSD effect are p-type semiconductors [11]. This difference in the electronic conduction may be essential in understanding the mechanism of the PSD effect.

On the other hand, for the Ag photodoping phenomenon, Ag^+ ions move in the doped region, whose composition is close to $AgAsS_2$ for the Ag/As–S system [7]. Since the doped region is a p-type semiconductor, a new idea has been proposed for explaining the Ag^+ migration, viz. a counterflow of Ag^+ ions in the direction opposite to the motion of the photoexcited holes [8, 9]. In addition, Tanaka et al. [12] observed a photo-induced chemical modification (PCM) phenomenon in $AgAsS_2$ glass, and this effect has been explained by the same concept as that for photodoping. The photoelectro-ionic interaction in Ag-rich glasses may also be responsible for the PSD phenomenon, even if the direction of ion flow in PSD is seemingly opposite to that in photodoping.

11.6.1 Photoelectro-Ionic Processes

The photodeposited Ag particles were found to be negatively charged under illumination [14]. This result fits very well into the explanation of the crystal growth of the Ag particles – Ag^+ ions are attracted by the Coulomb force of the negatively charged Ag deposits. However, it was still unclear why the Ag deposits acquire a negative charge under the illumination. To study this problem, we examined the difference in the photovoltaic effect when Ag and Au electrodes were used [23].

Figure 11.9(a) shows the sample configuration and the illuminated area. A small electrode ($\sim$0.5 mm in diameter and $\sim$500 Å thick), simulating an Ag deposit, was prepared on the glass surface by evaporation in vacuum. A back counter-electrode covered the opposite surface. Figure 11.9(b) shows the time dependence of the photovoltage of a small Ag electrode with respect to the Ag back counter electrode (Ag–Ag electrodes). The corresponding result for Au–Au electrodes is shown in Fig. 11.9(c). The photovoltage for the Ag–Ag electrodes is negative and seems to saturate at a negative value under illumination. This may support the fact that the Ag deposits are negatively charged under illumination. In contrast, the photovoltage for the Au–Au electrodes is positive and decays rapidly. The polarity of the photovoltaic effect is related to the energy-band bending of the glass in contact with Ag and Au electrodes (the electronic bands in the p-type glass bend downward for contact with Ag and upward for contact with Au (the work function is 4.3 eV for Ag and 5.1 eV for Au [26])). The time dependence of the magnitude is associated with the migration of Ag^+ ions under illumination.

For the crystal growth of Ag deposits in the PSD phenomenon, it may be essential that the Ag particles are negatively charged under illumination. The Ag^+ migration under the illuminated surface could then be due to the Coulomb force caused by the negatively-charged Ag particles, in a similar way to the formation of Ag clusters on n-type AgBr(Cl) photographic crystals.

However, the effect of the Coulomb force is limited to a depth of $\sim$1 μm (corresponding to the optical absorption depth, α^{-1}) from the illuminated surface, since in deeper regions, the force is be screened by the holes diffused into the interior of the glass (Fig. 11.10). If the Ag^+ migration is induced only by the Coulomb force, the amount of Ag metal segregated by PSD (much greater than that in photographic crystals) suggests that the Ag concentration at the illuminated surface should decrease strongly following the photodeposition.

In order to investigate the consumption of Ag^+ ions in the glass by PSD, the depth profile of the Ag concentration was measured from the illuminated surface to $\sim$50 μm depth, using a sample of As-based glass (45 at.% Ag) cross-sectioned after sufficient photodeposition [23].

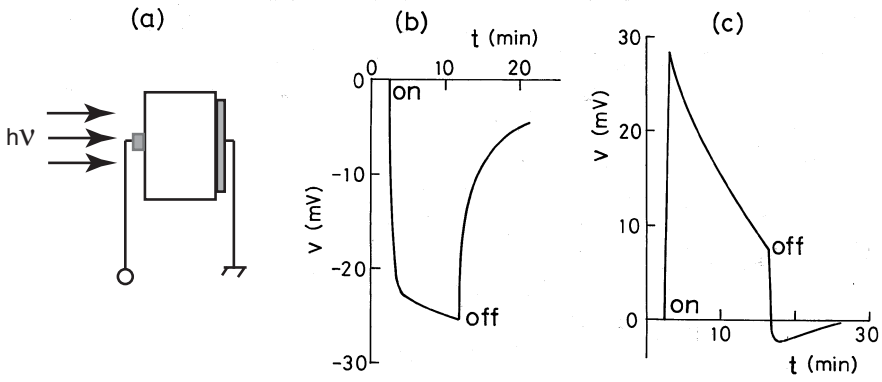

Figure 11.9: Photovoltaic effect of $Ag_{45}As_{15}S_{40}$ bulk glass measured by means of a small metal electrode [23]. (a) Illustration of the sample configuration and illuminated area. The small electrode is ∼0.5 mm in diameter and ∼500 Å in thickness. (b) The voltage of a small Ag electrode measured against the back counter electrode of an Ag film (Ag–Ag electrodes). (c) Data obtained for Au–Au electrodes. The experiments were done under illumination by 10 mW/cm^2 light Hg lamp at 20 °C.

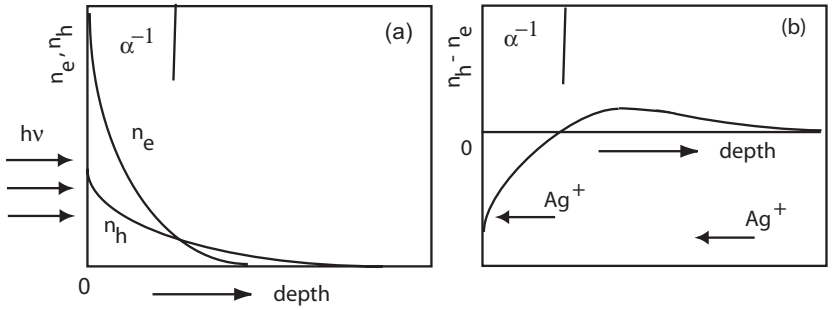

Figure 11.10: (a) Schematic steady-state distribution of photoexcited electrons (n_e) and holes (n_h) in p-type glasses ($\mu_h > \mu_e$, where μ_h and μ_e are the mobilities of holes and electrons) [23]. (b) The electric potential induced by this distribution [proportional to $(n_h - n_e)$]. α^{-1}represents the region (∼1 μm in depth) within which most incident photons are absorbed.

The analysis was carried out by an electron-probe microanalyzer with an energy-dispersive X-ray instrument. Accumulation of Ag^+ ions by the electron-beam irradiation was scarcely detected during the analyses, since the sample was coated with a ∼200 Å thick carbon film.

Under the glass surface that is not covered by the Ag deposits, the depth profile of Ag concentration was almost constant (∼45 at.%) throughout the sample depth and very different from the profile which might be expected if the Ag-ion movement were only caused by the Coulomb force due to the negatively-charged Ag deposits (cf. Fig. 11.3 in Ref. [23]). Furthermore, the Ag concentration under the Ag deposits was also constant at ∼45 at.% over the depth. The constant depth profile suggests that the Ag^+ migration in the PSD process may occur even in regions deeper than ∼1 μm (the penetration depth of the ∼700 nm light).

Since the glass is a p-type semiconductor, it may be considered that the Ag^+ ions in the deep region move toward the illuminated surface to counterflow the hole motion, as illustrated in Fig. 11.10(b). Consequently, the Ag^+ migration in the PSD process can be accounted for both by the Coulomb force induced by the electrons localized at the illuminated surface and coupled ion–hole fluxes in the deeper region.

The photoexcitation of electron–hole pairs does not occur at the glass surface under the Ag deposits, since the incident light cannot penetrate the Ag deposits with a thickness of $\sim$0.5 μm. Thus, the Ag^+ migration in the PSD process may occur only at the surface which is not covered by the Ag deposits. The Ag^+ ions diffuse to the surface, come into contact with the negatively-charged Ag deposits, and change to Ag atoms ($Ag^+ + e^- \rightarrow Ag^0$). This idea can account for the preferential radial growth of the Ag deposits [11, 27] and also explain the suppression of the formation of Ag deposits by overlaying metallic film [11].

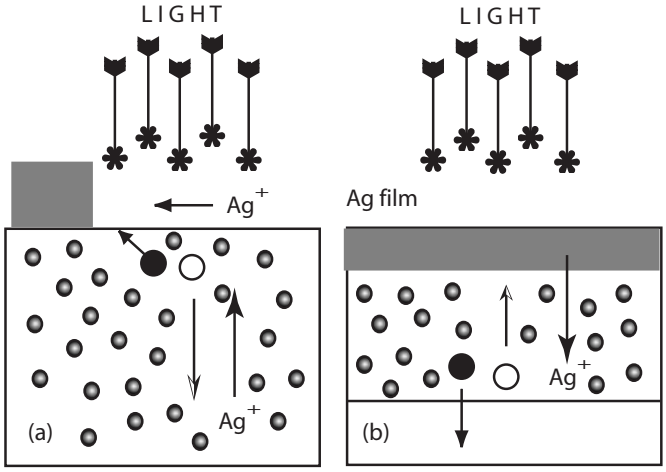

Figure 11.11: Schematic illustration of the mechanism of Ag^+ migration: (a) PSD phenomenon; (b) Ag photodoping. The solid and open circles represent the photoexcited electrons and holes, respectively. In both phenomena, the photoexcitation occurs in a region less than 1 μm from the illuminated surface. The region in (b) is enlarged for the depth direction.

The model proposed for the PSD process is illustrated in Fig. 11.11, together with a model for Ag photodoping. The PSD process can be described as the following steps:

(i) Photoexcitation of electron–hole pairs near the chalcogenide surface.

(ii) Diffusion of the holes into the interior of the glass.

(iii) Migration of Ag^+ ions toward the illuminated surface.

(iv) Formation of Ag nuclei on the surface.

(v) Crystal growth of the Ag nuclei.

The following points are essentially different from the photochemical reaction occurring in conventional photographic films. (i) The glasses showing the PSD effect are p-type semiconductors. (ii) The Ag^+ ions in the interior of glass can migrate in counterflow to the motion of the photoexcited holes. Thus, the amount of Ag metal segregated by PSD becomes much greater than that in photographic crystals.

For As-based glass (45 at.% Ag), the quantum efficiency of the PSD effect can be determined to be $\sim$1 % on average for the wavelength range from 300 to 600 nm [11]. This low efficiency may be ascribed, e.g. to recombination of the photoexcited electrons and holes.

11.6.2 Thermodynamic Aspect

The mechanism of Ag migration in the PSD process can be explained by diffusion of photoexcited holes, as for Ag photodoping and PCM phenomena. However, the following issues are still unclear. (i) Why does the PSD effect appear at very high Ag contents and why does it increase with the increasing Ag content? (ii) Why is the PSD phenomenon irreversible? (iii) Why can the photodeposited Ag particles be dissolved by annealing? (iv) Why does the temperature dependence of the PSD effect exhibit a maximum at around room temperature? These issues may be closely related to the thermodynamic properties of Ag-rich chalcogenide glasses [15].

In the case of photodoping in Ag/As_2S_3 samples, the As_2S_3 glass and metallic Ag form a glass with $\sim$25 at% Ag [7]. The total free energy of the system presumably decreases as a result of the solid-state reaction between Ag metal and As–S glass. Thus, Ag photodoping is an irreversible phenomenon, since the solid-state reaction is followed by a decrease in the total free energy (unstable $\rightarrow$ stable).

For the PSD phenomenon, excess Ag atoms (Ag^+ ions) are segregated by illumination with bandgap light and the Ag concentration of the glass itself decreases. If the free energy of metallic Ag is less than that of the Ag-rich glasses, in the same way, the total free energy of the system may decrease by the segregation of metallic Ag [15]. The reaction is also represented by an "unstable $\rightarrow$ stable" process and is an irreversible reaction. Thus, the PSD phenomenon is considered to be a photochemical reaction leading towards a thermodynamically more stable state caused by the segregation of excess Ag^+ ions.

The photosensitivity of the PSD effect is related both to the thermodynamic instability of the glasses with excess Ag^+ ions and to the diffusivity of the Ag^+ ions. These factors are closely connected with each other and may become largest at around the maximum Ag content in the corresponding chalcogenide system. In fact, for all the systems examined so far, the appearance of the PSD phenomenon is limited to concentrations near the maximum Ag content and the photosensitivity increases with increasing Ag content [5].

On the other hand, the PCM phenomenon is observed only at around 25 at.% Ag. In the PCM effect, the Ag concentration of a sample increases in the illuminated region and decreases in the unilluminated region [13]. The free energies of both regions increase by the migration of Ag^+ ions, since the free energy of Ag-rich Ag–As–S glasses takes a minimum at around 25 at.% Ag. This suggests that the system changes from stable to unstable under illumination. Thus, the PCM phenomenon can occur reversibly without annealing, in contrast to the PSD phenomenon. The lack of formation of Ag particles in the PCM process seems to

be due to the reaction of the "stable → unstable" type, rather than to a small increase of Ag concentration in the illuminated region (25 → ∼30 at.%).

It is an important question whether or not the PSD phenomenon can be observed for other metals, e.g. copper. It is known that Ge–S films can dissolve a large amount of Cu and the maximum content (62 at.%) is almost the same as the case of Ag (67 at.%) [28]. The Cu-rich Cu–Ge–S films with excess Cu atoms may also be unstable, since the films containing more than 62 at.% Cu precipitate Cu particles during preparation in the same way as for Ag–Ge–S films above 67 at.% Ag. However, the photo-induced surface deposition of Cu was not observed, although the Cu-rich films are p-type semiconductors [28]. We believe that the reason is that the Cu–Ge–S films do not exhibit ionic conduction of Cu even at 62 at.% Cu.

The erasure of Ag deposits means rediffusion of Ag^+ ions from metallic Ag into the interior of Ag-rich glass by pure thermal effects. The Ag^+ rediffusion can be explained by the idea that the solubility of Ag^+ ions in the Ag-rich glass increases with increasing temperature. This idea is based on the fact that no PSD effect is observed at temperatures above 80 °C [11]. When the solubility of Ag^+ ions is low, the glass becomes stable by segregation of Ag^+ ions. On the other hand, when the solubility of Ag^+ ions is sufficiently high, the glass can contain more Ag^+ ions. In this case, the metallic Ag can diffuse into the glass even if the glass is Ag-rich, in the same way as for Ag thermal doping observed in Ag/As_2S_3 samples. Thus, the thermal erasure of Ag deposits may be due to the higher solubility of Ag^+ ions at elevated temperatures.

The PSD effect has a maximum at around 20 °C and is not observed at either low temperatures (e.g. -196 °C, i.e. liquid N_2) or at high temperatures above $+80$ °C [11]. The diffusivity of Ag^+ ions generally decreases with decreasing temperature. Thus, the decrease of the PSD effect below 20 °C is explained by a decrease in diffusivity of Ag^+ ions at low temperatures (suppression of Ag^+ migration). On the other hand, the decrease of the PSD effect above 20 °C can be explained by an increase in solubility of Ag^+ ions at high temperatures. In view of the thermodynamic properties of Ag-rich glass, the peculiar temperature dependence of PSD effect can be understood in terms of a competition of two different factors, namely the diffusivity and solubility of Ag^+ ions in the glass [23].

11.7 Other Observations

In the case of photographic films, addition of small amounts of Au or S has long been known to increase the photosensitivity (sensitization) [25]. These additives have been considered to act as electron traps and subsequent nucleation centers for the formation of stable Ag specks in AgBr(Cl) photographic crystals. If such sensitization is applicable to the PSD phenomenon, a new photosensitive device with a very high resolution can be expected due to a marked increase in the nucleus density of Ag deposits.

We directly added 0.1–0.5 wt% (0.037–0.185 at.%) Au into the host glass ($Ag_{45}As_{15}S_{40}$). The effect of the addition of this small amount of Au on the PSD phenomenon was studied as a function of the Au content [29]. SEM observations have clearly shown that the nuclei density of Ag deposits increases by at least two orders of magnitude with an increase in Au content from 0 to 0.5 wt.%. The shape of the Ag deposits also changes from disc-like to pebble-like with increasing Au content. For the S-based films, the PSD effect of the samples with low

Ag content was enhanced by the addition of Au but little change was observed for the nuclei density and the shape of the Ag deposits [30].

The structure of Ag-rich glasses that exhibit the PSD effect was studied using $Ag_xAs_{60-x}S_{40}$ bulk glasses ($35 \leq x \leq 47.5$) [31]. The network structure of the glasses is similar to that of xanthoconite (Ag_3AsS_3 crystal). The local structure may be different in the composition ranges of $35 \leq x \leq 40$ (group I) and $40 \leq x \leq 47.5$ (group II, these exhibit the PSD effect). Group I contains excess As atoms that link the isolated AsS_3 pyramids. In contrast, group II contains excess Ag^+ ions that may lie between the AsS_3 pyramids and bind loosely with the surrounding S atoms. The excess Ag^+ ions may make the glasses thermodynamically unstable. As mentioned in Section 11.2, when the excess Ag^+ ions are segregated by illumination the glasses become stable.

Furthermore, surface deposition of fine Ag particles by electron-beam irradiation is observed for Ag-rich films on a glass substrate [5, 32]. This phenomenon is referred to as "electron-beam surface deposition" (ESD) of silver. The ESD phenomenon is mainly due to electron-induced charging of the irradiated region. Ag^+ ions in the films accumulate in the irradiated region, driven by the electric field induced by the charging, and fine Ag particles are formed by recombination of Ag^+ ions and electrons. The change in the optical properties of samples caused by the ESD effect is dramatic at wavelengths of 650–800 nm, in the same way as that caused by the PSD effect.

In the case of glasses with Ag contents below 30 at.%, only a volume expansion is observed in the irradiated region and surface deposition of Ag metal does not occur [33]. Since the Ag concentration in the irradiated region increases markedly (up to $\sim$60 at.%), the volume expansion is likely to be caused by the accumulation of Ag^+ ions. It is interesting that the surface deposition of metallic Ag is limited to Ag-rich glasses with excess Ag^+ ions for both photo-induced and electron beam induced phenomena.

11.8 Concluding Remarks

Ag-rich amorphous chalcogenide semiconductors exhibit a wide variety of changes in their physical properties due to long-range migration of Ag^+ ions, particularly when exposed to the bandgap light. This chapter reviewed the photo-induced surface deposition (PSD) of pure Ag particles on Ag-rich Ag–As(Ge)–S(Se) glasses, both bulk samples and thin films. This phenomenon have been explained in terms of the fact that Ag-rich chalcogenide glasses are mixed ion–electron (hole) conductors and are thermodynamically metastable.

The PSD phenomenon resembles the photochemical reaction in conventional photographic films. However, three points essentially distinguish the photochemical reaction and the PSD phenomenon: (i) the PSD phenomenon is *only* characteristic of Ag-rich *glasses* containing excess Ag^+; the crystallized samples do not exhibit the PSD effect; (ii) the Ag-rich glasses are p-type semiconductors; (iii) a large amount of Ag can be segregated by the PSD.

Acknowledgments

The author thanks Prof. K. Tanaka (Hokkaido University) for numerous discussions and Prof. S. Maruno (Professor Emeritus of Nagoya Institute of Technology) for much useful advice.

References

[1] K. Shimakawa, A.V. Kolobov, and S.R. Elliott, Adv. Phys. **44**, 475 (1995).
[2] K. Tanaka, Curr. Opin. Solid State Mater. Sci. **1**, 567 (1996).
[3] K. Tanaka, J. Non-Cryst. Solids **164/166**, 1179 (1993).
[4] Y. Kawamoto and M. Nishida, J. Non-Cryst. Solids **20**, 393 (1976).
[5] T. Kawaguchi, K. Tanaka, and S.R. Elliott, in Handbook of Advanced Electronic and Photonic Materials and Devices, H.S. Nalwa (Ed.), Vol. 5, Academic Press, San Diego, 2001, Chap. 3.
[6] K. Tanaka and M. Itoh, Optoelectronics **9**, 299 (1994).
[7] A.V. Kolobov and S.R. Elliott, Adv. Phys. **40**, 625 (1991).
[8] S.R. Elliott, J. Non-Cryst. Solids **130**, 85 (1991).
[9] K. Tanaka, J. Non-Cryst. Solids **137/138**, 1021 (1991).
[10] S. Maruno and T. Kawaguchi, J. Appl. Phys. **46**, 5312 (1975).
[11] T. Kawaguchi and S. Maruno, J. Appl. Phys. **77**, 628 (1995).
[12] K. Tanaka, N. Yoshida, and Y. Yamaoka, Philos. Mag. Lett. **68**, 81 (1993).
[13] N. Yoshida and K. Tanaka, J. Appl. Phys. **78**, 1745 (1995).
[14] T. Kawaguchi, S. Maruno, and K. Tanaka, J. Non-Cryst. Solids **164/166**, 1231 (1993).
[15] T. Kawaguchi, Jpn. J. Appl. Phys. **40**, 245 (2001).
[16] T. Kawaguchi and S. Maruno, Jpn. J. Appl. Phys. **33**, 4521 (1994).
[17] T. Kawaguchi and S. Maruno, Jpn. J. Appl. Phys. **36**, L85 (1997).
[18] T. Kawaguchi and S. Maruno, Jpn. J. Appl. Phys. **33**, 6470 (1994).
[19] T. Kawaguchi, S. Maruno, and K. Tanaka, J. Appl. Phys. **73**, 4560 (1993).
[20] T. Kawaguchi, S. Maruno, and S.R. Elliott, J. Appl. Phys. **79**, 9096 (1996).
[21] T. Kawaguchi, S. Maruno, and S.R. Elliott, J. Non-Cryst. Solids **211**, 187 (1997).
[22] T.H. James, The Theory of the Photographic Process, 4th ed., Macmillan, New York, 1977, Chap. 4.
[23] T. Kawaguchi, S. Maruno, and S.R. Elliott, J. Non-Cryst. Solids **202**, 107 (1996).
[24] T. Kawaguchi, Appl. Phys. Lett. **72**, 161 (1998).
[25] J.F. Hamilton, Adv. Phys. **37**, 359 (1988).
[26] CRC Handbook of Chemistry and Physics, 75th ed., CRC Press, Boca Raton, FL, 1994.
[27] T. Kawaguchi and S. Maruno, Jpn. J. Appl. Phys. **33**, 3417 (1994).
[28] T. Kawaguchi, S. Maruno, and S.R. Elliott, J. Non-Cryst. Solids **204**, 83 (1996).
[29] T. Kawaguchi, S. Maruno, and S.R. Elliott, J. Non-Cryst. Solids **212**, 166 (1997).
[30] T. Kawaguchi, Jpn. J. Appl. Phys. **37**, 6318 (1998).
[31] T. Kawaguchi, Jpn. J. Appl. Phys. **37**, 29 (1998).
[32] T. Kawaguchi, S. Maruno, and K. Masui, J. Non-Cryst. Solids **77/78**, 1141 (1985).
[33] K. Tanaka, in Physics and Applications of Non-Crystalline Semiconductors in Optoelectronics, A. Andriesh and M. Bertolotti (Eds.), Kluwer Academic, Dordrecht, 1997, p. 31.
[34] S. Maruno, M. Noda, and T. Yamada, J. Ceram. Soc. Jpn. **81**, 445 (1973).
[35] G.W. Roland, Metall. Trans. **1**, 1811 (1970).
[36] G.W. Roland, Econ. Geol. **65**, 241 (1970).

12 Photo-Induced Changes in Liquid Sulfur and Selenium

Yoshifumi Sakaguchi and Kozaburo Tamura

12.1 Introduction

It is well known that chalcogenide glasses containing sulfur and selenium show remarkable photo-induced changes [1]. However, it is *not* well known that elemental liquid sulfur and selenium also show significant photo-induced changes. Elemental liquid sulfur and selenium are semiconductors, which is due to their electronic structure. They belong to group VI of the periodic table and possess four valence p-electrons. Two of the p-electrons form covalent σ-bonds giving rise to a ring or polymeric structure in liquid sulfur and selenium. The remaining two electrons enter the lone-pair (LP) orbital. These p-electrons, especially LP electrons, play an important role in photo-induced changes.

From the viewpoint of photo-induced changes, liquids are positioned between isolated molecules and crystalline solids. It is known that photo-induced changes in electronic and structural properties are often observed in isolated molecules but hardly observed in crystalline solids, which is due to the fact that excitation of an electron hardly affects the whole crystal because of the strong constraint coming from the crystallinity with the long-range order. The effect may easily propagate and percolate the liquid, which enables us to observe the photo-induced cooperative phenomena in liquid sulfur and selenium.

In the present chapter we describe recent experimental and theoretical studies on the photo-induced changes in liquid sulfur and selenium. We start with the photo-induced polymerization in liquid sulfur in which S_8 ring molecules change to polymeric chains upon illumination by a laser. Polymerization in liquid sulfur has been attracting considerable experimental and theoretical attention for many decades [2–4]. Between the melting point (113 °C for orthorhombic sulfur) and the polymerization temperature of 159 °C sulfur forms a light-yellow low-viscosity liquid consisting of S_8 molecules which have the shape of a puckered ring. Above 159 °C it forms a highly viscous liquid in which a significant fraction of S_8 rings polymerize to form long polymeric chains. It is known that the structure [5–7] and thermodynamic properties such as viscosity [8], heat capacity [9, 10] and density [11–14] substantially change at the polymerization temperature. The measurements of the optical reflectivity [15, 16] and the optical absorption coefficient [17] also revealed that the polymerization produces considerable changes in the electronic energy levels of liquid sulfur. Tobolsky and Eisenberg [18] discussed the polymerization process based on an idea of a chemical reaction to explain the abrupt increase of viscosity at the polymerization temperature. For the understanding of the mechanism of the polymerization, studies on the dynamic behavior of the conversion between S_8 rings and polymeric chains are important.

Recently, the present authors have performed measurements of transient absorption spectra induced in liquid sulfur by illumination with a pulsed laser [19]. The study was performed with the following main objectives. The first objective was to study whether or not the polymerization can be induced when a pulsed laser with the bandgap energy illuminates S_8 rings in liquid sulfur. The second aim was to study the relaxation process in which photo-induced polymeric chains are relaxed to rings in thermal equilibrium. The results of these experiments are described below in detail.

Next we consider a possibility of the photo-induced semiconductor–metal (SC–M) transition in liquid selenium. Liquid selenium in the vicinity of its melting point consists of long polymeric chains, each containing as many as 10^5 atoms, and exhibits semiconducting behavior. With increasing temperature, the chain length becomes short [20,21], electrical conductivity increases [22] and the optical gap decreases [23]. It is known that further increase of temperature with application of pressure gives rise to the SC–M transition near the liquid–gas critical point ($T_c = 1615$ °C, $P_c = 385$ bar, $\rho_c = 1.85$ g cm^{-3} [24]) [25–29]. An NMR study [21] revealed that the chain molecule contains about ten atoms on average when the SC–M transition occurs. Tamura and collaborators carried out X-ray diffraction and EXAFS measurements [30–34] for fluid selenium up to the supercritical region, including the SC–M transition. It was found that the local structure substantially changes when the transition takes place. In an *ab initio* molecular-dynamic simulation by Shimojo et al. [35] it was found that the chain-like structure persists even in the metallic state, although the chain structure is disrupted. The SC–M transition in liquid selenium seems to be strongly related to the instability of the chain structure.

Trigonal selenium, the most stable crystalline form under normal conditions, consists of helical chains. LP electrons which are localized around selenium atoms and do not participate in covalent bonding play a crucial role in stabilizing the helical structure of trigonal selenium [36, 37]. LP electrons occupy the highest filled state forming the valence band, while the empty antibonding σ*-states form the conduction band. Between the valence and conduction bands there is an energy gap of about 2 eV, so that trigonal selenium behaves as a semiconductor. The bond length, bond angle and the dihedral angle of long polymeric chains in liquid selenium near the melting point are almost the same as those in trigonal selenium. The structural disorder in liquid selenium comes from the random variation of the sequence of dihedral angles along the chain in liquid selenium.

The SC–M transition observed near the critical point in liquid selenium must be related to instability of the chain structure, in which LP electrons play a crucial role. Therefore, it is interesting to study the effect of the photo-excitation of LP electrons on the structural and electronic properties of liquid selenium. The excitation of LP electrons to σ*-orbitals may affect the properties of liquid selenium, changing the strength of bonds, the conformation of the chain and the electronic states.

Recently, the present authors carried out measurements of transient absorption spectra of liquid selenium after illumination with a pulsed laser which excites LP electrons into the σ*-orbitals [38]. They observed an enormous change in the transmitted light intensity upon illumination with the pulsed laser. In addition, detailed analysis of the results suggested that the optical gap decreases with time and disappears after 0.5 μs when the pulsed laser illuminates liquid selenium at 350 °C with intensity of 15 mJ/pulse. They also carried out measurements of transient direct-current (dc) conductivity and observed a large increase of dc conductiv-

ity by a factor 10^5 on laser illumination [39]. The details of the transient dc conductivity measurements are described in a later section.

Finally, we discuss the results of *ab initio* molecular-dynamics simulations, which are very helpful for the understanding of the photo-induced changes in liquid sulfur and selenium and the possibility of the photo-induced SC–M transition [40], in the following sections.

12.2 Experimental

12.2.1 Optical Cells

The optical absorption spectrum in the high absorption region of semiconductors generally provides information about the inter-band transitions. The energy gap can be estimated from the fundamental absorption edge of the spectrum. To measure the spectrum in the high absorption region and to achieve homogeneous excitation of the sample, the use of a very thin film of the order of the light penetration depth, typically < 1 μm is needed. We have developed an optical cell for obtaining such thin films of liquids.

The cell is composed of a quartz tube connected to quartz plates with a thin sample space. The edges of the two plates were connected together by glass fusion and a thin and uniform gap was made between them. The space was filled with a liquid sample in the following way. The inside of the cell was evacuated, the solid sample in the reservoir was melted and Ar gas at atmospheric pressure was introduced into the cell to force the liquid specimen into the sample space.

For measurement of the transient dc conductivity of liquid selenium a different optical cell was developed. A thin liquid film is held between two quartz plates. Two electrodes made of gold were put into the channels on the quartz plates and the conductivity of the liquid film between the electrodes was measured. The distance between electrodes was about 0.1 mm. For more details about the cell structure see [41].

12.2.2 Measurement Set-Up

Figure 12.1 shows a schematic diagram of the apparatus used for the optical absorption measurements [19]. The third harmonic (355 nm) of the Nd:YAG pulsed laser was used for the photo-excitation of LP electrons in liquid sulfur and the second harmonic (532 nm) was used for liquid selenium [38]. The pulse width was 5–6 ns and the repetition rate was 10 Hz. The intensity of the pulsed laser was measured using a power meter combined with a beamsplitter. The pulsed laser beam was reflected by a mirror and illuminated the liquid sample contained in the quartz cell. A tungsten lamp was used as the probe light transmitted through the sample. The intensity was measured using a monochromator and a photomultiplier.

For the transient dc conductivity measurement of liquid selenium [39, 41] a standard resistance of 50 Ω was placed between the sample and a dc battery. The time variation of the voltage across the standard resistance before and after the laser illumination was measured using a wide-band preamplifier and a digital oscilloscope. The variation of the voltage reflects the change of the conductivity of liquid selenium.

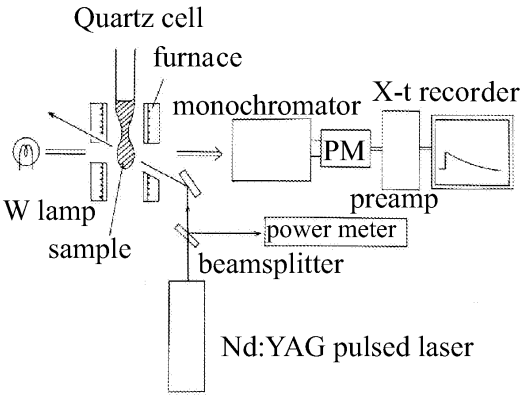

Figure 12.1: Schematic diagram of the apparatus used for the transient absorption measurements.

12.3 Photo-Induced Changes in Liquid Sulfur

12.3.1 Transient Absorption Measurements

In this section we discuss the results of transient optical-absorption measurements for liquid sulfur [19]. Figure 12.2 shows a logarithmic plot of the change in the transmission, $\Delta T/T$, versus time of liquid sulfur at 130 °C, where T is the transmittance in the thermal equilibrium state and ΔT the photo-induced change of the transmittance. The wavelength of the transmitted probe light is 390 nm, i.e. corresponds to an energy that is slightly larger than the optical gap of liquid sulfur [17] below the polymerization temperature T_p in thermal equilibrium. The intensities of the pulsed laser are denoted on the right-hand side of each curve in the figure. The photo-induced change, photodarkening in this case, is clearly observed upon illumination with the pulsed laser with intensity of about 1.0 mJ/pulse. With increasing laser power the value of $\Delta T/T$ increases, while the relaxation time remains unchanged. With further increase of the laser power, higher than 10 mJ/pulse, a new absorption feature with a short relaxation time appears. The values of the short and long relaxation times at 130 °C are found to be 60 s and 40 min, respectively. With increasing temperature, the relaxation time becomes shorter.

In order to understand the origin of photo-induced changes in liquid sulfur below T_p, the possibility that the laser-induced heating causes the changes, raising the temperature of liquid sulfur above T_p, was examined. Figure12.3 shows the plots of $\Delta T/T$ versus time at 130 °C during repeated illumination by a pulsed laser at 10 Hz and after stopping the illumination. Four curves are obtained for different intensities of the laser (0.05, 0.1, 0.2 and 1.0 mJ/pulse). The intensity of the pulsed laser is quite small compared with that used for the experiment depicted in Fig. 12.2. When the pulsed laser with 0.05 mJ/pulse is used, $\Delta T/T$ gradually increases with time and eventually saturates after 15 min. After stopping the illumination, $\Delta T/T$ decreases exponentially. When a stronger laser pulse (0.1 mJ/pulse) illuminates the sample, the saturated value of $\Delta T/T$ becomes larger and the time to reach the saturation value becomes shorter. The fast relaxation process becomes clearer when the intensity of the pulsed laser increases. The logarithmic plots of $\Delta T/T$ after stopping the illumination are shown in

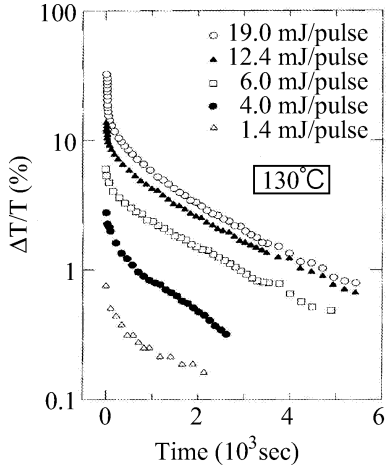

Figure 12.2: Logarithmic plots of $\Delta T/T$ versus time for liquid sulfur at 130 °C after the illumination by a single pulse of the laser with different intensities.

Fig. 12.4. One can clearly see a crossover between the fast and slow relaxation processes. The values of the relaxation time are 60 s and 10–20 min, respectively.

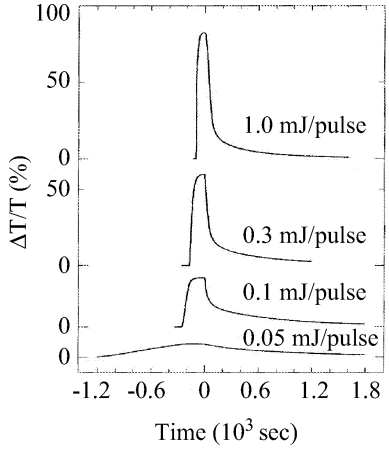

Figure 12.3: Plots of $\Delta T/T$ versus time for liquid sulfur at 130 °C during repeated illumination by a weak pulsed laser at 10 Hz and after stopping the illumination. The origin of the horizontal axis indicates the instance at which the illumination stops.

Assuming that the photon energy is totally consumed for heating the sample, the temperature of liquid sulfur is estimated to increase by 1 °C when a laser pulse (0.1 mJ/pulse) illuminates the sample, i.e. the temperature increase of the sample is negligibly small.

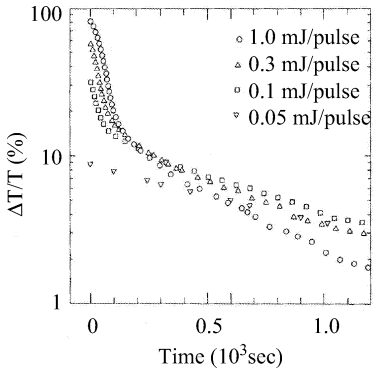

Figure 12.4: Logarithmic plots of $\Delta T/T$ versus time for liquid sulfur at 130 °C after stopping the repeated illumination of the pulsed laser.

12.3.2 Short- and Long-Living Products

The characteristic features of the photo-induced phenomena observed in liquid sulfur below T_p are as follows. First, the phenomena are not caused by laser heating. They must be strongly related to the structural instability of the S_8 ring induced by the photo-excitation of LP electrons located at the highest occupied states of molecular orbitals of the S_8 ring. Second, we have two kinds of photo-induced products with different relaxation times, namely short- and long-living products. The concentration of the long living products seems to be accumulated by repeated illumination with weak laser pulses. When the concentration of the long-living products exceeds a critical value the short-living products are created. It is interesting to note that when the short-living products are on the way back to the thermal equilibrium state after stopping the illumination, the long-living products start to appear with the same critical concentration corresponding to a value of $\Delta T/T$ equivalent to 10%.

12.3.3 What is a Short-Living Product?

The transient absorption measurements described in the previous section were made using a single wavelength of the probe light. In order to identify the short- and long-living products, it is important to know the spectral shape of the transient absorption spectra.

The transient absorption spectrum after illumination by a single laser pulse during repeated illumination by the pulsed laser was found to be quite different from that before the illumination: the spectrum substantially shifts to the low-energy side and a shoulder appears around 3.5 eV. The original spectrum is recovered after cessation of the illumination. Figure 12.5 shows the plots of the photo-induced deviation from the absorption coefficient in thermal equilibrium, $\Delta\alpha_p$, during the repeated illumination of liquid sulfur at 130 °C by a weak pulsed laser with intensity of 1.0 mJ/pulse (◯), and 20 s (□) and 180 s (△) after cessation of the illumination. As seen in the figure, a clear maximum in the spectrum was observed around 3.5 eV. Comparing the times at which the spectra in Fig. 12.5 were obtained with the horizontal axis in Fig. 12.4, we can see that the spectra denoted by (◯, □) and by (△) correspond to the short-living and long-living products, respectively.

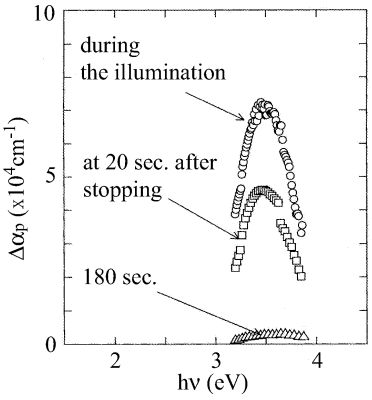

Figure 12.5: Plots of $\Delta\alpha_p$ versus photon energy for liquid sulfur at 130 °C, where $\Delta\alpha_p$ is the photo-induced deviation from the absorption coefficient in thermal equilibrium. Plots of $\Delta\alpha_p$ during repeated illumination by a weak pulsed laser with an intensity of 1.0 mJ/pulse are indicated by open circles, and those 20 and 180 s after stopping the illumination are shown by open squares and triangles, respectively.

Figure 12.6 shows difference spectra, $\Delta\alpha_T, \Delta\alpha_T = \alpha_T - \alpha_{130^\circ\mathrm{C}}$, at different temperatures, where α_T means the optical absorption coefficient in the thermal equilibrium state at a certain temperature T. These difference spectra are obtained by analyzing the optical absorption data without illumination [17]. As seen in Fig. 12.6 a distinct peak appears around 3.5 eV in the spectra above the polymerization temperature. It is known that these spectral changes originate from the creation of long polymeric chains containing 10^6 sulfur atoms [15, 17]. From the similarity between the spectra ◯ and □, shown in Fig. 12.5 and the spectra in Fig. 12.6, we can conclude that the *short-living products are long polymeric chains.* The comparison between two spectra denoted by ◯ in Fig. 12.7 and ◊ (the 400–130 °C data) in Fig. 12.6 demonstrates that the concentration of the photo-induced polymeric chains in liquid sulfur is about 60% [42].

Comparison of Figs. 12.5 and 12.6 also suggests that the long-living products are different from long polymeric chains but they also exist in a small fraction below T_p in the thermal equilibrium state.

12.3.4 What is a Long-Living Product?

An important conclusion deduced from the present experiments is that the long-living products are generated when a very weak laser illuminates S_8 rings and that the concentration increases with illumination time. When the concentration exceeds the critical value polymeric chains are produced. These polymeric chains change back to the stable S_8 rings after stopping the illumination. It should be noted that long-living products appear intermediately on the relaxation process from the polymeric chains to the S_8 rings. Therefore, the long-living products may consist of small molecules which eventually change back to S_8 rings.

Figure 12.7 shows the variation of $\Delta T/T$ with time in a sample which is heated very fast from the melting temperature to 130 °C and also cooled to 130 °C from 150 °C. The

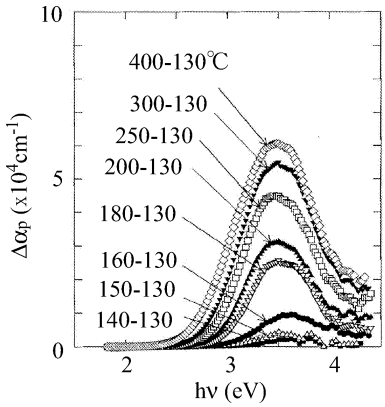

Figure 12.6: Plots of $\Delta\alpha_T$ versus photon energy. $\Delta\alpha_T$ is defined as $\Delta\alpha_T = \alpha_T - \alpha_{130^\circ\mathrm{C}}$ at different temperatures, where α_T is the optical absorption coefficient in thermal equilibrium state at a certain temperature T.

corresponding curves are denoted by open circles and triangles, respectively. It was found that the relaxation time is about 200 min for the heating procedure and about 45 min for the cooling procedure, which is almost the same as the relaxation time of the long-living products. The observed difference suggests that it is more difficult to generate the long-living products through the thermal rupture of the covalent bond of the S_8 ring than to change the excess long-living products back to the S_8 ring.

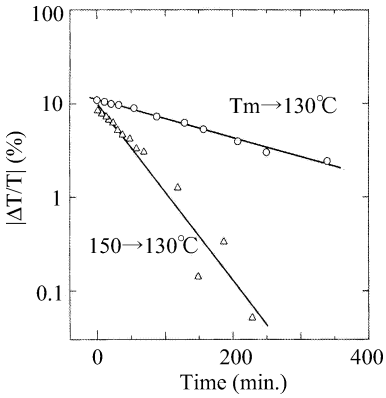

Figure 12.7: Variation of $\Delta T/T$ with time when the liquid sulfur is heated very fast to 130 °C from the melting point and cooled to 130 °C from 150 °C, which are denoted by open circles and triangles, respectively.

The effect of light illumination on physical and chemical properties of liquid sulfur near the melting point was first investigated more than 100 years ago. Lallemand discovered that a kind of sulfur insoluble in carbon disulfide (CS_2) [43] appears in a liquid mixture of sulfur and CS_2 illuminated by solar light. Berthelot [44] found that such insoluble sulfur can be created

in liquid sulfur by illumination with solar light which decreases the freezing point. From this result result Wigand [45] estimated the molecular weight of the insoluble sulfur molecule and predicted that the insoluble sulfur must consist of eight sulfur atoms. We can consider that the insoluble sulfur found by these previous investigations might be the same as the long-living product generated by weak illumination with a pulsed laser.

Charge-Transfer Complex

The most probable candidate for the long-living products may be a charge-transfer complex proposed by Wiewiorowsky and Touro [46] in order to explain the presence of metastable S_8 molecules below T_p produced by light illumination. The charge-transfer complex is considered to consist of an S_8 chain and the surrounding S_8 rings. Two electrons at the ends of the S_8 chain transfer to the surrounding S_8 rings and move around with paired spins. The idea of the charge-transfer complex having delocalized electrons with paired spins explains the experimental observation that ESR signals [47] can not be detected in spite of the existence of S_8 chain molecules below T_p [48]. It reminds us of spin pairing due to the so-called negative U with the help of a lattice deformation in solids. Wiewiorowsky et al. [49] considered that the freezing point depression observed in liquid sulfur is caused by the existence of a small number of charge-transfer complexes. They also studied the creation process of the 'charge-transfer complex' and found that 200 min are needed to reach thermal equilibrium when the sample is heated very fast to 130 °C from low temperatures, which is consistent with the data obtained by Sakaguchi and Tamura [19].

An Alternative Idea for Long-Living Product

An alternative idea to explain the origin of insoluble species existing below T_p was proposed by Steudel and Mausel [50]. Their basic idea is that insoluble species consist of a variety of S_n rings ($n \neq 8$) such as S_6, S_7, S_9, S_{12} and S_{20}. At present it is difficult to give a definite answer to the question of which one is the most likely candidate for the long-living products, the charge-transfer complex or S_n rings. The results shown in Figs. 12.3 and 12.4, however, may be helpful for the differentiation. The most important relevant result is that repeated illumination by a very weak pulsed laser accumulates the long-living products and the polymerization starts to occur when the critical value of $\Delta T/T$ is exceeded. Furthermore, in the relaxation process the slow relaxation appears when $\Delta T/T$ during the fast relaxation process decreases to the critical value, about 10%, which does not depend on the laser power. To explain such cooperative nature, the charge-transfer complex seems to be a more likely candidate.

12.3.5 Temperature Variation of Relaxation Time

Figure 12.8 shows the temperature variation of the relaxation time in a wide temperature range both below and above T_p. One can see that there are two relaxation processes below T_p and only one above T_p. The relaxation time of the slow relaxation process substantially decreases with increasing temperature and drops by a factor of 10^2 around T_p; the relaxation time of

the fast relaxation process gradually decreases. Note that the curves of the relaxation time for slow and fast relaxation processes cross at T_p.

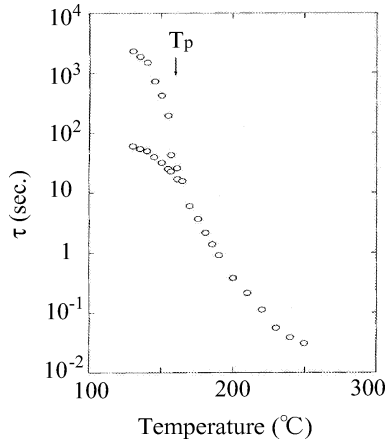

Figure 12.8: Temperature variations of relaxation time, τ, in a wide temperature range below and above T_p.

A possible explanation for these photo-induced phenomena is as follows. Below T_p, we may have three states, namely, rings, charge-transfer complexes and polymeric chains. The ring is the most stable species, the charge-transfer complex is metastable and the polymeric chain is unstable. A single shot of a weak pulsed laser easily produces the charge-transfer complex through the excitation over the potential barrier between two minimum states corresponding to the ring and the complex. With increasing intensity of the single shot of the laser a direct excitation from the most stable state (ring) to the unstable state (polymer) may occur in which instantaneous polymerization is expected because a large number of S_8 chains are instantaneously produced. The fast relaxation from the polymer to the complex, being followed by the slow relaxation from the complex to the ring, takes place below T_p.

Above T_p there exist a large number of S_8 rings together with polymeric chains. The illumination by a pulsed laser causes the opening of S_8 rings. The transient spectra above T_p, obtained by the measurement of $\Delta T/T$ at different photon energies, revealed that the products must be polymeric chains because the transient spectra also show maxima around a photon energy of about 3.5 eV.

12.3.6 Photo-Induced Polymerization as a Cooperative Phenomenon

The phenomenon induced by repeated illumination with a very weak pulsed laser shown in Figs. 12.3 and 12.4 is very interesting. The results reveal that the number of complexes becomes large with repeated illumination and polymeric chains can be generated when the concentration of long-living products exceeds a critical value. This fact suggests that a kind of structural instability takes place in long-living products at critical concentration. The instability may be caused by an electrostatic interaction such as dipole–dipole interaction between

them. The nature of the polymerization induced by repeated illumination with a weak laser seems to be cooperative.

Sakaguchi and Tamura [19] studied the photo-induced polymerization in detail, focusing on what happens when the intensity of the laser is increased. It was found that repeated illumination by a very weak laser (less than 0.07 mJ/pulse) only produces long-living products, probably charge-transfer complexes, while repeated illumination with pulses stronger than 0.07 mJ/pulse but less than about 20 mJ/pulse always produces polymers. They also investigated the effect of much stronger illumination than 20 mJ/pulse and found that there appears a visible pattern in the laser-illuminated area of liquid sulfur at 130 °C during repeated illumination with the pulsed laser [19, 51]. There are two different regions in the pattern, namely, homogeneous and inhomogeneous. The homogeneous region is transparent; in the inhomogeneous region parallel lines appear. The distance between the lines was found to be about 10 μm. It seemed that giant molecules with colloidal form lie along parallel lines. Such a pattern was observed when the quartz cell with a 1.0 or 0.3 μm thick sample space was used but never observed with a 7 μm thick sample space. Therefore, the appearance of the pattern must be strongly connected with the restricted geometry. In fact the length of one random chain [52] containing 10^5–10^6 sulfur atoms is estimated to be 0.1–0.3 μm, assuming that the bond length and the amplitudes of bond angle and dihedral angle are the same as those of S_8 ring but only the sign of the dihedral angle along the chain changes randomly. Therefore, it is not so unreasonable to consider that a thickness of 1.0 or 0.3 μm gives a two-dimensional restriction to the random chain. A kind of structural change from randomly oriented to densely packed chains may thus occur.

12.4 *Ab Initio* Molecular-Dynamics Simulation for Liquid Sulfur

12.4.1 Photo-Induced Bond Breaking in Isolated S_8 Ring

Shimojo et al. [53] performed *ab initio* molecular-dynamics (MD) simulations of an isolated S_8 molecule in order to investigate the instability of an S_8 ring illuminated by a pulsed laser. They showed that a bond in the S_8 ring is broken immediately after an electron in the highest occupied molecular orbital (HOMO) is excited to the lowest unoccupied molecular orbital (LUMO). This result strongly supports the possibility of photo-induced bond breaking in the S_8 ring followed by polymerization in liquid sulfur below T_p.

Figure 12.9 shows the time dependence of the S–S bond lengths in an S_8 cluster. The origin of time ($t = 0$) is the time at which an electron in the HOMO is excited to the LUMO. Before that ($t < 0$), the S–S bond lengths oscillate around their equilibrium distances, and the ring structure is retained. After the excitation ($t > 0$), where the LUMO as well as the HOMO are occupied by one electron, the length of one of the bonds suddenly increases, which means that the bond breaking takes place in the S_8 ring.

Figure 12.10 shows the evolution of the single-electron eigenvalues as a function of time. The electronic states below and above -0.4 au are characterized mainly as 3s and 3p orbitals, respectively. For $t < 0$, the electronic states below -0.17 a.u. are occupied by electrons, and there is a gap of about 0.1 a.u. between HOMO and LUMO. After the electron is excited,

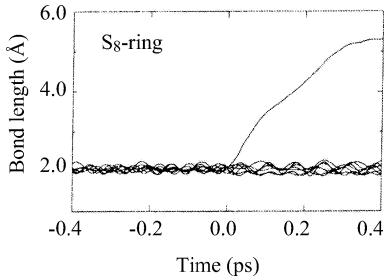

Figure 12.9: Time dependence of the S–S bond length in an isolated S_8 ring molecule studied by Shimojo et al. [53]. The bond lengths for eight S–S bonds are displayed. The origin of time is the instant at which an electron in the HOMO is excited to the LUMO.

the electronic structure is changed. At $t = 0$, the eigenvalue of the HOMO starts to increase, while that of the LUMO starts to decrease. They intersect at around 0.07 ps. This change in the electronic structure is considered to include the bond breaking, in other words, the bond breaking occurs to release the electronic energy due to the electron occupation of the LUMO.

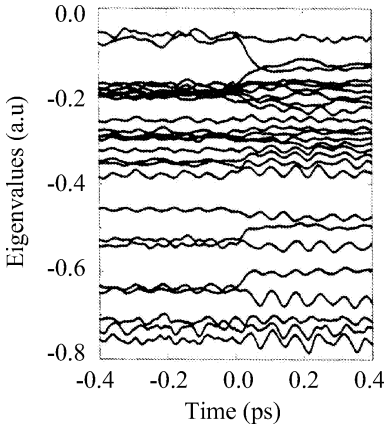

Figure 12.10: Time evolution of the single-electron eigenvalues of an isolated S_8 ring molecule studied by Shimojo et al. [53].

Shimojo et al. [53] also investigated the time evolution of the spatial distribution of wavefunctions for the HOMO and LUMO. Before the excitation of an electron, both wavefunctions spread over the whole ring, and the HOMO has bonding and LP character, while the LUMO has mainly antibonding character. After the excitation of an electron, the distribution of the wavefunction for the LUMO starts to change in a way that the amplitude of the wave function increases around the S–S bond which will break and decreases around other S–S bonds of the S_8 ring. Accompanying this change, the wave function for the HOMO changes its amplitude in the same way as that for LUMO does, and eventually the HOMO and the LUMO form bonding and antibonding orbitals, respectively, at the S–S bond to be broken. These facts are important for the bond breaking in the S_8 ring. It was asserted that the bond breaks so as to stabilize the antibonding LUMO when an electron is excited to the LUMO.

12.4.2 Photo-Induced Structural Change in Liquid Sulfur

In order to understand the photo-induced polymerization and the relaxation process in liquid sulfur, Munejiri et al. [54] performed first-principle MD simulations for the system consisting of a number of sulfur atoms. They revealed that the photo-induced bond breaking in liquid sulfur below T_p occurs in the same way as was observed in the isolated S_8 ring. They also proposed the molecular structure of the experimentally observed long-living products appearing in the relaxation process and a possible scenario of how the photo-induced polymerization occurs.

In their MD simulation, a system of 80 atoms, i.e. 10 S_8 molecules, was used. They confirmed that liquid sulfur consists of S_8 molecules with the shape of a puckered ring. The S_8 rings are very stable and no S–S bond broke during the simulation without electron excitation. When an electron is excited from HOMO to LUMO, it was found that one of the S_8 rings breaks immediately in the same way as was seen for an isolated S_8 ring. It was also found that when a bond in the S_8 ring breaks upon excitation, the S_8 ring changes its structure, while other S_8 rings remain in almost the same position maintaining the shape of the puckered ring.

12.4.3 Relaxation Process. A New Candidate for Long-Living Product

Munejiri et al. [54] also investigated the relaxation process. The most interesting finding is that the S_8 chain produced by the electron excitation does not reconstruct the original S_8 ring during the relaxation process but forms a 'tadpole-shaped' structure. Figure 12.11 shows the S_8 ring, the S_8 chain with a broken bond and the 'tadpole-shaped' S_8 molecule found in their simulation. The authors pointed out that the tadpole is very stable and suggested that the *tadpole is one of the possible structures for experimentally observed long-living products*.

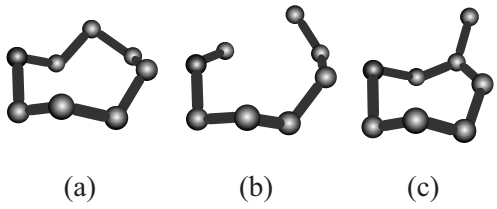

Figure 12.11: An S_8 ring, an S_8 chain with a broken bond and a tadpole-shaped S_8 molecule appearing in the relaxation process studied by Munejiri et al [54].

It is interesting to see that the tadpole has the shape of a three-fold coordinated site neighbored by a one-fold coordinated site with dangling bond, which reminds us of the 'valence alternating pair (VAP)' model proposed to explain the photo-induced changes in chalcogenide glasses. Unfortunately, Munejiri et al. [54] did not give any detailed description about the charge distribution in the tadpole.

They also investigated the photo-induced change when two electrons are excited at the same time. The first excitation of an electron causes a bond breaking of a certain S_8 ring. They observed that the second excitation of an electron causes the bond breaking of 'another'

S_8 ring; the second excitation never breaks the bond in the same S_8 ring. This permits us to consider that S_8 rings in liquid sulfur below T_p break one by one when illuminated by a very weak laser. Their simulation also suggested that two S_8 chains neither attack other S_8 rings nor change their own structures, maintaining the S_8 chain structure. The observation seems to contradict the theory by Tobolsky and Eisenberg [18] based on a chemical reaction in which chain ends attack the surrounding S_8 rings eventually causing continuous polymerization.

It is interesting to see what happens in the structure of these S_8 chains during the relaxation process. It was found that when the electron excitation is stopped neither of the two photo-created chains reconstructs the original S_8 ring but forms a tadpole structure. The two tadpoles are surrounded by S_8 rings and do not approach each other. The tadpole structure was found to be stable and survive for a long time, while the rearrangement of the bonding in the tadpole occurs. These structural properties in the relaxation process are consistent with the experimental suggestion: when the power of laser is weak, the S_8 ring does not polymerize but turns out to be a long-living product.

12.4.4 Polymerization

To investigate the polymerization process, Munejiri et al. [54] made a configuration in which the polymerization may occur by increasing the number of broken S_8 rings. They positioned four S_8 chains close to one another and performed the simulation, keeping four electrons in the excited state. After the electron excitation was stopped, they found that two S_{16} chains are formed by the four S_8 chains. They suggested that there are two processes of polymerization. One of the observed processes is that the two S_8 chains are connected by the edge atoms and turn into a long S_{16} chain. In another process, one of the S_8 chains first becomes a tadpole. When the other S_8 chain approaches that tadpole at one edge, the tadpole transforms into an S_8 chain, and the two S_8 chains become connected. The newly formed bonds were very stable and the two S_{16} chains survived throughout the simulation.

There are several questions regarding the tadpole. Does it have a paramagnetic property originating from unpaired spin at the dangling bond or is it non-magnetic? If an electron is transfered from a three-fold coordinated site to a one-fold coordinated site with a dangling bond, the paired spins at the one-fold site should be non-magnetic. Such a charge transfer is considered to occur in chalcogenide glasses producing a $C_3^+C_1^-$ defect pair which was suggested to be the origin of the photo-induced changes. Why is the tadpole so stable? This should be examined from the energetic point of view. What happens with the wavefunctions of the tadpole when two tadpoles approach each other and S_{16} polymer is generated? It is very important to investigate the elemental process of electronic and structural changes of two tadpoles approaching each other.

12.5 Photo-Induced Changes in Liquid Selenium

12.5.1 Transient DC Conductivity Measurements

In this section results of transient dc conductivity measurements [39] are described, in which the time variation of the voltage drop across the standard resistance after the laser illumina-

tion was measured using the method described in Section 12.2. The studies were performed changing two parameters: the intensity of the pulsed laser (over the 2–20 mJ/pulse range) and the temperature (over the 285–580 °C range).

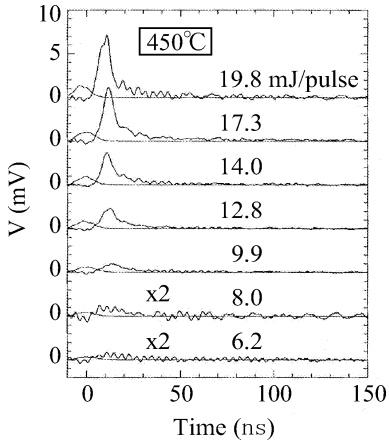

Figure 12.12: The voltage drop versus time when a pulsed laser with different intensities illuminates liquid selenium at 450 °C. The curves, which have peaks at 0 ns, indicate the pulse shape.

Figure 12.12 shows the voltage drop versus time when the pulsed laser illuminates liquid selenium at 450 °C. The intensities of the pulsed laser are indicated on each curve. The curves, each of which has a peak at 0 ns, indicate the pulse shape as a function of time. There is a small oscillation in the observed curves, which is considered to result from the electric circuit [39]. As seen in the figure, photo-induced changes occur upon illumination with a 6.2 mJ/pulse. With increasing laser intensity, the maximum voltage increases. The conductivity of liquid selenium corresponding to the maximum voltage for the intensity of 19.8 mJ/pulse is estimated to be 3.1 $\Omega^{-1}\,\mathrm{cm}^{-1}$ assuming that the photo-induced change takes place in the region of the penetration depth (885 Å) at 532 nm and at 450 °C [23], and using the value of the conductivity $\sigma = 9.9 \times 10^{-5}\ \Omega^{-1}\,\mathrm{cm}^{-1}$ [22] at 450 °C without illumination. The conductivity changes by more than four orders of magnitude. The process of reaching the maximum voltage takes about 5 ns for illumination with 6.2 and 8.0 mJ/pulse, and about 10 ns for illumination with pulses stronger than 9 mJ/pulse. Warren and Dupree [21] measured the correlation time for the molecular reorientation of liquid selenium over the temperature range 193–250 °C by means of NMR. When we extrapolate their data to 450 °C, the correlation time is estimated to be 10 ns. Such a long time suggests the possibility that the gradual increase of the voltage may be related to a gradual increase of the conductivity accompanying some structural changes in the chains of liquid selenium.

Two relaxation processes were observed when the intensity of the pulsed laser was stronger than 9 mJ/pulse. The relaxation times are 12 ns for the fast one and 94 ns for the slow one. The existence of two relaxation processes indicates that there are two components of electrical conduction and suggests that two different types of structure were formed after the illumination with the pulsed laser. On the other hand, there seems to be a single relaxation process with a relaxation time of 25 ns when the intensity of the pulsed laser is weaker than 9 mJ/pulse.

At 580 °C, the maximum voltage after the illumination with the 20.6 mJ/pulse reaches about 26 mV. The conductivity corresponding to this voltage is estimated to be 12 Ω^{-1} cm^{-1}. It should be noted that the conductivity changes by five orders of magnitude. According to Mott and Davis [55] and Mott [56], the minimum metallic conductivity should be about 20 Ω^{-1} cm^{-1} for liquid selenium. The value of the conductivity which we observed here is very close to this proposed value for liquid selenium.

Figure 12.13 shows the voltage drop across the standard resistance versus time for different temperatures. The laser intensity is fixed at 20 mJ/pulse. As clearly seen in the figure, the temperature increase seems to help the photo-induced changes in liquid selenium.

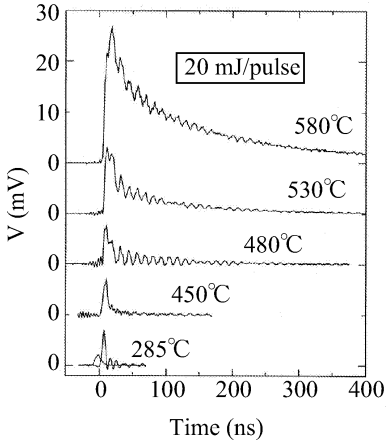

Figure 12.13: The voltage drop versus time when a pulsed laser with the intensity of 20 mJ/pulse illuminates liquid selenium at different temperatures. The curves, which have peaks at 0 ns, indicate the pulse shapes.

12.5.2 Maximum Voltage

Figure 12.14 shows the plots of the maximum voltage versus temperature for different laser intensities. As seen in the figure, the maximum voltage becomes extremely large above 500 °C for laser intensities of 10, 15 and 20 mJ/pulse.

Figure 12.15 shows plots of the maximum voltage versus laser intensity at different temperatures. As seen in the figure, there is a threshold of laser intensity at which the increase of the maximum voltage becomes large. At 450 °C, it is about 9 mJ/pulse. Above 500 °C, however, the threshold shifts to the low-intensity side. In addition, the value of the maximum voltage becomes large above 500 °C for laser intensities over the range 8–20 mJ/pulse. Thus, one can conclude that the nature of the photo-induced effect is changed at around 500 °C. As regards the structure of the selenium chain, at 500 °C, one selenium chain contains about 3000 atoms on average according to the estimation by Warren and Dupree [21]. When the pulsed laser illuminates liquid selenium at 500 °C with an intensity of 20 mJ/pulse, the ratio of the number of photons to the number of Se atoms in the illuminated region is estimated to be 1:2. Therefore, if the excitation of LP electrons causes the bond breaking, the chain length can

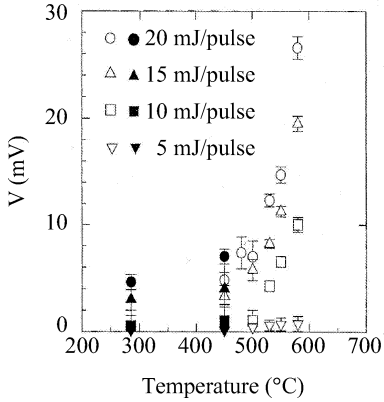

Figure 12.14: Maximum voltage versus temperature for different laser intensities.

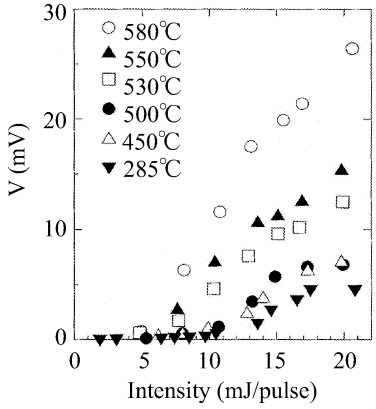

Figure 12.15: Maximum voltage versus laser intensity at different temperatures.

become short. In a short chain, the electronic states at the chain end are considered to affect the whole chain, resulting in a change of the chain conformation. Such short chains appear in fluid selenium near the liquid–gas critical point and show metallic character.

12.6 *Ab Initio* Molecular-Dynamics Simulation for Liquid Selenium

12.6.1 Bond Breaking in an Infinite Selenium Chain

To understand the experimentally observed photo-induced changes in liquid Se near the melting point, Hoshino and Shimojo [40] investigated the possibility that the bond breaking in an Se chain occurs when an electron is excited from the HOMO to the LUMO.

They took an Se helical chain composed of 14 atoms with 3.5-fold screw-rotation symmetry in the rectangular-parallelepiped cell and the periodic boundary conditions were imposed for the three directions. The neighboring chains were well separated, so that the model system can be considered as an assembly of isolated infinite chains. Their simulation was carried out at a temperature of 500 K.

When a photon is absorbed by an infinite Se chain, an electron in the HOMO is excited to the LUMO and after that the electron configuration was fixed. It is seen that, after the excitation, the LUMO and the HOMO are each occupied by one electron and one of the bond lengths starts to increase suddenly. The bond is considered to be broken. They investigated the time dependence of the single-electron energy eigenvalues. Before an electron is excited, there is a gap of about 1.5 eV between the HOMO and the LUMO, which are characterized mainly as the non-bonding 4p (LP) state and the antibonding 4p state, respectively. After the electron is excited, the eigenvalue of the HOMO starts to increase, while that of the LUMO starts to decrease. Since the LUMO is the antibonding state, it is energetically favorable to release the high energy due to the electron occupation of the LUMO by the bond breaking. Such a situation is similar to that observed in sulfur.

The time evolution of the wavefunctions of the LUMO was also investigated. Before the illumination the wavefunction spreads over the whole chain and has an antibonding character. After an electron is excited to the LUMO, the amplitude of the wavefunction increases around the Se–Se bond which will be broken, and decreases around other Se–Se bonds of the Se chain. At the same time the amplitude of the wavefunction of the HOMO is changed in a similar way to that of the LUMO. From these facts it was concluded that, when an electron is excited from the HOMO to the LUMO, one of the Se–Se bonds breaks so as to stabilize the antibonding LUMO state. As a result of the bond breaking, there appear states which have energy eigenvalues between the original HOMO and LUMO states whose wavefunctions have large amplitudes near both ends of the chains.

Hoshino and Shimojo [40] asserted that this bond breaking can be considered as one of the elemental processes of the photo-induced SC–M transition due to illumination with a pulsed laser [39]. Since real liquid Se near the melting point is an assembly of long helical Se chains, the laser illumination may produce many short chains which have energy eigenvalues in the middle of the gap and have wavefunctions with large amplitude near the ends of short chains. They considered that, as a result of these bond breakings, the gap of the electronic density of states disappears and the system becomes metallic.

The above simulation was essentially made for the infinite isolated chain. In real liquid Se, however, the *inter*-chain interaction is important. The bond breaking and the bond switching between different chains occur frequently due to the interchain interaction, in which lone-pair electrons play a crucial role. It would be interesting to study electronic and structural changes of the system containing many interacting chains when many electrons are excited simultaneously.

12.7 Final Remarks

In this chapter, studies of the photo-induced structural and electronic changes in liquid sulfur and selenium were described, focusing on the experimental results obtained by the present

authors. The photo-induced phenomena were discussed making use of the first-principle MD simulation by Hoshino and collaborators.

Liquid sulfur was found to be very sensitive to light. The role of LP electrons is important and the excitation of LP electrons from HOMO to LUMO induces enormous changes in the structure and electronic states of sulfur molecules. The excitation from HOMO to LUMO corresponds to illumination by a laser with the bandgap energy. When one uses a photon with a high energy sufficient to remove completely an LP electron from the sulfur ring, nothing happens because the ionized sulfur ring is stable. The use of a photon with the bandgap energy is essential and the excited electron should be kept in the LUMO states. This demonstrates that the photo-induced changes occur without a thermal origin.

The tadpole-shaped molecule discovered in the simulation for the relaxation process is very attractive. It is helpful to identify the metastable species and to consider the elemental process of the photo-induced polymerization. The structure and electronic properties of the tadpole molecule are also informative for the understanding of the photo-induced changes in chalcogenide glasses.

Photo-induced phenomena such as the generation of macromolecules of sulfur in strongly restricted geometry are interesting, and may indicate a new direction in the field of studies on photo-induced changes. Suppose liquid sulfur consisting of S_8 rings in the very small space with a thickness of, for example, 100 Å in which S_8 rings can move freely. What happens to the structure of liquid sulfur when a strong laser illumination produces long polymers instantaneously in such an extremely narrow space?

Concerning the photo-induced SC–M transition in liquid selenium, we do not have any direct evidence and still have several problems to be overcome experimentally. If a photo-induced SC–M transition in liquid selenium is confirmed, it will be very important from both academic and application points of view.

Acknowledgment

We are grateful to Professor K. Hoshino, Dr. F. Shimojo and Dr. S. Munejiri for valuable discussions and comments on the photo-induced phenomena in liquid sulfur and selenium. We are also grateful to Dr. A. Kolobov who has been interested in our work on photo-induced changes in liquids and encouraged us to write this chapter. Our work is partly supported by a Grant-in-Aid for Scientific Research from the Ministry of Education, Science, Sports and Culture of Japan.

References

[1] A.V. Kolobov and K. Tanaka, in Handbook of Advanced Electronic and Photonic Materials and Devices, H.S. Nalwa (Ed.), Vol. 5, Academic Press, San Diego, 2001, p. 47.

[2] R. Steudel, Top. Curr. Chem. **102**, 149 (1982).

[3] B. Meyer, Chem. Rev. **76**, 367 (1976).

[4] M. Schmidt, Angew. Chem. 85, 474 (1973).

[5] C.W. Thompson and N.G. Gingrich, J. Chem. Phys. **31**, 1598 (1959).

[6] R. Winter, C. Czornel, W-C. Pilgrim, W.S. Howells, P.A. Egelstaff, and T.J. Bodensteiner, J. Phys.: Condens. Matter **2**, 8497 (1990).
[7] R. Bellisent, L. Descotes and P. Pfeuty, J. Phys.: Condens. Matter **6**, A211 (1994).
[8] R. Bacon and R. Fanelli, J. Am. Chem. Soc. **65**, 639 (1943).
[9] F. Fehrer and A.Hellwig, Z. Anorg. Allg) Chem. **293**, 71 (1958).
[10] E. West, J. Am. Chem. Soc. **81**, 29 (1959).
[11] M. Kellas, J. Chem. Soc. **113**, 903 (1918).
[12] F. Fehrer,and A.Hellwig, Z. Anorg. Allg. Chem. **294**, 63 (1958).
[13] E. Sauer and B.Borst, Science **158**, 1567 (1967).
[14] H. Patel and B. Borst, J. Chem. Phys. **54**, 822 (1971).
[15] K. Tamura and F. Hensel, J. Non-Cryst. Solids **59**, 1079 (1983).
[16] K. Tamura, H-P. Seyer and F. Hensel, Ber. Bunsenges. Phys. Chem. **90**, 581 (1986).
[17] S. Hosokawa, T. Matsuoka and K. Tamura, J. Phys.: Condens. Matter **6**, 5273 (1994).
[18] A.V. Tobolsky and A. Eisenberg, J. Am. Chem. Soc. **81**, 780 (1959).
[19] Y. Sakaguchi and K. Tamura, J. Phys.: Condens. Matter **7**, 4787 (1995).
[20] C.H. Massen, A.G.L.M. Weijts and J.A. Poulis, Trans. Faraday Soc. **60**, 317 (1964).
[21] W.W. Warren Jr. and R. Dupree, Phys. Rev. B **22**, 2257 (1980).
[22] H. Gobrecht, D. Gawlik and F. Mahdjuri, Phys. Condens. Matter **13**, 156 (1971).
[23] S. Hosokawa and K. Tamura, J. Non-Cryst. Solids **117–118**, 52 (1990).
[24] S. Hosokawa, T. Kuboi and K. Tamura, Ber. Bunsenges. Phys. Chem. **101**, 12 (1997).
[25] A.A. Andreev, T. Turgunov and V.A. Alekseev, Sov. Phys.-Solid State **16**, 2362 (1975).
[26] V.A. Alekseev, V.G. Orcharenko, Ju.F. Ryzhkov and M.V. Sadovsky, JETP Lett. **24**, 189 (1976).
[27] H. Hoshino, R.W. Schmutzler and F. Hensel, Ber. Bunsenges. Phys. Chem. **80**, 27 (1976).
[28] H. Hoshino, R.W. Schmutzler and F. Hensel, Phil. Mag. **33**, 225 (1976).
[29] V.A. Alekseev, V.G. Orcharenko, Ju.F. Ryzhkov and M.V. Sadovsky, Phys. Lett. **A65**, 173 (1978).
[30] K. Tamura and M. Inui, J. Phys.: Condens. Matter **13**, R337 (2001).
[31] M. Inui, T. Noda, K. Tamura and C. Li, J. Phys.: Condens. Matter **8**, 9347 (1996).
[32] K. Tamura, J. Non-Cryst. Solids **205–207**, 239 (1996).
[33] Y. Soldo, J.L. Hazemann, D. Aberdam, M. Inui, K. Tamura, D. Raoux, E. Pernot, J.F. Jal and J. Dupuy-Philon, Phys. Rev. B **57**, 258 (1998).
[34] K. Tamura, Rev. High Press. Sci. Technol. **7**, 239 (1998).
[35] F. Shimojo, K. Hoshino, M. Watabe and Y. Zempo, J. Phys.: Condens. Matter **10**, 1199 (1998).
[36] H. Fukutome, Prog. Theor. Phys. **71**, 1 (1984).
[37] W.A. Harrison, Electronic Structure and Properties of Solids, Freeman, San Francisco, 1980, p. 93.
[38] Y. Sakaguchi and K. Tamura, J. Phys.: Condens. Matter **10**, 2209 (1998).
[39] Y. Sakaguchi and K. Tamura, J. Phys.: Condens. Matter **11**, 659 (1999).
[40] K. Hoshino and F. Shimojo, J. Phys.: Condens. Matter **10**, 11429 (1998).

[41] Y. Sakaguchi and K. Tamura, Rev. Sci. Instrum. **71**, 494 (2000).
[42] J.C. Koh and W. Klement Jr., J. Phys. Chem. **74**, 4280 (1970).
[43] A. Lallemand, C.R. Acad. Sci., Paris **70**, 182 (1870).
[44] M. Berthelot, C.R. Acad. Sci., Paris **70**, 941 (1870).
[45] A. Wigand, Z. Phys. Chem. **63**, 273 (1908).
[46] T.K. Wiewiorowsky and F.J. Touro, J. Phys. Chem. **70**, 3528 (1966).
[47] D.W. Gardner and G.K. Fraenkel, J. Am. Chem. Soc. **74**, 4280 (1956).
[48] P.W. Schenk and U. Thuemmler, Z. Elektrochem. **63**, 1002 (1959).
[49] T.K. Wiewiorowsky, A. Pathararathy and G.L. Slaten, J. Phys. Chem. **72**, 1890 (1968).
[50] R. Steudel and H-J. Mausel, Z. Anorg. Allg. Chem. **478**, 156 (1981).
[51] Y. Sakaguchi and K. Tamura, J. Non-Cryst. Solids **205–207**, 115 (1996).
[52] S. Oka, Proc. Phys.-Math. Soc. Jpn **24**, 657 (1942).
[53] F. Shimojo, K. Hoshino and Y. Zempo, J. Phys.: Condens Matter **10**, L177 (1998).
[54] S. Munejiri, F. Shimojo and K. Hoshino, J. Phys.: Condens. Matter **12**, 7999 (2000).
[55] N.F. Mott and E.A. Davis, Electronic Process in Non-Crystalline Materials, 2nd edn, Clarendon Press, Oxford, 1979, p. 187.
[56] N.F. Mott, Metal–Insulator Transitions, 2nd edn, Taylor and Francis, London, 1990, p. 241.

13 Staebler–Wronski Effect: Physics and Relevance to Devices

Paul Stradins and Michio Kondo

Light exposure in a-Si:H produces changes in photoconductivity (the Staebler–Wronski effect), creates Si dangling bond defects and deteriorates device performance. The Staebler–Wronski effect has been the most important issue of a-Si:H from both fundamental and application points of view for the last two decades and its mechanism has been studied extensively in terms of the carrier recombination processes and of hydrogen mediated structural change. The non-radiative bimolecular recombination of photo-carriers gives rise to defect creation during the dissipation of the phonon energy. Defect creation kinetics are insensitive to the exposure conditions such as temperature and light intensity. This suggests that the defect creation kinetics are not governed by the competition between different bulk recombination channels. Nevertheless, defect creation efficiency and their thermal stability strongly depend on the film microstructure and hydrogen content, particularly SiH_2 density in the film. Independent creation of defects in separated regions resulting in a wide distribution of defect creation rates is suggested. Time scales involved in defect creation suggest longer-living defect precursors. Another finding of much importance is that the carrier capture cross-section of the defect is intimately correlated with its thermal stability. This explains the very large changes in photoconductivity caused by relatively minor changes in defect concentration, as well as hysteresis loops between electron lifetime and defect concentration. This result implies a strong coupling between the electronic and structural nature of the defect. In fact, experimental evidence suggests structural changes in the medium range during the defect creation. The degradation of the devices has been well correlated with the defect creation in the bulk. The crucial parameter of the film property is the SiH_2 density in the film, which is mainly determined by the deposition rate. A successful control of the degradation by means of suppression of the SiH_2 density is demonstrated.

13.1 Introduction

Interaction between photons and material shows a wide variety of phenomena such as excitation of electronic states and subsequent relaxation with radiative or non-radiative emission of excess energy that sometimes results in the creation of new electronic or structural states. Radiation damage is a common issue in solids and their devices, and possible radiation sources are photons including cosmic rays, X-rays or γ-rays, and high-energy particles. When a high-energy electron irradiates crystalline silicon, for example, with an energy of $\sim 10^6$ eV, an isolated vacancy in the neutral state, V_0, is formed. The electronic state and thermal stability of the vacancy have been extensively studied [1].

In hydrogenated amorphous silicon (a-Si:H), on the other hand, it was found that the bandgap light ($h\nu > 1.7$ eV), that is, at photon energies much lower than those for the radiation damage of c-Si, causes large changes in photoconductivity (the Staebler–Wronski effect [2], 1977), indicating structural metastability of the amorphous network. Although the origin of photodegradation has been ascribed to the defect creation with some relevance to hydrogen, after more than 20 years of extensive research [3,4] the microscopic understanding of the mechanism is still an open question. a-Si:H being one of the most promising materials for inexpensive large area solar cell technology, this effect poses a challenge to the solar cell industry [5]. It is also a challenge to our understanding of the structural changes in disordered semiconductors.

Unlike in chalcogenide semiconductor glasses such as As_2S_3, in a-S:H light exposure does not produce significant changes in bulk optical or structural properties. However, large amounts of Si metastable dangling bond defects up to 10^{17} cm^{-3} are created, which act as charge carrier recombination centers. Besides defects, small changes in network structure are produced by light as confirmed by very sensitive detection techniques [6, 7]. These larger-scale changes are more likely to affect the carrier transport, while the deep defects strongly reduce the photocarrier lifetime.

It is largely accepted that the photodegradation is caused by Si dangling bond defects. Several defect creation models have been proposed. They follow the suggestion that an electronic bimolecular recombination [8] or trapping [9] event is important to trigger the structural reaction. The nature of the following structural reaction, however, is not clarified. The existing models suggest H atom insertion into a weak Si–Si bond [8] thus creating two spatially separated Si dangling bonds; H atom detachment from Si–H followed by its diffusion, trapping [10], and formation of double-H complexes [11]; creation of a pair of Si dangling bond and a highly mobile floating Si–Si bond, the latter diffusing away and reacting with defects, each other, or with Si–H [12–15]; and less specific atomic rearrangements involving wide distributions of energy barriers [9, 16, 17]. Light-induced defects have a wide distribution of annealing energy barriers [8, 18], thus they are unlikely associated with a single metastable configuration. It remains unclear how the hydrogen is involved in the defect creation. Pulsed ESR measurements reveal that H is excluded from the immediate vicinity of the light-induced defects and the defects are spatially isolated from each other [19]. On the other hand, solid evidence exists about the role of hydrogen in the annealing of the defects at elevated temperatures (above 150 °C). The annealing behavior of defects correlates with the temperature dependence of the atomic H diffusion, its dependence on doping, and the dispersive motion of hydrogen [20]. Clustered H also seems to be involved in defect creation [21, 22].

Despite being caused by the defects, photodegradation is not related to the defect creation in a straightforward and unique way [23–25]. Light exposures performed under different conditions (low temperature vs. high temperature, intense laser pulses vs. constant light illumination etc.) yield very different magnitudes of photodegradation for the same total amount of the defects created. As a consequence, hysteresis loops between the electron mobility–lifetime product and the number of defects in exposure–annealing cycles are observed [23, 25]. Defects that are thermally more stable affect the photoconductivity to a lesser extent [23, 25, 26]. Therefore, either very different defects are created under various conditions, or other entities are created along with defects that strongly affect carrier recombination. The existence of two different kinds of defects [23], wide distributions of the defect capture coefficients [17, 24],

and larger-scale structural changes in the network [6] accompanying defect creation were suggested. Partly because of the above non-unique relation between defects and photoconductivity, the photodegradation in solar cells is often difficult to relate to that in the i-layer bulk films.

This chapter deals with the physics of light-induced defect creation and its relation to the photodegradation in a-Si:H films and solar cells.

13.2 Creation of Si Dangling Bond Defects

Light-induced creation of Si dangling bond defects is likely initiated by a photocarrier recombination event followed by a structural reaction. The role of recombination was demonstrated by Staebler et al. by reduced photodegradation in pin structures under reverse bias [27]. Defect creation generally follows sublinear dependences both on time t and on the cw photocarrier generation rate G [8]:

$$N_D \sim G^m t^n \tag{13.1}$$

with $m \approx 0.6$ and $n \approx 0.33$ in the long-time limit. Defect densities N_D are typically measured by electron spin resonance (ESR) or by optical sub-gap absorption using photothermal deflection spectroscopy (PDS) or constant photocurrent method (CPM).

Stutzmann et al. [8] proposed that defect creation is triggered by bimolecular recombinations via localized tail states, which correspond to distorted Si–Si bonds. These events compete with recombinations via already existing defects. As the latter increase due to light exposure, the bimolecular recombination rate decreases leading to Eq. (13.1) [8]. This model assumes that defect creation rate mirrors the bimolecular recombination rate. This assumption can be tested by studying the defect creation kinetics under conditions where the bimolecular recombination dominates. Such a regime is realized at low exposure temperature T_e or at very high photocarrier generation rate G.

13.2.1 Defect Creation at Low Exposure Temperatures and Their Thermal Stability. Effect of High Electric Fields on Defect Creation

Light-induced degradation experiments were performed down to cryogenic temperatures [17, 24, 25, 28, 29]. At very low temperatures, recombination is mostly radiative and bimolecular owing to the large population of $\sim 10^{17}$ cm^{-3} electrons and holes trapped in the band tails [20]. Large densities of trapped photocarriers were confirmed by ESR [30] and by the photocurrent transients produced by re-excitation with IR light [31]. Thus at low T the defect recombination is weak leading to an almost constant bimolecular recombination rate. Under these conditions one expects to observe a linear increase of N_D with time t.

In the experiment, the defect density was monitored by relative changes in the sub-gap absorption α (1.3 eV) by CPM at 4.2 K. These relative changes in α agree well with those measured by CPM at 300 K on a sample degraded at room temperature and thus serve as a reliable measure of sub-gap absorption due to defects [24, 25]. Figure 13.1 shows the time

evolution of α due to light-induced defect creation at different exposure temperatures T_e [17]. At $T_e = 300$ K, $\Delta\alpha/\alpha_0$ increases with time sublinearly with n = 0.33 in agreement with Ref. [8]. At $T_e = 20$ K, the $\Delta\alpha/\alpha_0(t)$ is very similar to that at 300 K. These α changes are not related to the trapped carriers because they persist after applying bandgap and sub-gap measurement light, which greatly modifies the trapped carrier populations. Also, this long-term increase in α (1.3 eV) is not affected by the following prolonged ($\sim$1 h) exposures by strong infrared light with photon energies of 1–1.3 eV. Thus, it is due to the creation of metastable defect states at 20 K with very similar kinetics and efficiency as at 300 K. Similar defect creation is observed also at 4.2 K [25, 28, 29]. Surprisingly, less defects are created in the intermediate T_e range between 80 and 250 K.

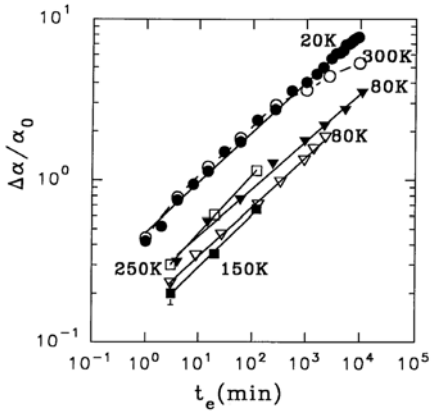

Figure 13.1: Kinetics of the increase in the sub-gap absorption due to the light-induced defect creation at different temperatures T_e. Cw light exposures were performed at photocarrier generation rate $G = 3.7 \times 10^{21}$ cm^{-3} s^{-1} [17].

All curves shown in Fig. 13.1 follow a sublinear t^n dependence with n ≈ 0.3, despite large differences in the relative contribution of bimolecular events in recombination. Figure 13.1 suggests that defect creation kinetics unlikely reflect the changes in the bimolecular recombination rate with the number of defects.

Therefore, even though the recombination processes over this wide T_e range vary drastically (from defect-controlled to largely bimolecular and from non-radiative to largely radiative), the defect creation remains remarkably robust and varies only within a factor of 3 in efficiency. Because the kinetics and G dependences are similar over the whole T range [17, 25], one can characterize the defect creation efficiency by N_D created by the same exposure at different T_e, see Fig. 13.2. Surprisingly, it exhibits a broad yet unexplained minimum between 80-250 K [17]. This is also observed in the degradation of photoconductivity [25].

Defect creation at low temperatures has been observed by other groups using ESR and luminescence techniques [18, 32–34]. Using the second harmonic ESR signal detection method combined with bleaching of the trapped charges by sub-gap light, Schultz et al. confirmed by ESR the creation of Si dangling bond defects at cryogenic temperatures [35].

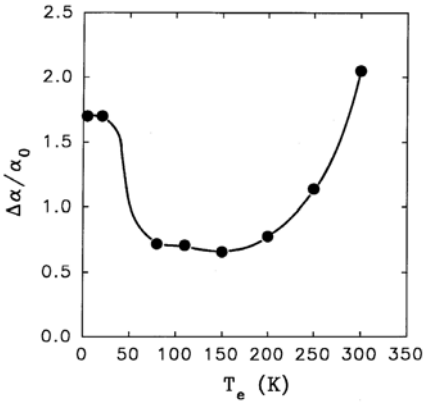

Figure 13.2: Increase in the sub-gap absorption due to the defect creation by identical cw light exposures for 2 h at different temperatures [17].

Defects created at low T_e have wide distributions of energy barriers for annealing [8, 18, 25]. Some of the defects created at 4.2 K are unstable at 200 K, while complete annealing is achieved only at 450 K [25, 36]. Zhang et al. [18] studied thermal stability of the defects created at 77 K by stepwise annealing. Their fitted distribution of activation energies is shown in Fig. 13.3. The exact shape of the distribution may be somewhat uncertain [37], yet it clearly spans over a wide energy range of 0.5–1.2 eV.

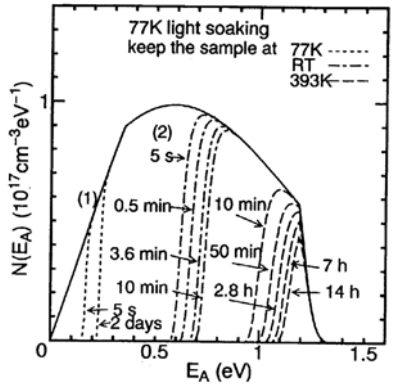

Figure 13.3: Fitted distribution of the annealing activation energies of the defects created by light exposure at 77 K (solid curve) and after keeping the exposed sample at various temperatures for times indicated [18].

In order to explain the robustness of the defect creation kinetics, one might consider that defect creation is triggered by some special recombination events. For example, it may be initiated by a geminate non-radiative recombination between the electron and hole. To test

this possibility, high electric field was applied during the defect creation at 4.2 K [17]. A 30% reduction in the defect creation efficiency under a field of 10^5 V/cm was demonstrated in a sample with coplanar electrodes. This effect is not due to the reduction of the total recombination rate in the film by spatial separation of the photocarriers as in p–i–n structures [27], but is rather due to changes in the recombination processes in the sample itself. It is possible that reduced degradation in compensated a-Si:H is due to similar built-in electric fields [3]. Despite the observed effect, geminate non-radiative processes are unlikely to be the main reason for the defect creation. First, the defect creation is very effective at high G (see the following section) where geminate recombinations are unlikely. Second, defect creation efficiency weakly depends on photon energy and is effective even at 1.1 eV excitation light [38]. Such a low-energy excitation is unlikely to provide enough energy for a single geminate non-radiative recombination to create a defect.

13.2.2 Defect Creation at Very High Photocarrier Generation Rates

Recombination is mostly bimolecular also at very high photocarrier generation rates G, such as during nanosecond laser pulses at $\sim 10^8$ suns. Large concentrations of photocarriers trapped in the valence (VB) and conduction band (CB) tails lead to the dominance of the bimolecular events over those via defects. When the product of trapped hole concentration and capture coefficient for electrons exceeds that for the defects, electrons in the extended states recombine mostly with trapped holes. In intrinsic a-Si:H, photoconductivity σ_p is mostly due to electrons. Thus, σ_p at very high G is expected to take the same value for different defect concentrations, provided that the transport properties remain unchanged. This value is governed by G, by the slopes of the CB and VB tails, by the capture coefficients into the tail states, and by extended state mobilities [39]. Photoconductivity is expected to increase with G approximately as $G^{0.5}$, reflecting the decrease of electron lifetime with trapped hole concentration.

Owing to the very short photocarrier lifetimes at high G, the photoconductivity values $\sigma_p(t)$ during the pulse correspond to the steady-state condition. This is confirmed by plotting $\sigma_p(t)$ against the corresponding $G(t)$ during the 5 ns laser pulse (Fig. 13.4). $\sigma_p(G)$ forms a single dependence $\sigma_p \sim G^{0.5}$ both for the rise and fall of the light intensity in the pulse and does not depend on how the value is reached. This demonstrates that recombination proceeds bimolecularly during the pulse with very short sub-nanosecond photocarrier lifetimes.

Similar behavior is observed for intense microsecond Xe flash pulses [39] where $\sigma_p(t)$ also takes quasi-steady-state values during the pulse. Thus, a graph of the steady-state photoconductivity in a-Si:H over 16 orders of magnitude in G can be composed from cw light, flash and laser pulse measurements (Fig. 13.5).

The annealed state was measured with small number of pulses to avoid its degradation. The photoconductivity dependences on G show two regions. In the first, low G region, σ_p steeply rises with G as $\sigma_p \sim G^\gamma$ with γ between 1 and 0.7 and is strongly affected by the Si dangling bond defects. The recombination is controlled by the defects and is monomolecular. Strong photodegradation is observed here. Note that a 10-fold increase in defect concentration produces more than 100-fold decrease in photoconductivity. This non-linear behavior is due to the difference in capture coefficients for native and light-induced defects and is discussed in Section 13.4.

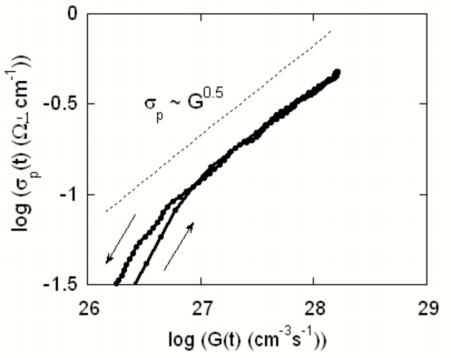

Figure 13.4: Instantaneous values of photoconductivity $\sigma_p(t)$ during the laser pulse plotted against the instantaneous values of the generation rate $G(t)$. Up and down arrows indicate the beginning and the end of the pulse, respectively [40].

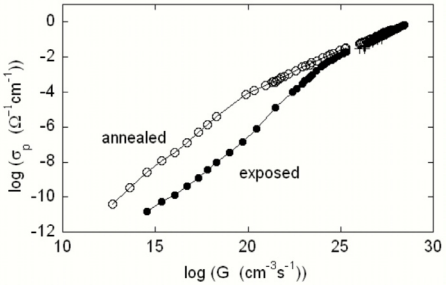

Figure 13.5: Steady-state photoconductivity of a-Si:H as a function of photocarrier generation rate for annealed ($N_D = 5 \times 10^{15}$ cm^{-3}) and light-exposed ($N_D = 5 \times 10^{16}$ cm^{-3}) states at $T = 300$ K. Data for $G \leq 10^{25}$ cm^{-3} s^{-1} and crosses are from Ref. [39], highest G data – ns laser pulses [40].

At high G we observe $\gamma \approx 0.5$. This is a bimolecular recombination regime where defects become irrelevant. For the annealed state it sets in at $G \sim 10^{20}$ cm^{-3} s^{-1} while for the exposed state it takes over at $G \sim 10^{24}$ cm^{-3} s^{-1}. This is due to the different concentrations of defects to compete with the bimolecular channel. Annealed and degraded state curves merge at very high G. Even the n-type and p-type a-Si:H approach the same dependence as doping also becomes irrelevant at very large G [39, 41].

Thus, at high G the bimolecular regime dominates. One therefore expects very efficient defect creation and linear dependences of $N_D(t)$ on both t and G because the bimolecular recombination rate is equal to G. Indeed, it was discovered [42, 43] that defects are created about 1000 times more efficiently by intense short laser pulses as compared with moderate cw light of 1–10 suns. Nevertheless, the time dependence remains sublinear with $n \approx 0.5$, while the G exponent of Eq. (13.1) is indeed close to $m = 1$ [42–44]. To explain the observed time dependence, Stutzmann et al. [42, 43] proposed that the defects are created by residual bimolecular recombination events *after* the pulse. As the photocarrier concentration decreases

after the pulse, the defects start to control the rate of the gradually weakening bimolecular recombination channel. Thus the time interval during which the defect creation takes place is given by the carrier lifetime after the pulse, which is inversely proportional to the defect concentration: $\tau \sim 1/N_D$. Solving the rate equation for defect creation in this case gives $m = 1$ and $n = 0.5$ [43].

This model leaves it unclear why the other, much more numerous bimolecular recombination events *during* the pulse do not trigger the defect creation. These recombination events are not influenced by defects [39, 45]. In addition, the decay of photoconductivity *after* the pulse is independent of the pulse energy [45]. The above assumption that this recombination tail controls the defect creation contradicts the experimentally observed linear G dependence of defect creation ($m = 1$).

These arguments were tested experimentally [40, 46]. Figure 13.6 shows photoconductivity transients produced by an intense 5 ns long laser pulse. Transients a, b, c, and d were taken at different stages of degradation by similar pulses at exposure times indicated on the figure. Transient e results from two-fold more intense pulse applied to the 2 min exposed film.

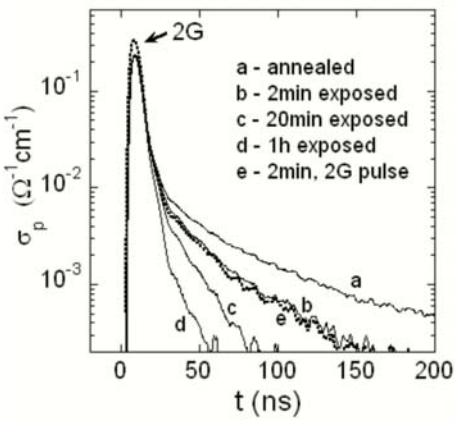

Figure 13.6: Transient photoconductivity during exposure to intense 5 ns bandgap light laser pulses of energy $E = 1.5$ mJ/cm^2 and the residual photoconductivity tails after the pulse (see text for details), after [40, 46].

First, the whole shape of the photoconductivity transient during the light pulse (within 5–20 ns) is independent of the state of degradation. This indicates that major recombination processes are not influenced by the defects, and that there are no light-induced changes in electron mobility or in CB and VB tails. It is only after the pulse, when conductivity drops about 20-fold that the defect recombination sets in and affects the photoconductivity transient. As shown above, a quasi-stationary state governed by very short (<1 ns) photocarrier lifetimes is established during the pulse [40]. Most of the recombination events (of the total of 2×10^{19} cm^{-3}) take place during the pulse and are bimolecular. Only a small fraction (estimated 1%) take place after the pulse and proceed through the defects (tails of the curves a–d). This small fraction of total recombination is unlikely to be responsible for the defect creation. First, it is almost independent of the excitation pulse energy: the long-time tail of $\sigma_p(t)$ re-

mains the same when the pulse energy is doubled, see curves d and e. Second, in another experiment, this tail of $\sigma_p(t)$ was greatly enhanced by applying a weaker, 6 μs long flash bias pulse simultaneously with the laser pulse. Nevertheless, no significant changes in the defect creation were observed [40]. Third, as will be shown in Section 13.2.3, creation of the new defects by pulses is not influenced by a large number of pre-existing defects. Therefore, defect creation is unlikely to be related to the residual recombination after the pulse. Rather, it is triggered by numerous bimolecular recombination events during the pulse.

To summarize, laser pulse exposure experiments show that defects are created very efficiently at high G where bimolecular recombination dominates. However, the defect creation kinetics even under these conditions are sublinear with $n = 0.5$. This dependence does not originate from the influence of existing defects. The latter do not influence the bimolecular recombination rate during the pulse. They do affect the residual recombination tail after the pulse, but the experiments show that this tail has no relevance to the defect creation. Finally, large amounts of pre-existing thermally stable defects have no influence on the creation of new defects, see the next section. Therefore, the origin of the sublinear kinetics of light-induced defect creation is neither related to changes in bimolecular recombination rate nor to any influence of the pre-existing defects on the creation of the new defects. It seems more likely that these kinetics originate from a disorder-related wide distribution of the creation time constants [17]. Experimentally observed wide distributions of the defect annealing activation energies (Fig. 13.3) indirectly support the above suggestion.

13.2.3 Influence Between Groups of Defects with Different Stability

To understand the mechanism of defect creation it is important to clarify the origin of the robust sublinear defect creation kinetics (Eq. (13.1)). The creation of new defects might be suppressed by the presence of the existing defects. This interaction might be either via photocarriers [8] or other mobile species [11,13]. As shown above, the photocarriers seem unlikely. Branz [11] suggested that defect creation is accompanied by a release of mobile H atoms from Si–H bonds. These mobile H atoms either recombine with the dangling bonds or form metastable complexes by pairing with each other on a weak Si–Si bond. The latter process stabilizes the newly created Si dangling bonds. In this model, it is the mobile H that realizes the interaction between the defects. When many defects pre-exist in the sample, mobile H recombines with them and the creation of new metastable H complexes is suppressed, as is the creation of new metastable defects. By solving coupled rate equations, sublinear creation kinetics for cw and pulse regime were obtained in agreement with the experiment [11]. Similar arguments are the basis of model by Biswas et al. [13] where instead of mobile H, mobile floating Si bonds are created together with the defects. They can either recombine with defects or form weak Si–Si bonds by pairing with each other. Their steady-state concentration depends on the defect concentration. In the above models, mobile atomic species establish a global link between different defects in the sample. It is important to test experimentally whether such an interaction between the defects exists.

For this, the following experiment was performed [47]. All light-induced defects were formally divided into two groups, which differ by their thermal stability. The first group, “soft” or S-defects, are those which anneal out by heating the sample to 360 K. The other group, “hard” or H-defects, remain stable upon heating to 360 K. By performing 360 K annealing

before and after exposure, one measures the changes in the concentrations of defects in both groups. Samples were subjected to identical exposure at 300 K by laser pulses for 8 h in two cases. In the first case, the films had been annealed at 470 K before the exposure and thus contained only a small amount of H-defects. In the second case, films contained numerous H-defects created by a prolonged pre-exposure at 360 K. Figure 13.7 shows the increase in the S-defect concentration $\Delta\alpha$(S) (given by sub-gap absorption α) due to exposure at 300 K as function of the pre-existing H-defect concentration given by α(H).

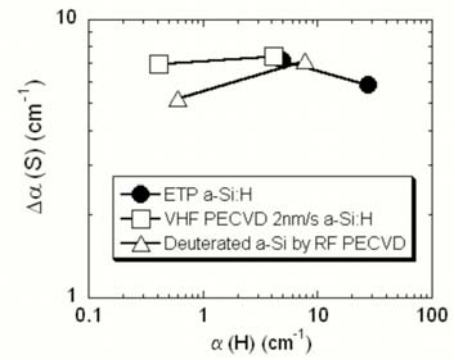

Figure 13.7: Increase in the unstable (S) defect concentration by laser pulse exposure at 300 K in the presence of different amounts of pre-existing stable (H) defects. Three different intrinsic a-Si:H films were prepared by expanding thermal plasma (ETP), VHF SiH_4 plasma, and deuteriated silane RF plasma. Defect densities are measured by the sub-gap absorption α (1.24 eV). Data from Ref. [47].

Surprisingly, the amounts of S-defects created in the presence of very different concentrations of H-defects are almost identical within experimental error. The latest experiments [48, 49] show that the creation of both S and H defects by laser pulses even follows similar kinetics with $n \approx 0.5$. These results strongly suggest that each group of defects is created independently and there seems to be no entity that establishes "global" link between them. Instead of the global interaction proposed in the above models [8, 11, 13], it seems more likely that defect creation and annealing might be a very local process restricted to the vicinity of special atomic structures like bivacancies [50], voids, or other unusual regions. In this case, no global link establishes between defects created in these separated regions. Defect creation rates might vary from region to region. Such a wide distribution of defect creation rates provides an alternative explanation for the sublinear creation kinetics without involving a global link between different groups of defects.

13.3 Effect of H-Content and Microstructure. Defect Precursors. Structural Changes

Defect creation depends on the film microstructure and hydrogen content. Defect creation is very effective in disordered a-Si:H films deposited at low substrate temperature and having high H content. In contrast, defect creation is suppressed in defective films with low H content

prepared by H effusion [51]. These variations might be due to both the H-content and film microstructure. The better correlation between the SiH_2 density rather than the SiH density in the film and the photocreated dangling bond density has been pointed out [52, 53]. Clustered H is also likely to be involved in photodegradation [22]. These effects could be ascribed to the structural flexibility of the network due to the lower coordination number of Si atoms, in spite of the absence of the direct experimental evidence of the contribution of the SiH_2 or SiH cluster to the defect creation. On the other hand, the defect creation efficiency varies little in a wide range of device quality films [24, 47]. However, defects created in these films have different thermal stability depending on the deposition method [47].

Defect creation by cw light is reduced in amorphous a-Si:H films containing a small fraction of microcrystallites [54]. This has been attributed to an alternative recombination path via crystallites [54]. On the other hand, the amorphous phase itself appears more ordered in films prepared near the microcrystalline threshold [55] and thus might have different light-induced defect properties (e.g. thermal stability).

Light-induced defect distribution in the depth of the film suggests that there are no defect precursors that diffuse long distances [56]. The defect depth profile is wider than that of the photocarrier generation rate, yet it can be explained by the commonly observed sublinear generation rate dependence (Eq. (13.1)) of creation efficiency [57].

Time scales of the defect creation were studied in order to establish the existence of slower defect precursors [46]. A sample was degraded by pairs of intense nanosecond laser pulses. Degradation was studied as a function of the delay time between the pulses in the pair. Defect creation by the second pulse might be enhanced by the defect precursors left after the first pulse. Experiment reveals two time scales in these dependences. The shorter one is approximately equal to the width of the light pulse and is likely due to the photocarriers surviving from the first pulse that contribute to the bimolecular recombination events of the second pulse. The second time scale is in the microsecond range and might be related to slower atomic precursors [40,46]. If related to mobile hydrogen [11], this would correspond to its diffusion by only few nm at room temperature. Separated regions suggested in Section 13.2.3 might restrict the diffusion of the hypothetical precursors.

Besides the defect creation, larger scale structural changes take place under light exposure [6]. The network flexibility allows spatially extended relaxation of the order of nm accompanied with defect creation. The photo-induced volume expansion (PVE) [7] has been thoroughly studied. PVE does not apparently correlate with defect creation, since it exhibits different kinetics and G dependence [58–61], and it strongly depends on the exciting photon energy [62]. The deposition condition dependence of PVE has also been studied [63, 64] and it does not apparently correlate with the defect creation efficiency. These effects are discussed in more detail in another chapter. Larger scale structural changes possibly affect charge carrier transport properties such as mobility, but this effect is too small to be detected in standard measurements. Small light-induced changes in the photoconductivity at high G (Section 13.2.2), drift mobility [65–67], and Urbach tail [68] all indicate small changes in transport properties. As shown below, photodegradation is mostly due to the changes in the photocarrier lifetime.

13.4 Light-Induced Degradation of Photoconductivity

At room temperature under a low photocarrier generation rate ($<10^{19}$ cm^{-3} s^{-1}), carrier transport is in the extended states and their lifetime is largely controlled by defects. Indeed, the inverse free electron lifetime τ^{-1} can be approximated by the following simplified expression:

$$\tau^{-1} = c_0 N_0 + c_1 N_1 + c_2 N_2 + c_3 p_t + \cdots \tag{13.2}$$

where the products of concentrations of recombination centers N_i and their capture coefficients c_i are summed over sets of species active in recombination [69]. They include N_0 native defects and p_t holes trapped in the VB tail. Light-induced defects here are represented by two sets N_1 and N_2. The latter reflect a wide range in the capture properties of the light-induced defects, as will be demonstrated below. If the concentration of neutral defects is relatively high and the photocarrier generation rate G is low, then the contribution of the VB tail states and the charge transfer from these states into defects can be neglected and the defects dominate the recombination. One would thus anticipate that a 10-fold increase in the defect concentration by light exposure lowers the mobility–lifetime product $\mu\tau$ 10 times. One would also expect the majority photocarrier lifetime to be a unique function of the total number of defects if they all have similar properties. The experimental result, however, is different as demonstrated by Fig. 13.8.

Figure 13.8 shows the normalized photoconductivity σ_p/eG temperature dependences for different intrinsic a-Si:H samples. σ_p/eG is equal to the electron mobility–lifetime product $\mu\tau$ except for the $T < 40$ K energy-loss hopping region. Standard glow discharge film from the University of Chicago, remote plasma CVD by Xerox, heated mesh PECVD by Electrotechnical Laboratory, and hot wire CVD film (with low 1.8% hydrogen content) by National Renewable Energy Laboratory were studied [24]. In the annealed state, the films are highly photoconductive at room temperature. After degradation for 120 h at room temperature by $G = 10^{22}$ cm^{-3} s^{-1} cw light, the σ_p at 300 K drops $\sim$100 times and takes similar values in all samples [24]. Surprisingly, this corresponds to an only nine-fold increase in the defect concentration ($\alpha/\alpha_0 = 9$). This strong reduction in σ_p at high temperatures is not related to possible shifts in the Fermi level [24]. The changes in σ_p are small in the low T region, indicating small changes in CB tail according to the energy-loss hopping model [70].

The degradation of σ_p becomes even stronger when the light exposures are performed at low temperatures. The bottom curve represents the same Chicago sample after 164 h light exposure at 20 K performed at $G = 3.7 \times 10^{21}$ cm^{-3} s^{-1}. This 20 K exposure produces almost the same number of defects ($\alpha/\alpha_0 = 8$) as the above 300 K exposure, yet it degrades σ_p much more. Thus, defects created at different temperatures have different effects on the photoconductivity. This is further evidenced by stepwise annealing, which gradually eliminates unstable defects. The 20 K exposed sample was annealed at 300 K for 30 min. This annealing reduced the total number of defects by only 20%, while the photoconductivity increased by more than a factor of 10 (dotted curve with double arrow), close to the 300 K exposure curve.

As seen from Fig. 13.8, the degradation of the photoconductivity is not related to the defect creation in a simple inverse-linear and unique way. First, the photoconductivity degrades by several orders of magnitude while the defect density is increased by less than a factor of 10 by light exposure. Second, equal numbers of defects produced under different conditions (different exposure T, or after partial annealing) give rise to very different photoconductivity

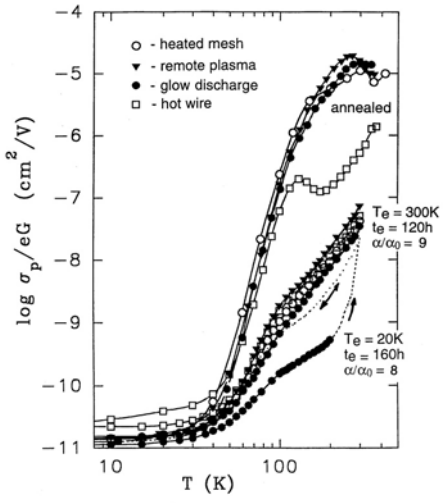

Figure 13.8: Normalized photoconductivity σ_p/eG as a function of T for different a-Si:H samples in the annealed (upper family of curves) and strongly degraded states (lower curves). Bottom curve: glow discharge a-Si:H after light-induced degradation at 20 K and the result of subsequent annealing at 300 K. Defect concentrations relative to the annealed state are given by the sub-gap absorption ratios α/α_0 at 1.3 eV; the measurement G is $\sim 10^{18}$ cm^{-3} s^{-1}; after [24].

values. The defects created at higher exposure temperature or left after partial annealing to higher temperature reduce the photoconductivity less. The latter effect was first demonstrated by Han and Fritzsche [23] by hysteresis loops between photoconductivity and sub-gap absorption upon light exposure and subsequent annealing. These loops were observed later by several groups [18,25,29,71,72]. It thus appears that more thermally stable defects have lower capture coefficients for photocarriers, as first suggested by Shepard et al. [26].

In Figure 13.9 the inverse mobility–lifetime product $(\mu\tau)^{-1}$ is plotted as a function of the number of defects produced by light exposure. Linear dependences are obtained [47], similar to Refs. [73–75]. Thus Eq. (13.2) can be approximated by $\tau^{-1} = c_{\text{eff}} N_D$, where c_{eff} is the effective defect capture coefficient for the ensemble of defects created. They are indeed strongly reduced at higher exposure temperatures (compare dark and open circles). This explains the non-unique dependence of σ_p on N_D. Large nonlinear changes in σ_p with defect concentration (Fig. 13.8) can also be explained by large differences between capture coefficients of defects having different thermal stability. Indeed, the capture coefficient of native (stable) defects c_0 in Eq. (13.2) is about 10 times lower than that for light-induced defects c_{eff} [47, 76]. Therefore, increasing N_D by factor 10 by light exposure reduces the photoconductivity by a factor of 100. In the experiment, this effect is typically seen as a sharp drop in the photoconductivity at the beginning of light exposure. This behavior is not evident from the linear plot of Fig. 13.9 since the native defect concentrations are low.

It may seem puzzling that the exposure curves in Fig. 13.9 are linear. Indeed, a whole spectrum of defects is created during the 300 K laser pulse exposure, with a wide distribution

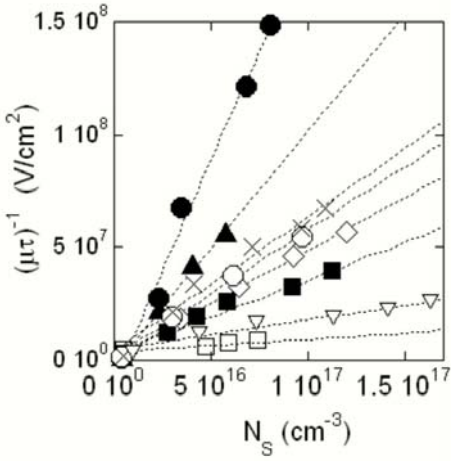

Figure 13.9: Relation between $(\mu\tau)^{-1}$ and defect spin concentration N_S due to light exposure (by nanosecond laser pulses). Exposure was performed at 300 K unless otherwise specified. Closed circles, Expanding Thermal Plasma film prepared at 250 °C; open circles, same sample exposed at 360 K. Dark triangles, VHF 20 Å/s film deposited at 250 °C; crosses – PSU H-diluted $R = 10$ RF a-Si:H; diamonds, D-diluted VHF film with $\mathrm{D}/(\mathrm{D}+\mathrm{H}) = 0.2$. Open triangles, VHF 5 Å/s, 350 °C a-Si:H. Closed squares, RF a-Si:D, open squares, same film exposed at 360 K [47].

of the annealing activation energies (see Section 13.2.1) and thus of their capture coefficients. In Eq. (13.2), two model sets of light-induced defects N_1 and N_2 can be associated with two different stability groups similar to S-and H-defects of Section 13.2.3. The capture coefficients of S-defects are higher than those of H-defects. Nevertheless, the creation of S- and H-defects has similar kinetics [48, 49]. Thus, their concentration ratio N_1/N_2 remains constant during the creation and Eq. (13.2) can be approximated as $\tau^{-1} = c_{\mathrm{eff}} N_D$. This might not be the case for prolonged cw exposures where S-defects tend to saturate [76].

The relation between the defect annealing energy distribution and their apparent capture coefficients is demonstrated in Fig. 13.10 [47]. The defects were created by laser pulse exposures in three different films and subsequently stepwise annealed to the temperatures indicated on the figure. Stepwise annealing destroys less stable defects with high capture coefficients, thus the annealing curves lie below the exposure curves and form hysteresis loops of different widths.

The width of the hysteresis loops depends on the width of the defect annealing energy distribution. Defects created in the high deposition rate ETP film at 300 K are relatively hard to anneal as demonstrated by the stepwise annealing experiments. They have a wide annealing energy distribution [48, 49]. This sample has the widest hysteresis loop (left loop, A). In contrast, light-induced defects in the $R = 10$ film (deposited near the microcrystalline threshold) are quite unstable: about 25% anneal out within 2 days at room temperature [47]. Their annealing energy distribution is narrow [48,49]. This corresponds to a narrow hysteresis loop (B, crosses). Wider spectrum of more stable defects is created in a standard VHF sample (B, triangles) in which the hysteresis loop is wider than in the $R = 10$ film. Defects with

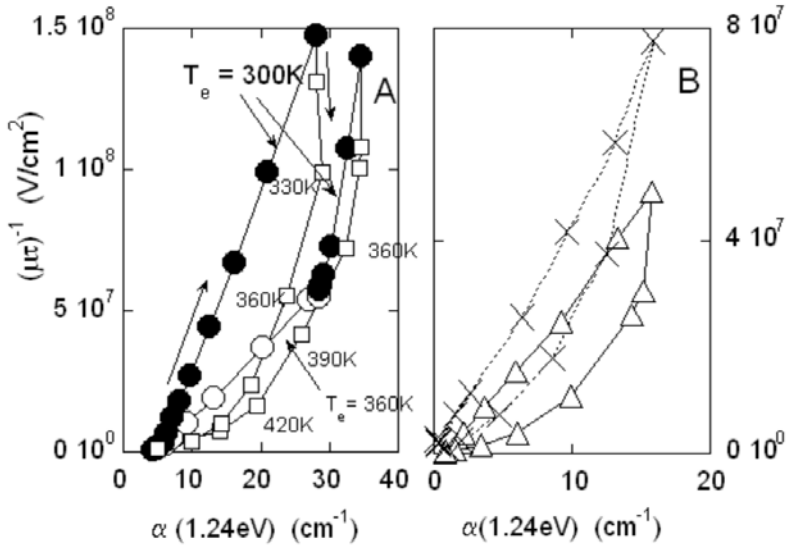

Figure 13.10: (A) Relation between electron inverse $\mu\tau$ product at 300 K and sub-gap absorption in Expanding Thermal Plasma (ETP) a-Si:H film. Closed circles, left exposure at 300 K; open circles, exposure at 360 K, followed by additional exposure at 300 K (closed circles, right). Open squares and the annealing temperatures indicate stepwise annealing. (B) Exposure at 300 K followed by stepwise annealing in VHF low rate a-Si:H (triangles) and PSU $R = 10$ transition region sample (crosses). Upper parts of the loops, exposure; lower parts, annealing [47].

a narrow activation energy distribution were created in the following experiment. The ETP sample was first strongly pre-exposed at 360 K (A, open circles) producing numerous stable H-defects. The exposure was continued at 300 K (A, closed circles, right). This exposure mostly generates unstable S-defects and only a few additional H-defects. These S-defects anneal out (open squares) at slightly above 360 K and thus have narrow activation energy distribution. They have high capture coefficients as evidenced by the steeper slope of the $(\mu\tau)^{-1} = f(\alpha)$. They exhibit very narrow hysteresis loop upon annealing. Thus, narrow defect annealing energy distributions correspond to narrow hysteresis loops, and vice versa.

Large variations in capture coefficients of the defects might be related to variations in their atomic surroundings or energy levels in the gap. The latter were investigated by sub-gap absorption $\alpha(h\nu)$ measurements by CPM at 4.2 K [36]. This technique detects optical transitions of majority photocarriers – electrons from the gap states to the conduction band. Figure 13.11 demonstrates changes in the spectral shape of $\alpha(h\nu)$. During the exposure at 4.2 K, α values at photon energies larger than 1.1eV increase monotonically (a) following the defect creation kinetics: $\alpha \sim t^{0.33}$, and they decrease monotonically (b) as defects anneal out. The lower-energy values of α ($<$1.1 eV), however, remain constant or even decrease during the exposure. Upon annealing, they exhibit an unexpected increase before the final decrease.

This increase starts at the same temperature 200 K above which the degraded $\mu\tau$ - product starts to recover, see Fig. 13.8.

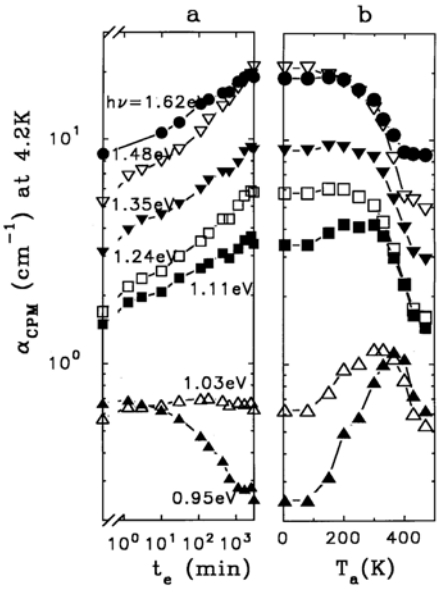

Figure 13.11: Changes in the sub-gap absorption at different photon energies due to the light exposure at 4.2 K (a) and subsequent partial anneal (b) at higher temperatures T_a [36].

These non-monotonic changes in α ($<$1.1 eV) might be related to changes in the defect states density or in their occupancy. Lower energy photons can excite electrons from only a part of the defect states distribution closer to CB, while higher energy ones are likely to excite all the defect states. The surprising constancy or decrease of low-energy α during exposure suggests that these states either become reduced in number, or their occupancy is lowered owing a weak p-type doping effect by some newly created states closer to VB edge. Most likely, additional states accessible for $h\nu < 1.1$ eV are also photocreated but they largely remain empty and thus are not detected by CPM. Annealing behavior of α ($<$1.1 eV) might be associated with a movement of defect energy levels closer to the CB edge as the metastable changes in structure around them anneal out [17, 36]. The second possibility - replenishment of the electron occupancy by annealing seems more consistent with the changes in $\alpha(h\nu)$ during the exposure (Fig. 13.11a).

Spectral changes similar to those of Fig. 13.11 were observed also for 300 K exposures [75, 77] and subsequent annealing [75] and were related to the disappearance of unstable defects and changes in electron mobility–lifetime product. The capture properties of defects seem to correlate with the spectral changes in $\alpha(h\nu)$. The explanation of this relation remains a challenge, which may help to understand the mechanism of defect creation and photodegradation. For example, floating bond states are expected to act as electron acceptors [14] and thus might be candidates for the above light-induced p-type doping effect. According to Shimizu

et al. [14] and Biswas et al. [13] they are created together with defects. On the other hand, the light-induced p-type doping suggested above is inconsistent with experimental observation that the Fermi level typically moves toward the midgap upon photodegradation independently of the type of doping.

13.4.1 Photodegradation of Solar Cells

Since the carrier diffusion length in a-Si:H is much lower than in crystalline Si, the photogenerated carriers are collected by the internal field. The spatial separation of the photocarriers prevents their recombination and accompanied defect creation. Under the open circuit condition, therefore, the degradation occurs most seriously, while under the short circuit or reverse biased condition the degradation is much less. The effect of the magnitude of the internal field also determines the thickness dependence of the degradation. The photocurrent and the degradation have a trade-off relation as shown in Fig. 13.12. This relation limits the i-layer thickness as well as the photocurrent value, resulting in the tandem cell structure to obtain sufficient efficiency.

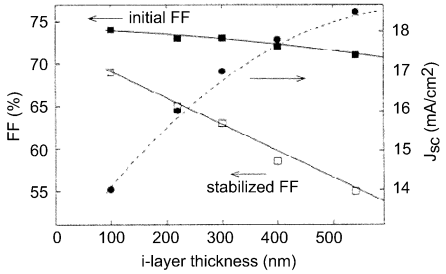

Figure 13.12: The fill factor FF of the a-Si:H solar cell before and after degradation, and its short circuit current J_{sc} plotted as functions of the i-layer thickness. The light soaking condition was simulated sunlight after standard atmospheric air mass (AM 1.5) at intensity 100 mW/cm^2; after [78].

Another crucial factor for industrial application is the effect of deposition rate upon the degradation. In the actual manufacturing process, a deposition rate of 1–2 nm/s is required for the a-Si:H intrinsic layer. It has been known that the photodegradation becomes more significant with increasing deposition rate [79]. The cause of this dependence has been ascribed to the increase in the SiH_2 density in the film with increasing deposition rate. The hydrogen content as a function of the deposition rate has been reported in a wide range of deposition rates [78]. As shown in Fig. 13.13, the reduction in the fill factor after the degradation increases with increasing SiH_2 density in the film.

It has been clarified that the SiH_2 density is dominated by the higher silane related species formed in the plasma particularly under high deposition rate conditions [80]. It has been reported that the SiH_2 density in the film is determined by the structural relaxation of adsorbed radicals in the surface region accompanied by hydrogen evolution, i.e. 2Si–H $\rightarrow$ Si–Si + H_2. The structural relaxation is disrupted by the higher silane radicals such as Si_2H_5, Si_3H_7 and so on because of their heavy mass and the steric hindrance [80], and the higher silane is more effectively formed in the plasma with higher electron temperature [81]. Therefore, there are

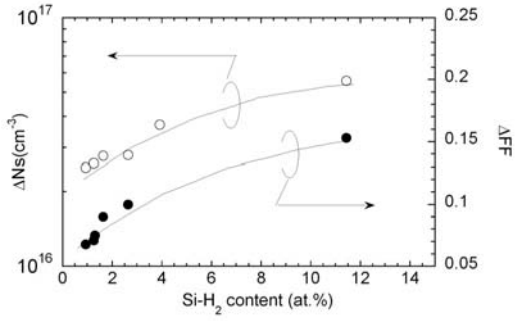

Figure 13.13: The reduction in the fill factor after the degradation as a function of SiH_2 density using a Schottky cell structure. The film thickness is nearly 1 μm. The films were deposited under various conditions.

two possible ways to suppress the SiH_2 density under a high deposition rate: to suppress the electron density and to elevate the deposition temperature. The lower electron temperature is obtained by means of plasma in the VHF region ($>$50 MHz). The structural relaxation is activated at higher deposition temperatures even in the presence of the higher silane radicals on the surface. As a consequence the photo degradation is significantly improved from 38% to 12% using the combination of the VHF plasma and a higher deposition temperature together with moderate hydrogen dilution [82] as shown in Fig. 13.14. The low-temperature deposition without hydrogen dilution results in severe degradation by 38%, which is improved by higher deposition temperature (20%) and further improved by hydrogen dilution (12%). A stabilized efficiency of 8.2% under 2 nm/s was obtained, which is the highest value among reported to date.

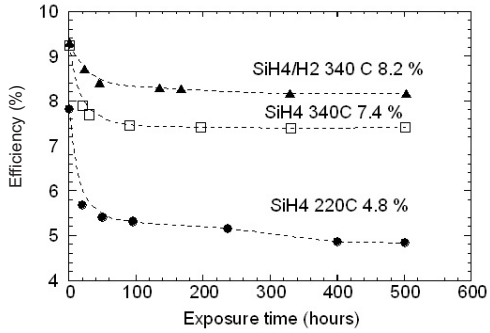

Figure 13.14: Photoinduced degradation behavior of the solar cell efficiency prepared under different conditions. The solar cell had an n–i–p structure with a textured ZnO coated stainless-steel substrate. The deposition rate is nearly constant at 2 nm/s for all of the cell; after [82].

To control degradation one needs to understand its mechanism and to relate the properties of bulk films with those in cells. Below we attempt to draw some link between them based on the results in Sections 13.2 and 13.4. Depositing an amorphous i-layer near the

microcrystalline transition by using H-diluted silane source gas has so far proven one of the most promising approaches [5, 83]. The photoconductive properties of the final degraded state depend on the light-induced defect creation efficiency, their thermal stability (distribution of annealing energies), and on their capture coefficients. The defect creation efficiency is remarkably similar over a wide range of device-quality films (see Fig. 13.8 and Ref. [47]). Cells, however, are operated at elevated temperatures and over extended periods of time, where defect density tends to saturate. This saturation value is more related to the defect annealing energy distribution than to their creation efficiency. These distributions depend on the film microstructure [48, 49]. For example, light-induced defects in the $R = 10$ film near the microcrystalline transition are remarkably unstable [47]. At elevated exposure temperature they saturate at low levels. This might explain the high stability of the solar cell with similar i-layers. If the activation energy distribution is broad, hard defects continue to accumulate under prolonged exposure at elevated temperature resulting in a high saturation value.

The capture properties of the defects are also likely to be important. Electron capture by defects in films depends on the exposure temperature and on the film deposition technique [47]. It is not clear whether the capture coefficients for electrons correlate with those for holes. Cell efficiency is strongly governed by the hole mobility–lifetime product [20]. However, a correlation of the cell properties with the electron $\mu\tau$ product has been emphasized [77]. In the experiment below, light-induced degradation of the bulk a-Si:H film was related to that of a solar cell with an identical i-layer [48]. The resulting changes in defect density of the film and inverse mobility–lifetime product for electrons are plotted against the cell short circuit current in Fig. 13.15. Photodegradation in both the film and the cell was performed at two different temperatures at the same nanosecond pulse generation rate G.

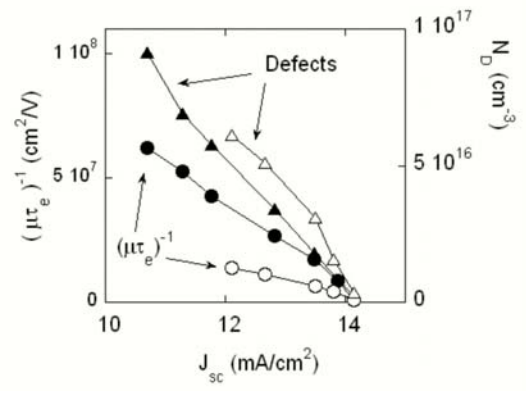

Figure 13.15: Inverse electron $\mu\tau$ (circles) and defect spin density (triangles) of the a-Si:H film plotted against the solar cell J_{sc} during the light exposure at 300 K (closed symbols) and 360 K (open symbols). The cell i-layer material is identical with the film; after [48].

As seen from the figure, neither the defect concentration nor the inverse electron $\mu\tau$ product uniquely correlates with the cell J_{sc} when defects are created at different exposure temperatures. The extent of cell degradation depends on the thermal stability of the created defects. This implies different cell degradation by defects having different capture coefficients for

electrons. On the other hand, degradation of the cell in Fig. 13.15 is not fully governed by the inverse electron $\mu\tau$ product either, which is proportional to the quantity $c_{\text{eff}}N_D$. This is likely due to a strong influence of hole processes and their different capture coefficients into defects.

13.5 Summary

Both the creation efficiency and kinetics of light-induced defects vary relatively little over a wide temperature range down to liquid He temperature. They are not governed by the competition between bimolecular and defect recombination channels. This is evidenced by sublinear time dependences of defect creation at low temperatures and at high photocarrier generation rate G where the bimolecular recombination dominates. These results indicate that defect creation is not triggered by the recombination events that dominate in the bulk. Rather, it might be triggered by recombination processes in special isolated regions such as near voids, in H-rich or H-poor regions, etc.

To explain the above very robust kinetics of the defect creation, models involving other metastable species created together with defects were proposed. These species might be mobile hydrogen [11] or Si–Si floating bonds [13, 14]. Creation of new defects is suppressed via capture of these species by the pre-existing defects. Experiment, however, does not provide any evidence for such an interaction between the defects. Large amounts of thermally more stable defects have no effect on the creation of less stable defects. Independent creation of defects in separated regions with wide distributions of creation rate constants might provide an explanation for the kinetics.

Photodegradation is caused by the changes in photocarrier lifetime. No significant changes in the mobility or band tail states take place. Thus, photodegradation is caused by light-induced defects that act as recombination centers. However, the capture properties of the defects vary over a wide range and correlate with the defect thermal stability as first suggested by Shepard et al. [26]. These large variations in capture coefficients are responsible for the observed non-linear relation between the photoconductivity and defect concentration and for the hysteresis loops between those quantities during the exposure–annealing cycles. The changes in electron mobility–lifetime product are related to the creation or disappearance of a certain number of defects with given thermal stability. Hence narrow hysteresis loops between $(\mu\tau)^{-1}$ and defect concentration result from narrow annealing energy distributions of the light-induced defects, while wide energy distributions produce wide loops.

Apparent capture coefficients might be influenced by hypothetical species that accompany defect creation. It is essential that these species are created and disappear together with defects because of the above relation between the defect capture coefficients and their thermal stability. Possible candidates are mobile H or Si floating bonds. The capture properties of the defect might be influenced by such a nearby species forming an electron trap [47]. Such a nearby trap serves as an intermediate state for non-radiative tunneling into the defect [84]. Defect capture might also be influenced by a weak doping effect by other species acting as electron acceptors, such as an Si floating bond. Identifying the cause of the large variations of the capture coefficients and their correlation with defect thermal stability presents a significant challenge and may elucidate the mechanism of photodegradation.

Photodegradation in solar cells is reduced by deposition at higher substrate temperatures, using deposition conditions that result in low plasma electron temperatures, and using H dilution. Defects having different thermal stability affect the degradation of solar cell differently. This suggests that the extent of the solar cell photodegradation depends on the defect capture coefficients for the photocarriers.

Acknowledgments

One of the authors (P.S.) thanks Prof. H. Fritzsche for numerous stimulating discussions and ideas on the experiments performed in his laboratory and elsewhere. The authors are grateful to Dr. A. Matsuda for invaluable suggestions, as well as S. Heck, T. Kamei, S. Shimizu, T. Nishimoto, M. Takai, R. Hayashi, T. Takagi and M.Q. Tran for fruitful collaboration.

References

[1] G.D. Watkins, J.R. Troxell and A.P. Chatterjee, Proc. of Intl. Conf. on Defects and Radiation Effects in Semiconductors **46**, 16 (1978).
[2] D.L. Staebler and C.R. Wronski, Appl. Phys. Lett. **31**, 292 (1977).
[3] H. Fritzsche, Mat. Res. Soc. Proc. **467**, 19 (1997).
[4] H. Fritzsche, Annu. Rev. Mat. Res. **31**, 47 (2002).
[5] R.A. Street (Ed.), Technology and Applications of Amorphous Silicon (Springer Series in Materials Science) Springer Verlag, Berlin, 2000 pp. 1-6, 252-299.
[6] H. Fritzsche, Solid State Commun. **94**, 953 (1995).
[7] T. Gotoh, S. Nonomura, M. Nishio, S. Nitta, M. Kondo and A. Matsuda, Appl. Phys. Lett. **72**, 2978 (1998).
[8] M. Stutzmann, W.B. Jackson and C.C. Tsai, J. Non-Cryst. Solids **77–8**, 363 (1985).
[9] D. Redfield and R.H. Bube, Appl. Phys. Lett. **54**, 1037 (1989).
[10] F. Yonezawa and A.S. Sakamoto, Optoelectronics **7**, 117 (1992).
[11] H.M. Branz, Phys. Rev. B **59**, 5498 (1999).
[12] S.T. Pantelides, Phys. Rev. B **36**, 3479 (1987).
[13] R. Biswas, Y.-P. Li and B.C. Pan, Mat. Res. Soc. Symp. Proc. **609**, A3.5 (2000).
[14] T. Shimizu, R. Durny and M. Kumeda, Mat. Res. Soc. Symp. Proc. **420**, 553 (1996).
[15] Y.S. Su and S.T. Pantelides, Phys. Rev. Lett. **88**, 165503 (2002).
[16] P.V. Santos and W.B. Jackson, Phys. Rev. B **44**, 10937 (1991).
[17] P. Stradins and H. Fritzsche, J. Non-Cryst. Solids **200**, 432 (1996).
[18] Q. Zhang, H. Takashima, J.-H. Zhou, M. Kumeda and T. Shimizu, Mat. Res. Soc. Proc. **336**, 269 (1994).
[19] S. Yamasaki and J. Isoya, J. Non-Cryst. Solids **166**, 169 (1993).
[20] R.A. Street, Hydrogenated Amorphous Silicon, Cambridge University Press, Cambridge, 1991, 417p.
[21] M. Kondo and K. Morigaki, J. Non-Cryst. Solids **137**, 247 (1991).
[22] M. Kondo and K. Morigaki, J. Non-Cryst. Solids **166**, 227 (1993).

[23] D. Han and H. Fritzsche, J. Non-Cryst. Solids **59–6**, 397 (1983).
[24] P. Stradins, H. Fritzsche and M.Q. Tran, Mat. Res. Soc. Symp. Proc. **336**, 227 (1994).
[25] P. Stradins and H. Fritzsche, Philos. Mag. B **69**, 121 (1994).
[26] K. Shepard, Z.E. Smith, S. Aljishi and S. Wagner, Appl. Phys. Lett. **53**, 1644 (1988).
[27] D.L. Staebler, R.S. Crandall and R. Williams, Appl. Phys. Lett. **39**, 733 (1981).
[28] P. Stradins and H. Fritzsche, Mat. Res. Soc. Proc. **297**, 571 (1993).
[29] P. Stradins, M.Q. Tran and H. Fritzsche, J. Non-Cryst. Solids **164–166**, 175 (1993).
[30] R.A. Street and D.K. Biegelsen, Solid State Commun. **44**, 501 (1982).
[31] H. Fritzsche, S. Heck and P. Stradins, J. Non-Cryst. Solids **200**, 153 (1996).
[32] M. Yoshida and K. Morigaki, J. Phys. Soc. Jpn. **59**, 1733 (1990).
[33] M. Yoshida and K. Morigaki, J. Phys. Soc. Jpn. **59**, 224 (1990).
[34] N.A. Schultz and P.C. Taylor, Phys. Rev. B **65**, art. no. 235207 (2002).
[35] N.A. Schultz and P.C. Taylor, Mat. Res. Soc. Proc. **609**, A3.4 (2000).
[36] P. Stradins and H. Fritzsche, Mat. Res. Soc. Proc. **467**, 85 (1997).
[37] T. Shimizu, M. Kumeda, Q. Zhang, J. Zhang and T. Ohtsuka, Mat. Res. Soc. Proc. **377**, 239 (1995).
[38] M. Fathallah, Philos. Mag. B **61**, 403 (1990).
[39] P. Stradins, H. Fritzsche, P. Tzanetakis and N. Kopidakis, Mat. Res. Soc. Proc. **420**, 729 (1996).
[40] P. Stradins, M. Kondo and A. Matsuda, Mat. Res. Soc. Proc. **609**, A3.1 (2000).
[41] P. Stradins, H. Fritzsche, N. Kopidakis and P. Tzanetakis, Mat. Res. Soc. Proc. **420**, 765 (1996).
[42] M. Stutzmann, J. Nunnenkamp, M.S. Brandt and A. Asano, Phys. Rev. Lett. **67**, 2347 (1991).
[43] M. Stutzmann, M.C. Rossi and M.S. Brandt, Phys. Rev. B **50**, 11592 (1994).
[44] P. Tzanetakis, N. Kopidakis, M. Androulidaki, C. Kalpouzos, P. Stradins and H. Fritzche, Mat. Res. Soc. Proc. **377**, 245 (1995).
[45] P. Tzanetakis, N. Kopidakis and H. Fritzsche, J. Non-Cryst. Solids **200**, 276 (1996).
[46] P. Stradins, M. Kondo and A. Matsuda, J. Non-Cryst. Solids **266**, 405 (2000).
[47] P. Stradins, S. Shimizu, M. Kondo and A. Matsuda, J. Non-Cryst. Solids **299**, 460 (2002).
[48] P. Stradins, S. Shimizu, M. Ito, M. Kondo and A. Matsuda, Abstracts of the Japanese Applied Physics Society 49th Spring Meeting **2**, 904 (2002).
[49] P. Stradins, M. Kondo and A. Matsuda, to be published (2003).
[50] S.B. Zhang and H.M. Branz, Phys. Rev. Lett. **87**, 105503 (2001).
[51] S. Shimizu, P. Stradins, M. Kondo and A. Matsuda, J. Non-Cryst. Solids **299**, 466 (2002).
[52] M. Ohsawa, T. Hama, T. Akasaka, T. Ichimura, H. Sakai, S. Ishida and Y. Uchida, Jpn. J. Appl. Phys. **24**, L838 (1985).
[53] N. Nakamura, T. Takahama, M. Isomura, M. Nishikuni, K. Yoshida, S. Tsuda, S. Nakano, M. Ohnishi and Y. Kuwano, Jpn. J. Appl. Phys. **28**, 1762 (1989).
[54] T. Kamei, P. Stradins and A. Matsuda, Appl. Phys. Lett. **74**, 1707 (1999).

[55] D.V. Tsu, B.S. Chao, S.R. Ovshinsky, S. Guha and J. Yang, Appl. Phys. Lett. **71**, 1317 (1997).

[56] S. Shimizu, P. Stradins, M. Kondo and A. Matsuda, Mat. Res. Soc. Proc. **664**, A14.3 (2001).

[57] S. Shimizu, P. Stradins, M. Kondo and A. Matsuda, Jpn. J. Appl. Phys. **41**, L1297 (2002).

[58] E. Stratakis, E. Spanakis, H. Fritzsche and P. Tzanetakis, J. Non-Cryst. Solids **266**, 506 (2000).

[59] E. Spanakis, E. Stratakis, P. Tzanetakis, H. Fritzsche, S. Guha and J. Yang, J. Non-Cryst. Solids **299**, 521 (2002).

[60] E. Spanakis, E. Stratakis, P. Tzanetakis, H. Fritzsche, S. Guha and J. Yang, Appl. Phys. Lett. **80**, 1734 (2002).

[61] P. Tzanetakis, Sol. Energy Mater. Sol. Cells (2003) to be published.

[62] N. Yoshida, Y. Sobajima, H. Kamiguchi, T. Iida, T. Hatano, H. Mori, Y. Nakae, M. Itoh, A. Masuda, H. Matsumura and S. Nonomura, J. Non-Cryst. Solids **299**, 516 (2002).

[63] S. Nonomura, N. Yoshida, T. Gotoh, T. Sakamoto, A. Matsuda and S. Nitta, J. Non-Cryst. Solids **266**, 474 (2000).

[64] T. Sakamoto, N. Yoshida, H. Harada, T. Kishida, S. Nonomura, T. Gotoh, M. Kondo, A. Matsuda, T. Itoh and S. Nitta, J. Non-Cryst. Solids **266**, 481 (2000).

[65] Q. Wang, H. Antoniadis and E.A. Schiff, Appl. Phys. Lett. **60**, 2791 (1992).

[66] K. Hattori, T. Hirao, M. Iida and H. Okamoto, J. Non-Cryst. Solids **266**, 352 (2000).

[67] S. Dong, Y. Tang, J. Liebe, R. Braunstein, R.S. Crandall, B.P. Nelson and A.H. Mahan, J. Appl. Phys. **82**, 702 (1997).

[68] N. Hata, P. Stradins, M. Isomura, M. Kondo and A. Matsuda, Extended Abstracts of Japanese Applied Physics Society 45th Spring Meeting **2**, 899 (1998).

[69] P. Stradins, Solar Energy Materials and Solar Cells (2003) to be published.

[70] B.I. Shklovskii, H. Fritzsche and S.D. Baranovskii, Phys. Rev. Lett. **62**, 2989 (1989).

[71] T. Shimizu, M. Imawi, T. Okagawa, A. Morimoko and M. Kumeda, Mat. Res. Soc. Proc. **258**, 455 (1992).

[72] G.S.L. Marucci, C. Minarini and A.Mittiga, J. Non-Cryst. Solids **198–200**, 482 (1996).

[73] L. Benatar, M. Grinberger, A. Fahrenbuch, A. Lopez-Otero, D. Redfield and R. Bube, Mat. Res. Soc. Proc. **258**, 461 (1992).

[74] P. Stradins, M. Kondo and A. Matsuda, Proceedings of IEEE 28th PVSC 853 (2000).

[75] S. Heck and H.M. Branz, Appl. Phys. Lett. **79**, 3080 (2001).

[76] P. Stradins, S. Shimizu, M. Kondo and A. Matsuda, Mat. Res. Soc. Proc. **664**, A12.1 (2001).

[77] J. Pearce, X. Niu, R. Koval, G. Ganguly, D. Carlson, R.W. Collins and C.R. Wronski, Mat. Res. Soc. Proc. **664**, A12.3 (2001).

[78] W.M.M. Kessels, A.H.M. Smets, D.C. Marra, E.S. Aydil, D.C. Schram and M.C.M. Van De Sanden, Thin Solid Films **383**, 154 (2001).

[79] B. Rech and H. Wagner, Appl. Phys. A–Mater. Sci. Process. **69**, 155 (1999).

[80] M. Takai, T. Nishimoto, M. Kondo and A. Matsuda, Appl. Phys. Lett. **77**, 2828 (2000).

[81] M. Takai, T. Nishimoto, T. Takagi, M. Kondo and A. Matsuda, J. Non-Cryst. Solids **266**, 90 (2000).

[82] T. Nishimoto, M. Takai, H. Miyahara, M. Kondo and A. Matsuda, J. Non-Cryst. Solids **299**, 1116 (2002).

[83] X.X. Xu, J. Yang and S. Guha, J. Non-Cryst. Solids **200**, 60 (1996).

[84] H. Dersch, L. Schweitzer and J. Stuke, Phys. Rev. B **28**, 4678 (1983).

14 Photo-Induced Structural Metastability in a-Si:H

Shuichi Nonomura

14.1 Introduction

Photo-induced metastability is a well-known phenomenon in amorphous materials [1] and is often observed in optical, transport, magnetic and structural properties such as photodarkening [1, 2], photo-induced electron spin resonance (ESR) [3–5] and photo-induced volume expansion [2, 4] in amorphous chalcogenide semiconductors. In hydrogenated amorphous silicon, the light soaking results in a decrease of photoconductivity (PC) and dark conductivity. The initial parameters recover upon thermal annealing at $\sim$150 °C. This phenomenon [6, 7] is called the Staebler–Wronski effect. It was demonstrated by numerous studies that the decrease of photoconductivity and dark conductivity caused by the light soaking is due to creation of defect states [8], which are located at around the mid-gap energy level [9]. These defects can be observed, for example, in ESR measurements (with $g = 2.005$) and the created defect is ascribed to the Si dangling bond. The defect creation is also observed in the mid-gap optical absorption spectrum [9] and as a decrease of photoluminescence intensity (PL). This photo-induced defect state act as a recombination center [7] for the carriers excited by light soaking, which produces the metastable change in PC, dark conductivity and PL [10]. Electrically injected carrier recombination also induces the defect creation [11] which suggests that the essential factor for the defect creation is a carrier recombination process. The photo-induced defects disappear after thermal annealing, i.e. the defect creation and annihilation is a reversible phenomenon. Although 25 years have passed after the first report of the Staebler–Wronski effect, the final picture and the best experimental method to elucidate the origin of the photo-induced metastability in a-Si:H remain unanswered questions until now.

In the application field of a-Si:H, especially in manufacturing activities of a-Si solar cells, the photo-induced defect creation is an important problem to be solved, because an increase of the recombination paths by the photo-induced defect creation results in lowering of the energy conversion efficiency by up to 10–20% of the initial value [7]. At the present stage, the market for Si thin film solar cells demands conversion efficiencies over 15%. A tandem type solar cell of a-Si:H/μc-Si:H is one of the possible ways to meet this demand. However, if a decrease of the current density due to photo-induced defect creation occurs in the a-Si:H top cell, the current density of the microcrystalline bottom cell also decreases because the two cells are connected in series. An improvement of the conversion efficiency for Si thin film solar cells is making steady progress. Recently, Kaneka Corporation published a conversion efficiency of 14.1% for small area (10×10 mm^2) and 11.7% for large area (910×455 mm^2) tandem type a-Si:H/μc-Si:H solar cells [12]. The conversion efficiency of 14.1% almost satisfies the target value of 15%, but the photo-induced degradation in the a-Si:H top cell still does not allow one

to achieve the goal value of 15%. The above aspects are the reason why the development of a method for the elimination of the Staebler–Wronski effect is an important and urgent problem, especially in thin film Si solar cells.

In 1995, Fritzsche [13] pointed out that the search for structural modifications by light soaking could provide clues to the microscopic mechanism of the Staebler–Wronski effect. Coincidentally with this suggestion, new results implying structural modifications have been reported based on experiments using infrared absorption [14], photoemission [15], polarized electroabsorption [16] and nuclear magnetic resonance [17]. In 1998, direct evidence for the structural metastability, viz. the photo-induced volume dilation, in a-Si:H [18–22] has been presented. In this chapter, we review the work done in our laboratory on structural metastability including the experimental technique (Section 14.2), fundamental properties (Section 14.3), and the effect of the deposition conditions of a-Si:H (Section 14.4.1) and cyanide treatment (Section 14.4.2).

14.2 Experimental Details

The laser optical-lever bending method [19, 23] was employed for sensitive detection of the volume change caused by light soaking in a-Si:H thin films. This technique is a derivative method the photothermal bending spectroscopy [24] designed for measurements of the absorption spectrum of thin films in the spectral range of low absorption. The sample is an a-Si:H film deposited on a thin quartz substrate, i.e. possessing a bimorph structure which contributes to the "amplification" of the change. The laser optical-lever method used allows for further "amplification". One edge of the sample is held on the sample holder, and the other edge is free. The expansion or contraction of the a-Si:H lattice is converted to the displacement of the sample's free edge.

Figure 14.1 shows a schematic diagram of the measurement system for the DC mode laser optical-lever bending method [19, 23]. A multi-mode Ar ion laser ($\lambda = 488$ and 514 nm) was used to induce the Staebler–Wronski effect in a-Si:H. A dye laser was used to provide the laser light with wavelengths of 570–630 nm. The light power for the light soaking was about 300 mW/cm^2, and the light soaking area on the sample was 2×10 mm^2. The intermittent light soaking was performed in order to avoid the temperature rise of the sample. The light-on and light-off periods were 5 min each and were controlled by a mechanical optical shutter. Under these light soaking conditions, the thermal annealing effect of the photo-induced defect was not observed. We used super invar metal for the sample holder, because this metal has extremely small expansion coefficient of 0.4×10^{-6} K^{-1} similar to those of glasses. The use of super invar prevents the displacement of the sample holder itself affected by drifting of the room temperature and the Joule heating generated from the laser light soaking in a-Si:H. An He–Ne laser ($\lambda = 632.8$ nm) was used as a probe beam for detecting the displacement of the sample's free edge, which results from the structural volume change. The probe beam, reflected from the sample's free edge, is fed into the position-sensitive detector (PSD). As shown in Fig. 14.1, the free edge is the smooth surface of quartz substrate without deposition of a-Si:H in order to prevent the dispersion of the reflected He–Ne laser light. The displacement of the probe beam is detected by PSD and magnified by a DC voltage amplifier after the current–voltage conversion circuit.

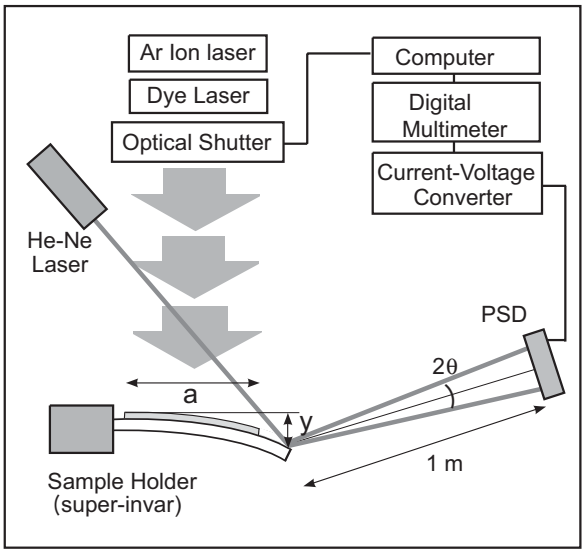

Figure 14.1: A schematic diagram of the DC mode laser optical-lever bending method in order to detect the photo-induced structural metastability in a-Si:H films.

The initial internal stress σ resulting from an a-Si:H film and a thin substrate was obtained from the bending angle θ using Stoney's equation [25]:

$$\sigma = E_S d_S^2 \tan(\theta/2)/3(1-\nu_S)d_f a \tag{14.1}$$

where E_s is Young's modulus, ν is Poisson's ratio, θ is the bending angle and a is the sample length. The subscripts s and f refer to the substrate and film, respectively. If y represents the displacement of the sample edge, $y/a = tan(\theta/2)$. This equation is correct under the condition $E_s d_s \gg E_f d_f$, because the values of E_f, E_s, n_f and n_s used in this study were 1.3×10^{11} Pa, 7.31×10^{10} Pa, 0.28 and 0.17, respectively. The photo-induced change of the internal stress $\Delta\sigma$ gives a photo-induced change of strain $\varepsilon = \Delta a/a$ described as

$$\varepsilon = \Delta a/a = (1-\nu_f)\Delta\sigma/E_f \tag{14.2}$$

The photo-induced volume change $\Delta V/V$ is calculated from the strain ε assuming the homogeneous structure of the film in three dimensions. The obtained detection limit of $\Delta V/V$ in our detection system was 2×10^{-7}. This high sensitivity means that our method has high potential for detecting small volume changes occurring due to thermal expansion, infinitely small structural changes, etc.

In this study both hydrogenated amorphous silicon (a-Si:H) and microcrystalline silicon (μc-Si) thin films have been used. The undoped films were prepared by two types of plasma enhanced chemical vapor deposition (PECVD) methods. One is a diode type PECVD used in our laboratory, and the other type used a triode type deposition developed by Matsuda [26]. Pure silane gas was used for preparation of a-Si:H films in our laboratory. In the case of the

triode type deposition, silane was diluted by hydrogen (SiH_4/H_2 = 1:4 sccm). The substrate temperature used was 100–550 °C. The substrate temperature was kept at 250 °C for the study of hydrogen dilution ratio dependence. The H dilution ratio r ($r = H_2/SiH_4$) was changed from 0 to 39. The substrate was mirror polished quartz with a thickness of 100 μm. The dimensions of the sample were 2 mm × 20 mm.

The p-type a-Si:H films were prepared using the diode type PECVD apparatus. B_2H_6 gas was used as the doping gas, and the doping ratio, B_2H_6/SiH_4, was changed from 10^{-4} to 10^{-2}. The n-type a-Si:H films were deposited using PH_3 and the same doping range of $PH_3/SiH_4 = 10^{-4}$–10^{-2}. The samples were deposited using the same deposition conditions as the undoped samples.

In order to study the influence of an externally applied stress related to the photo-induced structural change, we tried to make a-Si:H films with different initial stresses [23]. For this purpose, it is important to keep the same original amorphous structure in all samples. In order to meet this requirement, a special substrate holder was designed (Fig. 14.2). The lower part is a top view of the substrate holder. The three shaded rectangles are the setting positions for three substrates. Each cross-sectional view of the setting position is demonstrated in the upper part of the figure. The three holders have flat, convex and concave shapes and the quartz substrates were fitted to the holder using metal hooks. The central holder has flat shape, which produces a conventional standard sample. The left-hand side holder has a concave shape and the quartz substrate produces the external tensile stress in the a-Si:H film after the deposition. The convex shape sample holder supplies the compressive stress. Three types of a-Si:H films have the same amorphous Si network structure, because a-Si:H films are deposited on three substrates at one time.

It has been proposed [27–29] that crown-ether cyanide treatment is an effective method to remove defects from the surface of a-Si:H films and c-Si wafers. The crown-ether molecule possesses a hole of 2.7 Å diameter, which effectively captures a K^+ ion with a diameter of 2.66 Å. In this work, we used simple cyanide treatment without use of the crown-ether, because the measurement of $\Delta V/V$ is not affected by adsorption of small amount of K^+ ions on the a-Si:H surface. The a-Si:H film deposited on a thin quartz substrate was immersed in KCN solution (0.1 mol KCN in ethanol) for 2 min. Following this treatment, the sample was rinsed in ultrapure water at 25 °C. See Ref. [27] for more details.

14.3 Fundamental Properties of Photo-Induced Structural Metastability

In this section we describe the fundamental properties of photo-induced structural metastability responsible for the Staebler–Wronski effect. Figure 14.3 shows an example of the displacement signal by the intermittent light soaking. The noise level in the PSD output voltage before the light soaking corresponds to a normalized volume change of $\Delta V/V \sim 1 \times 10^{-7}$. The rapid output voltage increase during the light soaking is caused by the thermal expansion of an a-Si:H film due to Joule heating resulting from non-radiative recombination of excited electrons and holes. This signal intensity is denoted by ΔV_T. This change corresponds to a compressive stress (a thermally induced volume expansion) in a-Si:H. After turning off the

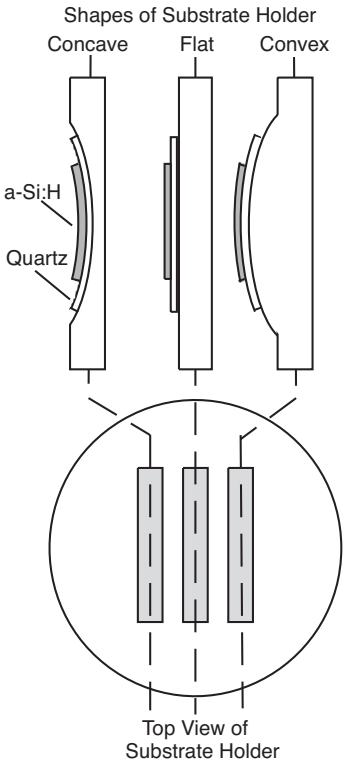

Figure 14.2: The top and cross-sectional views of the sample holder used for a-Si:H deposition.

light, the displacement signal quickly decreases (within 10 s) and returns to almost the same position as that before the light soaking. After 20 cycles of light soaking, a clear residual displacement signal ΔV_S was observed. The ΔV_S means a signal component induced by the photo-induced structural change in a-Si:H, which can be converted to Δa using Eq. (14.2). The value of ΔV_S as a function of the light soaking time is plotted in Fig. 14.3.

Figure 14.3 shows the raw data for the temporal evolution of the output voltage of PSD, ΔV_S. The output voltage gradually increases with the light soaking time (until 7 h in our experiment). The increase of the output voltage corresponds to the volume expansion of an a-Si:H film. The light was turned off after 7 h in order to confirm that the increase of the output voltage is irreversible. If the increase of the output voltage were caused by thermal expansion of the sample and/or the sample holder, the output voltage would have decreased during this longer light-off duration because of the cooling. The observed output voltage remained constant for 2 h (7–9 h in Fig. 14.4). It has been demonstrated elsewhere [30] that the photo-induced increase of the output voltage remained constant even for several days. No change of the photo-induced output voltage means that the photo-induced structural change is a persistent metastable state. If this photo-induced structural change is related to photo-induced defect creation, then this expansion should recover after thermal annealing at 200 °C

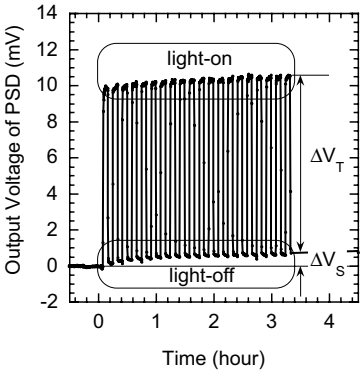

Figure 14.3: Raw data of PSD output voltage in the DC mode laser optical-lever bending system. The light of the Ar ion laser was shed periodically on a-Si:H films in order to avoid the thermal effect. Both light-on and light-off periods were 5 min. The detection limit of the $\Delta V/V$ estimated from the noise intensity is $\sim 2.5 \times 10^{-7}$.

and should exhibit an identical change in the second cycle of the light exposure. We observed that, indeed, the photo-induced volume expansion completely recovered after *in situ* thermal annealing at 200 °C for 2 h and that the identical volume expansion occurs in the second measurement cycle (Fig. 14.4). The normalized photo-induced volume expansion $\Delta V/V$ is characterized by a time evolution with light soaking similar to that of the photo-induced defect creation, i.e. the Stabel-Wronski effect, as shown in Fig. 14.5. Here, the defect density denoted by open squares was estimated using the constant photocurrent method (CPM). Figure 14.6 shows the $\log \Delta V/V$ versus $\log t$ plot of the $\Delta V/V$ shown in Fig. 14.5.

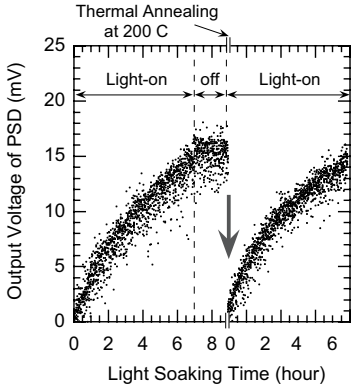

Figure 14.4: The time dependence of the PSD output voltage. Similar spectra for the first and second measurements were obtained for 0–7 h illumination.

Using the analogy with the photo-induced defect creation studies [31], we assume a power law of the form $\Delta V/V \propto G^m t^\gamma$ where G and t are the generation rate and the light soaking

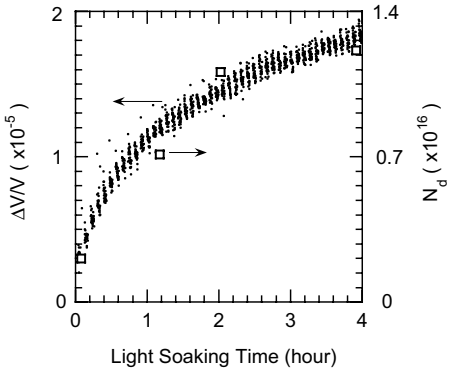

Figure 14.5: Comparison of the light soaking time dependence of $\Delta V/V$ and the photo-induced defect density estimated by the constant photocurrent method.

time, respectively, and γ is found to be 0.42. Other groups have also reported similar values of $\gamma = 0.42$–0.45 [32] and $\gamma = 0.44$ [33] in undoped a-Si:H films. All these values are larger than $\gamma = 0.33$ observed in the photo-induced defect creation [31]. The experimentally obtained value of the exponential factor of the generation rate is $m = 0.7$ [32], which is close to the 2/3 value widely accepted for the photo-induced defect creation [31]. The difference in the γ values suggests that the mechanism of the photo-induced $\Delta V/V$ is not exactly the same as that of the dangling bond creation observed in the ESR measurements.

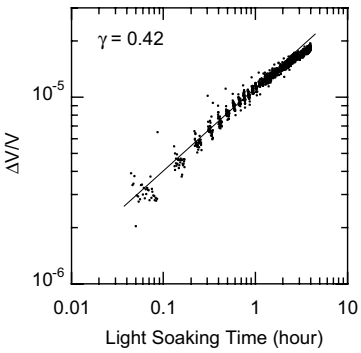

Figure 14.6: Log-log plots of $\Delta V/V$ versus light soaking time. The value of γ estimated from the slope of the solid line is 0.42.

We have studied the relationship between the initial stress and the photo-induced stress (volume expansion). In this experiment, the initial stress is derived from the curvature of a 100 μm thick a-Si:H film deposited on a thin quartz substrate. The sample has an upcurved shape after the deposition of a-Si:H (the a-Si:H film is on top) which means that the obtained initial stress was compressive. Its value was 300–400 MPa, in agreement with previous reports [22, 32, 34]. The photo-induced stress was also compressive.

The observed initial stress is considered to possess two components. One component is intrinsic stress influenced by the amorphous Si network structure of an a-Si:H film itself, which is determined by the deposition conditions. The other one is external stress induced by the thin quartz substrate. In order to obtain a-Si:H films possessing different initial stress, we used the special substrate holder described above. The concave shape sample holder produces a smaller initial stress of $\sim$320 MPa compared with that of the flat holder. The convex holder results in a larger initial stress of 600 MPa. Open circles in Fig. 14.7 denote the initial stress values in three-a-Si:H films. Because all three a-Si:H films were deposited simultaneously under the same deposition conditions they have the same amorphous Si network. The closed circles in Fig. 14.7 show the values of $\Delta V/V$ after 2 h of light soaking. The change of the initial stress was -34% (the convex shape sample) and $+24\%$ (the concave shape sample) compared with the initial stress of 485 MPa in the flat shape sample. On the other hand, the difference of $\Delta V/V$ was within 8%, and no correlation with the initial stress was observed. We can thus conclude that $\Delta V/V$ is not correlated with the external applied stress due to the substrate. We found that $\Delta V/V$ is strongly influenced by the intrinsic stress of the amorphous Si network structure of a-Si:H itself which is determined by the deposition conditions. The initial stress observed in a-Si:H films deposited in the flat substrate seems to correspond indirectly to the intrinsic stress of amorphous network itself. We believe that the observed photo-induced stress is the result of the dilatation, i.e. structural modification of the film.

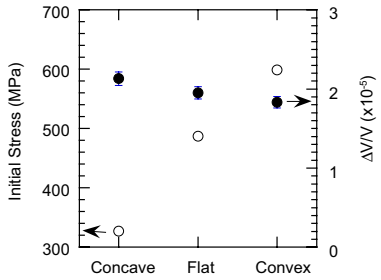

Figure 14.7: The changes of initial stress and the $\Delta V/V$ for a-Si:H films deposited on three quartz substrates with concave, flat and convex shapes.

14.4 Effect of Deposition Conditions and Cyanide Treatment on Photo-Induced Structural Metastability

14.4.1 Effect of Deposition Conditions on Photo-Induced Structural Metastability

To study the effect of the deposition conditions on photo-induced structural metastability, we performed measurements on various kinds of samples. Undoped a-Si:H films were prepared by PECVD, photo-CVD and hot-wire CVD [12] for the study of a photo-induced volume change, $\Delta V/V$. Figure 14.8 shows the $\Delta V/V$ of a-Si:H deposited at different deposition

temperatures from 100 °C to 550 °C. The $\Delta V/V$ value has a maximum around 300 °C and decreases at deposition temperatures higher than 300 °C. This tendency correlates with the smaller photo-induced defect creation at higher deposition temperatures and is explained by the defects created by effusion of hydrogen atoms from the a-Si:H network. The reduction of $\Delta V/V$ is also observed at lower deposition temperatures (100 °C to 250 °C). This reduction is also consistent with the increase of initial defect density at lower deposition temperature [30, 35]. The hydrogen content reaches ∼23% in the a-Si:H film at T_d = 100 °C, as shown in Fig. 14.9. In general, a-Si:H films prepared at lower temperature have a larger initial defect density and higher microvoid density than a-Si:H films deposited at ∼250 °C. The larger initial defect density allows for the non-radiative recombination path not contributing to the photo-induced defect creation. On the other hand, a high hydrogen content makes the a-Si:H network soft. These two reasons account for why the photo-induced defect creation is less efficient in both cases.

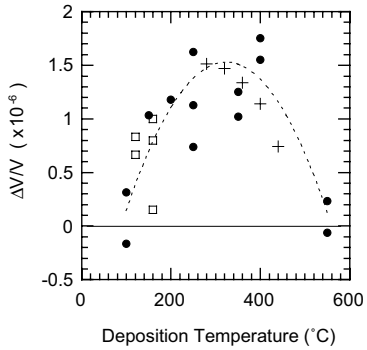

Figure 14.8: Dependence of $\Delta V/V$ on the deposition temperature of a-Si:H. The closed circles, open squares and crosses shows the $\Delta V/V$ of a-Si:H films deposited by PECVD, photo-CVD and hot-wire CVD, respectively.

Morigaki [36] has recently reported an increase of the photo-induced defect states under a light intensity of 700 mW/cm^2 and the photo-induced annealing of the dangling bonds at 1500 mW/cm^2 in a-Si:H with large hydrogen content. Our experimentally obtained small value of $\Delta V/V$ at T_d ∼100 °C is inconsistent with these results. The difficulty in the detection of $\Delta V/V$ might imply that a-Si:H films deposited at low temperature might have a different structure compared with that of a-Si:H with higher hydrogen content. Alternatively, the softening of the network by higher hydrogen content might obscure the photo-induced stress in spite of the defect creation.

The hydrogen dilution ratio is one of the important deposition parameters. High quality a-Si:H films applicable to solar cells are obtained at $H_2/SiH_4 \sim 10$. Fig. 14.10 shows the change of $\Delta V/V$ in a-Si:H films at different H_2/SiH_4 ratios from 0 to 39. The $\Delta V/V$ value becomes larger with increasing H_2/SiH_4 ratio and has a maximum value at $H_2/SiH_4 = 10$–15. This is the same dilution ratio as is used to obtain the high quality a-Si:H films applicable to solar cells.

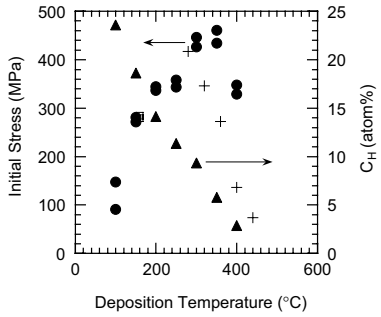

Figure 14.9: Dependence of the initial stress and hydrogen content on the deposition temperature of a-Si:H. The closed circles, open squares and crosses correspond to the initial stress of a-Si:H films deposited by PECVD, photo-CVD and Cat-CVD, respectively. The hydrogen contents are denoted by closed triangles.

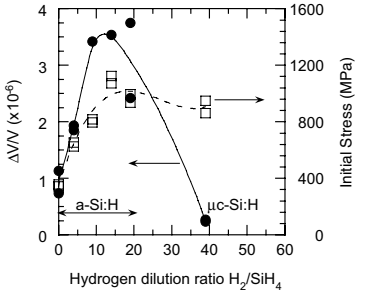

Figure 14.10: The change of $\Delta V/V$ with the hydrogen dilution ratio (H_2/SiH_4). The hydrogenated microcrystalline Si film is obtained at H_2/SiH_4 = 39.

The situation with defect generation in μc-Si:H is rather complicated. Thus, Nickel et al. observed photo-induced defect creation in a hydrogen passivated μc-Si:H film deposited at $\sim$600 °C [37]. Miere et al., on the other hand, reported that there was no change of photoconductivity induced by light soaking in a μc-Si:H film deposited at $\sim$200 °C [38]. Kondo et al. [39] demonstrated that in high quality μc-Si:H film with defect density of 5×10^{-15} cm^{-3} both an increase of defect creation and the formation of an oxide layer by the light soaking were taking place. It was also demonstrated that when the μc-Si:H film is covered by a thin a-Si:H layer (60 Å) no photo-induced defect creation occurs because covering by a-Si:H prevents surface oxidation. It was concluded that the increase of defect creation is caused by the band-bending resulting from the formation of an oxide layer on μc-Si:H films. The surface oxidation of μc-Si:H film was confirmed by Kunii et al. [40], who observed an increase of mid-gap absorption after exposure of μc-Si:H film to air. In a recent paper by Nickel et Rakel [41] a metastable increase of electrical conductivity with the cooling rate was reported. The possibility of creating a photo-induced metastable state might depend on the presence of amorphous phase inclusions in μc-Si:H film as well as on the amount and structure of the amorphous inclusions and the density of the defect states discussed above.

No photodegradation was observed in μc-Si:H solar cells [37]. It was therefore interesting to check whether or not such cells exhibit photo-induced dilatation. The μc-Si:H film used in this work was deposited at $H_2/SiH_4 = 39$ and had defect density below 10^{16} cm^{-3}. This sample exhibited a negligibly small value of $\Delta V/V = 2.5 \times 10^{-7}$. This result agrees with the absence of photo-induced defect creation in our μc-Si:H film prepared under identical deposition conditions and is also supported by the fact that prolonged light soaking of μc-Si:H solar cells did not reveal any degradation of the device parameters, e.g. the conversion efficiency [38].

We have demonstrated that the appearance of photo-induced structural metastability is related to photo-induced defect creation in μc-Si:H film. Spanakis et al. [42] also reported the qualitative correlation between the photo-induced $\Delta V/V$ and photo-induced defect creation in the study of hydrogenated amorphous $Si_{1-x}Ge_x$ alloys. It is well known that a-$Si_{1-x}Ge_x$:H alloys possess a diminished photo-induced defect creation ability in the Ge-rich region [43]. A significant decrease in $\Delta V/V$ was observed in $Si_{0.33}Ge_{0.67}$, i.e. in the composition where the photo-induced defect creation is greatly diminished.

We have studied the B_2H_6 doping effect on $\Delta V/V$ in a-Si:H films [44]. The doping gas ratio, B_2H_6/SiH_4, was changed from 10^{-4} to 10^{-2}. Other deposition parameters were kept constant in all a-Si:H films denoted in Fig. 14.11. The values of $\Delta V/V$ shown are for a light soaking time of 4 h. The intrinsic a-Si:H (at $B_2H_6/SiH_4 = 0$) has a photo-induced volume expansion of $\Delta V/V \approx 3 \times 10^{-6}$. A large increase of $\Delta V/V$ is found for the doping ratio $B_2H_6/SiH_4 = 10^{-4}$ and 10^{-3}. The observed large increase of $\Delta V/V$ agrees well with the photodegradation of the PC in a-Si:H films deposited with the same B_2H_6 doping gas ratio of 10^{-4} and 10^{-3}. An increase in the doping ratio to 5×10^{-3} resulted in a reduction of the $\Delta V/V$ value and for an even higher doping ratio of 10^{-2} no change of the $\Delta V/V$ could be observed. It should be noted that in the latter two a-Si:H films no photodegradation degradation was observed and, in fact, they showed a gradual *increase* of PC (the inverse Staebler–Wronski effect). This result correlates with the disappearance of $\Delta V/V$ (Fig. 14.11).

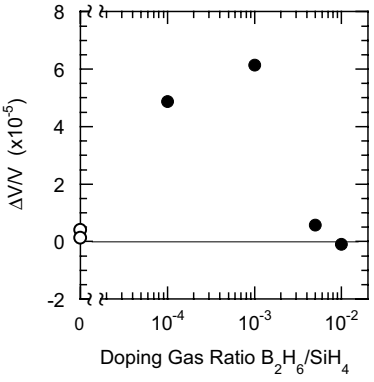

Figure 14.11: The change of $\Delta V/V$ with the doping ratio of B_2H_6/SiH_4. The open and closed circles show the $\Delta V/V$ of non-doped a-Si:H films and B_2H_6 doped a-Si:H films, respectively

The intrinsic a-Si:H film (i.e. $B_2H_6/SiH_4 = 0$) has an initial stress of 314 MPa. The initial stress becomes larger with an increase of the doping ratio and has a maximum value of 1016 MPa at $B_2H_6/SiH_4 = 10^{-3}$. The initial stress in films produced using higher doping ($B_2H_6/SiH_4 = 10^{-2}$) is smaller (452 MPa). For a different doping gas, PH_3, the magnitude of $\Delta V/V$ and the initial stress show changes with the doping ratio that are similar to the case of B_2H_6 doping [44]. This means that the behavior of $\Delta V/V$ is influenced by the incorporation of impurity atoms rather than by the position of the Fermi level. Incorporation of small amounts of impurity atoms ($>10^{-3}$) induces the creation of certain local regions in an a-Si:H network that are characterized by a higher concentration of precursors responsible for the photo-induced metastability. At higher doping gas ratio, the large amount of incorporated impurity atoms increase the disorder in a-Si:H network, which strongly modifies the local amorphous Si network and results in the reduction of photo-induced dilatation. The larger modification of the lattice reduces the photo-induced dilatation around the precursor of the photo-induced defect, which may decrease the probability of transformation of the precursor into the photo-induced metastable state.

Structural modification in an a-Si:H film takes place on the medium-range scale [19]. The obtained magnitude of $\Delta V/V$ in a wide range from 10^{-6} to 10^{-4} confirms that the appearance of $\Delta V/V$ correlates with the appearance of photo-induced defect creation, but the magnitude of $\Delta V/V$ has no one-to-one correspondence with the photo-induced defect density and the decrease of PC. Thus, Spanakis et al. [42] reported the surprisingly large magnitude of $\Delta V/V = 10^{-3}$ in a-$Si_{0.6}Ge_{0.4}$:H alloy with a photo-induced defect density of 4×10^{17} cm^{-3}. Park et al. pointed out that the photo-induced $\Delta V/V$ does not saturate even after 72 h of light soaking although the photo-induced defect density saturated after 1 h of light soaking [33].

It is difficult to understand how a simple bond-breaking model can account for the large values of $\Delta V/V$. A possible model to account for the Staebler–Wronski effect can be the following. First, the phonon energy released through the recombination of photoexcited carriers is consumed to transform the structure locally into a metastable, higher strained, state. A precursor for a dangling bond, D^0 [45], incidentally included in the strained area, changes to the dangling bond with subsequent modification of the local structure. Recently, Wronski et al. [45] reported that direct correlations were found between the electron mobility-lifetime products and the cell fill factor while no direct relationship was observed with the dangling bond density. It was suggested that presence of photo-induced defects different from the dangling bonds (the non-dangling bond defects, or non-D^0 defects), and the complexity of the processes responsible for the defect creation are important to explain the Staebler–Wronski effect. This approach is reasonable if one assumes that the structural change is an initial step in order to induce the D^0 and non-D^0 defects in the Staebler–Wronski effect.

The question of what the driving force is for creation of structural metastability in a-Si:H network is not clear at the present stage. Branz [46] came up with an idea that the photo-induced strain and network disorder are due to mobile H atoms generated from Si–H bonds. This is considered to be because Si-Si bonds are successively broken and reformed during the H diffusion. Biswas and Pan [47] suggested that the photo-induced volume dilation is due to flipped Si–H bonds accompanied by diffusion of hydrogen. Okamoto argued that none of these models could account qualitatively for the their experimental results on the observed photo-induced network distortion and the photo-induced structural dilation [48]. Our results suggest that one possible way to decrease the Staebler–Wronski effect in a-Si:H is to make the network

more rigid, which should prevent the transformation of the structure into the metastable state. This approach is supported by an experimental result of Nishimoto et al. [49] that a decrease of SiH_2 bond density incorporated in the a-Si:H network results in a decrease of photo-induced defect creation.

14.4.2 Effect of Cyanide Treatment on Photo-Induced Structural Metastability

It has recently been suggested that cyanide treatment may be an effective way to elucidate the nature of the Staebler–Wronski effect [27–29]. We have studied the effect of cyanide treatment on photo-induced dilatation in a-Si:H. The results are shown in Fig. 14.12. The experimental procedure was the following. Time evolution of $\Delta V/V$ was measured in an as-deposited a-Si:H film for 4 h (crosses in Fig. 14.12). The a-Si:H film was then subjected successively to cyanide treatment at 25 °C, rinsing in pure water and subsequent thermal annealing at 200 °C for 2 h in order to anneal the photodegradation. Open circles in Fig. 14.12 show the photo-induced $\Delta V/V$ in the film after the cyanide treatment. It is interesting that the magnitude of $\Delta V/V$ was markedly reduced (to one third of the original value) in the cyanide-treated film. The γ in the power law, however, remained unchanged ($\gamma = 0.42$–0.43). The latter result suggests that either the concentration of dangling-bond precursors is decreased or the structure of the film becomes more stable. More details can be found elsewhere [44]. We believe that the observed reduction in $\Delta V/V$ is caused by diffusion of cyanide ions into the a-Si:H network and their subsequent binding with either the photo-induced dangling bonds or with the precursors for the photo-induced dilatation such as microvoids and/or hydrogen-rich regions. We suggest that the binding of a cyanide ion with the precursors results in a more stable structure which is more difficult to dilate by photoexcitation.

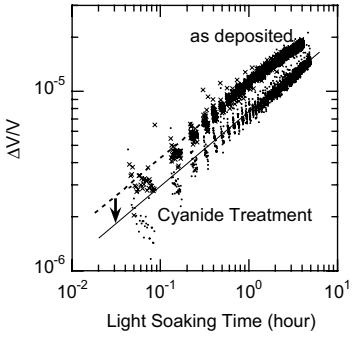

Figure 14.12: The light soaking time dependence of $\Delta V/V$ in the as-deposited a-Si:H film and the a-Si:H film subjected to successive cyanide treatment and the thermal annealing at 200 °C. The γ values of the two films are 0.42 and 0.43, respectively.

14.5 Summary

The photo-induced structural metastability of an a-Si:H film has been described. The volume expansion (dilation) $\Delta V/V$ of a-Si:H film by light soaking was detected by a highly sensitive laser optical bending method. The observed magnitude of $\Delta V/V$ changes in a wide range of 10^{-6}–10^{-4} in a-Si:H. The detected $\Delta V/V$ persists after light soaking but the initial parameters can be recovered by thermal annealing at 200 °C. Both of these features are similar to the characteristics of the Staebler–Wronski effect. It has been demonstrated that the photo-induced $\Delta V/V$ is determined by the intrinsic amorphous Si network structure, the latter being determined by the deposition conditions. The externally applied strain caused by a quartz substrate does not seem to play a role. Disappearance of the photo-induced structural metastability correlates with the absence of photo-induced defect creation. On the other hand, the obtained γ (assuming a $\Delta V/V \propto t^{\gamma}$ power law) is $\sim$0.42 and this value is larger than the 1/3 accepted in defect creation by light soaking time.

A possible scenario to account for the Staebler–Wronski effect can be the following. First, the energy generated during the photoexcited carrier recombination is consumed to transform the network structure locally into a metastable state characterized by higher strain. The precursors for D^0 and non-D^0 states are incidentally included in the strained local structure. The transformation of the amorphous Si lattice to the metastable state changes the precursors into D^0 and non-D^0 states. We believe that elimination of the local flexible regions in the structure of a-Si:H films is a possibly way to reduce the photo-induced structural metastability. The decrease (and, ideally, elimination) of $\Delta V/V$ is expected to solve the problems related to the Staebler–Wronski effect. We demonstrated that the cyanide treatment is an effective method to decrease the photo-induced structural metastability.

Acknowledgments

The author thanks Prof. N. Yoshida, Dr. T. Gotoh, Mr. Y. Sobajima and H. Kamiguchi for their experimental help. Helpful discussions with and suggestions by Professors K. Morigaki, K. Shimakawa, S. Nitta, H. Okamoto, M. Konagai, Ke. Tanaka and Y. Hamakawa are also greatly appreciated. This work is partially funded by NEDO as a part of the innovative PV Technology and Grant-in Aid for Science Research (B)(2) and the Mazda Foundation.

References

[1] K. Shimakawa, A. Kolobov and S.R. Elliott, Adv. Phys. **44**, 475 (1995).
[2] T. Tanaka, J. Non-Cryst. Solids **35&36**, 1023 (1980).
[3] J. Hautala, W.D. Ohlsen and P.C. Taylor, Phys. Rev. B **38**, 11048 (1988).
[4] Ke. Tanaka, Phys. Rev. B **57**, 5163 (1998).
[5] S.R. Elliott and K. Shimakawa, Phys. Rev. B **42**, 9766 (1990).
[6] D.L. Staebler and C.R. Wronski, Appl. Phys. Lett. **28**, 671 (1977).
[7] C.R. Wronski, Semiconductors and Semimetals **21** Part C, 347 (1984).
[8] H. Dersch, J. Stuke and J. Beichler, Appl. Phys. Lett. **38,** 456 (1981).

[9] N.M. Amer and W.B. Jackson, Semiconductors and Semimetals **21** Part B, 83 (1984).
[10] J.I. Pankove and J.E. Berkeyheiser, Appl. Phys. Lett. **37,** 705 (1980).
[11] H. Fritzche, Mat. Res. Soc. Proc. **467**, 19 (1997).
[12] K. Yamamoto, M. Yoshimi, Y. Tawada, S. Fukuda, T. Sawada, T. Meguro, H. Takata T. Suezaki, Y. Koi, K. Hayashi, T. Suzuki and A. Nakajima, Technical Digest of the International PVSEC-12, Jeju, Korea, 547 (2001).
[13] H. Fritzsche, Solid State Commun. **94**, 953 (1995).
[14] Z. Yiping, Z. Dianlin, K. Guanglin, P. Guangqin, L. Xianbo, Phys. Rev. Lett. **78,** 558 (1995).
[15] A. Ouhlal, A. Yelon and D.P. Masson, J. Non-Cryst. Solids **190**, 151 (1995).
[16] K.Shimizu, T. Shiba, T. Tabuchi and H. Okamoto, Jpn. J. Appl. Phys. **36**, 151 (1995).
[17] P. Hari, P.C. Taylor and R.A. Street, J. Non-Cryst. Solids **198**, 52 (1996).
[18] T. Gotoh, S. Nonomura, M. Hirata, N. Masui and S. Nitta, Solar Energy Mat. Solar Cells **49**, 13 (1997).
[19] T. Gotoh, S. Nonomura, M. Nishio and S. Nitta, Appl. Phys. Lett. **27**, 2978 (1998).
[20] K. Shimizu, T. Tabuchi, M. Ida and H. Okamoto, J. Non-Cryst. Solids **227–230**, 267 (1998).
[21] T. Gotoh, S. Nonomura, M. Nishio, N. Masui, S. Nitta, M. Kondo and A. Matsuda, J. Non-Cryst. Solids **227–230**, 236 (1998).
[22] K. Shimizu, T. Tabuchi, K. Hattori, H. Kida and H. Okamoto, MRS Symp. Proc. **507**, 735 (1998).
[23] S. Nonomura, T. Gotoh, M. Nishio, T. Sakamoto, M. Kondo, A. Matsuda and S. Nitta, Mat. Res. Soc. Symp. Proc. **557**, 337 (1999).
[24] T. Gotoh, S. Nonomura, S. Hirata and S. Nitta, Prog. Nat. Sci. **6**, S34 (1996).
[25] G.G. Stoney, Proc. Roy. Soc. **A28**, 172 (1909).
[26] A. Matsuda, in Proceedings International Seminar on Reactive Plasma, T. Goto (Ed.), Nagoya, 1991, p. 405.
[27] K. Kobayashi, A. Asano, S. Asada, T. Kubota, Y. Yamashita, K. Yoneda and Y. Tadokoro, J. Appl. Phys. **83**, 2098 (1998)
[28] H. Kobayashi, A. Asano, M. Takahashi, K. Yoneda and Y. Tadokoro, Appl. Phys. Lett. **25**, 4392 (2000).
[29] H. Kobayashi, Appl. Phys. Jpn. **71**, 860 (2002).
[30] S. Nonomura, N. Yoshida, T. Gotoh, T. Sakamoto, M. Kondo, A. Matsuda and S. Nitta, J. Non-Cryst. Solids **266–269**, 474 (2000).
[31] R.A. Street, Hydrogenated Amorphous Silicon, Cambridge University, Cambridge, 1991.
[32] E. Stratakis, E. Spanakis, H. Fritzsche and P. Tzanetakis, J. Non-Cryst. Solids **266–269**, 506 (2000).
[33] H. R. Park, J.Z. Liu, S. Wagner, Appl. Phys. Lett. **55**, 2658 (1989).
[34] M. Stutzmann, Appl. Phys. Lett. **47**, 21 (1985).
[35] S. Muramatsu, S. Matsubara, T. Watanabe, T. Shimada, T. Kamiyama, K. Suzuki, and A. Matsuda, Jpn. J. Appl. Phys. **30**, L2006 (1991).

[36] K. Morigaki, Physics of Amorphous Semiconductors, World Scientific, Imperial College, Singapore, 1999, p. 253.

[37] N.H. Nickel, W.B. Jackson and N,M, Johnson, Phys. Rev. Lett. **71**, 2733 (1993).

[38] J. Miere, R. Fluckinger, H. Keppner and A. Sah, Appl. Phys. Lett. **65**, 860 (1994).

[39] M. Kondo, T. Nishimiya, K. Saito, A. Matsuda, J. Non-Cryst. Solids **227–230**, 1031 (1998).

[40] Y. Kunii, J. Kitao, K. Mori, N. Yoshida and S. Nonomura, Solar Energy Mat. Solar Cells **74**, 415 (2002).

[41] N.H. Nickel and M. Rakel, J. Non-Cryst. Solids **299–302**, 502 (2002).

[42] E. Spanakis, E. Stratakis, P. Tzanetakis, H. Fritzsche, S. Guha and J. Yang, J. Non-Cryst. Solids **299–302**, 521 (2002).

[43] V. Chu, J.P. Conde, S. Aljishi, S. Wagner, Mat. Res. Soc. Symp. Proc. **118**, 167 (1988).

[44] S. Nonomura, H. Kobayashi, Y. Sobajima, T. Fujinaga, H. Kamiguchi and N. Yoshida, unpublished.

[45] C.R. Wronski, J.M. Pearce, R.J. Koval and R.W. Collins, Tech. Digest of the Int. PVSEC-12, Jeju, Korea, 33 (2001).

[46] H.M. Branz, Phys. Rev. B **59**, 5498 (1999).

[47] R. Biswas and B.C. Pan, Phys. Rev. B **57** 2253 (1998).

[48] H. Okamoto, Tech. Digest of the Int. PVSEC-11, Sapporo, Japan, 199 (1999).

[49] T. Nishimoto. M. Takai, H. Miyahara, M. Kondo and A. Matsuda, J. Non-Cryst. Solids **291–302**, 1116 (2002).

15 First Principles Molecular Dynamics and Photo Structural Response in Amorphous Silicon and Chalcogenide Glasses

David Drabold, Xiaodong Zhang, and Jun Li

15.1 Introduction

There is a striking range of novel phenomena which occur in non-oxide glasses, especially the chalcogenides (S, Se, Te), either in elemental form or alloyed with atoms from groups III, IV or V. The materials tend to have similar electronic state densities, possessing an optical gap of about 2 eV and exponential (Urbach) band tails at both band edges. They also have the important property that, although there are some gap states, they do not carry the traditional electron spin resonance (ESR) defect signature of unpaired spins. The lone-pair character of both the conduction and valence tails leads to very rich behavior under the influence of light. One light-induced process is "photo melting" of certain chalcogenide glasses such as a-Se [1] and g-As_2S_3 [2]; in which weak (even sub-gap) light shone on the glass leads to a viscosity change of *several* orders of magnitude. This process has been demonstrated *not* to be a thermal heating effect (in As_2S_3 for example the effect is *larger* at lower temperatures [2]). There is also the related property of giant photo-expansion [3]; large volume changes in light-exposed thin films; some chalcogenide films change thickness when light-soaked by *several percent*. Furthermore, there are also so-called "vector" effects [4, 5]; exposure to linearly or circularly polarized light results in linear or circular dichroism (from a light-induced anisotropic dielectric tensor). Brillouin light scattering experiments also have revealed a large, reversible and probably athermal photo-induced longitudinal acoustic mode softening in GeSe glasses [6], which has been connected to the important concepts of constraint counting and floppy modes [7]. The understanding of these effects is at present extremely incomplete, and these effects are known only in disordered forms of matter.

These materials are technologically important. For example, a-Se is a classical material for xerographic applications [9], and has recently been highlighted as a promising photoconductive material for digital X-ray radiography [10]. Certain chalcogenide alloys can be reversibly interchanged from amorphous to crystalline by suitable light exposure, a property which has been applied to high-density read–write memory/storage devices [11]. A new frontier which has only just begun to attract interest is athermal optical micro fabrication (micrometer length scale deformations can be accomplished via light exposure); this approach has already been used to make optical gratings and micro lenses [3]. The origin of this process is closely related to photo-induced fluidity. Glasses such as $As_{12}Ge_{33}Se_{55}$ are promising host media for rare-earth photonic devices [12].

For the case of chalcogenide glasses an important insight into the microscopic origin of the light-induced effects emerged in the 1970s and 1980s thanks to the work of several authors [13–19]. The lack of an ESR signal (implying no unpaired spins or a "negative Hubbard U" character [13]) in a system known on other grounds to have gap states led Street and Mott [14] to propose a picture in which photo-excited carriers thermalize rapidly into localized tail states, chemical arguments were then used to atomistically justify the "negative U" behavior (formation of valence alternation pairs with no ESR-active singly occupied electron states). Subsequent developments have been published by Elliott [18], Fritzsche [15] and Tanaka [19]. Beyond doubt these models are correct in their essential content and it is quite impressive how much progress can be made without detailed microscopic calculations. However, these treatments are limited to assumptions of locality and simple chemical bonding arguments which enable only a qualitative grasp of the phenomena (which vary considerably in detail with materials, temperature, intensity of light and other parameters). For a proper discussion of the experimental and theoretical situation, we recommend the review of Shimakawa and co-workers [20].

In a qualitative way, it is not surprising that glasses should exhibit some significant sensitivity to light, since the network is highly defective compared with crystalline forms of the materials (when they exist), and the simplest way to think of the effect of light is to consider the promotion of an electron to a low-lying antibonding state, which destabilizes the network. The effect is naturally stronger in a disordered system because the states which suffer modified occupations are usually localized; thus the structural changes are (initially) focused in the volume of space in which the electron wavefunctions associated with the occupation change are localized.

15.2 Method

Our approach to this problem is to adopt the methods of so called first principles simulations to the photostructural problem in glasses. Such a scheme has several key advantages: (1) it is based on a completely defined atomistic structural model for the glass (typically a cell with 100–300 atoms). It is possible to create models of amorphous silicon (a-Si), glassy chalcogenides and oxide glasses which are quite satisfactory when compared with known experiments (structural, electronic/optical and vibrational); (2) it is based upon a real electronic structure Hamiltonian, derived from density functional theory: the quantum mechanics is built in at a fundamental level; (3) the coupling between the electrons and lattice is at least reasonable; this electron–phonon coupling is obviously a key quantity for any simulation of photo-induced structural response; (4) in these simulations the locality (or lack thereof) in the rearrangements is not assumed; it is *computed*. These methods have been heavily applied to problems throughout materials physics and we are attempting to extend them to problems of light-induced effects in glasses. Our scheme also has weaknesses, particularly the short (picosecond) time scales of the simulation. Also, as for any simulation, one has to be able to interpret the mass of data spewing forth, and preferably learn something general about the physics of the material after performing the simulation. Finally, significant approximations connected with the electronic structure of the glass are assumed. With all these caveats however, this approach is comparatively "unbiased" and does not depend upon *a priori* as-

sumptions about the mechanism, barrier heights, etc. All of this emerges *automatically* (albeit approximately) from the computations.

15.2.1 Making the Structural Model of the Glass

We have empirically found that a simple simulation regime (molecular dynamics (MD) quench from the melt) can work quite well with certain glasses with a suitable simplified *ab initio* density functional Hamiltonian. This scheme *cannot* be expected to work for general amorphous systems [21]. We have conducted studies on a variety of Se alloy glasses which have convinced us that it is relatively easy to make realistic models (meaning adequate agreement with experiments) for stoichiometric compositions (such as As_2Se_3 [22] or $GeSe_2$ [23, 24]), but much more challenging to make models at compositions far from these. Almost certainly the ease of making quality models of these special compositions is connected to the *physical* glass forming process. In microscopic terms, this is connected to the similarity of the topological (and chemical) order in the liquid not far above the melting point and the glass. From a naive point of view this is altogether remarkable, since the time scale of quenching materials in the laboratory is dramatically longer than what we simulate on the computer.

Unexpected difficulties in model making can also arise in materials often supposed to be "simple" [25]. Beyond doubt, a-Si is the most studied disordered material. Yet "cook and quench" does a rather poor job of making models [26]. This is initially puzzling, since *ab initio* methods do accurately represent the relevant part of the Si phase diagram. This by itself, however, is clearly not a guarantee that computer melt quenching will result in a realistic physical model. There are at least two key limitations to these simulations: time scales (radically shorter in the simulation), and length scales (many simulations have been carried out for 64 atom cells, which are significantly strained). We note that one cannot make respectable a-Si in the laboratory by melt quenching: microcrystalline samples are the product of such experiments. One supposes that the problem for the simulation (and perhaps nature in this case!) is that MD simulations simply cannot unravel all the changes in topology necessary to model faithfully the amorphous solid state which is so topologically different from the six-fold liquid. Fortunately, alternative methods based on the Wooten–Weaire–Winer [27] bond-switching approach and Keating springs are brilliantly successful for a-Si. We suppose that the efficacy of this scheme originates in its imposition of the constraint of four-fold coordination for a-Si (an excellent approximation and a fine example of the use of *a priori* information in model building.)

The remarks in this section are largely independent of the choice of energy functional used. In some cases simple analytic interatomic potentials can succeed very well for modeling glasses. In other cases, highly accurate force fields derived from a proper quantum mechanical description of the material are necessary. However, the simulation regime (in the sense of the cooking, quenching and "annealing" process) should be optimized for whatever energy functional is chosen. Any MD approach suffers to varying degrees from the "time-scale problem" (unphysically rapid quenching in comparison to experiment). If one "anneals" a model, virtually all of the MD steps consist of oscillating in a harmonic (or nearly harmonic) well associated with the minimum in the system potential energy, which provides no information about the energy landscape away from the minimum. Such simulated annealing is therefore a very inefficient means to explore the configuration space of materials. One can instead go

to very high temperatures (quite near the melting point) to force the emergence of "more interesting" events, but the question arises of whether these are the same events seen (rarely) at lower temperatures. A development of great importance is recent work to allow access to a much larger part of the configuration space. A method which has been applied to amorphous systems is the "Activation–Relaxation Technique" (ART) of Barkema and Mousseau [28]. In this scheme, one "hunts" quite efficiently for saddles connecting basins of different energy minima, and one can explore dynamic events which occur on time scales vastly longer than the picosecond times of common MD simulations. Such calculations are also ideal for modeling diffusive phenomena (such as ion motion in a glassy host), and we expect significant advances to accrue from such studies.

15.2.2 Density Functional Theory and Molecular Dynamics

Since the application of density functional methods to problems of photostructural change is a recent idea, we think that it is useful to include a short self-contained summary of the method. For an authoritative review, see the book by Martin [29]. The complexity of electronic structure and force calculations arises from the many-body nature of the interactions between the electrons. Currently, it would seem that a direct attack on the many-electron problem is too difficult to have direct impact on amorphous systems, requiring as they do a large number of atoms to provide a model worth investigating. Thus, all the successful electronic structure calculations salient to amorphous insulators have involved some kind of mapping of the many-body problem into an effective one-electron problem. Historically, the Hartree and Hartree–Fock approaches were the first success in this direction; descendants of these methods are widely used today, particularly in quantum chemistry.

Of course, the true many-body Hamiltonian treats both the ions and electrons on a quantum mechanical basis. Because of the large mass difference between the electrons and nuclei, it is standard to decouple the nuclear and electronic degrees of freedom with the adiabatic or Born–Oppenheimer approximation [30], in which the electrons are assumed to respond instantly to motions of the ions (the electrons are taken to be in their ground-state for all instantaneous ionic conformations). Moreover, the nuclei are treated as classical particles which move in a potential determined by the electrons in their ground-state (computed for the given ionic coordinates).

For atomistic force calculations on solids, the current method of choice is density functional theory, due to Kohn, Hohenberg and Sham [29]. Its name comes from the predicted connection between the total ground-state electronic energy of a system and the electronic charge density. The following rigorous statements embody the foundation of zero-temperature density functional theory:

(1) The ground-state energy of a many electron system is a functional of the electron density $\rho(\mathbf{x})$:

$$E[\rho] \;=\; \int d^3x V(\mathbf{x})\rho(\mathbf{x}) \;+\; F[\rho], \tag{15.1}$$

where V is an external potential (due for example to interaction with ions, external fields, e.g., *not* with electrons), and $F[\rho]$ is a *universal* functional of the density. The trouble is

that $F[\rho]$ is not exactly known, although there is continuing work to determine it. The practical utility of this result derives from:

(2) The functional $E[\rho]$ is minimized by the true ground-state electron density.

It remains to estimate the functional $F[\rho]$, which in conjunction with the variational principle (2), allows real calculations. To estimate $F[\rho]$, the usual procedure is to note that we already know some of the major contributions to $F[\rho]$, and decompose the functional in the form:

$$F[\rho] = e^2/2 \int d^3x d^3x' \rho(\mathbf{x})\rho(\mathbf{x}')/|\mathbf{x}-\mathbf{x}'| + T_{ni}(\rho) + E_{xc}(\rho). \tag{15.2}$$

Here, the integral is just the electrostatic (Hartree) interaction of the electrons, T_{ni} is the kinetic energy of a *non-interacting* electron gas of density ρ, and $E_{xc}(\rho)$ is yet another unknown functional, called the "exchange-correlation" functional, which includes non-classical effects of the interacting electrons. Equation (15.2) is difficult to evaluate directly in terms of ρ (because of the term T_{ni}). Thus, one introduces single electron orbitals $|\chi_i\rangle$, for which $T_{ni} = \sum_{i\ occ}\langle\chi_i| - \hbar^2/2m\nabla^2|\chi_i\rangle$, and $\rho = \sum_{i\ occ}|\chi_i(\mathbf{x})|^2$ is the charge density of the physically relevant *interacting* system. The value of this decomposition is that $E_{xc}(\rho)$ is a smoothly and reasonably slowly varying functional of the density: we have included the most difficult and rapidly varying parts of F in T_{ni} and the Hartree integral, as can be seen from essentially exact many-body calculations on the homogeneous electron gas [31]. The Hartree and non-interacting kinetic energy terms are easy to compute and, if one makes the "local density approximation" (taking the electron density to be *locally* uniform), then with information about the homogeneous electron gas, functional (Eq. (15.2)) is fully specified.

With non-interacting orbitals $|\chi_i\rangle$, (with $\rho(\mathbf{x}) = 2\sum_{i\ occ}|\langle\mathbf{x}|\chi_i\rangle|^2$), the minimum principle plus the constraint that $\langle\chi_i|\chi_j\rangle = \delta_{ij}$ can be translated into an eigenvalue problem for the $|\chi_i\rangle$:

$$\{-\hbar^2\nabla^2/2m + V_{\text{eff}}[\rho(\mathbf{x})]\}|\chi_i\rangle = \epsilon_i|\chi_i\rangle, \tag{15.3}$$

where the effective (density) dependent potential V_{eff} (in practical calculations orbital dependent) is

$$V_{\text{eff}}[\rho(\mathbf{x})] = V(\mathbf{x}) + e^2 \int d^3x' \rho(\mathbf{x}')/|\mathbf{x}-\mathbf{x}'| + \delta\epsilon_{xc}/\delta\rho. \tag{15.4}$$

In this equation ϵ_{xc} is the parameterized exchange-correlation energy density from the homogeneous electron gas. The quantities to be considered as physical in local density functional calculations are the total energy (electronic or system), the ground-state electronic charge density $\rho(\mathbf{x})$, and related ground-state properties like the forces. In particular, it is tempting to interpret the $|\chi_i\rangle$ and ϵ_i as genuine electronic eigenstates and energies (and indeed this can often be useful); such identifications are not rigorous [32]. It is instructive to note that the starting point of density functional theory was to depart from the use of orbitals and formulate the electronic structure problem rigorously in terms of the electron density ρ; yet a practical implementation (which allows an accurate estimate of the electronic kinetic energy) led us immediately back to orbitals! This illustrates why it would be very worthwhile to know $F(\rho)$,

or at least the kinetic energy functional since we would then have a theory with a structure close to Thomas–Fermi form and would therefore be able to seek *one* function ρ rather than the cumbersome collection of orthonormal $|\chi_i\rangle$.

The usual implementation of the local density approximation (LDA) leads to a non-linear set of coupled integrodifferential equations. The origin of this non-linearity is that $V_{\rm eff}$ in the Schrödinger-like Eq. (15.3) is ρ-dependent, which in turn depends on the eigenvectors $|\chi_i\rangle$, which in turn depend on $V_{\rm eff}$ and so on. This non-linearity is dealt with in the usual way "iterating to self-consistency", an expensive inner loop on an already challenging computational task.

The development of practical density functional codes is a vast undertaking. Several "standard" codes are now in general use. Among these are SIESTA [33] and FIREBALL [34] which employ local basis sets and VASP [35], CASTEP [36], CPMD [37] and FHI98MD [38] which use a plane wave representation. Both classes of codes offer accurate solutions of the Kohn–Sham equations and each has its own strengths and limitations. In our work, we use FIREBALL and SIESTA.

15.2.3 Photostructural Change from Molecular Dynamics

In a single electron picture of the electronic structure of solids one imagines that in the presence of light the system Hamiltonian is [39]

$$H_{EM} = (\mathbf{p} + e/c\mathbf{A})^2/2m + V_{eff}(\mathbf{x}). \tag{15.5}$$

Here, V_{eff} is the Kohn–Sham potential and $\mathbf{A}$ is the vector potential associated with the electromagnetic (EM) field in Coulomb gauge [39]. $\mathbf{A}$ has a time dependence $\mathbf{A} \sim \mathbf{A_0}\mathrm{e}^{-i\omega t}$, where ω is the frequency of the light. One usually approaches this with time-dependent perturbation theory and Fermi's Golden Rule to obtain light-induced transition rates between valence and conduction states and quantities like dielectric functions. For our purposes, we seek the electronic (and consequent structural) changes arising from the EM field. In principle the "right" thing to do would be to solve the time-dependent Kohn–Sham (Schrödinger) equation:

$$i\hbar\partial\psi/\partial t = H_{EM}\psi, \tag{15.6}$$

while fully coupling the changes induced by $\mathbf{A}$ *back to the ion dynamics*. In this way, one would directly model EM field-induced transitions.

The calculation of the preceding paragraph is very difficult to implement, particularly for large supercell models of glasses (with typically 200+ atoms). As a way to alleviate these serious difficulties, we handle the transitions by simply changing electronic occupations. Our simulation of photostructural rearrangements is based upon the following reasoning: it is well known that topological or chemical irregularities in an amorphous network may lead to localized electron states in the gap or in the band tails. If such a system is exposed to bandgap light, then it becomes possible for the light to induce transitions of electrons from the top of the occupied states to low-lying unoccupied (conduction) states. For the present model we will not concern ourselves with the subtleties of how the EM field introduces the transition; we

will simply assume that a photo-induced promotion occurs. The key electronic band structure contribution to the interatomic force is

$$\mathbf{F}_\alpha = \sum_{n\ occ} \langle \psi_n | - \partial \mathbf{H}/\partial \mathbf{R}_\alpha | \psi_n \rangle, \tag{15.7}$$

where the index implies that the sum is carried out over occupied states. Then the effect of the electronic promotion is to deplete the original set of occupied states by one electron and add an electron to the unoccupied (conduction) states. If the light is exactly of bandgap energy, the electron will be promoted exactly from the top of the valence states to the bottom of the conduction states. Thus, the change in forces for atom/Cartesian component index α is

$$\delta \mathbf{F}_\alpha = \langle \psi_{N+1} | - \partial \mathbf{H}/\partial \mathbf{R}_\alpha | \psi_{N+1} \rangle - \langle \psi_N | - \partial \mathbf{H}/\partial \mathbf{R}_\alpha | \psi_N \rangle. \tag{15.8}$$

Here ψ_{N+1} is the lowest unoccupied molecular orbital (LUMO) and ψ_N is the highest occupied molecular orbital (HOMO). There are in fact additional terms arising from charge transfer, but these are relatively simple to handle. The likelihood of a light-induced structural change is then reduced in this model to the questions of whether $\delta \mathbf{F}_\alpha$ is large and if so, whether a new conformation becomes favorable. The key requirements are then that either or both of the states ψ_{N+1} or ψ_N are *well localized* and that the network admits the possibility of conformational change. If neither state is localized, then the change in forces from Eq. (15.8) will be "diluted" over the volume in which the state extends. Thus, in crystals (where all the states are extended), occupation changes of the type we describe here never lead to photostructural modification. Similarly, in models with overly large defect concentrations, no changes are observed either since the banding between defects (artificially) reduces the localization of the defect wavefunctions. Another statement is that a poorly localized wavefunction will have a small electron–lattice coupling with all the phonons, and no important photostructural effects are to be expected for this case. In general, it is necessary to investigate photostructural changes due to a collection of different initial and final states, although we may expect that only well localized states (necessarily near the gap) will be relevant.

It must be noted that the approach we suggest here is limited to *very* short (picosecond) time scales; longer times and longer length scales require additional methods and study. Still, we believe that the approach presented here is an essential first step to understanding these problems as well. Another "knob" on these simulations is how long to maintain the system in the excited state, which in turn depends on the size of models used. We have typically used times of the order of a few hundred fs by which an obvious light soaking pattern arrives; if times are much shorter than this, no rearrangements occur. This dimension of the "phase space" also needs to be more thoroughly explored.

15.3 Applications

In this section we describe the applications of these methods to particular amorphous and glassy systems. This work is in its infancy and more detailed studies are needed to understand the full potential (and limitations) of the approach. We believe that the results have been quite encouraging so far.

15.3.1 Amorphous Silicon

The most studied amorphous material is surely hydrogenated a-Si:H. Device-grade thin films of a-Si:H are routinely used in electronic applications (such as laptop displays), and are one of the key materials for photovoltaic applications. For photovoltaic applications, the response of the material to light soaking, and its resulting electronic degradation (the Staebler–Wronski effect (SWE) [40]) is absolutely central. The first application of this method was by Fedders, Fu and Drabold in 1992 [41].

There have been very many models put forward for the SWE. In analogy with the situation for the chalcogen glasses, these are usually plausible "cartoons" of what the SWE events are and how the defect creation proceeds. The better proposals carefully exploit the (many and complex) experimental properties of the effect and are well worth developing further with detailed calculations. For a review, see [40]. The logic of our calculation is the following: (1) there exist defects in a-Si which are uncommon (with a concentration less than 0.1%). These defects can take various forms: certainly some are dangling bonds (three-coordinated Si atoms) with an energy near mid-gap. Some are probably "strain" defects – nominally four-fold sites with bond angles far from the tetrahedral angle. It is not impossible that some are "floating" bonds (five-fold atoms), although the distinction from other defects can be rather ambiguous in practice. (2) Wavefunctions associated with these structural irregularities will be localized. (3) Electrons in localized states are very sensitive to lattice distortions (there is a large electron–phonon coupling for localized electrons [42]). (4) A large electron–phonon coupling may open the way to large and non-local rearrangements of the amorphous Si network. Note that the network must become "floppy" with light soaking for these rearrangements to occur – not only does the electron–phonon coupling have to be large, also the network must be non-rigid enough to permit structural change.

We performed the calculation on a very small (63 atom) model of a-Si [43]. We found that the simulation led to a complex sequence of bond forming and bond breaking with the net effect that defects were created. The effect was found to be quite *non-local* in qualitative agreement with spin resonance experiments [44]. In our simulation, there was a strained region of the cell which was especially active in rearrangements. As we discuss in detail elsewhere [41], the net effect of this process was to increase the number of dangling bond defects. This type of simulation needs to be extended in many ways (with current models, and more up-to-date electronic structure techniques), and a-Si:H is a particularly appropriate material to study since there is a wealth of excellent experiments (and many interesting ideas!) available.

This calculation is very interesting, and highly suggestive, but is far from a complete explanation of the SWE. For one thing, the calculation did *not* involve H, which is widely believed to be implicated in the SWE. Our approach needs to be applied to many different types of defects and strains. To achieve this, a wide array of models properly sampling the "space of defects" for a-Si:H needs to be assembled. We hope to pursue these studies in the near future.

15.3.2 Amorphous Selenium

Photostructural Effects in Models of a-Se

We made two models of a-Se (with 64 and 216 atoms) as described elsewhere [45,46]. These models were in suitable agreement with experiment (structural, vibrational and optical). Following the procedure of Section 15.2.3, we observed "photoannealing" – the *improvement* of the 64 atom model (initially this cell had a single "intimate" Valence Alternation Pair (IVAP); after occupation change and quenching the resulting model had no defects and a total energy improved over the first model. For the 216 atom model, which began with a single VAP, the final model possessed a single IVAP – so that there was "defect diffusion". It is quite possible that repeating the process with the 216 atom model with IVAP would also yield a defect-free model.

These results emphasize the effects of "local heating". When the occupation of a defect state (which may be localized in a compact volume of space) is changed, atoms which are within the volume suffer large changes in forces (from Eq. (15.8)). Thus, it is the local environment of the defects which are preferentially affected by occupation change and not the network at large (at least for sufficiently short times). Thus, the influence of light is locally to heat (anneal!) just those parts of the network with defects. There is thus a reasonable chance that the local annealing will *improve* the network rather than make it more defective. This statement depends of course upon the quality of the network; defective networks (thin films or systems which have not been annealed) are likely to improve.

Dynamical Inter-Chain Bond Formation [47,48]

Recent experiments on optically induced ESR by Kolobov et al. [47,49] showed that the ESR-active defect centers were created by breaking the inter-chain bonds under photo-excitation. They also observed fast and slow ESR signals for the film previously irradiated for several hours and then annealed at low temperature.

To attempt to elucidate the atomistics of this experiment, we began with an idealization: a pair of perfect Se chains as shown in Fig. 15.1. As in Section 15.2.3, we modeled the presence of light by promoting an electron from the top of the valence states to the bottom of the conduction states. Since the system is initially perfect, all sites are equivalent, and thus this amounts to putting an electron into an extended antibonding state and removing an electron from an extended bonding (valence) state. Now we add thermal disorder (we perform an MD simulation at $T = 300$ K). If the light was "off" (e.g. if the system was in the ground-state occupation), the system would execute small oscillations near the perfect conformation. In the excited state however, the system becomes unstable with respect to defect formation. We show that this is a consequence of the Coulomb interaction between positively charged threefold sites and negatively charged one-fold sites. We can also show how the defects change character through the simulation.

The process of the photostructural change of the parallel chains is shown in Fig. 15.1. The process can be understood in two stages. The first step is the defect creation process. This process lasts around 250 fs as indicated by Fig. 15.1(a–e). The second step is the process of stabilization of the defect as seen by Fig. 15.1(e–f). The dynamical inter-chain bond formation

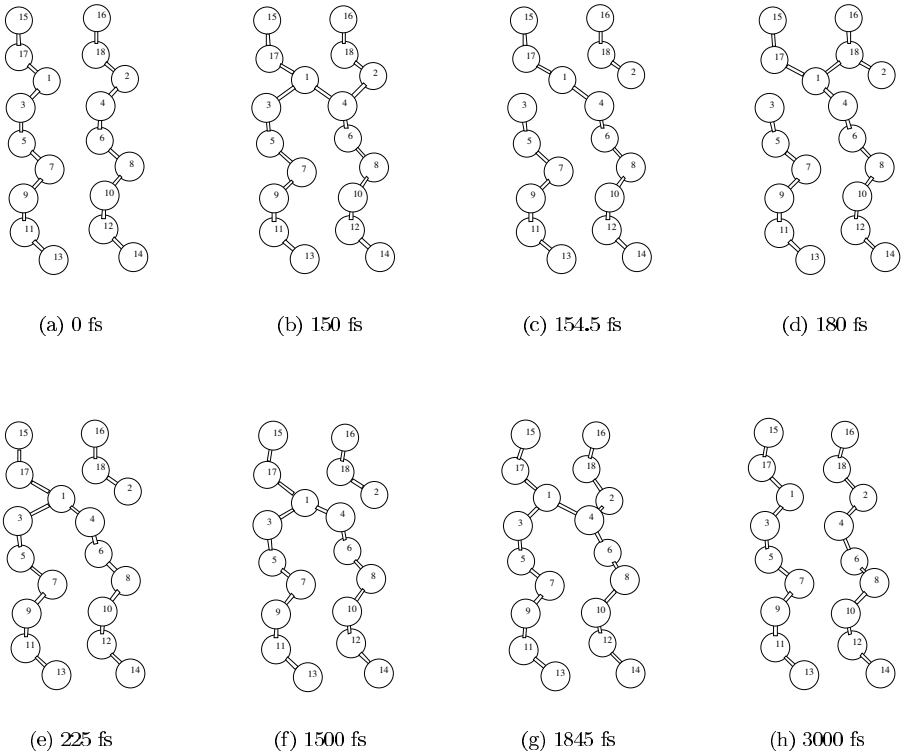

(a) 0 fs (b) 150 fs (c) 154.5 fs (d) 180 fs

(e) 225 fs (f) 1500 fs (g) 1845 fs (h) 3000 fs

Figure 15.1: The simulation of photostructural change of parallel Se chain. We maintain light excitation before 1500 fs; after 1500 fs, we relax the light excited conformation to optimal structure.

is clearly seen in Fig. 15.1b. To our knowledge, this is the first direct simulation to confirm this dynamical inter-chain bond observed in experiment [49].

The chemistry behind this process can be understood by looking at the charge evolution of the relevant atoms during the photo-excitation. The charges of the atoms are calculated by the standard Mulliken population analysis [50]. The time evolution of the Mulliken charge of relevant atoms during the photo-excitation is shown in Fig. 15.2. Initially, all the atoms in this two-chain configuration are equivalent. The initial effect of random thermal fluctuation and the photo-excitation process is to transfer charge from atoms 18 and 17 to atoms 1 and 2. This process can be seen from Fig. 15.2 at the beginning of the simulation (from 0 fs to 150 fs), where the charge of atom 1 and 2 increases (more negative [electron rich]) and the charge of atom 18 decreases (more positive [electron deficient]). However, with atoms 1 and 2 becoming more negatively charged, atom 18 becomes more positively charged, and the Coulomb interaction between atoms 18 and 1 will attract atom 1 to atom 18. After atom 1 moves close to atom 18, atom 1 is not geometrically equivalent to atom 2. *As atom 1 becomes a three-fold coordinated site due to Coulomb interaction, the role of atom 1 changes after the transfer. As shown in Fig. 15.2, the charge of atom 2 has a transition around 150 fs. The dynamical bond shown in Fig. 15.1b is formed around this time. This means that*

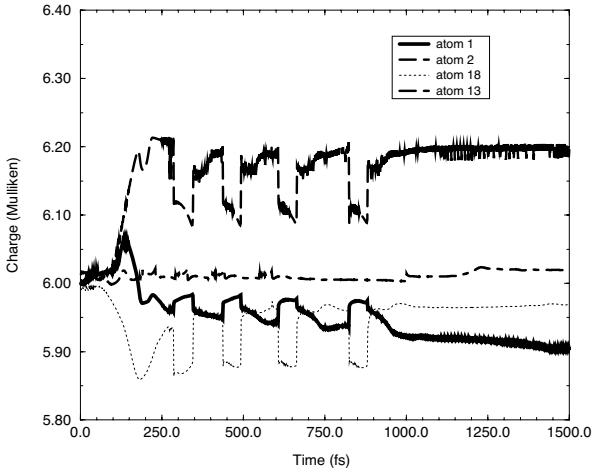

Figure 15.2: Time evolution of Mulliken charge for the atoms involved during the photo-excitation (parallel chain case). Atom 13 has charge near 6.0 and is shown as a reference atom which was inactive during the simulation. Charges larger than 6 are electron rich, smaller are deficient.

electron charge will move away from atom 1 during the photo-excitation process, after atom 1 makes the transition from two- to three-coordination. So, we can see that the dynamical bond formation is an intermediate process for defect creation by photo-excitation. The origin of this dynamical bond is the positive and negative charge centers formed by the photo excitation. The residual Coulomb interaction present during the photo-excitation causes atom 1 to become three-fold coordinated.

Figure 15.1b–e shows the reaction $2\,C_3 \rightarrow C_3^+ + C_1^-$. The two C_3 centers are atom 1 and atom 4 shown in Fig. 15.2b, and C_3^+ and C_1^- are atom 1 and 2 respectively shown in Fig. 15.1f. This dynamical process involves relaxation of the photo-created VAP defect under the condition of the photo-excitation. This relaxation process is also shown in Fig. 15.2 (150–250 fs). In the time interval 250–800 fs, we can still see some fluctuation of the charge of those relevant atoms. The photo-excited system is rather stable. It is interesting to observe that the VAP defects are somewhat charged even for the photo-excited system. During the time 250–1500 fs, the light excitation persists but the system reaches saturation and no new defects are created.

From another point of view, the modification of the occupations created an uncorrelated electron–hole pair, with both carriers in extended states (extended because the system was initially perfect). In the simulation, thermal disorder destroys the equivalence of the sites and causes the positive and negative charges to coalesce or "condense" onto defect centers (a VAP, C_3^+ and C_1^-). What is initially an uncorrelated pair changes character and instead produces stable charge defects in the chains.

After we turn off the light, the structure with light-created VAP defects takes about roughly the same amount time (after 350 fs) to relax back to the initial structure as the time (around 300 fs as shown in Fig. 15.2) spent to create these defects. This can also be observed by

tracking the time evolution of the energy of the system. Since the VAP defect created by light is a local bond rearrangement in this simulation, the structural change is reversible. In the real situation, the bond rearrangement is not necessary local and the structural change is also not necessarily reversible.

Light-Induced Electron Spin Resonance for Se Chains

In his PhD thesis [25], Zhang took an important step beyond the (explicitly spin non-polarized) local density approximation and examined the time dependence of the spin polarization for the dynamics discussed in the preceding section. These results should be directly relevant to light-induced ESR experiments. To enable this, it was necessary to use the powerful code SIESTA in conjunction with the local spin density approximation. We used the efficient program FIRE-BALL to generate the trajectory of the configuration for selenium parallel chain, and then we used the SIESTA to calculate the spin polarization every 10 configurations (time steps). Figure 15.3 shows the time evolution of the spin polarization of relevant atoms of selenium parallel chain. For comparison, we also plot the Mulliken charge calculated by SIESTA. It is

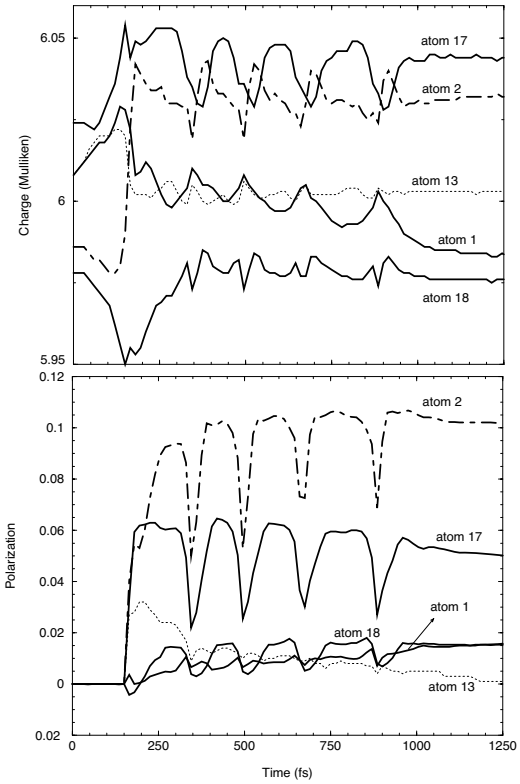

Figure 15.3: Time evolution of the spin polarization and Mulliken charge for selenium parallel chain during the light illumination.

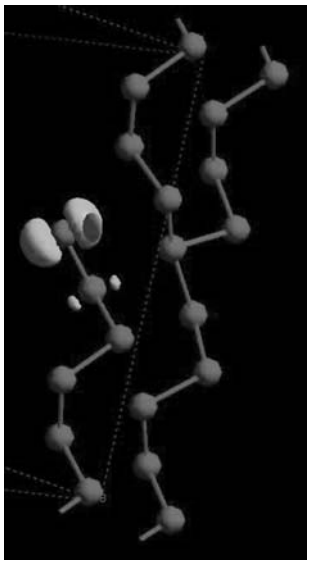

Figure 15.4: An unpaired electron spin in Se, extracted from a local spin density calculation with CASTEP (see text) for the Se chain during photo-excitation.

quite clear that those light excited defects carry net spin. Although the absolute charge calculated by SIESTA is not the same as that calculated by FIREBALL, they show a similar trend suggesting that our understanding of dynamical bond formation by weak Coulomb interaction is correct. In Fig. 15.4, we also plot the spin charge density of a light-excited configuration. It is interesting to see that the most spin charge is localized in the one-fold coordinated defect site. For this figure, we used the program CASTEP [36].

15.3.3 As_2Se_3

We have also simulated photostructural changes in g-As_2Se_3 [51]. For this system, it was not difficult to make a reasonably realistic model with 215 atoms by quenching from the melt. The predominant bonding unit in this material is the AsSe pyramid. Details on structural and vibrational properties have been published elsewhere [22]. For the present purposes, we note that the important defects in the model were *miscoordinated As*. In our model, there were two four-fold As and one two-fold As. Both led to localized band tail states (with the LUMO being associated with the four-fold defect and the HOMO with the two-fold as depicted in Fig. 15.5). This study strongly suggests that major rearrangements in this glass are primarily initiated from As-based defects rather than Se while adjacent Se-based defects are quite active in ensuing reactions. Where Se defects are concerned, there were 26 valence alternation pairs (26 three-fold and 26 one-fold coordinated atoms). Such a high density of Se-based defects, confirmed by recent experimental 3d core levels analysis [52], greatly reduces the localization of associated defect states. From the preceding paragraph, it can be seen that boosting an electron from HOMO to LUMO will preferentially affect local defect groups related to the HOMO and LUMO. In Fig. 15.6, we illustrate the effects of promotion.

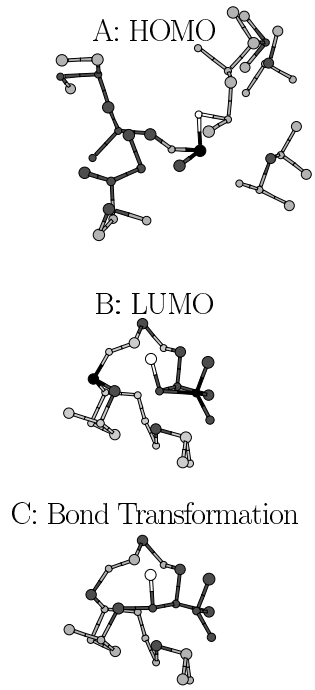

Figure 15.5: A view of atomic groups associated with edge states. Small circles stand for As and large for Se. Black (white) depicts over(under)-coordinated As or Se in the main structure. All sites may have unshown bonds with other atoms. (A), HOMO's group; (B), LUMO group; (C), Homopolar-heterpolar bond transformation within LUMO group at the onset of illumination.

We interpret the evolution in two time scales which emerge naturally from the simulation, short time (ST) stage and long time (LT) stage, as indicated in Fig. 15.6, and adopt the first minimum, about 2.8 Å, of the pair correlation function $G(r)$ of g-As_2Se_3 as a criterion to judge if a bond was broken or created. The ST phase involves two atomic reactions. Bond breaking in LUMO's group occurs at the onset of illumination and accounts for the steep fall of the LUMO eigenvalue. The correlated coordination changes can be viewed from Fig. 15.5B to Fig. 15.5C. Two homopolar bonds, As–As and Se–Se, around over-coordinated sites have broken and a new As–Se bond has been created. This suggests that the anti bonding character of the LUMO drives the weaker homopolar bonds to break and form energetically favored heteropolar bonds. This homopolar-to-heteropolar transformation may correspond to the experimentally observed "optical annealing" processes [20, 53]. Associated with this rearrangement, energy is transferred efficiently from light (electrons) to lattice, yielding the rapid growth of temperature indicated in Fig. 15.6, while other following reactions seem to be a low-efficiency process for optical–vibrational energy transfer. This observation indicates that As-based defects play a significant role in the photon absorption in this binary glass. The other reaction is a bond switch process occuring near the end of ST stage as shown in Fig. 15.7A.

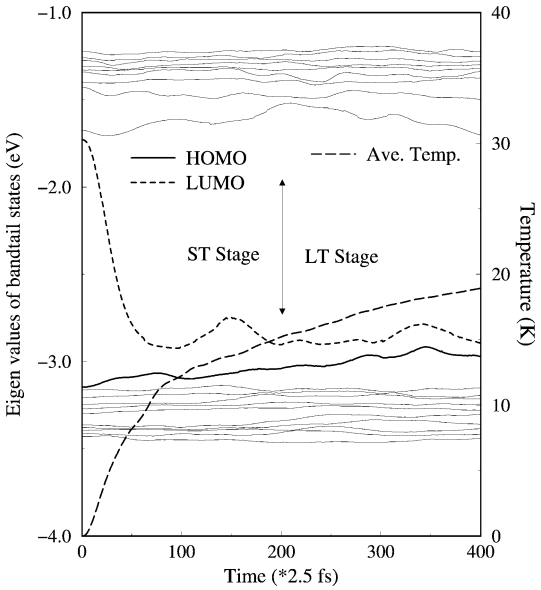

Figure 15.6: The first 1 ps evolution of eigenvalues of bandtail states and average temperature simulated for model of g-As_2Se_3 under illumination.

First an As–Se bond broke and an intimate pair (IP) was created. Subsequently As_2 went to combine with a nearby C_2, which was converted into a C_3 defect. This process indicates that light-induced unstable IPs are transformed into more stable random (not nearest neighbor or "intimate") pairs (RP) by bond switch processes. We found that bond switches are the main reaction in the relaxation of photoexcited states. The LT phase consists of a slow growth of the HOMO eigenvalue and concomitant atomic reactions which lag about 500 fs behind ST phase (see Fig. 15.6). The weaker response of the HOMO probably is due to smaller localization of the valence tail states compared with the conduction tail states, as we can infer from analysis of our computed eigenstates [54]. This also affects the time scale, since the local force changes are smaller for more extended states. Bond switch processes in LT phase are different from those at ST phase. An event is depicted in Fig. 15.7B. A bond around C_3 broke to create a P_2 defect. Subsequently the new As_2 defect combined with a nearby C_1 defect. Therefore, this bond switch process eliminates a random RP in as opposed to creating it at ST stage. There is also a bond switch process which does not eliminate RPs but changes the distribution of RPs that may be in the neighborhood of the original LUMO group. In other words, at LT stage, RPs have been rearranged in the adjoined structures to edge states. Combined with the bond switch at ST stage, Se-based defects are quite active during the relaxation of optically excited structure. It is worth pointing out that the rearrangement of RPs is coupled with the non-local vibration of the network, which is accumulated from ST stage. In ensuing simulation, bond switch processes seem to cease after LT phase. A saturation pattern occurs. A balance between network dynamics and photo-excitation develops after about 1.4 ps illumination. A regular non-local collective oscillation has been observed for later

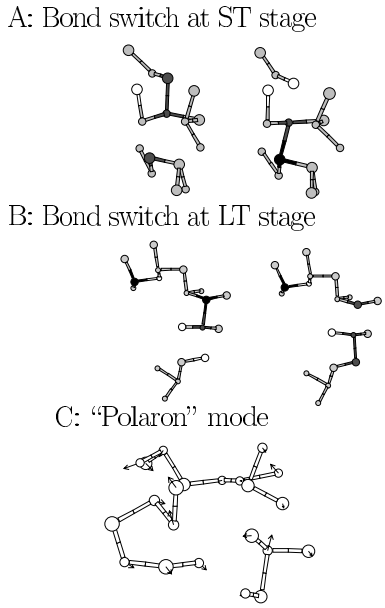

Figure 15.7: Two types of bond switch processes viewed from left to right. (A) ST stage: an intimate pair was created and transfered to an RP. Involved atoms belong to adjacent atomic group to the LUMO's structure as in the right part of Fig. 15.5C; (B) LT stage: an RP was eliminated. Atoms shown are those at the upper right corner of Fig. 15.5A. (C) Schematic of oscillating regions in the network. The arrow indicates the atomic motion with magnitude proportional to displacement.

times. This non-local collective motion involves an oscillation around the rearranged atomic groups of edge states and spans a long intermediate range (almost half of atoms in our model are involved). Figure 15.7C depicts a section of such oscillating regions featuring a periodic motion in the network. This may correspond to the self-trapped exciton effects proposed by Fritzsche [15]. In this model an intimate VAP constitutes a self-trapped exciton and can end up with random VAPs by further bond-switching reaction.

The above effects are certainly induced by light. If we let the model freely evolve for 1 ps without optical excitation, we observed no bond breaking, no bond switch, and no regular collective oscillation. We also noted that the electron–lattice energy transfer efficiency is very small in the whole process (Fig. 15.6).

Recently, Uchino and coworkers [55] have taken quite a different approach with quantum chemical calculations on small As–S clusters. The advantage of this approach is that the approximations for the electronic structure are probably more reliable than what we have presented. The difficulty is that the system sizes are small (typically 23 atoms, not counting passivating hydrogen), and also thermal simulation is not performed (local minima and transition paths are identified). It is encouraging that both calculations note the importance of mis-coordinated As to the photostructural process. As with our work, this research deserves further development.

15.3.4 Discussion

We have outlined a novel approach to modeling light-induced rearrangements in glasses. The method has some important advantages, mostly because it does not depend upon any *a priori* assumptions about the light-related changes in the glass. It can be implemented with structural models that *realistically mimic* the topology of a given network. Many features of the approach can be improved in systematic ways (with improved basis sets, better exchange-correlation functionals, etc.). The method also has weaknesses – probably most notably the use of Kohn–Sham orbitals as quasiparticle states (despite the apologies above). The scheme needs further development, both for theory and applications, but we believe that it is a promising tool in the arsenal of methods for understanding photo-induced changes in disordered systems.

Acknowledgments

We gratefully acknowledge collaboration and discussions with Ron Cappelletti, Himanshu Jain, Normand Mousseau, Peter Fedders, Punit Boolchand, Mike Thorpe, Otto Sankey, Alex Demkov, Serge Nakhmanson and Mark Cobb. This work was supported by the US National Science Foundation under grants DMR 0081006, 0074624 and 0205858.

References

[1] V. Poborchii, A. Kolobov and Ka. Tanaka, Appl. Phys. Lett. **74**, 215 (1999).
[2] H. Hisakuni and Ke. Tanaka, Science **270**, 974 (1995).
[3] Ke. Tanaka, Phys. Rev. B **57**, 5163 (1998); K. Tanaka and N. Yoshida, Solid. State Phenom. **55**, 153 (1997).
[4] See, for example, H. Fritzsche, Phys. Rev. B **52**, 15854 (1995).
[5] P. Krecmer, A.M. Moulin, R.J. Stephenson, T. Rayment, M.E. Welland and S.R. Elliott, Science **277**, 1799 (1997).
[6] P. Boolchand, private communication.
[7] M.F. Thorpe, J. Non-Cryst. Solids **57**, 355 (1983); J.C. Phillips, J. Non-Cryst. Solids **43**, 37 (1981).
[8] C.A. Spence and S.R. Elliott, Phys. Rev. B **39**, 5452 (1989).
[9] J. Mort, Physics Today **47**, 32 (1994).
[10] J. Rowlands and S. Kasap, Physics Today **50**, 24 (1997).
[11] S. Ohkubo, M. Okada, M. Murahata, T. Ide and T. Iwamaga, Jpn. J. Appl. Phys. **32**, 5230 (1993).
[12] See, for example, D.A. Turnbull and S.G. Bishop, J. Non-Cryst. Solids **223**, 105 (1998); S. Bishop, private communication.
[13] N.F. Mott and E.A. Davis, Electronic Processes in Non-crystalline Materials, Clarendon Press, Oxford University, 1978.
[14] R.A. Street and N.F. Mott, Phys. Rev. Lett. **35**, 1293 (1975).
[15] H. Fritzsche, Phil. Mag. B **68**, 561 (1993).
[16] M. Kastner, D. Adler and H. Fritzsche, Phys. Rev. Lett. **37**, 1504 (1976).

[17] D. Vanderbilt and J.D. Joannopolous, Phys. Rev. B **22**, 2927 (1980).

[18] S.R. Elliott, J. Non-Cryst. Sol **81**, 71 (1986).

[19] Ke. Tanaka, Curr. Opin. Solid State Mater. Sci. **1**, 567 (1996).

[20] K. Shimakawa, A. Kolobov and S.R. Elliott, Adv. Phys. **44**, 475 (1995).

[21] DA Drabold and Jun Li, Curr. Opin. Solid State Mater. Sci. **5**, 509 (2001).

[22] Jun Li and D.A. Drabold, Phys. Rev. B **61**, 11998 (2000).

[23] M. Cobb, D.A. Drabold and R.L. Cappelletti, Phys. Rev. B **54**, 12162 (1996).

[24] X. Zhang, D.A. Drabold, Phys. Rev. B **62**, 15695 (2000).

[25] X. Zhang, Dissertation, Ohio University (unpublished) 2001; http://www.phy.ohiou.edu/~drabold/xzhang.

[26] S. Nakhmanson, Dissertation, Ohio University (unpublished) 2001; http://www.phy.ohiou.edu/~drabold/serge.

[27] F. Wooten and D. Weaire, in: Solid State Physics, H. Ehrenreich, D. Turnbull, F. Seitz (Eds.), Academic Press, New York, 1987, p.40.

[28] G.T. Barkema and N. Mousseau, Phys. Rev. Lett. **77**, 4358 (1996); Comput. Sci. Eng. **1**, 74 (1999); N. Mousseau and G.T. Barkema, Phys. Rev. B **61**, 1898 (2000) and references therein.

[29] R.M. Martin, Electronic Structure of Matter, Cambridge University Press, Cambridge, 2003.

[30] M. Born and K. Huang, Dynamical Theory of Crystal Lattices, Clarendon Press, Oxford, 1954.

[31] D.M. Ceperley and G.J. Alder, Phys. Rev. Lett. **45**, 566 (1980).

[32] Note however that self-energy corrected LDA (GW quasiparticle calculations) have shown that the GW states are essentially identical with the Kohn–Sham orbitals for most cases. The significance of this is currently incompletely understood, but does offer additional rationale for the use of Kohn–Sham orbitals as quasiparticle states. See for example M.S. Hybertsen and S.G. Louie, Phys. Rev. B **34**, 5390 (1986).

[33] P. Ordejón, E. Artacho and J.M. Soler, Phys. Rev. B **53**, R10441 (1996); D. Sanchez-Portal, P. Ordejón, E. Artacho and J.M. Soler, Int. J. Quant. Chem. **65**, 453 (1997).

[34] O.F. Sankey and D.J. Niklewski, Phys. Rev. B **40**, 3979 (1989); A.A. Demkov, J. Ortega, O.F. Sankey and M. Grumbach, Phys. Rev. B **52**, 1618 (1995).

[35] G. Kresse and J. Hafner, Phys. Rev. B **47**, 558 (1993); Phys. Rev. B **49**, 14251(1994), J. Phys.: Condens. Matter **6**, 8245 (1994); G. Kresse and J. Futhmuller, Comput. Mater. Sci. **6**, 15 (1996); Phys. Rev. B **55**, 11169 (1996).

[36] V. Milman, B. Winkler, J.A. White, C.J. Pickard, M.C. Payne, E.V. Akhmatskaya, and R.H. Nobes, J. Quant. Chem. **77**, 895 (2000).

[37] R. Car and M. Parrinello, Phys. Rev. Lett. **55**, 2471 (1985).

[38] M. Bockstedte, A. Kley, J. Neugebauer and M. Scheffler, Comput. Phys. Commun. **107**, 187 (1997).

[39] P. Yu and M. Cardona, Fundamentals of Semiconductors, Springer, Berlin, 1996.

[40] H. Fritzsche, Annu. Rev. Mater. Res. **31**, 47 (2001).

[41] P.A. Fedders, Y. Fu and D.A. Drabold, Phys. Rev. Lett. **68**, 1888 (1992).

[42] D.A. Drabold, S. Nakhmanson and X. Zhang, In Properties and Applications of Amorphous Materials, M.F. Thorpe and L. Tichy (Eds.), NATO Science Series, II. Mathematics, Physics and Chemistry, Vol. 9, Kluwer, Dordrecht, 2001, p. 221.

[43] D.A. Drabold, P.A. Fedders, O.F. Sankey and J.D. Dow, Phys. Rev. B **42**, 5135 (1990).

[44] R.E. Norberg, P.A. Fedders, J. Bodart, R. Carey, Y.W. Kim, W. Paul and W. Turner, Mats. Res. Soc. Conf. Proc. **219**, 223 (1991).

[45] X. Zhang and D.A. Drabold, J. Non-Cryst. Solids **241**, 195 (1998).

[46] X. Zhang and D.A. Drabold, Phys. Rev. Lett. **83**, 5042 (1999).

[47] A.V. Kolobov, H. Oyanagi, Ka. Tanaka and Ke. Tanaka, Phys. Rev. B **55**, 726 (1997).

[48] X. Zhang and D.A. Drabold, Int. J. Mod. Phys. B. **24–25**, 3190 (2001).

[49] A.V. Kolobov, M. Kondo, H. Oyanagi, A. Matsuda and K. Tanaka, Phys. Rev. B **58**, 12004 (1998).

[50] A. Szabo and N.S. Ostlund, Modern Quantum Chemistry, McGraw-Hill, New York, 1989, p.151.

[51] Jun Li, D.A. Drabold, Phys. Rev. Lett. **85**, 2785 (2000).

[52] K. Antoine, J. Li, D.A. Drabold, H. Jain, M. Vlcek and A.C. Miller, J. Non-Cryst. Solids, in press.

[53] For example: A.J. Lowe, S.R. Elliott, and G.N. Greaves, Phil. Mag. B **54**, 483 (1986).

[54] A similar asymmetry in localization of valence and conduction tail states was seen in a-Si. See, for example, D.A. Drabold and J. Li, Mater. Res. Soc. Conf. Proc. **715**, A14.1 (2002) and references therein. The reason for this asymmetry is not clear, but appears to be a consistent feature in simulations of a-Si and many chalcogenide glasses.

[55] T. Uchino, D.C. Clary and S.R. Elliott, Phys. Rev. B **65**, 174204 (2002).

16 Soft Atomic Modes and Negative-U Centers as Sources of Metastable Transformations in the Structure and Dynamics of Glasses

Michael I. Klinger

The recent theory of the photostructural changes (PSC) in glassy semiconductors (GS) is surveyed. It appears to be the first quantum-mechanical theory of PSC actually based on the experimental observation that the PSC are found only in GS in which the basic localized charge carriers interacting with gap light are the well-known negative-U centers. The theory is able to answer the basic questions concerning the origin and features of the PSC. Explicit expressions for the transition probabilities in the kinetics of the PSC can be obtained. Metastable transformations in the universal dynamic anomalies, related to the PSC, in GS may be predicted, in accordance with some recently observed effects (in the tunneling dynamics) in GS. The most essential test of the theory is to experimentally verify the predicted suppression of the PSC in GS under moderately high pressures.

16.1 Introduction

As is observed in many experiments [1, 2], light of frequency comparable to the optical gap, $\omega \approx E_{opt}/\hbar$, can produce reversible metastable, sometimes long-lived, transformations in the structure, called "photostructural changes" (PSC), in glassy semiconductors (GS), particularly in chalcogenide glasses with the mobility-gap width $E_g \approx 1 - 3$ eV and $E_{opt} \simeq E_g$. In fact, EXAFS and Raman scattering experiments show that substantial changes occur in the medium-range order (MRO) structures forming such glasses [3], as well as in their short-range order [4]. Related considerable changes are produced in a variety of macroscopic physical and chemical properties of these glasses. The most outstanding effect appears to be the so-called "photodarkening" effect, a gap-light induced decrease ΔE_{opt} of the original optical gap width E_{opt} by up to around 10%, not observed in crystalline counterparts. Interesting anisotropic effects, dichroism and birefringence, associated with the PSC have also been revealed recently [1]. The nature of the PSC was one of challenging problems in the physics of GS since they were discovered about three decades ago. A number of models, involving different assumptions concerning the microscopic mechanisms, have been proposed to account in general for photo-induced metastable effects in semiconductors and insulators, in which the metastability was associated with generation and decay of electronic excitations (see, e.g., review [5]). However, as noted in some papers (see, e.g., [1], p. 481), such models, based on the assumption that adiabatic potentials of the local atomic configuration in an important atomic motion mode were different in its ground and optically excited electron states, were

merely plausible suggestions which accorded with known features of the effect. In fact, even for crystalline materials such models have been put on a proper theoretical footing only for defect generation in alkali metal halides and crystalline SiO_2. In other cases, the important atomic mode, as well as the parameters of the local atomic configuration, actually were not well defined. For the PSC [1, 2, 6], such models postulated that the adiabatic potential in its ground and excited electron states consisted of a lower branch as a double-well potential and an upper branch as a single-well potential, separated by a considerable split energy Δ with $\Delta/\hbar \gg \omega_v$, the vibration frequency. The process of creation and destruction of metastable defects was supposed to be due to competing light-induced Franck–Condon transitions from the lower branch to the upper one, and standard activated hopping transitions between the double-well potential minima. A standard kinetic equation for the metastable defects concentration c_d was analyzed and some features of its dependence on ω and T were revealed [1]. Experimental studies (see, e.g., [7]) of the photodarkening value ΔE_{opt}, assumed proportional to c_d, have shown qualitative agreement of some observed features with the expected ones. In spite of the stimulating role of the phenomenological models for experimental studies of the PSC and their interpretation, basic questions remained unanswered: (1) Why do photostructural changes occur only in GS? (2) What is the criterion for the existence of the postulated adiabatic potentials of a double-well potential shape, and is it realized in GS? (3) What are the relations between the characteristic energies of the PSC and $E_{opt} \simeq E_g$? (4) What are the expressions for the transition probabilities in the kinetics of the PSC?

These questions can be answered in the recent consistent theory [8] (see also [9]), taking into account that PSC are found only in GS in which basic localized charge carriers interacting with the gap light are negative-U centers. The latter, of the kind postulated by Anderson [10], have recently been theoretically identified [11] as electron (or hole) singlet pairs strongly self-trapped due to their interaction with nearby localized atomic soft modes. The soft modes were earlier theoretically found to contribute substantially, in general, to well-known low-temperature (-energy) dynamic anomalies of glasses [12]. As was shown, most soft modes, each of an average effective mass M_{sm} for a typical number of involved atoms, are quasi-harmonic ones. Their random spring constants k (measured below in the units of $k_0 \approx 10$ eV/ Å^2) are considerably smaller than the value $k_{ac} \equiv k_{ac}/k_0 \sim 1$ typical of the vast majority of atoms determining the standard acoustic dynamics.

Recently, a microscopic model for photo-induced metastability in amorphous As_2S_3 has been presented [13], by using clusters of atoms that model the local structure of the material. It seems that this structural model and the above-mentioned theoretical model of the PSC in GS could be agreed with each other as the latter was essentially related to negative-U centers [8] while the former was associated with the Street–Mott valence-alternating pairs of oppositely charged coordination defects which, in some sense, might be treated also as negative-U centers (see, e.g., [14]).

In what follows, Section 16.2 briefly describes the theory of the soft modes and their dynamics, the basic concepts, results and problems, and Section 16.3 describes the nature and properties of the negative-U centers as basic localized charge carriers with their ground-states in the mobility-gap of the electron spectrum of GS. Section 16.4 reports on the above-mentioned recent theory of the PSC related to the appropriate excited states of the negative-U centers in GS while Section 16.5 discusses the expected metastable transformations in the universal dynamic anomalies, correlated with the PSC, actually in the widely discussed tunneling

(non-vibrational) dynamics for very low excitation energies and the vibrational dynamics for moderately low energies. Section 16.6 discusses a prediction on the suppression of the soft-mode related metastable transformations under moderately high pressures. Some conclusions are presented in Section 16.7.

16.2 The Soft-Mode Dynamics of Glasses

In this section, a brief discussion is given of the role of the soft (non-acoustic) atomic motion modes and their excitations in the experimentally discovered [15] and widely studied [16] universal anomalies in glass atomic dynamics related to excitation energies $\varepsilon = \hbar\omega$ much lower than the Debye energy $\hbar\omega_D$, including some recent results. The concept of localized soft atomic modes was introduced in the theory which was able to characterize (partly at least) the dynamic anomalies in glasses [17,18], below referred to as the soft-mode dynamics theory (SMD), originally named "soft configuration model" [12] or "soft potential model" [19].

The universal dynamic anomalies occur in thermal, acoustic, dielectric properties and inelastic (Raman, neutron, X-ray) scattering spectra of glasses for low $\varepsilon \ll \hbar\omega_D$, $0 < \varepsilon \lesssim \varepsilon_b \approx 7.5$ meV, e.g., low temperatures $T \ll T_D \equiv \hbar\omega_D/k$, $0 \le T \lesssim T_b \approx 75$ K, or frequencies $\omega \ll \omega_D$, $0 < \nu \equiv \omega/2\pi \lesssim \nu_b \approx 1.5$ THz [16]. For very low $\varepsilon \lesssim \varepsilon_a \approx 0.1$ meV, i.e. $T \lesssim T_a \approx 1$ K and $\nu \lesssim \nu_a \approx 10^{-2}$ THz, the most striking anomalies appear to be the anomalous temperature dependence of the specific heat $C_g(T) \propto T^{\alpha}$, $\alpha \simeq 1$ (instead of the Debye T^3 dependence) and thermal conductivity $\chi_g(T) \propto T^{\sigma}$, $\sigma \simeq 2$. For moderately-low ε, $\varepsilon_a < \varepsilon \lesssim \varepsilon_b$, i.e., $T_a < T \lesssim T_b$ and $\nu_a < \nu \lesssim \nu_b$, the most impressive anomalies seem to be the THz frequency dynamics often referred to as high-frequency dynamics (HFD) and the correlated broad maximum ("hump") of $C_g(T)/T^3$ and "plateau" of $\chi_g(T)$ ($\approx constant$) around $T_M \approx h\nu_{BP}/4k_B \approx$ 10–20 K. Two types of glasses occur in experiments, in which the HFD either (i) reduces to the boson peak, a rather broad maximum of width $\Delta\nu \lesssim \nu_{BP}/3$ around $\nu_{BP} \approx 1$ THz in the vibrational density of states [20] in inelastic scattering spectra observed in B_2O_3 and some related glasses [20]; or (ii) the HFD involves both the boson peak and, above it, the accompanying high-frequency sound observed in SiO_2, CKN and some other glasses [21–23].

The BP intensity $I_{BP}(\omega \approx \omega_{BP})$, as well as the related dynamic structure factor, varies with increasing T as the Bose–Einstein distribution for appropriate harmonic vibrational excitations. The discovered anomalies suggested an existence of extra types of low-energy excitations in atomic dynamics of glasses, compared with that of respective crystals. Two types of such extra, non-Debye, excitations may exist with eigenstates of different nature. One type is acoustic excitations of high enough $\omega \approx \omega_{IR}^{(el)}$ around the Ioffe–Regel crossover [24] from weak elastic scattering of acoustic phonons by static-disorder induced structure fluctuations with a long mean-free-path $l_{ac}^{(el)}(\omega) \gg \lambda_{ac}(\omega) \gg a_1$ for low $\omega \ll \omega_{IR}^{(el)}$ to strong scattering with a short $l_{ac}^{(el)}(\omega) \lesssim \lambda_{ac}(\omega)$ for higher ω, $\omega_{IR}^{(el)} \lesssim \omega \ll \omega_D$; the phonon wavelength $\lambda_{ac}(\omega) \simeq 2\pi s_0/\omega$. s_0 is a typical sound velocity. The characteristic Ioffe–Regel crossover frequency $\omega_{IR}^{(el)}$ is defined by the equation $l_{ac}^{(el)}(\omega_{IR}^{(el)}) = \lambda_{ac}(\omega_{IR}^{(el)})$; a_1 is the mean atomic spacing. These excitations seem to predominate for glasses of the type (i); see, e.g., [25–28], and references therein. The acoustic excitations, elastically interacting with the static fluc-

tuations, can contribute to the atomic low-energy dynamics of glasses. In what follows, this contribution is referred to as "acoustic dynamics". Another mechanism for the HFD seems to be decisive for glasses of the type (ii), in which both the boson peak and the accompanying high frequency sound, essentially due to hybridization of acoustic excitations with some type of non-localized excitations of which the nature does not seem to be exactly identified [29–31] or with non-acoustic, non-localized but non-propagating, excitations identified [32] as the above-mentioned atomic soft-mode excitations (Section 16.5) in local atomic soft configurations which are characterized below.

In fact, at present some evidence exists in favor of an insufficiency of the acoustic dynamics, including excitations associated with the "elastic" Ioffe–Regel crossover, for explaining the universal dynamic anomalies of glasses. Indeed, a generally accepted fact is that the acoustic phonons are actually unimportant for very low $\varepsilon \lesssim \varepsilon_a$ for which the basic contribution to the dynamics is due to non-acoustic excitations which are atomic tunneling states in effective local random double-well potentials introduced by postulates in the standard tunneling model (see, e.g., [16]). On the other hand, there is experimental evidence that the tunneling dynamics is not essential for higher ε, $\varepsilon_a < \varepsilon \lesssim \varepsilon_b$, and thus extra, non-Debye, types of vibrational excitations, including the acoustic excitations in the "elastic" Ioffe–Regel crossover regime, can be responsible for the dynamic anomalies of glasses in this energy range. At the same time, it was shown in the SMD [12] that the tunneling states actually constitute only a part of the soft-mode excitations, and so the SMD is an extension of standard tunneling model to higher excitation energies $\varepsilon, \varepsilon_a < \varepsilon \lesssim \varepsilon_b$. The above-mentioned evidence in favor of an insufficiency of the acoustic dynamics is that no dynamic anomalies due to tunneling states are experimentally observed for very low $T \lesssim T_a$ in cases where no boson peak is observed for moderately low energies (see, e.g., [33]). This suggests that the contribution of the soft modes to the dynamic anomalies may be essential not only at very low $\varepsilon \lesssim \varepsilon_a$ where those are decisive, but also at the moderately low ε.

The basic concept of the SMD [12] was that two types of motions and related excitations, acoustic and soft-mode ones, co-exist and interact with each other, contributing to the anomalies in the low-energy dynamics of glasses. The main idea was that big, though rare, strongly anisotropic fluctuations of the local atomic configuration parameters (bond angles, dihedral angles, etc.) from the average values in the basic medium-range-order structures [1] unavoidably occur in a glass, as a topologically disordered solid, and give rise to the soft modes. The typical size of the soft modes, i.e., of the (quasi-) 1D fluctuations, is $L_{sm} \approx (2-3)a_1 \sim L_{MRO}$; the latter denotes the length scale of the above-mentioned basic medium-range-order structures forming a glass [34], while a_1 is the mean atomic separation. In this connection, both non-acoustic soft-mode vibrational excitations and non-vibrational, tunneling states excitations were revealed in the soft-mode dynamics.

Actually, in the anomalous *strongly anisotropic* local configuration the motion of relatively small groups of, say, of 5–10 atoms along the related distinguished mode x can just take place in an effective local potential $V_{sm}(x)$ with a small value of its spring parameter $\mid k(x) \mid \equiv \mid d^2V_{sm}(x)/dx^2 \mid \ll k_0$ and spring constant $k \equiv k(x_{\min}) \ll k_0$. Here, $x_{\min}$ (or $x_{\max}$) marks the potential minimum (or maximum) while $k_0 \approx 10 - 20$ eV/Å^2 is the value typical of the vast majority of atoms participating in the acoustic motions; both $k(x) > 0$, e.g., $k(x_{\min}) > 0$, and $k(x) < 0$, e.g., $k(x_{\max}) < 0$ for a double-well potential, may occur. Local configurations with $\mid k(x) \mid \ll k_0$, e.g., $k \ll k_0$, are rather labile, easily rearrangeable with

an anomalously high generalized susceptibility to distortions, $\chi = k^{-1} \gg \chi_0 = k_0^{-1}$ and related large displacement $\Delta x \approx (0.1 - 1.0)a_0 \gg (\Delta x)_0$; the atomic length $a_0 = 1$ Å$\equiv 1$ is the length unity in what follows and $(\Delta x)_0$ is the typical atomic displacement. Such a local atomic configuration and the related (quasi-)1D mode have been referred to as soft ones, and the local potential was expected, in general, to be anharmonic. In fact, it was shown that the soft modes were characterized by small random spring constants, $0 < k \ll k_0$, in a rather broad tail of the probability distribution density $P(k)$, far below its highest maximum for $k = k_0$. The theory of the soft modes and related excitations reveals a crossover in a relatively narrow energy range, $\varepsilon_a < \varepsilon < w$, from tunneling states in double-well potentials at $\varepsilon \lesssim \varepsilon_a$ to vibrational excitations (and classical overbarrier relaxations) at $w < \varepsilon \lesssim \varepsilon_b$; w is the revealed new characteristic energy scale of the SMD (see below). The basic relation derived in this theory characterizes the typical, i.e., most probable, anharmonic potential energy $V_{sm}(x)$ in the soft mode, which can be expressed, e.g., as follows [12]:

$$V_{sm}(x) \cong w(\eta x^2 + \xi x^3 + \lambda x^4), \tag{16.1}$$

instead of a standard harmonic single-well potential $V_0(x) \cong wx^2$. Here η, ξ, λ and the soft-mode displacement x ($\equiv u/a_0$) are dimensionless quantities. $\lambda = 1$, and $w = A\eta_L^2 \approx 1$ meV at $A = k_0 a_0^2/2 \approx 10$ eV; $\eta_L = (\varepsilon_0/A)^{1/3} \approx 10^{-2}$ is a small "non-adiabaticity" parameter, a measure of the effective atomic soft-mode mass M_{sm}, and $\varepsilon_0 = \hbar^2/M_{sm}a_0^2$. The unusually small characteristic soft-mode energy scale w ($\ll \hbar\omega_D \sim A\eta_L^{3/2}$), actually corresponds to the least possible (anharmonic) vibration energy; μ characterizes an effective quasi-molecule moving in a soft mode and typically comprising several atoms. By definition of the soft modes, basic random parameters of "softness", $\eta \lessgtr 0$, and asymmetry, $\xi \lessgtr 0$, belong to the tail of a characteristic broad probability distribution density $F(\eta, \xi)$, far below its highest maximum at $\eta = \eta_0 \simeq 1$ corresponding to $k = k_0 \equiv k(\eta_0, 0)$ for the vast majority of atoms with the noted standard single-well potentials. In fact, the tail comprises η and ξ, small in magnitude, actually at $|\eta| \lesssim \eta_{sm} \approx 0.1 \ll \eta_0 \simeq 1$ and $\xi^2 \lesssim \eta_{sm}$, corresponding to the small spring constants, $k \ll k_0$. As noted above, the soft-mode potentials occur around a boundary between *harmonically stable* ($\eta \gg \eta_L$) and *unstable* ($\eta < \eta_L$) single-well potentials which include those with very small positive values of the "softness" parameter η, $0 \lesssim \eta \lesssim \eta_L$, or double-well potentials with alternative values of η, e.g., $\eta < 0$. The soft-mode excitations were identified as the low-energy excited eigenstates ψ_{exc}, $H\ \psi_{exc} = \varepsilon_{exc}(\eta, \xi)\psi_{exc}$ of the Hamiltonian $H = -\varepsilon_0\ d^2/dx^2 + V_{sm}(x)$, with the excitation eigenenergies $\varepsilon \equiv \hbar\omega = \varepsilon_{exc}(\eta, \xi)$ at $\varepsilon \lesssim \varepsilon_b \approx 7.5\ w$. Although the soft modes in a glass may be considered as localized, their vibrational and non-vibrational (tunneling states) excitations, in principle, are quasi-localized in the above-mentioned relatively small groups of, say, of 5–10 atoms, as also confirmed by simulations. In other words, the excitation eigenstates are non-localized ones but not propagating waves, in the same sense as resonant, or quasi-local, local vibrations related to some kinds of defects in crystals are: such an excitation decays with its lifetime into co-existing acoustic phonons of close energies, due to their interactions $\delta V_{sm}(x, \mathbf{e})$, but the lifetime is still exceeding, though comparable to, the excitation frequency. In this connection, as usual, the excitations are well defined for such energy eigenfrequencies ω ($< \omega_{IR}^{(in)}$), for which their width $\gamma(\omega) < \omega$, i.e., not too close to the Ioffe–Regel crossover from weak to strong inelastic scattering of acoustic excitations by soft-mode ones at $\gamma(\omega_{IR}^{(in)}) = \omega_{IR}^{(in)}$. The

Hamiltonian $\delta V(x, \mathbf{e})$ for the interaction of a soft mode (its excitations) with acoustic modes (phonons) is so far approximately described in the simplest scalar form, as $V_{sm-ac}(x) \simeq \beta x \mathbf{e}$, where β is the coupling-energy parameter while $\mathbf{e}$ is the "small" acoustic strain tensor in the soft-mode location in the system. In general, both M_{sm} and $\mid \beta \mid$ are random parameters subject to distribution densities which are rather narrow so that their mean values may be used.

The soft-mode dynamics in glasses is actually characterized by the excitation spectra, $\varepsilon_{sm}(\eta, \xi)$, and by the transition (scattering) probabilities associated with the interaction Hamiltonian, as well as by the (single-) excitation density of states, $n_{sm}(\varepsilon)$, and the related atomic soft-mode concentration, c_{sm}. It has to be added that the vast majority of the soft-mode excitations are associated with (quasi-) harmonic vibrations, of which the low-temperature atomic concentration $c_{sm}^{(qh)} \simeq c_{sm}$ is orders of magnitude higher than the concentration $c_{sm}^{(TS)}$ of the non-vibrational atomic-tunneling-states excitations only in double-well potentials, with the typical very small value of the ratio $c_{sm}^{(TS)}/c_{sm}^{(qh)} \simeq c_{sm}^{(TS)}/c_{sm} \approx 10^{-3}$–$10^{-4}$. At ambient pressure and low temperatures ($p = 0$, $T/T_g \ll 1$), the low-energy anomalies in glass dynamics can approximately be interpreted qualitatively and in scale, to a considerable extent at least, with the concentration $c_{sm}^0 = c_{sm}(p = 0) \approx (1\text{–}5) \times 10^{-2}$.

However, c_{sm}^0 should be much lower, $c_{sm}^0 \ll 10^{-2}$, for "non-glassy" amorphous materials in which no pronounced low-energy dynamic anomalies are observed (e.g., in a-Si or amorphous water) (see [35]).

16.3 Negative-U Centers in Glassy Semiconductors

A fundamental manifestation of the soft modes appears to be an occurrence of negative-U centers which have been postulated to be the occupied localized states in the mobility gap of GS, largely of chalcogenide glasses (g-As_2S_3, g-GeS_2, etc.) with a typical mobility-gap width $E_g \approx 1\text{–}3eV$. A negative-U state was originally postulated by Anderson [10] to be a singlet ("diamagnetic") electron pair with energy (per particle) $E < E_F$ or hole pair with $E > E_F$, characterized by a negative correlation energy U of value $|U| \simeq E_g/2$ (E_F is the Fermi level located around the middle of the gap). This postulate and some theoretical conclusions have been applied for interpreting a large variety of experimental data for a series of anomalous electronic properties of GS: absence of a substantial paramagnetism and non-doping (pinning of the Fermi level), as well as peculiar ac conductivity and some photo-induced effects.

The quantum-mechanical theory of the negative-U states (centers) presented by Klinger and Taraskin [11] has shown that the states could be formed due to a non-polaronic self-trapping of an electron (hole) singlet pair in an atomic soft mode of a GS. The actual mobility-gap states are found in the theory to be the self-trapped pair states with characteristic self-trapping energies $W_2(< 0)$ of a very large value:

$$W_2 \simeq -2Q^2/k_{ef} \simeq -E_g, \text{ at } k_{ef} \simeq k_g \simeq Q^2/2E_g, \text{ and } |W_2| \simeq E_g \gg |W_{SP}|, \quad (16.2)$$

where $W_{SP} \equiv W_1^{(SP)} \simeq Q^2/2k_0$ is a self-trapping energy for a single standard small polaron, in a vibration mode with a typical spring constant, $k \approx k_0$, and Q is a typical electron-vibration coupling energy, $Q \approx 3eV$, for a GS. A standard small polaron is formed due

to a single-band self-trapping with only the parent band states (e.g., conduction-band states, for electrons) involved, at $|W_{SP}| \ll E_g$. The inequality $|W_2| \gg |W_{SP}|$ in Eq. (16.2) for negative-U centers holds just because of small spring constants $k_{ef} \simeq k_g \ll k_0$ for essential soft modes. Therefore, the negative-U state in a GS is formed, in the theory in question, due to a non-polaronic, two-band self-trapping process involving the parent and non-parent (e.g., valence) band states. This follows from direct calculations of the model Hamiltonian, $\hat{H}(x) = \hat{H}_{sm}(x) + \hat{H}_{HA} + \hat{H}_{el-sm}(x)$. The latter takes into account the soft-mode dynamics Hamiltonian, $\hat{H}_{sm}(x) = -(\hbar^2/2\mu)(d^2/dx^2) + V_{sm}(x)$ (with μ being the soft-mode effective mass), the well-known Hamiltonian of Haldane and Anderson, $\hat{H}_{HA}$, characterizing the hybridization of the "bare" electron parent band states ψ_i with each other (in the absence of atomic vibrations), and the Hamiltonian, $\hat{H}_{el-sm}(x)$ for the electron–soft mode-vibration interaction.

Moreover, Eq. (16.2) can be interpreted as due to the fact that the two-band pair self-trapping is related to the "bare" electron energy level (ε_0) lowering in the mobility gap and its hybridization with the "bare" non-parent band states ψ_i. The hybridization becomes decisive at the non-parent mobility edge (e.g., E_v) and creates a renormalized single-electron state $\Psi_{0\sigma}$ of a size $R_0 \gtrsim a_1$, with an energy level $E_{0\sigma}$,

$$\Psi_{0\sigma} = C_{00}^{(0)}\psi_0 + \sum_i C_{0i}^{(\sigma)}\psi_i \qquad \text{and} \qquad E_{0\sigma} \geq \varepsilon_0, \tag{16.3}$$

where $C_{00}^{(\sigma)}$ and $C_{0i}^{(\sigma)}$ determine the contributions of the states ψ_0 and ψ_i, respectively, and σ standing for spin projections ($\sigma = \pm\frac{1}{2}$). Since soft modes are characterized by small spring constants $k \sim 0.1k_0$, the self-trapping energy $|W_2|$ could exceed E_g, at realistic $E_g/|W_{sp}| \approx 10$. Then, the renormalized energy level $E_{0\sigma}$ is repelling off the mobility edge E_v due to the strong hybridization of states, so that indeed $|W_2| \simeq E_c - E_v = E_g$ (similarly for hole self-trapping). Thereby, essential soft modes are marked by a typical small spring constant $k_g \simeq Q^2/2E_g \ll k_0$.

It is also established in the theory that, as well as in the small-polaron theory, $W_2 = U - U_H + 2W_1$ and, moreover, $2|W_1| \approx |W_2|/2 \simeq E_g/2$ for the essential $k_{ef} \simeq k_g \ll k_0$ and the Hubbard correlation energy $U_H \ll E_g$. Thereby, the typical value of the negative correlation energy is

$$|U| \approx |W_2/2 \simeq E_g/2, \tag{16.4}$$

just as it was additionally postulated earlier [14] for fitting the appropriate experimental data. The theory under discussion and its basic Eqs. (16.2) and (16.4) allow us to characterize the spectral and thermodynamic properties of an SG as a semiconductor with mobility-gap negative-U states.

Excited electron states of the negative-U centers have been suggested in the theory in question (see Section 16.4) to determine non-equilibrium processes such as photo-induced phenomena in GS illuminated by gap-light of frequency $\omega \approx E_g/\hbar$, including the photo-induced structural changes (PSC) discovered long ago and studied in numerous experimental works and theoretical models.

16.4 Photo-Induced Metastable Transformations in Structure (Photostructural Changes)

Recently a consistent quantum-mechanical theory of the PSC has been established, in which the latter were identified with gap-light (radiation) generated structural defects associated with appropriate excited states of the negative-U centers and the above-mentioned (Section 16.1) basic questions on the origin and properties of the PSC in GS can be answered (see below). In particular, the answer to the widely discussed question of why the changes occur only in GS is that the negative-U centers in question are the basic localized charge carriers interacting with gap light only in these materials. In other words, the present theory takes into account that the PSC are found only in GS in which the basic localized charge carriers interacting with gap light are the negative-U centers [8, 9].

16.4.1 Photostructural Changes as Metastable "Defects" Due to Excited Negative-U Centers

The basic idea of the theory under discussion is that a high–energy excited state of a negative-U center generated by gap light is formed from its ground-state by a large change Δx_{exc} in the atomic soft mode displacement x, with $|\Delta x_{exc}| \sim 10x_0$ and x_0 being a typical amplitude of zero-point vibrations, e.g., $x_0 \approx 0.03$. Thereby, under certain realistic conditions (see below) metastable "defects" as excited states of the negative-U centers can be created in the original glass structure. As noted above, the displacement x, as well as a_1 and other lengths, are measured below in the atomic length units of a_0 = 1 Å, e.g., $a_1 \approx$ 2–3. In fact, metastability of the high–energy excitations is a general property of electron excitations strongly related to the soft modes, which is associated with the softness (relative ease of rearrangement) of the local atomic configuration and with the resulting barriers in the lower branch of the adiabatic potential for a negative-U center (see Fig. 16.1 and [12](a)). The most important result of the theory of the negative-U centers [11], which has to be accounted for here, is that the ground-state of such a negative-U center is characterized by a large change in soft-mode displacement, $|\Delta x_{ST}| \sim 10x_0$, with $\Delta x_{ST} \approx -\Delta x_{exc}$, and by a self-trapping energy W_2 (< 0) with a large magnitude, $|W_2| \simeq E_g$ (Eq. (16.2)).

The localized system that we consider is a singlet electron pair (with spatial coordinates $\mathbf{r}_1, \mathbf{r}_2$) interacting with a soft mode x to give rise to a negative-U center in its ground-state, with the wavefunction $\Psi_2^{(0)}(\mathbf{r}_1, \mathbf{r}_2)$, or in the excited state, with the wavefunction $\Psi_2^{(1)}(\mathbf{r}_1, \mathbf{r}_2)$. The Hamiltonian of our system $H_{2e,sm}$ can be written in the form [8, 9]

$$H_{2e,sm}(\mathbf{r}_1, \mathbf{r}_2; x) = H_{2e}(\mathbf{r}_1, \mathbf{r}_2) + H_{sm}(x) + H_{int}(\mathbf{r}_1, \mathbf{r}_2; x), \tag{16.5}$$

where $H_{2e}(\mathbf{r}_1, \mathbf{r}_2) = T_{2e} + V_{ee}$ is a standard Hamiltonian of a "fast" subsystem (a singlet pair of electrons of effective mass m), actually with a predominant kinetic energy term, and $H_{sm}(x) = T_{sm} + V_{sm}(x)$ is that of a "slow" soft-mode sub-system with a harmonic potential energy for most of the soft modes, $V_{sm}(x) \simeq kx^2/2$ at $0 < k \lesssim 0.1k_{ac}$, and T_{sm} is a kinetic energy determining a small non-adiabatic perturbation to the applied adiabatic approximation, at a typical small parameter $\eta \equiv (m/M_{sm})^{1/2} \sim 10^{-3}$. The interaction H_{int} between the electron pair and a finite soft mode displacement x in a basically covalent GS can be regarded

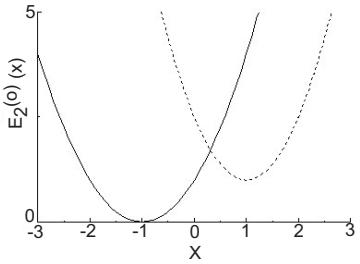

Figure 16.1: The "defect" adiabatic potential $E_2^{(\alpha)}(x)$ (in arbitrary units; $\alpha = 0, 1$) as a function of the soft mode displacement x. The continuous curve is for the ground-state, with its minimum at $x_2^{(0)} = -1$, and the broken curve is for an excited state, with its minimum at $x_2^{(1)} = 1$.

as a short-range one with the length scale $L_0 \approx a_1 \approx 2 - 3$, and be approximated, in general, in an additive form as

$$H_{int}(\mathbf{r}_1, \mathbf{r}_2; x) \simeq \sum_{j=1,2} \delta\Phi(\mathbf{r}_j; x), \tag{16.6}$$

where

$$\delta\Phi(\mathbf{r}; x) \simeq [D_1(\Theta)x + 0.5D_2(\Theta)x^2] \exp(-r/L_0).$$

with the electron radius-vector presented as $r \equiv (r, \Theta, \varphi)$. The parameter $D_1 \approx C_0 L_0^{-1}$, with C_0 being the interaction energy scale. On the other hand, $D_2 \approx C_0 L_0^{-2}$ gives rise to an extra contribution $\Delta k \propto D_2$ to the soft mode spring constant k, $k \longrightarrow k_{ef} = k + \Delta k$, where k_{ef} is the renormalized, effective, spring constant. In other words, a ground-state negative-U center may be considered as an extra weak effective covalent bond ($k_{ef} \ll k_0$) which is also characterized by a negative pair correlation energy of the same order of magnitude. Such weak effective bonds may relatively easily rearrange and thus favor either a decrease or an increase of the related local volume. Then, a metastable transformation may occur from a double-well potential to a single-well potential or vice versa, depending on the value of the light frequency in the gap light range (see [11](a)).

For the Hamiltonian $H_{2e,sm}$ of the system in question, the adiabatic potentials appear to be different for the ground and excited states of a negative-U center, of which the excited state corresponds to a metastable "defect" only when its adiabatic potential and that of the ground-state cross each other in accord with a relevant criterion discussed below. Two limit cases can be distinguished in Eq. (16.6): (I) both D_1 and D_2 do not depend on the angle Θ; (II) the angle dependence of $\delta\Phi(\mathbf{r}; x)$ is most pronounced. The limit case (I) appears to be of the simplest possible form $H_{int}(\mathbf{r}_1, \mathbf{r}_2; x)$ which is mainly explored below, giving rise to a small splitting of the crossing adiabatic potentials from each other. Some brief comments will only be addressed concerning the other limit case which rather corresponds to a large splitting of the crossing adiabatic potentials. As is common, it is assumed that the interaction energy C_0 is of the scale of a typical atomic elasticity energy measured below in the energy units of

$\varepsilon_0 = 1$ eV, $|C_0| \sim 10$. Moreover, the distributions of the random C_0 and L_0 are assumed such (e.g., sufficiently narrow) that their most probable values are close to the average values, so that the latter can be used for estimates.

As seen below, the resulting adiabatic potentials $E_2(x)$ of the soft mode may have a structure which is similar to that of a double-well potential with a deeper well, $E_2^{(0)}(x)$, related to a ground-state wavefunction $\Psi_2^{(0)}(\mathbf{r}_1, \mathbf{r}_2)$ of the negative-U center and a shallower one, $E_2^{(1)}(x)$, associated with a relevant, gap-light generated excited state wavefunction $\Psi_2^{(1)}(\mathbf{r}_1, \mathbf{r}_2)$ of the negative-U center. In order to describe the adiabatic potentials $E_2^{(\alpha)}(x)$ ($\alpha = 0, 1$) it is necessary to specify the form of the wavefunctions $\Psi_2^{(\alpha)}(\mathbf{r}_1, \mathbf{r}_2)$, which is approximated in the usual way:

$$\Psi_2^{(\alpha)}(\mathbf{r}_1, \mathbf{r}_2) \approx (1/2)^{1/2} \, [\phi_1^{(\beta)}(\mathbf{r}_1)\phi_1^{(\gamma)}(\mathbf{r}_2) + \phi_1^{(\beta)}(\mathbf{r}_2)\phi_1^{(\gamma)}(\mathbf{r}_1)], \tag{16.7}$$

with the single-electron ground-state wavefunction $\phi_1^{(0)}(\mathbf{r}) = (\pi\rho_0^3)^{-1/2} \exp(-r/\rho_0)$ and localized or non-localized excited-state wave functions $\phi_1^{(1)}$. The latter in what follows are singly ionized excited states (near the mobility edge), with largest soft mode displacements, orthogonal plane waves or equivalently excited bound states of size $\rho_1 \longrightarrow \infty$ (these are the only excited states for non-adiabatic small polarons). With the above choices, the pair wavefunction $\Psi_2^{(1)}(\mathbf{r}_1, \mathbf{r}_2)$ is orthogonal to $\Psi_2^{(0)}(\mathbf{r}_1, \mathbf{r}_2)$, and the present theory is qualitative and in some respects semi-quantitative, giving scale estimations but not numbers which could fit experimental data. Then, the adiabatic potentials $E_2^{(\alpha)}(x)$ related to the "defects" in question can be expressed in a standard way as

$$\begin{aligned} E_2^{(\alpha)}(x) &= \iint (d\mathbf{r}_1)(d\mathbf{r}_2)\Psi_2^{(\alpha)}(\mathbf{r}_1, \mathbf{r}_2)H_{2e,sm}(\mathbf{r}_1, \mathbf{r}_2; x)\Psi_2^{(\alpha)}(\mathbf{r}_1, \mathbf{r}_2) \qquad (16.8) \\ &= T_2^{(\alpha)} + 2Q^{(\alpha)}x + (1/2)\, k_{ef}^{(\alpha)} x^2 \\ &= W_2^{(\alpha)} + (1/2)\, k^{(\alpha)}(x - x_2^{(\alpha)})^2. \qquad (16.9) \end{aligned}$$

Here $W_2^{(\alpha)} = E_2^{(\alpha)}(x_2^{(\alpha)})k_{ef}^{(\alpha)}$ and $x_2^{(\alpha)}$ are functions of the model parameters C_0, k and L_0. The soft-mode coordinates of the two minima are $x_2^{(\alpha)} = -2Q^{(\alpha)}/k_{ef}^{(\alpha)}$, and $W_2^{(\alpha)}(< 0)$ is the pair self-trapping energy in the ground or excited state. In Eq. (16.9), $W_2^{(\alpha)} \simeq T^{(\alpha)} - 2(Q^{(\alpha)})^2/k_{ef}^{(\alpha)}$; in terms of $\Lambda_\alpha = 1+\rho_\alpha/2L_0$, the kinetic energy $T^{(\alpha)} = (2-\alpha)E_0\,(\Lambda_0-1)^{-2}$ where $E_0 = (\hbar^2/8mL_0^2)$ and m is the electron effective mass. Moreover, $Q^{(0)} = D_1/\Lambda_0^3$ and $Q^{(1)} = Q^{(0)}/2$, while the mentioned changes $\Delta k^{(\alpha)}$ in the effective spring constant $k_{ef}^{(\alpha)} = k + \Delta k^{(\alpha)}$ are $\Delta k^{(0)} = k_{ef}^{(0)} - k = D_2/\Lambda_0^3$ and $\Delta k^{(1)} = \Delta k^{(0)}/2$. Then, as follows from Eq. (16.2), most soft modes that contribute to the formation of ground-state negative-U centers are characterized by an effective spring constant $k_{ef}^{(0)} \simeq k_g = M_{sm}\Omega_{sm}^2 = 2(Q^{(0)})^2 E_g^{-1}[1+2E_0(\Lambda_0-1)^{-2}E_g^{-1}]^{-1}$, and the electron-induced additional spring constant $\Delta k^{(0)}$ can be appreciably less than k_g for appropriate realistic values of the parameters (Ω_{sm} is a typical soft mode frequency). In this connection, for the sake of simplicity of the following analysis, we confine our attention to the case of $D_2 \simeq 0$, so that the spring constants are all

equal, $k_{ef}^{(\alpha)} \simeq k \simeq k_g \approx 0.1 k_{ac}$. Then, with the obtained simple expressions for the adiabatic potentials $E_2^{(\alpha)}(x)$, our calculations show that the value of Λ_0, i.e., of the ground-state size ρ_0, found by minimizing the ground-state energy $E_2^{(\alpha)}(x_2^{(\alpha)})$, with respect to ρ_0, is a solution of the equation

$$E_0/(\Lambda_0 - 1)^3 = 3D_1^2/(k_g \Lambda_0^7) \simeq \gamma \Lambda_0, \tag{16.10}$$

where $\gamma = \hbar^2/3mL_0^2 E_g \lesssim 0.1$ for realistic values of the effective mass $m \simeq m_0$, the free electron mass. For such γ, $\rho_0/2L_0 \simeq \gamma^{1/3}(1 + \gamma^{1/3}/3)$, as also confirmed by numerical calculations. The combination of Eq. (16.9) and an extra energy minimum requirement, $E_0/(\Lambda_0 - 1)^4 > 7D_1^2/(k_g \Lambda_0^8)$, leads to the condition $(1 <) \Lambda_0 < 1.75$, i.e., $(0 <) \rho_0 < 1.5$ L_0, which is realized with the found value of $\rho_0(\gamma)$.

Finally, the criterion for an existence of metastable "defects" is that the soft-mode coordinate of the crossing point x_c for the adiabatic potentials in Fig. 16.1 lies between the coordinates $x_2^{(\alpha)}$ of the ground-state and excited-state minima. As by definition $E_2^{(0)}(x_c) = E_2^{(1)}(x_c)$, after simple algebra one finds that

$$x_c = -3D_1(\Lambda_0 - 1)/(k_g \Lambda_0^4), \tag{16.11}$$

and so the criterion for the existence of a "defect" state is that Λ_0 should lie between 1.5 and 3. Then, one concludes that actually $1.5 < \Lambda_0 < 1.75$, so the criterion is realizable for GS. In accordance with Eqs. (16.2) and (16.9)–(16.11), at $E_g = 2D_1^2/(k_g \Lambda_0^6)$, $E_2^{(\alpha)}(x_c)$ is higher in energy than the minimum of the energy of the excited state by the value of activation energy

$$E_{1c} = k_g (x_c - x_2^{(1)})^2/2 = [2D_1^2/(2k_g \Lambda_0^6)](1 - \kappa/\Lambda_0)^2 \equiv E_g \zeta^2, \tag{16.12}$$

with $\kappa = 1.5$ and $\zeta^2 \approx 1/49$ here. For finite D_2, at $\Delta k^{(0)} = D_2/\Lambda_0^3$ still noticeably less than $k^{(0)} \simeq k_g$, similar estimation results are expected, as confirmed in numerical calculations. In Eq. (16.12), the noted value of κ and upper limit of ξ^2 should not be understood too literally in this semi-quantitative theory. However, the scale of ζ^2 is still considerably less than the empirical one, e.g., $\zeta^2 \approx 0.5$–1.0. It may be anticipated that this smallness is related to the fact that in the limit case (I) under discussion, for which non-diagonal matrix elements of the interaction of Eq. (16.6) in the approximate negative-U states of Eq. (16.7) are zero and also the distributions of D_1, D_2, and D_0 are assumed to be such that their most probable values are close to the average valus and the latter can be used for estimates. A different situation in this connection may be characteristic of the other limit case (II), in which much larger non-diagonal matrix elements of H_{int} are expected to occur due to pronounced angle dependence in Eq. (16.9) (e.g., with $D_1 = C_1 L_0^{-1} \cos^2 \Theta$ and $D_2 = 0.5 C_0 L_0^{-2}[\cos^2 \Theta - (L_0/r) \sin^2 \Theta]$ at $C_1 \sim C_0$). In this case, the activation energy E_{1c} and ζ^2 may be much larger, even close to the empirical scale, e.g., with $\zeta^2 \gtrsim 1.0$. Accordingly, in some intermediate cases when an expression for $H_{int}(\mathbf{r}_1, \mathbf{r}_2; x)$ more general than in Eq. (16.6) is relevant, the activation energy E_{1c} may be close to the empirical scale of 1 eV. This suggestion has still to be checked more carefully in numerical calculations elsewhere, but the preliminary results are encouraging. It is worth adding that Eq. (16.10) is relatively weakly sensitive to the exact form of the expressions of $D_{1,2}(\Theta)$, while Eq. (16.12) is expected to be considerably more sensitive.

16.4.2 Kinetics and Transition Probabilities

Now, for the above theoretical model, a brief discussion is presented of kinetics of the PSC and the related probabilities for transitions between the adiabatic potential wells, $E_2^{(\alpha)}(x)$ ($\alpha = 0, 1$) in Fig. 16.1, giving rise to metastable "defects". The basic kinetic equation for the time evolution of the concentration $c_1(t) \equiv c_d(t)$ of the metastable "defects" is applied in a standard form,

$$\frac{dc_1}{dt} = [P_{0t1}^{(r)} c_0(t) - P_{1t0}^{(r)} c_1(t)] + [P_{0c1}^{(nr)} c_0(t) - P_{1c0}^{(nr)} c_1(t)], \tag{16.13}$$

for the simplest case with a steady-state concentration of the negative-U centers, $c_{nuc} = c_0 + c_1$ (e.g., $c_{nuc} \approx 10^{-3}$). The transition probabilities (per sec) $P_{0t1}^{(r)}$ and $P_{1t0}^{(r)}$ for successive inter-well radiative (via a transient state (t)) and intra-well relaxation transitions, as well as $P_{0c1}^{(nr)}$ and $P_{1c0}^{(nr)}$ for successive inter-well non-radiative (via an activated state at x_c) and intra-well relaxation transitions, are rather related to a bottleneck-like situation and can be expressed in terms of the above-mentioned parameters D_1, D_2, L_0 and $k^{(0)} = k_g$.

If the photon flux $Q_0 = \{\text{constant} > 0 \text{ for } t > 0 \text{ or } 0 \text{ for } t < 0\}$, the fractional concentration $f_1 = c_1/c_{nuc}$ of "defects" can be described by a standard phenomenological equation [6]:

$$f_1(t) = (f_0 - f_\infty) \exp(-t/\tau_f) + f_\infty, \text{ at } t > 0, \tag{16.14}$$

where $f_0 \equiv f(0) \geq 0$ and $f_\infty = f(t \gg \tau_f)$ is the steady-state value. Moreover, in terms of $P_{\alpha t\alpha'}^{(r)}$ and $P_{\alpha c\alpha'}^{(nr)}$, $f_\infty = \tau_f \tau_0^{-1}$ at $\tau_0^{-1} = P_{0t1}^{(r)}$ and $\tau_f^{-1} \cong P_{0t1}^{(r)} + P_{1t0}^{(r)} + P_{1c0}^{(nr)}$, since actually thermally induced "defects" are unimportant when the PSC are pronounced, i.e., $P_{0c1}^{(nr)}/P_{1c0}^{(nr)} \ll 1$. In terms of generalized cross-sections $\sigma_{\alpha t\alpha'} \equiv P_{\alpha t\alpha'}^{(r)}/Q_0$, one can see that $f_\infty \simeq Q_0/Q^*$ for small $Q_0 \ll Q^* = P_{1c0}^{(nr)}/\sigma_{0t1}$ while f_∞ exhibits a "saturation" for $Q_0 \gg Q^*$, as far as an (experimentally) accessible Q^* exists. If light is switched off at a time $t = \tau_\infty > \tau_f$, an effect of thermal relaxation of "defects" occurs, $f_1(t) \simeq f_\infty \exp[-(t - \tau_\infty)/\tau_b]$, for $t > \tau_\infty$, with a characteristic time $\tau_b(T)$ (see below).

For not too large Q_0, including $Q_0 \lesssim Q^*$(see below), the effective time $\tau_{\alpha t\alpha'}^{(r)}$ of the light-induced transitions actually is the time $\tau_{\alpha t}^{(FC)}$ of the related Franck–Condon transition from a vibrational state around the minimum in the α-th potential well to a respective transient state in the α'-th one,

$$\tau_{\alpha t\alpha'}^{(r)} \equiv 1/P_{\alpha t\alpha'}^{(r)} \simeq 1/Q_0 \sigma_{\alpha t}^{(0)} = \tau_{\alpha t}^{(FC)}, \qquad \text{with} \qquad \sigma_{0t1} \simeq \sigma_{0t}^{(0)}. \tag{16.15}$$

The Franck–Condon cross-section $\sigma_{\alpha t}^{(0)}$ can be readily obtained by equation for the adiabatic potentials of a negative-U center a well known formula of the cross-section associated with multi-phonon processes in self-trapped states [35]. In the case under discussion,

$$\sigma_{\alpha t}^{(0)}(\omega, T) \approx \sigma_0 \ \tanh(\hbar\Omega_{sm}/2T) \exp[-E_a^{(\alpha)}(\omega)/\theta_T], \tag{16.16}$$

where $E_a^{(\alpha)}(\omega) = (E_m^{(\alpha)} - \hbar\omega)^2/E_g$ is the activation energy at "high" $T \gg \hbar\Omega_{sm}/2$, $\sigma_0 \simeq 4\pi\omega|M_{\alpha t}|^2(2M_{sm})^{1/2}/3c_m\varepsilon(\omega)\hbar E_g^{1/2} \sim 10^{-14}$ cm^2 ($\approx L_{sm}^2$). $M_{\alpha t}$ is a standard electric

dipole transition matrix element, c_m is the light velocity and $\varepsilon(\omega)$ is the dielectric parameter of a GS. In Eq. (16.16) $\theta_T = (\hbar\Omega_{sm}/2)\mathrm{coth}(\hbar\Omega_{sm}/2T)$ and a typical soft mode frequency $\Omega_{sm} \approx 5 \times 10^{12}/s$, while $E_m^{(1)} = \gamma_1 E_g/4$ and $E_m^{(0)} = \gamma_0 E_g < E_g$ at $3/4 \lesssim \gamma_0 \lesssim 5/6 < \gamma_1 \lesssim 4/3$, not contradicting the fact that the observed maximum of light excitation spectrum occurs in the Urbach absorption tail at $\omega_{\max} < E_{opt}/\hbar$.

Thus the Frank–Condon cross-section changes with T as $T^{-1}\exp[-E_a^{(\alpha)}(\omega)/T]$ for $T > \hbar\Omega_{sm}/2 \approx 25$ K while it almost does not change at lower T, and, most importantly, $E_a^{(\alpha)}(\omega)$ is simply related to E_g due to Eq. (16.2). Certainly, Eqs. (16.13)–(16.16) hold in the present theory independent of the exact form of the expressions of $D_{1,2}(\Theta)$ in Eq. (16.6), as well as the expressions describing the probabilities of the intra-well relaxation transitions, included in the probabilities $P_{0c1}^{(nr)}$ and $P_{1c0}^{(nr)}$ in Eq. (16.13), estimated in what follows.

On the other hand, the expression for the probability (per second) of the thermal inter-well relaxation processes, in general, can be approximated in the present theory as

$$P_{1c0}^{(nr)} \simeq W_b \equiv \tau_b^{-1} = \Omega_b \exp(-E_{1c}/T) \ (\ll \Omega_{sm}), \tag{16.17}$$

as long as the finite time of intra-well vibrational relaxation τ_{VR} is in fact small, $\tau_{VR} \ll \tau_b$ (see below).

However, the expression for the probability Ω_b may be noticeably different in the two above-mentioned limit cases (I) and (II) of Eq. (16.6), as well as in intermediate cases. For the case (I), the effective frequency Ω_b for inter-well transitions at the activated state near the crossing point x_c of the adiabatic potentials (Fig. 16.1) is $\Omega_b = w_{LZ}$, the probability (per second) of the well-known semi-classical Landau–Zener transition, determining a small splitting $\Delta \approx \hbar w_{LZ}$ of the curves at x_c, basically due to weak non-adiabaticity. In fact, a typical estimation $w_{LZ}/\Omega_{sm} \approx Q^2\eta^2/\hbar\Omega_{sm}E_g \approx 10^{-3}$–$10^{-4}$ for appropriate realistic values of the parameters gives an accessible $Q^* \simeq W_b/\sigma_{0t}^{(0)} \lesssim w_{LZ}/\sigma_{0t}^{(0)} \approx (10^{23} - 10^{24})/\mathrm{cm}^2 s$, which significantly increases with T at $T < E_{1c}$. Eq. (16.15) holds not only for $Q_0 < Q^*$ but in general for not too large $Q_0 < Q^{**}$, as the cross-sections $\sigma_{0t1} \simeq \sigma_{0t}^{(0)}(1+Q_0\sigma_{0t}^{(0)}\tau_{VR}^{(1)})^{-1}$ accounts for the finite value of $\tau_{VR}^{(1)} \approx N_\alpha/w_1^{(1)}$; $w_1^{(1)}$ is the probability (per sec) of a single-phonon relaxation processes and $N_\alpha \approx [E_m^{(\alpha)} - E_2^{(\alpha)}(x_2^{(\alpha)})]/\hbar\Omega_\alpha$ is the number of such processes from the transient state energy to $E_2^{(\alpha)}(x_2^{(\alpha)})$. One can estimate $N_1 \approx E_g/4\hbar\Omega_{sm} \approx 10^2$ and $W_{VR}^{(1)} \equiv 1/\tau_{VR}^{(1)} \approx (10^{-2} - 10^{-3})\Omega_{sm}$ for actual $2T \lesssim T_g^{(GS)} \approx 500$ K, the glass transition temperature. Thus, as implied in Eq. (16.17), $\tau_{VR}^{(1)} \lesssim 0.1\tau_b$. Then, the value of $Q^{**} \simeq (\sigma_{\alpha t}^{(0)}\tau_{VR}^{(1)})^{-1}$ is considerably larger (although still accessible) and increases with T more weakly than Q^*, $Q^{**} \approx (10 - 10^2)Q^*$. In this connection, f_∞ changes considerably with ω, T and Q_0 at $Q_0 < Q^*$. However, it almost does not change with Q_0 and changes more weakly with T at $Q_0 > Q^*$. At the same time, the noted "saturation" is different at $Q^* < Q_0 < Q^{**}$, $f_\infty \approx \sigma_{0t}^{(0)}(\sigma_{0t}^{(0)} + \sigma_{0t}^{(1)})^{-1}$, and at $Q_0 > Q^{**}$, $f_\infty \simeq W_{VR}^{(1)}(W_{VR}^{(1)} + W_{VR}^{(0)})^{-1}$.

This holds in general as far as $W_b \ll \Omega_{sm}$, including the other limit case (II) and intermediate cases for which the explicit expressions for Ω_b and E_{1c}, presumably closer to the empirical values, will be considered elsewhere.

16.4.3 Concluding Remarks

In the cases with $W_b \ll \Omega_{sm}$, including the simplest case of Eqs. (16.11)–(16.12), Eqs. (16.5)–(16.17) of the present theory appear to answer the basic questions formulated in Section 16.1 and can be used for calculations of the kinetic characteristics of the PSC. The answer to the first question is that the PSC are due to metastable "defects" produced by the gap light generated excited states of negative-U centers which are basic localized charge carriers only in glassy semiconductors, in particular in chalcogenide glasses. The answer to the second question is that the explicit expression for the PSC criterion, i.e. for the existence of the negative-U center adiabatic potentials of the mentioned double-well potential shape, can indeed be obtained and shown to be realizable in GS. Moreover, it is shown in the theory that the characteristic energies of the PSC are proportional to the optical gap width $E_{opt} \simeq E_g$, in accordance with the experiment. Finally, explicit expressions for the transition probabilities in the kinetics of the PSC can be obtained from the theory (Eqs. (16.16)–(16.17)).

16.5 On Correlations Between Photo-Induced Transformations in Atomic Dynamics and Photostructural Changes

The purpose of this section is to discuss the possibility of occurrence of pronounced metastable transformations in the above-mentioned (Section 16.2) universal dynamic anomalies and some related recently observed effects in the tunneling dynamics in GS. As demonstrated in Section 16.5, the PSC occuring in these materials originate from excited negative-U centers ultimately related to the soft modes.

16.5.1 Are Pronounced Metastable Transformations Available in Atomic Tunneling Dynamics?

One can see from Section 16.4 that the negative-U centers excited by the gap-light are characterized by small effective spring constants $k_{ef}^{(exc)}$, which are even smaller than that, $k_{ef}^{(gr)} (\ll k_0)$, for the ground-states (Eqs. (16.6) and (16.9)), corresponding to an extra weak covalent bond which is even weaker than that for the ground-states. In general, this expected effect favors a relatively small increase of the volume and thus a transformation of a relatively small number Δc_{sm} (> 0) of soft modes "located" in single-well potentials into those in double-well potentials, particularly (but not limited to) for the gap-light of frequencies $\omega \lesssim \omega_g = E_g/\hbar$ at $0 \lesssim \omega_g - \omega \ll \omega_g$ in the optical-bandgap Urbach tail efficient also for the PSC in GS, with $\Delta c_{sm} \ll c_{sm}$. Thus, the expected effect can give rise to a relatively considerable increase of the atomic concentration of the soft modes in double-well potentials, and thereby of the concentration of the related atomic tunneling-states excitations with very small energies $\varepsilon \lesssim \varepsilon_a = k_B T_a$ at $T_a \approx 1$ K, provided that Δc_{sm} is not too small compared with the tunneling-states concentration $c_{sm}^{(TS)}$, e.g., at $\Delta c_{sm} \sim c_{sm}^{(TS)}$. In other words, the PSC are expected (at least for some frequency range of the gaplight) to enhance the universal dynamic anomalies associated with the atomic-tunneling states of the very low excitation energies.

This interpretation actually is in a qualitative agreement with the ideas suggested in recent experimental work [36]. While theoretical estimations of $\Delta c_{sm}/c_{sm}^{(TS)}$ have still to be given elsewhere, this ratio at present could presumably be estimated from interesting experimental data of the work cited above on the changes in low-temperature sound velocity and acoustic absorption around 150 MHz in a-As_2S_3 films illuminated at 5 K by the gap light. The absorption and the temperature dependence of the sound velocity are enhanced dramatically, and the elastic constants are softened by $8 \pm 1\%$. The structure of the films becomes more floppy, and this appears to be plausibly interpreted in this paper as due to an increase of the number of soft modes. This view is supported by the observed absolute decrease of the sound velocity during illumination, as well as by a decrease of the medium-range order in a-As_2S_3 earlier reported earlier [37]. Then, one could suggest that $\Delta c_{sm}/c_{sm}^{(TS)}$ is here still smaller than unity but considerable, e.g., $\Delta c_{sm}/c_{sm}^{(TS)} \sim 0.1$. It is not excluded, however, that the sign of Δc_{sm}, and thus the effect may become opposite for gap-light frequencies considerably exceeding the optical-gap width (see [11](a)).

16.5.2 Can Pronounced Metastable Transformations be Available in the HFD Related to Soft Modes?

The metastable transformations might occur also in the HFD related to vibrational soft-mode excitations (Section 16.2). For this case, a theoretical model and the resulting HFD, including both the boson peak and the correlated high-frequency sound, has recently been proposed [32], in which an isotropic elastic continuum matrix is considered, containing randomly distributed localized "defects" being atomic soft modes, of concentration $c_{sm}(\sim 10^{-2})$, with their "bare" harmonic (quasi-local) vibrational excitations. The only characteristic frequency of the model is a given random "bare" soft-mode frequency $\omega_0^{'}$, around its typical value $\omega_0 \approx 2\pi$ THz, chosen from the (vibrational) density of states $g_0(\omega_0^{'})$. The spectral properties of such a macroscopic system, which can be revealed from (e.g., scattering) experiments, such as the characteristic single-excitation density of states $g(\omega)$, can be calculated from the spectrum of eigenfrequencies $\omega = \omega(q; \varepsilon^{'})$ for propagating collective excitations with wavevector q, at a given value of $\omega_0^{'}$. The excitation spectrum is found to consist of two branches with the dispersion law $\omega = \omega_{1,2}(q; \omega_0^{'})$, which are separated by a gap of width $\Delta(\omega_0^{'}) = \omega_{2\,\min} - \omega_{1\,\max}$ at $\omega_{2\,\min} = \omega_0^{'}$, with a typical value of $\Delta(\omega_0) \sim 0.1\omega_0$ (see Fig. 16.1 in [32](a)). Actually, this spectrum corresponds to strong hybridization of the acoustic vibrations with the soft-modes. This hybridization is an essential feature of the excitations around the gap and is associated with an "inelastic" Ioffe–Regel crossover from weak inelastic scattering of acoustic phonons by soft-mode vibrations to strong scattering. In fact, the related acoustic mean-free path $l_{ac}^{(in)}(\omega)$ around the gap ($\omega \approx \omega_0^{'} \approx \omega_0$) is short in accordance with the definition of this crossover, $l_{ac-sm}^{(in)}(\omega) \approx \lambda_{ac}(\omega) = 2\pi s_0/\omega$ at $\omega \approx \omega_{IR}^{(in)} \approx \omega_0$ and $\nu_0 \sim 1$ THz, and the characteristic frequency $\omega_{IR}^{(in)} \approx \omega_0$ is practically independent of q, in accord with the physical sense of any Ioffe–Regel crossover. In the crossover range, the widths $\gamma_{1,2}$ of the eigenfrequencies $\omega_{1,2}$ are large in a sense that $\gamma_{1,2} = \kappa\omega_{1,2}$ with $0 < \kappa \lesssim 1$. The lower branch $\varepsilon_1(q; \varepsilon')$ considerably below the gap edge $\varepsilon_{1\,\max}$ is largely of acoustic origin, $\omega_1(q; \omega_0^{'}) \simeq s_0 q$. Moreover, the upper branch $\varepsilon_2(q; \varepsilon')$ considerably above the gap edge

$\varepsilon_{2\,\min} = \varepsilon'$ (at $\omega \leq \omega_{2\,\max} \ll \omega_D$) is of "mixed", strongly hybridized nature, although with an acoustic-like dispersion law, $\omega_2(q;\varepsilon') \simeq \omega_0^{'} + s_0 q$. The latter is expected to mark also non-localized, propagating, excitations of relatively high ω, $\omega_0 < \omega \lesssim \omega_{\max} \equiv p_{\max}\omega_0$ for $\omega_0^{'} \approx \omega_0$, similar to the observed high-frequency sound, with an experimental upper value $p_{\max}^{(\exp)} = \omega_{\max}^{(\exp)}/\omega_{BP} \gtrsim 2$–3 [22]. The mentioned vibrational excitations around the (pseudo)gap are also expected to be non-localized states, although different from the propagating high-frequency sound like states, because inelastic scattering is related to dephasing effects due to energy exchange.

Then, the basic spectral property under discussion, the density of states $g(\omega)$, as well as $g(\omega)/\omega^2$ measurable in inelastic incoherent neutron scattering experiments, can be approximately calculated [32](b). The results are presented in Fig. 16.2 at a typical gap width, $\delta = \Delta(\omega_0)/\omega_0 = 0.1$, and mean that $J(\varepsilon = \omega^2) = g(\omega)/2\omega$, as well as $g(\omega)/\omega^2$, exhibit in a qualitative accordance with recent experiments (see, e.g., [22]) both the broad asymmetric peak similar to a boson peak and the acoustic-like behavior similar to that of the high-frequency sound with $g(\omega) \propto \omega^{\delta}$ at $\delta \simeq 2$.

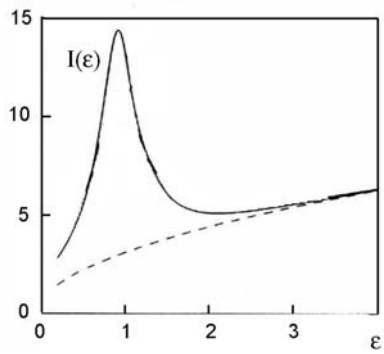

Figure 16.2: The vibrational DOS $J(\varepsilon = \omega^2) = g(\omega)/2\omega$ (in arbitrary units), at typical $\delta = 0.1$ and $\kappa \approx 0.3$; the dashed curve describes the Debye (gapless) spectrum.

The above-mentioned relatively small increase of the local volume and thus the transformation of few soft modes "located" in single-well potentials into those in double-well potentials by the gap-light can be characterized for the harmonic soft-mode vibrations under discussion by a much smaller parameter $c_{sm}/c_{sm}^{(qh)} (\lesssim c_{sm}^{(TS)}/c_{sm} \lesssim 10^{-3} - 10^{-4})$. However, this possible weak transformation does not necessarily affect the concentration $c_{sm}^{(qh)}$ of the (quasi-) harmonic soft modes involved here in the HFD. In fact (unlike the effect for the tunneling dynamics), it might give rise to a considerably weaker transformation (if any) in the HFD, due to effects in the location and shape of the boson peak and/or in the parameters of the high-frequency sound. Such effects appear to be weaker (to be discussed elsewhere) than the direct change of the soft-mode concentration.

16.6 Suppression of Photostructural Changes at High Pressure

The soft-mode excitations and related dynamic anomalies in glasses can be suppressed at a pressure much lower than, $p \gtrsim p_{ac} \approx E_B^{(s)}/a_1^3 \sim 10^6$ bar (for typical strong-bonding energy $E_B^{(s)}$ of about a few eV) which significantly affect the acoustic excitations of the same low energy. This essential difference is eventually associated with the very nature of the SMD of glasses (Section 16.2). On the one hand, one can characterize significant displacements as those of the Lindemann scale, $\delta_L \equiv u_L/a_1 \approx 0.1$, in both soft ($\Delta x_{sm}$) and acoustic ($\Delta x_{ac}$) modes, as follows: $\Delta x_{sm} = \chi_{sm} p_{sm} a_1^2 \approx \delta_L \approx \Delta x_{st} = \chi_{st} p_s a_1^2$, where p_{sm} denotes the introduced pressure scale characteristic of soft modes. On the other hand, in general, glasses contain both strong bonding forces, with $E_B^{(s)} \approx 1$ eV, and weak (weak covalent, van der Waals, etc.) bonding forces, with a typical energy $E_B^{(w)} \approx 0.1\, E_B^{(s)}$. For the latter, the characteristic pressure scale $p_w \approx E_B^{(w)}/a_1^3 \approx 0.1\ p_s$. Since the soft modes are characterized by small spring constants $k \approx 0.1 k_0$, and thus by weak bonding forces, the atomic displacements in soft modes indeed have to become significant, and the above-mentioned modes and their excitations are predicted to be strongly affected by moderately-high pressures around p_{sm} [12](b), [38], at

$$p \gtrsim p_{sm} \approx p_s(\chi_{st}/\chi_0) \approx 0.1\, p_s \approx 10^5 \text{ bar } \approx p_w. \tag{16.18}$$

Numerical calculations give rise to a relevant approximation for the PSC intensity $I_{PSC}(p)$, $I_{PSC}(p)/I_{PSC}(0) \propto c_{sm}(p)/c_{sm}(0) \approx \exp[-\psi(p)]$, as $I_{PSC}(p) \propto c_{sm}(p)$, the soft-mode concentration. The latter strongly decreases (by orders of magnitude) down to zero with increasing p, because the function $\psi(p)$ increases more rapidly than p (Fig. 16.3). This variation characterizes the predicted strong suppression of the soft modes and their excitations and thus the predicted effect of strong suppression of the related photostructural changes and possible metastable changes in the universal dynamic anomalies of glassy semiconductors, which is particularly strong for $p \approx p_{sm} \approx 10^5$ bar. The theoretical prediction under consideration appears to be supported, in scale at least, by some recent experimental data [39] for the boson peak (Section 16.2) in glassy SiO_2 densified under an applied pressure $p \approx 10^5$ bar, as discussed in [12](b), [38](b), and some earlier data [40] concerning the PSC related photodarkening effect in GS (Sections 16.1 and 16.4).

16.7 Conclusions

The recent theory of the photostructural changes [8] (see also [9]), surveyed above in Section 16.4, appears to be the first theory actually based on the experimental observation that the PSC are found only in GS, in particular in chalcogenide glasses, in which the basic localized charge carriers interacting with gap light are the well-known Anderson negative-U centers. The latter have been shown to be related to a non-polaronic kind of self-trapping of electron (hole) singlet pairs due to the electron (hole) interaction with the soft atomic motion modes characteristic of glasses, their low-energy excitations and related dynamic anomalies (Sections 16.2 and 16.3). As noted in the concluding remarks to Section 16.4, the theory under

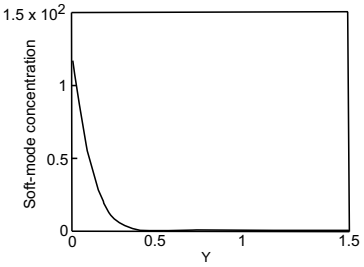

Figure 16.3: The dependence of the PSC intensity (in arbitrary units) on hydrostatic pressure, $y = p/p_{sm}$ at $0 < y \leq 1.5$.

discussion is able to answer in a natural way the basic questions concerning the origin and features of the PSC (Section 16.1).

The photostructural changes, induced by the gap light of substantial intensity I, are expected to give rise to the occurrence of additional localized electron states close to the mobility edges in the mobility gap, in the local atomic soft configurations containing actually a single soft mode. As far as this takes place, the optical gap width decreases, $E_{opt}(I) < E_{opt}(I \longrightarrow 0)$, which may correspond to the experimentally observed photodarkening. Since soft modes correspond to rare, highly anisotropic, quasi-1D fluctuations in atomic spring constants (Section 16.2), one also expects that anisotropic effects, e.g., dichroism and birefringence, that strongly depend on the light polarization, may occur in connection with the PSC, in accordance with recent experimental observations (see, e.g., [1, 41, 42] and references therein).

One problem of the theory under consideration is consistently to characterize qualitatively, and to a possible extent quantitatively, both the photodarkening phenomenon and the anisotropic effects, while another problem is to improve the quantitative aspect of the theoretical description of the metastable transformations (Section 16.5) in the soft-mode dynamics and related dynamic anomalies of the glasses (to be discussed elsewhere).

It appears that the most essential test of the relevance of the theory is to verify experimentally the predicted suppression of the soft modes (their dynamics and contribution to the dynamic anomalies) and thereby of the essentially related photostructural changes in glassy semiconductors, particularly in chalcogenide glasses, under moderately high pressures $p \sim p_{sm} \approx 10^5$ bar (Section 16.6).

Acknowledgment

It is my pleasure to thank Dr. A.V. Kolobov for bringing Ref. [40] to my attention.

References

[1] K. Shimakawa, A.V. Kolobov, and S.R. Elliott, Adv. Phys. **44**, 475 (1995).

[2] Ke. Tanaka, Rev. Solid State Sci. **4**, 641 (1990).

[3] J. Lowe, S.R. Elliott, and G.N. Greaves, Phil. Mag. B **54**, 483 (1986).

[4] A.V. Kolobov, H. Oyanagi, K. Tanaka, and Ke. Tanaka, Phys. Rev. B **55**, 726 (1997).
[5] M.I. Klinger, Ch. B. Lushchik, T.V. Mashovets, G.A. Kholodar, M.S. Sheinkman and Elango M.A., Sov. Phys. Usp. **147**, 528 (1985).
[6] A.V. Kolobov, B.T. Kolomiets, O.V. Konstantinov, and V.M. Lyubin, J. Non-Cryst. Solids **45**, 335 (1981).
[7] V.L. Averyanov, A.V. Kolobov, B.T. Kolomiets, and V.M. Lyubin: J. Non-Cryst. Solids **45**, 343 (1981).
[8] M.I. Klinger, V. Halpern, and F. Bass, Phys. Stat. Solids (b) **230**, 39 (2002).
[9] F. Bass, V. Halpern, and M.I. Klinger, Phys. Lett. A **278**, 165 (2000).
[10] P.W. Anderson, Phys. Rev. Lett. **34**, 953 (1975).
[11] M.I. Klinger and S.N. Taraskin, Phys. Rev. B **57**, 12898 (1995).
[12] M.I. Klinger, (a) Phys. Rep. **165**, 275 (1988); (b) Phil. Mag. B **81**, 1273 (2001).
[13] T. Uchino, D.C. Clary, and S.R. Elliott, Phys. Rev. B **65**, 174204 (2002).
[14] N.F. Mott and E.A. Davis, Electronic Processes in Non-Crystalline Materials, Clarendon press, Oxford, 1979.
[15] R.C. Zeller and R.O. Pohl, Phys. Rev. B **4**, 2029 (1971).
[16] W.A. Phillips (Ed.), Amorphous Solids, Springer, Berlin (1981).
[17] M.I. Klinger, in Problems of Modern Physics, A.P. Alexandrov (Ed.), Nauka, Leningrad, 1980, p. 293.
[18] M.I. Klinger and V.G. Karpov, Sov. J. Techn. Phys. Lett. **6**, 1473 (1980); Solid State Comm. **37**, 975 (1981).
[19] M. Ramos and U. Buchenau, in Tunneling Systems in Amorphous and Crystalline Solids, P.Esquinazi (Ed.). Springer, Berlin, 1998, p. 527.
[20] R. Shuker and R. Gammon, Phys. Rev. Lett. **25**, 222 (1970).
[21] A. Matic, D. Engberg, C. Masciovecchio, and L. Borjesson, Phys. Rev. Lett. **86**, 3803 (2001).
[22] G. Ruocco and F. Sette, J. Phys.: CM **13**, 9141 (2001).
[23] A. Matic, L. Borjesson, G. Ruocco, C. Masciovecchio, A. Mermet, F. Sette, and R. Verbeni, EuroPhys. Lett. **54**, 77 (2001).
[24] A.F. Ioffe and A.R. Regel, Prog. Semicond. **4**, 237 (1960).
[25] S.N. Taraskin and S.R. Elliott, J. Phys.: CM **11**, A219 (1999).
[26] S.N. Taraskin, J.J. Ludlam, G. Natarajan, and S.R. Elliott, Phil. Mag. B **82**, 197 (2001).
[27] W. Schirmacher, G. Diesemann, and C. Ganter, Phys. Rev. Lett. **81**, 136 (1998).
[28] J. Kantelhardt, S. Russ, and A. Bunde, Phys. Rev. B **63**, 064302 (2001).
[29] W. Goetze and M.R. Mayr, Phys. Rev. E **61**, 587 (2000).
[30] J. Horbach, W. Kob, and K. Binder, Eur. J. Phys. B **19**, 531 (2001).
[31] T.S. Grigera, V. Martin-Mayor, G. Parisi, and P. Verrocchio, J. Phys.: CM **14**, 2167 (2002).
[32] M.I. Klinger and A.M. Kosevich, (a) Phys. Lett. A **280**, 365 (2001); (b) Phys. Lett. A **295**, 311 (2002).
[33] C.A. Angell, J. Phys.: CM **12**, 6463 (2000).
[34] S.R. Elliott, Physics of Amorphous Materials, Longman, New York, 1990.

[35] M. Lax, J. Chem. Phys. **20**, 1752 (1952).
[36] J. Honolka, G. Kasper, and S. Hunklinger, Europhys. Lett. **57**, 382 (2002).
[37] H. Fritzsche, Phil. Mag. B **68**, 561 (1993).
[38] M.I. Klinger, (a) J. Non-Cryst. Solids **232–234**, 257 (1998); (b) Phys. Lett. A **254**, 255 (1999).
[39] M. Arai, Y. Inamura, and T. Otomo, Phil. Mag. B **79**, 1733 (1999).
[40] G. Pfeiffer and M.A. Paesler, J. Non-Cryst. Solids **114**, 130 (1989).
[41] A.V. Kolobov, V.M. Lyubin, T. Yasuda, and Ka. Tanaka, Phys. Rev. B **55**, 23 (1997).
[42] V.M. Lyubin and V.K. Tikhomirov, J. Non-Cryst. Solids **114**, 133 (1989).

17 Hypervalent Bonds as Active Centers Providing Photo-Induced Transformations in Glasses

Sergei A. Dembovsky and Elena A. Chechetkina

A consistent chemical bond approach is used for explanation of photostructural changes and related phenomena (photoluminescence, photo-ESR, mid-gap absorption) in chalcogenide glasses. In contrast to the overwhelming majority of the models that use chemical-bond arguments, our model is supported by direct quantum-chemistry calculations made on an *ab initio* level. The proposed active centers are hypervalent bonds (HVB) that interact with the surrounding continuous random network in both local and collective ways. The collective behavior of HVB, which leads to dramatic macroscopic change (photodarkening, photoexpansion, etc.), is assumed to be a result of self-organization of HVB in the form of a bond wave. Contemporary computation chemistry and physics of evolving systems are combined in order to achieve a deeper understanding of photo-induced instability in glasses.

17.1 Introduction

The major problem with the present-day understanding of photo-induced phenomena in glassy semiconductors seems to be a gap between "good physics", that reveals in a wide variety of experiments and their model interpretations (see, e.g. review [1]), and "poor chemistry". The latter means that the chemical-bond arguments used in the models fail when tested by direct quantum-chemistry studies. A notable example is VAP, a defect that was proposed in 1976 [2] and remains the most popular up to now. When the first quantum-chemical study of Se was undertaken [3], VAP occurred *not* as the *negative-U* defect as required tentatively. The arguments that Se is a particular glass, in which photostructural changes at room temperature and some other features are absent, are erroneous. Even in 1980 it was shown [4] that the difference in the photodarkening ability between Se and "typical" glasses such as As_2S_3 is only due to the relatively low glass transition temperature of Se. Provided the temperature is low enough, the photodarkening is clearly observed in Se. Thus, in order to describe the specificity of glassy semiconductors as *negative-U* materials, one needs a defect of another type than VAPs.

The second problem is that both "microscopic" properties, such as luminescence [5] and ESR [6], and "macroscopic" properties, such as density [7] and fluidity [8], are sensitive to photo-excitation and are often related to each other (see, e.g., photoluminescence, photoexpansion and photoconduction as a function of temperature in Ref. [9]). This means that active centers to be found possess a strong coupling between *electronic* and *atomic (nuclear)* subsystems, on the one hand, and between different *scales*, on the other hand. The latter is observed

clearly in atomic structure, for which the photo-induced changes in the short-range order, SRO (e.g., in the form of first coordination number [10]), medium-range order, MRO (first sharp diffraction peak [11]), and long-range order, LRO (anisotropy [12]), have been reported.

We focus our attention on a *chemical bond*, because it is just the object whose atomic and electronic components are naturally related with each other (compare bond length and bond order, radial distribution function and electronic density distribution along and in the orthogonal direction, etc.). To be a well defined "defect", the chemical bond that one needs should differ essentially from ordinary bonds that form a continuous random network (CRN). Since CRN represents the *ideal* structure of a glass, incorporation of a "defective" chemical bond into CRN is a necessary step for approaching the *real* glass structure. Below we consider the *hypervalent bond* (HVB) as a decisive defect, and we believe that self-organization of HVB in the form of a *bond wave* is a way to describe the real glass on every structural level, from SRO to LRO.

17.2 What Kind of Bond is Needed?

One of the principal recent results in the field of light-induced effects in glassy semiconductors is the fact that the first coordination number, Z_1, *increases* in the process of photo-excitation [10]. This fact is disastrous for most existing models since they are based either on the formation of light-induced dangling bonds which decrease Z_1, and/or VAP which, being a combination of a super-coordinated chalcogene atom and a sub-coordinated one, keep the average Z_1 constant.

On the other hand, the problem of increased atomic coordination in a glass as compared with the corresponding crystal was a stimulus that initiated our approach. Already in 1981 one of the authors [13] collected available structural data and emphasized the situation of the increased first coordination number (especially in liquid and amorphous film states of chalcogenide glasses) – the fact that has led him to the conclusion that, in addition to ordinary bonds forming both ideal CRN and crystalline lattice, *hypervalent bonds* (HVB) must exist in glasses (see also review [14] for details). In this way the notion about HVB as a specific chemical-bond defect in glass was introduced more than 20 years ago.

The first model of HVC in glass was electron-rich three-centered bonds (TCB), analogous to those realized in molecules of halogens and rare-gas halides (XeF_2, etc. [15]). This analogy arises naturally since glasses have a relatively high concentration of lone-pair (LP) electrons [16] that are needed for the formation of TCBs starting with an ordinary two-center covalent bond. The distinction is that the TCB in a glass does not belong to a free molecule, like in XeF_2, etc., but rather exists as a "defect" bonding state, being the so-called "quasi-molecular defect" embedded into ideal CRN.

The TCB was used for interpretation of various features of glasses observed in a wide temperature range, from melt temperatures ($T > T_m, T_m$ being the melting point of the corresponding crystal) to a few kelvin [16–18]. At high temperatures, the thermally-generated HVB replace dangling bonds in the process of thermally-induced destruction of CRN, creating a dynamic continuous mixed-bonded network that explains the characteristic high-viscosity of glass-forming liquids. At the other side of the temperature range (at about 1–10 K) HVB, representing naturally soft atomic configurations and two-well potentials, provide the well-known

low-temperature anomalies in heat capacity, heat conduction, etc. However, the question of whether TCBs are realized in glasses remained open. Molecular dynamic simulation of a-Se by Hohl and Jones [19] confirmed the TCBs geometry (C_3–C_3 pairs were found to represent 82% of defects in liquid Se), but the TCBs also require a specific electronic structure (two bonding electrons and two non-bonding electrons are shared between three atoms), the realization of which can be proved only by quantum-chemistry methods that give both atomic and electronic structure.

17.3 A Quantum-Chemistry Study: HVB *versus* VAP

In our early quantum-chemistry work performed on a semi-empirical MNDO (modified neglect of differential overlap) level we detected the TCBs in a-S [20] and in a-Si:H [21]. In the latter case the TCBs belong to the class of electron-deficient TCBs, analogous to that realized in boron hydrides and in substances with hydrogen bonds [15], in contrast to electron-rich TCBs in glasses. Soon after that the TCB in SiO_2 was described by Dianov et al [22] in the framework of MNDO. Although this TCB, namely, ≡Si- - -O- - -Si≡, has the parameters surprisingly similar to those predicted by us for TCB in SiO_2 earlier [18], this is *not* HVB since all atoms have a normal coordination (four-coordinated silicon, Si_4, and two-coordinated oxygen, O_2). On the other hand, in a series of our following studies, which were made on a *non-empirical* level, it was shown that "classical" TCB in glasses is a rather rare case, while a number of low-energy HVB configurations is a standard situation (see reviews [23] and [24] for oxide and chalcogenide glasses, respectively, and [14] for a brief summary). Thus, the TCBs represent a first generalized image of HVB. However, special quantum-chemical study is needed in order to estimate what exactly HVB realize in the glass under consideration. For example, in a-Se we investigated a number of HVB configurations having three- and four-fold coordinated atoms, the Se_4^0 center being the lowest-energy one among them [25].

According to our study, HVB in a glass represents the *negative-U* defect (neutral state is diamagnetic) in contrast to VAP, as is illustrated in Fig. 17.1 for Se. The same result was obtained earlier for S [24], although the S_4^0 energy with respect to the ground S_2^0 state is somewhat higher, and the well is less pronounced, than for Se_4^0. It should be noted that the bonds of the C_4^0 center are not equivalent: two of them are shorter and stronger than the other two, and an interchange between the pairs of bonds requires overcoming a barrier in the two-well potential of C_4^0.

Thus, a widely used model of VAP as a metastable *negative-U* defect needs serious reconsideration, also taking into account the results of Vanderbilt and Joannopoulos [3]. The VAP concept seems to be regenerated now on a new computational level. Namely, although classical VAP and IVAP suggested in [2] hardly exist, a specific VAP-dipole (VAP-d), in which C_3^+ and C_1^- atoms are linked directly (e.g. >Se–Se), represents a metastable center with a relatively low energy (0.9 eV for VAP-d *versus* 0.4 eV for C_4^0 in the case of Se [25]). Note that MD simulation [19] also reveals defects of the VAP-d geometry, whose relative concentration was evaluated to be about 12% in liquid Se.

By means of contemporary quantum-mechanical methods not only the atomic and electronic structures of a hypervalent bonding configuration but also their contribution into the gap states and vibration spectra can be evaluated. As to photo-induced phenomena, addi-

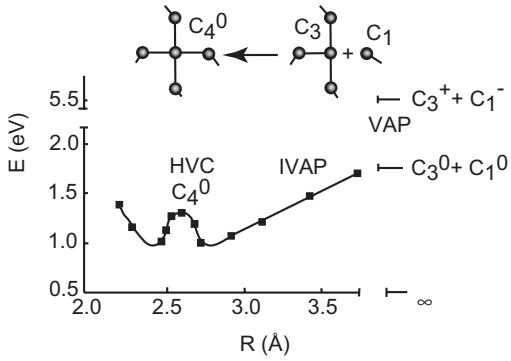

Figure 17.1: Transformation of VAP through IVAP to HVC of the C_4^0 type for Se when decreasing the space between C_3 and C_1 centers (after [25]).

tional vibration bands that develop under photo-excitation, e.g. two peaks at about 160 cm^{-1} and 275 cm^{-1} for a-Se [26] are of particular interest. Computational IR spectra of different defect-containing clusters in a-Se reveal for C_4^0 two strong bands located at 181 cm^{-1} and 261 cm^{-1} [27]. Taking into account the method uncertainty for the band position (about 20 cm^{-1}), the calculated bands coincide well with the experimentally observed ones. Note also that computational bands for VAP-d in a-Se are located at 200, 286, and 337 cm^{-1} [27]. Although IR and Raman spectra are not equivalent, first of all in terms of the relative intensities of the individual bands, this is a good argument that HVB in the form of Se_4^0 can be an active center playing an important role in photo-induced phenomena in a-Se.

17.4 General Model of PSC and Related Phenomena

The first model that used HVB (in the form of hypothetical TCBs) and that connected naturally "macroscopic" and "microscopic" aspects of the photo-induced transformation in glassy semiconductors was proposed by us 15 years ago [28]. In our opinion, the general points of the model remain valid and in this section we briefly describe this model and formulate new problems that go beyond its limits.

The initial structure is considered as CRN, e.g. the network of two-folded atoms in the case of Se which is used as the simplest prototype. A mesoscopic region of such CRN with conditionally regular arrangement of C_2 atoms is shown as the first line in Fig. 17.2. Then the defects in the form of HVB/TCB are introduced in CRN; one of them is shown in the second line in Fig. 17.2. Bandgap light ($E_{exc} \geq E_g$, where E_g is the optical bandgap energy) induces *excitons* that couple with pre-existing HVB (Fig. 17.3, region (a)) and drag them through CRN, as is shown by lines 2–4 (and so on) in Fig. 17.2. The elementary stage of this transfer is the $B_1D + B_2 \rightarrow (B_1DB_2) \rightarrow B_1 + B_2D$ process, where B denotes the basic/ground state or an ordinary covalent bond, and (B_1DB_2) is the transition state (not shown in Fig. 17.2) arising when HBV links the initially separated chains. The details of this process, namely, the nature of the transition state (B_1DB_2) and the energy of elementary transfer ϵ_t, remain unknown.

We believe that the LP excitation with the subsequent formation of a many-center complex (B_1DB_2) corresponds to the ϵ_t barrier, and both the complex formation and its destruction proceed without breaking of strong covalent bonds, so $\epsilon_t \ll \epsilon_{DB}$, where ϵ_{DB} is the energy for creation of a dangling bond which can be estimated from the atomization energy as $\epsilon_{DB} = E_a/N$= 49 kcal/mol = 2.1 eV for Se (compare with E_g=1.9 eV for a-Se).

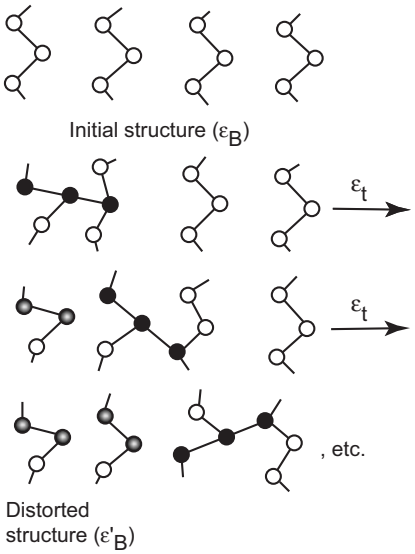

Figure 17.2: Light-induced drift of HVB (in the hypothetical form of TCB), after [28]. The atoms which are part of HVB are shown by black circles. Two jumps of HVB are shown. The CRN structure behind is distorted and the atoms that are shifted from their initial positions are shown by shaded circles.

A series of such transfers/jumps of HVB takes place until the exciton energy is exhausted (see Fig. 17.3, region (b)), the number of jumps being $n < E_g/\varepsilon_t$. Since the structural relaxation is arrested below T_g (remember that $T \ll T_g$ is the condition for the photostructural changes under consideration), each HVB leaves a distorted track behind it (see shaded atoms in Fig. 17.2), so a *mesoscopic* structural change appears. Provided that the track structure imitates the structure of a defect which forms the track, then the average coordination in the track, $< Z_1 >$, increases in accordance with the increased coordination of atoms belonging to HVB. Of course, in order to obtain a *macroscopic* effect, a relatively high concentration of HVB and a relatively long migration path, n, are needed.

When HVB stops, one or several of the following *microscopic* events at the terminal point take place. If the remaining energy is too low for the excitation of the defect, HVB is either preserved in CRN or decays producing an ordinary bond ($D \rightarrow B$). The probability of each pathway is determined by the CRN configuration near the terminal point. When the energy reserve is sufficient, excitation of HVB, $D \rightarrow D^*$, is possible with the subsequent appearance of photo-ESR and photoluminescence (PL), as is shown in Fig. 17.3, region (c). The excited paramagnetic state D* has a mid-gap energy, ϵ^*_D, because of a large Stokes shift of the PL

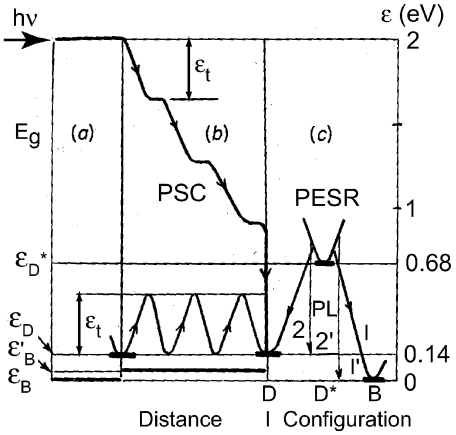

Figure 17.3: A generalized scheme of photo-induced phenomena (after [28]). Photostructural changes (PSC) as a result of HVB jumps (three jumps with the activation barriers ϵ_t are shown), photo-ESR and two-band photo-luminescence (PL). The energies are those for Se.

line(s). The mid-gap absorption, that develops together with photo-ESR [6] may indicate a direct excitation of a trapped HVB with the subsequent thermalization. One can also propose a continuous process $D{\rightarrow}(+h\nu_{MGA}){\rightarrow}D^*{\rightarrow}(-\nu_{L2}){\rightarrow}D{\rightarrow}(+h\nu_{MGA}){\rightarrow}D^*$, as a model for the non-Stokes PL; however, detailed experiments on the spectral response of PL are needed to investigate this possibility.

The terminate HVB-defect "waits" for a next exciton, and then migrates further with a final destruction or excitation. As a result, all the pre-existing HVB/defects either disappear *(D→B)* or get stuck in CRN, so photostructural changes are *saturated*. "Microscopic" response, photo-ESR and PL, proceeding in terminal points, seem to have slower kinetics, but eventually all the system reaches a stationary state. The next cycle of illumination–annealing reproduces the initial one, i.e. annealing at about T_g restores the initial structure completely, including the restoration of all pre-existing HVB and their distribution in CRN. This is the origin of the characteristic *reversibility* of photo-induced phenomena. It should be noted that a deviation from completely reversible behavior is possible (the first cycle can differ from the following ones [29]); however, a general model aims only at explanation of general features of the phenomena.

Comparing our model [28] with the existing ones, one can see both similarities and differences. The light-induced creation of an exciton which finally recombines either to the new localized or to the old group-state geometry as considered in [30] correlates with our exciton-assisted HVB drift followed by the exciton recombination at the terminal point (see Fig. 17.3). However, the exciton in our model is only a conductor for the optical excitation, while HVB play an active role in structural and electronic changes. The formation of dynamical interchain bonds after [10] correlates with our transfer of HVB from one chain to another (Fig. 17.2) and with the formation of the (B_1DB_2) interchain complex. Note, however, that HVB is an "interchain" bond itself. Finally, we agree completely with Kolobov et al. [1,10] as concerns the decisive role of LP electrons (which is not surprising just because valence band in glassy semi-

conductors is formed by LP electrons) in both the formation of "dynamical interchain bonds" and ESR effects, although the detailed interpretations differ. The chemical bond arguments in [10] are similar to that used for VAP in the classical paper [2]. However, the attractive simplicity can lead to erroneous conclusions. It is a too rough approximation to use the initial molecular orbitals and/or their energy for describing a new bonding state. For example, when TCB is realized, a new, non-bonding molecular orbital appears [15]. Thus, *ab initio* quantum-mechanics calculations seem to be the only way to probe one or another model, excited and transition states being a special problem.

For example, let us consider the LP excitation under illumination. In our model we consider two types of excitation: (i) the *paired* one, that corresponds to HVB migration (Fig. 17.2) with the formation of (B_1DB_2) complex as a transition state, and (*ii*) the *un*paired one, that corresponds to the formation of an ESR-active state D^*. Using the description of this center as a hole localized on an Se atom [6], we proposed that one of the LP electrons moves away from the Se atom, although still belonging to this atom. As a result, a positively charged and electron-deficient state of Se atom (hole) arises and, as to the LP electrons, the splitting of the LP orbital takes place with the appearance of two unpaired electrons of different origin. They can be compared with interconnected T (triclinic) and B (broad isotropic) ESR centers in a-Se, whose concentrations are equal at low temperature [31]. It seems likely that the T center corresponds to the nearest strongly localized (LP)* electron, while the B center corresponds to the distant and slightly localized (LP)* electron.

In fact, the considered one-electron LP excitation corresponds to the principal scheme of the well-known "*harpoon mechanism*", proposed by Polanyi [32] in the early 1930s and confirmed later using special methods of study of kinetics of elementary reactions in the gaseous state (see, e.g. [33, 34]). This mechanism describes a general class of reactions initiated by long-range one-electron transfer with the formation of hypervalent intermediates. In our case, the "harpoon" is a distant (LP)* electron, which can correspond to both the defect state and the ground/basic state, as is shown in region (c) in Fig. 17.3 ($D \leftrightarrow D^* \leftrightarrow B$). The latter means, however, that the formation of a new HVB ($B \rightarrow D^* \rightarrow D$) is initially a *one-electron* process as was proposed earlier [17]. Moreover, it seems likely that *switching* of covalent bonds – a necessary stage of viscous flow – is initiated by means of one-electron LP excitation too. This conclusion follows from our experiment of the giant influence of an alternating magnetic field on viscosity of selenium (up to several times) [35]. This possibility is very attractive because in such a way a really *non-breaking* mechanism of the bond switching – the lowest-energy one – can be realized in the form of directed percolation of one-electron excitations. Thus, the harpoon-like excitation of LP has to be carefully tested by means of *ab initio* quantum-chemistry study, like the one performed in Ref. [34] for a classical harpoon reaction.

17.5 Self-Organization of HVB: a Bond-Wave Model

Photo-induced phenomena are known to proceed at the same time on different levels/scales: microscopic (registered by photo-ESR and photoluminescence), mesoscopic (on the scale of the so-called medium-range order, observed primary by first sharp diffraction peak, FSDP), and macroscopic (photoconduction and photostructural changes such as photodarkening, photoexpansion, etc., photo-induced anisotropy being a particular case). The existing models

(see, e.g. review [1]) consider primarily the microscopic level, while a need for meso- and macroscopic description becomes more and more evident. See, e.g., ref. [36], in which a "macroscopic" model of layer- or chain-like clusters is used (in our opinion, this is more likely a "mesoscopic" model due to the cluster scale). In our model [28] we tried to reach the macroscopic level by an assumption that one defect (HVB) interacts with the continuous random network (CRN) many times, being dragged through the CRN by means of excitons during continuous bandgap illumination. However, there exists a much more effective way of such an interaction that is realized not by means of single defects (HVB) but by their collective formation named a *bond wave*.

The bond wave represents a spatio-temporal correlation of elementary acts of bond exchange, $D(HVB) \leftrightarrow B$(ordinary bond) in our case. The bond-wave model was introduced by one of the present authors earlier in order to explain thermodynamic (relatively low melting and boiling points of glass-forming substances) [37], structural (FSDP) [38], and dynamic (viscosity–temperature dependence) [39] properties of glasses. For the convenience of the reader a simplified image of the bond wave is given in Fig. 17.4 in the form of a TCB wave in two-coordinated CRN. From a *structural* point of view, the bond wave represents an equidistant system of planes (surfaces) populated with "defect" bonds, HVB in our case; the system dimensions are not restricted, in principle. From a *dynamic* point of view, the planes move as a whole at $T > T_g$ (above T_g the wave velocity is temperature dependent), and stop below T_g, when the bond wave "freezes" (strictly, only the 3D wave stops, and the waves of reduced dimensionality, 2D, 1D, 0D, can exist below the glass transition causing the so-called secondary relaxation processes). From an *electronic* point of view, both one-electron and two-electron waves can be realized, depending on the nature of the transition state in the elementary act of bond exchange.

Remember that above we related the two-electron LP excitation with the HVB jump between two adjacent chains using the scheme $B_1D + B_2 \rightarrow (B_1DB_2) \rightarrow B_1 + B_2D$. As long as the chains (1 and 2) remain separated after the defect moves away, there is no switching of covalent bonds as a result of the process. On the other hand, taking into account that HVB is weaker and longer compared with an ordinary covalent bond, one can conclude that the wavefront/layer populated by HVB represents a region of expansion in a more dense/rigid CRN. This means that the corresponding HVB wave, as a system of such layers moving through CRN, can be identified as an *acoustic bond wave*. In the case of one-electron LP excitation, which was related above with the magneto-active $D \leftrightarrow$D*$\leftrightarrow$ B process at the terminal point (see region c in Fig. 17.3), the corresponding HVB wave is magneto-active too. Using the above assumption that such a one-electron process is the initial stage for switching of covalent bonds, we introduce a *switching bond wave* as a collective one-electron excitation of LP. This wave is able to provide viscous flow, considered as collective bond switching, on one the hand, and can interact with magnetic field, on the other hand. Then our experiments on the magnetic field influence on the viscosity of Se [35] can be interpreted in the following way.

Since the magnetic field in the above experiments [35] was very *weak* compared to *kT*, the field action is not a trivial force interaction between the field and spins. It seems likely that the field, using collective D^* states as sensors, gives the *direction* in which the bond wave moves in CRN. Indeed, the sign of the effect (a decrease or an increase of viscosity) depends on the field direction with respect to the flow direction [35]. Thus, the magnetic field plays a role of an *information field* for the switching bond wave in the glass; the term "information field" used

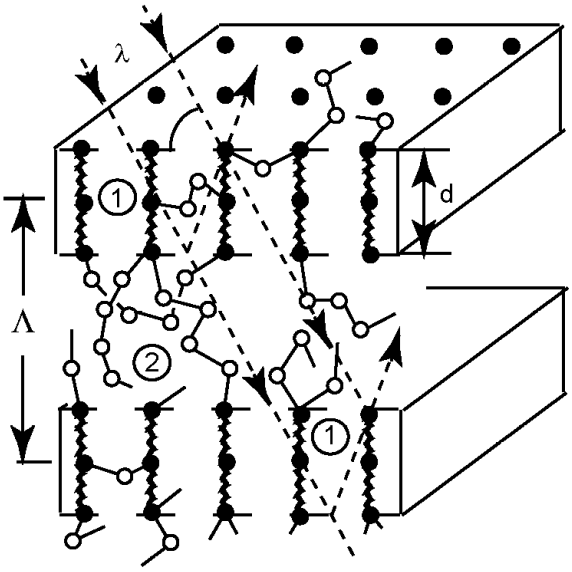

Figure 17.4: An "elementary cell" of the bond wave after [38]. Two wave-fronts populated with HVB (black circles linked by a string), '1', and a piece of CRN between them, '2', are shown. Λ is the wavelength and $d = 2\pi Q_1$ is the layer thickness (Q_1 is the FSDP position). The Bragg reflection from the layers that corresponds to the FSDP is shown by arrows.

here has the same meaning as in the theory of self-organization [40]. Using information fields of different nature (magnetic, electric, polarized light, mechanical stress, temperature gradient, etc.) one can form a required structure. For example, an anisotropic cell-like structure, which forms when three randomly directed bond waves intersect each other, is shown in Fig. 17.5. When an internal information field forces the bond wave to select a particular direction, then anisotropic layer-like structure arises. This is the key point for the interpretation of light-induced anisotropy.

To be more consistent, we should propose a quantum-chemical method for modeling of HVB waves. Unfortunately, it is too large a formation for such a study. On the other hand, it is possible to use a mixed approach. For example, the quantum chemistry/molecular mechanics method [41] permits the investigation of a large cluster as consisting of a central part modeled by quantum-chemistry methods, and its environment modeled using classical molecular mechanics methods.

17.6 Conclusions

Both chemical-bond analogies (TCB, harpoon mechanism) and quantum-chemistry *ab initio* calculations were used for discussion of photo-induced phenomena from the point of view of chemical bonding. The calculations reveal a variety of hypervalent configurations in glasses,

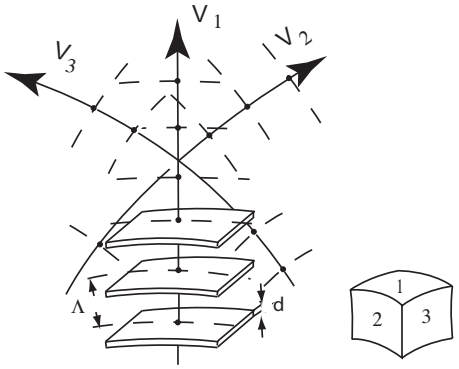

Figure 17.5: Three co-existing bond waves in the random case; V_i is the ith wave velocity vector (after [38])

both transient and metastable, the low-energy metastable hypervalent bonds (HVB) being also negative-U centers. An interconnected understanding of light-induced phenomena at different levels, from microscopic to macroscopic, however, can not be solved on the chemical level only. In order to describe a collective behavior of HVB, the notion about HVB wave that spread within the continuous random network, thus modifying its initial state, is used. Although quantum-chemical modeling of HVB wave is impossible at this stage, contemporary methods of computational chemistry that combine opportunities of different approaches can give us a good approximation. Since the characteristic metastability of glass is determined by specific instability of chemical bonding, both computational chemistry and physics of evolving systems (synergetics) are needed for a real progress in our understanding of how the glass responds to external stimuli.

Acknowledgments

The authors wish to thank A.S. Zyubin and F.V. Grigor'ev for valuable discussions. This work was supported by the Russian Foundation of Basic Research (Grant No. 00-03-32646).

References

[1] A.V. Kolobov, and K. Tanaka, J. Optoel. Adv. Mater. **1**, 3 (1999).
[2] M. Kastner, D. Adler, and H.Fritzsche, Phys. Rev. Lett. **37**, 1504 (1976).
[3] D. Vanderbilt, and J.D. Joannopoulos, Phys. Rev. B **22**, 2927 (1980); B **27**, 6311 (1983).
[4] K. Tanaka, J. Non-Cryst. Solids **35–36**, 1023 (1980).
[5] B.T. Kolomiets, T.N. Mamontova, I.A. Domoryad, and A.A. Babaev, Phys. Stat. Sol. (a) **7**, K29 (1971).
[6] S.G. Bishop, U. Strom, and P.C. Taylor, Phys. Rev. Lett. **34**, 1346 (1977).
[7] H. Hamanaka, K. Tanaka, and S. Iizima, Solid State Commun. **23**, 63 (1977).
[8] H. Hisakuni, and Ke. Tanaka, Science **270**, 974 (1995).

[9] Ke. Tanaka, J.Non-Cryst. Solids **266–269**, 889 (2000).
[10] A.V. Kolobov, H. Oyanagi, K. Tanaka, and Ke. Tanaka, Phys. Rev. B **55**, 726 (1997).
[11] K. Tanaka, Appl. Phys. Lett. **26**, 243 (1975).
[12] V.G. Zhdanov, B.T. Kolomiets, V.M. Lyubin, and V.K. Malinovsky, Phys. Stat. Sol. (a) **52**, 621 (1979).
[13] S.A. Dembovsky, Mater. Res. Bull. **16**, 1331 (1981).
[14] S.A. Dembovsky, and E.A. Chechetkina, J. Optoel. Adv. Mater. **3**, 3 (2001).
[15] G.C. Pimentel, and R.D. Spratley. Chemical Bonding Clarified Through Quantum Mechanics, Holden-Day, San Francisco, 1970.
[16] S.A. Dembovsky, and E.A.Chechetkina, J. Non-Cryst. Solids **64**, 95 (1984).
[17] S.A. Dembovsky, and E.A. Chechetkina, J. Non-Cryst. Solids **85**, 346 (1986).
[18] S.A. Dembovsky, and E.A. Chechetkina., Glass Formation, Nauka, Moscow, 1990, in Russian.
[19] D. Hohl, and R.O. Jones, Phys. Rev. B **43**, 3856 (1991).
[20] A.S. Zyubin, and S.A. Dembovsky, Solid State Commun. **89**, 335 (1994).
[21] A.S. Zyubin, and S.A. Dembovsky, Solid State Commun. **87**, 175 (1993).
[22] E.M. Dianov, V.O. Sokolov, and V.B. Sulimov, J. Non-Cryst. Solids **211**, 197(1997).
[23] S.A. Dembovsky, A.S. Zyubin, and O.A.Kondakova, Russ. Chem. J. **45**, 92 (2001).
[24] S.A. Dembovsky, and A.S. Zyubin, Russ. J. Inorg. Chem. **46**, 121 (2001).
[25] A.S. Zyubin, F.V. Grigor'ev, and S.A. Dembovsky, Russ. J. Inorg. Chem. **46,** 1350 (2001).
[26] A.V. Kolobov, H. Oyanagi, and K. Tanaka, MRS Bull. **24**, 32 (1999).
[27] F.V. Grigor'ev, A.S. Zyubin, and S.A. Dembovsky, Semiconductors **37**, 616 (2003).
[28] S.A. Dembovsky, and E.A. Chechetkina, Philos. Mag. **B53**, 367 (1986).
[29] D.K. Biegelsen, and R.A. Street, Phys. Rev. Lett. **44**, 803 (1980).
[30] Q. Ma, W. Zhou, D. Sayers, and M.A. Paesler, Phys. Rev. B **52**, 10025 (1995).
[31] A. Kolobov, M. Kondo, H. Oyanagi, R. Durny, A. Matsuda, and K.Tanaka, Phys. Rev. B **56**, R485 (1997).
[32] M. Polanyi, Atomic Reactions, Williams and Norgate, London, 1932.
[33] H.F. Davis, A.G. Suits, and Y.T. Lee, J. Chem. Phys. **96**, 6710 (1992).
[34] J.N. Harvey, D. Schroder, W. Koch, D. Danovich, S. Shaik, and H. Schwarz, Chem. Phys. Lett. **278**, 391 (1997).
[35] S.A. Dembovsky, E.A. Chechetkina, and S.A. Kozyukhin, JETP Lett. **41**, 88 (1985).
[36] A. Ganjoo and K. Shimakawa, J. Optoel. Adv. Mater. **4**, 595 (2002).
[37] E.A. Chechetkina, J. Non-Cryst. Solids. **128**, 30 (1991).
[38] E.A. Chechetkina, J. Phys.: Condens. Matter **7**, 3099 (1995).
[39] E.A. Chechetkina, J. Non-Cryst. Solids. **201**, 146 (1996).
[40] H. Haken. Information and Self-Organization: A Macroscopic Approach in Complex Systems, Springer, Berlin, 1988; Springer Series in Synergetics, Vol. 4.
[41] J.R. Shoemarker, L.W. Burggraf, and M.S. Gordon, J. Phys. Chem. A **103**, 3245 (1999).

18 Phase-Change Optical Storage Media

Takeo Ohta and Stanford R. Ovshinsky

18.1 Introduction

In modern society, dramatic changes are taking place in the fields of energy and information. There is a deep connection between them – information is encoded energy and it is energy in the form of light and electric fields that couples to the atomic orbital to bring about the changes in materials that represent information.

Soon after starting in the mid-1950s of an unexpected field of amorphous and disordered materials wherein the constraints of the crystalline lattice were lifted so that new degrees of freedom for the atomic design of synthetic materials were made possible Ovshinsky announced amorphous semiconductor switching and memory effect "Ovonic" in 1968 [1].

This opened a new materials research area [2, 3] and since 1971 both OMS (Ovonic memory switching) and laser recording phase-change memory have been rapidly developing. Significant progress was made increasing the data rate, reliability and in other related areas [4, 5]. A landmark was reached in 1989 when Ohta announced over million-cycle stable phase-change optical disc technology [6]. Matsushita/Panasonic were the first to succeed in the development of new rewritable phase-change optical disc products with first shipments in 1990 [7]. Now phase-change rewritable optical disc technology has become the main stream of the optical disc world as demonstrated by the new rewritable compact discs (CDs) and digital versatile discs (DVDs), which are based upon it [8].

In the present chapter we describe how amorphous order–disorder phase-change memory became the enabling technology for DVD media, high-density technology developments and the next generation phase-change media.

18.2 Phase-Change Overwrite Optical Disc

18.2.1 Phase-Change Optical Memory Phenomena

Phase-change chalcogenide materials was first reported by Feinleib et al. in 1971 [3]. Fritzsche made a groundbreaking presentation on amorphous semiconductors at the American Physical Society Meeting held in Philadelphia, Pennsylvania (USA) and also in Japan at the conference of Japan Applied Physics (Spring) in 1971 [9]. Ovshinsky's pioneering patents in 1968 [10] and 1972 [11] established the phase-change data storage field.

Ohta proposed sub-oxide thin film phase-change media (TeO_x) which led to write-once optical disc products for video image file storage in 1982 [12, 13]. There are many thin film

sub-oxide materials such as GeO_x, SbO_x, and MoO_x with additives of Sn or In that undergo a structural transformation. All of these materials, when in the as-deposited state, are amorphous. Upon heating, they exhibit a darkening effect [12]. Table 18.1 shows change in the optical constants of the sub-oxide films following heat treatment. For rewritable phase-change optical disc, chalcogenide systems including GeSbTe and SbTe eutectics with various modifiers are applied to achieve reversible direct overwrite cycle performance.

Table 18.1: Optical constants of suboxide films at $\lambda = 830$ nm [12]

Suboxide	As deposited		After heat treatment		Conditions
	$\alpha_1(\text{cm}^{-1})$	n_1	$\alpha_2(\text{cm}^{-1})$	n_2	
SbO_x	2.5×10^4	1.8	6.1×10^4	1.9	250 °C, 5 min
TeO_x	0.8×10^5	3.1	1.0×10^5	3.6	250 °C, 5 min
MoO_x	5.6×10^3	1.8	1.1×10^4	2.1	250 °C, 5 min
GeO_x(Te)	4.9×10^4	2.5	1.8×10^5	2.8	250 °C, 5 min

18.2.2 The Phase-Change Memory Mechanism

Figure 18.1 shows the model of phase-change data storage. The enthalpy of the material when in the amorphous phase is higher than when the material is in the crystalline phase. When the structure changes from amorphous to crystalline, the optical absorption edge of the material shifts to a longer wavelength. This is accompanied by a change in the complex refractive index $N = n + ik$ (n is the refractive index and k is extinction coefficient). This causes the reflectivity of the film to change, which is the basis of the storage and retrieval means. The information can be detected by changes in the reflectivity just like CD disc playback. When crystalline film at "a" is exposed to a high-power laser spot, the temperature of the irradiated region increases to over the melting temperature T_m and the state changes "b" to "c" and "d", as show in Figure 18.1. After the laser irradiation, the temperature decreases rapidly through a super cooled state between "c" and "e" to room temperature, "f". When the cooling rate is above the critical cooling rate (3.4 K/ns) [14], the portion of the film at "f" remains in the amorphous phase. When a lower power level laser spot irradiates the amorphous region "f", the temperature increases above "e", the glass transition temperature (T_g), and then the amorphous structure is transformed to the crystalline structure and the mark is erased. Above T_g, when softening – not melting – takes place, a higher mobility state initially induced by lone pair electron absorption provides the ability for atoms to move slightly at very high speed to establish the new configurations leading to either crystallization or returning to the amorphous state, depending on conditions.

18.2.3 Phase-Change Overwriting Method

The requirement for overwriting a phase-change material is a high enough crystallization so that in the time the laser spot moves the distance of its diameter, the irradiated region can be

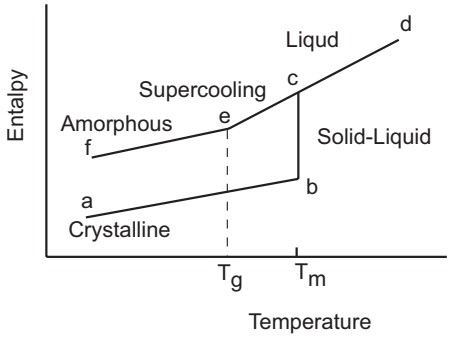

Figure 18.1: Model of the phase-change memory (T_g, glass transition temperature; T_m, melting temperature).

changed to a fully crystalline state and previously recorded information is erased [15]. Terao et al. announced the overwrite data on In–Se phase-change material in 1986 [16]. The critical cooling rate depends on the constituent atomic elements and their concentrations. Our experiments [14] have allowed us to estimate that the critical cooling rate of the GeTe–Sb_2Te_3–Sb system is 3.4 K/ns, which is sufficient for application as direct overwrite media at linear speed above 8 m/s.

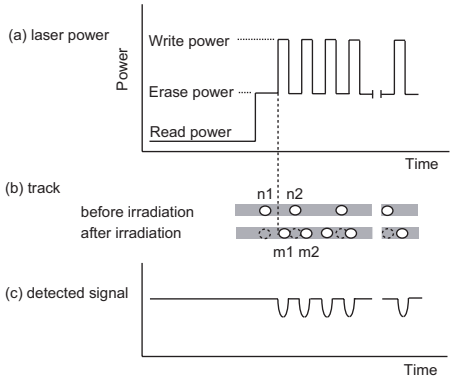

Figure 18.2: Direct overwriting method by optical mean only on phase-change optical disc [15, 16].

Figure 18.2 illustrates the operating principle of phase-change overwriting: Figure 18.2(a) shows a laser power modulation waveform, Fig. 18.2(b) shows written marks on a track before and after overwriting, and Fig. 18.2(c) shows a read-out signal after overwriting.

18.3 Phase-Change Materials

18.3.1 Bonding Features of Chalcogenide Phase-Change Materials

Chalcogenide compounds are notable for their easy transition from the crystalline state to the amorphous states. Those compounds include the elements Te, Se and/or S, which are in the group VI of the Periodic Table and show the chain structure in the amorphous state [17]. Additive of As in Te works to form the ring network structure as $As_{25}Te_{75}$ [17, 18]. The chain-like bonding in Te and Se is important in facilitating the structural changes.

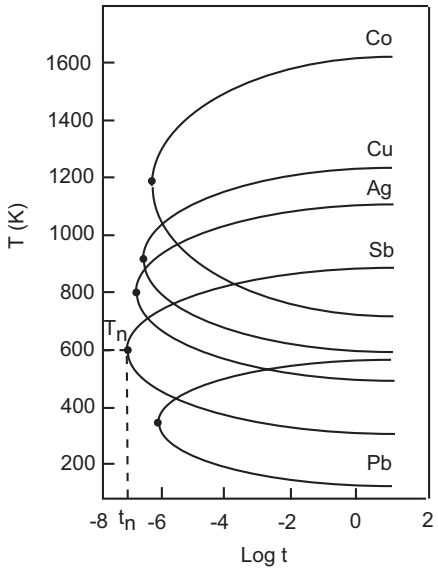

Figure 18.3: T–T–T curve (time–temperature–transformation curve) for Co, Cu, Ag, Sb and Pb elements corresponding to a volume fraction crystallization of 1×10^6 [20].

Okuda et al. reported [19] the mechanism of amorphous-crystalline phase change in terms of Avrami equation and investigated its dynamic transition using T–T–T (time-temperature-transition) curves [20]. The T–T–T curves of Co, Cu, Ag, Sb, Pb are shown in Figure 18.3. The nose temperature (T_n) and the time (t_n) of the temperature coming to T_n, the melting temperature (T_m), and the critical crystallization time (volume fraction of crystallization of 10^{-6}) are given in Table 18.2. The critical cooling rates of crystallization of these elements are given by the equation $R_c = (T_m - T_n)/t_n$. The log R_c values of these elements decrease in the order Sb > Ag > Cu > Co > Pb. These elements will control the crystallization rate of the phase-change materials.

18.3.2 Phase-Change Optical Disc Materials for Optical Disc Memory

Functional phase-change rewritable media can be made based on the $Te_{85}Ge_{15}$ eutectic composition [3, 4, 21]. The melting temperature shows a minimum (375 °C) at the eutectic com-

Table 18.2: Estimated values of T_g, T_g/T_m and calculated values of T_n, t_n, log R_c of elements [19]

Element	T_m(K)	T_g(K)	T_g/T_m	T_n(K)	t_n(s)	Log R_c (K/s)
Sb	895	182	0.20	600	7.41×10^{-8}	9.61
Ag	1235	250	0.20	800	2.98×10^{-7}	9.16
Cu	1357	298	0.22	900	3.38×10^{-7}	9.13
Co	1768	445	0.25	1200	6.54×10^{-7}	8.94
Pb	601	152	0.25	375	7.07×10^{-7}	8.50
Te	722	285	0.39	500	5.75×10^{-6}	7.54
Ge	1212	750	0.62	945	8.96×10^{-4}	5.47

position, and it is expected that the viscosity will increase at this composition. Addition of small amounts of Sb and S increases both ease of formation and stability of the amorphous phase as e.g. in the material of composition $Ge_{15}Te_{81}Sb_2S_2$ [3].

Phase-change materials for overwriting by one laser spot need to have high-speed crystallizing characteristics. Three different families of phase-change material systems that are suitable for this application are In–Sb–Te [22], Ge–Te–Sb [6,23-25], Ag–In–Sb–Te [26]. These families have different crystallization processes. The two major kinds of phase change optical disc materials are nucleation dominant materials typified by Ge–Sb–Te, and edge growth dominant materials typified by the $Sb_{69}Te_{31}$ eutectic material system.

In–Sb–Te

Crystalline growth dominates over nucleation in In–Sb–Te. When the erase laser power irradiates written marks to a point where the film just melts, after irradiation recrystallization will proceed from the mark edge and the mark is erased. In the In–Sb–Te alloy, careful choice of overwrite laser power levels allows one to achieve very high erase ratios.

GeTe–Sb_2Te_3–Sb (GST)

In GST media, the crystallization process is governed by nucleation rather than crystal growth. Recrystallized amorphous marks in GeTe–Sb_2–Te_3–Sb films have a large number of small crystallites in their grain structure. This suggests a two-step erase process. In the first step, a large number of crystalline nuclei are formed and then crystal grain growth occurs leading to erasure of the amorphous mark. The erase process proceeds in the solid state and the power tolerance becomes comfortably wide. However, the erase ratio is lower than in In–Sb–Te films.

Ohta and Yamada's groups developed the GeTe–Sb_2Te_3–Sb system and achieved a crystallization speed of 30–100 ns with small crystalline grain size [6, 23]. Figure 18.4 shows the crystallization temperature of this system. The latent heat of transformation from crystalline to liquid (16.3 kcal/kg) and amorphous to liquid (8.5 kcal/kg) was obtained from these measurements [27].

Ag–In–Sb–Te (AIST)

The AIST family is generally characterized as having growth dominated crystallization and high erase ratio [26]. The origin of the large erase ratio is ascribed to the low thermal conductivity components present in the thin film structure, which is composed of a mixture of $AgSbTe_2$ phase-change component in an amorphous In–Sb matrix. The overwrite cycle performance of Ag–In–Sb–Te system is around 10 000 or more, and the limitation of this overwrite cycle is still being investigated.

Sb-rich, Sb–Te (FGM)

At the Optical Data Storage Conference in 2000, eutectic composition systems such as $Sb_{69}Te_{31}$ were proposed [28, 29] as fast growth materials (FGM). These crystal growth dominant compositions might be superior for high-density, high data rate recording, phase-change optical discs. As the density of the phase-change optical disc increases, the recorded marks become smaller ($<$200 nm), and growth dominant material can lead to shorter crystallization times. The eutectic composition of $Sb_{69}Te_{31}$ is indicated on the line from Sb_2Te_3 to Sb in Fig. 18.4. The composition at that point is 0.18 (Sb_2Te_3) and 0.82 Sb. The reason why this eutectic composition shows rapid crystallization characteristics is being investigated.

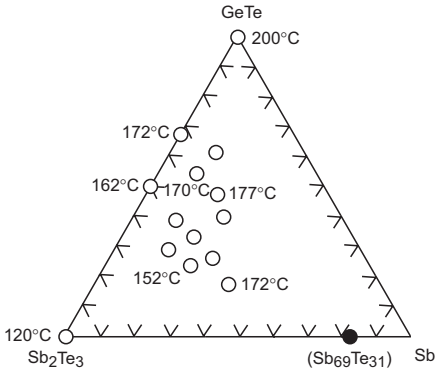

Figure 18.4: Crystallization temperature of quasi ternary GeTe–Sb_2Te_3–Sb alloy system [6]. Heating: 100 °C /min

GaSb system

At the PCOS2002 conference, Okuda suggested that explosive material elements such as Ga, Ge, and Sb will assist the crystallization process and Tashiro announced high-speed crystallization material in the GaSb system [30, 31].

18.4 Breakthrough Technologies of the Phase-Change Optical Disc Media

18.4.1 Basic Layer Structure

In the early phases of its development, the most important subject of phase-change optical discs was performance degradation over write–erase cycles. A basic phase-change optical disc is a four-layer structure. The four layers are a bottom dielectric layer (155 nm), an active layer (24 nm), an upper dielectric layer (45 nm), and a reflection layer (100 nm).

The total layer structure design is based on optical and thermal considerations. The first priority is the amplitude of the optical signal. This corresponds to the reflection difference between that of the amorphous state (R_a) and of the crystalline state (R_c). These reflectivities can be calculated using multi-layer optical methods. Next, the disc sensitivity is optimized by simultaneously considering optical absorption for the amorphous state and for the crystalline state, and the thermal structure to introduce a rapid cooling structure.

In early phase-change media, the overwrite cycle life characteristics on a spinning disc were rather small compared with the static cycle test. This was resolved by selecting materials that are thermally stable and whose thermal expansion coefficients are rather small. The optical, thermal, and mechanical characteristics of the layers used in phase-change optical disc media are summarized in Table 18.3. One difficulty in modeling the thermal characteristics of recordable optical media is use of accurate values for the thermal constants. The thermal coefficients of most materials are different when in bulk and thin-film forms. Peng and Mansuripur addressed this issue by developing a new method for measurement of the thermal coefficients of the layers in phase-change optical disc media. This method can determine the coefficients of the various layers by reflectivity measurements of heated and laser-exposed samples [32]. The principle of this elegant method is use of the basic thermal diffusion equation along with known transition temperatures for melting and the crystallization of phase-change thin films [32, 33].

The newly developed materials of GeTe–Sb_2Te_3–Sb used in the active layer and ZnS–SiO_2 used in the protective layer have resolved the issue of variations of signal amplitude and noise level with cycle life. The grain size of ZnS–SiO_2 is very small at around 2 nm [34]. The ZnS–SiO_2 dielectric layer is thermally stable and does not show grain growth even after annealing at 700 °C for 5 min.

18.4.2 Million Overwrite Cycle Phase Change Optical Disc [6]

Another degradation mechanism which has to be counteracted to extend rewrite cycle life is space deformation of the disc layers on a sub-nanometer level, which works as a motive force for sub-nanometer displacement of the active layer components. The deformation is driven by thermal expansion of the layers during the recording process. The deformation is generally asymmetric along the laser scanning direction, greater toward the forward edge and less toward the backward edge. Inoue et al. calculated the thermal deformation of the phase-change optical disc layers [35] during the recording process. This phenomenon can be reduced by adding a layer that has small thermal expansion coefficient between the phase-change layer and the upper dielectric layer. The thermal expansion coefficient of SiO_2 (5.5×10^{-7}) and of

Table 18.3: Optical, mechanical and thermal properties of materials

Material	Refractive index $\lambda = 650$ nm	Density (kg/m^3)	Young's modulus (N/m^2)	Poisson's ratio	Specific heat (J/(kg K))	Thermal conductivity W/(m K)	Coefficient of linear expansion
GeTe–Sb_2Te_3–Sb (Amorphous)	$4.21 + 1.89$i	—	—	—	—	—	—
GeTe–Sb_2Te_3–Sb (Crystalline) 2:1:0.5 (mol ratio)	$4.56 + 4.23$i	6150	5.49×10^{10}	0.33	0.209×10^3	0.581	1.1×10^{-5}
ZnS–SiO_2 4:1 (mol ratio)	2.0	3650	7.81×10^{10}	0.2	0.563×10^3	0.657	7.4×10^{-6}
SiO_2	1.46	2202	7.81×10^{10}	0.2	0.753×10^3	1.313	5.5×10^{-7}
Al alloy	$2.2 + 7.5$i	2750	7.03×10^{10}	0.345	0.892×10^3	0.215×10^3	2.2×10^{-5}
Polycarbonate	1.58	1200	2.26×10^9	0.3	0.126×10^2	0.223	7.0×10^{-5}

ZnS–SiO_2 (6.1×10^{-6}) serves this purpose very well. Use of an added SiO_2 layer increases the dynamic overwrite cycle characteristics to over 2×10^6 cycles [6, 35]. The new five-layer structure, which has the additional SiO_2 layer, shows more than 1 000 000 overwrite cycles. Figure 18.5 shows more than 2 million cycle characteristics of the phase-change optical disc with the additional SiO_2 layer [6, 35].

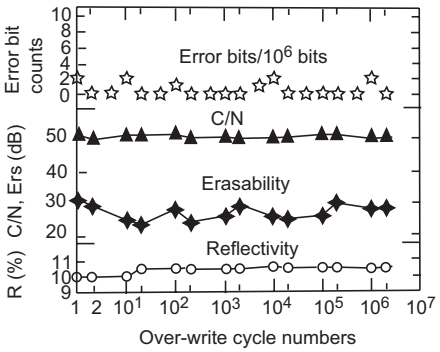

Figure 18.5: Two million overwrite cycle test results of phase-change optical disc with additional SiO_2 protection layer [6].

The sensitivity of the phase-change optical disc was rather low in the first commercial disc products, requiring 21 mW of laser power on the disc. We found that the sensitivity and the cycle characteristics are basically not a trade-off relation. It has been shown that the overwrite cycle characteristics and record sensitivity can be simultaneously optimized, and the high sensitivity PD phase-change optical disc was developed that has more than 500 000 overwrite capability and 10 mW recording sensitivity optimized through layer thickness [36].

18.5 Thin Substrate Technology of Phase Change Optical Disc Promotes DVD

Increased storage density can be achieved in optical discs by using more powerful, larger numerical aperture (NA) lens to form a smaller laser spot. However, the sensitivity to tilt angle in the disc increases dramatically with increasing numerical aperture. Satoh and Ohta were the first to demonstrate that a thin disc substrate, which is effective for resolving the disc tilt sensitivity at high numerical aperture, could be successfully made and used in an optical disc during high-density recording [37]. Their system combined emerging technologies such as a red laser diode, a large numerical aperture (0.6) lens, and thin disc substrate (0.6 mm) [37, 38]. They proposed a high-density 90 mm diameter phase-change optical disc for ISO standardization in 1995 [39]. Figure 18.6 shows the crosstalk characteristics of optical discs made using 1.2 mm and 0.6 mm substrates with a high numerical aperture lens (NA = 0.6). As can be seen in the figure, the thinner substrate shows lower crosstalk than the thick substrate disc when the tilt angle increases. These technologies were adopted into DVD in 1995.

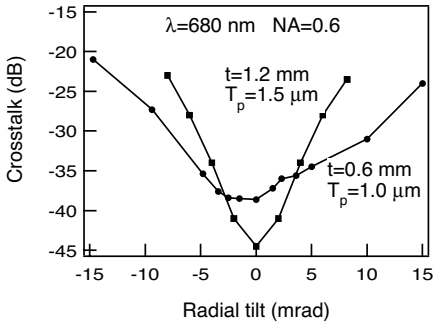

Figure 18.6: Comparison of the tilt angle dependence of crosstalk for substrate thickness of $t = 1.2$ mm and thin substrate of $t = 0.6$ mm [37]. Lens numerical aperture: NA = 0.6. Laser wavelength: 680 nm.

A simple overwrite disc function and compatibility of the phase-change with ROM discs is also featured in the DVD specification of rewritable DVD-RAMs, DVD-RWs and +RWs.

18.6 High-Density Recording Technologies for Phase Change Optical Discs

18.6.1 Short-Wavelength Blue Laser and High Numerical Aperture Lens Recording

Phase-change optical storage discs have high signal output and record sensitivity over a wide spectrum of light from infrared of 830 nm to blue–violet of 405 nm. When blue laser light of wavelength 425 nm and lens numerical aperture of 0.6 [40] are applied, the recording density is estimated to be 9 Gbit/in^2. The next increase in recording density will result from a combination of an even larger numerical aperture lens and a short wavelength (405 nm) blue laser. The newly proposed blu-ray disc technology incorporates these components with a 0.85 numerical aperture lens and a new disc structure incorporating a thin (0.1 mm) cover layer, with recording and reading of the data done through the thin, cover-layer side. This new system has a recording capacity of 22.4 GB/side on a 120 mm diameter disc [41].

18.6.2 Dual-Layer Recording

Another approach to increase the storage capacity is dual-layer recording, creating volumetric rather than two-dimensional surface recording. Dual-layer DVD optical discs that read out from one side have been commercialized for 8.5 GB discs for longer cinema titles. Nagata et al. announced a phase-change rewritable dual layer optical disc also having a capacity of 8.5 GB, and a density of 6.4 Gbit/in^2, nearly doubling the previous density [42]. The first layer in a dual-layer, phase-change optical disc should have transmission of about 50% in the crystalline state for recording in the second layer through the first layer. Using a blue laser with a 0.6 NA lens gives a capacity of 27 GB in a dual-layer disc [43].

Blue lasers and a high (0.85) NA lens can be used together in dual-layer, phase-change optical discs and this combination increases the density even more. The recording capacity of the dual-layer structure is between 40 GB and 50 GB/side, and the carrier-to-noise ratios (CNRs) of the layers are 51 dB and 49 dB, respectively [44, 45].

18.6.3 Multi-Level Recording

A third approach to increased storage density is multi-level (ML) recording on phase-change optical discs. Ovshinsky demonstrated ML recording of phase-change electric switching memory in 1997, showing 16 switching levels [46]. ML recording, for example, 4-ary recording gives $\log_2 4 = 2$ bits per mark, doubling the recording density of conventional binary recording.

ML recording requires a high C/N ratio for accurate detection of the M-ary signal. At ODS2000, O'Neil and Wong demonstrated eight-level phase-change recording technology and announced a CD-RW system having a capacity of 2 GB [47]. Horie et al. proposed a new recording strategy for multi-level recording on a phase-change optical disc, the phase-change film material being FGM [48]. Flynn et al. proposed In–(SbTe) as a new material for ML recording media and found that slow melt crystallization characteristics are required for high-quality signal recording [49].

Ohta et al. proposed to divide this large reflectivity signal into multi-level signals on a phase-change optical disc using the Mark Radial Width Modulation (MRWM) method [50].

Although most multi-level recording strategies use a fixed mark length, Honguh and Murakami proposed a run-length-limited (RLL) code for multi-level recording adding spacing to the minimum and maximum run-length constraints. This code shows a magnification factor of 1.76 for a (1,7) code applied to multi-level recording [51].

Miyagawa and Mansuripur showed a different multi-level recording method using a phase-change optical medium. They define 256 distinct patterns that are each recorded in a data block length of 1.6 μm. Each block corresponds to 8 bits of information [52]. Tsu and Strand demonstrated that the short pulse write strategy improves the mark shape and mark edge quality [53].

18.6.4 Near-Field Recording and Super-RENS Recording

The storage capacity of optical media can be increased by using more powerful high NA lenses. Terris et al. proposed to use a solid immersion lens (SIL) [54] which has a numerical aperture larger than 1.0. Kishima et al. developed a near-field optical head using a super-hemispherical solid immersion lens (Super-SIL) to increase recording density of phase-change optical discs [55]. They used a spin on glass (SOG) disc medium designed to optimize the coupling of the evanescent field present in near-field systems. The laser beam is incident on the coated side of the disc, which is coated with a multi-layer stack comprised of SiN (25 nm) / SiO_2 (SOG) (82 nm groove and 57 nm land)/SiN (20 nm)/ZnS–SiO_2 (85 nm)/$Ge_2Sb_2Te_5$ (12 nm)/ZnS–SiO_2 (20 nm)/Al alloy (100 nm)/glass substrate. In order to couple efficiently the evanescent field to the medium, the air gap between the disc surface and the optical head is only 50 nm. A recording density of 50.4 Gbit/in^2 is achieved using an extremely small 160 nm track pitch and an 80 nm minimum bit length.

In 1999, Tominaga announced a new high-density recording method called Super-RENS (Super-REsolution Near-field Structure) that can record and read marks beyond the diffraction limit [56]. Super-RENS is unique for optical near-field recording whose near-field aperture is generated within the optical disc itself with an added Sb mask layer. During the recording process, the laser spot heats up the Sb layer, which shows non-linear optical characteristics at higher temperatures. When the laser beam heats the Sb layer in the center of the Gaussian spot, a small aperture opens and functions to create an evanescent field so the laser can record marks smaller than the diffraction limit. Recently Super-RENS media using AgOx as the mask layer were reported showing an improved CRN of 32 dB using reflection readout mode at a mark size of 200 nm [57]. For comparison, in a conventional 4.7 GB DVD, the minimum mark size is 400 nm. Super-RENS near-field recording shows potential for four times higher density recording.

18.6.5 High Data Rate, High-Density Recording on Phase-Change Disc

The maximum data rate of a phase-change optical disc is related to the crystallization speed of the active layer. When overwriting data on the track, the previously recorded data are erased by the laser spot within the time the spot traverses over each location on the disc. Rewritable DVD materials such as GST and AIST have a crystallization time of 30–50 ns and, therefore, have the characteristic of a more than 10 Mbps recording data rate. A second limit comes from the cooling speed of the disc structure. If the cooling speed is low, the laser spot cannot form amorphous marks because the heat does not diffuse away fast enough to quench the amorphous structure. At ISOM2001, Kato et al. announced a 140 Mbit/s recording rate [58] in the disc structure with a rapid cooling layer of Al_2O_3, and using an AIST recording material modified with germanium.

18.6.6 Combination Technology

Short-wavelength blue lasers increase the density by the ratio of the wavelength $(650/405)^2$ to produce an increase of about 2.6-fold.

Introducing a magnification factor of multi-level recording of $M = 4(\times 1.76)$, the recording density will further increase. Using a combination of multi-level recording with a dual layer disc structure and blue lasers, the density reaches 30G bit/in^2 with a 0.6 lens NA.

The second strategy to increase storage density is to use a lens of 0.85 NA and a 0.1 mm thin overcoat layer. The recording density can be double $[(0.85/0.6)^2]$ that of a conventional DVD by using the larger numerical aperture lens. The recording density is predicted to be 60 Gbit/in^2 and the capacity will rise to 83 GB on a single side of a 120 mm disc. Figure 18.7 shows the area recording density growth of phase-change optical discs.

The Super-RENS effect can be combined with the above technologies, resulting in the potential for increasing the density by a factor of four to achieve 240 Gbit/in^2 in the future.

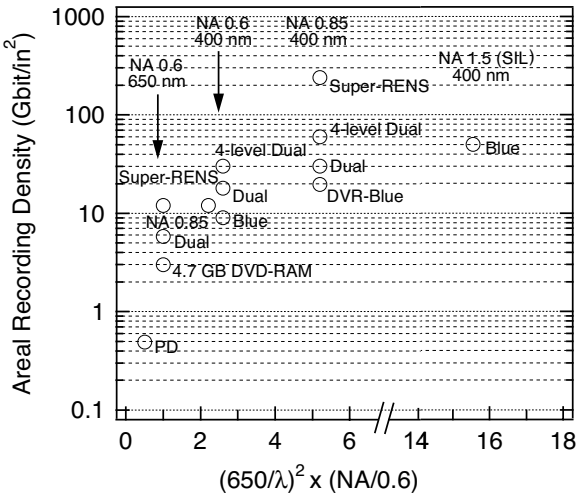

Figure 18.7: Area recording density growth of phase-change optical disc.
Version 1 ($\lambda = 830$ nm, NA $= 0.5$). PD ($\lambda = 780$ nm, NA $= 0.5$). 4.7 GB DVD-RAM ($\lambda = 650$ nm, NA $= 0.6$). 50 GB dual-layer disc, blue wavelength, NA $= 0.85$. multi-level recording. Super-RENS (640 nm, NA $= 0.6$).

18.7 Future Directions of the Phase-Change Storage Media

18.7.1 Ultra Short Pulse (Femtosecond) Laser Recording

Recent advances in lasers having pulse widths in the pico- and femtosecond regime have allowed new studies of materials. High-speed fiber communication, high-resolution laser processing and ultra short time resolution measurements are important applications. Femtosecond laser pulses are used to observe ultra high-speed chemical reactions and bio-molecular dynamics. Photo-induced refractive index changes in silicate glass induced by multi-photon absorption process [59] can be observed using 120 fs laser pulses at a laser wavelength of 800 nm. Laser processing on metals and ceramics can be done almost without laser ablation using femtosecond laser irradiation.

Although phase changes are initiated by direct electronic excitation through optical absorption, the thermal energy created when the electrons drop to their ground state must be controlled in order to provide for optimal recorded mark formation. The heating time of the phase-change material as a result of conventional laser spot recording on a disc is rather long and therefore there is substantial heat diffusion during the recording process. Heat diffusion accompanying conventional laser recording can limit the performance of future high-density and high data rate optical discs. Space that is heated by thermal diffusion must be left between the recorded marks. The variation of the position of the mark and its edges during writing are the major limiters jitter characteristics and hence conventional recording density.

Ohta et al. were the first to examine the response of phase-change thin film media to femtosecond laser pulses to investigate capabilities for ultra short pulse laser recording [60].

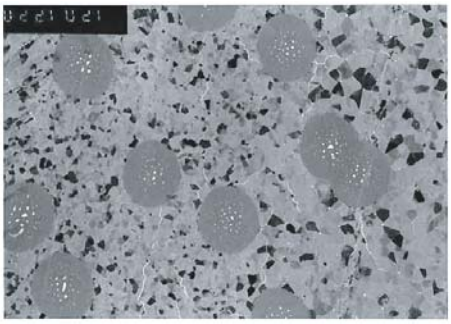

Figure 18.8: TEM observation of amorphous marks formed by femtosecond laser pulse on the phase-change optical disc media [60].

The sample disc had a structure comprised of a polycarbonate substrate/155 nm ZnS–SiO_2 layer/24 nm GeSbTe layer/ 45 nm ZnS–SiO_2 layer. The disc did not have the conventional reflection layer. The femtosecond laser beam was incident on the coated side. Figure 18.8 shows the transmission electron microscope (TEM) observation of the mark formed by the 120 femtosecond laser exposure. Shaw et al. predicted femtosecond switching in Ovonic memory devices [61], and this experiment shows that order-to-disorder phase-change can be completed using a single 120 femtosecond laser pulse. The femtosecond response experiment of the phase-change materials and the observations of the process provide mean to more fully expand the fundamental understanding of the phase-change phenomena. This first experiment shows the amorphous mark recording data rate of phase-change optical disc is expected to be more than Tbit/s.

18.8 Conclusion

An innovative proposal of Ovshinsky on amorphous phase-change memory in 1968 was attractive for the material science and research and technology development field. Due to engineering and analytical efforts the advantage of this technology became obvious. A million-overwrite cycle performance of the phase-change optical disc was a major breakthrough in the technology which realized the first product. The next major step in high-density rewritable phase-change optical disc development was the use of a thin disc substrate which led to a appearance of DVDs and rewritable DVDs in 1996. These consumer-use rewritable phase-change optical disc became the mainstream of the optical disc world. Phase-change technology can be expected to advance significantly in the coming decades. Optical discs with dramatically increased density (240 Gbit/in^2) and data-processing rate (Tbit/s) are expected in the near future.

Acknowledgments

The authors are grateful to all members of ECD (Energy Conversion Devices Inc.), in particular to Dave Strand, David Tsu and Kelly D. Flynn for their innovative work on amorphous ma-

terials. Also important contributors to optical disc development are Noboru Yamada and Isao Satoh at Matsushita. The authors appreciate important contributions to phase-change optical disc storage made by Koichiro Kishima (Sony), Michikazu Horie (Mitsubishi Chemical), Tatsuya Kato (TDK), Junji Tominaga (AIST), Naoyasu Miyagawa, Kenji Narumi (Matsushita), whose excellent results were discussed in this chapter.

Our thanks are extended to Masud Mansuripur of the Optical Science Center of the University of Arizona for profitable discussions and collaborative research on optical storage. The authors would like to express their deep gratitude to Iris Ovshinsky for her immense help and kind support of all our work on phase-change amorphous materials.

References

[1] S.R. Ovshinsky, Phys. Rev. Lett. **21**, 1450 (1968).

[2] E.J. Evans, J.H. Helbers, and S.R. Ovshinsky. J. Non-Cryst. Solids **2**, 334 (1970).

[3] J. Feinleib, J. de Neufville, S.C. Moss, and S.R. Ovshinsky, Appl. Phys. Lett. **18**, 254 (1971).

[4] S.R. Ovshinsky and H. Fritzche, Metall. Trans. **2**, 641 (1971).

[5] S.R. Ovshinsky and P.H. Klose, J. Non-Cryst. Solids, **8-10**, 892 (1972).

[6] T. Ohta, M. Uchida, K. Yoshioka, K. Inoue, T. Akiyama, S. Furukawa, K. Kotera, S. Nakamura, Proc. SPIE **1078**, 27 (1989).

[7] Panasonic Catalog, Mutlifunction rewitable optical disc, LF-7110 (1990).

[8] Panasonic Catalog, Rewritable optical disc DVD-RAM 4.7GB, LF-D100J, DY-HB47(2000).

[9] M.H. Cohen, H. Fritzsche, and S.R. Ovshinsky, Phys. Rev. Lett. **22**, 1065 (1969).

[10] S.R. Ovshinsky, Symmetrical current controlling device, USP 3 271 591.

[11] S.R. Ovshinsky, Method and apparatus storing and retrieving information, USP 3 530 441.

[12] T. Ohta, M. Takenaga, N. Akahira, and T. Yamashita, J. Appl. Phys. **53**, 8497 (1982).

[13] T. Yoshida, T. Ohta, and S. Ohara, Proc. SPIE **329**, 40 (1982).

[14] T. Ohta, K. Inoue, S. Furukawa, T. Akiyama, M. Uchida, and S. Nakamura, Electro. Commun. Tech. Res. Meet. Rep. CPM89-84 (1989) p. 41.

[15] T. Ohta, T. Nakamura, N. Akahira, and T. Yamasita, Method of overwrite optical disc media, Japanese patent No. 1668522.

[16] M. Terao, N. Nishida, Y. Miyauchi, S. Horigome, T. Kaku, N. Ohta, Proc. SPIE **695**, 105 (1986).

[17] R. Grigorovici, Amorphous and liquid semiconductors, J. Tauc (Ed.), Plenum Press, London, 1974, chapter 2.

[18] J. Cornet and D. Rossier, J. Non-Cryst. Solids **12**, 85 (1973).

[19] M. Okuda, H. Naito, T. Matsushita, JJAP Series 6, Proc. Int. Symp. on Optical Memory, 1991, p. 73.

[20] H.A. Davies, Phys. Chem. Glasses **17**, 159 (1976).

[21] W. Klemm and G. Frischmuth, Z. Anorg. Chem. **218**, 249 (1934).

[22] Y. Maeda, H. Andoh, I. Ikuta, M. Nagai, Y. Katoh, H. Minemura, N. Tsuboi, and Y. Satoh, Appl. Phys. Lett. **54**, 893 (1989).

[23] N. Yamada, E. Ohno, N. Akahira, K. Nishiuchi, K. Nagata and M. Takao, Proc. Int. Symp. on Optical Memory, 1987, p. 61.

[24] M. Suzuki, I. Doi, K. Nishimura, I. Morimoto, and K. Mori, Proc. Optical Memory Symposium'88, 1988, p. 41.

[25] N. Kh. Abrikosov and G.T. Danilova-Dobroyakova, Inorg. Mater. **1**, 187 (1965).

[26] H. Iwasaki, Proc. SPIE **3109**, 12 (1997).

[27] N. Yamada, E. Ohno, K. Nishiuchi, and N. Akahira, J. Appl. Phys. **69**, 2849 (1991).

[28] G.F. Zhou, H.J. Borg, J.C.N. Rijpers, M.H.R. Lankhorst, and J.J.L. Horikx, Proc. SPIE **4090**, 108 (2000).

[29] M. Horie, T. Ohno, N. Nobukuni, K. Kiyono, T. Hashizume, and M. Mizuno, Proc. SPIE **4342**, 77 (2001).

[30] M. Okuda, H. Inaba, and S. Usuda, Proc. PCOS2002, 2002, p. 1.

[31] H. Tashiro, M. Harigaya, K. Ito, M. Shinkai, K. Tani, N. Yiwata, A. Watada, K. Makita, and K. Kato, Proc. PCOS2002, 2002, p. 11.

[32] C. Peng and M. Mansuripur, Appl. Opt. **39**, 2347 (2000).

[33] C. Peng and M. Mansuripur, Measurement of the thermal coefficients of rewritable phase change optical recording media, ODSC (Optical data storage center of The State Univ. of Arizona), Semi-annual Report, July 31, 2001.

[34] T. Ohta, K. Inoue, S. Furukawa, K. Yoshioka, M. Uchida, and S. Nakamura, Rapid cooling phase-change optical disc with ZnS–SiO2 dielectric layer, Electro. Commun. Tech. Res. Meet. Rep. CPM90-35, 1990, p. 43.

[35] K. Inoue, S. Furukawa, K. Yoshioka, K. Kawahara, and T. Ohta, Proc. ASME **2**, 593 (1992).

[36] T. Ohta, K. Yoshioka, H. Isomura, T. Akiyama, and R. Imanaka, Proc. SPIE **2514**, 302 (1995).

[37] T. Ohta, K. Inoue, T. Ishida, Y. Gotoh and I. Satoh, Jpn. J. Appl. Phys. **32**, 5214 (1993).

[38] T. Sugaya, T. Taguchi, K. Shimura, K. Taiara, Y. Honguh, and H. Satoh, Jpn. J. Appl. Phys. **32**, 5402 (1993).

[39] 1.3 GB 90 mm Phase-change optical disc, ISO/IEC JTC: Project 1.23.14760, 1995.

[40] M. Kato, Y. Kitaoka, K. Yamamoto, and K. Mizuuchi, MORIS/ISOM 97, Yamagata, Tech. Digest of Joint MORIS/ISOM 97, 1997, We-F-01, p. 46.

[41] M.J. Dekker, N. Pfeffer, M. Kuijper, I.P.D. Ubbens, W.M.J. Coene, E.R. Meinders, and H.J. Borg, Proc. SPIE **4090**, 28 (2000).

[42] K. Nagata, K. Nishiuchi, S. Furukawa, N. Yamada, and N. Akahira, Jpn. J. Appl. Phys. **38**, 1679 (1999).

[43] T. Akiyama, M. Uno, H. Kitaura, K. Narumi, K. Nishiuchi, and N. Yamada, Jpn. J. Appl. Phys. **40**, 1598 (2001).

[44] K. Narumi, S. Furukawa, T. Nishihara, H. Kitaura, R. Kojima, K. Nishiuchi, and N. Yamada, Tech. Digest ISOM2001, 2001, Fr-K-02, p. 202.

[45] K. Hayashi, K. Hisada, and E. Ohono, Tech. Digest ISOM2001, 2001, Pd-33, p. 312.

[46] S.R. Ovshinsky, Proc. 9th Symp. on Phase Change Recording, PCOS1997, 1997, p. 44.

[47] M.P. O'Neill and T.L. Wong, Tech. Digest ODS2000, 2000, WB2, p. 170.

[48] K. Kiyono, M. Horie, T. Ohno, T. Uematsu, T. Hashizume, M.P. O'Nell, K. Balasubramanian, R. Narayan, D. Warland, and T. Zhou, Tech. Digest ISOM2000, 2000, MC1, p.37.

[49] K.D. Flynn, D. Strand, and T. Ohta, Proc 14th Symp, PCOS2002, 2002, p. 43.

[50] T. Ohta, K. Nishiuchi, K. Narumi, Y. Kitaoka, H. Ishibashi, N. Yamada, and T. Kozaki, Jpn. J. Appl. Phys. **9**, 770 (2000).

[51] Y. Honguh and T. Murakami, Electron. Commun. Jpn. Part 3, **77**, 85 (1994).

[52] N. Miyagawa and M. Mansuripur, Tech. Digest ISOM2001, 2001, Fr-N-04, p. 240.

[53] D. Tsu and D. Strand, Proc. SPIE **4342**, 124, 2001, p. 124.

[54] B.D. Terris, H.J. Mamin, D. Rugar, W.R. Studenmund, and G.S. Kino, Appl. Phys. Lett. **65**, 388 (1994).

[55] K. Kishima, I. Ichimura, K. Saito, K. Yamamoto, Y. Kuroda, A. Iida, S. Masuhara, and K. Osato, Jpn. J. Appl. Phys. **41**, 1894 (2002).

[56] J. Tominaga, Tech. Digest ODS99, 1999.

[57] H. Fuji, J. Tominaga, L. Men, T. Nakano, H. Katayama, and N. Atoda, Jpn. J. Appl. Phys. Part (1) **39**, 980 (2000).

[58] T. Kato, H. Hirata, H. Inoue, H. Shingai, and H. Utsunomiya, Tech. Digest ISOM2001, 2001, Fr-K-01, p. 200.

[59] K. Miura, J. Qiu, H. Inoue, T. Mitsuyu, and K. Hirao, Appl. Phys. Lett. **71**, 3329, 1997.

[60] T. Ohta, N. Yamada, H. Yamamoto, T. Mitsuyu, T. Kozaki, J. Qiu, and K. Hirao, MRS 2001 Spring, Proc. Vol. 674 (2001) V1.1.1.

[61] M.P. Shaw, S.H. Hilmberg, and S.A. Kostylev, Phys. Rev. Lett. **23**, 521 (1973).

19 Application of Ge–Sb–Te Glasses for Ultrahigh-Density Optical Storage

Junji Tominaga

Te-based chalcogenides remain materials of interest for ultrahigh density optical data storage. A multilayer combination of GeSbTe and Sb allows one to obtain less than 100 nm optical resolution due to electromagnetic field interaction between optical near-field and surface plasmons generated on the films. Super-resolution near-field structure (super-RENS) may provide new ideas for applications of chalcogenide thin films.

19.1 Introduction

Chalcogenide glasses, mainly composed of Ge, Sb and Te, have long been attracting attention as one of the key materials for erasable optical data storage [1–3]. In the late 1990s, research and development activities finally led to the realization of optical data storage with a 4.7 GB capacity in a 12 cm plastic disc, the so-called digital versatile disc random access memory (DVD-RAM) [4, 5]. Here, a GeSbTe thin glass film with a thickness of only 20 nm is used for photo-thermal switching between amorphous and crystalline phases for recording and reproducing digital data. As is well known, chalcogenide glasses are photosensitive and a change of the refractive index can also be reversibly induced entirely within the amorphous state (reversible photostructural changes). However, the change of the refractive index due to the photostructural change is rather small in comparison with the index change required to reproduce the signals and is not sufficient to circumvent large noise levels caused by the media structure and the laser source. In compact disc, for example, a large contrast in reflection is needed with a modulation of more than 60%.

The usefulness of GeSbTe glasses in optical data storage is determined not only by the large refractive index difference between the amorphous and crystalline states, but also by the structural transition time being matched to the data access speed of computer systems. Since the great invention using TeGeSbS by Ovshinsky in the 1960s [6], laser-induced phase transition and its application to optical data storage have attracted much attention with the objective of developing an erasable type of optical disc systems without any magnetic heads. Especially during the last decade, a great amount of R&D effort was expended by various electric and chemical companies and several universities with the goal to increase the refractive index difference and improve the reliability in erasing cycles. Since the 1980s, different combinations of chalcogenides have been examined, however, only two compounds have finally survived, namely, GeSbTe and AgInSbTe [7, 8]. The most useful and valuable composition in the GeSbTe system is $Ge_2Sb_2Te_5$, which is a pseudo-binary Sb_2Te_3–GeTe composition; the

other two compositions are $GeSb_4Te_7$ and $GeSb_2Te_4$. As is well known, $Ge_2Sb_2Te_5$ glass is now used as a recording layer of DVD-RAM. On the other hand, several different compositions of AgInSbTe are adapted in compact disc re-writable (CD-RW) and DVD-RW discs. With both $Ge_2Sb_2Te_5$ and AgInSbTe glasses, the storage capacity in a 12 cm disc is expected to be pushed up to 25-30 GB in the near future by using a 405 nm blue laser source. In order to increase further the storage capacity of optical disc (up to 100 GB), a modified structure and recording method have been proposed such as a multilayer medium with double recording layers and mark area recording. However, almost all current optical readout systems utilize *far-field optics* which imposes the diffraction limit on their resolving power, similar to Heisenberg's uncertainly principle in quantum physics [9]. In other words, the optical beam spot size cannot be reduced beyond the diffraction limit, which is defined as

$$\Phi > \lambda/(2NA) \tag{19.1}$$

Here, Φ, λ and NA are the laser spot diameter, light wavelength and numerical aperture ($<$1.0) of the lens, respectively. As two marks or pits are not allowed in the same spot, the mark resolution readable in the optical system Δ is Φ/2. In the most advanced optical system using a blue laser (405 nm), the available lens NA is 0.85. These values limit the resolution Δ at 120 nm. As long as the *far-field optics* is used, the resolution is strictly determined by Eq. (19.1).

In order to overcome the limitations imposed on Δ by the *far-field optics* and to increase the optical capacity further beyond 100 GB, application of *near-field optics* was proposed in the early 1990s and several different types of near-field recording (NFR) have been developed [10–12]. To realize NFR with higher data capacity, one has to take care of both the recording media and the detailed nature of *near-field optics* including *surface* or *localized surface plasmons*. In the initial stages of research it was not clear whether the current optical recording materials – GeSbTe and AgInSbTe – were still applicable to record rigidly a small size pit or mark in a less than 100 nm region and to hold it thermally stable for a long time at room temperature. It was also unknown if the refractive index change caused by the structural phase transition of the chalcogenides can produce a large enough optical contrast (modulation) by electromagnetic field coupling with optical near-field generated very close to the layer. Although such unavoidable issues have been unsolved, the research and development of NFR have been carried out due to the efforts of few chemists who have joined the research.

In this chapter, we describe NFR from the point of view of chemistry and materials science, and discuss the future of NFR with optical nonlinear films.

19.2 Optical Near-Field and Surface Plasmons

Optical near-field is a non-propagating electromagnetic field, the so-called trapped light or a photon at a small optical aperture (smaller than the wavelength of the light) or at a protrusion of a metallic surface. Unlike propagating far-field light, the electromagnetic near-field intensity exponentially reduces with the distance from the aperture or the protrusion. Let us imagine a pinhole on a non-transparent screen as shown in Fig. 19.1. A relatively large hole whose diameter of more than the wavelength of the light is depicted in Fig. 19.1(a), and a small hole whose diameter is less than the wavelength of the is shown in Fig. 19.1(b).

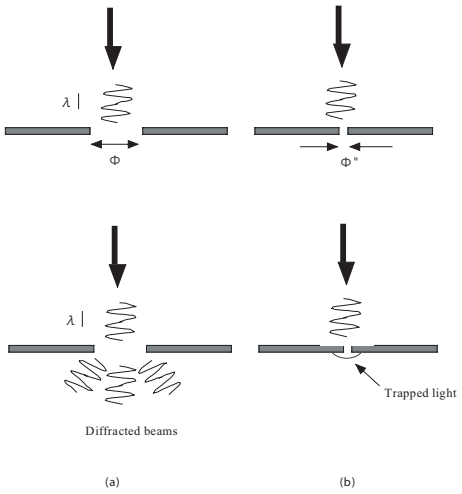

Figure 19.1: Diffraction from pinholes. (a) Diameter ϕ is lager than the incident light wavelength λ, and (b) smaller than the wavelength.

The Fraunhofer diffraction problem is easily solved [9], and the diffraction angle θ_m is given by

$$\phi \sin\theta_m = m\lambda \tag{19.2}$$

Here, ϕ is the pinhole diameter, λ is the wavelength of the light, and m are integers ($\pm 1, 2, 3, \ldots$). Therefore, if $\phi > \lambda$, Eq. (19.2) can be satisfied; however, $\sin\theta_m$ has to be >1, if we require $\phi < \lambda$. This means that the light cannot penetrate the pinhole and most of the incident light bounces. However, if the screen is made of metal or is covered with a metal thin film, the incident light wave swings electrons on the surface, resulting in the generation of a trapped electrical field at the pinhole. This trapped electromagnetic field is *optical near-field*. According to Eq. (19.2), the field cannot propagate as far-field light or as a diffracted beam because this requires an unrealizable condition of $\sin\theta_m > 1$. Therefore, the trapped photon cannot interact with anything, unless a probe is placed close to the near-field source ($<$100 nm).

Surface plasmon is an electromagnetic field normally generated at an interface between a dielectric medium and a metal [13]. However, the propagation normal to the interface is not allowed, and the intensity reduces exponentially. Both *optical near-field* and *surface plasmon* are thus spatially restricted electromagnetic fields, which are completely or partially prohibited from propagation. In order to generate, for example, a surface plasmon, specific conditions must be satisfied. In Fig. 19.2(a), propagation of electromagnetic field in two different media characterized by ε_1 and ε_2 is schematically shown assuming a two-dimensional model (x–z plane). According to Maxwell's equations the field in the media is described by

$$\mathbf{E} = (E_{1x} + E_{1z}) \exp(jk_{1x}x - jk_{1z}z - j\omega t) \tag{19.3}$$

in medium 1 ($z > 0$) and

$$\mathbf{E} = (E_{2x} + E_{2z})\exp(jk_{2x}x - jk_{2z}z - j\omega t) \tag{19.4}$$

in medium 2 ($z < 0$).

It should be noted that dispersion relationship between k_{is} and ε_i ($i = 1, 2$ and $s = x, z$) is determined by

$$k_{ix}^2 + k_{iz}^2 = (\omega/c)^2\varepsilon_i \qquad (i = 1, 2) \tag{19.5}$$

At the boundary ($z = 0$), the electrical field $\mathbf{E}$ must be equal in medium 1 and 2, that is, $E_{1x} = E_{2x}$ and, according to Eq. (19.4),

$$\varepsilon_1 E_{1z} = \varepsilon_2 E_{2z} \tag{19.6}$$

In addition, the electrical field divergence in each medium 1 and 2 must be zero. Therefore, we obtain the following relationship among ε_i and k_{iz} ($i = 1, 2$):

$$\varepsilon_1/k_{1z} = -\varepsilon_2/k_{2z} \tag{19.7}$$

The dispersion relation of k_x is finally

$$k_x^2 = (\omega/c)^2[\varepsilon_1\varepsilon_2/(\varepsilon_1 + \varepsilon_2)] \tag{19.8}$$

In comparison with Eq. (19.5), in order for the field not to propagate along z, k_{iz} has to be imaginary, but k_x must be real. This condition is only satisfied when one of the dielectric constants ε_i is $\varepsilon_i < 0$ and $\mid \varepsilon_i \mid > \varepsilon_s (i \neq s)$. Generally, dielectric constants of metals have negative values. Therefore, the requirements can be satisfied if one selects a combination of a dielectric medium and metal for generating the surface plasmon. As shown in Fig. 19.2(b), Eq. (19.5) describes a momentum circle composed of k_x and k_z. Both k_x and k_z move on the circle to satisfy the dispersion relation. However, once k_x goes beyond the circle, k_z has to be imaginary in order to satisfy Eq. (19.5). Thus, the electrical field can only propagates along x as a surface plasmon, and the field along the z direction is exponentially reduced.

19.3 GeSbTe Glass and its Characteristics for NFR

As discussed in Section 19.2, the optical near-field and surface plasmons are special electromagnetic fields generated only on a material surface. Although the penetration depth of the field normal to the surface depends on each material, the field intensity is exponentially weakened on a scale of less than 100 nm. However, Eq. (19.2) does not impose any restrictions on the pinhole diameter ϕ and, therefore, the optical near-field is not restricted by the diffraction limit of Eq. (19.1). The intensity of the field localized at a small aperture or pinhole generally decreases as the size becomes smaller. Therefore, if one uses optical near-field in ultrahigh-density optical data storage, the output signals from smaller data pits are weakened as the data storage capacity is increased. This is an important trade-off in any NFR system.

Of course, in order to realize NFR, not only the optics for the recording and readout but also the proper choice of a recording material are very important factors. Although the first

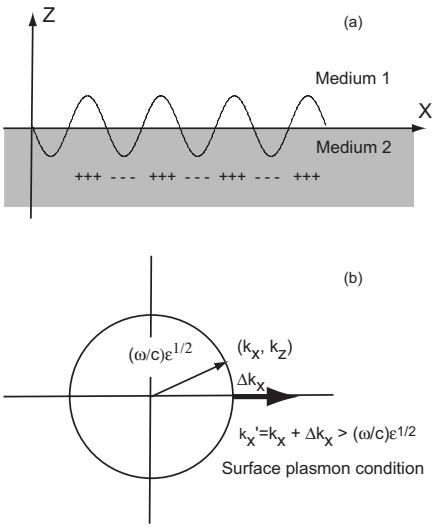

Figure 19.2: A model for the explanation of surface plasmon generation, and (b) the angular momentum relationship between k_x and k_z, for the condition of surface plasmon generation.

NFR was proposed and demonstrated using a magneto-optical (MO) metal alloy, almost all subsequent studies of NFR have been oriented to developing NFR flying heads with a small optical aperture or specially designed lens, the so-called solid immersion lens [12]. Also, numerous and different attempts have been made to control with the needed precision the space required to feel the near-field, the task being complicated by the high-speed requirement in order to increase the data transfer rate up to the current DVD systems [11, 14]. Unfortunately, very few groups including ours have paid sufficient attention to materials [15, 16]. Even now, it remains unknown whether the current magneto-optical or phase-change materials including GeSbTe or AgInSbTe are truly applicable to produce a nanometer-size pit and stable mark. In an MO film, the thermal stability of a magnetic domain is an issue when the mark size is smaller than 100 nm; in phase-change (PC) media, stability of the amorphous mark surrounded by the crystalline phase becomes a fatal issue for such small bit sizes. In both MO and PC data storage, small-size mark recording remains *terra incognita* while reliability at room temperature has to be guaranteed for more than 100 years. Moreover, the media surface has to be tough to withstand a flying NFR head crash, i.e. the surface has to be covered with a hard coating, whose thickness introduces a trade-off with the near-field signal intensity. Because of the nature of the near-field, the medium design should be simpler and thinner ($<$50–100 nm) in order to retrieve the signal intensity with low intensity loss. Otherwise the flying head would cause a crash at the medium surface with a small shock, resulting in data loss in the worst case. Therefore, the recording materials for NFR have to satisfy the following conditions:

1. Large optical contrast of refractive index change before and after recording.

2. Negative dielectric constant of one of the phases.

3. Toughness and hardness.
4. Small crystalline grain and good thermal stability.
5. Smooth surface on a nanometer scale.

From the point of view of the above severe restrictions, unfortunately, GeSbTe can only satisfy the first two conditions; other conditions are not satisfied. Especially the thermal stability of the recorded marks (amorphous) is not high ($\sim$160 °C), because it is expected that a huge amount of laser energy will be dissipated and produce heat around the pinhole in attempts to retrieve the near-field signal with good signal-to-noise ratio (SNR) using a flying NFR head (see Fig. 19.3). Additionally, GeSbTe exhibits a volume change between the amorphous and crystalline states.

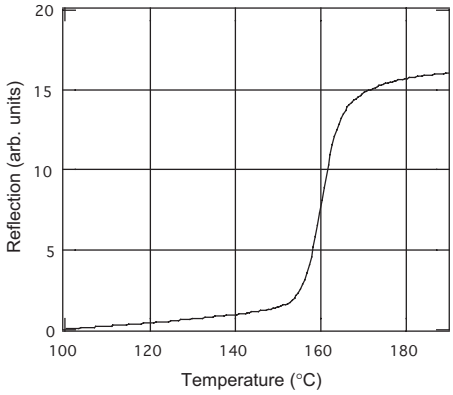

Figure 19.3: Typical phase transition of as-deposited amorphous $Ge_2Sb_2Te_5$ layer against temperature change. The heat ramp rate is 10 °C/min.

Figure 19.4 shows an atomic force microscope (AFM) image of a crystalline GeSbTe mark recorded by using an NFR fiber probe. The film thickness is 50 nm. After the NFR, the thickness is reduced by approximately 10% of the initial thickness. As mentioned before, the near-field intensity decreases exponentially with the distance from the surface. Thus, a 10 nm thickness variation may cause a quite large artifact in the signal intensity. According to the above discussion, we cannot say that GeSbTe glass is a suitable recording medium for NFR.

However, its large optical constant variation before and after the phase transition (the dielectric constants of the crystalline phase and of the as-deposited amorphous phase are $-7.76 - 35.19j$ and $12.58 - 20.03j$, respectively, at 635 nm which is a typical wavelength to read DVD data) is a very attractive property. A protection film generally used in DVD-RAM is a composite of ZnS and SiO_2, whose dielectric constant is 4.41. Therefore, the crystalline phase has a potential to generate a surface plasmon: $k_x > (\omega/c)$, while the as-deposited amorphous area cannot. Thus, surface plasmon is expected to be generated only at the crystalline marks. The extension of the surface plasmon along the crystalline mark is $\sim$170 nm and the plasmon penetration depth is $\sim$40 nm in ZnS-SiO_2 and $\sim$20 nm in GeSbTe [13]. Therefore, the GeSbTe has a potential for reducing the mark size down to 20 nm. This would allow the data capacity to be increased up to 1 Terabyte!

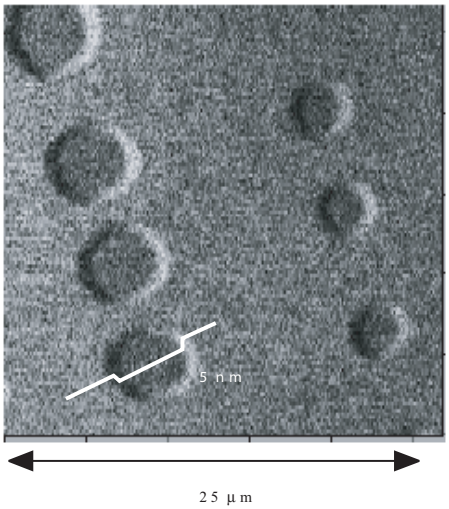

Figure 19.4: AFM image of GeSbTe thin film (50 nm thickness) on a glass substrate by NFR.

19.4 NFR Optical Disc Using GeSbTe Glass

Up to now, we have discussed the issue of NFR and the required characteristics. In order to realize NFR using GeSbTe glass, we need a second probe disturbing the generated near-field or surface plasmon, and evacuating it as light scattering in far-field. A new technique not using mechanical systems – NFR flying aperture or solid immersion lens – but an optical nonlinear Sb film was proposed in 1998 by our group. This multilayered structure is depicted in Fig. 19.5 and is called super-resolution near-field structure (super-RENS). Super-RENS is not a "lens" but works like an objective lens very close ($<$50 nm) to the GeSbTe recording film. A SiN layer (dielectric constant $\sim$4.4 at 635 nm) is sandwiched between the Sb and GeSbTe layers. The Sb film is deposited by sputtering and is crystalline because of the low phase-transition temperature ($<80°$C). The refractive index of the film with a thickness of more than 10 nm is $3.11 + 5.66j$ at 633 nm. The penetration depth of the optical near-field into the Sb film is $\sim$20 nm, and that into SiN is $\sim$100 nm. The extension of the plasmon into the Sb layer is an order of magnitude larger than that into GeSbTe, and is $\sim$1300 nm. The thickness of the Sb film is selected to be about the plasmon's penetration depth. Even when a higher numerical aperture of $\sim$1.0 is used, there is no way to generate surface plasmon at the interface between the SiN and Sb films unless total attenuated reflection is used. On the other hand, if small mark trains are once recorded in the GeSbTe layer, the surface plasmon may be generated over the trains. As discussed above in relation to Eq. (19.2), if the mark size and space between the marks are smaller than the wavelength, the condition $\sin\theta_m > 1$ has to be fulfilled and the incident laser beam partly generates surface plasmon.

The super-RENS was formed on a transparent polycarbonate substrate disc in the order shown in Fig. 19.5 by a vacuum deposition technique such as sputtering, and the disc characteristics were investigated. The disc was set in an optical disc drive tester (DDU-1000, Pulstec

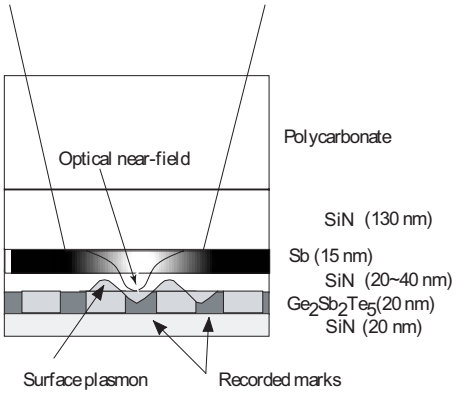

Figure 19.5: Super-resolution near-field structure (super-RENS) using Sb and GeSbTe layers.

Industrial) with a laser wavelength of 635 nm and a lens numerical aperture of 0.6. The laser spot size was approximately 1000 nm, the diffraction limit was ∼530 nm, and the resolution mark size was ∼265 nm. The disc was rotated at a constant linear velocity of 3.0–6.0 m/s and a recording high power laser beam irradiated the disc along tracks to record several different mark trains. The mark sizes could vary. The duty was set at 50%. The recording power of the laser was 5.5 mW. As shown in Fig. 19.6, in reading the recorded tracks containing trains of marks of different sizes (same mark size within the train) with a 1.0 mW readout power, the measured resolution (300 nm) is in good agreement with the theoretical one and smaller mark signals are not at all reproduced. However, smaller marks beyond the resolution limit (down to 60 nm in size) are clearly detected if the readout laser power is increased up to 3.5 mW. Even the 100 nm mark trains possess a carrier to noise ratio of 25 dB.

Figure 19.7 shows actual output signals detected spectrum analyzer at 1.0- and 3.5-mW readout. The signal was reversibly detected (or not) by changing the readout power. The super-RENS effect is scientifically very interesting and has a potential to read out small marks beyond the diffraction limit. The transmission electron microscope (TEM) images of the Sb and GeSbTe layers after the recording of a 150 nm mark trains are shown in Fig. 19.8.

In the recording track (groove), the 150 nm marks were not clearly identified in the $Ge_2Sb_2Te_5$ layer. Rather unexpectedly, the recorded marks seem to be crystalline. At the same time, the non-recorded area also changed to the crystalline state. The non-recorded lands clearly show the as-deposited amorphous phase. On the other hand, the Sb layer looks similar on lands and grooves; the phase is crystalline in both cases. No specific damage was observed after the recording and reading out. Based on this TEM image, it is suggested that the recorded groove be transformed from the as-deposited amorphous to the crystalline state, which means the groove is exposed to a very high temperature of more than 160 °C. The recorded marks are also once heated up to the high temperature, but after the short-pulse recording, the mark is rapidly cooled; the cooling time overcomes the phase-transition time to the crystalline phase. It is clear that the heat source to transform the $Ge_2Sb_2Te_5$ layer to the crystalline state is generated by the Sb layer. Our computer simulation predicts the temperature at the center of the Sb layer to be more than 600 °C, which is close to the melting point of bulk Sb. Therefore,

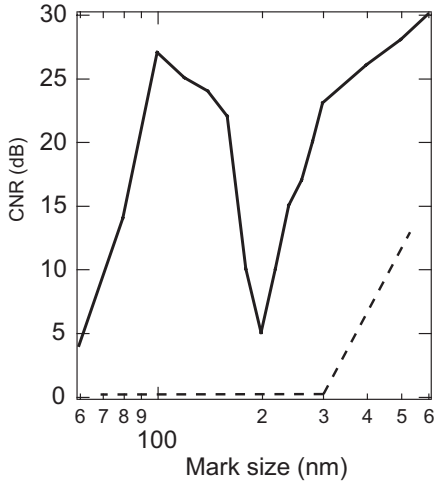

Figure 19.6: Readout characteristics of a super-RENS disc. Dotted line, 1.0-mW readout power, and solid line, 3.5 mW readout power [17].

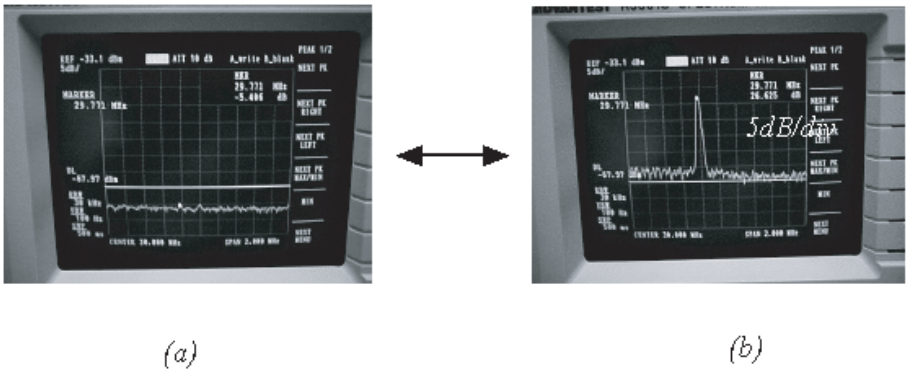

Figure 19.7: Actually observed readout signals from a100 nm mark train recorded in a super-RENS disc. Output signal at readout power of 1.0 mW (a) and 3.5 mW (b). The disc rotation speed is 6.0 m/s. The wavelength and NA used in the readout were 635 nm and 0.6, respectively [17].

an optical aperture generated by the refractive index change of the heated Sb film must be the main reason for the observed super-resolution [16, 18]. It was found that the ability of the Sb film to retrieve the small mark signals critically depends on its thickness (Fig. 19.9).

The most suitable Sb film thickness is approximately 15 nm. If the thickness is further increased, the intensities drop considerably, while the intensities decrease gradually in the case of thinner films. As discussed above, the penetration depth of the surface plasmon in the Sb layer is roughly 20 nm, which may correlate with the thickness dependence of the signal intensity from the super-RENS disc.

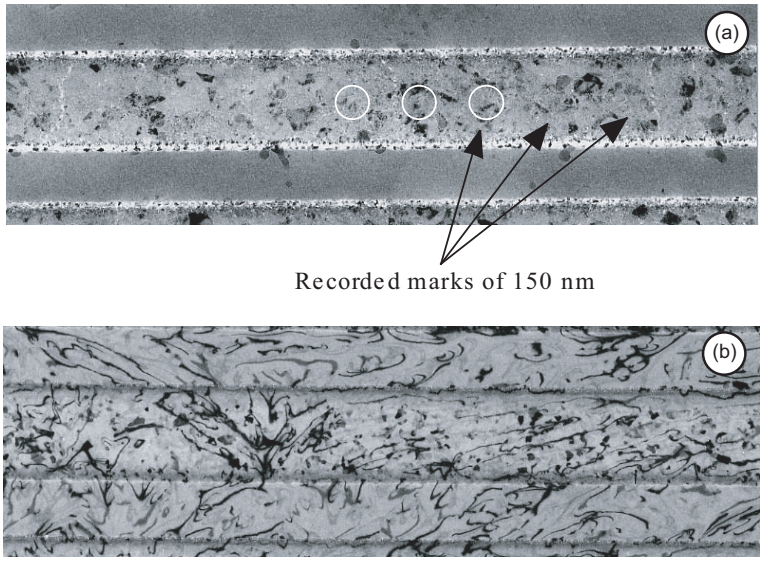

Figure 19.8: TEM images of the super-RENS disc after recording 150 nm mark trains and reading out at 3.5 mW. a, $Ge_2Sb_2Te_5$; b, Sb.

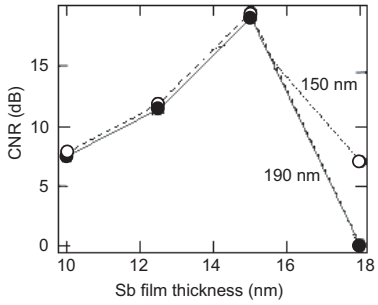

Figure 19.9: Signal intensity dependence on the Sb film thickness. The read-out intensities from marks with size smaller than the resolution limit is shown for two different mark sizes [17].

19.5 Summary

GeSbTe and Sb phase-change layers remain valuable for research and study in order to increase the optical data storage density in phase-change recording. Their optical properties, especially related to optical near-field and surface plasmons, have not yet been completely revealed. The potential of PC recording and its data capacity are very high – no limit on the recording mark size has been detected, although thermal stability becomes the main issue in the current optical recording systems using a focused laser beam. We expect that further research on super-RENS technology can solve the problem in the near future.

Acknowledgment

The author wishes to thank to Dr. T. Nakano of LAOTECH for helpful discussions on near-field optics and surface plasmons.

References

[1] N. Yamada, E. Ohno, K. Nishiuchi, N. Akahira, and M. Takao, J. Appl. Phys. **69**, 2849 (1991).

[2] K.A. Agaev and A.G. Talybov, Sov. Phys. Cryst. **11**, 400 (1966).

[3] I.I. Petrov, R.M. Imamov and Z.G. Pinsker, Sov. Phys. Cryst. **13**, 339 (1968).

[4] M. Terao, A. Hirotsune, Y. Miyauchi, M. Miyamoto, T. Nishida, and K. Andoh, Proc. SPIE **3109**, 60 (1997).

[5] M. Miyamoto, K. Andoh, Y. Anzai, A. Hirotsune, J. Ushiyama, T. Toda, H. Kando, M. Terao, T. Nishida, and T. Maeda, Technical Digest ODS 98, p. 142.

[6] J. Feinleib, J. DeNewfville, S.C. Moss, and S.R. Ovshinsky, Appl. Phys. Lett. **18**, 254 (1971).

[7] H. Iwasaki, M. Harigaya, O. Nonoyama, Y. Kageyama, M. Takahashi, K. Yamada, H. Deguchi, and Y. Ide, Jpn. J. Appl. Phys. **32**, (1993) 5241.

[8] H.J. Borg and J.P.W.B. Duchateau, Proc. SPIE **3109**, 20 (1997).

[9] E. Hecht, Optics, Addison-Wesley, Reading MA, 1987.

[10] E. Betzig, J. K. Trautman, R. Wolfe, E. M. Gyorgy, P. L. Finn, M. H. Kryder and C. H. Chang, Appl. Phys. Lett. **61**, 142 (1992).

[11] H. Ukita, Y. Katagiri and H. Nakada, Proc SPIE **1499**, 248 (1991).

[12] B. D. Terris, H. J. Mamin, D. Rugar, W. R. Studenmund and G. S. Kino, Appl. Phys. Lett. **65**, 388 (1994).

[13] H. Raether, Surface Plasmons on Smooth and Rough Surfaces and on Gratings, Springer-Verlag, Heidelberg, 1988.

[14] B. D. Terris, H. J. Mamin and D. Rugar, Appl. Phys. Lett. **68**, 141 (1996).

[15] J. Tominaga, T. Nakano and N. Atoda, Appl. Phys. Lett. **73**, 2078 (1998).

[16] J. Tominaga, T. Nakano, T. Fukaya, N. Atoda, H. Fuji and A. Sato, Jpn. J. Appl. Phys. **38**, 4089 (1999).

[17] J. Tominaga, H. Fuji, A. Sato, T. Nakano, and N. Atoda, Jpn. J. Appl. Phys. **39**, 957 (2000).

[18] A. Sato, J. Tominaga, T. Nakano, H. Fuji and N. Atoda, Proc. SPIE **3864**, 157 (1999).

20 Evaluation of Multiplexing in High-Density Holographic Memories

Juan Maria González-Leal, Pavel Krecmer, Jiri Prokop, and Stephen R. Elliott

The design and realization of a unique instrument capable of concurrently recording and evaluating various types of multiplexed holograms is described. Theoretical considerations on the specific criteria that holographic media need to satisfy, as well as the analysis of the diffraction efficiency of thick holographic diffraction gratings, are also presented. Some preliminary results of the recording and evaluation of chalcogenide films, which have recently emerged again as potentially promising holographic data-storage media, are reported.

20.1 Introduction

In the last decade, enormous improvements in computer technology have meant a renaissance of holography as a new potential solution for the ever-growing demand for faster and bigger data-storage devices, and/or faster data-transfer rates over optical networks. Indeed, it is only holography that promises true, massively parallel data writing and retrieval on optical discs, speeding up current data-storage technology by orders of magnitude [1–3]. At the same time, it also provides the capability of storing several terabits of data on a single CD-type format optical disc.

Unlike conventional optical data storage (CDs or DVDs, for instance), where individual bits are stored as distinct optical changes on the surface of a recording medium, in holographic data storage an entire *page* of information of around 1 Mbit, which is arranged by a spatial light modulator (SLM), is stored as an optical interference pattern within a thick, photosensitive material. A sketch of the basic principles of this technology for the writing and reading process is shown in Fig. 20.1. It is obvious that the parallel character of holography massively increases the read/write rates. They can be even further increased by using pulsed lasers. Optical transfer rates as high as 10 Gbit/s have been demonstrated with a 500 μJ/pulse laser, pulsed at 1 kHz [4].

On the other hand, the three-dimensional character of the (thick) recording media and, thus, the physics fundamentals of volume holography, make it possible, in addition, to superimpose a large number of these interference patterns or gratings in the same location; these can be recovered independently, as long as they are distinguishable by the direction or the period of the gratings. Such methods of overlapping pages of information are generally referred to as hologram multiplexing, and there are several basic ways to carry it out, namely, angle multiplexing, phase-coded multiplexing, peristrophical multiplexing, shift multiplexing and wavelength multiplexing [3]. Once several pages have been recorded at the same location,

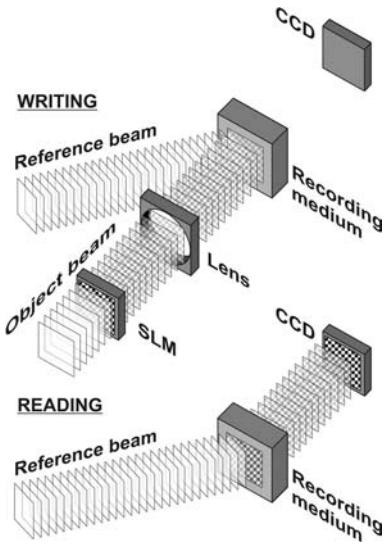

Figure 20.1: Basic principles of the recording and readout processes in holographic data-storage technology. The SLM arranges the digital data to be stored, in the form of a matrix of bits (page of information). The optical interference pattern of this object beam delivering the data and a reference beam is recorded through the medium volume. The page of information stored can be recovered by illuminating the medium with the reference beam at the same angle as used for recording.

any particular data page can then be read out independently by illuminating the stored gratings with the reference light beam that was used to record that page. Because a hologram is stored throughout the thickness of the medium, this reference light beam is diffracted by the interference patterns in such a fashion that only the desired object beam is significantly reconstructed. Figures 20.2 and 20.3 illustrate the recovery of two different pages of information stored in the same volume of the recording medium, which were recorded by changing the angle of the reference beam (angular multiplexing) or by rotating the sample (peristrophical multiplexing), respectively.

By their very nature, different holographic materials will perform in different ways, and for various ways of multiplexed-hologram writing. Moreover, the above multiplexing methods are also, by their very nature, dependent on each other and, thus, to use the full dynamic range of a material (i.e., how many independent holograms can be written in the same volume of the sample) it is necessary to combine several methods of multiplexing.

Although some efforts have been made to develop specific instrumentation for holographic data storage [4, 5], current research on glassy holographic media still suffers from a lack of suitable systems capable of concurrently recording and evaluating various types of multiplexed holograms. The Holographic Optical Storage Tester (HOST) built in the IBM Research Division [5], for instance, was designed to perform only angular multiplexing in photorefractive crystals, paying special attention to the signal-to-noise ratio (SNR) of retrieved holographic data and the resulting bit-error rate (BER) of the retrieved digital data. The Stanford/HDSS digital holographic disc storage demonstrator [4], on the other hand, is an-

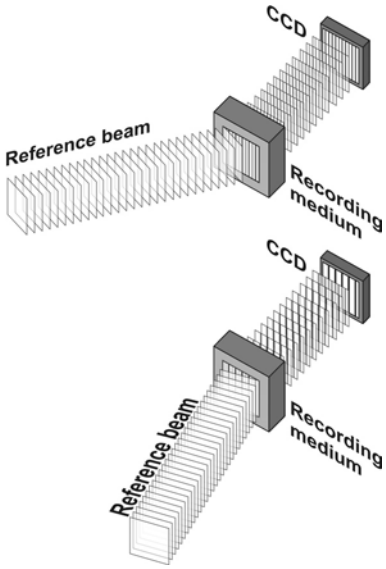

Figure 20.2: Angular multiplexing is performed by changing the direction of the reference beam relative to the surface of the sample; the holograms are distinguished by the period of gratings.

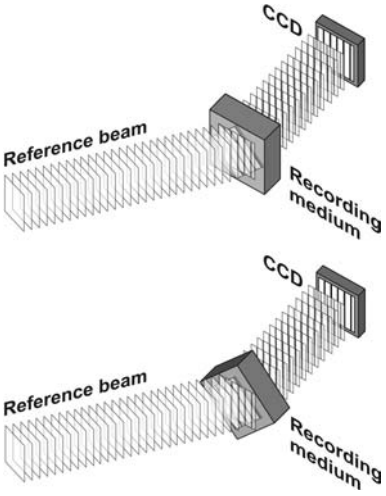

Figure 20.3: Peristrophical multiplexing of the holograms is performed by rotation of the sample with respect to the axis perpendicular to its surface. Holograms are distinguished by the direction of the gratings.

other high-precision tester but, like the previous one, performs only one type of multiplexing, namely, shift multiplexing. The aim of this chapter is to present the system concept, the implementation, and the performance of a unique precision tester for the recording and evaluation

of volume holograms using different multiplexing methods, the so-called HOLOMETER. After completion, the HOLOMETER will provide a very useful tool for the characterization of a variety of materials for holographic data storage.

Finally, we also give an overview of the specific criteria that holographic media need to satisfy, as well as some theoretical considerations on the analysis of the diffraction efficiency of thick holographic diffraction gratings.

20.2 Holographic Data-Storage Media

As usual, new technologies are always supported by other, previously established technologies. Thus, the availability of new short-wavelength solid-state lasers and high-precision linear and rotary micropositioners, and the improved performance of SLMs and CCD or CMOS photodetector arrays, among other facilities, have been necessary to make holographic data storage a viable technology. The main challenge from now on is, therefore, to find suitable holographic storage media. In the few past years, most of the efforts in this search have been addressed towards photorefractive crystals and both organic and inorganic photopolymers [2, 6–8]. Nevertheless, some of the properties of these materials are currently less than optimal. Hence, a search for new materials is essential.

The properties of foremost importance for holographic storage media can be broadly characterized as 'optical quality', 'recording properties', and 'stability'. These directly affect the data density and capacity that can be achieved, the data rates for input and output, and the BER. Optical quality requires very high standards of optical homogeneity and fabrication over the full area of the storage medium. Recording properties are characterized in terms of sensitivity and dynamic range: sensitivity refers to the extent of refractive-index modulation produced per unit exposure (energy per unit area). Recording sensitivity is commonly expressed in terms of the square root of diffraction efficiency, η:

$$S = \eta^{1/2}/(Ilt) \text{ (typically in cm/J)} \tag{20.1}$$

where I is the total incident light intensity, $l = 1/\alpha$ is the effective optical thickness (α being the intensity absorption coefficient), and t is the exposure time. Nevertheless, for the sake of comparison of different media, it is more useful to define the sensitivity as

$$S' = S \times l \text{ (typically in cm}^2\text{/J)}. \tag{20.2}$$

Dynamic range concerns the total response of the medium when it is divided up among many holograms multiplexed in a common volume of material. This property, which depends on the magnitude of the modulation in both the refractive index and the absorption coefficient, is often parameterized by the so-called M-number (M#):

$$M\# = \sum_{i=1}^{N} \eta_i^{1/2} \tag{20.3}$$

where N is the maximum number of holograms that can be stored in a location of the recording medium, and η_i is the maximum diffraction efficiency of the ith hologram. Finally, thermal,

environmental and long-term (ageing) stability is a desirable property, indeed for any data-storage medium.

Challenges to be achieved for volume holographic data-storage media can be summarized as follows:

- Amplitude of the modulation of refractive index: $\Delta n \geq 0.004$.
- Record wide range of spatial frequencies: 0.1 μm $\lesssim \Lambda \lesssim$10 μm.
- Medium thickness: $L \geq 200$ μm.
- Low exposure threshold: $\lesssim$25 mJ/cm^2.
- Stable image for low diffraction efficiencies.
- Small angular deviations from Bragg-matching condition: volume shrinkage $\lesssim 0.1\%$.
- Low light scattering: $\lesssim 10^{-4}$ sr^{-1}, $\sim 10^{-6}$ η.
- Low absorbance after recording: $(\alpha L) < 0.05$.
- Phase uniformity/homogeneity: $<\pi/5$.
- Lifetime (after recording): $>$10 years.
- Pre-recording shelf life: $>$1 year.

20.3 HOLOMETER

20.3.1 Concept

The HOLOMETER is a fully automated apparatus that has been designed to explore the parameter space of holographic recording materials and recording physics. To accomplish this, the tester must not only have the highest possible precision in all its controlled and measured parameters, but must allow the operator to have complete computer control of all of them.

20.3.2 Implementation

A sketch of the HOLOMETER is shown in Fig. 20.4. The device is composed of two mechanical arms (Newport, model X95-1), a photodiode for the measurement of diffraction efficiency (Centronic, model OSI100), a laser source and the necessary focusing and collimating optics, an SLM (Kopin, model CyberDisplay 320 mono), CMOS camera (Navitar, model 1-13664) and Fourier lenses for imaging experiments, electronics and a controlling PC, and the sample holder. The *object* arm is fixed and bears the object-beam optics. The *reference* arm is placed on a precision rotation stage (PI, model M-062.DD), enabling measurement over a wide range of angles (resolution 5 μrad) and holds the reference-beam collimating optics and/or phase mask and polarization optics (waveplates). To allow flexibility of the system over a wide range of angles, the beam is delivered to both arms by fiber optics from the output of a laser.

The universal sample holder (see Fig. 20.5) allows shifting in the three spatial directions, as well as rotation of the sample around both the axes parallel and perpendicular to its surface, in order to perform angular multiplexing and peristrophical multiplexing, respectively.

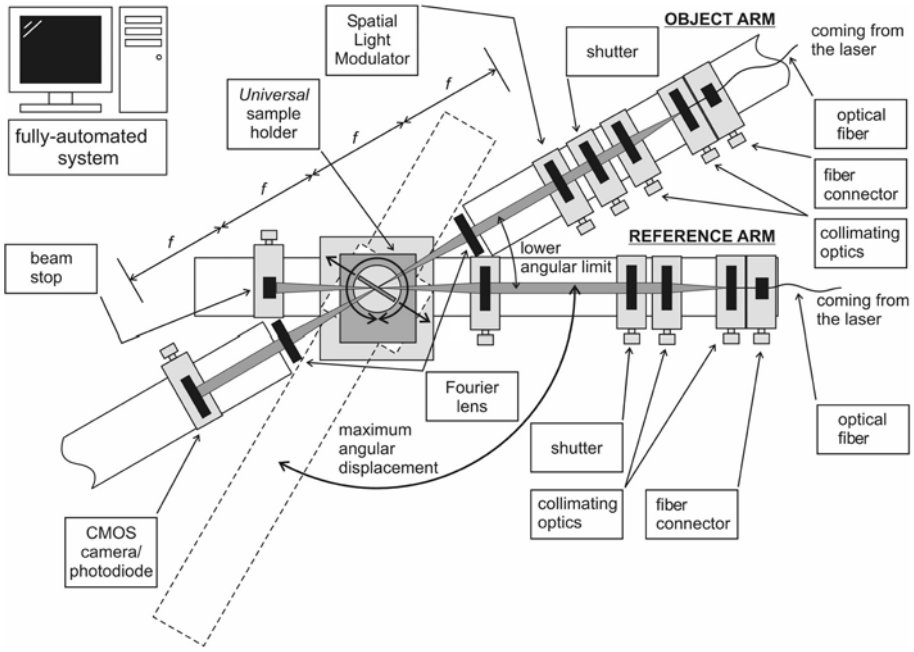

Figure 20.4: Schematic drawing of the HOLOMETER. The reference and object beams are delivered to both arms by fiber optics from the output of a laser. Fourier lenses are arranged in the so-called 4-f configuration for imaging experiments. The system is fully controlled by a PC.

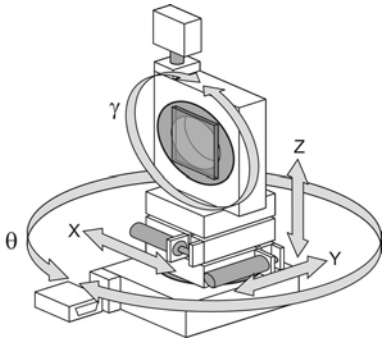

Figure 20.5: The universal sample holder provides five degrees of freedom for the positioning of the sample and performing different kinds of multiplexing.

As in systems dealing with time, in which the frequency domain shows notable advantages over the time domain as far as the stability of the system and, therefore, the SNR, is

concerned, in holographic data-storage systems it is also convenient to work in the spatial frequency domain, in such a way that the precise positioning of the recording medium is less critical. Bearing in mind this principle, a lens of focal length f is used in a Fourier configuration to image the Fourier transform of the page of information arranged by the SLM onto the storage medium. The reconstructed wave front is then transformed back by another Fourier-transform lens and imaged onto the CMOS camera. Figure 20.4 shows the so-called 4-f configuration for the system SLM–lens–medium–lens–camera. The recording medium is placed in the common focal plane of the two lenses, and the SLM and CMOS camera in the other focal planes of the lenses.

The HOLOMETER is fully controlled by a personal computer (AMD Athlon 600 MHz). The various components of the tester are controlled through a variety of interfaces. The general-purpose interface-bus (GPIB) interface is used to monitor the intensity of the diffracted light beam through the digital multimeter (Agilent, model 34401A), which is connected to the photodiode. Parallel ports (COM 1 and COM 2) are used to control both the translation and rotation stages. A timer/counter module (National Instruments, model NI PXI 6601) performs the synchronization of the shutters (Vincent Associates, model UNIBLITZ VS25V2T1), via the corresponding connector block (National Instruments, model BNC-2121) which controls the four-channel driver (Vincent Associates, model VMM-D4).

The control software has been developed by using the object-oriented graphical-programming language LabVIEW 6.i (National Instruments). LabVIEW allows the implementation of virtual instruments (VIs) that have interactive user-interface controls, indicators, graphs, etc., which simulate the front panel of a physical instrument.

20.3.3 Performance

Basically the tester is based on the recording of the interference pattern of two non-collinear laser beams. Analysis of the diffraction efficiency of an individual volume holographic diffraction grating provides crucial information about the angle, phase, shift or wavelength selectivity of the photosensitive materials under test and, consequently, about the potential maximum number of holograms that can be stored by using a particular multiplexing method. Apart from revealing information about the dynamic range of a recording medium, these measurements also provide information about the magnitude of the changes induced by light in the optical properties of the material under study.

As already mentioned, the HOLOMETER allows control by computer of the angle between the laser beams, the phase of the reference beam, the orientation of the sample with respect to the laser beams, the position of the light spot on the sample, and the wavelength of the laser, in order to perform different multiplexing methods. Thus, the recording and read-out of an individual hologram, or a sequence of multiplexed holograms by using different types of multiplexing methods, are simple routines. Furthermore, long-term tasks can be run without user action. In addition, specific algorithms have been developed and implemented into the main software for the analysis of the measurements, e.g. the measurement of the so-called parameter $M\#$, which is a figure of merit for holographic data-storage media, is automatically calculated after running a writing/reading sequence of multiplexed holograms.

20.4 Diffraction of Light by a Volume Grating

The diffraction of a plane electromagnetic wave by a sinusoidally stratified thick hologram grating (see Fig. 20.6) has been investigated theoretically by a number of authors and many methods have been suggested. Most entail some form of approximation, and some are more accurate than others. For an in-depth discussion of a variety of different methods, see Ref. [9]. Among these, one of the simplest, but the most successful, approaches in the Bragg regime is the use of coupled-wave theory, making the study of Kogelnik's work [10] compulsory reading. However, although most of the problems concerning diffraction gratings with sinusoidal fringe patterns uniform throughout the depth can be solved by his extensive study, the formulation does not consider any possible attenuation in the refractive-index modulation, Δn, and/or in the absorption modulation, $\Delta\alpha$, along the thickness of the holographic media, L, which is the case, for example, for chalcogenide glasses when the light used has a photon energy comparable to the bandgap of the glass. Attenuation in Δn and/or $\Delta\alpha$ leads to a considerable deviation in the angular selectivity profiles from the line shape predicted by Kogelnik's formulation [11, 12].

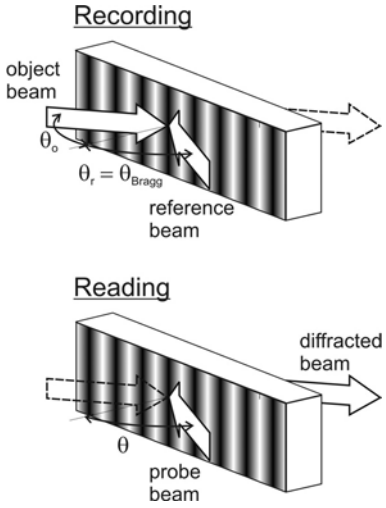

Figure 20.6: Schematic of recording and readout geometry of a diffraction grating: θ_r is the angle of incidence of the reference beam, θ_0 the angle of incidence of the object beam, and θ the angle of incidence of the probe beam during reading.

Starting with Maxwell's equations for a nonmagnetic medium ($\mu = 1$):

$$\nabla^2 \boldsymbol{E} + k^2 \boldsymbol{E} = 0 \tag{20.4}$$

where

$$k^2 = \varepsilon(\omega/c)^2 - j\omega\sigma,$$

with ω being the frequency of the wave and c the speed of light in vacuum, and considering a sinusoidal spatial modulation defined by the so-called grating vector, $\boldsymbol{K}$, for both the dielectric

constant,

$$\varepsilon = \varepsilon_0 + \Delta\varepsilon\cos(\boldsymbol{K}\cdot\boldsymbol{r})$$

(or equivalently, the refractive index, $n = n_0 + \Delta n\cos(\boldsymbol{K}\cdot\boldsymbol{r})$) and the conductivity,

$$\sigma = \sigma_0 + \Delta\sigma\cos(\boldsymbol{K}\cdot\boldsymbol{r})$$

(or equivalently the absorption coefficient, $\alpha = \alpha_0 + \Delta\alpha\cos(\boldsymbol{K}\cdot\boldsymbol{r})$), where $\boldsymbol{r} = (x, y, z)$ is a position vector, and the subscript '0' stands for the average value of these quantities, it is possible to derive, after some algebra, the coupled-wave equations with respect to the probe, $\boldsymbol{E}_p$, and diffracted, $\boldsymbol{E}_d$, waves for the case of *uniform* gratings:

$$c_p\frac{dE_p}{dz} + \frac{\alpha_0}{2}E_p = -j\kappa\exp(j\Delta k_z z)E_d, \tag{20.5}$$

$$c_d'\frac{dE_d}{dz} + \frac{\alpha_0}{2}E_d = -j\kappa\exp(-j\Delta k_z z)E_p, \tag{20.6}$$

where

$$j = \sqrt{-1},$$

$$c_p = \cos\theta,$$

$$c_d' = -\cos(2\phi - 2\theta_{Bragg} + \theta),$$

$$\Delta k_z = K[\cos(\phi - \theta_{Bragg} + \theta) - \cos\phi],$$

and κ is the coupling constant, which is defined as

$$\kappa = \frac{1}{2}(k\Delta n + j\frac{\Delta\alpha}{2}). \tag{20.7}$$

Here, θ is the angle of incidence of the probe beam measured inside the medium, θ_{Bragg} stands for the internal angle of incidence satisfying the Bragg condition, ϕ is the so-called *slant* angle, which is the angle of the grating vector, $\boldsymbol{K}$, with respect to the normal of the medium, Δk_z is the z component of the wavevector mismatch $\Delta\boldsymbol{k}$ given by $\boldsymbol{k}_d = \boldsymbol{k}_d' + \Delta\boldsymbol{k} = \boldsymbol{k}_p - \boldsymbol{K}$, and $\boldsymbol{k} = 2\pi/\lambda$ is the wavenumber of the incident light in free space with wavelength λ. All of these quantities are clearly illustrated in Fig. 20.7.

It is important to note that the present approach is somewhat different from the original work of Kogelnik [10] concerning the definition of the wavevector, $\Delta\boldsymbol{k}$, modelling the Bragg-angle detuning. This is because Eqs. (20.5) and (20.6), and the factor c_d' introduced here, have different forms to those from [10]. The present definition of $\Delta\boldsymbol{k}$ is plausibly valid when working around the Bragg angle, which is the case for the measurement of the selectivity profiles for the diffraction efficiency.

The system of differential equations defined by Eqs. (20.5) and (20.6) can be solved analytically by using the boundary conditions: $E_d(0) = 0$ and $E_p(0) = 1$. Since we are only concerned with an analytical expression for the diffraction efficiency, which is given by

$$\eta = \frac{c_d'}{c_p}\frac{E_d(L)E_d^*(L)}{E_p(0)E_p^*(0)} = \frac{c_d'}{c_p}E_d(L)E_d^*(L), \tag{20.8}$$

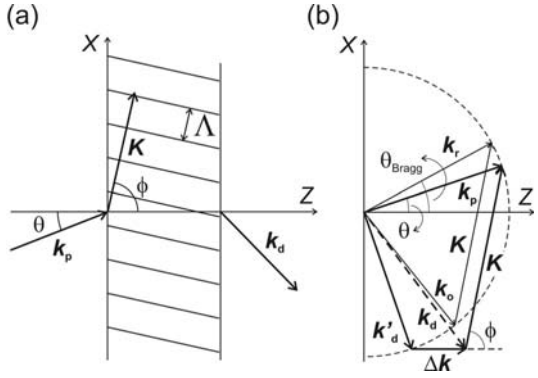

Figure 20.7: Schematic of grating vector components (a) and a cross-sectional view of the k-sphere showing the present approach for the mismatch vector (b). $\boldsymbol{k}_p$ is the wavevector of the probe wave, $\boldsymbol{k}_d$ the wavevector of the diffracted wave, $\boldsymbol{K}$ the grating vector, Λ the grating period, ϕ the slant angle, $\boldsymbol{k}_r$ the wavevector of the reference wave, $\boldsymbol{k}_0$ the wavevector of the object wave, $\Delta\boldsymbol{k}$ the mismatch vector and $\boldsymbol{k'}_d = \boldsymbol{k}_p - \boldsymbol{K} - \Delta\boldsymbol{k}$.

only the solution for the amplitude of the diffracted wave, $E_d(z)$, for a uniform thick lossy dielectric grating, is given:

$$E_d(z) = j2a\sqrt{\frac{c_p}{c'_d}}\exp(-bz/2)\frac{\sinh[\sqrt{b^2-4(a^2+c)}z/2]}{\sqrt{b^2-4(a^2+c)}} \tag{20.9}$$

where

$$a = \kappa/(4\sqrt{c_p c'_d}),$$

$$b = \alpha_0(1/c_p + 1/c'_d)/2 - j\Delta k_z,$$

$$c = \alpha_0[\alpha_0/(2c_p) - j\Delta k_z]/(2c'_d).$$

The measurement of the dependence of the diffraction efficiency, η, on the angle or wavelength around the values of these quantities for which the Bragg condition is verified, as shown in Fig. 20.8, gives relevant information about a potential holographic data-storage medium. Plots obtained in such a fashion are usually called Bragg-selectivity profiles and they are strongly dependent on the medium thickness (see Fig. 20.9) and both the refractive-index and absorption-coefficient modulations (see Fig. 20.10). Looking at these figures, the basic principle of multiplexed holographic data storage is clear: *new gratings (holograms) can be recorded at the diffraction minima of the closest adjacent gratings without any significant overlapping between them*. This principle is illustrated in Fig. 20.11.

So far, we have followed the traditional model for the definition of the modulation of the refractive index and absorption coefficient, i.e. a sinusoidal variation around both the background refractive index and absorption coefficient, as shown in Fig. 20.12(a), with a mathematical formulation given by $n = n_0 + \Delta n_0 \cos(\boldsymbol{K}\cdot\boldsymbol{r})$ and $\alpha = \alpha_0 + \Delta\alpha_0 \cos(\boldsymbol{K}\cdot\boldsymbol{r})$. However, this is not a realistic model because it would involve changes in these quantities at

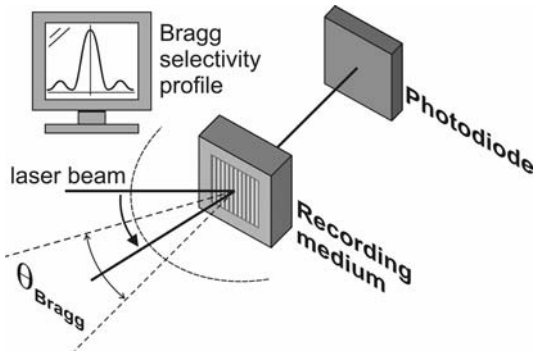

Figure 20.8: Analysis of the selectivity profiles for the diffraction efficiency provides crucial information on the holographic recording process.

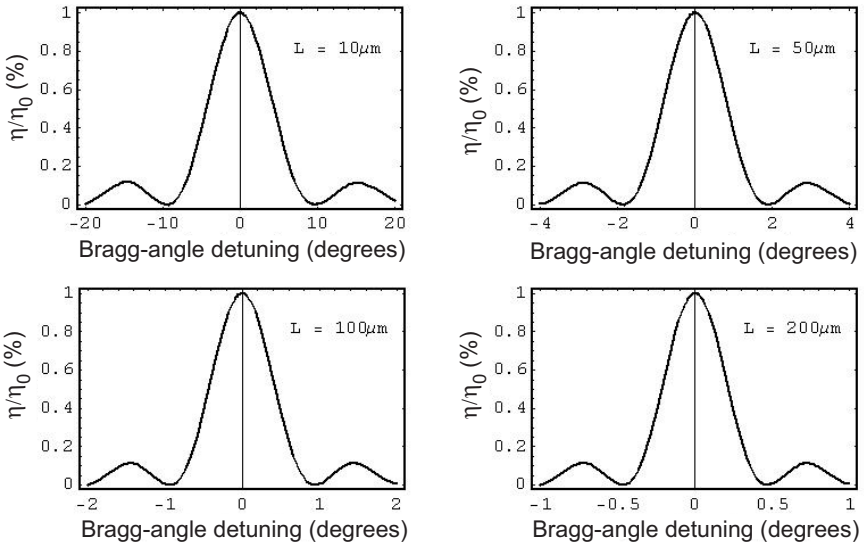

Figure 20.9: The selectivity profiles are strongly dependent on the medium thickness. Thus, the thicker the material, the higher is the selectivity and, in turn, the larger the number of holograms that can be stored in the same volume of the medium. Normalized selectivity profiles have been obtained for λ = 633 nm, $\theta_r = \theta_0 = 15^\circ$, n_0 = 1.5, $\alpha_0 = \Delta\alpha_0 = 0$ and Δn_0 verifying $\pi \Delta n_0\ L/(\lambda \cos\theta_r) = \pi/2$ in order to reach maximum diffraction efficiency for this grating [10].

the zero-intensity locations of the holographic pattern. Such a modulation would also suggest that both positive and negative light-induced changes would occur in the material at the same time. Therefore, a more realistic model accounting for the modulation in a so-called uniform thick grating would be given by $n = n_0 + \Delta n_0\ [1 + \cos(\boldsymbol{K} \cdot \boldsymbol{r})]$ and $\alpha = \alpha_0 + \Delta\alpha_0\ [1 + \cos(\boldsymbol{K} \cdot \boldsymbol{r})]$, which is illustrated in Fig. 20.12(b). It is easy to prove that the above-introduced

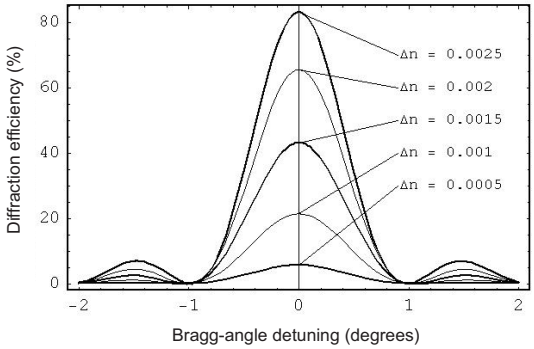

Figure 20.10: The selectivity profiles are also dependent on the amplitude of the changes in both the refractive index and absorption coefficient. The higher the modulation in the refractive index, for instance, the higher is the maximum diffraction efficiency and, in turn, the clearer the distinction between the different holograms. Selectivity profiles have been obtained for λ = 633 nm, $\theta_r = \theta_0 = 15^\circ$, n_0 = 1.5, $\alpha_0 = \Delta\alpha_0 = 0$ and L = 100 μm.

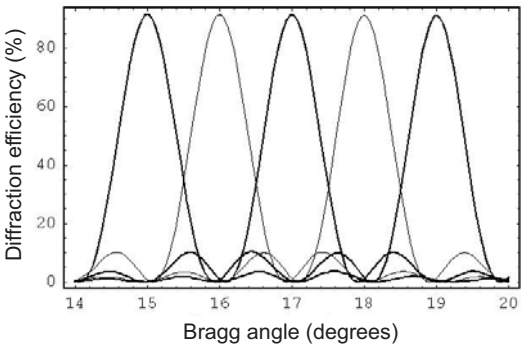

Figure 20.11: New gratings (holograms) can be recorded at the diffraction minima of the closest adjacent gratings without any significant overlapping between them. Selectivity profiles have been obtained for λ = 633 nm, n_0 = 1.5, $\alpha_0 = \Delta\alpha_0 = 0$, Δn_0 verifying $\pi\Delta n_0\ L/(\lambda \cos\theta_r) = \pi/2$ [10], L = 100 μm, and for the same angles θ_r and θ_0, ranging from 15 to 19°.

system of coupled differential equations now reads as follows:

$$c_p \frac{dE_p}{dz} + \frac{1}{2}(\alpha_0 + j\kappa)E_p = -j\kappa \exp(j\Delta k_z z)E_d, \tag{20.10}$$

$$c'_d \frac{dE_d}{dz} + \frac{1}{2}(\alpha_0 + j\kappa)E_d = -j\kappa \exp(-j\Delta k_z z)E_p, \tag{20.11}$$

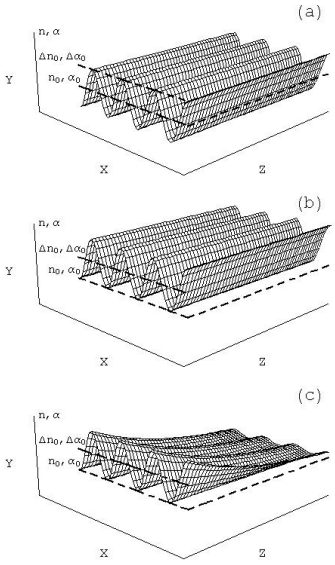

Figure 20.12: Sinusoidal modulation of the refractive index, n, and the intensity absorption coefficient, α, for a uniform grating (b) and a non-uniform grating (c). The modulation that was considered originally by Kogelnik [10] to develop the coupled-wave theory is also plotted in (a) for illustrative purposes. The surface of the medium is in the x–y plane, with the thickness direction being along the z-axis.

and the amplitude of the diffracted wave is

$$E_d(z) = j2a\sqrt{\frac{c_p}{c'_d}}\exp(-bz/2)\frac{\sinh[\sqrt{b^2-4(a^2+c)}z/2]}{\sqrt{b^2-4(a^2+c)}} \tag{20.12}$$

where

$$a = \kappa/(4\sqrt{c_p c'_d}),$$

$$b = (\alpha_0 - j\kappa)(1/c_p + 1/c'_d)/2 - j\Delta k_z,$$

$$c = (\alpha_0 - j\kappa)[(\alpha_0 - j\kappa)/(2c_p) - j\Delta k_z]/(2c'_d).$$

However, we can still go a step further in the definition of an even more realistic model accounting for the modulation in thick gratings. The magnitude of the photo-induced local structural changes in amorphous chalcogenide films, which are the basis of the holographic recording in such materials, is expected to follow an exponential decrease with thickness, corresponding to the exponential decrease in light intensity along the thickness (Beer–Lambert law). Therefore, an exponential attenuation, both in the modulation of the refractive index,

$$\Delta n = \Delta n_0 \exp(-\alpha_{rec} z/sin|\phi|), \tag{20.13}$$

and in the modulation of the absorption coefficient,

$$\Delta\alpha = \Delta\alpha_0 \exp(-\alpha_{rec} z/sin|\phi|), \tag{20.14}$$

as shown in Fig. 20.12(c), are also expected. Δn_0 and $\Delta\alpha_0$ stand for the largest modulation of the refractive index and absorption coefficient (at z = 0), respectively, and α_{rec} is the intensity absorption coefficient for the recording wavelength, λ_{rec}, which would differ from α_0 when light beams with different wavelengths are used for recording and readout. However, the HOLOMETER works at the same wavelength in both cases and, for the sake of a reduction in the number of parameters involved in the formulation presented in this chapter, we will consider that $\alpha_{rec} = \alpha_0$ from now on.

The system of differential equations defined by Eqs. (20.10) and (20.11) can now be rewritten for a *non-uniform* thick lossy dielectric grating as

$$c_p \frac{dE_p}{dz} + \frac{1}{2}(\alpha_0 + j\kappa_0 \exp[-\alpha_0 z/\sin|\phi|])E_p = -j\kappa_0 \exp[-\alpha_0 z/\sin|\phi|] \exp(j\Delta k_z z) E_d, \tag{20.15}$$

$$c'_d \frac{dE_d}{dz} + \frac{1}{2}(\alpha_0 + j\kappa_0 \exp[-\alpha_0 z/\sin|\phi|])E_d = -j\kappa_0 \exp[-\alpha_0 z/\sin|\phi|] \exp(-j\Delta k_z z) E_p, \tag{20.16}$$

where

$$\kappa_0 = \frac{1}{2}(k\Delta n_0 + j\frac{\Delta\alpha_0}{2}). \tag{20.17}$$

Owing to the extreme difficulty of solving this system of equations analytically, a numerical method has been used to determine the amplitude of the diffracted wave emanating from the medium, $E_d(L)$, when reading is performed at angles, θ, around the Bragg angle, θ_{Bragg}. As in the previous case, the same set of boundary conditions, namely, $E_d(0)$ = 0 and $E_p(0)$ = 1, is considered.

20.5 Testing the Holographic Data-Storage Potential of Chalcogenide Glasses

The variety of light-induced effects that chalcogenide glasses exhibit is well known [13], and many efforts have been made to exploit their technological potential. So far, the development of the phase-change rewritable optical memory disc by Energy Conversion Devices Inc. has been by far the most successful application of chalcogenide glasses. Another technological field which has attracted the interest of researchers is the fabrication of diffractive optical elements. Although there are a few reports in the literature dealing with holographic diffraction gratings [14–20] based on chalcogenide films, they have been mostly concerned with thin films, and thus with thin gratings. Typical thicknesses of the chalcogenide films studied in the

cited representative papers have always been less than 10 μm. However, volume holographic data storage crucially depends on the thickness of the medium and this is a key factor for this technology: Bragg selectivity, and hence data density, increases with increasing thickness of the recording medium [1–3, 9, 10]. Therefore, revealing data about the potential use of chalcogenide glasses as holographic data storage recording media do not exist so far.

Amorphous chalcogenide films of different compositions, both reasonably thick ($\sim$65 μm) and thin ($\sim$1 μm), were deposited onto silica glass substrates (refractive index, 1.51) by thermal evaporation in vacuum from the melt-quenched bulk glasses. Antireflection layers (refractive index, 1.38) were evaporated onto the thick-film samples (see Fig. 20.13) in order to improve the transmission of the optical system. Optical characterization of the thin films from transmission spectra, taken at normal incidence [21], allowed the determination of both the refractive index and the absorption coefficient at the laser wavelength for the *blank* holographic medium. Values for these optical parameters were found to be 2.40 and 197 cm^{-1}, respectively, for a representative chalcogenide composition.

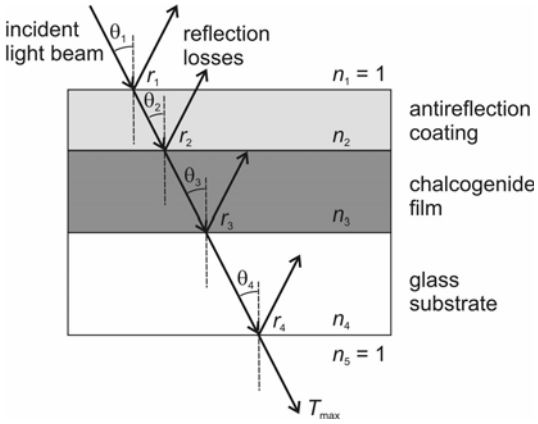

Figure 20.13: Cross-sectional view of the samples used in this work. A sketch of the light path through the sample showing the reflection losses is also displayed.

A number of diffraction gratings, with both different periods, Λ, and slant angles, ϕ, were recorded in the samples by using the HOLOMETER. The diffraction efficiency for the first-order-diffracted light was measured around the Bragg angle in order to check the angular selectivity of the grating. It is important to note that $E_d(L)$ and, in turn, the value for the diffraction efficiency, η, derived from it, in the whole of the above-introduced mathematical formulation, does not take into account either losses due to the reflections at the interfaces of the sample, or the presence, for example, of an antireflection coating, as in the present case. Hence, these features have been included in the formulation as an additional term giving the maximum transmission, T_{max}, of the *blank* thick sample (see Fig. 20.13) at the wavelength used for readout, as a function of the angle of incidence:

$$T_{\max} = \frac{\prod_{i=1}^{4}(1 - r_i^2)}{\sqrt{(A+B)(C+D)}} \tag{20.18}$$

where

$$r_i = \frac{n_{i+1}\cos\theta_{i+1} - n_i\cos\theta_i}{n_{i+1}\cos\theta_{i+1} + n_i\cos\theta_i}$$

is the Fresnel reflection coefficient for light polarized perpendicular to the plane of incidence, at the interface separating media i and $i+1$, and angles with respect to the normal of the interface in each media being θ_i and θ_{i+1} (see Fig. 20.13), and

$$A = \left[-1 + r_1(r_2 - r_3) + r_2 r_3\right]^2,$$

$$B = \left[r_2 - r_3 + r_1(-1 + r_2 r_3)\right]^2 r_4^2,$$

$$C = \left[1 - r_1(r_2 + r_3) + r_2 r_3\right]^2,$$

$$D = \left[r_2 + r_3 - r_1(1 + r_2 r_3)\right]^2 r_4^2.$$

Absorption effects are not considered in Eq. (20.18) because they already appear intrinsically within the system of equations. Therefore, the diffraction efficiency for such a three-layer (antireflection coating/chalcogenide/substrate) holographic recording system is finally given by

$$\eta' = T_{max}\eta. \tag{20.19}$$

Analysis of the experimental selectivity profiles of non-uniform volume hologram diffraction gratings, written in chalcogenide-based three-layer samples, was carried out by using a best-fitting algorithm on the basis of Eq. (20.19).

Figure 20.14 collects the experimental results for η' as a function of Bragg-angle detuning, $\Delta\theta = \theta - \theta_{Bragg}$, for a representative $\sim$1000 lines/mm unslanted thick hologram grating ($\theta_r = \theta_0 = 15.5^\circ$) based on a thick (65 μm) amorphous chalcogenide film. Readout was performed by using a laser intensity 20 times lower than the laser intensity used for recording. The maximum diffraction efficiency for this particular holographic grating was 12.5%. Angular selectivity was around 2°. Values of the grating parameters, Δn_0 = 0.0061 and $\Delta\alpha_0$ = 173 cm^{-1}, as well as the hologram thickness, L = 65.64 μm, were obtained by using the already-mentioned best-fitting algorithm based on Eq. (20.19), and the corresponding best-fitting curve is shown in Fig. 20.14. Values of Δn_0 = 0.0039, $\Delta\alpha_0$ = 128 cm^{-1} and L = 61.29 μm were found when the uniform-grating approach presented here was considered in Eq. (20.19). The corresponding best-fitting curve in this case is also plotted in Fig. 20.14 for the sake of comparison.

As already mentioned, attenuation in Δn_0 and $\Delta\alpha_0$ leads to a considerable deviation in the angular selectivity profiles from the line shape predicted by Kogelnik's formulation. In particular, minima in the diffraction efficiency around the central maximum at $\Delta\theta = 0$ no longer decrease to zero. Moreover, it can be seen in Fig. 20.14 that the experimental selectivity curve for the diffraction efficiency shows an asymmetric shape, which is also caused by the non-uniformity of the grating recorded in the material. The traditional coupled-wave formulation does not account for these effects, at least for physically reasonable values of the magnitude of the modulation (minima uplift can be obtained, but at the expense of involving

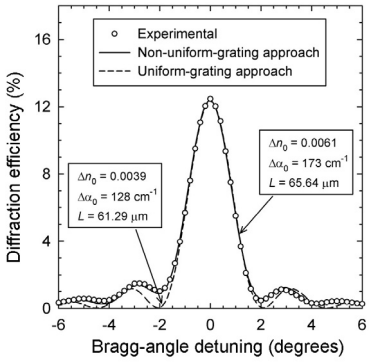

Figure 20.14: Experimental angular selectivity profile of a ∼1000 lines/mm unslanted diffraction grating recorded in a 65 μm amorphous chalcogenide film with refractive index $n = 2.40$ and absorption coefficient $\alpha_0 = 197$ cm^{-1}. Recording angles for the reference and signal beams were both $\theta_r = \theta_0 = 15.5°$. Solid and dashed lines correspond to, respectively, the best-fitting curves on the basis of the formulation presented in this work for both non-uniform and uniform thick holographic gratings. Values for the amplitude of the modulation of the refractive index, Δn_0, and absorption coefficient, $\Delta\alpha_0$, as well as the medium thickness, L, derived from the data fit, in both cases, are shown in the insets.

unphysical negative values for the intensity absorption coefficient(!)). The formulation developed here matches the experimental results in an excellent way, and physically coherent results have been found. It is worth noting that the value found from this curve fitting for the film thickness, L = 65.64 μm, is in good agreement with the value, 64.57 μm, measured by a quartz microbalance placed in the evaporation chamber, as well as with the mechanically measured value, 68 μm, using a depth gauge (Mitutoyo, model 547-257, the resolution of this gauge being ± 1 μm).

20.6 Summary

Details about the building of the HOLOMETER instrument, as well as theoretical considerations about the requisites for holographic data-storage media, and a formulation suitable for the analysis of thick holograms based on chalcogenide glasses, have been provided. A more realistic model for the modulation of the refractive index and absorption coefficient, which considers their light-induced attenuation along the thickness, has been taken into account for the analysis of the Bragg-selectivity profiles. The coupled-wave formulation developed here matches the experimental results in an excellent way. Some preliminary results of the recording and evaluation of thick hologram gratings based on thick amorphous chalcogenide films have been reported. These results seem to be very promising with regard to the possibility of the HOLOMETER becoming a standard characterization set-up available to a wide community of researchers concerned with holographic data storage, as well as the suitability of chalcogenide glasses as holographic media.

Acknowledgments

This work was partially supported by the Paul Research Instrument Fund of the Royal Society and by a Marie Curie Fellowship of the European Community programme "Improving Human Research Potential and the Socio-Economic Knowledge Base" under contract number HPMF-CT-2000-01031.

References

[1] J.F. Heanue, M.C. Bashaw and L. Hesselink, Science **265**, 749 (1994).

[2] J. Ashley, M.-P. Bernal, G.W. Burr, H. Coufal, H. Guenther, J.A. Hoffnagle, C.M. Jefferson, B. Marcus, R.M. Macfarlane, R.M. Shelby and G.T. Sincerbox, IBM J. Res. Dev. **44**, 341 (2000).

[3] G. Barbastathis and D. Psaltis, in Holographic Data Storage, (Springer Series in Optical Sciences, Vol. 76), H.J. Coufal, D. Psaltis and G. Sincerbox (Eds.), Springer-Verlag, Berlin, 2000, p. 21.

[4] S.S. Orlov, E. Bjornson, W. Phillips and L. Hesselink, in Proceedings of the 29th Applied Imagery and Pattern Recognition Workshop (AIPR'2000, Washington, DC), J. Aanstoos (Ed.), IEEE Computer Society, Los Alamitos, USA, 2000, p. 71.

[5] M.-P. Bernal, H. Coufal, R.K. Grygier, J.A. Hoffnagle, C.M. Jefferson, R.M. Macfarlane, R.M. Shelby, G.T. Sincerbox, P. Wimmer and G. Wittmann, Appl. Opt. **35**, 2360 (1996).

[6] R.R.A. Syms, Practical Volume Holography, Clarendon Press, Oxford, 1990, p. 132.

[7] S.J. Zilker, ChemPhysChem **1**, 72 (2000).

[8] See Part II: Recording Media, in Holographic Data Storage, (Springer Series in Optical Sciences, Vol. 76), H.J. Coufal, D. Psaltis and G. Sincerbox (Eds.), Springer Verlag, Berlin, 2000.

[9] L. Solymar and D.J. Cook, Volume Holography and Volume Gratings, Academic Press, New York, 1981.

[10] H. Kogelnik, Bell Syst. Tech. J. **48**, 2909 (1969).

[11] N. Uchida, J. Opt. Soc. Am. **63**, 280 (1973).

[12] D.A. Waldman, H.-Y.S. Li and M.G. Horner, J. Imag. Sci. Technol. **41**, 497 (1997).

[13] A.V. Kolobov and Ka. Tanaka, in Handbook of Advanced Electronic and Photonic Materials and Devices, Vol. 5, H.S. Nalwa, (Ed.), Academic Press, San Diego, 2001, p. 47.

[14] C.H. Kwak, J.T. Kim and S.S. Lee, Opt. Lett. **13**, 437 (1988).

[15] E. Hajto, P.J.S. Ewen, R.E. Belford and A.E. Owen, Thin Solid Films **200**, 229 (1991).

[16] V. Boev, E. Sleeckx, M. Mitkova, P. Markovsky, P. Nagels and K. Zlatanova, Vacuum **47**, 1211 (1996).

[17] A. Ozols, N. Nordman, O. Nordman and P. Riihola, Phys. Rev. B **55**, 14236 (1997).

[18] V. Palyok, A. Mishak, I. Szabó, D.L. Beke and A. Kikineshi, Appl. Phys. A **68**, 489 (1999).

[19] O. Nordman, J. Opt. Soc. Am. B **16**, 631 (1999).

[20] A. Stronski, M. Vlcek, A. Sklenar, P.E. Shepeljavi, S.A. Kostyukevich and T. Wagner, J. Non-Cryst. Solids **266–269**, 973 (2000).

[21] J.M. González-Leal, R. Prieto-Alcón, J.A. Angel, D.A. Minkov and E. Márquez, Appl. Opt. **41**, 7308 (2002).

21 Optical Waveguides Photo-Written in Glasses with a Femtosecond Laser

Kazuyuki Hirao and Kiyotaka Miura

21.1 Introduction

In general, it is difficult to produce an interaction effect between glass and light by a one-photon process when the excitation wavelength does not agree with the absorption region of the glass. However, various types of interactions with glass can be produced by using an ultrashort-pulse laser operating at the nonresonance wavelength with pulse widths of femtosecond order [1, 2]. Ultrashort light pulses are useful for observing and evaluating at a very high time resolution the dynamics of the phenomena that occur in materials at speeds ranging from pico- to femtoseconds. Such phenomena include direct interaction between light and atoms or molecules, the saturation processes associated with the coherent state of materials, and the elementary processes of chemical reactions. A short pulse width also means that extremely high peak power can be obtained and that high-intensity light can easily be achieved by focusing the laser. The development of high-energy-density femtosecond pulse lasers prompted us to investigated the unexplored potential for inducing multiphoton photochemical reactions.

We recently discovered that refractive index changes of the order from 10^{-2} to 10^{-3} can be induced within various types of glasses by irradiating the glass with focused femtosecond laser pulses [3]. By using a femtosecond laser with a high repetition rate, permanent optical waveguides can be successfully written in various glasses, where refractive index changes are continuously induced along a path traversed by the focal point [4, 5]. We found that the photo-reduction of samarium ions can occur simultaneously with the refractive index change. More recently, it was confirmed that photo-reduction of rare earth ions in several glasses can be produced by irradiation with femtosecond laser pulses [6].

In this chapter, we describe the preparation and optical characterization of photo-written optical waveguides formed in bulk glasses by ultrashort laser pulses in the femtosecond region. The combination of photo-induced refractive index change and photo-reduction is also discussed.

21.2 Experimental Details

The irradiation source employed was a regeneratively amplified 800 nm Ti:sapphire laser that emitted 10 Hz or 200 kHz mode-locked pulses. The pulse width of the laser was continuously adjusted from 110 to 250 fs by changing the dispersive pathlength of a pair of prisms. The

average power of the laser pulses at the sample location was approximately controlled in the 1–800 mW range by using neutral-density filters inserted between the laser and the prism compressor.

As samples we used fused and synthetic silica, Ge-doped silica, borosilicate, borate, phosphate, fluorophosphate, fluoride, and chalcogenide glasses. All experiments were performed at room temperature.

21.3 Experimental Results

21.3.1 Photo-Written Waveguides

Figure 21.1 shows an array of the refractive index changes inside a silica glass induced by a single pulse, the peak power being 10^9 W/cm^2. The spots have diameters of roughly 400 nm, as measured with a confocal laser scanning microscope. This is significantly smaller than the focal-beam size and the wavelength of the laser (800 nm). This may be due to the self-focusing of the laser and non-linear effect of the glass, which resulted from the interaction between the laser and the glass. The spot size of refractive index change increases with increasing number of irradiation pulses and the peak power of each pulse. Using a microellipsometer, we measured refractive index profiles across the cross-sections of refractive index change lines that were formed perpendicular to the laser beam with a $10\times$ lens. The laser power, pulse width, and repetition rate were 470 mW, 130 fs and 200 kHz, respectively. For pure silica and the Ge-doped silica glasses, the laser irradiation produced refractive index increases of approximately 0.015 and 0.01, respectively, at the center.

The refractive index increase values observed here are large enough for the creation of optical devices or three-dimensional memory. We observed a densification phenomenon in the silica glass irradiated by the femtosecond laser from the measurement of Raman spectra. Therefore, the increases in the refractive index can be related to local densification which finally occurs inside the glass, though the initial process of refractive index changes may be accompanied by various phenomena such as the formation of color centers or lattice defects, or melting of a very small area.

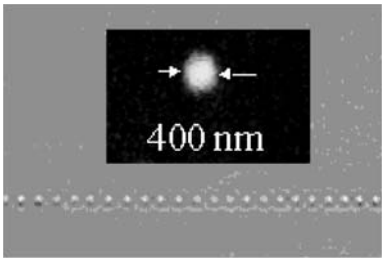

Figure 21.1: Refractive index changes inside silica glass induced by a series of single pulse shots.

By using a femtosecond laser with a high repetition rate, it is possible to write waveguides, where laser damage spots are continuously induced along a path traversed by the focal point. Waveguides could be written inside various glasses such as fused and synthetic silica,

Ge-doped silica, borosilicate, borate, phosphate, fluorophosphate, fluoride, and chalcogenide glasses. Typical photo-written waveguides formed inside fluoride glass are shown in Fig. 21.2; the waveguides shown were created using 800 nm, 120 fs, 200 kHz mode-locked pulses. The waveguides were written by translating the sample (a) parallel or (b) perpendicular to the axis of the laser beam at a rate of 20 μm/s and focusing the laser pulses through a 10$\times$ or 50$\times$ microscope objective, respectively. The cross-section of a waveguide written by translating the sample parallel to the axis of the laser beam is shown in Fig. 21.3 (a) and that written by translating the sample perpendicular to the axis of the laser beam is shown in Fig. 21.3(b). Both cross-sections are almost circular. When the samples were translated parallel to the laser beam, the shape of the cross-sections remained unchanged despite changes in the average laser power or the magnification of the objective, with diameters of approximately 7–30 μm. The core of the waveguides produced when the samples were translated perpendicular to the laser beam became more elliptical as the numerical aperture was decreased because of the self-focusing. Therefore, a high-numerical-aperture objective should be used to form waveguides with a circular core. Writing waveguides perpendicular to the incident laser beam provides most flexibility for writing planer patterns and allows one to create multiple-pattern layers by simply changing the focus depth of the beam. To obtain information on the densification due to structural changes in the laser-irradiation region, we observed the unpolished surface of the core-end of the waveguide using atomic force microscopy. We found that the shrinkage of the surface gradually increased from the outside of the core towards the center, which allows us to conclude that the densification of the glass occurs in the laser-irradiated region.

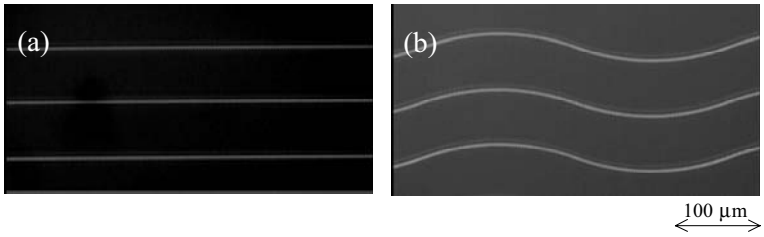

Figure 21.2: Photo-written waveguides in fluoride glass formed using 800 nm 200 kHz mode-locked pulses. The waveguides were written by translating the sample (a) parallel or (b) perpendicular to the axis of the laser beam at a rate of 20 μm/s and focusing the laser pulses through a 10$\times$ or 50$\times$ microscope objective, respectively.

21.3.2 Power Dependence

We examined the effects of the average power, the pulse width, and the number of laser passes on the refractive index and core size of optical waveguides. The relationship between the diameter of the core formed by translating the sample parallel to the axis of the laser beam and the average power of the laser is shown in Fig. 21.4. The core diameters increased with increasing average laser power at a constant pulse width.

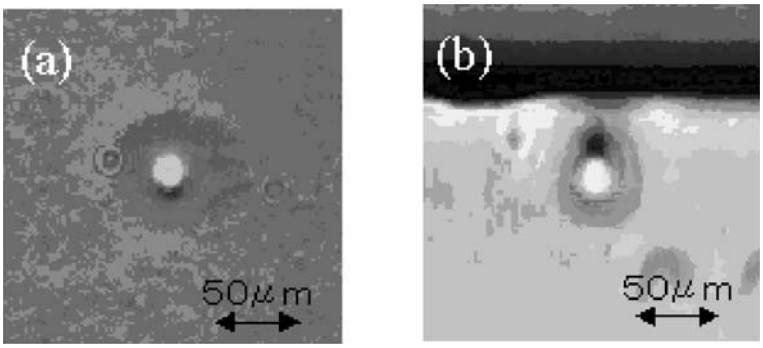

Figure 21.3: Cross-sections of waveguides written by (a) translating the sample parallel to the axis of the laser beam, and (b) translating the sample perpendicular to the axis of the laser beam.

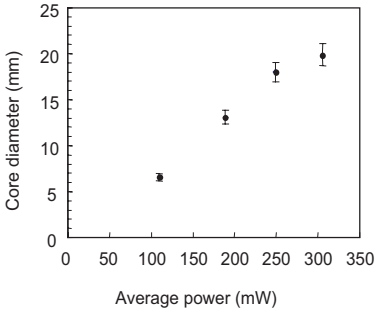

Figure 21.4: Relationship between the diameter of a core formed by translating the sample parallel to the axis of the laser beam and the average power of the laser. The error bars correspond to the scatter in measured values. The pulse width of the laser was 120 fs.

21.3.3 Guided Light Intensity Profiles

The intensity profiles of the guided light for waveguides produced at different pulse widths at a constant average power are shown in Fig. 21.5. The peak intensity increased as the pulse width decreased when the average power was kept constant. This result shows that the change in the refractive index increases as the pulse width is decreased. In other words, the refractive-index change increases with the peak power, which is equal to the average power over the pulse width. Note that the core diameters decreased as the peak power was increased.

As shown in Fig. 21.6, the intensity profiles of the guided light varied with the number of laser passes over the same area. The core diameters remained unchanged independent of the number of passes, although increasing the number of passes resulted in an increase of the guided-light intensity due to an increase of the refractive index of the core area. These results indicate that the induced refractive-index difference and the core diameter can be controlled by adjusting the writing conditions.

We observed the field-intensity distributions of the guided light in a waveguides written in fluoride glass at different average powers by using a CCD camera. The intensity distributions

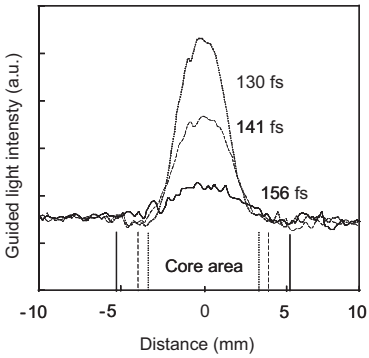

Figure 21.5: Intensity profiles of the guided light for waveguides produced at different pulse widths. Average power of the laser was 150 mW.

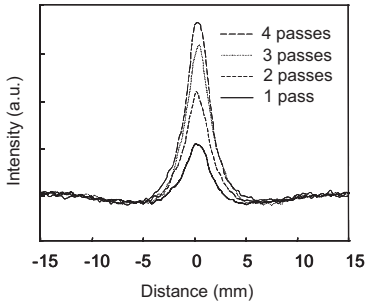

Figure 21.6: Intensity profiles of the guided light varied with the number of laser passes over the same area. Average power and pulse width were 170 mW and 120 fs, respectively.

of the far field at 800 nm for 15 mm long fluoride-glass waveguides are shown in Fig. 21.7(a) and (b), where the core diameters were 8 and 27 μm, respectively. At a core diameter of 8 μm, it was possible to propagate only a fundamental mode that was nearly Gaussian, while a complicated intensity distribution resulting from the overlap of several modes was observed in a waveguide with the core diameter of 27 μm. Studies of the wavelength dependence of the mode profiles at several wavelengths ranging from 633 nm to 1 μm revealed that the cut-off wavelength of the waveguide in Fig. 21.7(a) was around 800 nm.

Figure 21.8 shows the result of Hermite–Gaussian fitting for the intensity distributions of the near field for the waveguide shown in Fig. 21.7(a), on an assumption that the refractive index of the core decreases in proportion to the square of the distance from the center. The calculated result is in good agreement with the experimental data, indicating that this waveguide is a graded-index one with a quadratic refractive-index distribution. The refractive indices of the core center and base glass calculated from the result of the fitting were 1.502 and 1.499, respectively.

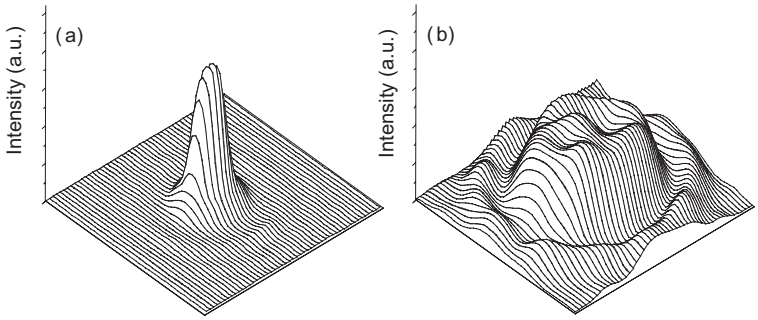

Figure 21.7: Intensity distributions of the far field at 800 nm for 15 mm long fluoride-glass waveguides where the core diameters were (a) 8 and (b) 27 μm.

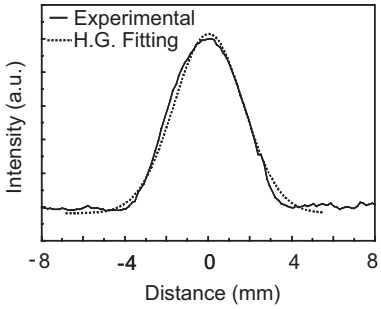

Figure 21.8: Result of Hermite–Gaussian fitting for the intensity distributions of the near field. The sample was the same as that observed in Fig. 21.7(a).

We have shown that permanent optical waveguides can be written in fluoride glass by using a femtosecond laser with a repetition rate of 200 kHz. Examination of the effects of the writing conditions on the refractive index and core size of optical waveguides showed that (i) the diameter and refractive index of the core increase with the average laser power at a constant pulse width, (ii) the refractive index of the core increases and the core diameter decreases as the pulse width is decreased at a constant average laser power, and (iii) the refractive index of the core increases with the number of laser passes, while the core diameter remains unchanged.

These results demonstrate that the parameters of waveguides can be controlled by adjusting the writing conditions.

21.4 Discussion

At present, we do not have a clear answer for the mechanism of the refractive index variation. We have examined the laser-irradiation region in silica glass by an atomic force microscope (AFM). Figure 21.9 shows the AFM image of the surface of a core end on silica glass. The shrinkage of the surface gradually increases from the outside of the core towards the center and

reaches a maximum of 45 nm. This result suggests that the densification of the glass occurs in the laser-irradiated region. The observed increases in the refractive index can be related to local densification which finally occurred inside the glass. It is quite possible, however, that the initial processes of the optical waveguide formation may be accompanied by various phenomena such as the formation of color centers or lattice defects, or melting of a very small area.

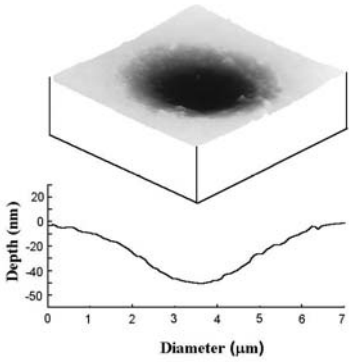

Figure 21.9: An AFM profile of the damage spot

The creation of defects in the glasses with high SiO_2 content resulting from 810 nm radiation suggests that the damage mechanism involves a multi-photon process. To our knowledge, the optical damage at this wavelength has not been previously reported, and it is speculated that the high pulse energy of the femtosecond laser is responsible for this effect. We believe that the photo-induced refractive index increase in glasses is a complex process which is due to both densification and defect generation.

21.5 Conclusions

Optical waveguides have been successfully fabricated in various glasses by ultra-fast pulses from a femtosecond laser. In addition, it was confirmed that single-mode waveguides could be written with femtosecond laser pulses. These facts open up new possibilities in the field of integrated optics and three-dimensional optical circuits, especially for compact, all-solid-state lasers, amplifiers and optical switches.

The existing knowledge of the mechanisms behind the permanent changes of the refractive index in various glasses is insufficient. The results presented in this paper demonstrate that it may be possible to fabricate three-dimensional optical integrated circuits in the interior of glasses with compositions using laser writing.

Acknowledgments

We acknowledge helpful discussions with Y. Kondo, H. Inouye, S. Fujiwara and T. Suzuki of the Hirao Active Glass Project, ERATO, JST, Japan. We thank N. Nishimura of Central Glass Co., Ltd. for his help with the fluoride glass fabrication.

References

[1] E. N. Glezer, M. Milosavljevic, L. Huang, R. J. Finlay, T.-H. Her, J. P. Callan, and E. Mazur, Opt. Lett. **24**, 2023 (1996).

[2] Y. Kondo, T Suzuki, H. Inouye, K. Miura, T. Mitsuyu, and K. Hirao, Jpn. J. Appl. Phys. **37**, 94 (1998).

[3] K. M. Daivis, K. Miura, N. Sugimoto and K. Hirao, Opt. Lett. **21**, 1729 (1996).

[4] K. Miura, J. Qiu, H. Inouye, T. Mitsuyu and K. Hirao, Appl. Phys. Lett. **71**, 3329 (1997).

[5] K. Miura, H. Inouye, J. Qiu, and K. Hirao, Nucl. Instrum. Methods Phys. Res. B **141**, 726 (1998).

[6] J. Qiu, K. Miura, T. Suzuki, Y. Kondo, T. Mitsuyu and K. Hirao, Appl. Phys. Lett. **74**, 10 (1999).

22 Applications of the Photodissolution Effect in Chalcogenide Glasses

Peter J.S. Ewen

The metal photodissolution effect that occurs in a wide range of chalcogenide glasses has many potential applications in areas requiring the fabrication of high-resolution or high-aspect ratio surface relief or embedded structures, such as diffraction gratings, photonic bandgap devices, components for integrated optics, and resists for nanolithography. Because these materials are also transparent to IR radiation they are particularly suited to producing devices and components for operation at IR wavelengths. This paper outlines the key features of the effect as far as imaging is concerned and surveys developments in the applications of the effect over the past decade. The advantages of the effect in comparison with the photodarkening phenomenon that occurs in chalcogenide glasses are also assessed.

22.1 Introduction

Since its discovery in the mid 1960s by Kostyshin and co-workers, the metal photodissolution (MPD) effect has been extensively studied, partly through interest in the fundamental mechanism of the phenomenon, but also because of its potential applications. In their original paper, Kostyshin *et al.* [1] noted the high-resolution capability of the process and predicted its use in micro-imaging.

The MPD effect and its applications have been the subject of earlier reviews [2–5]. The purpose of the present chapter is to summarize the work which has been done on the applications of the MPD effect since these earlier reviews were published. The following section contains a brief explanation of the effect together with a description of those of its properties which are important as far as applications are concerned. Subsequent sections cover the different application areas: high-resolution lithography; IR grating fabrication; IR optical components; and miscellaneous applications. A more detailed account of the mechanism of the MPD effect and its general properties is presented by Wágner and Frumar in Chapter 10.

22.2 The MPD Effect and its Imaging Properties

22.2.1 The Basic Effect

When a chalcogenide layer in contact with a layer of certain metals is illuminated, metal ions dissolve in the glass and migrate through it in the direction of illumination, thereby altering the composition and structure of the glass and changing its physical properties, particularly

its solubility and optical constants. This effect is termed "photodiffusion", "photodoping" or "photodissolution", and is illustrated in Fig. 22.1.

The effect is essentially a light-induced chemical reaction between the metal and the chalcogenide to form a new material, which may be a single compound or a phase-separated mixture. This reaction product separates the metal and chalcogenide layers, so that for the reaction to proceed, the new material must be both an ionic and electronic conductor, i.e. it must allow the metal ions and electrons to diffuse through it to reach the product/chalcogenide interface (x–y in Fig. 22.1), where they can continue to react with the chalcogenide. The process is analogous to the tarnishing of metal films. The purpose of the light is to lower the kinetic barrier preventing the reaction at room temperature, so that the light stimulating the effect is expected to be absorbed near the doped/undoped interface x–y, which has been confirmed experimentally [3, 6].

22.2.2 Material Systems Exhibiting the Effect

The effect has been observed in numerous chalcogenide systems, e.g. As–S, As–Se, Ge–Se, Ge–S, As–S–Te and As–Se-Te and is probably a characteristic of most amorphous chalcogenides. It occurs in melt-quenched glasses as well as films (either annealed or unannealed). A variety of metals, metal compounds and alloys (e.g. Ag, Cu, Zn, Ag_2S, Ag_2Se and alloys in the Ag–Cu system) have been used as the metal-ion source, which can be in the form of an evaporated film, a bulk substrate [7] or even a thin coating produced by dipping the chalcogenide into a solution of a metal compound [8]. Because such a large number of metal/chalcogenide combinations exhibit this effect there is considerable potential for optimizing the performance of imaging media based on it.

22.2.3 The Metal Concentration Profile

The amount of metal that can be introduced into a chalcogenide glass by photodissolution can be considerable, e.g. 30–40 atomic percent in some cases [9–11]. (For this reason "photodoping" is not really an appropriate term for the effect since doping generally suggests the introduction of small amounts of extraneous atoms. However, the term "photodoping" is widely used in the literature, the reaction product often being referred to as the "photodoped" material and the initial chalcogenide as the "undoped" glass.) In addition, the metal ions can be driven quite deep into the chalcogenide by photodissolution, for example in the $Ag/As_{16}S_{80}Te_4$ combination, Ag was found to penetrate at least 20 μm into the glass [12]. It should be noted that this is not necessarily the maximum penetration depth for this combination nor is it necessarily a typical value for all metal/chalcogenide combinations. It is not known whether in principle there is an effective upper limit to the penetration depth for a particular metal/chalcogenide combination.

One of the characteristics of the photodissolution effect is that the interface between the reaction product and the chalcogenide (x–y in Fig. 22.1) is usually relatively sharp, much sharper than that resulting from the Fickian distribution expected if the metal ions simply diffused into the chalcogenide in the same way as, for example, dopant diffuses into a semiconductor. Also, the metal concentration throughout the reaction product layer is essentially constant [9, 11, 12], so that the metal concentration profile during the process is often termed

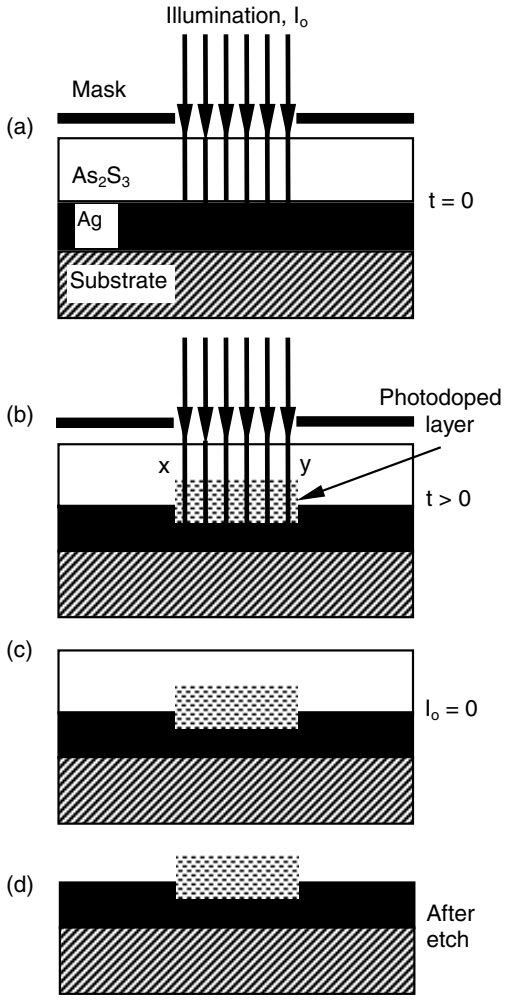

Figure 22.1: Schematic illustration showing a cross-section through an As_2S_3 film undergoing photodissolution with Ag, and the process of image formation. (a) The initial bi-layer system is illuminated at time $t = 0$. (b) During illumination the photodoped layer grows and the doped/undoped interface x–y progresses up through the film. (c) When the illumination is switched off an embedded structure remains in the film. (d) A surface relief structure can be produced by etching away the undoped material.

"step-like", although it should be noted that this does not necessarily imply a perfectly abrupt interface between the photodoped and undoped material, only that the interface is sharper than that resulting from simple diffusion.

22.2.4 Spectral Sensitivity

Photodissolution can be stimulated by photons with energies anywhere between the deep-UV (190 nm) [13] and the IR (800 nm) [14] spectral regions, the exact range of energies depending on the sample geometry and material compositions (it also occurs under X-ray, electron-beam or ion-beam irradiation [15–17]). The chalcogenide/metal combination may be illuminated from the chalcogenide side or, for very thin metal films, the metal side, although in the latter case the maximum thickness of photodoped layer achievable will be correspondingly small. The spectral sensitivity of the process depends on absorption in the chalcogenide/metal for illumination from the chalcogenide/metal side, as well as on the spectral dependence of the basic process. If the chalcogenide film thickness is greater than $\sim$100 nm and illumination is from the chalcogenide side as in Fig. 22.1 then the sensitivity in the UV will fall with increasing photon energy due to the high absorption of the chalcogenide layer in the UV. As the efficiency of the basic process is expected to decrease as the photon energy decreases, the sensitivity in the red spectral region will fall with decreasing photon energy. It should be noted that the process can still be stimulated with photons of energy below the bandgap energy for the undoped chalcogenide [14].

22.2.5 Imaging Properties

The MPD effect has two important features as far as imaging applications are concerned. First, because the dissolving metal ions do not migrate outside of the illuminated area an exact image of the intensity distribution at the surface of the chalcogenide film is created in the interior. Second, because such large amounts of metal (e.g. 30–40 atomic percent) can be driven into the glass, its structure and hence its properties are significantly altered: for example the difference in refractive index between the doped and undoped material may be as high as 0.5 (at visible and IR wavelengths [18]) and the doped material may be impervious to etchants that remove the undoped chalcogenide [19, 20]. Figure 22.1 shows schematically how images are formed using the effect and how either embedded or surface relief structures may be obtained in the film.

For most metal/chalcogenide combinations at room temperature the metal ions will dissolve into the glass only under illumination, so that if illumination ceases there is no further movement of the metal ions and no degradation of the stored image. However, at higher temperatures (e.g. $>$175 °C for the Ag/As_2S_3 system) thermally stimulated isotropic diffusion of the metal ions may occur.

22.3 Applications of the Effect

22.3.1 High-Resolution Lithography

One of the earliest and most important application areas for the MPD effect was in high-resolution lithography. This work was pioneered by groups at Bell Telephone Laboratories in the USA [21] and NTT laboratories in Japan [20]. The development of new resists is critical in sustaining the continuing trend in device miniaturization and in the 1980s chalcogenide resists

based on MPD were seen as a promising alternative to conventional organic resists, particularly because they overcame the "standing wave" problem. Although interest in chalcogenide resists has since declined, owing to improvements in organic resists, it may yet revive, because ultimately they have a higher resolution capability than conventional resists, which are based on large organic molecules.

The early work on resists employing the MPD effect has been surveyed in previous reviews [2, 4, 5, 20–24] and will not be covered here. Instead, the advantages of these resists will be summarized and only the most recent work described.

Resolution Capability

Mizushima and Yoshikawa [20] have demonstrated that features as small as 1 nm can be produced by these resists. The ultimate resolution achievable with any resist is fixed by the size of the "molecular" units from which it is made. In the case of these chalcogenide resists the diameter of the smallest such unit is a few interatomic distances.

The resolving power of a chalcogenide resist is also enhanced by the so-called "edge-sharpening" effect [21, 25] which tends to compensate for diffraction and interference effects in the aerial image.

Sensitivity to UV and Other Forms of Radiation

Chalcogenide resists are sensitive to UV light, either from conventional sources [25,26] or excimer lasers [13, 25, 27]. For example, Fig. 22.2 shows the sensitivity of the Ag_2Te/As_2S_3 system from 1.96–6.42 eV (632.8–193 nm) [25]. They can also be patterned using electron beams [16, 20, 28, 29], X-rays [15] or ion beams [17, 28].

Top-Surface Sensitivity

The usual configuration for these resists is to have the metal above the chalcogenide layer. For exposure from the metal source side, the resist system will have top-surface sensitivity [25], which eliminates standing wave effects and is important when depth of focus is small.

Contrast

The resist contrast, γ, is defined by

$$\gamma = 1/\ln(D_0/D_i)$$

where D_i is the threshold dose required for a photodoped layer to first appear and D_0 is the minimum dose required for the chalcogenide film to be photodoped from top to bottom.

These resists generally have a high contrast, γ. Typical values are given in Table 22.1.

Compatibility with Existing Process Technology

In addition to matching or surpassing the performance of organic resists, chalcogenide resists are also compatible with standard processing techniques such as plasma etching and spin

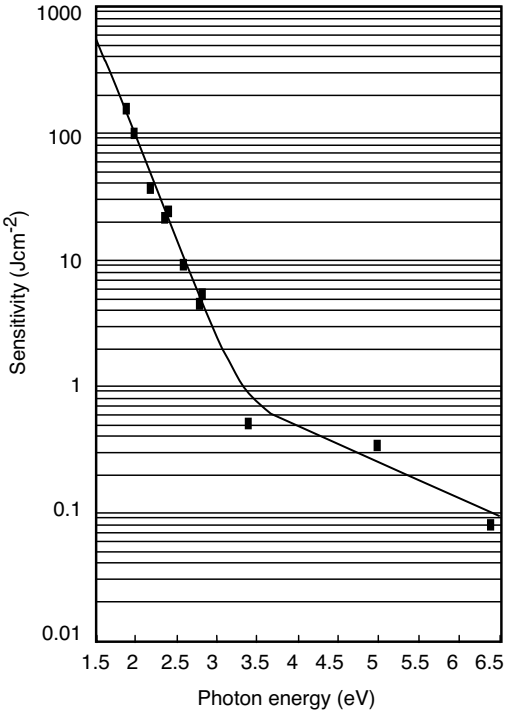

Figure 22.2: Sensitivity of the Ag_2Te/As_2S_3 system between 632.8 and 193 nm [25].

Table 22.1: Typical contrast values for chalcogenide resists based on the MPD effect, and for different exposure methods.

Exposure source	Contrast, γ	References
Conventional UV	$5 < \gamma < 15$	25, 26
Excimer laser	$\gamma \sim 10$	13, 27
Electron beam	$5 < \gamma < 9$	20, 28, 29
X-rays	$\gamma \sim 3.5$	15

coating. The resist layers can also be deposited by vacuum evaporation or sputtering, so that a complete ultra-clean, all-vacuum process can be set up [4].

Metal/Chalcogenide Resist Systems in Use

The most extensively studied resist system based on the MPD effect is Ag_2Se/Ge–Se [20, 21], although much work has also been carried out on Ag/As–S resists [30]. Eneva et al. [31] have investigated the combination Ag/$Ge_{30}S_{70}$ as a possible red-sensitive resist for the fabrication

of diffractive optical elements. Resists based on Ag_2Te/As_2S_3 have also been studied [13,25], particularly for use in 193 nm excimer laser lithography. They were found to yield a high contrast (of up to $\gamma = 15$) and also exhibited the "edge-sharpening" effect. Although the sensitivity (100 mJ/cm^2 at 193 nm) was slightly poorer than for Ag/As_2S_3 it was felt that the telluride-based system was superior in terms of ease of use and reproducibility.

Characteristic Curves

Bello and Jishi [32] have determined theoretically the characteristic curves for Ag/As_2S_3 photoresist, that is curves of normalized thickness remaining after development vs. exposure. They find that the curves yield a high contrast and are also unaffected by the standing-wave effect provided diffraction effects are negligible. Diffraction effects are significant in situations where the pattern dimensions are comparable with the exposure wavelength.

22.3.2 IR Diffractive Optical Elements

In addition to the wide range of photo-induced effects they exhibit, chalcogenide glasses have another important property, namely they are infrared transmitting materials, with passbands (depending on composition) from the visible to beyond 15 μm. By combining these two useful properties, diffractive optical elements for operation in the IR spectral region can be produced, since light-induced effects such as MPD can be used to produce the surface-relief or embedded structures required for devices such as gratings, Fresnel lenses and kinoforms. Diffractive optical elements have several potential uses, for example in beam combining, filtering and spectral analysis, and may have advantages over conventional refractive or reflective IR components as regards weight, cost and ease of manufacture. The early work on this application of the MPD effect was summarized in a previous review [5].

In the fabrication of IR gratings, the MPD effect has two advantages over the other photo-induced effects exhibited by chalcogenides: it results in a large change in the refractive index, n, of the glass (Δn values of up to ~ 0.5 can be obtained [18]); and it produces a large change in the etch resistance of the glass. Differential etch rates of up to $\sim 400{:}1$ can be achieved between the photodoped and undoped material [19, 20, 33, 34], depending on the glass composition, the amount of metal introduced and the etchant. Figure 22.3 shows how the etch rate varies with Ag content for the case of photodoped As_2S_3.

A large change in refractive index is required for the embedded structures used in bulk phase gratings, and high differential etch rates enable deep surface relief structures to be created. For efficient operation, IR gratings must be relatively deep (>1 μm), which is in contrast to the case for the lithographic applications, where much thinner films are used (<0.2 μm).

The required depths, d, for different types of grating element at different wavelengths of operation have been calculated from theory [18] and typical values for a square-wave grating profile are given in Table 22.2.

Photodoping to a depth of 20 μm has been reported for $Ag/As_{16}S_{80}Te_4$ [12] and if this is typical of chalcogenide systems then most of the structures in Table 22.2 should be achievable.

Much of the work on diffractive elements made by MPD has been done using the Ag/As–S combination but other chalcogenide systems (As_2Se_3, $GeSe_2$ [35] and $Ge_{30}S_{70}$ [31]) have also been investigated.

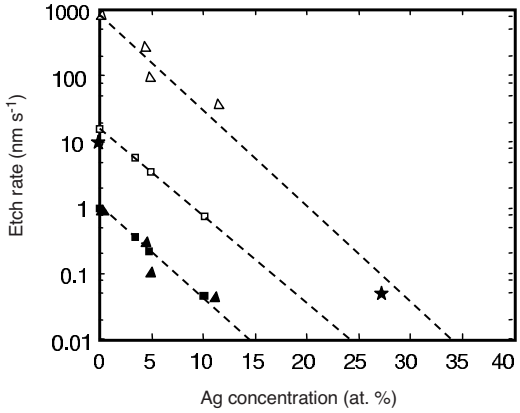

Figure 22.3: Etch rate of Ag-photodoped As_2S_3 in 1 N (△) and 0.1 N (□) NaOH solutions for different amounts of Ag. (Data are calculated from measurements in Refs. [33] and [19] for 1 N and 0.1 N NaOH, respectively.) Filled points (▲, ■) show the rates relative to those for the undoped material. The straight lines are a linear guide for the eye and have been extrapolated to large Ag contents. Also shown are the etch rates (★) of undoped and Ag-photodoped As_2S_3 for dry etching with CF_4 plasma [34].

Table 22.2: Depth of profile, d, required for optimum operation of a square-wave grating at different replay wavelengths [18].

	Depth, d/(μm)		
Replay wavelength/(μm)	0.632	4.0	10.6
Bulk phase grating	1.39	8.77	23.2
Surface relief grating	0.48	3.0	8.06
Blazed zone plate	0.38	2.4	6.42

Because MPD is essentially a diffusion-controlled process the required exposure time increases as the square of the grating depth, so that long exposures are required for thick structures. However, the speed of the MPD process can be increased by an order of magnitude by simultaneously applying heat (photothermal doping) [36]. Provided the temperature is not too great (less than ∼100 °C for the Ag/As_2S_3 system) purely thermal doping, which is isotropic and hence affects grating linewidth, is comparatively negligible. To produce gratings holographically at elevated temperatures would be problematic because of, for example, the creation of air currents, but mask exposure of a heated sample may be viable.

The speed of the MPD process can also be enhanced by the use of multilayered structures. It has been shown that samples consisting of alternate layers of Ag and $As_{33}S_{67}$ yield a photodissolution rate that is 1–2 orders of magnitude faster than for the conventional bilayer structure [37]. Using this technique a 2.3 μm thick bulk phase grating was produced by mask exposure in a sample with 20 alternating layers. Each Ag layer must be sufficiently thin

that it is transparent at the exposure wavelength, and provided the chalcogenide layer is thick enough, the Ag in the unexposed regions is depleted by lateral photodissolution, so that these regions also become transparent.

In the conventional bilayer structure, MPD can be stimulated by exposure from the chalcogenide side or from the metal side, although in the latter case the metal layer must be sufficiently thin to allow the light to pass through to reach the doped/undoped interface. However, using a thin metal layer as the source results in a shallow photodoped region, or one that is only lightly doped, which in turn implies a small change in n and etch resistance. For deep structures, or large values of Δn and differential etch rate, thicker metal layers must be used as the source.

Because such thick layers are not transparent at IR wavelengths, any of the metal source remaining after exposure must be removed by etching. This means that in the conventional bilayer structure the metal layer must be deposited above the chalcogenide, which implies that imaging must take place through the substrate. This constraint can be circumvented by first depositing the metal on the substrate and then patterning it prior to depositing the chalcogenide on top [38]. The combination is then flood illuminated from the chalcogenide side and the grating pattern in the metal is transferred into the glass by photodissolution. In this case, heating to increase the rate of photodissolution can easily be carried out simultaneously with illumination.

High diffraction efficiencies ($>90\%$) should be achievable with these gratings provided their depth and period have been optimized and they have an anti-reflection coating. Theoretical predictions for bulk (i.e. embedded) gratings with different profiles are illustrated in Fig. 22.4 [36], which shows how diffraction efficiency varies with depth normalized to the grating period, which was fixed at 0.79λ, λ being the replay wavelength. A triangular profile yields the highest efficiency (99%).

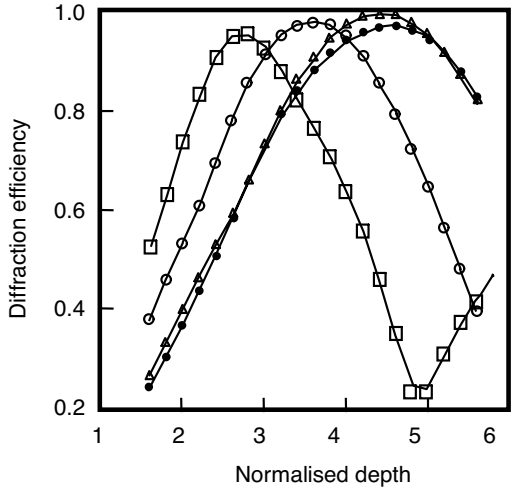

Figure 22.4: Theoretical first-order diffraction efficiencies of bulk phase gratings with various profiles: □, square; ○, sinusoidal; △, triangular; ●, parabolic [36].

An important technological requirement for grating devices is that their performance at elevated temperatures should be stable. For gratings produced by the MPD effect, there is the possibility that thermal diffusion may cause some redistribution of the metal ions over time. This may have little effect for surface relief devices but the performance of bulk gratings might deteriorate. In the case of bulk gratings made with $Ag/As_{33}S_{67}$ it was found that gratings held at 100 °C in the dark over 6 months did not deteriorate significantly, although there was evidence of some redistribution of the Ag ions [36].

The MPD effect can, of course, be used to produce gratings for operation in the visible [35, 39–41], although the advantages of chalcogenides over the wide range of other materials that can be used for "visible" grating fabrication are less obvious. Gerke et al. [40] have investigated the use of dry etching in the fabrication of gratings for the visible produced by MPD in the $Ag/GeS_{0.5}Se_{3.5}$ system. The development of anisotropic dry-etching techniques is useful as it provides a route for obtaining blazed relief structures.

Blazed structures can also be made by producing a grating with a symmetrical profile in an undoped chalcogenide film (e.g. using photodarkening and subsequent etching) and then depositing Ag on the grating at an angle to the normal [41]. The Ag can then be photodoped or thermally doped into the grating to give etch resistance to part of the profile. A second etching step is then carried out which removes material from the unprotected regions, yielding an asymmetric profile.

22.3.3 IR Optical Components

The MPD effect offers a general process for creating embedded or surface relief microstructures in chalcogenide films or on the surface of bulk chalcogenide substrates. Hence the effect can, in principle, be used to produce many other types of structure in addition to the one-dimensionally periodic grating structures described in the previous section, for example Fresnel zone plates, structured antireflection surfaces [42, 43], or binary optical elements [44]. Many of the technology issues pertaining to grating fabrication (resolution, etch resistance, depth achievable, stability, etc.) which were dealt with above are also applicable to these other structures and will not be discussed further. The following sections summarize the various types of component that have been made or proposed based on the MPD effect. These are generally intended for operation at IR wavelengths, in order to take advantage of the IR transparency of these materials.

Microlens Arrays

Microlens arrays consist of an array of microscopic-sized lenses fabricated on a planar substrate and find applications in integrated optics, image processing and optical computing [45]. Eisenberg and co-workers [46, 47] have produced microlens arrays in undoped As–S films using the normal photo-induced solubility change that occurs in many chalcogenide compositions. For example, a 40×40 array of 12 μm diameter lenses with a 12 μm pitch was fabricated in a 0.35 μm thick film. After the array had been formed, a layer of Ag was evaporated over it and exposed to UV light. By photodoping Ag into the glass in this way it was possible to increase its refractive index (from 2.5 to 2.9) and hence alter the focal length of the microlenses (from 34 μm to 27 μm).

A microlens array can also be fabricated directly using the MPD effect itself. One possible method has been demonstrated by Wagner et al. [11], who produced a 24×24 array of 20 μm diameter lenses by photodissolving Ag into $As_{33}S_{67}$ (see Fig. 22.5). In this technique, lens-shaped surface relief is produced by the volume expansion accompanying photodissolution.

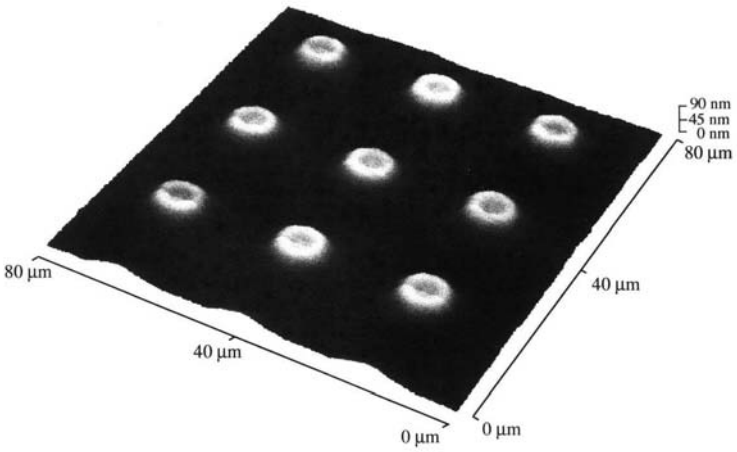

Figure 22.5: Atomic force microscope image of part of a microlens array produced by Ag photodissolution into an $As_{33}S_{67}$ film. The surface relief is 90 nm high and is due to the volume expansion accompanying photodoping [11].

Waveguides

The MPD effect can in principle be used to define strip waveguides, although due to the increased absorption at red wavelengths which accompanies photodoping, only IR wavelengths could be propagated. The waveguiding properties of As_2S_3 photodoped with Ag have been investigated by Ogawa et al. [48], who found that a small, lightly doped region could be used to deflect a 632.8 nm laser beam propagating through an undoped As_2S_3 film. This was attributed to a refractive index gradient at the boundary of the doped region and was proposed as the basis of a micro-optical waveguide element.

Photonic Bandgap Structures

Photonic bandgap (PBG) structures are essentially media with a periodic spatial modulation in refractive index and have applications, for example, in reflectors, cavities and waveguiding [49]. Creating such structures in chalcogenide films would help realize the potential of PBG devices in the IR spectral region.

A rule-of-thumb is that the period of these structures should be *smaller* than the wavelength of operation but that the depth (for 2D structures) should be *greater* than the wavelength. This implies that aspect ratios >1 are required for these structures. The work on

MPD-based resists has demonstrated that high-resolution features can be defined in *thin* films using UV exposure and the work on IR gratings has shown that deep structures (i.e. of at least several microns depth) can be produced using MPD.

However, producing features that are both fine *and* deep using the MPD effect is problematic [50] because the UV light required for high-resolution patterning penetrates only a fraction of a micron into a chalcogenide sample, because of strong absorption in these materials. There are possibilities for circumventing this problem but they add to process complexity, for example, thin photodoped regions created at the surface of a chalcogenide film can be used as a mask for anisotropic etching of the undoped chalcogenide underneath. An alternative approach might be to use MPD (or another photo-induced effect) to produce the coarser waveguide structures in which the PBG arrays are made, and then to create the PBG features in the waveguide using a technique such as focused ion-beam (FIB) milling [50]. An example of this technique is shown in Fig. 22.6, which shows an $As_{33}S_{67}$ waveguide produced by photodarkening, and an array of holes milled in it using an FIB [51].

22.3.4 Miscellaneous Applications

X-Ray Recording Medium

As mentioned above, in the section on lithography, MPD can also be stimulated by X-rays. Somemura et al. [52] have investigated MPD in the Ag–Se/Ge–Se system as a basis for recording soft X-ray holograms for use in e.g. 3D X-ray microscopy. Soft X-ray exposure of an Ag–Se/Ge–Se film induces a reflectance change with no additional processing required. This combination has a potential resolution of 10 nm and good sensitivity.

Ion-Selective Membranes and Solid-State Batteries

As–S and As–Se films photodoped with Ag or Cu have been investigated as ion-selective membranes for sensing Ag or Cu ions [53, 54]. These films are intended for use as the membranes in ion-selective field-effect transistors. The role of the dopants is to improve the electroconductivity of the membranes. Chemical sensors have a wide variety of uses, for example in medical diagnosis, pollution monitoring and chemical process control.

Ag photodoping in multilayer structures composed of films of $GeSe_3$ and superionic glasses has been investigated with a view to their use in solid-state batteries [55]. However, for this particular metal/chalcogenide combination only a small amount of Ag could be extracted electrochemically after photodoping.

UV Dosimetry

It has been suggested [56] that the MPD effect could be used as the basis of a personal dosimeter for measuring cumulative exposure to UV radiation. The technique is based on the well-known resistance monitoring technique that is often used to measure the kinetics of the effect. Exposure dosage is determined by measuring the increase in the resistance of the metal layer that is dissolving into the chalcogenide during illumination.

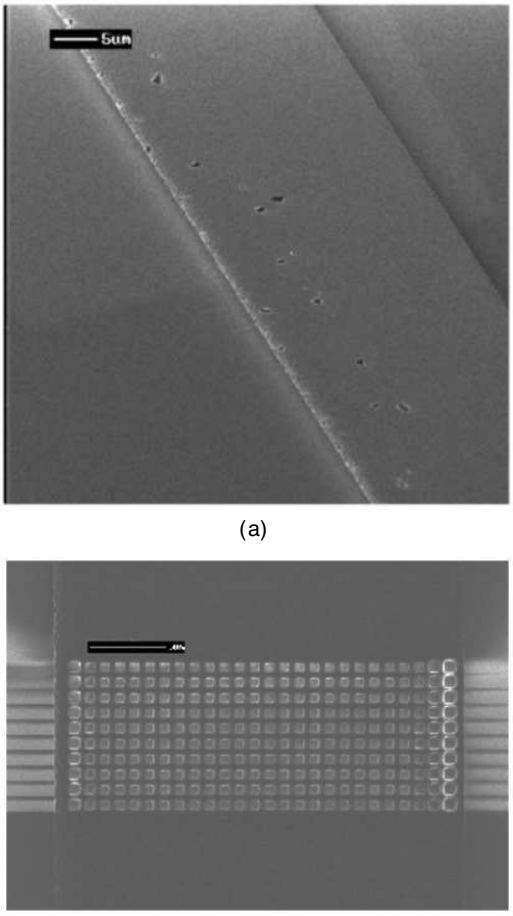

(a)

(b)

Figure 22.6: SEM images of: (a) a 25 μm wide, 2.5 μm deep waveguide produced in an $As_{33}S_{67}$ film using photodarkening and wet etching; (b) a 10×25 array of 0.5 μm square holes produced by FIB milling in a 2.5 μm deep waveguide [51]. The scale marker in each picture indicates a distance of 5 μm.

Gray-Scale Mask Fabrication

It has also been proposed that MPD using Ag/Ge–Se could be used to produce high-resolution gray-scale masks [57]. The columnar structure of Ge–Se films could give a possible edge precision of 100 Å and should prevent undercutting during etching, thus allowing pixels to be placed close together.

Memories and Other Devices

Kozicki and co-workers [58–61] have investigated dendrite formation in photodoped chalcogenide films and proposed that it could be used as the basis of a variety of devices including programmable read-only memories, programmable resistance/capacitance devices and field-configurable connections. The basic device consists of two metal electrodes with a layer of photodoped material sandwiched between them. When an appropriate voltage difference is applied across the electrodes, metal ions come out of the photodoped glass and form an electrodeposit between them, thereby forming a connection.

The ion conduction that occurs in the photodoped layer is an important aspect of the operation of these devices and also for the electrochemical applications such as sensors and batteries [62].

22.4 Comparison of MPD and Photodarkening as Techniques for Producing Structures

The widely studied photodarkening effect that occurs in chalcogenides can also be used to produce images or structures in films or bulk samples of these glasses [5, 24]. In this section the advantages and disadvantages of photodarkening and MPD as fabrication methods are compared.

Process Complexity

MPD yields a somewhat more complex fabrication process as two layers must be deposited (metal and chalcogenide), and for some applications any metal remaining after exposure must be etched away. In contrast, for photodarkening only a single layer needs to be deposited.

Etching

Very high differential etch rates (up to 400:1) between exposed and unexposed regions can be achieved using the MPD effect using either wet or dry etching. The differential etch rates achievable using photodarkening and wet etchants can also be good, although problems with undercutting can occur in thicker films [63]. Differential etch rates for dry etching using photodarkening are much poorer [34, 40, 64].

Exposure Time

Exposure time is not a problem when imaging in thin films using the MPD effect. However, because MPD involves diffusion, exposure time increases as the square of the structure depth, which means that long exposure times are required to produce structures more than a few microns deep, e.g. for IR gratings. This necessitates the use of stable exposure systems and for volume manufacturing may lead to problems of low throughput or equipment wear. For these thicker structures, exposure time is less of an issue in the case of photodarkening.

Imaging Requirements

For patterning thin films there are no special imaging requirements when using MPD but to produce thicker photodoped structures a thicker metal layer is required as the source, hence exposure must be from the chalcogenide side. This in turn requires that the illumination wavelength is in the visible rather than the UV, since UV light is strongly absorbed by chalcogenides and may not penetrate to the metal layer. In addition, if any unreacted metal is to be removed after exposure, the metal layer must be above the chalcogenide, so that exposure must take place through the substrate. This requirement can be circumvented by pre-patterning the metal layer [38] but this adds additional steps to the fabrication process.

To produce thick structures using photodarkening, visible rather than UV illumination is again required.

Suitability for Embedded Structures

Applications such as bulk phase gratings and certain photonic bandgap structures require the sample to have regions of one material embedded in another, each material having a different refractive index. For example, for the grating case, alternating stripes of high and low refractive index material are required. Generally, the larger the refractive index difference, the better is the device performance. The MPD effect can yield large refractive index differences between the doped and undoped material (up to 0.5). However, photodarkening produces a much smaller change in refractive index (<0.1).

In addition, embedded structures produced by MPD are more stable at elevated temperatures – the difference in refractive index produced by photodarkening tends to decrease on heating.

Homogeneity

For some applications (e.g. gratings and photonic bandgap structures) the uniformity of the exposed region may be important. In the case of MPD we have some evidence from scattering experiments that heavily doped regions may not always be homogeneous (even when a single phase glass composition exists, as in the case of Ag photodoping into $As_{33}S_{67}$). In contrast, photodarkened material is homogeneous and has low scattering losses.

Maximum Depth of Structure Achievable

Photodoping to a depth of more than 20 μm has been reported for the Ag/$As_{16}S_{80}Te_4$ system [12], but it is not known whether this is a typical value for all chalcogenides. For photodarkening, structures 5 μm deep have been reported [65] and even deeper ones may be achievable by optimizing the exposure wavelength and etchant.

22.5 Conclusions

This chapter has outlined the key features of the MPD effect as far as imaging is concerned and surveyed developments in the applications of the effect in various fields over the past decade.

The strengths and weaknesses of MPD as the basis of an imaging or fabrication process have been considered. In terms of etching and suitability for embedded structures, MPD is superior to photodarkening, but involves greater process complexity and can involve more demanding exposure requirements than the latter. The details of the particular application will determine which photo-induced effect is most appropriate as the basis for the fabrication technique.

An important issue regarding applications is, of course, cost. Much of the work done on MPD has used Ag as the metal source, which is comparatively expensive. Recently, however, photodoping with Cu has been revisited [66] and suggested as the basis of a more competitive process. Studies of new metal/chalcogenide combinations may also overcome some of the problems associated with MPD as a fabrication method, for example by yielding improvements in the speed of the process.

References

[1] M.T. Kostyshin, E.V. Mikhailovskaya, and P.F. Romanenko, Sov. Phys. – Solid State **8**, 451 (1966).

[2] A.V. Kolobov and S.R. Elliot, Adv. Phys. **40**, 625 (1991).

[3] A.E. Owen, A.P. Firth, and P.J.S. Ewen, Phil. Mag. B **52**, 347 (1985).

[4] K. Tanaka, J. Non-Cryst. Solids **138**, 1021 (1991).

[5] P.J.S. Ewen and A.E. Owen, in High Performance Glasses, M. Cable and J.M. Parker (Eds.), Blackie, Glasgow, 1992, p. 287.

[6] A.V. Kolobov, S.R. Elliott, and M.A. Taguirdzhanov, Phil. Mag. B **61**, 859 (1990).

[7] P.J.S. Ewen, W.T. Taylor, A.P. Firth, and A.E. Owen, Phil. Mag. B **48**, L15 (1983).

[8] S. Petrova, P. Simidchieva, and A. Buroff, Proc. Conf. "Amorphous Semiconductors – 84", E. Fahri-Vateva and A. Buroff (Eds.), Bulgarian Academy of Sciences, Sofia, 1984, p. 256.

[9] M. Janai, Phys. Rev. Lett. **47**, 726 (1981).

[10] M. Yamaguchi, I. Shimizu, and E. Inoue, J. Non-Cryst. Solids **47**, 341 (1982).

[11] T. Wagner, G. Dale, P.J.S. Ewen, A.E. Owen, and V. Perina, J. Appl. Phys. **87**, 7758 (2000).

[12] E. Inoue, H. Kokado, and I. Shimizu, J. Jpn. Soc. Appl. Phys. (Suppl.) **43**, 101 (1974).

[13] J.M. Lavine and M.J. Buliszak, J. Vac. Sci. Technol. B **14**, 3489 (1996).

[14] S.A. Lis and I.M. Lavine, Appl. Phys. Lett. **42**, 675 (1983).

[15] K. Saito, Y. Utsugi, and A. Yoshikawa, J. Appl. Phys. **63**, 565 (1988).

[16] G.H. Bernstein, W.P. Liu, Y.N. Khawaja, M.N. Kozicki, and D.K. Ferry, J. Vac. Sci. Technol. B **6**, 2298 (1988).

[17] R. Klabes, A. Thomas, G. Kluge, W. Beyer, R. Grotzschel, and P. Suptitz, Phys. Stat. Sol. A **106**, 57 (1988).

[18] C.W. Slinger, A. Zakery, P.J.S Ewen, and A.E. Owen, Appl. Opt. **31**, 2490 (1992).

[19] N. Tohge, T. Minami, and T. Tsubaki, J. Mat. Sci. Lett. **8**, 935 (1989).

[20] Y. Mizushima, and A. Yoshikawa, in Amorphous Semiconductor Technologies and Devices, Y. Hamakawa (Ed.), Omsha, Tokyo, 1981, p. 277.

[21] K.L. Tai, E. Ong, and R.G. Vadimsky, Proc. Electrochem. Soc. **82–89**, 9 (1982).

[22] A.V. Kolobov, J. Non-Cryst. Solids **166**, 1159 (1993).

[23] Y. Utsugi, A. Yoshikawa, and T. Kitayama, Microelectronic Eng. **2**, 281 (1984).

[24] S.R. Elliott, in Materials Science and Technology, Vol. 9, R.W. Cahn, P. Haasen and E.J. Kramer (Eds.), VCH, Weinheim, 1991, p. 375.

[25] S.A. Dumford and J.M. Lavine, J. Vac. Sci. Technol. B **12**, 44 (1994).

[26] M.N. Kozicki, S.W. Hsia, A.E. Owen, and P.J.S. Ewen, J. Non-Cryst. Solids **138**, 1341 (1991).

[27] K.J. Polasko, R.F.W. Pease, E.E. Marinero, and M.R. Cagan, J. Vac. Sci. Technol. B **3**, 319 (1985).

[28] K. Balasubramanyam, L.J. Chen, A.L. Ruoff, and E.D. Wolf, J. Appl. Phys. **53**, 5975 (1982).

[29] Y.C. Liang, H. Yamanaka, and K. Tada, Thin Solid Films **165**, 55 (1988).

[30] S.A. Kostyukevych, Proc. SPIE **3424**, 20 (1998).

[31] J. Eneva, A. Gushterov, B. Tomerova, and B. Mednikarov, J. Mat. Sci.: Mat. Electron. **10**, 529 (1999).

[32] A.F. Bello, R.A. Jishi, and J. Imaging Sci. Technol. **36**, 562 (1992).

[33] J. Plocharski, J. Przyluski, and H. Wycislik, J. Non-Cryst. Solids **56**, 325 (1983).

[34] M.S. Chang and J.T. Chen, Appl. Phys. Lett. **33**, 892 (1978).

[35] I.Z. Indutnyi, A.V. Stronski, S.A. Kostioukevitch, P.F. Romanenko, P.E. Schepeljavi, and I.I. Robur, Opt. Eng. **34**, 1031 (1995).

[36] P.J.S. Ewen, A. Zekak, C.W. Slinger, G. Dale, D.A. Pain, and A.E. Owen, J. Non-Cryst. Solids **164–166**, 1247 (1993).

[37] T. Wagner and P.J.S. Ewen, J. Non-Cryst. Solids **266–269**, 979 (2000).

[38] G. Dale and P.J.S. Ewen, IEE Proc. – Optoelectron. **144**, 426 (1997).

[39] I.Z. Indutnyi, M.T. Kostishin, P.F. Romanenko, P.F., and A.V. Stronskii, J. Inf. Rec. Mater. **19**, 329 (1991).

[40] R.R. Gerke, T.G. Dubrovina, P.A. Dmitrikov, and M.D. Mikhailov, J. Opt. Technol. **64**, 1008 (1997).

[41] M.V. Sopinskyy, P.F. Romanenko, I.Z. Indutnyy, and E.F.Venger, J. Optoelectron. Adv. Mater. **3**, 383 (2001).

[42] E.B. Grann, M.G. Moharam, and D.A. Pommet, J. Opt. Soc. Am. **A12**, 333 (1995).

[43] E.B. Grann and M.G. Moharam, J. Opt. Soc. Am. **A13**, 988 (1996).

[44] M.B. Stern, Microelectron. Eng. **32**, 369 (1996).

[45] D. Daly and T. Hessler, Photonics Spectra **35(7)**, 120 (2001).

[46] N.P. Eisenberg, M. Manevich, M. Klebanov, V. Lyubin, and S. Shtutina, Proc. 3rd EOS Topical Meeting on Microlens Arrays, 11th, 12th May 1995, Teddington, UK, 1995, p. 29.

[47] N.P. Eisenberg, M. Manevich, M. Klebanov, V., Lyubin, and S. Shtutina, J. Non-Cryst. Solids **200**, 766 (1996).

[48] T. Ogawa, M. Wakaki, S. Tatumi, Y. Miyanishi, and J. Lee, Proc. SPIE **2778**, 275 (1996).

[49] J.D. Joannopoulos, R.D. Meade, and J.N. Winn, Photonic Crystals: Molding the Flow of Light, Princeton University Press, Princeton, 1995.

[50] G. Dale, R.M. Langford, P.J.S. Ewen, and C.M. Reeves, J. Non-Cryst. Solids **266–269**, 913 (2000).

[51] P.J.S. Ewen, A.E. Owen, and G. Dale, Final Report on EPSRC Grant GR/L73296 (1999).

[52] Y. Somemura, A. Yoshikawa, and Y. Utsugi, Jpn. J. Appl. Phys., **31**, 3712 (1992).

[53] R. Tomova, J. Assa, R. Stoycheva-Topalova, and A. Buroff, J. Non-Cryst. Solids **260**, 195 (1999).

[54] R. Tomova, G. Spassov, R. Stoycheva-Topalova, and A. Buroff, J. Non-Cryst. Solids **266–269**, 985 (2000).

[55] J. Kawamura, J. Iriyama, and Y. Nakamura, Solid State Ionics **90**, 303 (1996).

[56] M.N. Kozicki, US Patent 5500532 (1996).

[57] B. Block, A.O. Thornton, J. Ingwersen, and W. Daschner, US Patent 6033766 (2000).

[58] M.N. Kozicki, M. Yun, L. Hilt, and A. Singh, in Solid-State Ionic Devices, E.D. Wachsman, J.R. Akridge, M. Liu, and N. Yamazoe (Eds.), Electrochemical Society Series **99**, 298 (1999).

[59] M.N. Kozicki, M.Yun, S.J. Yang, J.P. Aberouette, and J.P. Bird, Superlattices Microstructures **27**, 485 (2000).

[60] M.N. Kozicki and W.C. West, US Patent 5761115 (1998).

[61] M. Mitkova and M.N. Kozicki, J. Non-Cryst. Solids **299–302**, 1023 (2002).

[62] M. Kawasaki, J. Kawamura, Y. Nakamura, and M. Aniya, Solid State Ionics **123**, 259 (1999).

[63] S. Mamedov and A. Kisliuk, J. Vac. Sci. Technol. B **14**, 1864 (1996).

[64] K. Petkov, R. Todorov, L. Tichy, and P.J.S. Ewen, Proc. 19th Int. Congress on Glass, 1–6 July 2001, Edinburgh.

[65] M. Vlcek, P.J.S. Ewen, and T. Wagner, J. Non-Cryst. Solids **227–230**, 743 (1998).

[66] M.V. Sopinskyy and M.T. Kostyshin, J. Optoelectron. Adv. Mater. **3**, 411 (2001).

23 Engineering Glassy Chalcogenide Materials for Integrated Optics Applications

Kathleen Richardson, Thierry Cardinal, Martin Richardson, Alfons Schulte, and Sudipta Seal

23.1 Introduction

Next generation devices for telecommunication and related applications will rely on the development of materials which possess optimized physical properties that are compatible with packaging requirements for systems in planar or fiber form. This allows suitable "integration" to existing fiber-based applications and hence requires appropriate consideration to material choice, its stability and long-term aging behavior. Included within this chapter are results of recent efforts to engineer materials suitable for such integration. First, needs for integrated optics and the attractiveness of chalcogenide-based glasses (ChGs) are reviewed. Second, the flexibility offered within the As–S–Se glass system is discussed, and comparisons are drawn between glasses in bulk and film forms. Following a description of the chemical systems and the properties evaluated on materials in bulk glass and film form, results of efforts to create components and characterize key structural attributes of such elements are described. The property differences and characterization tools employed to realize these data are presented. Efforts have been made in these studies to process and characterize the resulting structures in the form to be used in their final device geometry. Lastly, the ability to photo-induce changes within these glasses are discussed and key issues of such modification are reviewed. Described are results of efforts to tailor optical properties concurrent with structural stability, and to evaluate changes to these properties which result during photo-modification and subsequent aging.

23.2 Chalcogenide Glasses for Near-Infrared (NIR) Optics

Two characteristics of As–S–(Se) compounds – a large glass forming region and a wide optical transmission band, with potentially low loss for the 1.3–1.55 μm telecommunications window – make them excellent candidates for infrared guiding applications. The ability to process these glasses in substantial quantities in their bulk form, and their demonstrated capability of fabricating good optical quality thin films formed by thermal evaporation and other deposition techniques, enables the realization of relatively low cost As–S–(Se) integrated optical components. With appropriate consideration of function and application, such components can be "integrated" onto a single "chip" or substrate.

In complementary work to that described elsewhere in this text, we and our collaborators have demonstrated a range of optical functions that can be realized in these glasses, including rare earth (Pr and Er) doping and emission in key telecommunication wavelengths, fabrication

of waveguides (channel, self-written, fs-written), that can laterally or vertically couple light to various locations within a planar structure, and gratings (relief and phase) that can spectrally filter or modulate light. The results, summarized below, illustrate the attractiveness of these materials for such applications.

ChGs are photosensitive when exposed to bandgap energy ($E_g \sim 2.35$ eV for As_2S_3) [1,2]. Taking advantage of these photosensitive effects (photodarkening and photoexpansion) in ChGs, allows the creation of bulk waveguide structures [3], or the patterning of photo-induced relief gratings and guided wave structures in ChG films [4–6]. Recent results by our group in this area are presented later in this chapter. The interplay between micro-structure and desirable properties of devices is illustrated in materials suitable for use in high-speed optical communication applications. Such applications require all-optical processing and switching capabilities which must be compatible with system configurations, possess ultrafast broadband response time, as well as low linear and nonlinear loss. Additionally, the material must be amenable to the small sizes and stability requirements needed for future "on chip" devices. Chalcogenide glasses (ChGs) have shown promise in that they exhibit properties compatible with the above requirements at 1.3 and 1.55 μm wavelengths [7]. Recent experiments on As–S, As–S–Se and related compounds have demonstrated flexibility in forming fiber and film devices such as narrow-band spectral Bragg filters [8] and lens-arrays, rare earth doped structures [9,10] as well as couplers and self-written planar waveguides made from single and multilayer film structures [11].

Key to the realization of components in any optical communication system, is a knowledge that the material can carry out its function and maintain stability over specified thermal, mechanical and environmental conditions, for a defined lifetime. Hence, the most attractive material is only useful if a full understanding of its performance can be made in its "use" geometry. Thus, results of our studies to engineer chalcogenide glasses for optical applications have focused on the key property performance of the glasses in the final device geometry. We have sought to define fundamental differences associated with processing and use, to identify long-term stability issues and resolve them, with compositional and processing modifications.

23.3 Bulk Chalcogenide Glasses (ChG): Composition and Optical Properties

Two kinds of glass samples have been used throughout the results reported here: binary stoichiometric arsenic trisulfide (As_2S_3 or $As_{40}S_{60}$) or its selenide analogue, originating from a commercial source or prepared by a distillation process. The commercial samples, depending on the lot, exhibited regions with dark particles observed by optical microscopy. These dark particles were identified as carbon particles by Fourier transform infrared (FTIR) spectroscopy, through measurement of an optical vibration mode at 1500 cm^{-1} characterizing the C–S bonds. In order to improve the optical quality of glasses by removing potentially absorptive inclusions, a distillation procedure was established. The second type of samples were ternary As–S–Se glasses containing $\leq$40 mol% As. The fabrication procedure employed to obtain inclusion-free bulk glass material is described in detail in [12].

Table 23.1: Compositions, density ρ, glass transition temperature T_g, and energy gap E_g of bulk binary and ternary glasses.

Glass number	Composition	ρ (g/cm^3) ($\pm$ 0.01)	T_g (°C) ($\pm$ 2°C)	E_g (eV)
1	$As_2S_3(As_{40}S_{60})$	3.20	215	2.13
2	$As_{40}S_{45}Se_{15}$	3.56	207	1.88
3	$As_{40}S_{30}Se_{30}$	3.92	202	1.72
4	$As_{40}S_{15}Se_{45}$	4.27	196	1.62
5	$As_{40}Se_{60}$	4.59	191	1.54
6	$As_{32}S_{34}Se_{34}$	3.74	154	1.75
7	$As_{24}S_{38}Se_{38}$	3.63	131	1.74
8	$As_{18}S_{41}Se_{41}$	3.50	114	1.72
9	$As_{24}S_{76}$	2.67	147	2.06
10	$As_{24}S_{57}Se_{19}$	3.11	137	1.72
11	$As_{24}S_{19}Se_{57}$	4.05	122	1.51
12	$As_{24}Se_{76}$	4.46	116	–
13	$As_{14}S_{43}Se_{43}$	3.43	100	1.70

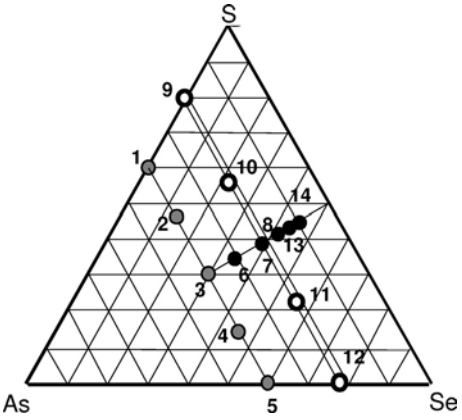

Figure 23.1: Ternary phase diagram depicting the three series of glasses examined within the As–S–Se system.

The bulk glass compositions examined for variation of optical properties with structure [13] are illustrated in the ternary phase diagram shown in Fig. 23.1. The physical properties are summarized in Table 23.1. Shown in Fig. 23.1 are three series of glasses; compositions along the line $x\ As_{40}S_{60} - (1-x)\ As_{40}Se_{60}$ form glasses where the molar ratio As/(S + Se) was held constant at 2:3, and a systematic replacement of sulfur by selenium was made. These compositions are represented as shaded circles and are labeled as compositions 1–5. Compositions maintaining a molar ratio S/Se = 1 were examined as a function of molar ratio As/(S + Se). These compositions are represented in Fig. 23.1 as solid circles and represent a systematic

reduction in As(S,Se)$_{3/2}$ pyramidal units and a concurrent increase in chalcogen-containing interconnecting chain members. To evaluate the role of chalcogen type and concentration on both structure and linear and nonlinear optical properties, a series of compositions, (numbered 8–12) were included. All glasses in this series contained 24 mol% As with an (S + Se) content equal to 76 mol%, and are shown as heavy-lined open circles.

As can be seen in Table 23.1, there is a systematic red shift of the bandgap, E_g, which is correlated with the progressive substitution of selenium for sulfur in the glass. Concurrently, an increase in density and decrease in T_g for increasing Se content occur. In the As–S and As–Se systems, a decrease of the As(S,Se) ratio produces a blue shift of the band gap [14]. For glasses with Se/S = 1, the bandgap shows much less of a change. It is important to consider the point where the two-photon absorption (2PA) of a candidate glass becomes significant. For use at the telecommunication wavelength of 1.55 μm, this point ($h\nu/2$) is near 2.0 eV. Hence glasses with a bandgap near or below this level may have appreciable nonlinear absorption that could compromise performance in high power applications.

In Fig. 23.2, several characteristic Raman excitation wavelengths are illustrated with respect to a plot of the glasses' absorption coefficients for compositions with constant As/(S + Se) molar ratio. As will be discussed later, the selection of a probe wavelength for Raman structural studies within this system becomes important, as excitation at wavelengths within or close to the bandgap may promote absorption. The magnitude of this absorption in most cases (observed for power levels as low as hundreds of microwatts) is sufficient to impart measurable photo-induced structural changes. Often, such changes result in a discoloration, or the well-referenced phenomenon of photodarkening. As will be described within this work, all Raman-based structural studies have utilized low-power (< 25 mW), near-infrared ($\lambda = 840$ nm) excitation, unless stated otherwise.

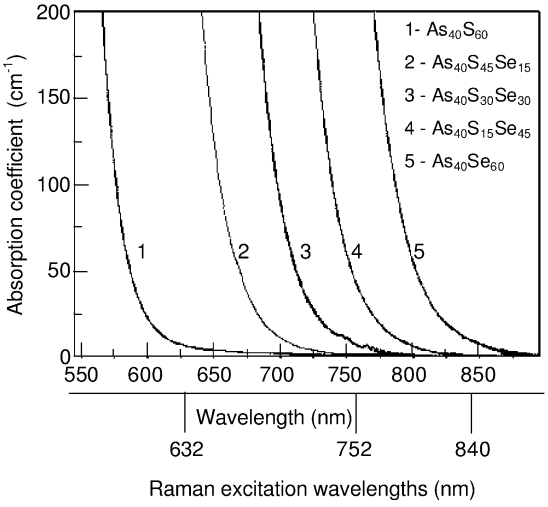

Figure 23.2: Absorption coefficient (cm^{-1}) versus wavelength for As$_{40}$(S + Se)$_{60}$ glasses illustrating the red shift in the absorption band with Se addition (from [7]). Shown for comparison are the glass band edge as compared with Raman excitation wavelengths.

The linear optical properties within the As–S–Se glass system exhibit predictable systematic variation. Like the bandgap variation with Se addition depicted in Fig. 23.2, the same glasses show a monotonic increase in linear index, n, with Se addition, when measured at 1.55 μm. This change in index for the same twelve glasses depicted in Fig. 23.1 is shown in Fig. 23.3a. The change of index with composition can be directly related to the variation in glass network structure associated with the compositional variation. The effect of an increase in 2-coordinated chalcogen (S or Se) at the expense of 3-coordinated As gives rise not only to a decrease in density, but also a concurrent decrease in refractive index. This is shown in Fig. 23.3b where index is plotted as a function of structural connectivity. This connectivity, is often described by a glass average coordination number (ACN), where the higher the ACN, the larger is the extent of connectivity. ACN within the glass system has been calculated using the following equation:

$$\text{ACN} = 3x + 2y$$

where x and y are the respective molar fractions of As and chalcogen species, respectively, and the integer represents the normal coordination state of the atom in the glass network. The systematic substitution of Se for S does not change the ACN as shown in Fig. 23.3b (as x and * for stoichiometric (40 mol%) and As-deficient (24 mol% As) compositions, respectively). However, for equi-molar chalcogen glasses (shown as triangles) the impact of decreasing content of 3-coordinated (As) species on the glass network and refractive index is clearly seen in the systematic decrease in n.

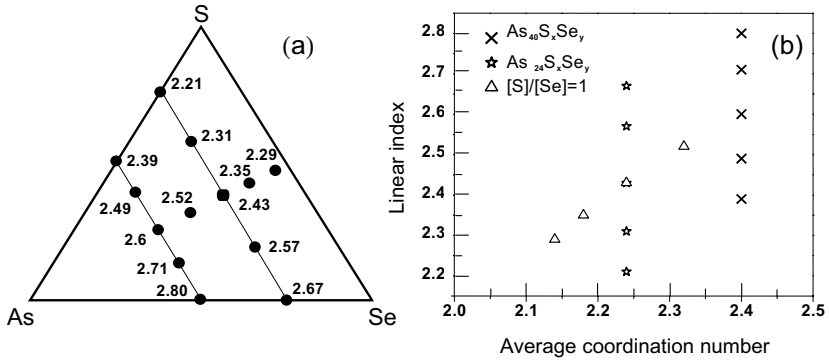

Figure 23.3: Variation in linear refractive index (n) measured at 1.55 μm as determined from Fresnel loss measurements (a) for the three series examined within the As–S–Se system ($n \pm 0.007$), and (b) the corresponding relationship between index and average coordination number (ACN) of the glass network (from [31]).

The structural changes which impact linear index variation shown in Fig. 23.3 also lead to a variation in the glass nonlinear refractive index. Here, not only are the structural species important but their electronic character also plays a role. We have carried out extensive analysis on bulk and ChG film [15, 16] materials using X-ray photoelectron spectroscopy (XPS), to probe the variation in structural and electronic properties as a function of composition and following exposure to a variety of environmental conditions [17]. These studies have confirmed

a systematic variation in position of the band edge, and limited variation in properties when exposed to severely oxidizing conditions. Understanding changes in electronic structure aid in the interpretation of many optical properties.

The normalized nonlinear index n_2 as compared with fused silica for selected glasses measured using z-scan at 1.55 μm [12] is shown in Fig. 23.4a. The enhancement of nonlinear optical properties (n_2) by substitution of selenium for sulfur in $As_{40}S_{60}$ has been attributed to an increasing number of covalent, homopolar bonds. On the other hand, distinctly large nonlinear optical property values with *ordinary linear values* in $As_{24}S_{38}Se_{38}$ (composition 7 in Fig. 23.3) may be due to Se–Se bonds, created by an As deficiency. Hence, what the chemical species is, and what its electronic structure is, impact both linear and nonlinear optical properties of the material.

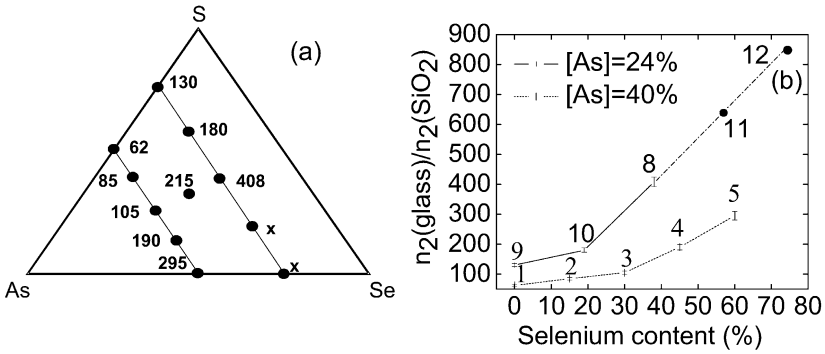

Figure 23.4: Variation in nonlinear refractive index as measured at 1.55 μm via z-scan (a) within the As–S–Se system, and (b) plotted as a function of Se content. (Extrapolated data points are preliminary data from a limited set of measurements.)

In the light of the above structural discussion, it is thought that the homopolar bonds and their electron-laden lone pairs allow strong coupling of the electric field vector of the probing laser light to the material leading to an enhanced nonlinearity. This is illustrated in Fig. 23.4b which shows the variation in measured and extrapolated values of the n_2 ratio with chalcogen content. Increasing the chalcogen content (from 60 to 76 mol%) leads to an increase in the n_2 ratio to silica and we believe the pronounced rise is attributable to the much larger quantity of Se–Se bonds (versus S–S or S–Se) as determined by Raman spectroscopy [13]. While S–S and S–Se bonds also possess two lone pairs per atom, these pairs have lower orbital electron densities and are present in much fewer numbers as compared with more polarizable Se–Se bonds. Structural analysis of these glasses has shown that the S present in these equi-molar compositions tends to remain with the As pyramidal units, while the Se form the dominant chain species. It is repeated here however, that the enhancement to n_2 offered by increasing the concentration of the n_2-enhancing species (in this case Se) comes at a price. Increasing Se content increases the linear (and nonlinear) absorption of the glass. This means that the enhancement seen is more dominated by a now present, resonance effect (the glass absorption edge falls below the $h\nu/2$ guideline for non-resonant behavior); this means that the increased absorption realized in the material can also contribute to other deleterious effects, such as

measurement-induced structural modification. Such modification under specific conditions, could lead to changes in the material structure/properties during use. Hence, a choice needs to be made whereby the magnitude of n_2 is weighted against a deleterious concurrent increase in absorption. For switching applications, both properties need be considered in the selection of an optimal material.

23.4 Chalcogenide Thin Films and Comparison with Bulk Glass

Chalcogenide thin films have been studied extensively for their variation from the parent bulk glass material and their stability in physical properties following deposition. As properties of a glass are a function of its thermal history it is not unexpected that films or fibers may have properties that vary from those seen in their melt-derived bulk analogues. Similar measurement of fiber properties within the As–Se system [18] showed similar variation in properties with forming conditions. As–S–Se films evaluated in this study show a range of property variation from their parent bulk glasses.

All glass films examined in our studies have been processed at Laval University's Centre Optique, Photonique at Laser (COPL) facilities using a clean room fabrication facility dedicated to processing ChG materials. Processing conditions, summarized for films and subsequently fabricated gratings, are discussed in detail in [11, 19]. In all cases, films are deposited from thermally evaporated parent bulk glasses, onto room temperature, oxidized silicon substrates under a vacuum of nominally 10^{-7} Torr. Glassy films processed by these techniques were confirmed to be amorphous in nature and vary in composition from the parent bulk by less than 5 mol%. [7] Most single- or multilayer films that have been prepared are approximately 2 μm in thickness or less [20]. Shown in Fig. 23.5 is a scanning electron micrograph of a multilayer ChG film structure midway through its lithographic processing steps, en route to becoming a channel waveguide. To fabricate the multilayer film structure, two bulk glass compositions were loaded into the deposition chamber and alternately deposited to form a multilayer structure. A channel within the core ternary glass serves to guide.

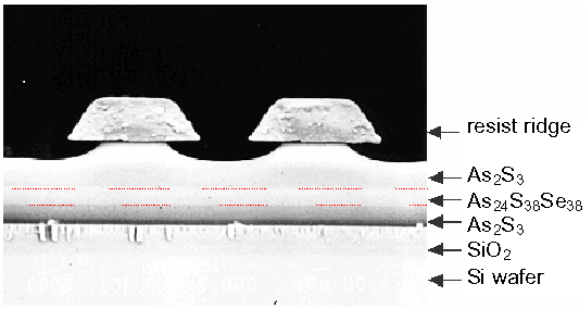

Figure 23.5: SEM micrograph of a multilayer $As_{24}S_{38}Se_{38}/As_2S_3$ ridge directional coupler midway through its lithographic processing protocol.

To compare the properties of films with those of their bulk counterparts, a series of optical and structural analyses were carried out. As described in detail by Laniel et al. [21] a systematic set of measurements were performed on films prepared under identical deposition conditions to examine the variation in film refractive index. refractive index data were collected at wavelengths surrounding the 1.55 μm telecom wavelength, and these data are summarized in Table 23.2. Shown are data for glasses numbered 1–8 from the bulk glass ternary series. Bulk glass starting compositions are shown, and unless listed (in parentheses below the parent composition), film compositions were identical with that of the parent material, as quantified through use of microprobe analysis. Values of index prior to and following a two-hour annealing at 120 °C are also tabulated.

Within the error of the measurements, no apparent variation in index was measured via the grating coupling technique over the 1.53–1.60 μm spectral range of the measurements. As compared with changes in bulk glass refractive indices with composition shown in Fig. 23.3a, film indices exhibited slightly larger variation with composition. This variation may be attributable to subtle compositional variations and the higher cooling rate with which the film structure assembles from the vapor phase. The ability for molecular species to assemble in the vapor phase [22] would give rise to a notably more ordered, connected molecular structure as compared with systems where no molecular ordering is believed to occur (e.g. in ternary As–S–Se glasses). Annealing of the as-deposited films resulted in a further increase in index and density, as the frozen network structure relaxes and further polymerizes. As illustrated in the subsequent section, these structural changes can be readily identified with Raman spectroscopy. Films exhibited an almost 2% higher linear index as compared with bulk glasses, and annealing increased the film density (decreased the as-deposited film volume) and index by a further 2%.

Densification and thickness changes have been reported in other studies within our group for fresh, annealed and aged films, as examined using Rutherford backscattering spectroscopy (RBS) [23,24]. Structural relaxation and subsequent rearrangement occur in both the short and long timeframes and dictate the aging kinetics of the materials. These changes are quantified in subsequent sections as corroborated by Raman spectroscopic analysis. Such long-term property modification, if any, is important in specific device structures.

23.5 Structural Characterization of Chalcogenide Glasses

23.5.1 Raman Spectroscopy

Inelastic scattering of light – or Raman scattering – in a material yields structural and dynamic information on a molecular level. The Raman spectrum provides a "fingerprint" of the molecular species present. The non-destructive nature of the probe, flexibility in sampling arrangements, and a technical revolution [25,26] in multichannel detection and prefilters have opened up many new areas where Raman measurements have proven valuable [27,28].

As discussed earlier, efforts to optimize film properties and device performance have focused on identifying the chemical and structural origin of the linear and nonlinear response in terms of the material processing conditions used in creating the optical element [13]. Important to this study, NIR Raman spectroscopy affords new opportunities in the non-destructive

Table 23.2: refractive index and dispersion data for chalcogenide films: as-deposited (n-a) and following annealing (a). Composition data shown are from electron microprobe analyses of resulting film. Compositional variation from the parent bulk (starting composition shown in italics) is noted where film stoichiometry showed differences.

Glass Number	Composition		Refractive index at 1.53 μm	Error	Refractive index at 1.55 μm	Error	Refractive index at 1.575 μm	Error	Refractive index at 1.60 μm	Error
1	$As_{40}S_{60}$	a	2.4035	0.0086	2.4050	0.0061	2.3964	0.0102	2.4012	0.0066
		n-a	2.3439	0.0044	2.3439	0.0037	2.3439	0.0060	2.3427	0.0030
2	$As_{36}S_{49}Se_{15}$	a	2.4707	0.0064	2.4636	0.0023	2.4618	0.0023	2.4655	0.0020
	(As$_{40}$S$_{45}$Se$_{15}$)	n-a	2.4139	0.0020	2.4098	0.0020	2.4118	0.0020	2.4155	0.0020
3	$As_{39}S_{29}Se_{32}$	a	2.5727	0.0030	2.5709	0.0062	2.5714	0.0030	2.5686	0.0081
	(As$_{40}$S$_{30}$Se$_{30}$)	n-a	2.5074	0.0035	2.4949	0.0024	2.5000	0.0026	2.4972	0.0041
4	$As_{40}S_{14}Se_{46}$	a	2.6750	0.0052	2.6766	0.0084	2.6766	0.0178	2.6655	0.0051
	(As$_{40}$S$_{15}$Se$_{45}$)	n-a	2.6239	0.0063	2.6270	0.0063	2.6286	0.0063	2.6350	0.0064
5	$As_{40}Se_{60}$	a	2.8318	0.0059	2.8318	0.0077	2.8257	0.0030	2.8282	0.0030
		n-a	2.7842	0.0144	2.7707	0.0040	2.7715	0.0040	2.7835	0.0100
6	$As_{32}S_{34}Se_{34}$	a	2.5400	0.0028	2.5414	0.0028	2.5455	0.0069	2.5527	0.0051
		n-a	2.5050	0.0024	2.5041	0.0026	2.5064	0.0041	2.5223	0.0041
7	$As_{24}S_{38}Se_{38}$	a	2.4666	0.0023	2.4650	0.0023	2.4666	0.0042	2.4666	0.0031
		n-a	2.4445	0.0029	2.4445	0.0089	2.4445	0.0043	2.4464	0.0029
8	$As_{18}S_{41}Se_{41}$	a	2.3764	0.0020	2.3745	0.0020	2.3745	0.0020	2.3745	0.0020
		n-a	2.3691	0.0023	2.3673	0.0023	2.3709	0.0037	2.3691	0.0037

analysis of materials, which are strongly absorbing in the visible. A distinct advantage over the more conventional approach using the visible range of the spectrum is the ability to obtain the Raman spectrum of photosensitive compounds without interference from photoreactions caused by the probe beam. In chalcogenide glasses shifting the excitation wavelength to 840 nm (below the bandgap) allows one to obtain high-quality Raman spectra without material modification. The higher spatial resolution necessary to characterize planar films can be achieved with a microscope attachment.

In the microstructural analysis of single- and multilayer waveguide devices, Raman spectroscopy employing integrated optical techniques can be extremely powerful [66]. The material of interest is cast into a slab waveguide, thereby significantly increasing both the scattering volume and the electrical field intensity within the film. In spite of its sensitivity, waveguide Raman spectroscopy (WRS) using guided mode excitation [29,30] has not been applied to the structural characterization of chalcogenide glasses until recently [31, 32]. Discussed here are selective results of such experiments where chalcogenide film Raman spectra were measured using guided mode excitation.

Raman scattering in the NIR is excited with 840 nm radiation from a tunable Ti:sapphire laser (30–50 mW), as depicted in Fig. 23.6. The scattered Raman light is analyzed with a single-grating spectrograph equipped with a thinned, back-illuminated CCD detector. The Rayleigh line is suppressed with a semiconductor bandgap filter [33]. The spectra shown in the following were not corrected for the instrument profile, nor was any smoothing or background correction performed.

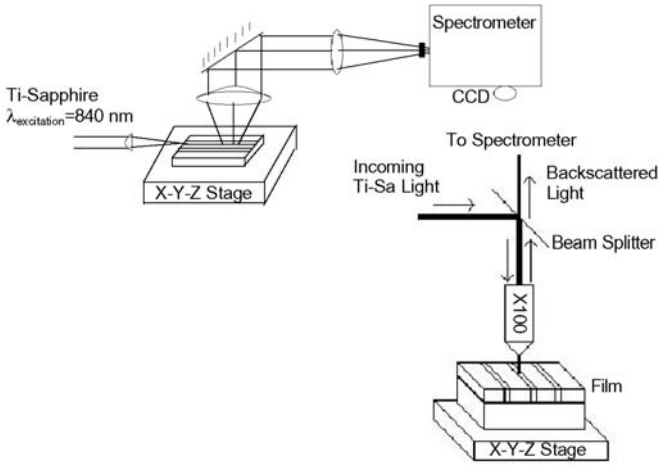

Figure 23.6: Experimental setup for near-infrared Raman spectroscopy. Sampling arrangements for micro- (backscattered geometry) and waveguide excitation (90° geometry) are shown.

23.5.2 NIR Raman Spectroscopy of Bulk Chalcogenide Glasses

Figure 23.7 illustrates the near-infrared Raman spectra (incident and scattered polarization resolved along the z-axis) for a series of binary and ternary ChG compounds. The spectra

were obtained at a spectral resolution of 1.5 cm^{-1} which is verified by resolving the isotope splitting of the symmetric stretch vibration of Cl in CCl_4 near 459 cm^{-1}.

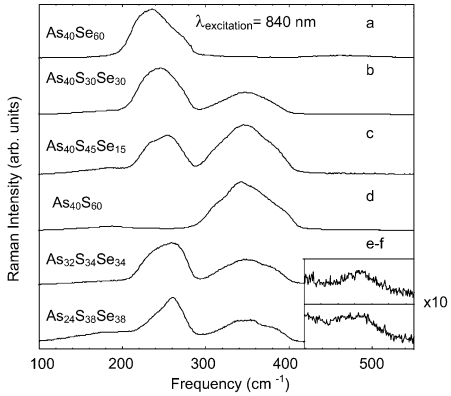

Figure 23.7: Raman spectra of bulk glasses obtained with near-infrared excitation (λ = 840 nm) as a function of compositional variation. Spectral resolution is 1.5 cm^{-1}.

The increased spectral resolution of the bulk spectra clearly shows that each of the dominant bands consist of several overlapping components. The dominant feature in the binary sulfide and selenide compounds are bands at 345 cm^{-1} ($As_{40}S_{60}$) and 230 cm^{-1} ($As_{40}Se_{60}$), respectively. These spectra are in good agreement with previous studies [34], and the strong, broad band is attributed to an anti-symmetric As–(S,Se)–As stretching vibration in the $As(S,Se)_3$ pyramids. According to the analysis of Lucovsky and Martin [35], the normal modes of the bulk glasses (e.g. clusters of $As(S,Se)_3$) molecules with weak intermolecular coupling) are obtained by treating the molecular pyramid modes ($As(S,Se)_3$) and bridging chain modes (As–(S,Se)–As) independently. In the ternary compounds with S/Se = 1 molar ratio and decreasing As content, a progressive decrease of these broad bands is observed, indicative of a decrease in the number of As-containing pyramidal sites. New bands appearing around 255 cm^{-1} and 440–480 cm^{-1} form in the now chalcogen-rich glasses, and are attributed to Se–Se and S–S homopolar bonds. These units serve as chalcogen chains connecting the remaining pyramidal units. The small number of S–S bonds indicated by a weak band near 495 cm^{-1} for equal concentrations of S and Se suggests that the S stays with the remaining pyramids, and that it is the Se which dominates the connecting chain units. Local structural investigations using Raman spectroscopy have been carried out on As–S–Se glasses previously [34] but compared with bulk glasses, only limited comparison of the structural differences attributable to different molecular entities created during film or fiber processing have been directly made [22].

Deviations from bulk glass properties in oxide fibers have been well studied and clearly illustrate the processing-induced structural property modifications possible in highly coordinated oxide glasses [36, 37]. The extent of such compositional variation, and the resulting structural units formed, varies with the specific fiber or film processing technique used, and can be extreme or subtle depending on such variables as deposition rate, substrate temperature, deposition, draw environment (vapor chemistry) or draw rate. One might expect, as has

been observed in As_2Se_3 film and fiber materials [21], that this deviation from bulk would be larger for As–S materials than that observed in oxide glasses. Neutron scattering and X-ray diffraction studies on bulk sulfide and selenide glasses and glasses deposited as thin films [22] have shown variations in structural units on the intermediate range order scale. Depending on processing conditions, polymeric cages (based on As_4S_4 units) or less connected groups of As–S pyramidal units, were observed. More importantly, since they are different from the traditional units formed in the "bulk", they are much more *metastable*, and can be structurally modified or eliminated with post-deposition processing. Knowledge of how structural features form and how they impact physical properties including optical properties is crucial to optimize desirable film properties and stability.

23.5.3 NIR Waveguide and Micro-Raman Spectroscopy of Chalcogenide Films

Waveguide Raman spectroscopy (WRS), using guided mode excitation [29, 30] has been applied to thin organic and polymeric films, to probe spontaneous [38] and coherent [39] scattering, and very recently, to sol–gel derived planar germanosilicate [40] waveguides and lead titanate [41] films. The refractive index of these organic and oxide materials allows the use of high-index glass prisms such as LaSF5 ($n \sim 1.8$) for coupling a range of propagation vectors into the waveguide structure. In spite of its sensitivity, WRS has not been applied to the structural characterization of chalcogenide glasses until recently [31, 32] most likely owing to their high index ($\sim$2.45) and lack of suitable prism couplers and difficulties associated with working in the near-infrared.

Figure 23.8 illustrates the variation in Raman spectra obtained in an As_2S_3 channel (film) waveguide structure, as probed across the waveguide endface. In the cases shown, the excitation beam (840 nm) was launched into the waveguide's end-face at various lateral positions (a–d), illustrating the sensitivity of the probe to regions near the edge (c) or center (a, d) of the guide structure.

The WRS spectra obtained from bulk As_2S_3, in amorphous and crystalline form, and an as-deposited film are shown in Fig. 23.9. Though the As_2S_3film has a thickness of just 1.5 μm, the high signal-to-noise ratio achieved by guided mode excitation is evident and the low-frequency Raman peaks are well separated from interfering Rayleigh scattering.

The distinction observed between bulk spectra and that of the film structure emphasizes the resulting structural differences associated with film processing conditions. Certain key components such as the band at 345 cm^{-1} remain in all spectra. However, new substructures appear in the film spectra as compared with the broad features of the bulk spectra. These differences from bulk are due to the different (molecular) arrangements of the constituent atoms within the film. These sharp, molecular-signature structures were confirmed not to be due to crystallinity within the film, but most likely result from the formation of as-deposited As_4S_4 units [22,42]. Several sharp molecular bands superimposed on a network-like continuum have also been observed in Raman spectra excited with near band energies (647 nm) [42–44]. By using a longer excitation wavelength (840 nm) and due to the absence of changes in the spectra when varying the power (10–50 mW) we rule out photo-induced changes from the probe beam [45].

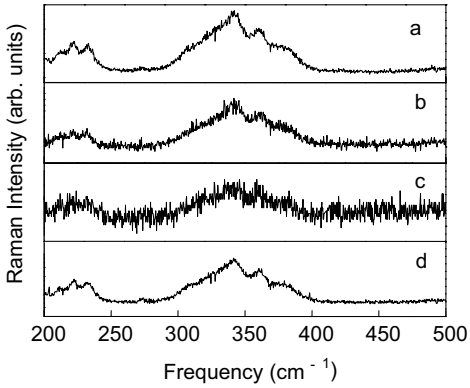

Figure 23.8: Waveguide Raman spectra of single layer, As_2S_3 channel structure. Panels (a) to (d) show a sequence traversing along the lateral direction (L to R) on the endface of the waveguide traversing from channel to channel. Excitation wavelength is 840 nm.

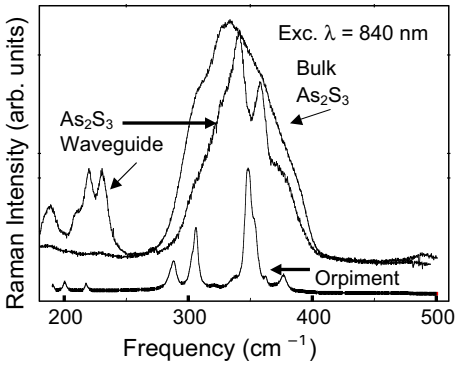

Figure 23.9: Structural features in film and bulk As_2S_3 Raman spectra as compared with high-purity crystal (from [66]). (Crystalline specimen courtesy of Prof. M. Frumar, University of Pardubice, Czech Republic).

23.6 Photo-Induced Changes in Glassy Chalcogenides

Recent publications have proposed the possibility of a refractive index change by femtosecond laser exposure of glasses in their transparent spectral region [46–48]. Most papers have reported this effect in silica or germanosilicate glasses [46]. Waveguide writing has been achieved by generating line damage inside various glasses and especially in chalcogenides [47]. Self-written waveguides have also been reported in $As_{40}S_{60}$ glass films using a femtosecond 800 nm source propagating through the films axis [48] and in bulk [7].

The photo-induced phenomenon has been widely investigated in amorphous materials. Chalcogenide glasses are well known to exhibit reversible photo-induced effects to bandgap light exposure [49–53]. The low optical bandgap of chalcogenide glasses make them highly

sensitive to visible exposure. Exposure to bandgap wavelength light induces a photodarkening in $As_{40}S_{60}$ glasses, a reduction of the glass bandgap, and a refractive index change in the exposed region according to the Kramers–Kronig relation. An important aspect of the photodarkening is that it was not observed in crystalline materials but only in disordered materials, leading to the conclusion that photodarkening effects are related to the increase of randomness of the glass network [54].

A correlation between reversible photo-induced effects and structural change has been discussed by different authors [13, 53, 55, 56] for bulk and well-annealed thin film materials. The increase of homopolar As–As and S–S chemical bonds, and of the disorder of the glass network was considered to contribute to the photodarkening effect. However, the relation between structure and photodarkening is not well established.

Discussed in this section are results of studies evaluating the effects of writing over a range of exposure conditions on ChG materials in bulk and film form. In addition to writing waveguides, we are interested in understanding the thresholds whereby laser interaction with the ChG material transitions from reversible to irreversible photostructural change, and onto permanent damage resulting from ablation.

23.6.1 Exposure Sensitivity of Chalcogenide Glasses

Photo-induced changes to a material can occur over a range of exposure conditions and in ChG materials are a function of material photosensitivity. In early work by our collaborators, [11] the photosensitivity of As_2S_3 was compared with the highly nonlinear $As_{24}S_{38}Se_{38}$ composition used in multilayer waveguide structures. It was shown that under identical exposure conditions, the ternary material exhibited dramatically reduced induced index changes following illumination with a continuous wave (CW) 514.5 nm source.

The extent of changes (both structural and optical) have been shown to vary widely with wavelength of the irradiating light (with respect to the bandgap), intensity (ns versus ps or fs pulses as compared with CW), and cumulative exposure dose. The resulting material modification associated with these conditions, range from the well-documented (reversible or irreversible) photodarkening, to irreversible destructive modification to the glass bonds during laser ablation. We are investigating the variation in structural changes imposed on bulk and film ChG materials associated with these widely differing exposure regimes, in an attempt to maximize the means by which the glasses can be modified for a range on on-chip components.

The mechanism of fs interaction in materials remains a topic of extensive research. It has been studied in detail at the University of Central Florida (UCF) with the aim of micromachining bulk materials in ambient atmosphere [53, 57]. Efforts to utilize these sources in the fundamental regimes of modification possible in ChG materials are briefly described in [57, 58], along with the fundamental mechanisms believed to be dominant in the drilling of deep holes in a range of oxide and non-oxide glass materials.

Of recent interest is the ability to generate a broad range of material response using fs laser pulses. In an effort to quantify the variation in ChG material response, we systematically increased the power density on an As_2S_3 film, evaluated the photoexpansion and ablation, and discerned where the cross-over in material behavior occurred. These results, discussed in [59], are depicted in Fig. 23.10. Shown in Fig. 23.10a are the resulting spots illuminated with sub-100 fs pulses, with power density of the exposure, shown on the x-axis. Fig. 23.10b illustrates

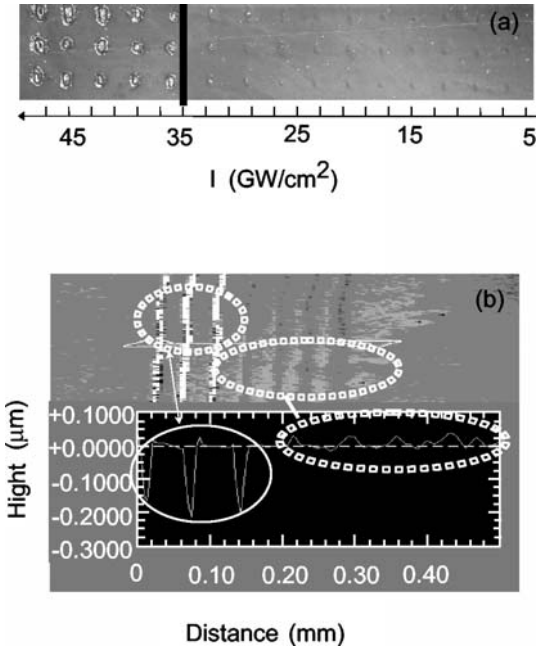

Figure 23.10: (a) Array of features written in an As_2S_3 film using fs pulses of a Ti:sapphire ($\lambda = 800$ nm) laser illustrating the power density threshold (in GW/cm^2) where photoexpansion (right of black line) transcends to laser ablation (left of black line). (b) White light interferogram and linescan illustrating topographic variation in lines written under the power density regimes identified in (a). The left features (top and bottom) correspond to trenches ablated during writing, whereas the faint regions of photoexpansion (right) occur in these films for power densities less than 35 GW/cm^2.

the change in film surface relief associated with transitioning into the ablation regime. Here, the photoexpansion seen with sub-threshold exposure, gives rise to ablative material removal, as seen in the New View 5000 White Light interferometer scans, at a threshold of 35 GW/cm^2. The mechanisms of material modification in these two forms of materials are markedly different.

23.6.2 Photo-Induced Waveguides in Bulk ChG Materials

We have written permanent waveguides in both bulk [7] and film As_2S_3 glasses [58] using a train of 850 nm femtosecond laser pulses and have measured both the induced index variation and structural changes induced through the photo-modification. An index variation in the bulk material, correlated to photodarkening was reported and corresponds to a local increase comparable with the magnitude observed in other bulk ChG studies. Micro-Raman spectroscopy has shown the local chemical change associated with the refractive index variation. It is believed that local changes in nonlinear absorption occur during the writing process, leading to a structural change and local index modification. Correlation of these optical changes with the structural modification within the bulk glass are illustrated in Fig. 23.11.

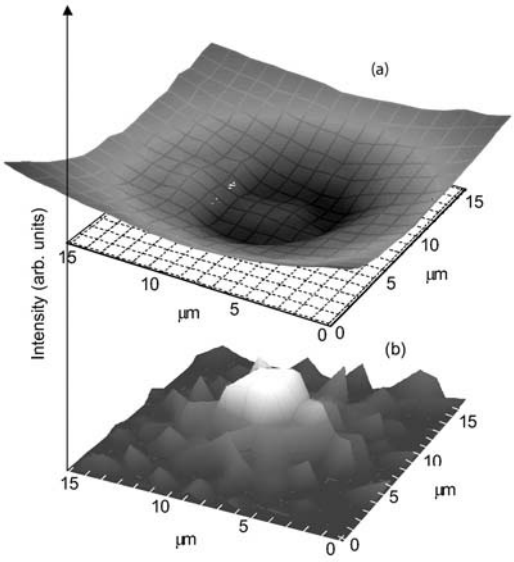

Figure 23.11: (a) Three dimensional map of Raman scattering illustrating the local evolution of the Raman bands centered at 345 cm^{-1} (a) and at 236 cm^{-1} (b) for the central region of a waveguide written in bulk As_2S_3 (from [3]). These maps correspond to the creation of homopolar As–As bonds (b) at the expense of previously existing As–S bonds (a).

The refractive index variation between the waveguide (exposed region of the glass sample) and the cladding (unexposed region) was evaluated following waveguide writing. An induced index change of $+0.04$ was associated with the formation of the 9 mm diameter circular waveguide formed by moving the sample through a well-characterized focal region. A key finding of the study defined the structural mechanism associated with the writing process in the As_2S_3 material. The concurrent destruction of As–S bonds within the glass network and the associated formation of As–As bonds during the bulk material modification is quantified by a two-dimensional micro-Raman analysis (excitation $\lambda = 752$ nm). The spatial variation of these two key bond types are shown in the plots in Fig. 23.11a and b. Figure 23.11a illustrates the local depletion of As–S bonds in the central waveguide region, as reflected in the decrease of Raman intensity of the As–S 345 cm^{-1} peak. This change is accompanied by a corresponding increase in the 236 cm^{-1} band (Fig. 23.11b) attributable to local formation of "wrong" As–As bonds. As no homopolar bonds are theoretically present in the stoichiometric bulk As_2S_3, their *formation* is characteristic of (fs) laser modification. As will be described in the next section, this mechanism is converse to the that seen during waveguide writing in films, where homopolar bonds that exist in as-deposited films actively participate in the local structural rearrangement during laser interaction.

23.6.3 Photo-Induced Changes in ChG Films

Photo-induced effects have been observed in a variety of chalcogenide glasses [41, 42]. These effects include optical transmissivity and reflectivity variations, refractive index changes, and variations in chemical reactivity. Two-photon induced refractive index changes by exposure in the 800 nm region have been measured [60]. The ultimate long-term stability of chalcogenide-based optical elements relies on the generation of photo-induced structures which undergo limited structural relaxation with time. ChGs typically exhibit lower glass transition temperatures (T_g) than oxide glasses and hence can exhibit significant sub-T_g relaxation at, or near, room temperature [18]. This relaxation can result in structural changes that modify the *as-written* glass structure and performance of the optical element. To ascertain the effects of structural relaxation resulting from aging, spectroscopic analyses of As_2S_3 film structures were performed following annealing and in freshly written ($<$1 month) and aged ($\sim$3 years under ambient conditions) Bragg gratings. In all cases, a depletion in as-deposited/as-written As–As and S–S bonds and modification of As–S bonds, was observed. The extent of such changes depended on the initial, as-formed concentrations of each type of bond, and how the film was aged or annealed. Changes in waveguide Raman spectra for As_2S_3 structures prior to and after annealing, and following 514 nm exposure similar to that used in grating writing are shown in Fig. 23.12 and are discussed in [23, 24]. The sharp features seen in the Raman spectrum of the as-deposited film illustrated in Fig. 23.12 are not present in bulk ChGs and correspond to molecular units that can undergo reconfiguration over time.

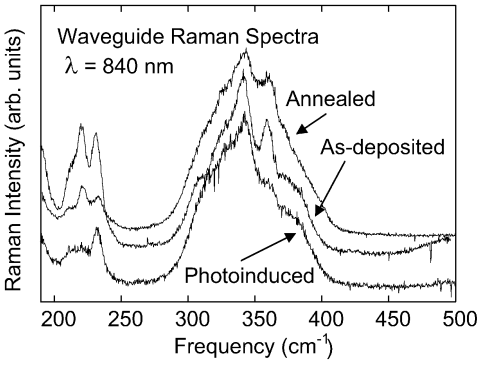

Figure 23.12: Variation in waveguide Raman spectra for fresh, annealed, and photostructurally modified As_2S_3 channel waveguide (exposure λ = 514.5 nm). Excitation wavelength is 840 nm (from [66]).

Characterization of grating structures shortly after writing, and after prolonged room temperature aging shows that while small amounts of the *as-written* relief structure stayed in the *aged* grating structure, few molecular species seen in as-deposited structures remained, and a considerable reduction in induced index change (δn) occurs.

The polarization dependence of such writing processes has been studied in ChG, most recently by our Laval colleagues in As_2S_3, and others in As–Se glasses in [61] and references therein. We are currently examining the concurrent glass structural modification in the Saliminia-written [62] structures, using micro-thermal analysis techniques [63].

The effects of photo-induced changes are evident in the Raman spectra as well. By exciting Raman scattering with sub-bandgap energies ($\lambda = 840$ nm) at low-power levels (25 mW) photostructural changes due to the probe beam are avoided. Large changes are seen in the Raman band near 235 cm^{-1} which is associated with As–As bond vibrations. Several mechanisms for photo-induced changes in chalcogenides, including bond redistribution and coordination defects, have been suggested [60]. Trigonal AsS_3 pyramidal units can be transformed into a five-fold coordinated As site having four As–S bonds and one As–As bond via a photoionization process [44]. The variation in film age and deposition technique dictates how far the film structure is from the local equilibrium state and the impact of such structural changes on expected grating optical performance. These issues are currently being examined, and recent results have shown that homopolar bonds seen in as-deposited films (shown near 200 cm^{-1} in Fig. 23.12), remain, even after aging periods of several years. Not only do these well-aged films retain their photosensitivity (i.e. undergo induced refractive index modification and structural changes (expansion)), but the magnitudes of both are comparable to that seen in freshly formed films, illuminated shortly after deposition. These results will undoubtedly lead to further progress in forming stable, written structures in these ChG materials.

23.6.4 Grating Fabrication in As_2S_3 Glassy Films

Unlike the grating fabrication techniques described above for ChG films illuminated through masks or with interfering CW beams, femtosecond (fs) lasers also appear to be a promising tool for the direct write micro-structuring of optical materials. It was demonstrated that unamplified femtosecond lasers could produce optical breakdown and structural change in bulk transparent materials using tightly focused pulses of just 5 nJ [55].

Using an extended cavity unamplified Kerr-lens mode locked Ti:sapphire laser ($\lambda = 800$ nm, repetition rate 28 MHz, sub-50 fs pulse duration, up to 20 nJ/pulse), relief and volume gratings with a 20 μm period were fabricated on a 1.66 μm thick, As_2S_3 thin film [64]. The output of the laser was focused by a 15×, 0.28 *NA* reflective objective onto a target attached to a 3D motorized translation system.

The sample was processed in two regimes: first, the intensity was kept below the ablation threshold, generating a volume grating resulting from photoexpansion and an induced index change. The resulting structure from a Zygo New View 5000 is shown in Fig. 23.13a. In the second regime, intensities *above* the ablation threshold produced a relief grating with grooves of 0.2 μm depth (Fig. 23.13b). Previous studies have linked bulk glass structural and optical property changes (photosensitivity) through Raman spectroscopy, showing that nonlinear absorption-induced index changes were linked to local bonding changes in As_2S_3 [13]. Following this approach, waveguides over 1 cm in length and $\sim$10 μm in diameter were fabricated in As_2S_3 thin films by direct transverse writing using the same unamplified Ti:sapphire laser [67]. Further studies are under way including the measurement of the refractive index change by the refracted near-field technique. Concurrently, we are evaluating long-term stability in both photoexpansion and induced index with age, including studies on pre-aged films, which have undergone most of their short-term, post-deposition relaxation.

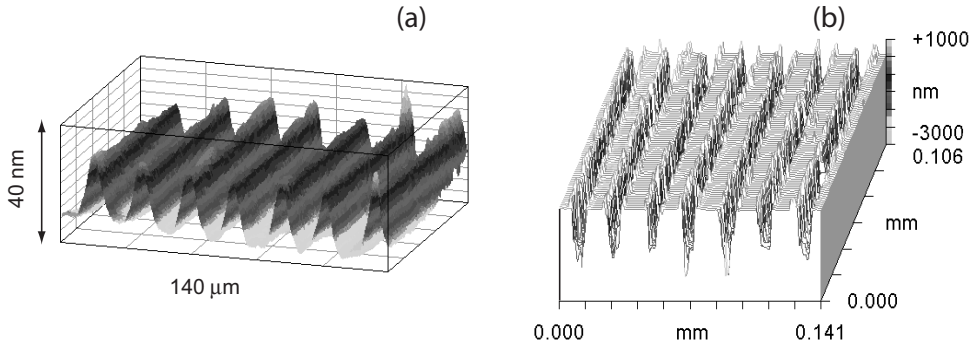

Figure 23.13: Surface profile of (a) the phase and (b) topographic relief in gratings on an As_2S_3 film produced with sub-50 fs laser pulses from the extended cavity unamplified Ti:sapphire oscillator (from [65]).

23.7 Conclusions and Outlook

This chapter has summarized a variety of results whereby ChG materials have been processed and characterized with the aim of understanding key material attributes in geometries suitable for use in integrated optical components. Within the narrow composition space where we have focused on obtaining a thorough grasp of bulk/film property trends and variation, clear learnings have been realized associated with the linear and nonlinear optical properties of these glasses and their relation to glass structure. It been shown by these efforts and those of others that compositional-tailoring of glasses to known properties can yield structures and components with good optical quality and promise of potential in-service stability. Such know-how thus allows identification of materials that can be deposited onto glass or Si chip substrates and modified to carry out key functions suitable for moving and amplifying light.

Photo-induced structural changes can be realized in ChG materials to induce structure and refractive index changes. Such modification can be used to write structures, either with CW bandgap light, or near-bandgap light employing short (fs) pulses. The photosensitivity offered by ChG materials allow polarization-dependent features to be written which may offer promising component opportunities once stabilization techniques employing pre-aging are optimized. This material flexibility, along with the technology know-how associated with true, three-dimensional structuring capabilities offered through direct write techniques, illustrate further routes to clever device engineering.

Emerging results of ongoing interest and research in ChG materials will allow a range of key components with stable optical and physical properties to be realized for next generation optical elements. Characterization of key structural features on materials in their final device configuration allows for a thorough understanding of the inter-relationship between processing and end use. Such analysis is essential in predicting long-term stability requisite for device applications.

Acknowledgments

It is a pleasure to acknowledge a host of students and collaborators who have contributed to the results discussed herein, in particular C. Rivero, A. Zoubir, G. Nootz, P. Sharek, C. Lopez, L. Shah, M. Marchivie, K. Zollinger, M. deCastro, A. Graham, W. Li, C. Wilson, K. Elshot, M. Couzi, J. Fick, D. Hagan, and R. Irwin. We are also grateful to our Canadian colleagues and their students for their long-term partnership and friendship, specifically A. Villeneuve, T. Galstian, R. Vallee, E. Knystautas, K. Turcotte, V. Hamel, K. LeFoulgoc, C. Meneghini, J. F. Viens, A. Saliminia, N. Hô, and J. Laniel. All of these participants took part in processing and characterization efforts illustrated in the results presented herein, and have contributed to this mutually rewarding collaboration. This work was carried out with the support of a number of research, equipment, and educational grants, including NSF awards DMR-9974129, DUE-9850934, INT-0129235, ECS-0123484, ECS-0225930, EEC-9732420, and CHE-9732161, and IGERT grant DGE-0114418. The authors acknowledge the assistance of staff at the AMPAC Material Characterization Facility (MCF), University of Central Florida.

References

[1] A. Villeneuve, T.V Galstian, M. Duguay, and K. Richardson, J. Light. Technol. **15**, 1343 (1997).

[2] S. Ramachandran, S. Bishop, J.P. Guo, and D.J. Brady, IEEE Phot. Tech. Lett. **8**, 1041 (1996).

[3] O.M. Efimov, L.B. Glebov, K.A. Richardson, E. Van Stryland, T. Cardinal, S.H. Park, M. Couzi, and J.L. Bruneel, J. Opt. Mater. **17**, 379 (2001).

[4] A.M. Andriesh, Y.A. Bykovskii, E.P. Kolomeiko, A.V. Makovkin, V.L. Smirnov, and A.V. Shmal'ko, Sov. J. Quantum Electron. **7**, 347 (1977).

[5] M. Asobe, T. Kanamori, and K. Kubodera, IEEE J. Quant. Electron. **29**, 2325 (1993).

[6] S. Ramachandran and S.G. Bishop, Appl. Phys. Lett. **74**, 13 (1999).

[7] K.A. Richardson, J.M. McKinley, B. Lawrence, S. Joshi, and A.Villeneuve, J. Opt. Mater. **10**, 155 (1998).

[8] K. Tanaka, N. Toyosawa, and H. Hisakuni, Opt. Lett. **20**, 1976 (1995).

[9] J. Fick, A. Villeneuve, E. Knystautas, S. Roorda, and K. Richardson, J. Non-Cryst. Solids **272**, 200 (2000).

[10] C. Meneghini, J.F.Viens, A. Villeneuve, E.J. Knystautas, M.A. Duguay, and K.A. Richardson, J. Optical Society B **15**, 1305 (1997).

[11] J.F. Viens, C. Meneghini, A. Villeneuve, T.V. Galstian, E. Knystautas, M. Duguay, K.A., Richardson, and T. Cardinal, J. Lightwave Technol. **17**, 1184 (1999).

[12] K.A. Richardson, J.M. McKinley, B. Lawrence, S. Joshi, and A. Villeneuve, J. Opt. Mater. **10**, 155 (1998).

[13] T. Cardinal, K. Richardson, H. Shim, G. Stegeman, A. Schulte, R. Beathy, K. LeFoulgoc, C. Meneghini, J.F. Viens, and A.Villeneuve, J. Non-Cryst. Solids **256 & 257**, 353 (1999).

[14] E. Hajto, P.J.S. Ewen, and A.E. Owen, J. Non-Cryst. Solids **164–166**, 901 (1993).

[15] S. Seal, K.A. Richardson, C. Lopez, A. Graham, D.K. Verma, K. Turcotte, J. Laniel, A. Saliminia, T.V. Galstian, and A. Villeneuve, Phys. Chem. Glasses **43**, 59 (2002).

[16] W. Li, S. Seal, C. Lopez, and K.A. Richardson, J. Appl. Phys. **92**, 7/02 (2002).

[17] S. Seal, W. Li, K.A. Richardson, D.K. Verma, A. Shulte, C. Lopez, A. Graham, and C. Rivero, J. Corros., in press (2002).

[18] K.A. Cerqua-Richardson, PhD Thesis, NYS College of Ceramics at Alfred University (1992).

[19] A. Saliminia, A.Villeneuve, T.V. Galstian, S. LaRochelle, and K.A. Richardson, J. Lightwave Technol. **17**, 837 (1999).

[20] C. Lopez, K.A. Richardson, S. Seal, D.K. Verma, A. Graham, A. Villeneuve, T.V. Gastian, K. Turcotte, A. Saliminia, J. Laniel, M. deCastro, A. Schulte, and C. Rivero, J. Am. Ceram. Soc. **85**, 1372 (2002).

[21] J. Laniel, J.M. Ménard, A. Villeneuve, R. Vallée, C. Lopez, and K.A. Richardson, Proc. SPIE Photonics North 2002: International Conference on Applications of Photonic Technology (ICAPT), vol. 4833, Quebec (2002).

[22] A. Apling, A.J. Leadbetter, and A. Wright, J. Non-Cryst. Solids **23**, 369 (1977).

[23] C. Rivero, P. Sharek, G. Nootz, C. Lopez, K.A. Richardson, and A. Schulte, Proc. SPIE Engineering Thin Films with Ion Beams, Nanoscale Diagnostics, and Molecular Manufacturing, vol. 4468, San Diego, CA (2001).

[24] C. Rivero, P. Sharek, G. Nootz, C. Lopez, W. Li, K. Richardson, A. Schulte, G. Braunstein, R. Irwin, V. Hamel, K. Turcotte, and E. Knystautas, Thin Solid Films, **425**, 59 (2003).

[25] R. L. McCreery, Raman Spectroscopy for Chemical Analysis, Wiley, New York, 2000.

[26] B. Chase, Appl. Spectrosc. **48**, 14A (1994).

[27] P. Colomban and J. Corset (Eds.), J. Raman Spectrosc., Special Issue: Raman (Micro) Spectrometry and Materials Science (1999).

[28] W.H. Weber and R. Merlin (Eds.), Raman Scattering in Materials Science, Springer, New York, 2000.

[29] S.L. Zhang and B.F. Zhu (Eds.), Proc. XXVIIth Intl. Conf. on Raman Spectrosc., Wiley, New York, 2000.

[30] J.F. Rabolt, in Fourier Transform Raman Spectroscopy, D. B. Chase and J. F. Rabolt (Eds.), Academic Press, San Diego, 1994, p. 133.

[31] C. Rivero, A. Schulte, C. Lopez, K. Richardson, K. Turcotte, V. Hamel, A. Villeneuve, and T. Galstian, OSA Topical Meeting on Nonlinear Guided Waves, Clearwater, FL, 2001.

[32] A. Schulte, C. Rivero, K. Richardson, K. Turcotte, J. Laniel, V. Hamel, A. Villeneuve, A. Saliminia, and T. Galstian, Opt. Commun. **198**, 125 (2001).

[33] A. Schulte, Appl. Spectrosc. **46**, 891 (1992).

[34] A. Freitas, J. Strom, and D.J. Treacy, J. Non-Cryst. Solids **59&60**, 615 (1983).

[35] G. Lucovsky and R. Martin, J. Non-Cryst. Solids **8–10**, 185 (1972).

[36] M. Goldstein and T. H. Davies, 1955, J. Am. Ceram. Soc. **38**, 223 (1955).

[37] H. Stockhorst and P. Bruckner, J. Phys. (Coll.) **43**, C9 (1982).

[38] Y. Levy, C. Imbert, J. Cipriani, S. Racine, and R. Dupeyrat, Opt. Commun. **11**, 66 (1974).

[39] W.M. Hetherington III, N.E.Van Wyck, E.W. Koenig, G.I. Stegeman, and R.M. Fortenberry, Optics Lett. **8**, 88 (1984).

[40] C. Duverger, J.M. Nedelec, M. Benatsou, M. Bouazoui, B. Capoen, M. Ferrari, and S. Turrell, J. Mol. Struct. **480–481**, 169 (1999).

[41] C. Urlacher, O. Marty, J.C. Plenet, J. Serughetti, and J. Mugnier, Thin Solid Films **349**, 63 (1999).

[42] M. Frumar, M. Vlcek, Z. Cernosek, Z. Polak, and T. Wagner, J. Non-Cryst. Solids **213&214**, 215 (1997).

[43] P. Krecmer, M. Vlcek, and S.R. Elliot, J. Non-Cryst. Solids **227–230**, 682 (1998).

[44] T. Uchino, D.C. Clary, and S.R. Elliott, Phys. Rev. Lett. **85**, 3305 (2000).

[45] A. Schulte, M. Marchivie, K. Zollinger, C. Rivero, A. Graham, C. Lopez, K.A. Richardson, K. Turcotte, and A. Villeneuve, Proc. of the XVIIth International Conference on Raman Spectrosc., (ICORS) **17**, 616 (2000).

[46] H.B. Sun, Y, Xu, S. Joudkazis, K. Sun, M. Watanabe, S. Matsuo, H. Misawa, and J. Nishii, Opt. Lett. **26**, 325 (2001).

[47] K. Hirao and K. Miura, J. Non-Cryst. Solids **239**, 91 (1998).

[48] K. Minoshima, A.M. Kowalevicz, I. Hartl, E.P. Ippen, and J.G. Fujimoto, Opt. Lett. **26**, 1516 (2001).

[49] F. Korte, S. Adams, A. Egbert, C. Fallnich, A. Ostendorf, S. Nolte, M. Will, J.P. Ruske, B.N. Chichkov, and A. Tunnermann, Opt. Express **7**, 1545 (2000).

[50] E. Matthias, M. Reichling, J. Siegel, O.W. Kading, S. Petzoldt, H. Skurk, P. Bizenberger, and E. Neske, Appl. Phys. A (Solids and Surfaces) **A58**, 129 (1994).

[51] N. Bloembergen, IEEE J. Quantum Electron. **QE-10**, 375 (1974).

[52] Schott Glass Technologies Inc., Optical Glass Catalog, 400 York Avenue, Duryea, PA 18642.

[53] L. Shah, PhD Thesis, School of Optics, University of Central Florida (2001).

[54] A. Braun, G. Korn, X. Liu, D. Du, J. Squier, and G. Mourou, Opt. Lett. **20**, 73 (1995).

[55] C.B. Schaffer, A. Brodeur, J.F. Garcia, and E. Mazur, Opt. Lett. **26**, 93 (2001).

[56] A.M. Streltsov and N.F. Borrelli, Opt. Lett. **26**, 42 (2001).

[57] L. Shah, J. Tawney, M. Richardson, and K. Richardson, Appl. Surf. Sci. **183**, 151 (2001).

[58] A. Zoubir, L. Shah, K. Richardson, and M. Richardson, Proc. SPIE, **4760-5**, 2 High Power Laser Ablation in Materials, Taos NM (2002).

[59] K.A. Richardson, A. Zoubir, C. Rivero, C. Lopez, L. Shah, and M.C. Richardson, Proc. of the XIIIth International Symposium on Non-Oxide Glasses, Parubice, Czech Republic (2002).

[60] C. Meneghini and A. Villeneuve, J. Opt. Soc. Am. B **15**, 2946 (1998).

[61] G. Chen, H. Jain, M. Vlcek, S. Khalid, J. Li, D.A. Drabold, and S.R Elliott, Appl. Phys. Lett. **82**, 706 (2003).

[62] A. Saliminia, T. Galstian, and A. Villeneuve, Phys. Rev. Lett. **85**, 4112 (2000).

[63] TA Instruments, Micro-thermal Analysis (μTA-2990) System, Delaware, 2000.

[64] A. Zoubir, M.C. Richardson, C. Rivero, C. Lopez, N. Hô., N., R. Vallée, and K.A. Richardson, Proc. Conference on Lasers and Electro-Optics, paper #CMZ4, Long Beach CA (2001).

[65] A. Saliminia, T.V. Galstian, A. Villeneuve, K. LeFoulgoc, and K.A. Richardson, J. Opt. Soc. B **17**, 1343 (2000).

[66] A. Schulte and K.A. Richardson, "Near-Infrared Raman Spectroscopy of Chalcogenide Glasses for Integrated Optics," in Recent Research Developments in Non-Crystalline Solids, Transworld Research Network, P.O. 36/248 (1) Vallakkadavu, Trivandrum - 695 008, Kerala, India (2001).

[67] C. Lopez, K. Richardson, M. Balu, D. Hagan, A. Zoubir, M.C. Richardson, J. Laniel, J.M. Menard, A.Villeneuve, and R.Vallée, OSA Annual Meeting, Orlando FL (2002).

Index